Doctoral Dissertation
Doctoral Program in Electrical, Electronics and Communications Engineering
(31th Cycle)

High Performance Control Techniques for Multiphase eDrives

Sandro Rubino
* * * * * *

Supervisor
Prof. Radu Iustin Bojoi

Politecnico di Torino
March 3, 2019

I hereby declare that, the contents and organisation of this dissertation constitute my own original work and does not compromise in any way the rights of third parties, including those relating to the security of personal data.

…….....

Sandro Rubino

Turin, March 3, 2019

Summary

The recent energy-policies are leading to a relevant reduction in the use of fossil fuels for both energy production and transports sectors. As a consequence, an impressive electrification process involving many production sectors has recently been started. Nevertheless, this important technology step is requiring robust and reliable solutions able to replace the existing ones. Nowadays, thanks to recent advancements of the power electronics, many electrical solutions able to help towards a more sustainable future have been developed. The dissertation research activity is focused on one of these. In detail, the analysis and control of multiphase electrical machines.

Currently, the multiphase solutions are largely employed in high-power and/or safety-critical applications such as the shipboard applications. Indeed, the distribution of the electric power on more phases allows at keeping the current and/or the voltage levels to acceptable limits that can be handled with the commercial fast power electronics components. Concerning the system reliability, this is significantly improved as the higher number of phases leads to the redundancy from both power converter and electrical machine points of view. For these reasons, in the current scenario where the transports electrification is playing a leading role, the multiphase solutions are gaining a growing attention by the industrial producers. Nevertheless, there is a strong interest in the development of modular multiphase configurations able to use the well-consolidated three-phase technologies, thus reducing costs and design times. This kind of systems are usually called as “multiple three-phase machines/drives” and they represents the research context of this dissertation.

The multiple three-phase drive topologies allows at implementing the concept of modularity in terms of electrical machine winding and power converter structure. Indeed, the machine’s stator consists of multiple three-phase winding sets with isolated neutral points. An independent three-phase power converter unit supplies each three-phase set.

In this way, the drive is configured as multiple three-phase units operating in parallel. Despite the large spreads of these multiphase drive topologies, few control solutions able to deal with a direct control of the main variables (current, flux, torque) belonging to each three-phase winding set have been developed, to exploit all the degrees of freedom offered by the multiple three-phase drives. For this reason, the main goal of this dissertation is to extend the modularity of the multiple three-phase structures also in terms of drive control scheme, thus without limiting itself to the machine configuration and power converter structure.

In detail, this dissertation deals with the design and implementation of a Direct Flux Vector Control (DFVC) scheme for multiple three-phase Induction Motor (IM) drives. The proposed control solution performs a direct and independent regulation of both stator flux amplitude and torque contribution belonging to each three-phase winding set, thus defining an equivalent modular Direct Torque Control (DTC) scheme for this kind of machines. The control scheme is designed to be fully compatible with the multiple three-phase drive topologies, using modular Voltage Supply Inverter (VSI) structures together with independent Pulse Width Modulation (PWM) voltage control of each three-phase power converter unit.

The performance of the control has been validated by means of experimental tests carried out with a multi-modular power converter feeding a quadruple three-phase induction machine prototype. The experimental results demonstrate the effectiveness and feasibility of the proposed control scheme, in terms of full drive controllability in all operating condition. Additional studies on the design and implementation of modular control schemes for multiple three-phase synchronous motor drives are on-going.

Contents

List of Figures

Fig. 4. 10. View of the digital controller DS1103 PPC Controller Board (left) and the power converter FPGA motherboard (right).
Fig. 4. 11. Schematic block diagram of the test rig for the experimental validation of the DFVC scheme using PI controllers.
Fig. 4. 12. Schematic block diagram of the test rig for the experimental validation of the DFVC scheme using DB controllers.
Fig. 4. 13. Drive scheme using a single outer controller.
Fig. 4. 14. From top to bottom: measured speed (10^3 · r/min); reference and observed machine torque (Nm); estimated mechanical power (kW).
Fig. 4. 15. From top to bottom: single units observed torque (Nm); single units observed flux amplitude (mVs); single units measured d_{sk}-axis current (A); single units measured q_{sk}-axis current (A); single units observed load-angle (deg).
Fig. 4. 16. For each k-unit DFVC scheme, from top to bottom: reference and observed torque (Nm); reference and observed flux amplitude (mVs); measured d_{sk}-axis current (A); reference and measured q_{sk}-axis current (A); observed load-angle (deg).
Fig. 4. 17. From top to bottom: measured speed (10^3 · r/min); reference and observed machine torque (Nm); estimated mechanical power (kW).
Fig. 4. 18. From top to bottom: single units observed torque (Nm); single units observed flux amplitude (mVs); single units measured d_{sk}-axis current (A); single units measured q_{sk}-axis current (A); single units observed load-angle (deg).
Fig. 4. 19. For each k-unit DFVC scheme, from top to bottom: reference and observed torque (Nm); reference and observed flux amplitude (mVs); measured d_{sk}-axis current (A); reference and measured q_{sk}-axis current (A); observed load-angle (deg).
Fig. 4. 20. Fast torque transient from no-load up to 150% rated torque (24 Nm) at -6000 r/min. Ch1: $i_{s1\text{-}a}$ (10 A/div), Ch2: $i_{s2\text{-}a}$ (10 A/div), Ch3: $i_{s3\text{-}a}$ (10 A/div), Ch4: $i_{s4\text{-}a}$ (10 A/div). Time resolution: 5 ms/div.
Fig. 4. 21. From top to bottom: measured speed (10^3 · r/min); reference and observed machine torque (Nm); estimated mechanical power (kW).
Fig. 4. 22. From top to bottom: single units observed torque (Nm); single units observed flux amplitude (mVs); single units measured d_{sk}-axis current (A); single units measured q_{sk}-axis current (A); single units observed load-angle (deg).
Fig. 4. 23. For each k-unit DFVC scheme, from top to bottom: reference and observed torque (Nm); reference and observed flux amplitude (mVs); measured d_{sk}-axis current (A); reference and measured q_{sk}-axis current (A); observed load-angle (deg).

Fig. 4. 24. Ch1: $i_{s1\text{-}a}$ (10 A/div), Ch2: $i_{s2\text{-}a}$ (10 A/div), Ch3: $i_{s3\text{-}a}$ (10 A/div), Ch4: $i_{s4\text{-}a}$ (10 A/div).

Fig. 4. 25. From top to bottom: measured speed (10^3 · r/min); reference and observed machine torque (Nm); estimated mechanical power (kW).

Fig. 4. 26. From top to bottom: single units observed torque (Nm); single units observed flux amplitude (mVs); single units measured d_{sk}-axis current (A); single units measured q_{sk}-axis current (A); single units observed load-angle (deg).

Fig. 4. 27. For each k-unit DFVC scheme, from top to bottom: reference and observed torque (Nm); reference and observed flux amplitude (mVs); measured d_{sk}-axis current (A); reference and measured q_{sk}-axis current (A); observed load-angle (deg).

Fig. 4. 28. Ch1: $i_{s1\text{-}a}$ (10 A/div), Ch2: $i_{s2\text{-}a}$ (10 A/div), Ch3: $i_{s3\text{-}a}$ (10 A/div), Ch4: $i_{s4\text{-}a}$ (10 A/div).

Fig. 4. 29. From top to bottom: measured speed (10^3 · r/min); reference and observed machine torque (Nm); estimated mechanical power (kW).

Fig. 4. 30. From top to bottom: single units observed torque (Nm); single units observed flux amplitude (mVs); single units measured d_{sk}-axis current (A); single units measured q_{sk}-axis current (A); single units observed load-angle (deg).

Fig. 4. 31. For each k-unit DFVC scheme, from top to bottom: reference and observed torque (Nm); reference and observed flux amplitude (mVs); measured d_{sk}-axis current (A); reference and measured q_{sk}-axis current (A); observed load-angle (deg).

Fig. 4. 32. Ch1: $i_{s1\text{-}a}$ (10 A/div), Ch2: $i_{s2\text{-}a}$ (10 A/div), Ch3: $i_{s3\text{-}a}$ (10 A/div), Ch4: $i_{s4\text{-}a}$ (10 A/div).

Fig. 4. 33. From top to bottom: measured speed (10^3 · r/min); reference and observed machine torque (Nm); estimated mechanical power (kW).

Fig. 4. 34. From top to bottom: single units observed torque (Nm); single units observed flux amplitude (mVs); single units measured d_{sk}-axis current (A); single units measured q_{sk}-axis current (A); single units observed load-angle (deg).

Fig. 4. 35. For each k-unit DFVC scheme, from top to bottom: reference and observed torque (Nm); reference and observed flux amplitude (mVs); measured d_{sk}-axis current (A); reference and measured q_{sk}-axis current (A); observed load-angle (deg).

Fig. 4. 36. Ch1: $i_{s1\text{-}a}$ (10 A/div), Ch2: $i_{s2\text{-}a}$ (10 A/div), Ch3: $i_{s3\text{-}a}$ (10 A/div), Ch4: $i_{s4\text{-}a}$ (10 A/div).

Fig. 4. 37. Machine phase-currents for 200% of the rated torque (32 Nm) in generation at -3500 r/min using the optimal stator flux amplitude reference. Ch1:

$i_{s1\text{-}a}$ (7.5 A/div), Ch2: $i_{s2\text{-}a}$ (7.5 A/div), Ch3: $i_{s3\text{-}a}$ (7.5 A/div), Ch4: $i_{s4\text{-}a}$ (7.5 A/div). Time resolution: 10ms/div.

Fig. 4. 38. From top to bottom: measured speed (10^3 · r/min); reference and observed machine torque (Nm); estimated mechanical power (kW).

Fig. 4. 39. From top to bottom: single units observed torque (Nm); single units observed flux amplitude (mVs); single units measured d_{sk}-axis current (A); single units measured q_{sk}-axis current (A); single units observed load-angle (deg).

Fig. 4. 40. For each k-unit DFVC scheme, from top to bottom: reference and observed torque (Nm); reference and observed flux amplitude (mVs); measured d_{sk}-axis current (A); reference, measured and maximum limit q_{sk}-axis current (A); observed load-angle (deg).

Fig. 4. 41. From top to bottom: measured speed (10^3 · r/min); reference and observed machine torque (Nm); estimated mechanical power (kW).

Fig. 4. 42. From top to bottom: single units observed torque (Nm); single units observed flux amplitude (mVs); single units measured d_{sk}-axis current (A); single units measured q_{sk}-axis current (A); single units observed load-angle (deg).

Fig. 4. 43. For each k-unit DFVC scheme, from top to bottom: reference and observed torque (Nm); reference and observed flux amplitude (mVs); measured d_{sk}-axis current (A); reference and measured q_{sk}-axis current (A); observed load-angle (deg).

Fig. 4. 44. Ch1: $i_{s1\text{-}a}$ (7.5 A/div), Ch2: $i_{s2\text{-}a}$ (7.5 A/div), Ch3: $i_{s3\text{-}a}$ (7.5 A/div), Ch4: $i_{s4\text{-}a}$ (7.5 A/div).

Fig. 4. 45. Ch1: $i_{s1\text{-}a}$ (7.5 A/div), Ch2: $i_{s2\text{-}a}$ (7.5 A/div), Ch3: $i_{s3\text{-}a}$ (7.5 A/div), Ch4: $i_{s4\text{-}a}$ (7.5 A/div).

Fig. 4. 46. From top to bottom: measured speed (10^3 · r/min); reference and observed machine torque (Nm); estimated mechanical power (kW).

Fig. 4. 47. From top to bottom: single units observed torque (Nm); single units observed flux amplitude (mVs); single units measured d_{sk}-axis current (A); single units measured q_{sk}-axis current (A); single units observed load-angle (deg).

Fig. 4. 48. For each k-unit DFVC scheme, from top to bottom: reference and observed torque (Nm); reference and observed flux amplitude (mVs); measured d_{sk}-axis current (A); reference and measured q_{sk}-axis current (A); observed load-angle (deg).

Fig. 4. 49. Ch1: $i_{s1\text{-}a}$ (7.5 A/div), Ch2: $i_{s2\text{-}a}$ (7.5 A/div), Ch3: $i_{s3\text{-}a}$ (7.5 A/div), Ch4: $i_{s4\text{-}a}$ (7.5 A/div).

Fig. 4. 50. From top to bottom: measured speed (10^3 · r/min); reference and observed machine torque (Nm); estimated mechanical power (kW).

Fig. 4. 51. From top to bottom: single units observed torque (Nm); single units observed flux amplitude (mVs); single units measured d_{sk}-axis current (A); single units measured q_{sk}-axis current (A); single units observed load-angle (deg).

Fig. 4. 52. For each k-unit DFVC scheme, from top to bottom: reference and observed torque (Nm); reference and observed flux amplitude (mVs); measured d_{sk}-axis current (A); reference, measured and maximum limit q_{sk}-axis current (A); observed load-angle (deg).

Fig. 4. 53. From top to bottom: measured speed (10^3 · r/min); reference and observed machine torque (Nm); estimated mechanical power (kW).

Fig. 4. 54. From top to bottom: single units observed torque (Nm); single units observed flux amplitude (mVs); single units measured d_{sk}-axis current (A); single units measured q_{sk}-axis current (A); single units observed load-angle (deg).

Fig. 4. 55. For each k-unit DFVC scheme, from top to bottom: reference and observed torque (Nm); reference and observed flux amplitude (mVs); measured d_{sk}-axis current (A); reference, measured and maximum limit q_{sk}-axis current (A); observed and maximum limit load-angle (deg).

Fig. 4. 56. Ch1: $i_{s1\text{-}a}$ (7.5 A/div), Ch2: $i_{s2\text{-}a}$ (7.5 A/div), Ch3: $i_{s3\text{-}a}$ (7.5 A/div), Ch4: $i_{s4\text{-}a}$ (7.5 A/div).

Fig. 4. 57. Ch1: $i_{s1\text{-}a}$ (7.5 A/div), Ch2: $i_{s2\text{-}a}$ (7.5 A/div), Ch3: $i_{s3\text{-}a}$ (7.5 A/div), Ch4: $i_{s4\text{-}a}$ (7.5 A/div).

Fig. 4. 58. From top to bottom: measured speed (10^3 · r/min); reference and observed machine torque (Nm); estimated mechanical power (kW).

Fig. 4. 59. From top to bottom: single units observed torque (Nm); single units observed flux amplitude (mVs); single units measured d_{sk}-axis current (A); single units measured q_{sk}-axis current (A); single units observed load-angle (deg).

Fig. 4. 60. For each k-unit DFVC scheme, from top to bottom: reference and observed torque (Nm); reference and observed flux amplitude (mVs); measured d_{sk}-axis current (A); reference, measured and maximum limit q_{sk}-axis current (A); observed and maximum limit load-angle (deg).

Fig. 4. 61. From top to bottom: measured speed (10^3 · r/min); reference and observed machine torque (Nm); estimated mechanical power (kW).

Fig. 4. 62. From top to bottom: single units observed torque (Nm); single units observed flux amplitude (mVs); single units measured d_{sk}-axis current (A); single units measured q_{sk}-axis current (A); single units observed load-angle (deg).

Fig. 4. 63. For each k-unit DFVC scheme, from top to bottom: reference and observed torque (Nm); reference and observed flux amplitude (mVs); measured d_{sk}-axis current (A); reference, measured and maximum limit q_{sk}-axis current (A); observed and maximum limit load-angle (deg).

Fig. 4. 64. Single units flux amplitude and rotor flux amplitude (mVs).
Fig. 4. 65. From top to bottom: measured speed ($10^3 \cdot$ r/min); reference, observed and predicted machine torque (Nm); estimated mechanical power (kW).
Fig. 4. 66. From top to bottom: single units observed and predicted torque (Nm); single units observed and predicted flux amplitude (mVs); single units measured and predicted d_{sk}-axis current (A); single units measured and predicted q_{sk}-axis current (A); single units observed and predicted load-angle (deg).
Fig. 4. 67. For each k-unit DFVC scheme, from top to bottom: reference, observed and predicted torque (Nm); reference, observed and predicted flux amplitude (mVs); measured and predicted d_{sk}-axis current (A); reference, measured and predicted q_{sk}-axis current (A); observed and predicted load-angle (deg).
Fig. 4. 68. For each k-unit model predictive estimator (MPE), from top to bottom: reference, observed and predicted torque (Nm); (α,β) observed and predicted fluxes (mVs); (α,β) measured and predicted currents (A).
Fig. 4. 69. From top to bottom: measured speed ($10^3 \cdot$ r/min); reference, observed and predicted machine torque (Nm); estimated mechanical power (kW).
Fig. 4. 70. From top to bottom: single units observed and predicted torque (Nm); single units observed and predicted flux amplitude (mVs); single units measured and predicted d_{sk}-axis current (A); single units measured and predicted q_{sk}-axis current (A); single units observed and predicted load-angle (deg).
Fig. 4. 71. For each k-unit DFVC scheme, from top to bottom: reference, observed and predicted torque (Nm); reference, observed and predicted flux amplitude (mVs); measured and predicted d_{sk}-axis current (A); reference, measured and predicted q_{sk}-axis current (A); observed and predicted load-angle (deg).
Fig. 4. 72. For each k-unit model predictive estimator (MPE), from top to bottom: reference, observed and predicted torque (Nm); (α,β) observed and predicted fluxes (mVs); (α,β) measured and predicted currents (A).
Fig. 4. 73. Ch1: $i_{s1\text{-}a}$ (10 A/div), Ch2: $i_{s2\text{-}a}$ (10 A/div). Time resolution: 5 ms/div.
Fig. 4. 74. From top to bottom: measured speed ($10^3 \cdot$ r/min); reference, observed and predicted machine torque (Nm); estimated mechanical power (kW).
Fig. 4. 75. From top to bottom: single units observed and predicted torque (Nm); single units observed and predicted flux amplitude (mVs); single units measured and predicted d_{sk}-axis current (A); single units measured and predicted q_{sk}-axis current (A); single units observed and predicted load-angle (deg).
Fig. 4. 76. For each k-unit DFVC scheme, from top to bottom: reference, observed and predicted torque (Nm); reference, observed and predicted flux amplitude (mVs); measured and predicted d_{sk}-axis current (A); reference, measured and predicted q_{sk}-axis current (A); observed and predicted load-angle (deg).

Fig. 4. 77. For each *k*-unit model predictive estimator (MPE), from top to bottom: reference, observed and predicted torque (Nm); (α,β) observed and predicted fluxes (mVs); (α,β) measured and predicted currents (A).
Fig. 4. 78. Ch1: $i_{s1\text{-}a}$ (10 A/div), Ch2: $i_{s2\text{-}a}$ (10 A/div). Time resolution: 5 ms/div.
Fig. 4. 79. From top to bottom: measured speed (10^3 · r/min); reference, observed and predicted machine torque (Nm); estimated mechanical power (kW).
Fig. 4. 80. From top to bottom: single units observed and predicted torque (Nm); single units observed and predicted flux amplitude (mVs); single units measured and predicted d_{sk}-axis current (A); single units measured and predicted q_{sk}-axis current (A); single units observed and predicted load-angle (deg).
Fig. 4. 81. For each *k*-unit DFVC scheme, from top to bottom: reference, observed and predicted torque (Nm); reference, observed and predicted flux amplitude (mVs); measured and predicted d_{sk}-axis current (A); reference, measured and predicted q_{sk}-axis current (A); observed and predicted load-angle (deg).
Fig. 4. 82. For each *k*-unit model predictive estimator (MPE), from top to bottom: reference, observed and predicted torque (Nm); (α,β) observed and predicted fluxes (mVs); (α,β) measured and predicted currents (A).
Fig. 4. 83. Ch1: $i_{s1\text{-}a}$ (10 A/div), Ch2: $i_{s2\text{-}a}$ (10 A/div). Time resolution: 5 ms/div.
Fig. 4. 84. From top to bottom: measured speed (10^3 · r/min); reference, observed and predicted machine torque (Nm); estimated mechanical power (kW).
Fig. 4. 85. From top to bottom: single units observed and predicted torque (Nm); single units observed and predicted flux amplitude (mVs); single units measured and predicted d_{sk}-axis current (A); single units measured and predicted q_{sk}-axis current (A); single units observed and predicted load-angle (deg).
Fig. 4. 86. For each *k*-unit DFVC scheme, from top to bottom: reference, observed and predicted torque (Nm); reference, observed and predicted flux amplitude (mVs); measured and predicted d_{sk}-axis current (A); reference, measured, predicted and maximum limit q_{sk}-axis current (A); observed, predicted and maximum limit load-angle (deg).
Fig. 4. 87. Single units flux amplitude and rotor flux amplitude (mVs).

List of Tables

Chapter 1

INTRODUCTION

Table of Contents

List of Figures

List of Tables

In the recent years, due to the worrying evolution of the climatic changes, we are witnessing a massive redefinition of the technological development plans. As main consequence, the current and future energy-policies will impose a relevant reduction in the use of fossil fuels for both energy production and transports sectors [1]. Nowadays, the renewable energy sources together with the energy-saving policies represent the most promising solutions for achieving the environment sustainability targets.

In this context, both wind and photovoltaic energy productions are undergoing an impressive technological development in order to improve their production capability together with the energy efficiency. However, in parallel with the advancements in the energy production also the transport sector is experiencing relevant changes. Indeed, following the future European directives [2], [3] concerning the reduction of both global and local emissions, the main automotive companies are moving towards the electrification of the vehicles. In addition, interesting innovations are emerging in both aircraft and aerospace sectors with the current paradigms of More Electric Aircraft (MEA) and More Electric Engine (MEE) [4], [5].

The above examples make the idea how the next future will be focused on a heavy electrification process that will involve many production areas. However, this important technological step will require smart and reliable solutions able to replace the existing conventional ones. A key factor is certainly represented by the recent advancements of the power electronics which is experiencing a real revolution not only in terms of achieved quality levels, but also a significant reduction of the production costs. Thanks to significant efforts in both academic and industrial research activities, many electrical solutions for a more sustainable future have been developed. The thesis focuses on the multiphase electrical solutions, with emphasis on the modelling and control.

The main advantages of multiphase drives is to reduce the current per phase without increasing the phase voltage [6]. Starting from the 1990s, multiphase drives have become a competitive solution in marine applications for both ship propulsion and power generation and still to date they represent a standard in the sector.

However, the interest in the use of multiphase electrical solutions has started seriously to grow with the development of the power electronics since it has been possible to take great advantages from the use of such systems. The first one is surely related to the distribution of the electric power on more phases which allows at keeping the current and/or the voltage levels to acceptable limits that can be handled with commercial fast power electronics components. This feature results particularly convenient in high power systems since it is possible to obtain high dynamic performance which are difficult to reach with the conventional thyristor technology. Another important advantage on the use of multiphase drives is their intrinsic fault tolerance behaviour. Indeed, thanks to the higher number of phases, it is possible to improve the system reliability by means of the redundancy from both power converter and electrical machine points of view. This factor has made

the multiphase electrical systems particularly attractive for safety-critical applications such as the shipboard applications mentioned above.

Despite these important advantages, the use of multiphase drives is quite limited to the high power and safety-critical applications. The main reason can be found in the historical evolution of the three-phase drives which have reached the full consolidation only in the last years. Indeed, only in recent times it has been possible to find a complete know-how in power electronics, electrical machines design, electric drives control strategies together with a wide availability of cheap and powerful platforms for the implementation of advanced controls. Moreover, the spread of multiphase solutions in the industry has been strongly hindered due the lack of a complete technical literature able to overcome the complexity of the topic in straightforward way. However, thanks to the impressive efforts made by several research activities [7]–[10], this issue can be nowadays considered solved.

Currently, the multiphase electrical solutions have gained the required maturity level such to represent a competitive alternative to the conventional three-phase drives [7]. Indeed, in the current scenario where the transportation electrification process will play a leading role, the multiphase solutions are gaining a growing attention by many industrial producers. In detail, there is a strong interest in the development of modular multiphase structures able to use the well-consolidated three-phase technology so reducing costs and design times [5]. This kind of systems are usually called as “multiple three-phase machines/drives” and their features will be fully described in the next paragraphs.

Therefore, the dissertation deals with the analysis, design and implementation of high-performance control techniques for multiphase electrical drives using multiple three-phase configurations.

1.1 Review of previous research

The first research activities on multiphase electrical systems date back more than a century ago with the development of the symmetrical coordinates applied to polyphase networks [11]. Nevertheless, the most relevant contributions about the multiphase solutions have been published over the past 30 years by covering a wide range of topics. In the technical literature, there are many paper surveys providing the state of the art in this field of the research [7]–[10]. Starting from the first attempts to provide a technology status review [7], [8], [12] until to the recent surveys on the latest advancements [9], [10], [13], the research on the multiphase electrical solutions includes the following chapters:

1) Applications
2) Machine configurations and modelling
3) Machine design
4) Power converters and modulation techniques
5) Drive topology
6) Drive control techniques
7) Fault analysis and post-fault control strategies

After an overview on the applications of the multiphase drives, a brief review of the state of the art in each above research topic will be provided in the next subsections.

1.1.1 Applications

According with the introduction, the multiphase drives result a convenient solution for both high-power (MW levels) and for low voltage/high currents applications due the distribution of the total electric power in a higher number of phases with respect to the three-phase counterparts. Furthermore, thanks to their intrinsic fault-tolerant behaviour, the multiphase systems are widely used in safety-critical applications like the naval ones [7], [13]. However, there are many recent examples on the use of multiphase drives in both transports and energy production sectors [13].

Naval

In the marine applications, it is possible to find many examples of multiphase solutions used for both ship propulsion [14]–[22] and shipboard generation [23], [24]. As example, the world's first electric warship UK "Daring class" Type-45 Destroyer is equipped with two 20 MW/15-phase induction motors fed by pulse width modulation (PWM) insulated gate bipolar transistor (IGBT) inverters [25]. Other solutions for ship propulsion are based on 9-phase [19] and 12-phase machines [18], [20].

Aircraft

Interesting application examples of multiphase solutions can be found in the aircraft industry [26], [27] due the current paradigms of More Electric Aircraft (MEA) and More Electric Engine (MEE) [4], [5]. Some low-power solutions for electric actuators use 6-phase [28]–[30] or 4-phase motor drives [5], [31]. However, there are several research projects on the use of multiphase drives as starter/alternator for the on-board electrical generation [32], [33]. Moreover, there are outstanding attempts in the use of multiphase drives for powering electric aircraft [34]. Recently, a 260 kW/6-phase permanent magnet motor with one of the highest power-over-weight ratios of the history (5 kW/kg) has been designed by Siemens AG. The final aim of this research project will be the hybridization of the regional airliners to reduce their fuel consumption [34].

Automotive

The penetration of multiphase drives is rather low in automotive applications due the low value of the power levels (hundreds of kW) such to justify the use of conventional three-phase solutions. However, there are some attempts into using multiphase solutions for low voltage systems fed at 48 Vdc in order to keep the currents levels to reasonable limits [35]. Relevant examples of multiphase solutions currently in production consist of a 5-phase starter/alternator and a 5-phase generator belonging to Robert Bosch Gmbh [36], both with integrated power electronics.

Wind Energy

In parallel with the transportation electrification, the multiphase solutions are gaining a growing attention also in the energy production, especially in the high-power wind generation (MW levels) [37]–[39]. Indeed, by removing the gearbox between the propeller and the electric generator it is possible increase the overall efficiency. In addition, the complexity of the system is further reduced. Nevertheless, this solution requires a direct drive generator characterized by high values of torque and currents together with a challenging design of the power converter interfaced to the electric grid. To overcome this issue, a commercial series of 5 MW wind turbines based on 12-phase permanent magnet generators has been recently launched by Siemens Gamesa [40].

Lifting Systems

Finally, it is worth noting the use of multiphase solutions by the Hyundai Group to produce the ultra-high-speed elevators (until 18 m/s with 30 persons). Indeed, in this specific application a 1.1 MW/9-phase permanent magnet machine is employed [41], [42].

The above cited examples represent the proof how the multiphase drives may represent the next evolution of the electrification, especially for all those applications characterized by considerable values of power and most of all without a challenging design of the power converters in terms of voltage and current levels.

1.1.2 Machine configurations and modelling

The machine configuration has a large influence on defining the drive's structure and related control scheme. With reference to the technical literature [8], [13], the multiphase electrical machines are usually designed to obtain symmetrical or asymmetrical configurations of the stator winding.

Symmetrical configuration

A symmetrical multiphase configuration is characterized by an uniform spatial displacement between the magnetic axes belonging to two consecutive stator phases. For a three-phase machine, this angle is the well-known 120 electrical degrees, while in a generic multiphase machine it depends by the total number of phases. As example, a symmetrical 5-phase machine has a spatial displacement of 72 electric degrees between the magnetic axes belonging to two consecutive stator phases, as shown in Fig. 1. 1.

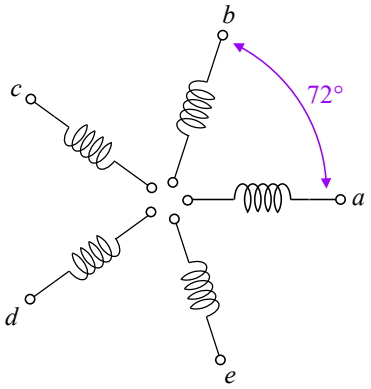

Fig. 1. 1. Symmetrical 5-phase machine configuration.

Asymmetrical configuration

When the number of phases is even or an odd number that is not prime, the machine can be configured as n sets having l phases each [13]. In this case, if the spatial displacement between the magnetic axes of the first phases belonging to two consecutive sets is $180/(l \cdot n)$, then a machine with asymmetrical configuration is obtained.

As example, an asymmetrical 12-phase machine has a spatial displacement of 15 electric degrees between the magnetic axes of the first phases belonging to two consecutive sets, as shown in Fig. 1. 2. For this specific case, the number of sets n can be either 4 or 2 depending on if 3-phase ($l = 3$) or 6-phase ($l = 6$) units are considered. In the first case, the machine is usually called as "quadruple three-phase machine" while in the second one as "dual six-phase machine". Typically, three-phase units are employed ($l = 3$) and this dissertation will be focused on this case because of the large interest shown by the industry.

The main reason on the use of the two above configurations is strictly related to the issues on the electromechanical machine modelling. In detail, the definition of the reference transformations which are fundamental for the implementation of high-performance drive strategies. In the three-phase systems the problem has been rapidly solved thanks to both Clarke [43] and Park transformations [44], [45].

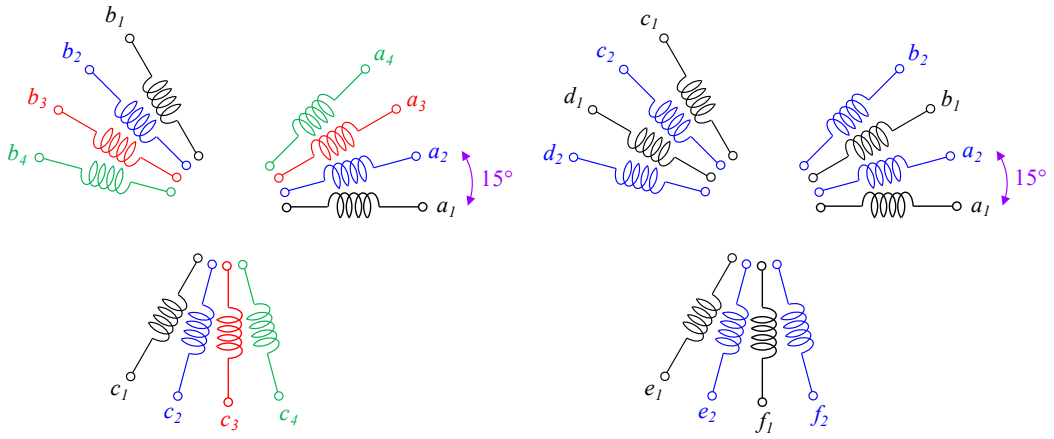

Fig. 1. 2. Asymmetrical 12-phase machine configurations: quadruple three-phase (left) and dual six-phase (right).

Nevertheless, these ones represent just a specific case of application of the symmetrical coordinates' theory [11]. An outstanding attempt in the use of that theory for obtaining a reference transformation able to handle any symmetrical multiphase machine was done by [46]. Nevertheless, this approach was not able to deal with the asymmetrical configurations which gained a lot of attention before the development of power converters with PWM modulation. As example, the asymmetrical 6-phase machine in dual three-phase configuration resulted as the most considered multiphase solution in high power applications. The main reason was related to the absence of the sixth harmonic in the torque ripple caused by the fifth and seventh harmonics of the stator currents [8].

Historically, to face with the asymmetrical configurations, the multiphase machines modelling has been developed following two different approaches, both with the goal to deal with all possible cases, as will be described below.

Vector Space Decomposition (VSD) approach

The first modelling approach is called Vector Space Decomposition (VSD) and it extends the results obtained with the symmetrical configurations [46] to the asymmetrical ones. Developed for the first time in [47], this approach decomposes the machine original space into multiple orthogonal subspaces. The reference transformation is performed by means of a matrix having a dimension equal to the total number of phases and it is computed through a simple algorithm based on the harmonic decoupling. For symmetrical multiphase configurations, the obtained transformation matrix is the same of the one computed by means the symmetric coordinates' theory [11], [46]. A detailed procedure to compute the VSD transformation matrix for any asymmetrical multiphase configurations has been recently published in [48].

The main advantage of the VSD approach consists of the simplicity of the results. Indeed, among the VSD subspaces, only one is responsible for the electromechanical energy conversion and in addition with similar equations to the ones of the three-phase machines [8], [47].

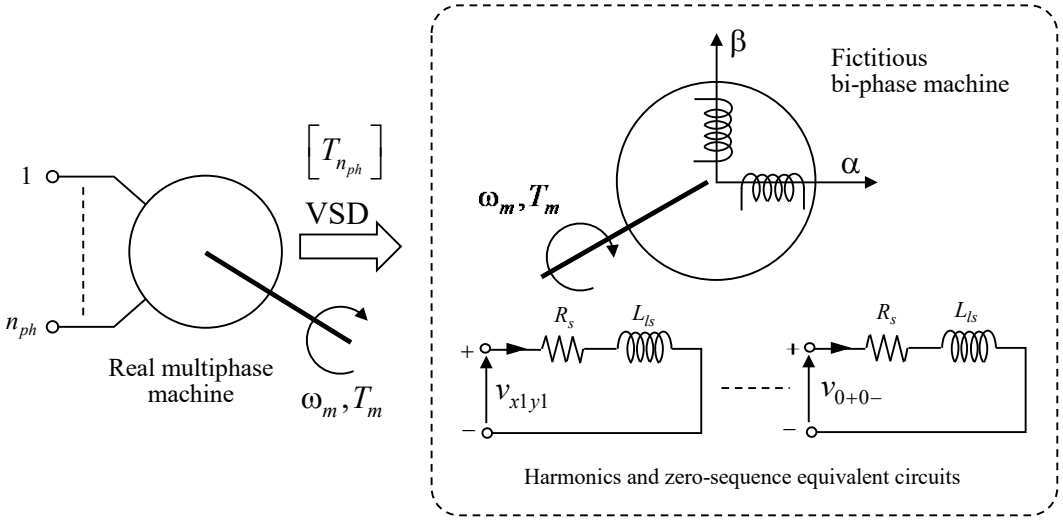

Fig. 1. 3. Meaning of the VSD approach based on the generalized reference transformation using the VSD transformation matrix.

Concerning the other subspaces, they are just representative of the additional degrees of freedom of the machine but without any role in the torque production as they have the meaning of harmonic and homopolar patterns, as shown in Fig. 1. 3. Currently, the VSD results the most employed modelling approach and a deeper analysis will be reported next.

Multi-Stator (MS) approach

The main alternative to the VSD modelling is represented by the Multi-Stator approach (MS). Developed for the first time in [49] for a 6-phase asymmetrical induction machine, this approach is convenient when the machine is configured as multiple *l*-phases sets. The main advantage of the MS approach is the high degree of modularity which allows the clear separation of the flux and torque contributions belonging to each set. In addition, the number of *l*-phases belonging to each set can be arbitrary since the MS approach uses a dedicated reference transformation for each of these sets. In this way, each set can be independently treated by the other ones. As example, if the machine is configured in multiple three-phase sets ($l = 3$), then the MS approach will apply a dedicated Clarke's transformation for each of them [13], as shown in Fig. 1. 4.

Therefore, it is possible to understand how the MS approach can deal with any modular multiphase configuration. Conversely, the validity of the VSD approach is limited to the symmetrical and asymmetrical multiphase configurations. The only limit on the use of the MS approach is related to the existence of the specific reference transformation used to deal with the single set. As example, if a 12-phase machine in double six-phase configuration is considered, then the MS approach will apply two specific six-phase reference transformation matrices. Nevertheless, each of them can be only computed by using the VSD algorithm. According with the limits of this one, only if each six-phase set is characterized by a symmetrical or asymmetrical configuration, then the MS approach can be applied. Otherwise, the transformation matrix of the single set cannot be defined and consequently also the

MS approach will be unable to deal with that machine configuration. This is the only case where the MS approach has the same limits of the VSD one.

In terms of obtained electromechanical model, the MS approach leads to a more complicated equation system with respect to one computed with the VSD modelling. Indeed, to highlight the torque contribution of each single set, the electromagnetic model of the machine is characterized by strong magnetic couplings between the units [13], [50]. This is the main consequence to the full use of the all degrees of freedom offered by the machine compared to the VSD approach where the electromechanical energy conversion is modelled in average way through the main subspace only. Recently, the MS approach is gaining a growing attention by the industry due the relevant implications on the drive control schemes [13]. With the aim at proposing high-performance control techniques for modular multiphase motor drives, the control schemes developed in this dissertation are MS-based.

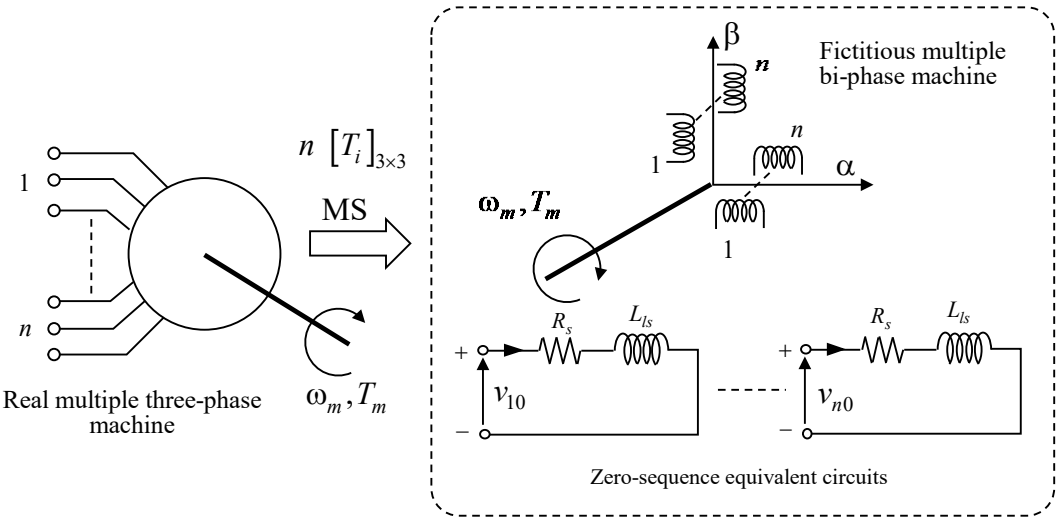

Fig. 1. 4. Meaning of the MS approach based on multiple three-phase Clarke transformation matrices.

Nevertheless, in recent years there have been several attempts into defining new modelling methods able to combine the benefits of both VSD and MS approaches [51]. With reference to the technical literature, the most important attempt is surely represented by the Decoupled Multi-Stator approach (DMS) [52], [53].

Decoupled Multi-Stator (DMS) approach

Starting from the MS-model of the machine, the DMS approach introduces a further reference transformation able to remove the magnetic couplings between the units. In this way, the resulting electromagnetic model of the machine becomes like the one obtained through the VSD approach. Nevertheless, the modularity is respected since the model is built starting from the MS approach [53]. The decoupling transformation introduced by the DMS approach is based on the computation of the common and differential modes of the machine [54], thus assuming a general validity among the modular multiphase configurations.

Despite the great advantages offered by the DMS approach, it has been applied only on the 6-phase machine model in double three-phase configuration [53]. Indeed, there are relevant difficulties into defining a general algorithm able to compute the decoupling transformation for more complicated multiphase configurations. One of the main contributions of this dissertation consists of the solution of this issue. In detail, a computation algorithm able to decouple the main modular multiphase configurations is provided, as it will be shown in the dedicated chapters.

Application of modelling approaches on drive control strategies

Most of the employed multiphase configurations can be modelled by means of the VSD and MS approaches. However, the choice of an approach over another depends by many factors. For some machine configurations, the use of a specific approach becomes mandatory since the VSD and MS ones are not always interchangeable. As example, the VSD approach can be just applied on symmetrical and asymmetrical configurations while the MS one requires a modular configuration of the machine. Therefore, some multiphase drive strategies must necessarily be based on a single approach when specific machine configurations are employed. As example, all the symmetrical configurations having a prime number of phases (5-phase, 7-phase, …) can be exclusively modelled by means of the VSD approach. Being the 5-phase motor drives one of the most employed multiphase solutions, it is possible to understand how the VSD approach has received more attention than the MS one.

However, when modular machine configurations are considered, the drive strategy can be based using both approaches. As example, the 6-phase machine using both symmetrical and asymmetrical configurations [47], [49]. In this case, independently by the fact if the drive employs a modular topology with two independent three-phase units or not, both VSD and MS approaches can be used. The choice is related to the specifications that the drive strategy must satisfy. Indeed, the use of the VSD approach allows at highlighting both the energy conversion and the harmonic pattern of the machine through a simple equation system. Nevertheless, this approach is not be able to deal with a modular drive strategy since an average control of the machine power is performed [8], [47]. Conversely, the use of the MS approach can guarantee the direct control of the currents flowing in each three-phase winding set, thus obtaining a modular drive strategy despite the energy conversion is modelled with a complex equation system [13], [49].

In conclusion, the use of both VSD and MS approaches for the implementation of drive control strategies is quite consolidated. It is not possible to establish the best approach among them since the choice is related to many factors. Therefore, in the technical literature there are many research activities where both methods have been used with satisfying results. Relevant works on the use of the VSD approach on modular drive topologies can be found in [47], [55]. However, in the recent years the development of drive strategies based on the MS approach is

gaining an ever more attention [33], [42], especially on the multiple three-phase drive topologies characterized by a high number of sets. Indeed, in these systems the modularity of the drive strategy represents the most important feature, as will be described next.

Last, but not less important, are the attempts on the use of the DMS approach for six-phase permanent magnet motor drives [52], [53]. In this case, the control strategy combines the advantages of both VSD and MS approaches with the aim at obtaining high control performance of the drive. Unfortunately, the six-phase machine results the only developed case due the difficulties into computing the decoupling transformation for more complex modular multiphase configurations, as described in the previous paragraphs.

In conclusion, the multiphase machines modelling can be performed using different approaches. However, the choice of one approach over another depends by multiple factors, starting from the considered machine configuration up to the features required to the drive structure together with the related control algorithm.

1.1.3 Machine design

The research on the multiphase machines typologies has been characterized by a different development with respect to the three-phase counterparts. Being the multiphase machines historically used in the high-power applications, the research has been focused on the most reliable and robust technologies like the induction motors (IM) one [7], [9], [10]. The choice of the IMs was also justified for their capability to work with square wave supply employing both Voltage Source Inverters (VSI) and Current Source Inverters (CSI) typologies.

Nevertheless, in the last two decades the focus of the multiphase machines design has moved towards the permanent magnet (PM) motors types, due the needing to improve the performance of the drives under both efficiency and power density points of view [56]. In detail, the current research regards the development of both Surface Mount Permanent Magnet (SMPM) and Interior Permanent Magnet (IPM) machines. Indeed, these machine solutions can become an interesting alternative for automotive applications due the obtainable advantages not only in terms of power density and efficiency, but also regarding their inherent fault-tolerant capability.

Worthy of mentioning are the wound rotor synchronous machines. In the past, this machine typology had undergoing an impressive development being employed in the three-phase alternators for the large-scale energy production. Currently, the wound rotor synchronous multiphase machines represent one the best solutions for ultra-high-power applications [57] and also in the aircraft sector for their possible use as starter/alternators. Indeed, the use of PM generators in the aircraft sector is still strongly hindered by the technical problems related to the no-load back-emf voltages. The use of wound rotor synchronous multiphase machines solves these issues since the excitation magnetic field can be easily regulated. In addition, it is

possible to take all the advantages related to the multiphase solutions in terms of current and voltage levels.

Winding layouts

A relevant aspect related to the multiphase machines design is the winding layout. Indeed, different solutions can be employed depending by the machine type. The IM are usually designed with Distributed Winding (DW). Moreover, to avoid leakage mutual couplings between the stator phases, a full-pitch configuration is usually recommended. About the synchronous machines, the choice of the winding layout is strictly related to the target application. Indeed, together with the conventional DW, there is a growing interest in the use of Fractional-Slot Concentrated Windings (FSCW). The main advantages of these ones include short end-turns, high slot fill factor, low cogging torque and the possibility to obtain high values of the phase inductances [9]. In this way, the short-circuit current of the machine is limited with relevant improvements of the flux-weakening capability.

In conclusion, the design of multiphase machines is performed similarly to the one of the three-phase counterparts, thus following the standard rules to obtain an air-gap magnetomotive force having a specific harmonic content [58].

1.1.4 Power converters and modulation strategies

Most of the solutions are based on 2-levels VSIs as the multiphase systems allow at keeping both current and voltage levels at acceptable limits, thus avoiding the use of complex multilevel configurations. In addition, the use of many conversion levels leads to the implementation of modulation strategies with a low level of application in the industry. The main limit is represented by the exponential increment of the power converter's instantaneous discrete states that depends by both the number of phases and the number of conversion levels. Indeed, there are few examples on the use of 3-levels multiphase VSIs. Anyway, their application is usually limited on the 5-phase and 6-phase configurations [39], [59].

Power converter structures

The structure of the multiphase power converters generally depends by the supplied machine configuration. As example, for symmetrical multiphase configurations having a prime number of phases (5-phase, 7-phase, ...) a single multiphase VSI structure is usually employed [8], [13]. Conversely, when modular configurations like the asymmetrical ones are employed, also the power converter is typically structured in a modular way. As example, a power converter feeding multiple three-phase machines is usually designed as multiple three-phase power modules operating in parallel [13]. In this way, thanks to the use of the well-consolidated three-phase technologies, both costs and development times are significantly reduced [5]. This feature is appreciated by the industrial manufacturers, thus justifying the growing interest on these specific multiphase configurations [10].

In the recent years, the use of modular power converters has led to the development of many "series/parallel" multiphase configurations [10], [60]–[62]. As example, the solution presented in [63] employs a 6-phase generator connected to two 3-phase VSIs having their respective dc-links connected in series, thus forming a high voltage dc transmission system. This kind of multiphase structures can have great interest in the offshore wind farms where High-Voltage DC (HVDC) systems are usually employed [64].

Modulation strategies

In the technical literature, the definition of modulation strategies for multiphase VSIs results one of the most developed research topics [7], [8], [65]. Indeed, each multiphase VSI modulation technique must be defined by considering many aspects. Starting from the power converter's structure up to the employed machine configuration, each of these factors has a large impact not only in terms of algorithm's complexity but also relevant consequences on the drive's energy efficiency [47].

Despite the complexity of the issue, the Pulse Width Modulation (PWM) techniques for multiphase VSIs have been developed with the same mathematical approaches of the three-phase case like the Carrier-Based PWM (CB-PWM) [66]–[72] and the Space Vector Modulation (SV-PWM) [73]–[82]. For three-phase VSIs, the two methods have a good degree of interchangeability since they obtain the same results with similar computational efforts. Nevertheless, in the multiphase VSIs the choice of one method over the other one is strictly related to the employed machine configuration (modular or not) together with the modelling approach upon which the drive control algorithm is implemented (VSD-based or MS-based).

Space Vector Modulation (SV-PWM)

The multiphase SV-PWM is the generalization of the conventional three-phase case. Therefore, this method uses a switching pattern that involves all possible power converter's instantaneous states. General approaches for the implementation of *n*-dimensional SV-PWM strategies can be found in [81], [82]. However, the SV-PWM techniques are usually combined with the VSD modelling approach due the great advantage into decomposing the starting *n*-dimensional space in multiple orthogonal subspaces having a specific physical meaning each [47]. In detail, a single main subspace for the energy conversion and the other ones with the meaning of harmonic and homopolar models of the system, as well-established by the VSD theory.

The SV-PWM techniques are usually defined to optimize the energy conversion together with the aim at minimizing the harmonic content [83]. Consequently, the VSD is the most suitable approach since it is possible to configure the SV-PWM algorithm to generate the voltage vectors for the energy conversion in the main subspace, while minimizing any possible voltage component in the other ones, thus avoiding useless harmonic and homopolar currents.

However, this operation is not easy to perform since each instantaneous state of the power converter is mapped in all subspaces and with different effects in each of them [47], [83], as shown in Fig. 1. 5 - Fig. 1. 6 for a 5-phase system. In addition, the number of discrete states and the number of subspaces depend by the number of phases [83]. A relevant attempt for a symmetrical 9-phase machine can be found in [84].

Finally, another issue into using the SV-PWM techniques is the reconfiguration of the algorithm after an open-phase fault event. The fault-tolerance operation of multiphase drives aims at keeping unchanged the torque production to the same levels before the fault event. However, all the machine's waveforms (currents, fluxes) must continue to be within the limits of the power converter/machine and with a limited harmonic content.

To guarantee these conditions, an SV-PWM technique must be able to keep the control of all VSD subspaces using the remained discrete states. In addition, due the asymmetries introduced by the open phase-fault, both harmonic and homopolar currents must be controlled to a not-zero value.

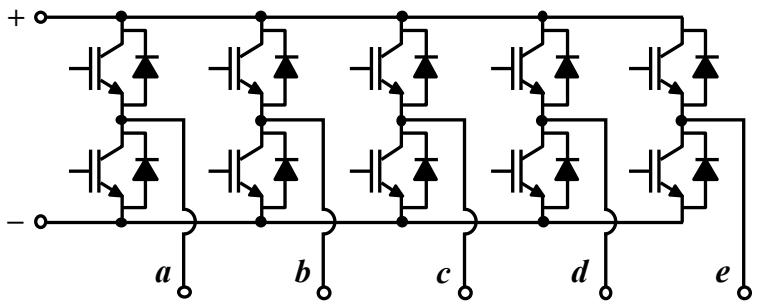

Fig. 1. 5. 5-phase VSI.

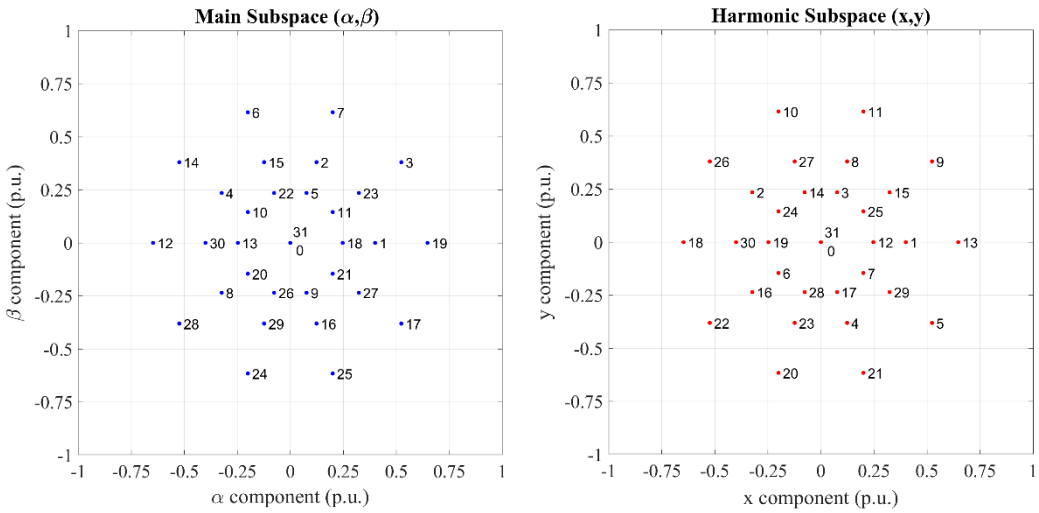

Fig. 1. 6. Normalized 5-phase VSI power converter's discrete states: voltage components on the main subspace (left) and in the harmonic one (right).

In case of an open-phase fault event, the number of lost instantaneous states is x^{y-1} where x is the number of conversion levels of the power converter (usually 2-levels configuration are employed) while y is the number of phases before the open-phase fault event. As example, a 9-phase power converter having a 2-levels structure is characterized by 2^9 (512) instantaneous states. Each of them is mapped in 4 different subspaces plus a zero-sequence component, as established by the VSD theory [47], [83]. After an open-phase fault event, the algorithm must be reconfigured to guarantee the optimal control of all subspaces by means of the 2^8 (256) remained available states. Therefore, through this example it is possible to understand why for systems having a high number of phases, the multiphase SV-PWM techniques (> 6) are not recommended.

Carrier Based PWM (CB-PWM)

The main alternative to the SV-PWM method is represented by the CB-PWM techniques. The main advantage of these solutions is their simple implementation since an independent control of each single-phase voltage is performed. This feature is obtained regardless of whether each single phase is fed by a conventional "inverter-leg" or even by an "H-bridge" structure. This last configuration is employed in the open-end winding multiphase machines to improve the fault-tolerance capability of the drive [13].

All the CB-PWM techniques are based on the computation of the phase duty-cycle. In addition, the element which distinguishes a technique over another is represented by the definition of the zero-sequence voltage, as for the three-phase VSIs [85]. Indeed, among the multiphase CB-PWM techniques it is possible to find the generalization of the three-phase PWM strategies [86], [87]. Therefore, through a proper definition of the zero-sequence voltage it is possible to optimize specific features of the drive such the switching losses or the modulation range [86].

In conclusion, the use of CB-PWM strategies allows at implementing simpler post-fault reconfiguration of the algorithms.

Modular strategies

Historically, the most employed multiphase solutions are the symmetrical 5-phase machine and the 6-phase one, using both symmetrical and asymmetrical configurations. In addition, the stator windings have a single neutral point. These are the reasons why the concepts about the multiphase modulation strategies have been mainly developed for these solutions, thus making their validity quite limited. Nevertheless, with the recent development of the modular multiphase solutions the results obtained from that research activities are regaining a growing attention.

Up to now, the concept of modularity has been described in terms of machine configuration and power converter structure. Nevertheless, it can be also extended from the multiphase PWM strategies point of view. The main advantage on the use of modular modulation strategies is the possibility to obtain a straightforward control of multiphase converters having a high number of phases. However, such techniques can be implemented only when both machine and power converter

employ a modular configuration. As example, in the multiple three-phase machines, the stator winding is structured in multiple independent three-phase windings which operate in parallel. In this case, each three-phase set can be fed by an independent three-phase VSI, thus allowing the voltage control of each single unit by means of a conventional three-phase PWM technique [86], [87]. Through this example, it is possible to understand how there is not a specific limit on the number of three-phase sets since the PWM strategy is implemented in modular way.

Nevertheless, these configurations can be implemented only if the winding belonging to each set has an its neutral point physically isolated by the other ones, as shown in Fig. 1. 7. In fact, the use of a modular modulation technique implies the application of a specific zero-sequence voltage for each set. Consequently, the overall combination of these ones can lead to a relevant voltage excitation of the homopolar subspaces of the machine, as highlighted by the VSD modelling [47], [83]. Therefore, the only way to avoid useless homopolar currents is the use of multiple independent neutral points.

The example of the multiple three-phase structures can be extended to more complex multiphase configurations. As example, a 15-phase machine using a "triple five-phase" configuration employs three 5-phase windings with three isolated neutral points. In this case, each set is fed by an independent 5-phase VSI, thus with the possibility at implementing a 5-phase PWM strategy for each of them. In addition, in this case the adoption of a CB-PWM technique over an SV-PWM one is not so relevant since the 5-phase case is the easiest to manage [78]. This example is the proof how the results obtained by the modulation strategies defined on multiphase machines using a single neutral point are still useful and with a current practical interest.

Finally, the modular modulation techniques usually do not need any reconfiguration of the algorithm after an open-phase fault event. Indeed, the modular multiphase drives are generally designed with the goal to disconnect the whole faulty set from the power supply (including the converter) [13]. In terms of modulation strategy, this operation corresponds into disabling the execution algorithm of the PWM voltage control related to the faulty set.

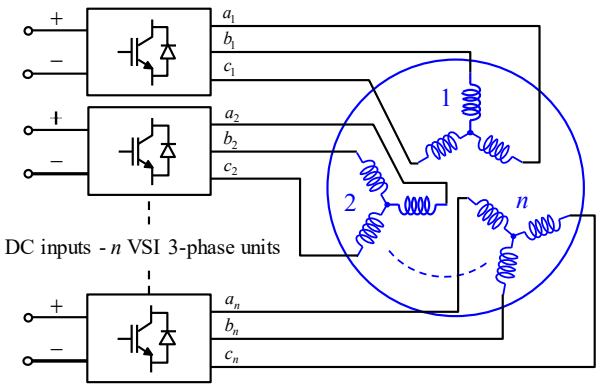

Fig. 1. 7. Multiple three-phase machine fed by multiple VSI three-phase units.

In conclusion, the recent development of modular modulation strategies is allowing the overcoming of the issues related to the voltage control of multiphase VSIs having a high number of phases. In addition, a straightforward reconfiguration of the PWM algorithms after an open-phase fault event is obtained. For these reasons, the interest on modular multiphase solutions is growing ever more in the industry, thus leading to a replacement process of the historical multiphase configurations.

1.1.5 Drive topology

The concept of drive topology has been partially introduced through the previous paragraphs. However, more specifically it corresponds with the definition of the whole drive system in terms of power converter structure and machine configuration. With reference to the technical literature [8], [13], the most employed drive topologies are the following:

- Conventional multiphase structure with single neutral point
- Modular structure with independent *l*-phase units

As previously described, the single neutral point configurations have represented a standard in the context of the multiphase electrical solutions. To this category belong the multiphase drives having a prime number of phases (5-phase, 7-phase, ...). In these machine configurations, the stator winding cannot be set in modular way. Therefore, the symmetrical configuration with single neutral point represents the simplest solution despite it does not fulfil the requirements of fault-tolerance operation [13], [88]. Indeed, for these drive topologies the power converter consists of a conventional multiphase VSI, as shown in Fig. 1. 8. Nevertheless, this drive topology still today results largely employed, especially the 5-phase case [7], [9].

The main alternative to the single neutral point configurations is represented by the modular structures. Most of the multiphase solutions belong to this category and currently there is a growing interest in their development.

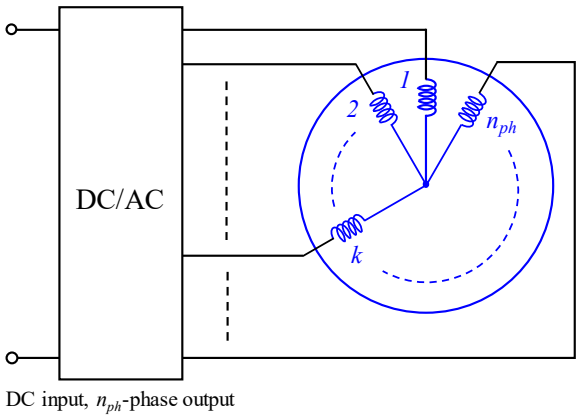

Fig. 1. 8. Multiphase drive topology with single neutral point.

The concept of modularity has been expressed under many points of view, starting from the machine configurations up to the implementation of PWM strategies. Despite the modularity of a drive topology can be obtained in many ways, two specific configurations are collecting the interest of the industry. The first one consists of a solution where multiple of independent single-phase units are employed. In this case, each machine phase is fed by a dedicated single-phase inverter [13], [88], as shown in Fig. 1. 9. This solution possesses the highest degree of modularity together with the best fault-tolerant operation of the drive. Indeed, in case of fault each single-phase converter can be easily disconnected from the supply source. In addition, to improve the fault-tolerance capability of the system, this drive topology is usually used to fed FSCW synchronous machines. Finally, another interesting advantage is related to the output voltage range of the converter. Usually, each single-phase power converter consists of a H-bridge structure fed by a DC source [13]. Therefore, through this solution the widest output voltage range is obtained since the maximum peak of the phase voltage corresponds with the DC source voltage.

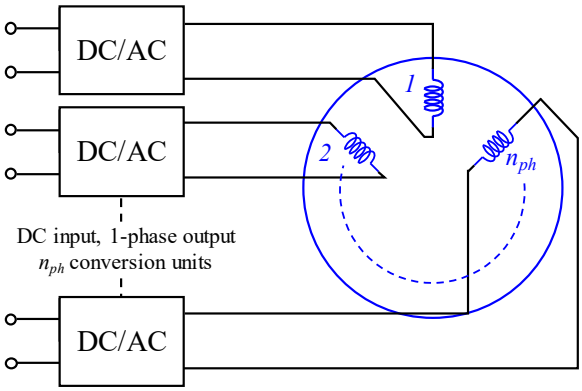

Fig. 1. 9. Multiphase drive topology using multiple single-phase units.

The second most employed modular drive topology is represented by the multiple three-phase solutions. For these solutions, the machine stator consists of independent three-phase windings with isolated neutral points [8], [13]. Indeed, each three-phase set is fed by an independent three-phase converter (Fig. 1. 10), thus making possible the use of a modular modulation strategy. From the fault-tolerant point of view, this topology offers less degrees of freedom with respect to the previous one. Indeed, when a fault occurs, the whole three-phase faulted unit (three-phase winding set plus dedicated converter) is disconnected from the DC power supply [13]. The main advantage of the multiple three-phase drives is the possibility to use the well-consolidated three-phase technologies, thus leading to a significant reduction of the costs and design times. According with the introduction, this dissertation is focused on the development of control strategies for multiple three-phase motor drives and therefore more details will be provided later.

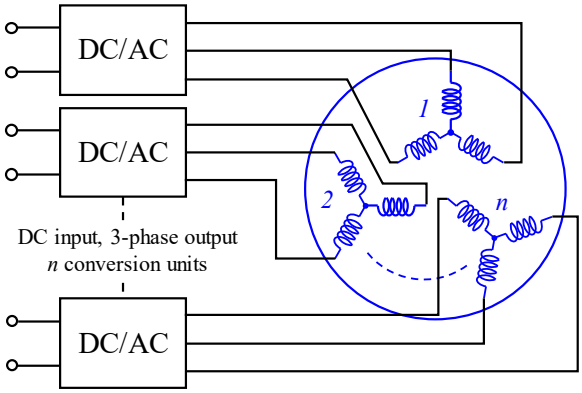

Fig. 1. 10. Multiphase drive topology with multiple three-phase units.

The drive topology has a large influence on the definition of the control strategy. Indeed, most of the control algorithms for multiphase motor drives are based on the employed modelling approach (VSD - MS). However, these ones have been developed upon base of the main multiphase machine configurations.

Therefore, once the drive topology has been chosen, the control strategy is de facto defined even if marginally.

1.1.6 Drive control solutions

The versatility of the multiphase solutions in terms of machine configurations, modelling approaches and power converter structures has led to the development of an impressive variety of drive control techniques. In terms of electromechanical energy conversion, the multiphase machines control has strong similarities with the one of the three-phase counterparts. Indeed, thanks to the application of the multiphase modelling approaches (VSD - MS), most of the concepts related to the vector control of three-phase machines are still valid [8]. However, the complexity of the topic makes necessary the classification of the multiphase drive control techniques upon base their main features.

From technical literature [7]–[9], [13], the control techniques discussed according to the following aspects:

- Control scheme
- Regulation type

An in-depth analysis about each of these aspects is reported below.

Control scheme

The development of control strategies for multiphase electrical machines can be considered similar to the one of the three-phase counterparts. Indeed, thanks to the VSD and MS modelling approaches, it has been possible to adapt most of the control typologies developed on the three-phase drives [7]–[9]. Nevertheless, it is necessary to highlight how the higher degrees of freedom offered by the multiphase machines have also represented a strong hinder in the implementation of several control strategies like the well-known Direct Torque Control (DTC) [8], [9].

Typology	References
VC	[42], [52], [53], [89]-[110], [112], [113]
DTC	[118]-[129]
DFVC	[33]

Table 1. 1. Multiphase drive control techniques.

Anyway, the level of know-how in this field of the research makes necessary a classification of the main control strategies developed for the multiphase motor drives. With reference to the technical literature, the following control schemes can be mainly distinguished (Table 1. 1):

- Vector Control (VC)
- Direct Torque Control (DTC)
- Direct Flux Vector Control (DFVC)

An in-depth analysis about each of these control techniques are reported in the following subsections.

Vector Control (VC)

The definition of VC scheme is quite general and can be referred to different variables (flux, currents). However, the most developed variant is represented by the Current Vector Control (CVC) schemes in which a direct regulation of the stator currents to get the required electromagnetic torque together with a specific level of the machine's flux is performed (Table 1. 2). Because of the operating principles of the multiphase machines are the same of three-phase ones, the CVC can be implemented in a rotating (d,q) frame, thus obtaining a Field Oriented Control (FOC) scheme [89], [90]. The meaning of d-axis is the same of the three-phase motor drives, independently by the employed modelling approach (VSD, MS, DMS). Therefore, it corresponds with the electrical rotor position for synchronous machine. Conversely, for asynchronous machines the d-axis usually represents the position of the rotor flux vector with respect to a stationary frame [89].

A multiphase CVC scheme can be implemented in many ways, depending by the employed modelling approach and the considered reference frame (stationary or rotating). However, as confirmed by the technical literature, the most employed control scheme for multiphase drives is the FOC one based on the VSD approach [7], [9]. The reasons of this are many. One over all, it represents the simplest extension of the FOC schemes applied on the conventional three-phase motor drives. Indeed, the VSD approach allows at decomposing the machine original space in multiple orthogonal subspaces where only the main one is responsible for the electromagnetic torque production (sinusoidal machines). Moreover, with similar equations to the ones of the three-phase machines. Therefore, through the VSD approach, it is possible to adopt any three-phase FOC scheme to perform the electromechanical energy conversion of a multiphase machine [91]–[105]. The only element to add is the control of the harmonic and homopolar subspaces (these latter depending by the machine configuration in terms of neutral point status).

Nevertheless, unlike the main subspace where the variables (flux, currents) in steady-operation are dc quantities, in the harmonic and homopolar subspaces they are ac quantities [8], [47]. Therefore, due the limited performance of the conventional Proportional Integral (PI) controllers, the use of the Proportional Resonant (P-RES) ones becomes necessary to guarantee a proper operation of the drive [91], [92]. Nevertheless, the tuning of these kind of regulators is not easy since the resonant frequency of each of them must be updated according to the motor fundamental frequency in which the electromechanical energy conversion is performed. In addition, when the ratio between the switching frequency and the fundamental one becomes too low, the performance of the P-RES controllers drastically drop due to the combination of discretization issues together with the down-sampling ones. Only the discretization issues can be solved properly by means of the use of strict analytical methods [106].

If a modular drive topology is employed, the use of P-RES controllers can be avoided if FOC schemes based on the MS approach are implemented. In this case, the control strategy consists of multiple FOC sub-schemes which operate in parallel [42], [107]–[110]. One for each *l*-phases unit. Indeed, the MS approach decomposes the original machine model in *n* overlapped subspaces, where *n* is the number of units composing the drive [8], [13]. Each subspace is representative of a specific unit. Therefore, the equation system associated to each subspace is representative of the torque contribution due to a single set. For this reason, upon the equation system of each subspace/unit a dedicated FOC scheme is implemented. This way to manage the degrees of freedom of the machine allows to avoid the use of harmonic and homopolar patterns. Consequently, regardless of the considered subspace, all the variables in steady-operation are dc quantities, thus allowing the use of conventional PI regulators to guarantee a proper operation of the drive [13], [107]. However, the main disadvantage of a MS-based FOC scheme consists of strong magnetic couplings between the *n* units composing the drive. Therefore, specific decoupling algorithms must be implemented. As this dissertation concerns the implementation of MS-based control techniques, further details will be provided next.

In parallel with the development of the above control solutions, there also interesting attempts into proposing FOC schemes based on the DMS approach [52], [53]. A DMS-based scheme is designed starting from a MS-based one, thus inheriting the advantages in terms of modularity. Nevertheless, unlike the MS-based schemes, all the magnetic couplings between the units are removed through the application of a specific decoupling transformation. The effect of this one is to perform a redefinition of the MS subspaces with the goal at obtaining the common and differential modes of the machine. In this way, the energy conversion is concentrated in the common mode subspace while the unbalances between the units in terms of flux and torque productions are projected in the differential subspaces. Therefore, the final configuration of a DMS-based scheme is like to the one obtained with a VSD-based scheme but with the difference that all variables (flux, currents) in steady-operation are dc quantities, thus allowing the use of PI regulators

to guarantee a proper operation of the drive. Another advantage of a DMS-based scheme is the straightforward reconfiguration of the control strategy after an open-phase fault event since it is just necessary to perform a simple recalculation of the reference variables belonging to the differential modes' subspaces. Despite the great advantages on the use of a DMS-based FOC scheme, it has been implemented just on a dual three-phase PM motor drive [53] due the issues on the computation of the decoupling transformation for more complex modular multiphase configurations.

The technical literature reports different versions of the FOC scheme for multiphase IM drives. Indeed, as for the three-phase counterparts, there is the possibility at implementing Indirect FOC (iFOC) schemes in which the rotor flux position is computed by means of the reference currents values, thus avoiding the implementation of a flux observer [111]. The iFOC schemes are easy to implement but they cannot guarantee high dynamic performance in terms of electromagnetic torque production. Nevertheless, their application on the multiphase IM drives has received more attention unlike the three-phase counterparts [93]–[96], [109]. The reason is quite practical. The multiphase solutions have been historical employed in high power or safety critical applications in which there are not dynamic requirements, thus making the iFOC schemes a valid control solution.

Finally, together with the development of FOC schemes, there are also several research activities where CVC schemes operating in the stationary reference frame (SCC) are proposed. One of the first attempts is reported in [112] for a dual three-phase IM drive. However, these control solutions are gaining an ever more attention due the recent development of the predictive control algorithms [9], [113]. More details about this kind of control strategies will be provided in the next subsections.

Typology	Modelling Approach	References
FOC	VSD	[91], [92], [97]-[105]
	MS	[42], [107]–[110]
	DMS	[52], [53]
iFOC	VSD	[93]–[96]
	MS	[109]
SCC	VSD	[112]-[113]

Table 1. 2. Current Vector Control (CVC) techniques.

Direct Torque Control (DTC)

The DTC schemes represent one of the most competitive control solutions for three-phase motor drives as they can obtain high dynamic performance without the use of inner current control loops [114]–[116]. The working principle of the DTC schemes is completely different with respect to the VC ones. Indeed, the electromechanical energy conversion is performed by means of two parallel scalar controls corresponding to the regulation of the stator flux and electromagnetic torque respectively.

Typology	Drive Topology	References
ST-FOC	5-phase	[117]–[119]
	6-phase	[120]–[126]
DB-DTC	6-phase	[127]

Table 1. 3. Direct Torque Control (DTC) techniques.

In addition, unlike the FOC schemes, the DTC ones can be implemented in the stationary frame, thus avoiding the use of the rotational transformations.

According with the literature, the DTC schemes can be designed to work with both variable and constant switching frequency. To the first category belongs to the well-known Direct Self Control (DSC) and Switching Table based DTC (ST-DTC) schemes [114], [128]. To the second one belongs the PWM based DTC (PWM-DTC) where a constant switching frequency is imposed due the use of a PWM modulator [116].

The performance achieved by the DTC schemes on the three-phase drives have led to several research works having the goal to extend this control typology also on the multiphase machines [117]–[127], [129]. Nevertheless, the results obtained in this field of the research are still today limited to specific machine configurations like the 5-phase [117]–[119] and 6-phase ones [120]–[127]. It is important to highlight how most of the efforts have been done in the development of ST-DTC schemes (Table 1. 3), thus following the same tendency of the three-phase drives. In addition, to simplify the machine modelling, DTC schemes based on the VSD approach have been mainly developed.

The design of ST-DTC schemes for multiphase machines having a high number of phases is strongly hindered by the exponential increment of the power converter discrete states. In detail, the main issue is the definition of switching tables able to guarantee the simultaneous control of the all machine subspaces. Indeed, due the absence of inner control loops, the switching tables must be designed to perform the electromechanical energy conversion in the main subspace but at the same time limiting the circulation of harmonic and homopolar currents in the other ones. With reference to the literature, recent works on the application of ST-DTC schemes on 5-phase motor drives can be found in [117], [119]. Regarding the 6-phase machine, different switching tables design solutions are experimented in [125] with good regulation performance. Finally, noteworthy is the solution reported in [127] where a Dead-Beat DTC (DB-DTC) scheme for dual three-phase IM drives is proposed.

In conclusion, due to the difficulties into limiting the circulation of currents in the harmonic and homopolar subspaces, the development of DTC techniques for multiphase drives characterized by a high number of phases is still today considered an unsolved issue. A possible solution could be the use of PWM-DTC schemes [116] although there are few attempts into their implementation [127].

Direct Flux Vector Control (DFVC)

The Direct Flux Vector Control (DFVC) has been recently proposed for three-phase drives as alternative to the conventional FOC and DTC strategies [130]. Being implemented in the rotating frame defined by the position of the stator flux vector, the DFVC scheme possesses a high degree of generality. Indeed, it has been successfully implemented in both induction and synchronous motor drives [131]–[133], thus assuming the meaning of an unified ac control strategy. The DFVC can be considered an evolution of the DTC with the advantage of having constant switching frequency due the use of a PWM modulator. Nevertheless, the state variables controlled by the DFVC scheme correspond with the stator flux amplitude and the torque-producing current component, thus combining the advantage of both FOC and DTC schemes. As for the DTC schemes, the direct stator flux regulation allows to obtain better performance at high speed together with the flux-weakening operation of the drive. Nevertheless, the indirect regulation of the torque through the direct control of the torque-producing current component allows to obtain a good level of decoupling between the control axes. In this way, similar advantages of the FOC schemes are obtained.

A recent attempt into applying the DFVC scheme on a dual three-phase IM drive is reported in [33]. Through this work, it has been possible to demonstrate how the DFVC can represent a smart control solution for multiple three-phase motor drives. Indeed, the DFVC scheme allows to overcome all the limits which characterize the DTC strategies anyway retaining similar dynamic performance, as shown in [33], [130]. For this reason, one of the main goals of this dissertation consists of defining a general DFVC scheme for multiple three-phase IM drives able to obtain high dynamic performance in all operating conditions. Furthermore, being the proposed control solution based on the MS approach, a full and independent control of each three-phase unit is obtained, thus implementing the modularity concept also in terms of drive control strategy. Further details about the application of the DFVC scheme on multiphase drives will be reported in the dedicated chapters.

Regulation type

The regulation type consists of the computation method of the power converter reference commands. It must not be confused with the modulation strategies or the control scheme. Indeed, the latter just represents a computation method of specific reference variables (currents, fluxes, torque) able to guarantee the electromechanical energy conversion. Therefore, the control typology can consist in a VC scheme or a DTC one depending by the specifications of the drive. Conversely, the regulation type is the method by which the machine's variables are manipulated to satisfy the references.

Independently by the fact if three-phase or multiphase drives are considered, the following regulation types are usually employed:

- Regulation with standard controllers
- Regulation with hysteresis controllers
- Regulation by means of predictive algorithms

With reference to the technical literature, there are many other methods that have been developed for the electric drives (neural networks, fuzzy logics etc.) [104], [105]. However, the aforementioned are the most relevant as they are also used in the multiphase solutions.

Although indirectly, the regulation by means of standard controllers have been introduced in the section related to the control scheme. Indeed, a typical example of these ones is represented by the use of PI regulators for the implementation of control loops. In the motor controls context, usually the outputs of the regulators belonging to the inner loops correspond with the reference voltages to be applied to the machine. Therefore, the standard controllers' outputs often represent the inputs of the algorithms implementing the PWM strategies for the generation of the power converter commands.

About the regulation by means of hysteresis controllers, a typical application example is represented by the ST-DTC schemes. In this case, the power converter commands are generated directly through hysteresis controllers which outputs are elaborated by predefined tables containing the switching patterns.

However, in this subsection a deeper analysis is dedicated to the third regulation type related to implementation of predictive algorithms. In the recent years, the development of predictive control schemes for multiphase drives has gained an impressive attention such to represent a possible technological evolution in this field of the research [9], [113]. The implementation of a predictive control scheme can be performed in many ways. However, in the motor drives context, the Model Predictive Control (MPC) schemes represent the most developed solution.

Model Predictive Control (MPC)

In the three-phase motor drives, the MPC techniques have recently emerged as competitive alternative to the conventional feedback control algorithms [134], [135]. The main advantages on their use are the improvement of the dynamic performance together with a less demanding control tuning procedure, thus making these solutions particularly interesting for the application engineers. For these reasons, in the recent years they have been started several research activities with the aim at designing MPC schemes for multiphase drives, thus combining their advantages. Due the complexity of the topic, few control solutions have been proposed [113]. Nevertheless, these are fairly diversified such to have defined a good level of know-how in this field of the research.

As previously described, the MPC does not represent a control typology. It just consists of an alternative computation method of the power converter reference voltages.

Two main categories of MPC schemes can be identified from the literature [134] (Table 1. 4):

- Finite Control Set MPC (FCS-MPC)
- Continuous Control Set MPC (CCS-MPC)

In the FCS-MPC schemes, the reference voltages are selected among the power converter's discrete states according with the optimization of a user-defined cost function. The FCS algorithms directly perform the computation of the power converter switching pattern since the PWM modulator is not employed. Therefore, the FCS-MPC schemes are usually characterized by a variable switching frequency like the ST-DTC schemes. The main advantage on the use of FCS-MPC schemes is the possibility to obtain average switching frequencies usually lower than conventional feedback schemes, thus reducing the switching losses and nevertheless obtaining similar dynamic performance.

The advantages obtained by the FCS-MPC algorithms on the three-phase drives have led to many attempts into extending their validity on the multiphase solutions [136]–[168]. However, as for the ST-DTC schemes, the exponential increment of the power converter's discrete states strongly hinders the implementation of multiphase FCS-MPC schemes. Currently, satisfactory experimental results have been obtained just on the 5-phase and 6-phase motor drives [113]. The main issues are exactly the same found in the implementation of multiphase ST-DTC schemes. The only exception is represented by the replacement of the combination consisted of hysteresis controllers plus switching tables with an optimization algorithm of the cost function. However, this operation is even more complex since the cost function must be evaluated in each possible power converter's discrete state, thus requiring impressive computational efforts when multiphase machines with a high number of phases are considered. Moreover, the reconfiguration of the FCS-MPC schemes after an open-phase fault event is not easy to perform as the cost function must be optimized with a lower number of available states, thus encountering similar issues to the SV-PWM algorithms.

From the literature [113], the multiphase FCS-MPC schemes are more employed than the CCS-MPC ones. As main consequence, different FCS-based control schemes have been developed, depending by the optimized variables in the cost function. Therefore, among all the developed multiphase FCS-MPC schemes, it is possible to find the following control typologies (Table 1. 4):

- FCS-MPC for CVC schemes implemented in the stationary frame [136]–[140], [142], [144]–[147], [149], [150], [152], [154], [158]–[161], [164], [168]; the cost function is designed for current control of the all VSD subspaces. In detail, this solution aims at controlling the currents in the main subspace to perform the energy conversion (ac quantities) and at the same time keeping to zero the currents belonging to the harmonic and homopolar subspaces.

MPC Category	Control Typology	References
FCS-MPC	SCC	[136]–[140], [142], [144]–[147], [149], [150], [152], [154], [158]–[161], [164], [168]
	FOC	[143], [148], [151], [163], [165]
	DCPC	[153], [155]
	DTC	[141]
CCS-MPC	FOC	[156], [157], [165]

Table 1. 4. Model Predictive Control (MPC) techniques.

- FCS-MPC for FOC schemes [143], [148], [151], [163], [165]; the only difference with respect to the previous case is represented by the currents belonging to the main subspace which are referred with respect to the rotating (d,q) frame (dc quantities).
- FCS-MPC for Direct Control of Phase Currents (DCPC) schemes [153], [155]; the cost function is designed for the control of the all phase currents. There is not the use of any reference transformation.
- FCS-MPC for DTC schemes [141]; the cost function is designed similar to the CVC and FOC ones. The only difference is represented by the variables belonging to the main subspace corresponding with the stator flux amplitude and electromagnetic torque.

It can be noted how all the FCS-MPC schemes have been developed using the VSD approach to obtain a simple machine model, thus avoiding further complications. In addition, the CVC schemes implemented in the stationary frame result the most employed solution due the advantages in the design of the cost function. Indeed, this one must be designed for the control of a single variable typology, ac steady-state quantities in this specific case.

Unlike the FCS-MPC schemes, in the CCS-MPC ones the voltage range corresponds with the all possible average voltage vectors which the power converter can apply. Therefore, the CCS-MPC schemes are executed at constant switching frequency since a PWM modulator is employed [113]. Although the cost functions can be also implemented in these schemes, the computation of the reference voltages is usually performed by using a deadbeat approach [169], [170], thus obtaining high dynamic performance and low harmonic distortion of the machine waveforms. Therefore, the reference voltages are computed by using the inverse machine model together with the reference commands and the predicted values of the control variables, thus making the number of power converter discrete states not so relevant. As a consequence, the CCS-MPC algorithms can represents a possible solution into defining general MPC schemes for multiphase machines [113].

Another advantage on the use of CCS-MPC schemes is the versatility in terms of employed modelling approach. Indeed, unlike the FCS-MPC schemes, the use of the VSD approach is not mandatory. Therefore, it is possible to implement MS-based CCS-MPC schemes when modular multiphase configurations are employed,

thus obtaining the related advantages in terms of modularity of the control strategy and easy reconfiguration of the algorithm after an open-phase fault event.

Finally, as for the FCS-MPC algorithms, the CCS-MPC ones can be applied on any control typology. However, with reference to the technical literature (Table 1. 4) there are only few attempts at implementing CCS-MPC algorithms for FOC schemes [156], [157], [165]. Indeed, the CCS-MPC algorithms can optimize less variables with respect to the FCS-MPC schemes. Moreover, the implementation of CCS-MPC algorithms usually require huge computational efforts, especially when modular configurations of the drive strategy are employed.

1.1.7 Fault analysis and post-fault control strategies

Thanks to their intrinsic fault-tolerant capability, the multiphase drives have found large employment in the safety-critical applications in which any service interruption can lead to significant money losses. As example, the oil and gas applications in which high power modular multiphase solutions are often employed [57]. Therefore, the development of post-fault drive strategies has resulted one of the most considered research topics [7], [10].

In the multiphase drives the fault sources are typically represented by the power converter and the electrical machine [10]. About the first one, the most frequent faults are usually referable to the power switches. Conversely, the electrical machines can be subjected to both open and short connection of one or more phases. From the literature, the open-phase faults events from both power converter and electrical machine result the most considered cases since they usually do not compromise the post-fault operation of the drive drastically. However, the reconfiguration of a drive control strategy after a fault event is usually preceded by the detection of the same. This operation is not easy to perform especially when the fault regards the electrical machine [10]. For this reason, among the research activities focused on the fault-tolerant operation of the multiphase drives, it is possible to find several contributions in which fault detection techniques have been developed [171]–[177]. As example, a real-time approach for the detection of faults in machines having an odd number of phases is reported in [172], [173]. Currently, there are few contributions into both diagnosis and detection of the failures on multiphase drives, thus is not yet possible to provide a real state of the art in this field of the research. Conversely, there are many published works in which different fault-tolerant control strategies for multiphase drives have been developed [61], [97], [144], [175], [178]–[199].

By considering an open-phase fault event, a post-fault drive strategy can be implemented in many ways, depending by which variables it is necessary to optimize. After an open-phase fault event the multiphase machines can still guarantee the torque production. In any case, this working condition is usually characterized by a performance derating. Indeed, when one or more phases are lost, it is necessary to increase the value of the currents in the healthy ones in order to keep the torque production level as close as possible to the one preceding the fault

event. Nevertheless, there is not a univocal method into doing this operation [7], [8], [10].

Without any limit on the current's levels, the torque production after an open-phase fault event is not compromised. However, it is necessary to take in account the limitations on the maximum current allowed by both power converter and electrical machine. Regarding the power converter, the overcoming of the current limits can lead to irreversible damages on the power switches, thus the protection system of the converter rapidly avoids this condition by stopping the devices switching. This event must be avoided since it corresponds with the service interruption of the drive.

Conversely, the machine current limits are usually related to the maximum allowed thermal stresses beyond which severe damages on the windings insulation system are caused [200]. With reference to [10], the post-fault strategies can be categorized in two main groups:

- Minimum Loss (ML) strategies: for a given torque reference the currents commands are computed according with the minimization of the copper losses [184], [191]. In the ML strategies, there is no restriction on the magnitude of the phase currents. Indeed, the post-fault operation of the drive is often characterized by unequal amplitude values of the phase currents. Therefore, a detailed thermal analysis is necessary to avoid local heating.
- Maximum Torque (MT) strategies: for a given torque reference the currents commands are computed according with the minimization of their amplitude [183], [201], [202]. In the MT strategies, equal amplitudes of the phase currents are imposed, so better heating operating conditions are obtained.

In any case, both ML and MT post-fault strategies are designed at having limited torque oscillations, thus avoiding dangerous vibrations [197]. Therefore, the currents of the healthy phases must continue to generate air-gap magnetomotive forces with limited harmonic content. This issue is particularly important in multiphase drives employing a conventional single neutral point configuration. Indeed, in this drive topology the open-phase fault leads to an asymmetric configuration of the magnetic axes belonging to the stator phases, thus making more complex the computation of the currents' references. Finally, in terms of machine modelling the post-fault strategies usually do not apply any change in the reference transformation, especially when the VSD approach is employed [61], [180]. As main consequence, after an open-phase fault event a specific control of the currents belonging to the harmonic and homopolar subspaces must be performed. Nevertheless, there are several attempts in which the recalculation of the reference transformation is performed [144], [178], [203]–[205], although numerical methods with limited validity are employed.

Finally, with the recent development of the modular drive topologies also the post-fault control strategies result simplified. In these configurations, the faulted

units (stator winding plus power converter) are simply disconnected from the power supply [13], [33], [113]. For this reason, the post-fault strategy must be simply designed into computing the reference variables (fluxes, currents) for the remaining healthy sets. This operation is quite easy to perform being each single unit an independent polyphase system, thus able to guarantee an optimal torque production without relevant oscillations [13]. In addition, each set is always characterized by a uniform amplitude of the phase currents. For this reason, the post-fault drive techniques for the modular multiphase configurations are usually defined following a MT strategy.

1.1.8 Conclusion

The most relevant contributions on the development of multiphase motor drives have been published in the last three decades by covering many technical aspects [7]–[10], [13]. In this paragraph, a literature survey providing the state of the art in this field of the research has been reported. With reference to it, the multiphase solutions have been historically employed in both high power and safety-critical applications [8]. Currently, they represent a standard in the marine applications for both ship propulsion and on-board generation. However, in the current scenario in which the transportation electrification is playing a key-role for the reduction fossil fuel emissions [1]–[3], the multiphase motor drives can represent a smart and reliable solution [7], [13].

The research on the multiphase drives has been split up in different subtopics, thus achieving a high level of know-how under many aspects. Starting from the machine modelling up to the drive control techniques [7]. Nowadays, the multiphase solutions can be considered a competitive alternative to the conventional three-phase ones [7], [9], [10]. Nevertheless, among all the possible multiphase configurations, there is a strong interest in the development of the modular ones. With reference to the literature survey, it has been shown how the modularity of the drive topology leads to several advantages [10], [13]. Among these, one of the most important is represented by the modular modulation strategies as they allow a straightforward control of multiphase VSIs having a high number of phases. Another relevant advantage is the possibility to employ modular modelling approaches [49], [53] with the aim into implementing modular control techniques, thus obtaining relevant simplifications also on the post-fault reconfiguration of the drive strategies [13].

In the recent years, among the modular multiphase configurations, the multiple three-phase drives have gained a growing attention by the industrial manufacturers [13], [34], [40], [41]. Indeed, these solutions can use the well-consolidated three-phase technologies, thus leading to a significant costs reduction [5]. For this reason, the dissertation is focused on the implementation of high-performance control techniques for this specific drive topology. In conclusion, the multiple three-phase drives represent the research context of this dissertation and more details will be provided in the next paragraph along with the all introduced novelties.

1.2 Research contributions

This dissertation deals with the analysis, design and implementation of innovative control techniques for multiple three-phase induction motor drives. The main goal of the research activity consists of the development of a modular control scheme able to fully exploit all the degrees of freedom offered by these specific multiphase drive topologies.

The proposed control techniques have been developed by using the MS-approach [13], [49]. Conversely, the VSD-approach has been used only for comparison purposes, being it not suitable for dissertation goal.

The research activity has led to the following major results and novelties:

1) MS and VSD state-space model computation for multiple three-phase induction machines having an arbitrary number of three-phase winding sets.
2) Design and implementation of a modular Direct Flux Vector Control (DFVC) scheme for multiple three-phase induction motor drives having an arbitrary number of three-phase units. The proposed control scheme allows at implementing an independent regulation of both stator flux amplitude and torque contribution belonging to each three-phase unit.
3) Design and implementation of a Model Predictive DFVC (MPC-DFVC) scheme for multiple three-phase induction motor drives having an arbitrary number of three-phase units. To obtain the best dynamic drive performance, a deadbeat regulation (CCS-MPC) is performed.

In each proposed control solution, the post-fault drive operation has been implemented. The open-phase fault events due to a power electronics failure have been considered.

The experimental validation has been performed on a 12-phase asymmetrical induction machine using a quadruple three-phase configuration.

1.3 Dissertation outline

This thesis is divided into 4 chapters as follows:

- **Chapter 1** provides a literature survey of current state of the art in the multiphase electrical systems. The list follows of research contributions and discussion of novelties. Finally, the list of publications derived from the Ph.D. work is reported.
- **Chapter 2** provides the general modelling of the multiple three-phase induction machine using both Multi-Stator (MS) and Vector Space Decomposition (VSD) approaches.
- **Chapter 3** provides the design and digital implementation of a Direct Flux Vector Control (DFVC) scheme for multiple three-phase Induction Motor (IM) drives.

- **Chapter 4** provides the experimental validation of the proposed control solution. On the basis of the experimental results, full drive controllability in all operating condition is validated.

1.4 List of publications

Journal Papers

1) S. Rubino, R. Bojoi, S. A. Odhano and P. Zanchetta, "Model Predictive Direct Flux Vector Control of Multi-three-Phase Induction Motor Drives," in *IEEE Transactions on Industry Applications*, vol. 54, no. 5, pp. 4394-4404, Sept.-Oct. 2018.
2) A. Amerise, M. Mengoni, L. Zarri, A. Tani, S. Rubino and R. Bojoi, "Open-End Windings Induction Motor Drive with a Floating Capacitor Bridge at Variable DC Link Voltage," in *IEEE Transactions on Industry Applications* (Early Access).

Conference Papers

1) S. Rubino, A. Mazza, G. Chicco and M. Pastorelli, "Advanced control of inverter-interfaced generation behaving as a virtual synchronous generator," 2015 *IEEE Eindhoven PowerTech*, Eindhoven, 2015, pp. 1-6.
2) S. Rubino, R. Bojoi, A. Cavagnino and S. Vaschetto, "Asymmetrical twelve-phase induction starter/generator for more electric engine in aircraft," 2016 *IEEE Energy Conversion Congress and Exposition (ECCE)*, Milwaukee, WI, 2016, pp. 1-8.
3) R. Bojoi, S. Rubino, A. Tenconi and S. Vaschetto, "Multiphase electrical machines and drives: A viable solution for energy generation and transportation electrification," 2016 *International Conference and Exposition on Electrical and Power Engineering (EPE)*, Iasi, 2016, pp. 632-639.
4) S. Rubino, R. Bojoi, M. Mengoni and L. Zarri, "Optimal flux selection for multi three-phase machines in normal and fault conditions," 2017 *IEEE International Electric Machines and Drives Conference (IEMDC)*, Miami, FL, 2017, pp. 1-8.
5) A. Amerise, M. Mengoni, L. Zarri, A. Tani, S. Rubino and R. Bojoi, "Open-ended induction motor drive with a floating capacitor bridge at variable DC link voltage," 2017 *IEEE Energy Conversion Congress and Exposition (ECCE)*, Cincinnati, OH, 2017, pp. 3591-3597.
6) S. Rubino, R. Bojoi, S. A. Odhano and P. Zanchetta, "Model predictive direct flux vector control of multi three-phase induction motor drives," 2017 *IEEE Energy Conversion Congress and Exposition (ECCE)*, Cincinnati, OH, 2017, pp. 3633-3640.

7) A. Tenconi, S. Rubino and R. Bojoi, "Model Predictive Control for Multiphase Motor Drives – a Technology Status Review," 2018 *International Power Electronics Conference (IPEC-Niigata* 2018 - *ECCE Asia)*, Niigata, 2018, pp. 732-739.
8) A. Boglietti, R. Bojoi, S. Rubino and M. Cossale, "Load Capability of Multiphase Machines under Normal and Open-Phase Fault Conditions," 2018 *IEEE Energy Conversion Congress and Exposition (ECCE)*, Portland, OR, 2018, pp. 242-247.
9) S. Odhano, P. Zanchetta, S. Rubino and R. Bojoi, "Modulated Model Predictive Direct Power Control of DFIM Considering Magnetic Saturation Effects," 2018 *IEEE Energy Conversion Congress and Exposition (ECCE)*, Portland, OR, 2018, pp. 5442-5449.
10) S. Rubino, R. Bojoi, E. Armando and A. Tenconi, "Model Predictive Direct Flux Vector Control of Surface Permanent Magnet Motor Drives," 2018 *IEEE Energy Conversion Congress and Exposition (ECCE)*, Portland, OR, 2018, pp. 5458-5465.
11) S. Rubino, R. Bojoi, E. Levi and O. Dordevic, "Vector Control of Multiple Three-Phase Permanent Magnet Motor Drives," *IECON 2018 - 44th Annual Conference of the IEEE Industrial Electronics Society*, Washington, DC, 2018, pp. 5866-5871.

References

[1] 'COP 21 Paris France Sustainable Innovation Forum 2015 working with UNEP'. [Online]. Available: http://www.cop21paris.org/. [Accessed: 12-Dec-2018].

[2] E. Parliament, 'Resolution on "Winning the Battle Against Global Climate Change"'.

[3] 'European Environment Agency's home page', *European Environment Agency*. [Online]. Available: https://www.eea.europa.eu. [Accessed: 12-Dec-2018].

[4] J. A. Rosero, J. A. Ortega, E. Aldabas, and L. Romeral, 'Moving towards a more electric aircraft', *IEEE Aerosp. Electron. Syst. Mag.*, vol. 22, no. 3, pp. 3–9, Mar. 2007.

[5] W. Cao, B. C. Mecrow, G. J. Atkinson, J. W. Bennett, and D. J. Atkinson, 'Overview of Electric Motor Technologies Used for More Electric Aircraft (MEA)', *IEEE Trans. Ind. Electron.*, vol. 59, no. 9, pp. 3523–3531, Sep. 2012.

[6] H. Kim, K. Shin, S. Englebretson, N. Frank, and W. Arshad, 'Analytical model of multiphase permanent magnet synchronous machines for energy and transportation applications', in *2013 International Electric Machines Drives Conference*, 2013, pp. 172–179.

[7] E. Levi, 'Multiphase Electric Machines for Variable-Speed Applications', *IEEE Trans. Ind. Electron.*, vol. 55, no. 5, pp. 1893–1909, May 2008.

[8] E. Levi, R. Bojoi, F. Profumo, H. A. Toliyat, and S. Williamson, 'Multiphase induction motor drives - a technology status review', *IET Electr. Power Appl.*, vol. 1, no. 4, pp. 489–516, Jul. 2007.

[9] F. Barrero and M. J. Duran, 'Recent Advances in the Design, Modeling, and Control of Multiphase Machines—Part I', *IEEE Trans. Ind. Electron.*, vol. 63, no. 1, pp. 449–458, Jan. 2016.

[10] M. J. Duran and F. Barrero, 'Recent Advances in the Design, Modeling, and Control of Multiphase Machines—Part II', *IEEE Trans. Ind. Electron.*, vol. 63, no. 1, pp. 459–468, Jan. 2016.

[11] C. L. Fortescue, 'Method of Symmetrical Co-Ordinates Applied to the Solution of Polyphase Networks', *Trans. Am. Inst. Electr. Eng.*, vol. XXXVII, no. 2, pp. 1027–1140, Jul. 1918.

[12] G. K. Singh, 'Multi-phase induction machine drive research—a survey', *Electr. Power Syst. Res.*, vol. 61, no. 2, pp. 139–147, Mar. 2002.

[13] R. Bojoi, S. Rubino, A. Tenconi, and S. Vaschetto, 'Multiphase electrical machines and drives: A viable solution for energy generation and transportation electrification', in *2016 International Conference and Exposition on Electrical and Power Engineering (EPE)*, 2016, pp. 632–639.

[14] T. J. McCoy, 'Electric Ships Past, Present, and Future [Technology Leaders]', *IEEE Electrification Mag.*, vol. 3, no. 2, pp. 4–11, Jun. 2015.

[15] 'Publications', *McCoy Consulting, LLC*. [Online]. Available: http://mccoy-consulting.com/publications.html. [Accessed: 12-Dec-2018].

[16] T. Ericsen, N. Hingorani, and Y. Khersonsky, 'Power electronics and future marine electrical systems', *IEEE Trans. Ind. Appl.*, vol. 42, no. 1, pp. 155–163, Jan. 2006.

[17] S. Castellan, R. Menis, M. Pigani, G. Sulligoi, and A. Tessarolo, 'Modeling and Simulation of Electric Propulsion Systems for All-Electric Cruise Liners', in *2007 IEEE Electric Ship Technologies Symposium*, 2007, pp. 60–64.

[18] T. Mazzuca and M. Torre, 'The FREMM architecture: A first step towards innovation', in *Automation and Motion 2008 International Symposium on Power Electronics, Electrical Drives*, 2008, pp. 574–579.

[19] B. Gamble, G. Snitchler, and T. MacDonald, 'Full Power Test of a 36.5 MW HTS Propulsion Motor', *IEEE Trans. Appl. Supercond.*, vol. 21, no. 3, pp. 1083–1088, Jun. 2011.

[20] F. Scuiller, J. Charpentier, and E. Semail, 'Multi-star multi-phase winding for a high power naval propulsion machine with low ripple torques and high fault tolerant ability', in *2010 IEEE Vehicle Power and Propulsion Conference*, 2010, pp. 1–5.

[21] J. Dai, S. W. Nam, M. Pande, and G. Esmaeili, 'Medium-Voltage Current-Source Converter Drives for Marine Propulsion System Using a Dual-Winding Synchronous Machine', *IEEE Trans. Ind. Appl.*, vol. 50, no. 6, pp. 3971–3976, Nov. 2014.

[22] L. Parsa and H. A. Toliyat, 'Five-phase permanent magnet motor drives for ship propulsion applications', in *IEEE Electric Ship Technologies Symposium, 2005.*, 2005, pp. 371–378.

[23] G. Sulligoi, A. Tessarolo, V. Benucci, M. Baret, A. Rebora, and A. Taffone, 'Modeling, simulation and experimental validation of a generation system for Medium-Voltage DC Integrated Power Systems', in *2009 IEEE Electric Ship Technologies Symposium*, 2009, pp. 129–134.

[24] G. Sulligoi, A. Tessarolo, V. Benucci, A. M. Trapani, M. Baret, and F. Luise, 'Shipboard Power Generation: Design and Development of a Medium-Voltage dc Generation System', *IEEE Ind. Appl. Mag.*, vol. 19, no. 4, pp. 47–55, Jul. 2013.

[25] 'Type 45 destroyer', *Wikipedia*. 04-Dec-2018.

[26] C. Gerada, K. Bradley, X. Huang, A. Goodman, C. Whitley, and G. Towers, 'A 5-Phase Fault-Tolerant Brushless Permanent Magnet Motor Drive for an Aircraft Thin Wing Surface Actuator', in *2007 IEEE International Electric Machines Drives Conference*, 2007, vol. 2, pp. 1643–1648.

[27] X. Huang, A. Goodman, C. Gerada, Y. Fang, and Q. Lu, 'Design of a Five-Phase Brushless DC Motor for a Safety Critical Aerospace Application', *IEEE Trans. Ind. Electron.*, vol. 59, no. 9, pp. 3532–3541, Sep. 2012.

[28] M. Galea, Z. Xu, C. Tighe, T. Hamiti, C. Gerada, and S. Pickering, 'Development of an aircraft wheel actuator for green taxiing', in *2014 International Conference on Electrical Machines (ICEM)*, 2014, pp. 2492–2498.

[29] C. Gerada, M. Galea, and A. Kladas, 'Electrical machines for aerospace applications', in *2015 IEEE Workshop on Electrical Machines Design, Control and Diagnosis (WEMDCD)*, 2015, pp. 79–84.

[30] M. Rottach, C. Gerada, and P. W. Wheeler, 'Design optimisation of a fault-tolerant PM motor drive for an aerospace actuation application', in *7th IET International Conference on Power Electronics, Machines and Drives (PEMD 2014)*, 2014, pp. 1–6.

[31] B. C. Mecrow *et al.*, 'Design and testing of a four-phase fault-tolerant permanent-magnet machine for an engine fuel pump', *IEEE Trans. Energy Convers.*, vol. 19, no. 4, pp. 671–678, Dec. 2004.

[32] G. Rizzoli, G. Serra, P. Maggiore, and A. Tenconi, 'Optimized design of a multiphase induction machine for an open rotor aero-engine shaft-line-embedded starter/generator', in *IECON 2013 - 39th Annual Conference of the IEEE Industrial Electronics Society*, 2013, pp. 5203–5208.

[33] R. Bojoi, A. Cavagnino, A. Tenconi, and S. Vaschetto, 'Control of Shaft-Line-Embedded Multiphase Starter/Generator for Aero-Engine', *IEEE Trans. Ind. Electron.*, vol. 63, no. 1, pp. 641–652, Jan. 2016.

[34] Siemens, 'Electromobility: Electrically Powered Flight'. [Online]. Available: https://www.siemens.com/innovation/en/home/pictures-of-the-future/mobility-and-motors/electromobility-electrically-powered-flight.html. [Accessed: 12-Dec-2018].

[35] R. Bojoi, A. Cavagnino, M. Cossale, and A. Tenconi, 'Multiphase Starter Generator for a 48-V Mini-Hybrid Powertrain: Design and Testing', *IEEE Trans. Ind. Appl.*, vol. 52, no. 2, pp. 1750–1758, Mar. 2016.

[36] G. Wolf and N. Pfitzke, 'Five-phase generator', US7989996B2, 02-Aug-2011.

[37] S. Brisset, D. Vizireanu, and P. Brochet, 'Design and Optimization of a Nine-Phase Axial-Flux PM Synchronous Generator With Concentrated Winding for Direct-Drive Wind Turbine', *IEEE Trans. Ind. Appl.*, vol. 44, no. 3, pp. 707–715, May 2008.

[38] Z. Xiang-Jun, Y. Yongbing, Z. Hongtao, L. Ying, F. Luguang, and Y. Xu, 'Modelling and control of a multi-phase permanent magnet synchronous generator and efficient hybrid 3L-converters for large direct-drive wind turbines', *IET Electr. Power Appl.*, vol. 6, no. 6, pp. 322–331, Jul. 2012.

[39] I. Gonzalez-Prieto, M. J. Duran, H. S. Che, E. Levi, M. Bermúdez, and F. Barrero, 'Fault-Tolerant Operation of Six-Phase Energy Conversion Systems With Parallel Machine-Side Converters', *IEEE Trans. Power Electron.*, vol. 31, no. 4, pp. 3068–3079, Apr. 2016.

[40] 'The leader in renewable energy I Siemens Gamesa'. [Online]. Available: https://www.siemensgamesa.com/en-int. [Accessed: 12-Dec-2018].

[41] 'INNOVATIONS | HYUNDAI ELEVATOR'. [Online]. Available: http://www.hyundaielevator.com/en/company/info/summary. [Accessed: 12-Dec-2018].

[42] E. Jung, H. Yoo, S. Sul, H. Choi, and Y. Choi, 'A Nine-Phase Permanent-Magnet Motor Drive System for an Ultrahigh-Speed Elevator', *IEEE Trans. Ind. Appl.*, vol. 48, no. 3, pp. 987–995, May 2012.

[43] W. C. Duesterhoeft, M. W. Schulz, and E. Clarke, 'Determination of Instantaneous Currents and Voltages by Means of Alpha, Beta, and Zero Components', *Trans. Am. Inst. Electr. Eng.*, vol. 70, no. 2, pp. 1248–1255, Jul. 1951.

[44] R. H. Park, 'Two-reaction theory of synchronous machines generalized method of analysis-part I', *Trans. Am. Inst. Electr. Eng.*, vol. 48, no. 3, pp. 716–727, Jul. 1929.

[45] R. H. Park, 'Two-reaction theory of synchronous machines-II', *Trans. Am. Inst. Electr. Eng.*, vol. 52, no. 2, pp. 352–354, Jun. 1933.

[46] D. C. White and H. H. Woodson, *Electromechanical Energy Conversion*. Wiley, 1959.

[47] Y. Zhao and T. A. Lipo, 'Space vector PWM control of dual three-phase induction machine using vector space decomposition', *IEEE Trans. Ind. Appl.*, vol. 31, no. 5, pp. 1100–1109, Sep. 1995.

[48] I. Zoric, M. Jones, and E. Levi, 'Vector space decomposition algorithm for asymmetrical multiphase machines', in *2017 International Symposium on Power Electronics (Ee)*, 2017, pp. 1–6.

[49] R. H. Nelson and P. C. Krause, 'Induction Machine Analysis for Arbitrary Displacement Between Multiple Winding Sets', *IEEE Trans. Power Appar. Syst.*, vol. PAS-93, no. 3, pp. 841–848, May 1974.

[50] I. Zoric, 'Multiple Three-Phase Induction Generators for Wind Energy Conversion Systems', doctoral, Liverpool John Moores University, 2018.

[51] M. Zabaleta, E. Levi, and M. Jones, 'Modelling approaches for triple three-phase permanent magnet machines', in *2016 XXII International Conference on Electrical Machines (ICEM)*, 2016, pp. 466–472.

[52] S. Kallio, M. Andriollo, A. Tortella, and J. Karttunen, 'Decoupled d-q Model of Double-Star Interior-Permanent-Magnet Synchronous Machines', *IEEE Trans. Ind. Electron.*, vol. 60, no. 6, pp. 2486–2494, Jun. 2013.

[53] J. Karttunen, S. Kallio, P. Peltoniemi, P. Silventoinen, and O. Pyrhönen, 'Decoupled Vector Control Scheme for Dual Three-Phase Permanent Magnet Synchronous Machines', *IEEE Trans. Ind. Electron.*, vol. 61, no. 5, pp. 2185–2196, May 2014.

[54] Y. Hu, Z. Q. Zhu, and M. Odavic, 'Comparison of Two-Individual Current Control and Vector Space Decomposition Control for Dual Three-Phase PMSM', *IEEE Trans. Ind. Appl.*, vol. 53, no. 5, pp. 4483–4492, Sep. 2017.

[55] I. Zoric, M. Jones, and E. Levi, 'Arbitrary Power Sharing Among Three-Phase Winding Sets of Multiphase Machines', *IEEE Trans. Ind. Electron.*, vol. 65, no. 2, pp. 1128–1139, Feb. 2018.

[56] G. Pellegrino, A. Vagati, B. Boazzo, and P. Guglielmi, 'Comparison of Induction and PM Synchronous Motor Drives for EV Application Including Design Examples', *IEEE Trans. Ind. Appl.*, vol. 48, no. 6, pp. 2322–2332, Nov. 2012.

[57] A. Tessarolo, G. Zocco, and C. Tonello, 'Design and Testing of a 45-MW 100-Hz Quadruple-Star Synchronous Motor for a Liquefied Natural Gas Turbo-Compressor Drive', *IEEE Trans. Ind. Appl.*, vol. 47, no. 3, pp. 1210–1219, May 2011.

[58] J. Pyrhonen, T. Jokinen, and V. Hrabovcova, *Design of Rotating Electrical Machines*. John Wiley & Sons, 2009.

[59] M. Darijevic, I. Zoric, and M. Jones, 'Optimised Modulation of Five-Phase Open-End Winding Drive', in *PCIM Europe 2017; International Exhibition and Conference for Power Electronics, Intelligent Motion, Renewable Energy and Energy Management*, 2017, pp. 1–8.

[60] I. Zoric, M. Jones, and E. Levi, 'Voltage balancing control of a symmetrical nine-phase machine with series-connected DC links', in *2017 IEEE 26th International Symposium on Industrial Electronics (ISIE)*, 2017, pp. 1052–1057.

[61] H. S. Che, M. J. Duran, E. Levi, M. Jones, W. Hew, and N. A. Rahim, 'Postfault Operation of an Asymmetrical Six-Phase Induction Machine With Single and Two Isolated Neutral Points', *IEEE Trans. Power Electron.*, vol. 29, no. 10, pp. 5406–5416, Oct. 2014.

[62] H. S. Che, E. Levi, M. Jones, M. J. Duran, W. Hew, and N. A. Rahim, 'Operation of a Six-Phase Induction Machine Using Series-Connected Machine-Side Converters', *IEEE Trans. Ind. Electron.*, vol. 61, no. 1, pp. 164–176, Jan. 2014.

[63] M. J. Durán, S. Kouro, B. Wu, E. Levi, F. Barrero, and S. Alepuz, 'Six-phase PMSG wind energy conversion system based on medium-voltage multilevel converter', in *Proceedings of the 2011 14th European Conference on Power Electronics and Applications*, 2011, pp. 1–10.

[64] F. Blaabjerg and Z. Chen, *Power Electronics for Modern Wind Turbines*. Morgan & Claypool, 2006.

[65] E. Levi, 'Advances in Converter Control and Innovative Exploitation of Additional Degrees of Freedom for Multiphase Machines', *IEEE Trans. Ind. Electron.*, vol. 63, no. 1, pp. 433–448, Jan. 2016.

[66] O. Ojo, G. Dong, and Z. Wu, 'Pulse-Width Modulation for Five-Phase Converters Based on Device Turn-on Times', in *Conference Record of the 2006 IEEE Industry Applications Conference Forty-First IAS Annual Meeting*, 2006, vol. 2, pp. 627–634.

[67] O. Ojo and G. Dong, 'Generalized discontinuous carrier-based PWM modulation scheme for multi-phase converter-machine systems', in *Fourtieth IAS Annual Meeting. Conference Record of the 2005 Industry Applications Conference, 2005.*, 2005, vol. 2, pp. 1374-1381 Vol. 2.

[68] N. Bodo, E. Levi, and M. Jones, 'Investigation of Carrier-Based PWM Techniques for a Five-Phase Open-End Winding Drive Topology', *IEEE Trans. Ind. Electron.*, vol. 60, no. 5, pp. 2054–2065, May 2013.

[69] A. Iqbal, E. Levi, M. Jones, and S. N. Vukosavic, 'A PWM Scheme for a Five-Phase VSI Supplying a Five-Phase Two-Motor Drive', in *IECON 2006 - 32nd Annual Conference on IEEE Industrial Electronics*, 2006, pp. 2575–2580.

[70] D. Casadei, D. Dujic, E. Levi, G. Serra, A. Tani, and L. Zarri, 'General Modulation Strategy for Seven-Phase Inverters With Independent Control of Multiple Voltage Space Vectors', *IEEE Trans. Ind. Electron.*, vol. 55, no. 5, pp. 1921–1932, May 2008.

[71] L. Zarri, M. Mengoni, A. Tani, G. Serra, and D. Casadei, 'Minimization of the Power Losses in IGBT Multiphase Inverters with Carrier-Based Pulsewidth Modulation', *IEEE Trans. Ind. Electron.*, vol. 57, no. 11, pp. 3695–3706, Nov. 2010.

[72] D. Casadei, M. Mengoni, G. Serra, A. Tani, and L. Zarri, 'A new carrier-based PWM strategy with minimum output current ripple for five-phase inverters', in *Proceedings of the 2011 14th European Conference on Power Electronics and Applications*, 2011, pp. 1–10.

[73] G. Carrasco and C. A. Silva, 'Space Vector PWM Method for Five-Phase Two-Level VSI With Minimum Harmonic Injection in the Overmodulation Region', *IEEE Trans. Ind. Electron.*, vol. 60, no. 5, pp. 2042–2053, May 2013.

[74] Ó. Lopez, J. Alvarez, J. Doval-Gandoy, and F. D. Freijedo, 'Multilevel Multiphase Space Vector PWM Algorithm', *IEEE Trans. Ind. Electron.*, vol. 55, no. 5, pp. 1933–1942, May 2008.

[75] O. Lopez, J. Alvarez, J. Doval-Gandoy, and F. D. Freijedo, 'Multilevel Multiphase Space Vector PWM Algorithm With Switching State Redundancy', *IEEE Trans. Ind. Electron.*, vol. 56, no. 3, pp. 792–804, Mar. 2009.

[76] E. A. R. E. Ariff, O. Dordevic, and M. Jones, 'A Space Vector PWM Technique for a Three-Level Symmetrical Six-Phase Drive', *IEEE Trans. Ind. Electron.*, vol. 64, no. 11, pp. 8396–8405, Nov. 2017.

[77] S. Moinoddin, H. Abu-Rub, A. Iqbal, S. M. Ahmed, O. Dordevic, and E. Levi, 'Space vector pulse-width modulation technique for an eleven-phase voltage source inverter with sinusoidal output voltage generation', *IET Power Electron.*, vol. 8, no. 6, pp. 1000–1008, 2015.

[78] P. S. N. de Silva, J. E. Fletcher, and B. W. Williams, 'Development of space vector modulation strategies for five phase voltage source inverters', in *Second International Conference on Power Electronics, Machines and Drives (PEMD 2004).*, 2004, vol. 2, pp. 650-655 Vol.2.

[79] G. Grandi, G. Serra, and A. Tani, 'Space vector modulation of a seven-phase voltage source inverter', in *International Symposium on Power Electronics, Electrical Drives, Automation and Motion, 2006. SPEEDAM 2006.*, 2006, pp. 1149–1156.

[80] H.-M. Ryu, J.-H. Kim, and S.-K. Sul, 'Analysis of multiphase space vector pulse-width modulation based on multiple d-q spaces concept', *IEEE Trans. Power Electron.*, vol. 20, no. 6, pp. 1364–1371, Nov. 2005.

[81] A. Lega, M. Mengoni, G. Serra, A. Tani, and L. Zarri, 'Space Vector Modulation for Multiphase Inverters Based on a Space Partitioning Algorithm', *IEEE Trans. Ind. Electron.*, vol. 56, no. 10, pp. 4119–4131, Oct. 2009.

[82] J. Prieto, F. Barrero, M. J. Durán, S. T. Marín, and M. A. Perales, 'SVM Procedure for$n$-Phase VSI With Low Harmonic Distortion in the Overmodulation Region', *IEEE Trans. Ind. Electron.*, vol. 61, no. 1, pp. 92–97, Jan. 2014.

[83] J. W. Kelly, E. G. Strangas, and J. M. Miller, 'Multiphase space vector pulse width modulation', *IEEE Trans. Energy Convers.*, vol. 18, no. 2, pp. 259–264, Jun. 2003.

[84] D. Dujic, M. Jones, and E. Levi, 'Space Vector PWM for Nine-Phase VSI with Sinusoidal Output Voltage Generation: Analysis and Implementation', in *IECON 2007 - 33rd Annual Conference of the IEEE Industrial Electronics Society*, 2007, pp. 1524–1529.

[85] D. Casadei, G. Serra, A. Tani, and L. Zarri, 'General Inverter Modulation Strategy for Multi-Phase Motor Drives', in *2007 IEEE International Symposium on Industrial Electronics*, 2007, pp. 1131–1137.

[86] A. M. Hava, R. J. Kerkman, and T. A. Lipo, 'A high-performance generalized discontinuous PWM algorithm', *IEEE Trans. Ind. Appl.*, vol. 34, no. 5, pp. 1059–1071, Sep. 1998.

[87] 'Wiley-IEEE Press: Pulse Width Modulation for Power Converters: Principles and Practice - D. Grahame Holmes, Thomas A. Lipo'. [Online]. Available: http://www.wiley.com/WileyCDA/WileyTitle/productCd-0471208140,miniSiteCd-IEEE2.html. [Accessed: 13-Dec-2018].

[88] J. W. Bennett, B. C. Mecrow, D. J. Atkinson, and G. J. Atkinson, 'Safety-critical design of electromechanical actuation systems in commercial aircraft', *IET Electr. Power Appl.*, vol. 5, no. 1, pp. 37–47, Jan. 2011.

[89] W. Leonhard, *Control of Electrical Drives*, 3rd ed. Berlin Heidelberg: Springer-Verlag, 2001.

[90] P. Vas, *Sensorless Vector and Direct Torque Control*. Oxford University Press, 1998.

[91] M. Mengoni *et al.*, 'Control of a fault-tolerant quadruple three-phase induction machine for More Electric Aircrafts', in *IECON 2016 - 42nd Annual Conference of the IEEE Industrial Electronics Society*, 2016, pp. 5747–5753.

[92] A. G. Yepes, J. Malvar, A. Vidal, O. López, and J. Doval-Gandoy, 'Current Harmonics Compensation Based on Multiresonant Control in Synchronous Frames for Symmetrical$n$-Phase Machines', *IEEE Trans. Ind. Electron.*, vol. 62, no. 5, pp. 2708–2720, May 2015.

[93] L. Hou, Y. Su, and L. Chen, 'DSP-based indirect rotor field oriented control for multiphase induction machines', in *IEEE International Electric Machines and Drives Conference, 2003. IEMDC'03.*, 2003, vol. 2, pp. 976–980 vol.2.

[94] S. N. Vukosavic, M. Jones, E. Levi, and J. Varga, 'Rotor flux oriented control of a symmetrical six-phase induction machine', *Electr. Power Syst. Res.*, vol. 75, no. 2, pp. 142–152, Aug. 2005.

[95] H. Xu, H. A. Toliyat, and L. J. Petersen, 'Five-phase induction motor drives with DSP-based control system', *IEEE Trans. Power Electron.*, vol. 17, no. 4, pp. 524–533, Jul. 2002.

[96] A. S. Abdel-Khalik, M. I. Masoud, and B. W. Williams, 'Improved Flux Pattern With Third Harmonic Injection for Multiphase Induction Machines', *IEEE Trans. Power Electron.*, vol. 27, no. 3, pp. 1563–1578, Mar. 2012.

[97] H.-M. Ryu, J.-W. Kim, and S.-K. Sul, 'Synchronous-frame current control of multiphase synchronous motor under asymmetric fault condition due to open phases', *IEEE Trans. Ind. Appl.*, vol. 42, no. 4, pp. 1062–1070, Jul. 2006.

[98] R. Bojoi, A. Tenconi, G. Griva, and F. Profumo, 'Vector Control of Dual-Three-Phase Induction-Motor Drives Using Two Current Sensors', *IEEE Trans. Ind. Appl.*, vol. 42, no. 5, pp. 1284–1292, Sep. 2006.

[99] R. Bojoi, G. Griva, and F. Profumo, 'Field Oriented Control of Dual Three-Phase Induction Motor Drives using a Luenberger Flux Observer', in *Conference Record of the 2006 IEEE Industry Applications Conference Forty-First IAS Annual Meeting*, 2006, vol. 3, pp. 1253–1260.

[100] R. Kianinezhad, B. Nahid-Mobarakeh, F. Betin, and G. A. Capolino, 'Sensorless field-oriented control for six-phase induction machines', in *Fourtieth IAS Annual Meeting. Conference Record of the 2005 Industry Applications Conference, 2005.*, 2005, vol. 2, pp. 999-1006 Vol. 2.

[101] L. Parsa and H. A. Toliyat, 'Five-phase permanent-magnet motor drives', *IEEE Trans. Ind. Appl.*, vol. 41, no. 1, pp. 30–37, Jan. 2005.

[102] R. Shi, H. A. Toliyat, and A. El-Antably, 'Field oriented control of five-phase synchronous reluctance motor drive with flexible 3/sup rd/ harmonic current injection for high specific torque', in *Conference Record of the 2001 IEEE Industry Applications Conference. 36th IAS Annual Meeting (Cat. No.01CH37248)*, 2001, vol. 3, pp. 2097–2103 vol.3.

[103] Y. Hu, Z. Zhu, and K. Liu, 'Current Control for Dual Three-Phase Permanent Magnet Synchronous Motors Accounting for Current Unbalance and Harmonics', *IEEE J. Emerg. Sel. Top. Power Electron.*, vol. 2, no. 2, pp. 272–284, Jun. 2014.

[104] L. Zheng, J. E. Fletcher, B. W. Williams, and X. He, 'Dual-Plane Vector Control of a Five-Phase Induction Machine for an Improved Flux Pattern', *IEEE Trans. Ind. Electron.*, vol. 55, no. 5, pp. 1996–2005, May 2008.

[105] M. Mengoni, L. Zarri, A. Tani, L. Parsa, G. Serra, and D. Casadei, 'High-Torque-Density Control of Multiphase Induction Motor Drives Operating Over a Wide Speed Range', *IEEE Trans. Ind. Electron.*, vol. 62, no. 2, pp. 814–825, Feb. 2015.

[106] R. I. Bojoi, G. Griva, V. Bostan, M. Guerriero, F. Farina, and F. Profumo, 'Current control strategy for power conditioners using sinusoidal signal integrators in synchronous reference frame', *IEEE Trans. Power Electron.*, vol. 20, no. 6, pp. 1402–1412, Nov. 2005.

[107] R. Bojoi, M. Lazzari, F. Profumo, and A. Tenconi, 'Digital field-oriented control for dual three-phase induction motor drives', *IEEE Trans. Ind. Appl.*, vol. 39, no. 3, pp. 752–760, May 2003.

[108] R. Bojoi, F. Profumo, and A. Tenconi, 'Digital synchronous frame current regulation for dual three-phase induction motor drives', in *IEEE 34th Annual Conference on Power Electronics Specialist, 2003. PESC '03.*, 2003, vol. 3, pp. 1475–1480 vol.3.

[109] G. K. Singh, K. Nam, and S. K. Lim, 'A simple indirect field-oriented control scheme for multiphase induction machine', *IEEE Trans. Ind. Electron.*, vol. 52, no. 4, pp. 1177–1184, Aug. 2005.

[110] R. Bojoi, F. Farina, M. Lazzari, F. Profumo, and A. Tenconi, 'Analysis of the asymmetrical operation of dual three-phase induction machines', in *IEEE International Electric Machines and Drives Conference, 2003. IEMDC'03.*, 2003, vol. 1, pp. 429–435 vol.1.

[111] M. J. Duran, E. Levi, and F. Barrero, 'Multiphase Electric Drives: Introduction', in *Wiley Encyclopedia of Electrical and Electronics Engineering*, Hoboken, NJ, USA: John Wiley & Sons, Inc., 2017, pp. 1–26.

[112] R. Bojoi, E. Levi, F. Farina, A. Tenconi, and F. Profumo, 'Dual three-phase induction motor drive with digital current control in the stationary reference frame', *IEE Proc. - Electr. Power Appl.*, vol. 153, no. 1, pp. 129–139, Jan. 2006.

[113] A. Tenconi, S. Rubino, and R. Bojoi, 'Model Predictive Control for Multiphase Motor Drives – a Technology Status Review', in *2018 International Power Electronics Conference (IPEC-Niigata 2018 -ECCE Asia)*, 2018, pp. 732–739.

[114] I. Takahashi and Y. Ohmori, 'High-performance direct torque control of an induction motor', *IEEE Trans. Ind. Appl.*, vol. 25, no. 2, pp. 257–264, Mar. 1989.

[115] G. S. Buja and M. P. Kazmierkowski, 'Direct torque control of PWM inverter-fed AC motors - a survey', *IEEE Trans. Ind. Electron.*, vol. 51, no. 4, pp. 744–757, Aug. 2004.

[116] T. G. Habetler, F. Profumo, M. Pastorelli, and L. M. Tolbert, 'Direct torque control of induction machines using space vector modulation', *IEEE Trans. Ind. Appl.*, vol. 28, no. 5, pp. 1045–1053, Sep. 1992.

[117] X. Kestelyn, E. Semail, and D. Loroil, 'Direct torque control of multi-phase permanent magnet synchronous motor drive: application to a five-phase', in *IEEE International Conference on Electric Machines and Drives, 2005.*, 2005, pp. 137–143.

[118] H. A. Toliyat and H. Xu, 'A novel direct torque control (DTC) method for five-phase induction machines', in *APEC 2000. Fifteenth Annual IEEE Applied Power Electronics Conference and Exposition (Cat. No.00CH37058)*, 2000, vol. 1, pp. 162–168 vol.1.

[119] L. Zheng, J. E. Fletcher, B. W. Williams, and X. He, 'A Novel Direct Torque Control Scheme for a Sensorless Five-Phase Induction Motor Drive', *IEEE Trans. Ind. Electron.*, vol. 58, no. 2, pp. 503–513, Feb. 2011.

[120] K. Hatua and V. T. Ranganathan, 'Direct torque control schemes for split-phase induction machine', *IEEE Trans. Ind. Appl.*, vol. 41, no. 5, pp. 1243–1254, Sep. 2005.

[121] F. Farina, R. Bojoi, A. Tenconi, and F. Profumo, 'Direct Torque Control with Full Order Stator Flux Observer for Dual-Three Phase Induction Motor Drives', *IEEJ Trans. Ind. Appl.*, vol. 126, no. 4, pp. 412–419, 2006.

[122] K. Marouani, F. Khoucha, A. Kheloui, L. Baghli, and D. Hadiouche, 'Study and Simulation of Direct Torque Control of Double-Star Induction Motor Drive', in *2006 12th International Power Electronics and Motion Control Conference*, 2006, pp. 1233–1238.

[123] R. Kianinezhad, B. Nahid, F. Betin, and G. A. Capolino, 'A novel Direct Torque Control (DTC) method for dual three phase induction motors', in *2006 IEEE International Conference on Industrial Technology*, 2006, pp. 939–943.

[124] A. Taheri, A. Rahmati, and S. Kaboli, 'Efficiency Improvement in DTC of Six-Phase Induction Machine by Adaptive Gradient Descent of Flux', *IEEE Trans. Power Electron.*, vol. 27, no. 3, pp. 1552–1562, Mar. 2012.

[125] A. Taheri, A. Rahmati, and S. Kaboli, 'Comparison of Efficiency for Different Switching Tables in Six-Phase Induction Motor DTC Drive', *J. Power Electron.*, vol. 12, pp. 128–135, Jan. 2012.

[126] J. K. Pandit, M. V. Aware, R. V. Nemade, and E. Levi, 'Direct Torque Control Scheme for a Six-Phase Induction Motor With Reduced Torque Ripple', *IEEE Trans. Power Electron.*, vol. 32, no. 9, pp. 7118–7129, Sep. 2017.

[127] R. Bojoi, F. Farina, G. Griva, F. Profumo, and A. Tenconi, 'Direct torque control for dual three-phase induction motor drives', *IEEE Trans. Ind. Appl.*, vol. 41, no. 6, pp. 1627–1636, Nov. 2005.

[128] M. Depenbrock, 'Direct self-control (DSC) of inverter-fed induction machine', *IEEE Trans. Power Electron.*, vol. 3, no. 4, pp. 420–429, Oct. 1988.

[129] R. Karampuri, J. Prieto, F. Barrero, and S. Jain, 'Extension of the DTC Technique to Multiphase Induction Motor Drives Using Any Odd Number of Phases', in *2014 IEEE Vehicle Power and Propulsion Conference (VPPC)*, 2014, pp. 1–6.

[130] G. Pellegrino, R. I. Bojoi, and P. Guglielmi, 'Unified Direct-Flux Vector Control for AC Motor Drives', *IEEE Trans. Ind. Appl.*, vol. 47, no. 5, pp. 2093–2102, Sep. 2011.

[131] S. A. Odhano, R. Bojoi, A. Boglietti, Ş. G. Roşu, and G. Griva, 'Maximum Efficiency per Torque Direct Flux Vector Control of Induction Motor Drives', *IEEE Trans. Ind. Appl.*, vol. 51, no. 6, pp. 4415–4424, Nov. 2015.

[132] G. Pellegrino, E. Armando, and P. Guglielmi, 'Direct Flux Field-Oriented Control of IPM Drives With Variable DC Link in the Field-Weakening Region', *IEEE Trans. Ind. Appl.*, vol. 45, no. 5, pp. 1619–1627, Sep. 2009.

[133] G. Pellegrino, E. Armando, and P. Guglielmi, 'Direct-Flux Vector Control of IPM Motor Drives in the Maximum Torque Per Voltage Speed Range', *IEEE Trans. Ind. Electron.*, vol. 59, no. 10, pp. 3780–3788, Oct. 2012.

[134] P. Cortes, M. P. Kazmierkowski, R. M. Kennel, D. E. Quevedo, and J. Rodriguez, 'Predictive Control in Power Electronics and Drives', *IEEE Trans. Ind. Electron.*, vol. 55, no. 12, pp. 4312–4324, Dec. 2008.

[135] P. Correa, M. Pacas, and J. Rodriguez, 'Predictive Torque Control for Inverter-Fed Induction Machines', *IEEE Trans. Ind. Electron.*, vol. 54, no. 2, pp. 1073–1079, Apr. 2007.

[136] F. Barrero, M. R. Arahal, R. Gregor, S. Toral, and M. J. Duran, 'A Proof of Concept Study of Predictive Current Control for VSI-Driven Asymmetrical Dual Three-Phase AC Machines', *IEEE Trans. Ind. Electron.*, vol. 56, no. 6, pp. 1937–1954, Jun. 2009.

[137] F. Barrero, M. R. Arahal, R. Gregor, S. Toral, and M. J. Duran, 'One-Step Modulation Predictive Current Control Method for the Asymmetrical Dual Three-Phase Induction Machine', *IEEE Trans. Ind. Electron.*, vol. 56, no. 6, pp. 1974–1983, Jun. 2009.

[138] R. Gregor *et al.*, 'Predictive-space vector PWM current control method for asymmetrical dual three-phase induction motor drives', *IET Electr. Power Appl.*, vol. 4, no. 1, pp. 26–34, Jan. 2010.

[139] M. J. Duran, J. Prieto, F. Barrero, and S. Toral, 'Predictive Current Control of Dual Three-Phase Drives Using Restrained Search Techniques', *IEEE Trans. Ind. Electron.*, vol. 58, no. 8, pp. 3253–3263, Aug. 2011.

[140] F. Barrero *et al.*, 'An Enhanced Predictive Current Control Method for Asymmetrical Six-Phase Motor Drives', *IEEE Trans. Ind. Electron.*, vol. 58, no. 8, pp. 3242–3252, Aug. 2011.

[141] J. A. Riveros, F. Barrero, E. Levi, M. J. Durán, S. Toral, and M. Jones, 'Variable-Speed Five-Phase Induction Motor Drive Based on Predictive Torque Control', *IEEE Trans. Ind. Electron.*, vol. 60, no. 8, pp. 2957–2968, Aug. 2013.

[142] M. J. Duran, J. A. Riveros, F. Barrero, H. Guzman, and J. Prieto, 'Reduction of Common-Mode Voltage in Five-Phase Induction Motor Drives Using Predictive Control Techniques', *IEEE Trans. Ind. Appl.*, vol. 48, no. 6, pp. 2059–2067, Nov. 2012.

[143] C. S. Lim, E. Levi, M. Jones, N. A. Rahim, and W. P. Hew, 'FCS-MPC-Based Current Control of a Five-Phase Induction Motor and its Comparison with PI-PWM Control', *IEEE Trans. Ind. Electron.*, vol. 61, no. 1, pp. 149–163, Jan. 2014.

[144] H. Guzman, M. J. Duran, F. Barrero, B. Bogado, and S. Toral, 'Speed Control of Five-Phase Induction Motors With Integrated Open-Phase Fault Operation Using Model-Based Predictive Current Control Techniques', *IEEE Trans. Ind. Electron.*, vol. 61, no. 9, pp. 4474–4484, Sep. 2014.

[145] H. Guzman, F. Barrero, and M. J. Duran, 'IGBT-Gating Failure Effect on a Fault-Tolerant Predictive Current-Controlled Five-Phase Induction Motor Drive', *IEEE Trans. Ind. Electron.*, vol. 62, no. 1, pp. 15–20, Jan. 2015.

[146] H. Guzman *et al.*, 'Comparative Study of Predictive and Resonant Controllers in Fault-Tolerant Five-Phase Induction Motor Drives', *IEEE Trans. Ind. Electron.*, vol. 63, no. 1, pp. 606–617, Jan. 2016.

[147] C. Martín, M. R. Arahal, F. Barrero, and M. J. Durán, 'Five-Phase Induction Motor Rotor Current Observer for Finite Control Set Model Predictive Control of Stator Current', *IEEE Trans. Ind. Electron.*, vol. 63, no. 7, pp. 4527–4538, Jul. 2016.

[148] M. Cheng, F. Yu, K. T. Chau, and W. Hua, 'Dynamic Performance Evaluation of a Nine-Phase Flux-Switching Permanent-Magnet Motor Drive With Model Predictive Control', *IEEE Trans. Ind. Electron.*, vol. 63, no. 7, pp. 4539–4549, Jul. 2016.

[149] J. Rodas, F. Barrero, M. R. Arahal, C. Martín, and R. Gregor, 'Online Estimation of Rotor Variables in Predictive Current Controllers: A Case Study Using Five-Phase Induction Machines', *IEEE Trans. Ind. Electron.*, vol. 63, no. 9, pp. 5348–5356, Sep. 2016.

[150] J. Rodas, C. Martín, M. R. Arahal, F. Barrero, and R. Gregor, 'Influence of Covariance-Based ALS Methods in the Performance of Predictive Controllers With Rotor Current Estimation', *IEEE Trans. Ind. Electron.*, vol. 64, no. 4, pp. 2602–2607, Apr. 2017.

[151] C. Xue, W. Song, and X. Feng, 'Finite control-set model predictive current control of five-phase permanent-magnet synchronous machine based on virtual voltage vectors', *IET Electr. Power Appl.*, vol. 11, no. 5, pp. 836–846, 2017.

[152] I. Gonzalez-Prieto, M. J. Duran, J. J. Aciego, C. Martin, and F. Barrero, 'Model Predictive Control of Six-Phase Induction Motor Drives Using Virtual Voltage Vectors', *IEEE Trans. Ind. Electron.*, vol. 65, no. 1, pp. 27–37, Jan. 2018.

[153] H. Lu, J. Li, R. Qu, L. Xiao, and D. Ye, 'Reduction of unbalanced axial magnetic force in post-fault operation of a novel six-phase double-stator axial

flux PM machine using model predictrive control', in *2016 IEEE Energy Conversion Congress and Exposition (ECCE)*, 2016, pp. 1–8.

[154] I. González-Prieto, M. J. Duran, N. Rios-Garcia, F. Barrero, and C. Martín, 'Open-Switch Fault Detection in Five-Phase Induction Motor Drives Using Model Predictive Control', *IEEE Trans. Ind. Electron.*, vol. 65, no. 4, pp. 3045–3055, Apr. 2018.

[155] M. Salehifar and M. Moreno-Equilaz, 'Fault diagnosis and fault-tolerant finite control set-model predictive control of a multiphase voltage-source inverter supplying BLDC motor', *ISA Trans.*, vol. 60, pp. 143–155, Jan. 2016.

[156] R. Salehi Arashloo, M. Salehifar, L. Romeral, and V. Sala, 'A robust predictive current controller for healthy and open-circuit faulty conditions of five-phase BLDC drives applicable for wind generators and electric vehicles', *Energy Convers. Manag.*, vol. 92, pp. 437–447, Mar. 2015.

[157] J. L. R. Martinez, R. S. Arashloo, M. Salehifar, and J. M. Moreno, 'Predictive current control of outer-rotor five-phase BLDC generators applicable for off-shore wind power plants', *Electr. Power Syst. Res.*, vol. 121, pp. 260–269, Apr. 2015.

[158] M. Salehifar, M. Moreno-Eguilaz, G. Putrus, and P. Barras, 'Simplified fault tolerant finite control set model predictive control of a five-phase inverter supplying BLDC motor in electric vehicle drive', *Electr. Power Syst. Res.*, vol. 132, pp. 56–66, Mar. 2016.

[159] M. R. Arahal, F. Barrero, S. Toral, M. Duran, and R. Gregor, 'Multi-phase current control using finite-state model-predictive control', *Control Eng. Pract.*, vol. 17, no. 5, pp. 579–587, May 2009.

[160] C. Martín, M. R. Arahal, F. Barrero, and M. J. Durán, 'Multiphase rotor current observers for current predictive control: A five-phase case study', *Control Eng. Pract.*, vol. 49, pp. 101–111, Apr. 2016.

[161] C. Martín, M. Bermúdez, F. Barrero, M. R. Arahal, X. Kestelyn, and M. J. Durán, 'Sensitivity of predictive controllers to parameter variation in five-phase induction motor drives', *Control Eng. Pract.*, vol. 68, pp. 23–31, Nov. 2017.

[162] H. Guzmán, M. J. Durán, and F. Barrero, 'Speed control of five-phase induction motor drives with an open phase fault condition and predictive current control methods', in *IECON 2012 - 38th Annual Conference on IEEE Industrial Electronics Society*, 2012, pp. 3647–3652.

[163] C. S. Lim, E. Levi, M. Jones, N. A. Rahim, and W. P. Hew, 'Experimental evaluation of model predictive current control of a five-phase induction motor using all switching states', in *2012 15th International Power Electronics and Motion Control Conference (EPE/PEMC)*, 2012, p. LS1c.4-1-LS1c.4-7.

[164] A. Iqbal, R. Alammari, M. Mosa, and H. Abu-Rub, 'Finite set model predictive current control with reduced and constant common mode voltage for a five-phase voltage source inverter', in *2014 IEEE 23rd International Symposium on Industrial Electronics (ISIE)*, 2014, pp. 479–484.

[165] C. Xue, W. Song, and X. Feng, 'Model predictive current control schemes for five-phase permanent-magnet synchronous machine based on SVPWM', in *2016 IEEE 8th International Power Electronics and Motion Control Conference (IPEMC-ECCE Asia)*, 2016, pp. 648–653.

[166] D. Winterborne and V. Pickert, 'Improving direct instantaneous torque control of switched reluctance machines with predictive flux constraints', in *8th IET International Conference on Power Electronics, Machines and Drives (PEMD 2016)*, 2016, pp. 1–6.

[167] H. J. Brauer, M. D. Hennen, and R. W. D. Doncker, 'Multiphase Torque-Sharing Concepts of Predictive PWM-DITC for SRM', in *2007 7th International Conference on Power Electronics and Drive Systems*, 2007, pp. 511–516.

[168] B. Bogado, F. Barrero, M. R. Arahal, S. Toral, and E. Levi, 'Sensitivity to electrical parameter variations of Predictive Current Control in multiphase drives', in *IECON 2013 - 39th Annual Conference of the IEEE Industrial Electronics Society*, 2013, pp. 5215–5220.

[169] J. S. Lee, C. Choi, J. Seok, and R. D. Lorenz, 'Deadbeat-Direct Torque and Flux Control of Interior Permanent Magnet Synchronous Machines With Discrete Time Stator Current and Stator Flux Linkage Observer', *IEEE Trans. Ind. Appl.*, vol. 47, no. 4, pp. 1749–1758, Jul. 2011.

[170] C. Choi, J. Seok, and R. D. Lorenz, 'Wide-Speed Direct Torque and Flux Control for Interior PM Synchronous Motors Operating at Voltage and Current Limits', *IEEE Trans. Ind. Appl.*, vol. 49, no. 1, pp. 109–117, Jan. 2013.

[171] J. Apsley and S. Williamson, 'Analysis of multiphase induction machines with winding faults', *IEEE Trans. Ind. Appl.*, vol. 42, no. 2, pp. 465–472, Mar. 2006.

[172] L. Zarri *et al.*, 'Behavior of multiphase induction machines with unbalanced stator windings', in *8th IEEE Symposium on Diagnostics for Electrical Machines, Power Electronics Drives*, 2011, pp. 84–91.

[173] L. Zarri *et al.*, 'Detection and Localization of Stator Resistance Dissymmetry Based on Multiple Reference Frame Controllers in Multiphase Induction Motor Drives', *IEEE Trans. Ind. Electron.*, vol. 60, no. 8, pp. 3506–3518, Aug. 2013.

[174] D. Foito, J. Maia, V. Fernão Pires, and J. F. Martins, 'Fault diagnosis in six-phase induction motor using a current trajectory mass center', *Measurement*, vol. 51, pp. 164–173, May 2014.

[175] M. Salehifar, R. S. Arashloo, J. M. Moreno-Equilaz, V. Sala, and L. Romeral, 'Fault Detection and Fault Tolerant Operation of a Five Phase PM Motor Drive Using Adaptive Model Identification Approach', *IEEE J. Emerg. Sel. Top. Power Electron.*, vol. 2, no. 2, pp. 212–223, Jun. 2014.

[176] R. N. Andriamalala, H. Razik, G. Didier, F. M. Sargos, C. r D. Silva, and E. r c D. Silva, 'A Model of Dual Stator Winding Induction Machine in case of Stator and Rotor Faults for Diagnosis Purpose', in *Conference Record of the 2006 IEEE Industry Applications Conference Forty-First IAS Annual Meeting*, 2006, vol. 5, pp. 2340–2345.

[177] H. Razik *et al.*, 'A model of double star induction motors under rotor bar defect for diagnosis purpose', in *2005 IEEE International Conference on Industrial Technology*, 2005, pp. 197–202.

[178] M. A. Fnaiech, F. Betin, G. Capolino, and F. Fnaiech, 'Fuzzy Logic and Sliding-Mode Controls Applied to Six-Phase Induction Machine With Open Phases', *IEEE Trans. Ind. Electron.*, vol. 57, no. 1, pp. 354–364, Jan. 2010.

[179] J. M. Apsley, 'Open-circuit fault mitigation for multiphase induction motors with a unified control structure', in *5th IET International Conference on Power Electronics, Machines and Drives (PEMD 2010)*, 2010, pp. 1–6.

[180] A. Tani, M. Mengoni, L. Zarri, G. Serra, and D. Casadei, 'Control of Multiphase Induction Motors With an Odd Number of Phases Under Open-Circuit Phase Faults', *IEEE Trans. Power Electron.*, vol. 27, no. 2, pp. 565–577, Feb. 2012.

[181] J.-R. Fu and T. A. Lipo, 'Disturbance-free operation of a multiphase current-regulated motor drive with an opened phase', *IEEE Trans. Ind. Appl.*, vol. 30, no. 5, pp. 1267–1274, Sep. 1994.

[182] L. Alberti and N. Bianchi, 'Experimental Tests of Dual Three-Phase Induction Motor Under Faulty Operating Condition', *IEEE Trans. Ind. Electron.*, vol. 59, no. 5, pp. 2041–2048, May 2012.

[183] A. S. Abdel-Khalik, M. I. Masoud, S. Ahmed, and A. Massoud, 'Calculation of derating factors based on steady-state unbalanced multiphase induction machine model under open phase(s) and optimal winding currents', *Electr. Power Syst. Res.*, vol. 106, pp. 214–225, Jan. 2014.

[184] S. Dwari and L. Parsa, 'An Optimal Control Technique for Multiphase PM Machines Under Open-Circuit Faults', *IEEE Trans. Ind. Electron.*, vol. 55, no. 5, pp. 1988–1995, May 2008.

[185] N. Bianchi, S. Bolognani, and M. D. Pre, 'Strategies for the Fault-Tolerant Current Control of a Five-Phase Permanent-Magnet Motor', *IEEE Trans. Ind. Appl.*, vol. 43, no. 4, pp. 960–970, Jul. 2007.

[186] A. Mohammadpour and L. Parsa, 'Global Fault-Tolerant Control Technique for Multiphase Permanent-Magnet Machines', *IEEE Trans. Ind. Appl.*, vol. 51, no. 1, pp. 178–186, Jan. 2015.

[187] F. Baudart, B. Dehez, E. Matagne, D. Telteu-Nedelcu, P. Alexandre, and F. Labrique, 'Torque Control Strategy of Polyphase Permanent-Magnet Synchronous Machines With Minimal Controller Reconfiguration Under Open-Circuit Fault of One Phase', *IEEE Trans. Ind. Electron.*, vol. 59, no. 6, pp. 2632–2644, Jun. 2012.

[188] A. Mohammadpour and L. Parsa, 'A Unified Fault-Tolerant Current Control Approach for Five-Phase PM Motors With Trapezoidal Back EMF Under Different Stator Winding Connections', *IEEE Trans. Power Electron.*, vol. 28, no. 7, pp. 3517–3527, Jul. 2013.

[189] Z. Sun, J. Wang, G. W. Jewell, and D. Howe, 'Enhanced Optimal Torque Control of Fault-Tolerant PM Machine Under Flux-Weakening Operation', *IEEE Trans. Ind. Electron.*, vol. 57, no. 1, pp. 344–353, Jan. 2010.

[190] A. A. A. Hafez, R. Todd, A. J. Forsyth, and A. M. Cross, 'Direct current ripple compensation for multi-phase fault-tolerant machines', *IET Electr. Power Appl.*, vol. 5, no. 1, pp. 28–36, Jan. 2011.

[191] X. Kestelyn and E. Semail, 'A Vectorial Approach for Generation of Optimal Current References for Multiphase Permanent-Magnet Synchronous Machines in Real Time', *IEEE Trans. Ind. Electron.*, vol. 58, no. 11, pp. 5057–5065, Nov. 2011.

[192] N. K. Nguyen, F. Meinguet, E. Semail, and X. Kestelyn, 'Fault-Tolerant Operation of an Open-End Winding Five-Phase PMSM Drive With Short-Circuit Inverter Fault', *IEEE Trans. Ind. Electron.*, vol. 63, no. 1, pp. 595–605, Jan. 2016.

[193] H. Xu, H. A. Toliyat, and L. J. Petersen, 'Resilient current control of five-phase induction motor under asymmetrical fault conditions', in *APEC. Seventeenth Annual IEEE Applied Power Electronics Conference and Exposition (Cat. No.02CH37335)*, 2002, vol. 1, pp. 64–71 vol.1.

[194] L. Zheng, J. E. Fletcher, and B. W. Williams, 'Current optimization for a murti-phase machine under an open circuit phase faur condition', in *The 3rd IET International Conference on Power Electronics, Machines and Drives, 2006. PEMD 2006*, 2006, pp. 414–419.

[195] L. Parsa and H. A. Toliyat, 'Fault-tolerant five-phase permanent magnet motor drives', in *Conference Record of the 2004 IEEE Industry Applications Conference, 2004. 39th IAS Annual Meeting.*, 2004, vol. 2, pp. 1048–1054 vol.2.

[196] C. B. Jacobina, I. S. Freitas, T. M. Oliveira, E. R. C. da Silva, and A. M. N. Lima, 'Fault tolerant control of five-phase AC motor drive', in *2004 IEEE 35th Annual Power Electronics Specialists Conference (IEEE Cat. No.04CH37551)*, 2004, vol. 5, pp. 3486-3492 Vol.5.

[197] R. Kianinezhad, B. Nahid-Mobarakeh, L. Baghli, F. Betin, and G. A. Capolino, 'Torque Ripples Suppression for Six-Phase Induction Motors Under Open Phase Faults', in *IECON 2006 - 32nd Annual Conference on IEEE Industrial Electronics*, 2006, pp. 1363–1368.

[198] J. Wang, K. Atallah, and D. Howe, 'Optimal torque control of fault-tolerant permanent magnet brushless machines', *IEEE Trans. Magn.*, vol. 39, no. 5, pp. 2962–2964, Sep. 2003.

[199] B. C. Mecrow, A. G. Jack, J. A. Haylock, and J. Coles, 'Fault-tolerant permanent magnet machine drives', *IEE Proc. - Electr. Power Appl.*, vol. 143, no. 6, pp. 437–442, Nov. 1996.

[200] N. Bianchi, E. Fornasiero, and S. Bolognani, 'Thermal Analysis of a Five-Phase Motor Under Faulty Operations', *IEEE Trans. Ind. Appl.*, vol. 49, no. 4, pp. 1531–1538, Jul. 2013.

[201] S. Dwari and L. Parsa, 'Fault-Tolerant Control of Five-Phase Permanent-Magnet Motors With Trapezoidal Back EMF', *IEEE Trans. Ind. Electron.*, vol. 58, no. 2, pp. 476–485, Feb. 2011.

[202] R. S. Arashloo, J. L. R. Martinez, M. Salehifar, and M. Moreno-Eguilaz, 'Genetic algorithm-based output power optimisation of fault tolerant five-phase brushless direct current drives applicable for electrical and hybrid electrical vehicles', *IET Electr. Power Appl.*, vol. 8, no. 7, pp. 267–277, Aug. 2014.

[203] R. Kianinezhad, B. Nahid-Mobarakeh, L. Baghli, F. Betin, and G. Capolino, 'Modeling and Control of Six-Phase Symmetrical Induction Machine Under Fault Condition Due to Open Phases', *IEEE Trans. Ind. Electron.*, vol. 55, no. 5, pp. 1966–1977, May 2008.

[204] M. Deilamani, R. Kianinezhad, S. G. H. Seifossadat, and M. Keramatzade, 'A new insight into six phase induction machine modeling under open phase fault condition', in *International Aegean Conference on Electrical Machines and Power Electronics and Electromotion, Joint Conference*, 2011, pp. 201–204.

[205] H. Guzmán, M. J. Durán, and F. Barrero, 'A comprehensive fault analysis of a five-phase induction motor drive with an open phase', in *2012 15th International Power Electronics and Motion Control Conference (EPE/PEMC)*, 2012, p. LS5b.3-1-LS5b.3-6.

Chapter 2

MODELING OF MULTIPLE THREE-PHASE INDUCTION MACHINE

Table of Contents

List of Figures

List of Tables

In this chapter, a general Multi-Stator (MS) model of a multiple three-phase induction machine is reported. The machine uses sinusoidal distribution of windings and a squirrel cage rotor. The proposed MS modelling is defined for a machine having an arbitrary number of three-phase winding sets. In addition, to deal with the most generic case, the stator parameters of the three-phase sets are considered different from each other.

Finally, a comparison with the results obtained by means of the Vector Space Decomposition (VSD) approach is reported. In this way, it will be shown why the MS approach results very convenient for the implementation of modular drive control schemes.

2.1 Multi-Stator (MS) modelling approach

A generic multiple three-phase induction machine (IM) with the following hypotheses is considered (Fig. 2. 1):

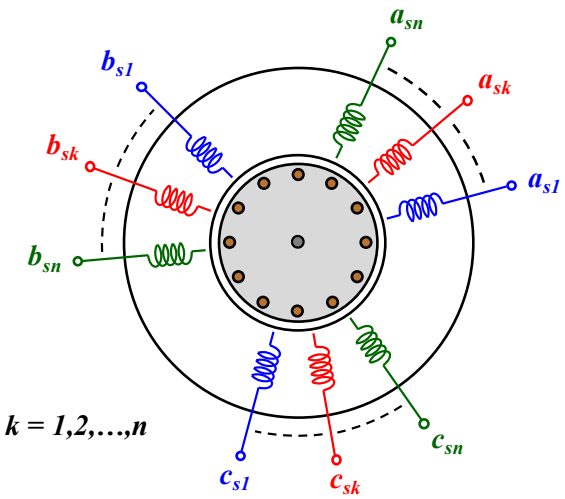

Fig. 2. 1. Multiple three-phase squirrel cage induction machine.

1) The stator is composed by n three-phase winding sets with arbitrary angle displacements;
2) Each three-phase winding set is composed by identical single-phase windings with sinusoidal distribution and with a reciprocal angle displacement of 120° electrical degrees;
3) Squirrel cage rotor modelled as an equivalent three-phase winding composed by identical single-phase windings with sinusoidal distribution and with a reciprocal angle displacement of 120° electrical degrees;
4) Ideal iron characterized by the absence of losses and magnetic saturation phenomena;
5) The air gap thickness is considered uniform, thus neglecting the presence of both stator slots and rotor cage;
6) Full decoupling between the leakage fluxes for both stator and rotor windings.

2.1.1 Electromechanical model in phase coordinates

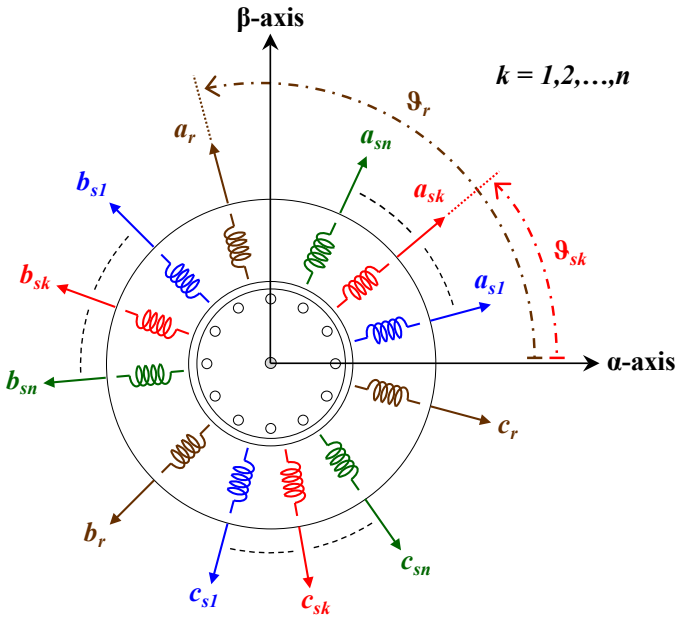

Fig. 2. 2. Equivalent MS magnetic scheme of a multiple three-phase squirrel cage induction machine.

With reference to the starting hypotheses 1)-6), it is possible to consider the machine scheme shown in Fig. 2. 2. For each three-phase winding set the magnetic axes belonging to phases are highlighted. In addition, the following assumptions are considered:

- Each three-phase winding set is identified by means the position of the magnetic axis belonging to the first phase. This axis is conventionally indicated with the letter "*a*".
- The position of the magnetic axis belonging to the first phase of each three-phase winding set is indicated with the letter "ϑ". The position of each magnetic axis is defined with respect to a stationary (α,β) frame. In detail, this angle is computed with respect to the α-axis by considering an anticlockwise rotation direction.
- The position of the magnetic axis belonging to each stator winding is invariant. Conversely, the position of the magnetic axis belonging to the first phase of the rotor winding corresponds with the real electrical rotor position ϑ_r.

According with the above assumptions, the positions of the magnetic axes belonging to the phases of a generic three-phase stator *k*-set is expressed as follows:

$$\begin{bmatrix} \vartheta_{sk-a} \\ \vartheta_{sk-b} \\ \vartheta_{sk-c} \end{bmatrix} = \begin{bmatrix} \vartheta_{sk-a} \\ \vartheta_{sk-a} + \frac{2\pi}{3} \\ \vartheta_{sk-a} - \frac{2\pi}{3} \end{bmatrix} = \begin{bmatrix} \vartheta_{sk} \\ \vartheta_{sk} + \frac{2\pi}{3} \\ \vartheta_{sk} - \frac{2\pi}{3} \end{bmatrix} \tag{2.1}$$

Similarly, the positions of the magnetic axes belonging to the phases of the three-phase rotor winding is expressed as follows:

$$\begin{bmatrix} \vartheta_{r-a} \\ \vartheta_{r-b} \\ \vartheta_{r-c} \end{bmatrix} = \begin{bmatrix} \vartheta_{r-a} \\ \vartheta_{r-a} + \frac{2\pi}{3} \\ \vartheta_{r-a} - \frac{2\pi}{3} \end{bmatrix} = \begin{bmatrix} \vartheta_{r} \\ \vartheta_{r} + \frac{2\pi}{3} \\ \vartheta_{r} - \frac{2\pi}{3} \end{bmatrix} \tag{2.2}$$

Finally, the position of the stationary α-axis is conventionally made coincident with the magnetic axis belonging to the first phase of the first set. This condition is expressed as follows:

$$\vartheta_{s1-a} = \vartheta_{s1} = 0 \tag{2.3}$$

With reference to the unified theory of the electrical machines [1], the electromagnetic model of any multiphase machine in the continuous time-domain is described by the following equation systems:

- Stator magnetic model
- Rotor magnetic model
- Stator electric model
- Rotor electric model

The complete description of both magnetic and electric models is following reported. Once the electromagnetic model of the machine is computed, it is possible to define the electromechanical energy conversion relationships.

Stator magnetic model in phase coordinates

The stator magnetic model consists of the equation system containing all the current-to-flux relationships of the stator phases. For a multiple three-phase machine, the number of stator phases is a multiple of three and it depends by the number of winding sets *n*. Therefore, the stator magnetic model is composed by $3 \cdot n$ equations. Each of these describes the relationship between the flux linkage of a specific phase winding as a function of the all machine currents. Thanks to the magnetic linearity hypothesis 4), it is possible to apply the superposition principle. Therefore, the flux linkage contribution related to each machine current can be computed separately. In addition, according with hypothesis 6), there are not magnetic mutual leakage phenomena between the stator phases. Consequently, the magnetic model of each three-phase stator *k*-set is expressed as follows:

$$\begin{bmatrix} \lambda_{sk-a} \\ \lambda_{sk-b} \\ \lambda_{sk-c} \end{bmatrix} = L_{l,sk} \cdot \begin{bmatrix} i_{sk-a} \\ i_{sk-b} \\ i_{sk-c} \end{bmatrix} + \sum_{z=1}^{n} \left(\left[M_{sk-sz} \right] \cdot \begin{bmatrix} i_{sz-a} \\ i_{sz-b} \\ i_{sz-c} \end{bmatrix} \right) + \left[M_{sk-r} \right] \cdot \begin{bmatrix} i_{r-a} \\ i_{r-b} \\ i_{r-c} \end{bmatrix} \tag{2.4}$$

where:

- $\left[\lambda_{sk-a} \quad \lambda_{sk-b} \quad \lambda_{sk-c}\right]^t$ is the vector of the stator fluxes linkage for the three-phase *k*-set defined in the own stator phase coordinates $(abc)_k$;
- $\left[i_{sk-a} \quad i_{sk-b} \quad i_{sk-c}\right]^t$ is the vector of the stator currents for the three-phase *k*-set defined in the own stator phase coordinates $(abc)_k$;
- $\left[i_{sz-a} \quad i_{sz-b} \quad i_{sz-c}\right]^t$ is the vector of the stator currents for the three-phase *z*-set defined in the own stator phase coordinates $(abc)_z$;
- $\left[i_{r-a} \quad i_{r-b} \quad i_{r-c}\right]^t$ is the vector of the rotor currents for the three-phase rotor set defined in the own rotor phase coordinates $(abc)_r$;

while:

- $L_{l,sk}$ is the self-leakage phase inductance for the three-phase *k*-set;
- $\left[M_{sk-sz}\right]$ is the 3×3 mutual magnetizing inductance matrix between the stator phase windings of *k*-set and the stator phase windings of the *z*-set;
- $\left[M_{sk-r}\right]$ is the 3×3 mutual magnetizing inductance matrix between the stator phase windings of *k*-set and the rotor phase windings.

With reference to (2.4), the mutual magnetizing inductance matrices $\left[M_{sk-sz}\right]$ and $\left[M_{sk-r}\right]$ must be computed. In detail, it is necessary to define the relationship for the computation of the mutual magnetizing inductance between two generic phase windings of the machine.

Mutual magnetizing inductance between two generic phase windings

Two generic phase windings '*x*' and '*y*' are considered. With reference to the electromagnetic theory [1], the definition of mutual magnetizing inductance is the following:

$$M_{y-x} = \left.\frac{\lambda_{y-x}}{i_x}\right|_{i_y=0} = M_{x-y} = \left.\frac{\lambda_{x-y}}{i_y}\right|_{i_x=0} \tag{2.5}$$

The Equation (2.5) must be interpreted as follows. The mutual magnetizing inductance M_{y-x} is related to the flux linkage λ_{y-x} of the '*y*' phase winding caused by the current injection i_x in the '*x*' phase-winding. Similarly, the mutual magnetizing inductance M_{x-y} is related to the flux linkage λ_{x-y} of the '*x*' phase winding caused by the current injection i_y in the '*y*' phase-winding.

The computation of the mutual magnetizing inductance M_{y-x} is performed by using the scheme shown in Fig. 2. 3.

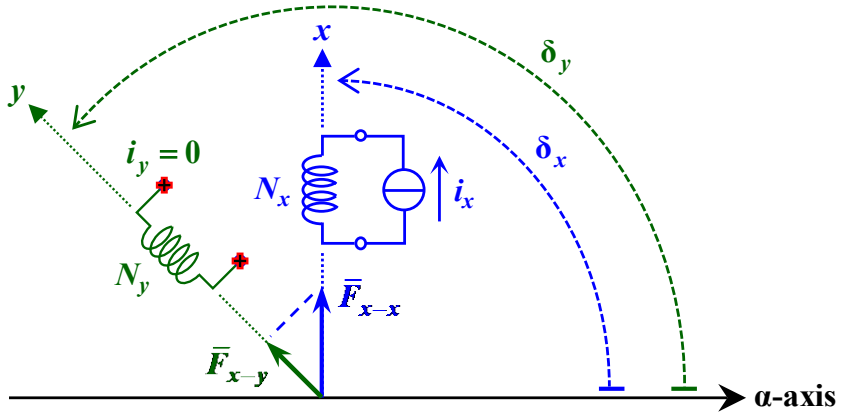

Fig. 2. 3. Scheme for the computation of the mutual magnetizing inductance $M_{y\text{-}x}$.

The current injection i_x in the 'x' phase winding generates a magnetomotive force vector $\overline{F}_{x-x}$ which is aligned with the magnetic x-axis. The amplitude of the magnetomotive force vector F_{x-x} is computed as follows:

$$F_{x-x} = \left|\overline{F}_{x-x}\right| = N_x \cdot i_x \tag{2.6}$$

where N_x represents the number of turns of the 'x' phase-winding. According with the initial assumptions, the position δ_x of the magnetic axis belonging to the 'x' phase winding is computed with respect to the stationary α-axis. The amplitude value in (2.6) can be also negative depending by the sign of the current i_x.

Concerning the magnetic effects on the 'y' phase winding, they can be evaluated through the computation of the magnetomotive force acting on the magnetic 'y' axis. By indicating with δ_y the position of the magnetic axis belonging to the 'y' phase winding, the projection F_{y-x} of the magnetomotive force vector $\overline{F}_{x-x}$ on such axis is computed as follows:

$$F_{y-x} = \left|\overline{F}_{y-x}\right| = F_{x-x} \cdot \cos\left(\delta_y - \delta_x\right) = N_x \cdot i_x \cdot \cos\left(\delta_y - \delta_x\right) \tag{2.7}$$

Thanks to hypotheses 4)-5), the machine structure can be considered magnetically isotropic, leading to a unique value of equivalent air gap magnetic reluctance $\Re_{eq}$, as shown in Fig. 2. 4. Therefore, the magnetic flux ϕ_{y-x} generated by the magnetomotive force vector $\overline{F}_{x-x}$ along the magnetic 'y' axis is computed as follows:

$$\phi_{y-x} = \left|\overline{\phi}_{y-x}\right| = \frac{F_{y-x}}{\Re_{eq}} = \frac{N_x \cdot i_x}{\Re_{eq}} \cdot \cos\left(\delta_y - \delta_x\right) \tag{2.8}$$

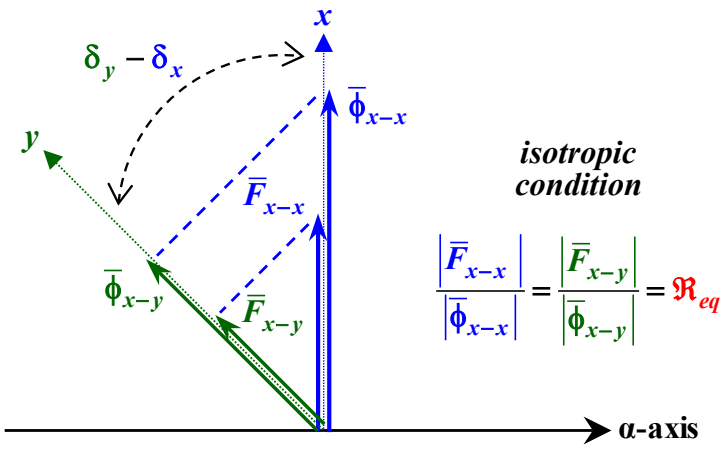

Fig. 2. 4. Scheme for the computation of the magnetic fluxes.

Finally, the flux linkage λ_{y-x} of the 'y' phase winding, caused by the current injection i_x in the 'x' phase-winding, is computed as follows:

$$\lambda_{y-x} = N_y \cdot \phi_{y-x} = \frac{N_x \cdot N_y}{\Re_{eq}} \cdot i_x \cdot \cos\left(\delta_y - \delta_x\right) \tag{2.9}$$

where N_y represents the number of turns of the 'y' phase winding.

Therefore, according with (2.5), the mutual magnetizing inductance between the phase windings 'x' and 'y' is computed as follows:

$$M_{y-x} = \left.\frac{\lambda_{y-x}}{i_x}\right|_{i_y=0} = \frac{N_x \cdot N_y}{\Re_{eq}} \cdot \cos\left(\delta_y - \delta_x\right) \tag{2.10}$$

The cosine is an even function. Therefore, the mutual magnetizing inductance does not depend by the phase winding in which the current injection is performed, leading to the following result:

$$M_{y-x} = \frac{N_x \cdot N_y}{\Re_{eq}} \cdot \cos\left(\delta_x - \delta_y\right) = \frac{N_x \cdot N_y}{\Re_{eq}} \cdot \cos\left(\delta_y - \delta_x\right) = M_{x-y} \tag{2.11}$$

By means of (2.11), the matrices $\left[M_{sk-sz}\right]$ and $\left[M_{sk-r}\right]$ can be computed, leading to the computation of the stator magnetic model of the machine.

Mutual magnetizing inductance matrix between two generic three-phase windings

Two generic three-phase windings 'x' and 'y' are considered. The application of (2.11) requires the computation of the angular differences among the magnetic axes belonging to 'x' and 'y' winding sets, as shown in Fig. 2. 5. According with (2.1), the angular difference among two generic magnetic axes can be defined using the positions of the magnetic axes of the first phases belonging to each winding set, as shown in Table 2. 1.

set x / set y	$a_y \to \vartheta_y$	$b_y \to \vartheta_y + 2\pi/3$	$c_y \to \vartheta_y + 4\pi/3$
$a_x \to \vartheta_x$	$\vartheta_x - \vartheta_y$	$\vartheta_x - \vartheta_y - 2\pi/3$	$\vartheta_x - \vartheta_y - 4\pi/3$
$b_x \to \vartheta_x + 2\pi/3$	$\vartheta_x - \vartheta_y + 2\pi/3$	$\vartheta_x - \vartheta_y$	$\vartheta_x - \vartheta_y - 2\pi/3$
$c_x \to \vartheta_x + 4\pi/3$	$\vartheta_x - \vartheta_y + 4\pi/3$	$\vartheta_x - \vartheta_y + 2\pi/3$	$\vartheta_x - \vartheta_y$

Table 2. 1. Angular differences among the magnetic axes belonging to '*x*' and '*y*' winding sets.

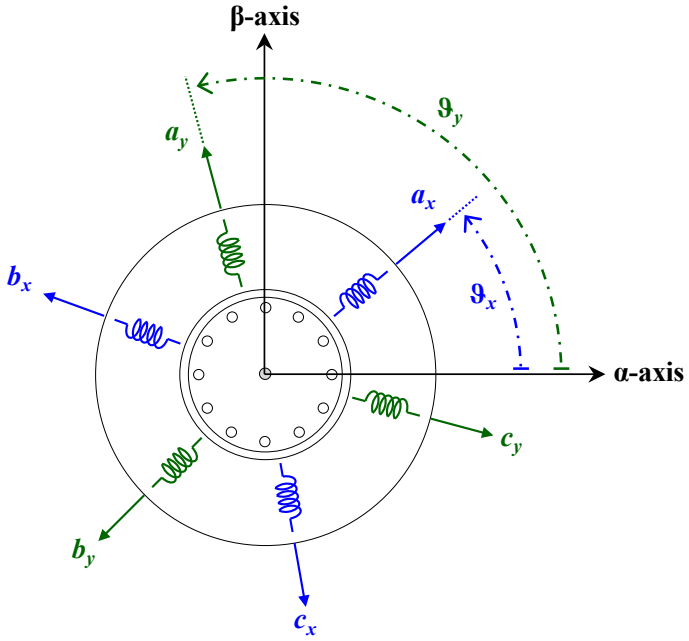

Fig. 2. 5. Scheme for the computation of the mutual magnetizing inductance matrix between two generic '*x*' and '*y*' three-phase windings.

According with hypothesis 2), each three-phase winding set is characterized by a unique number of turns. As a consequence, the phase windings belonging to the '*x*' set are characterized by N_x turns. Similarly, the phase windings belonging to the '*y*' set are characterized by N_y turns.

Therefore, with reference to (2.11) and Table 2. 1, the mutual magnetizing inductance matrix $[M_{sk-sz}]$ between the stator phase windings of *k*-set and the stator phase windings of *z*-set is computed as follows:

$$[M_{sk-sz}] = \frac{N_{sk} \cdot N_{sz}}{\Re_{eq}} \cdot \begin{bmatrix} \cos(\Delta\vartheta_{sk-sz}) & \cos\left(\Delta\vartheta_{sk-sz} - \frac{2\pi}{3}\right) & \cos\left(\Delta\vartheta_{sk-sz} - \frac{4\pi}{3}\right) \\ \cos\left(\Delta\vartheta_{sk-sz} + \frac{2\pi}{3}\right) & \cos(\Delta\vartheta_{sk-sz}) & \cos\left(\Delta\vartheta_{sk-sz} - \frac{2\pi}{3}\right) \\ \cos\left(\Delta\vartheta_{sk-sz} + \frac{4\pi}{3}\right) & \cos\left(\Delta\vartheta_{sk-sz} + \frac{2\pi}{3}\right) & \cos(\Delta\vartheta_{sk-sz}) \end{bmatrix} \tag{2.12}$$

where:

- $\Delta\vartheta_{sk-sz} = \vartheta_{sk} - \vartheta_{sz}$ is the angular difference among the magnetic axes of the first phases belonging to *k*- and *z*- sets;
- N_{sk} is the number of turns characterizing the *k*-set;
- N_{sz} is the number of turns characterizing the *z*-set.

Similarly, the mutual magnetizing inductance matrix $[M_{sk-r}]$ between the stator phase windings of *k*-set and the rotor phase windings is computed as follows:

$$[M_{sk-r}] = \frac{N_{sk} \cdot N_r}{\Re_{eq}} \cdot \begin{bmatrix} \cos(\Delta\vartheta_{sk-r}) & \cos\left(\Delta\vartheta_{sk-r} - \frac{2\pi}{3}\right) & \cos\left(\Delta\vartheta_{sk-r} - \frac{4\pi}{3}\right) \\ \cos\left(\Delta\vartheta_{sk-r} + \frac{2\pi}{3}\right) & \cos(\Delta\vartheta_{sk-r}) & \cos\left(\Delta\vartheta_{sk-r} - \frac{2\pi}{3}\right) \\ \cos\left(\Delta\vartheta_{sk-r} + \frac{4\pi}{3}\right) & \cos\left(\Delta\vartheta_{sk-r} + \frac{2\pi}{3}\right) & \cos(\Delta\vartheta_{sk-r}) \end{bmatrix} \tag{2.13}$$

where:

- $\Delta\vartheta_{sk-r} = \vartheta_{sk} - \vartheta_r$ is the angular difference among the magnetic axes of the first phases belonging to *k*-set and the rotor winding;
- N_r is the number of turns characterizing the equivalent rotor winding.

With reference to (2.4), the computation of both $[M_{sk-sz}]$ and $[M_{sk-r}]$ leads to the complete definition of the stator magnetic model in phase coordinates.

Rotor magnetic model in phase coordinates

The rotor magnetic model consists of the equation system containing the current-to-flux relationships of the rotor cage. Therefore, with reference to hypothesis 3), the rotor magnetic model consists of 3 equations. The procedure for the computation of the rotor magnetic model is like the one used for the stator magnetic model. Consequently, the magnetic model of the rotor winding is expressed as follows:

$$\begin{bmatrix} \lambda_{r-a} \\ \lambda_{r-b} \\ \lambda_{r-c} \end{bmatrix} = L_{l,r} \cdot \begin{bmatrix} i_{r-a} \\ i_{r-b} \\ i_{r-c} \end{bmatrix} + \sum_{z=1}^{n} \left([M_{r-sz}] \cdot \begin{bmatrix} i_{sz-a} \\ i_{sz-b} \\ i_{sz-c} \end{bmatrix} \right) + [M_{r-r}] \cdot \begin{bmatrix} i_{r-a} \\ i_{r-b} \\ i_{r-c} \end{bmatrix} \tag{2.14}$$

where:

- $[\lambda_{r-a} \quad \lambda_{r-b} \quad \lambda_{r-c}]^t$ is the vector of the rotor fluxes linkage for the three-phase rotor set defined in the own rotor phase coordinates $(abc)_r$;

while:

- $L_{l,r}$ is the self-leakage phase inductance of the equivalent rotor winding;
- $\left[M_{r-sz}\right]$ is the 3×3 mutual magnetizing inductance matrix between the rotor phase windings and the stator phase windings of the *z*-set;
- $\left[M_{r-r}\right]$ is the 3×3 self-mutual magnetizing inductance matrix of the rotor phase windings.

With reference to (2.11) and Table 2. 1, the mutual magnetizing inductance matrix $\left[M_{r-sz}\right]$ is computed as follows:

$$\left[M_{r-sz}\right]=\frac{N_{sz}\cdot N_r}{\Re_{eq}}\cdot\begin{bmatrix}\cos\left(\Delta\vartheta_{r-sz}\right) & \cos\left(\Delta\vartheta_{r-sz}-\frac{2\pi}{3}\right) & \cos\left(\Delta\vartheta_{r-sz}-\frac{4\pi}{3}\right)\\ \cos\left(\Delta\vartheta_{r-sz}+\frac{2\pi}{3}\right) & \cos\left(\Delta\vartheta_{r-sz}\right) & \cos\left(\Delta\vartheta_{r-sz}-\frac{2\pi}{3}\right)\\ \cos\left(\Delta\vartheta_{r-sz}+\frac{4\pi}{3}\right) & \cos\left(\Delta\vartheta_{r-sz}+\frac{2\pi}{3}\right) & \cos\left(\Delta\vartheta_{r-sz}\right)\end{bmatrix} \tag{2.15}$$

where:

- $\Delta\vartheta_{r-sz}=\vartheta_r-\vartheta_{sz}$ is the angular difference among the magnetic axes of the first phases belonging to the rotor winding and the stator *k*-set;

Finally, the self-mutual magnetizing inductance matrix $\left[M_{r-r}\right]$ of the rotor phase windings is computed as follows:

$$\left[M_{r-r}\right]=\frac{N_r\cdot N_r}{\Re_{eq}}\cdot\begin{bmatrix}\cos\left(\Delta\vartheta_{r-r}\right) & \cos\left(\Delta\vartheta_{r-r}-\frac{2\pi}{3}\right) & \cos\left(\Delta\vartheta_{r-r}-\frac{4\pi}{3}\right)\\ \cos\left(\Delta\vartheta_{r-r}+\frac{2\pi}{3}\right) & \cos\left(\Delta\vartheta_{r-r}\right) & \cos\left(\Delta\vartheta_{r-r}-\frac{2\pi}{3}\right)\\ \cos\left(\Delta\vartheta_{r-r}+\frac{4\pi}{3}\right) & \cos\left(\Delta\vartheta_{r-r}+\frac{2\pi}{3}\right) & \cos\left(\Delta\vartheta_{r-r}\right)\end{bmatrix} \tag{2.16}$$

where:

- $\Delta\vartheta_{r-r}=\vartheta_r-\vartheta_r=0$.

With reference to (2.14), the computation of both $\left[M_{r-sz}\right]$ and $\left[M_{r-r}\right]$ leads to complete definition of the rotor magnetic model in rotor phase coordinates.

In conclusion, the magnetic model of a multiple three-phase IM machine is composed by $3\cdot(n+1)$ algebraic equations, containing all the current-to-flux relationships of the phase windings.

Stator electric model in phase coordinates

The stator electric model consists of the equation system containing all the flux-to-voltage relationships of the stator phases. Therefore, the stator electric model is composed by $3 \cdot n$ equations. Using the passive sign convention, for each three-phase stator k-set the electric equations are as follows:

$$\begin{bmatrix} v_{sk-a} \\ v_{sk-b} \\ v_{sk-c} \end{bmatrix} = R_{sk} \cdot \begin{bmatrix} i_{sk-a} \\ i_{sk-b} \\ i_{sk-c} \end{bmatrix} + \frac{d}{dt} \begin{bmatrix} \lambda_{sk-a} \\ \lambda_{sk-b} \\ \lambda_{sk-c} \end{bmatrix} \tag{2.17}$$

where:

- $\begin{bmatrix} v_{sk-a} & v_{sk-b} & v_{sk-c} \end{bmatrix}^t$ is the vector of the stator voltages for the three-phase k-set defined in the own stator phase coordinates $(abc)_k$;

while:

- R_{sk} is the phase resistance for the three-phase k-set.

With reference to (2.17), the electric model of each three-phase set corresponds with the application of the Faraday's law of induction, obtaining the same electrical equations of a conventional three-phase machine.

Rotor electric model

The rotor electric model consists of the equation system containing all the flux-to-voltage relationships of the rotor cage. Therefore, with reference to hypothesis 3), the rotor magnetic model is composed by 3 equations. Using the passive sign convention, the rotor electric model is identical with the one of a conventional three-phase IM machine:

$$\begin{bmatrix} v_{r-a} \\ v_{r-b} \\ v_{r-c} \end{bmatrix} = R_r \cdot \begin{bmatrix} i_{r-a} \\ i_{r-b} \\ i_{r-c} \end{bmatrix} + \frac{d}{dt} \begin{bmatrix} \lambda_{r-a} \\ \lambda_{r-b} \\ \lambda_{r-c} \end{bmatrix} \tag{2.18}$$

where:

- $\begin{bmatrix} v_{r-a} & v_{r-b} & v_{r-c} \end{bmatrix}^t$ is the vector of the rotor voltages for the three-phase rotor set defined in the own rotor phase coordinates $(abc)_r$;

while:

- R_r is the phase resistance of the equivalent rotor winding.

Because a squirrel cage IM typology is considered, the equivalent rotor winding is short-circuited, leading to the following equations:

$$\begin{bmatrix} v_{r-a} & v_{r-b} & v_{r-c} \end{bmatrix}^t = [0]_{3\times1} = \begin{bmatrix} 0 & 0 & 0 \end{bmatrix}^t \tag{2.19}$$

In conclusion, the electric model of a multiple three-phase IM machine consists of 3·(*n*+1) differential equations, containing all the flux-to-voltage relationships of the phase windings.

Electromagnetic model in phase coordinates

The computation of both electric and magnetic models has been performed by considering each three-phase *k*-set separately. Anyway, with the aim at obtaining an overall electromagnetic model of the machine, it is necessary to merge the electromagnetic equations for all sets, including the rotor winding. To avoid a cumbersome mathematical formulation, each three-phase vector defined in phase coordinates (*abc*) will be indicated from now on as follows:

$$\begin{bmatrix} x_{sk-a} \\ x_{sk-b} \\ x_{sk-c} \end{bmatrix} = \left[x_{sk,abc} \right] \quad , \quad \begin{bmatrix} x_{r-a} \\ x_{r-b} \\ x_{r-c} \end{bmatrix} = \left[x_{r,abc} \right] \qquad (x = v, i, \lambda) \tag{2.20}$$

Using (2.20), the Equations (2.4), (2.14) and (2.17)-(2.18) are expressed as follows:

$$\left[\lambda_{sk,abc} \right] = L_{l,sk} \cdot \left[i_{sk,abc} \right] + \sum_{z=1}^{n} \left(\left[M_{sk-sz} \right] \cdot \left[i_{sz,abc} \right] \right) + \left[M_{sk-r} \right] \cdot \left[i_{r,abc} \right] \tag{2.21}$$

$$\left[\lambda_{r,abc} \right] = L_{l,r} \cdot \left[i_{r,abc} \right] + \sum_{z=1}^{n} \left(\left[M_{r-sz} \right] \cdot \left[i_{sz,abc} \right] \right) + \left[M_{r-r} \right] \cdot \left[i_{r,abc} \right] \tag{2.22}$$

$$\left[v_{sk,abc} \right] = R_{sk} \cdot \left[i_{sk,abc} \right] + \frac{d}{dt} \left[\lambda_{sk,abc} \right] \tag{2.23}$$

$$\left[v_{r,abc} \right] = R_{r} \cdot \left[i_{r,abc} \right] + \frac{d}{dt} \left[\lambda_{r,abc} \right] \tag{2.24}$$

By merging (2.21) for all sets *k*=1,2,…,*n* and including (2.22), the complete magnetic model of the machine in phase coordinates is obtained as follows:

$$\begin{Bmatrix} \left[\lambda_{s1,abc} \right] \\ \left[\lambda_{s2,abc} \right] \\ \dots \\ \left[\lambda_{sn,abc} \right] \\ \left[\lambda_{r,abc} \right] \end{Bmatrix} = \left[L_L \right] \cdot \begin{Bmatrix} \left[i_{s1,abc} \right] \\ \left[i_{s2,abc} \right] \\ \dots \\ \left[i_{sn,abc} \right] \\ \left[i_{r,abc} \right] \end{Bmatrix} + \left[L_M \right] \cdot \begin{Bmatrix} \left[i_{s1,abc} \right] \\ \left[i_{s2,abc} \right] \\ \dots \\ \left[i_{sn,abc} \right] \\ \left[i_{r,abc} \right] \end{Bmatrix} = \left[L \right] \cdot \begin{Bmatrix} \left[i_{s1,abc} \right] \\ \left[i_{s2,abc} \right] \\ \dots \\ \left[i_{sn,abc} \right] \\ \left[i_{r,abc} \right] \end{Bmatrix} \tag{2.25}$$

where:

$$\left[L_L\right]=\begin{bmatrix} L_{l,s1}\cdot\left[I_d\right]_{3\times3} & \left[0\right]_{3\times3} & \dots & \left[0\right]_{3\times3} & \left[0\right]_{3\times3} \\ \left[0\right]_{3\times3} & L_{l,s2}\cdot\left[I_d\right]_{3\times3} & \dots & \left[0\right]_{3\times3} & \left[0\right]_{3\times3} \\ \dots & \dots & \dots & \dots & \dots \\ \left[0\right]_{3\times3} & \left[0\right]_{3\times3} & \dots & L_{l,sn}\cdot\left[I_d\right]_{3\times3} & \left[0\right]_{3\times3} \\ \left[0\right]_{3\times3} & \left[0\right]_{3\times3} & \dots & \left[0\right]_{3\times3} & L_{l,r}\cdot\left[I_d\right]_{3\times3} \end{bmatrix} \tag{2.26}$$

$$\left[L_M\right]=\begin{bmatrix} \left[M_{s1-s1}\right] & \left[M_{s1-s2}\right] & \dots & \left[M_{s1-sn}\right] & \left[M_{s1-r}\right] \\ \left[M_{s2-s1}\right] & \left[M_{s2-s2}\right] & \dots & \left[M_{s2-sn}\right] & \left[M_{s2-r}\right] \\ \dots & \dots & \dots & \dots & \dots \\ \left[M_{sn-s1}\right] & \left[M_{sn-s2}\right] & \dots & \left[M_{sn-sn}\right] & \left[M_{sn-r}\right] \\ \left[M_{r-s1}\right] & \left[M_{r-s2}\right] & \dots & \left[M_{r-sn}\right] & \left[M_{r-r}\right] \end{bmatrix} \tag{2.27}$$

$$\left[L\right]=\left[L_L\right]+\left[L_M\right] \tag{2.28}$$

Concerning the terms $\left[0\right]_{3\times3}$ and $\left[I_d\right]_{3\times3}$, they have the following meaning:

$$\left[0\right]_{3\times3}=\begin{bmatrix} 0 & 0 & 0 \\ 0 & 0 & 0 \\ 0 & 0 & 0 \end{bmatrix} \quad , \quad \left[I_d\right]_{3\times3}=\begin{bmatrix} 1 & 0 & 0 \\ 0 & 1 & 0 \\ 0 & 0 & 1 \end{bmatrix} \tag{2.29}$$

Conversely, by merging (2.23) for all sets k=1,2,…,n and including (2.24), the complete electric model of the machine in phase coordinates is obtained:

$$\begin{Bmatrix} \left[v_{s1,abc}\right] \\ \left[v_{s2,abc}\right] \\ \dots \\ \left[v_{sn,abc}\right] \\ \left[v_{r,abc}\right] \end{Bmatrix}=\left[R\right]\cdot\begin{Bmatrix} \left[i_{s1,abc}\right] \\ \left[i_{s2,abc}\right] \\ \dots \\ \left[i_{sn,abc}\right] \\ \left[i_{r,abc}\right] \end{Bmatrix}+\frac{d}{dt}\cdot\begin{Bmatrix} \left[\lambda_{s1,abc}\right] \\ \left[\lambda_{s2,abc}\right] \\ \dots \\ \left[\lambda_{sn,abc}\right] \\ \left[\lambda_{r,abc}\right] \end{Bmatrix} \tag{2.30}$$

where:

$$\left[R\right]=\begin{bmatrix} R_{s1}\cdot\left[I_d\right]_{3\times3} & \left[0\right]_{3\times3} & \dots & \left[0\right]_{3\times3} & \left[0\right]_{3\times3} \\ \left[0\right]_{3\times3} & R_{s2}\cdot\left[I_d\right]_{3\times3} & \dots & \left[0\right]_{3\times3} & \left[0\right]_{3\times3} \\ \dots & \dots & \dots & \dots & \dots \\ \left[0\right]_{3\times3} & \left[0\right]_{3\times3} & \dots & R_{sn}\cdot\left[I_d\right]_{3\times3} & \left[0\right]_{3\times3} \\ \left[0\right]_{3\times3} & \left[0\right]_{3\times3} & \dots & \left[0\right]_{3\times3} & R_{r}\cdot\left[I_d\right]_{3\times3} \end{bmatrix} \tag{2.31}$$

With the aim at obtaining a compact formulation, the following variables are defined:

$$\{\mathrm{V}\}=\begin{Bmatrix}[v_{s1,abc}]\\[v_{s2,abc}]\\ \dots \\ [v_{sn,abc}]\\[v_{r,abc}]\end{Bmatrix},\quad \{\mathrm{I}\}=\begin{Bmatrix}[i_{s1,abc}]\\[i_{s2,abc}]\\ \dots \\ [i_{sn,abc}]\\[i_{r,abc}]\end{Bmatrix},\quad \{\Lambda\}=\begin{Bmatrix}[\lambda_{s1,abc}]\\[\lambda_{s2,abc}]\\ \dots \\ [\lambda_{sn,abc}]\\[\lambda_{r,abc}]\end{Bmatrix} \tag{2.32}$$

Finally, by replacing (2.32) in (2.25) and (2.30), the complete electromagnetic model of an IM in phase coordinates is obtained:

$$\begin{cases}\{\mathrm{V}\}=[R]\cdot\{\mathrm{I}\}+\dfrac{d}{dt}\{\Lambda\}\\ \{\Lambda\}=[L]\cdot\{\mathrm{I}\}\end{cases} \tag{2.33}$$

The equation system (2.33) represents the most generic form by which the electromagnetic model of an any electrical machine is described [1].

Electromagnetic torque in phase coordinates

The definition of the electromechanical model requires the computation of the electromagnetic torque generated by the machine. This one can be obtained using many approaches. A straightforward method consists of the computation of the energetic balance [2]. According with it, for each differential time range *dt*, the electrical machine operation is regulated by the following energetic balance:

$$\forall\ dt: \qquad dE_E - dE_M = dE_T + dE_W \tag{2.34}$$

where:

- dE_E is the infinitesimal variation of the electrical energy;
- dE_M is the infinitesimal variation of the mechanical energy;
- dE_T is the infinitesimal variation of the thermal energy;
- dE_W is the infinitesimal variation of the magnetic field energy.

Each of these contributions can be computed directly. Concerning dE_E, it corresponds with the temporal integration of the machine electric power:

$$dE_E = \{\mathrm{I}\}^t\cdot\{\mathrm{V}\}\cdot dt \tag{2.35}$$

The contribution dE_M corresponds to the temporal integration of the mechanical power generated by the machine electromagnetic torque T:

$$dE_M = T \cdot d\vartheta_m = T \cdot \frac{d\vartheta_r}{p_p} \tag{2.36}$$

where:

- $d\vartheta_m$ is the infinitesimal variation of the mechanical rotor position;
- $d\vartheta_r$ is the infinitesimal variation of the electrical rotor position;
- p_p is the pole pairs number of the machine.

Thanks to hypothesis 4), the thermal energy is exclusively generated by the Joule losses of the machine. Therefore, dE_T is computed as follows:

$$dE_T = \{\mathrm{I}\}^t \cdot [R] \cdot \{\mathrm{I}\} \cdot dt \tag{2.37}$$

Concerning dE_W, it is computed as temporal derivation of the power stored in the machine magnetic field:

$$\frac{dE_W}{dt} = \frac{d}{dt}\left(\frac{1}{2} \cdot \{\mathrm{I}\}^t \cdot [L] \cdot \{\mathrm{I}\}\right) \Rightarrow dE_W = d\left(\frac{1}{2} \cdot \{\mathrm{I}\}^t \cdot [L] \cdot \{\mathrm{I}\}\right) \tag{2.38}$$

By replacing (2.35)-(2.38) in (2.34), the energetic balance is expressed as follows:

$$\{\mathrm{I}\}^t \cdot \{\mathrm{V}\} = \frac{T}{p_p} \cdot \frac{d\vartheta_r}{dt} + \{\mathrm{I}\}^t \cdot [R] \cdot \{\mathrm{I}\} + \frac{d}{dt}\left(\frac{1}{2} \cdot \{\mathrm{I}\}^t \cdot [L] \cdot \{\mathrm{I}\}\right) \tag{2.39}$$

Finally, by replacing the left member of (2.39) with the electromagnetic model of the machine defined in (2.33), the result is as follows:

$$\{\mathrm{I}\}^t \cdot \frac{d}{dt}\left([L] \cdot \{\mathrm{I}\}\right) = \frac{T}{p_p} \cdot \frac{d\vartheta_r}{dt} + \frac{d}{dt}\left(\frac{1}{2} \cdot \{\mathrm{I}\}^t \cdot [L] \cdot \{\mathrm{I}\}\right) \tag{2.40}$$

Using some mathematical manipulations, (2.40) is expressed as follows:

$$T = \frac{1}{2} \cdot p_p \cdot \{\mathrm{I}\}^t \cdot \frac{d[L]}{d\vartheta_r} \cdot \{\mathrm{I}\} \tag{2.41}$$

In magnetic linearity conditions 4), (2.41) allows the electromagnetic torque computation of any electrical machine. With the aim at obtaining a specific formulation for this kind of machine, (2.28) is replaced in (2.41), leading to the following result:

$$T = p_p \cdot \sum_{k=1}^{n}\left(\left[i_{sk,abc}\right]^t \cdot \frac{d\left[M_{sk-r}\right]}{d\vartheta_r} \cdot \left[i_{r,abc}\right]\right) \tag{2.42}$$

From (2.42) it is noted how the electromagnetic torque is the sum of the contributions of the *n* stator sets interacting with the three-phase rotor. Finally, using (2.13), the extended computation of (2.42) leads to the following result:

$$T = p_p \cdot \sum_{k=1}^{n} \left[\frac{N_{sk} \cdot N_r}{\Re_{eq}} \cdot \left(T_{s,r} + T_{s,r-1} + T_{s,r+1} \right) \right] \tag{2.43}$$

where:

$$\begin{cases} T_{s,r} = \left(i_{sk-a} \cdot i_{r-a} + i_{sk-b} \cdot i_{r-b} + i_{sk-c} \cdot i_{r-c} \right) \cdot \sin\left(\Delta\vartheta_{sk-r} \right) \\ T_{s,r-1} = \left(i_{sk-a} \cdot i_{r-c} + i_{sk-b} \cdot i_{r-a} + i_{sk-c} \cdot i_{r-b} \right) \cdot \sin\left(\Delta\vartheta_{sk-r} + \frac{2\pi}{3} \right) \\ T_{s,r+1} = \left(i_{sk-a} \cdot i_{r-b} + i_{sk-b} \cdot i_{r-c} + i_{sk-c} \cdot i_{r-a} \right) \cdot \sin\left(\Delta\vartheta_{sk-r} + \frac{4\pi}{3} \right) \end{cases} \tag{2.44}$$

With reference to (2.44), each torque contribution is given by the product between a stator phase current and a rotor phase current, thus respecting the induction machine operating principle.

Mechanical model

The mechanical model of an electrical machine consists of two equations. The first one consists of the torque balance on the mechanical shaft. Using the simplest formulation, this equation can be expressed as follows:

$$T - T_L = I_{eq} \cdot \frac{d\omega_m}{dt} \Rightarrow T - T_L = \frac{I_{eq}}{p_p} \cdot \frac{d\omega_r}{dt} \tag{2.45}$$

where:

- T_L is the overall load torque, including eventual friction contributions;
- I_{eq} is the overall momentum of inertia around the axis of rotation, considering both the machine's rotor and mechanical load;
- ω_m is the mechanical speed of the rotor shaft;
- ω_r is the electrical speed of the rotor shaft.

The second mechanical equation corresponds with the temporal integration of the mechanical speed to get the mechanical rotor position:

$$\omega_m = \frac{d\vartheta_m}{dt} \Rightarrow \omega_m = \frac{1}{p_p} \cdot \frac{d\vartheta_r}{dt} = \frac{\omega_r}{p_p} \tag{2.46}$$

where:

- ϑ_m is the mechanical position of the rotor shaft;
- ϑ_r is the electrical position of the rotor shaft.

Like any ac machine, the relationship between the mechanical and electrical variables is exclusively related to the number of pole pairs p_p of the machine.

Energy conversion model in phase coordinates

The computation of the electromagnetic and mechanical models allows to define the electromechanical equation system of the machine, describing the energy conversion processes. In detail, the energy conversion model in phase coordinates is composed by the combination of the following equation systems:

$$\begin{cases} \{\mathrm{V}\} = [R]\cdot\{\mathrm{I}\} + \dfrac{d}{dt}\{\Lambda\} & Eq.\ 2.33 \\ \{\Lambda\} = [L]\cdot\{\mathrm{I}\} & Eq.\ 2.33 \\ T = p_p \cdot \sum_{k=1}^{n}\left(\left[i_{sk,abc}\right]^t \cdot \dfrac{d\left[M_{sk-r}\right]}{d\vartheta_r} \cdot \left[i_{r,abc}\right] \right) & Eq.\ 2.42 \\ \dfrac{d\omega_r}{dt} = \dfrac{p_p}{I_{eq}} \cdot \left(T - T_L\right) & Eq.\ 2.45 \\ \dfrac{d\vartheta_r}{dt} = \omega_r & Eq.\ 2.46 \end{cases} \tag{2.47}$$

The equation system (2.47) represents the complete electromechanical MS model of a generic multiple three-phase induction machine in phase coordinates. In conclusion, it is described as follows:

- $3\cdot n$ stator magnetic equations (2.21);
- 3 rotor magnetic equations (2.22);
- $3\cdot n$ stator electrical equations (2.23);
- 3 rotor electrical equations (2.24);
- 1 electromagnetic torque equation (2.42);
- 2 mechanical equations (2.45), (2.46).

As happens for the three-phase machines, the electromechanical model in phase coordinates can be manipulated using the reference transformations. In this way, it is possible to get an equation system able to highlight the flux and torque production of each single three-phase winding set, resulting suitable for machine control purposes.

2.1.2 Electromechanical model in stationary coordinates

Like for the three-phase machines, the computation of the electromechanical model in the stationary (α,β) frame allows to reduce the equation system complexity, leading to more manageable formulations. Concerning the MS approach [3], it requires the application of the general three-phase Clarke transformation to get the machine model in the stationary (α,β) frame [2].

Using the amplitude-invariant form, the general three-phase Clarke transformation is defined as follows [2]:

$$[T_i] = \frac{2}{3} \cdot \begin{bmatrix} \cos(\vartheta_i) & \cos\left(\vartheta_i + \frac{2\pi}{3}\right) & \cos\left(\vartheta_i + \frac{4\pi}{3}\right) \\ \sin(\vartheta_i) & \sin\left(\vartheta_i + \frac{2\pi}{3}\right) & \sin\left(\vartheta_i + \frac{4\pi}{3}\right) \\ 1/2 & 1/2 & 1/2 \end{bmatrix} \tag{2.48}$$

where ϑ_i indicates the position of the magnetic axis belonging to the first phase '*a*' of the considered three-phase *i*-set. According with the initial assumptions, the position angle is computed with respect to the stationary α-axis by considering an anticlockwise rotation direction, as shown in Fig. 2. 2.

With the aim at getting the electromagnetic model of the machine in stationary coordinates, the application of the Clarke transformation to both electric and magnetic models is following reported.

Stator magnetic model in stationary coordinates

According with the MS approach, the computation of the stator magnetic model in stationary (α,β) frame must be performed by considering each three-phase *k*-set separately. For convenience, (2.21) is further reported, however with a change in the notation of the rotor variables:

$$\left[\lambda_{sk,abc}\right] = L_{l,sk} \cdot \left[i_{sk,abc}\right] + \sum_{z=1}^{n} \left(\left[M_{sk-sz}\right] \cdot \left[i_{sz,abc}\right]\right) + \left[M_{sk-r}\right] \cdot \left[i^{r}_{r,abc}\right] \tag{2.49}$$

The superscript '*r*' indicates that the considered variable is defined in the rotor coordinates, making necessary its redefinition to the *k*-set stator ones. With the aim at performing this operation, the transformation ratio between the generic stator *k*-set and the rotor winding is introduced:

$$t_{sk-r} = \frac{N_{sk}}{N_r} \tag{2.50}$$

Therefore, the rotor variables can be easily referred to the *k*-set stator coordinates as follows:

$$\left[i^{sk}_{r,abc}\right] = \frac{1}{t_{sk-r}} \cdot \left[i^{r}_{r,abc}\right] \quad , \quad \left[v^{sk}_{r,abc}\right] = t_{sk-r} \cdot \left[v^{r}_{r,abc}\right] \quad , \quad \left[\lambda^{sk}_{r,abc}\right] = t_{sk-r} \cdot \left[\lambda^{r}_{r,abc}\right] \tag{2.51}$$

By replacing (2.51) in (2.49), the magnetic model of the stator *k*-set having rotor variables defined in the *k*-set stator coordinates is obtained:

$$\left[\lambda_{sk,abc}\right] = L_{l,sk} \cdot \left[i_{sk,abc}\right] + \sum_{z=1}^{n} \left(\left[M_{sk-sz}\right] \cdot \left[i_{sz,abc}\right] \right) + \left[M_{sk-r}\right] \cdot t_{sk-r} \cdot \left[i_{r,abc}^{sk}\right] \quad (2.52)$$

Starting from a generic variable in phase coordinates $(abc)_k$, the application of the three-phase Clarke transformation leads to the definition of the stationary (αβ0) components. In terms of mathematical formulation, this operation is described as follows:

$$\left[x_{sk,\alpha\beta 0}\right] = \begin{bmatrix} x_{sk-\alpha} \\ x_{sk-\beta} \\ x_{sk-0} \end{bmatrix} = \left[T_{sk}\right] \cdot \left[x_{sk,abc}\right] \quad , \quad \left[x_{r,\alpha\beta 0}^{sk}\right] = \begin{bmatrix} x_{r-\alpha}^{sk} \\ x_{r-\beta}^{sk} \\ x_{r-0}^{sk} \end{bmatrix} = \left[T_r\right] \cdot \left[x_{r,abc}^{sk}\right] \quad (2.53)$$
$$\left(x = v, i, \lambda\right)$$

where:

- $\left[T_{sk}\right]$ is the three-phase Clarke transformation for the stator *k*-set, this one is computed using the position angle ϑ_{sk};
- $\left[T_r\right]$ is the three-phase Clarke transformation for the rotor set, this one is computed using the rotor electrical position ϑ_r.

Therefore, the application of (2.53) on (2.52) leads to the computation of the *k*-set stator magnetic model in terms of stationary (αβ0) variables, obtaining the following result:

$$\left[\lambda_{sk,\alpha\beta 0}\right] = L_{l,sk} \cdot \left[i_{sk,\alpha\beta 0}\right] + \sum_{z=1}^{n} \left(\left[M_{sk-sz,\alpha\beta 0}\right] \cdot \left[i_{sz,\alpha\beta 0}\right] \right) + \left[M_{sk-r,\alpha\beta 0}\right] \cdot t_{sk-r} \cdot \left[i_{r,\alpha\beta 0}^{sk}\right] \quad (2.54)$$

where:

$$\left[M_{sk-sz,\alpha\beta 0}\right] = \left[T_{sk}\right] \cdot \left[M_{sk-sz}\right] \cdot \left[T_{sz}\right]^{-1} = \frac{3}{2} \cdot \frac{N_{sk} \cdot N_{sz}}{\Re_{eq}} \cdot \begin{bmatrix} 1 & 0 & 0 \\ 0 & 1 & 0 \\ 0 & 0 & 0 \end{bmatrix} \quad (2.55)$$

$$\left[M_{sk-r,\alpha\beta 0}\right] = \left[T_{sk}\right] \cdot \left[M_{sk-r}\right] \cdot \left[T_r\right]^{-1} = \frac{3}{2} \cdot \frac{N_{sk} \cdot N_r}{\Re_{eq}} \cdot \begin{bmatrix} 1 & 0 & 0 \\ 0 & 1 & 0 \\ 0 & 0 & 0 \end{bmatrix} \quad (2.56)$$

With the aim at obtaining a more compact formulation, the following variables are introduced:

$$m_{sk-sz} = \frac{3}{2} \cdot \frac{N_{sk} \cdot N_{sz}}{\Re_{eq}} \quad , \quad m_{sk-r} = \frac{3}{2} \cdot \frac{N_{sk} \cdot N_{r}}{\Re_{eq}} \tag{2.57}$$

By separating the (α,β) components from the zero-sequence '0' one, (2.54) is expressed as follows:

$$\begin{cases} \begin{bmatrix} \lambda_{sk-\alpha} \\ \lambda_{sk-\beta} \end{bmatrix} = L_{l,sk} \cdot \begin{bmatrix} i_{sk-\alpha} \\ i_{sk-\beta} \end{bmatrix} + \sum_{z=1}^{n} \left(m_{sk-sz} \cdot \begin{bmatrix} i_{sz-\alpha} \\ i_{sz-\beta} \end{bmatrix} \right) + m_{sk-r} \cdot t_{sk-r} \cdot \begin{bmatrix} i_{r-\alpha}^{sk} \\ i_{r-\beta}^{sk} \end{bmatrix} \\ \lambda_{sk-0} = L_{l,sk} \cdot i_{sk-0} \end{cases} \tag{2.58}$$

Finally, (2.58) can be further simplified by introducing the complex vector notation defined as follows:

$$\begin{bmatrix} x_{sk-\alpha} \\ x_{sk-\beta} \end{bmatrix} = x_{sk-\alpha} + j \cdot x_{sk-\beta} = \overline{x}_{sk,\alpha\beta} \quad , \quad \begin{bmatrix} x_{r-\alpha}^{sk} \\ x_{r-\beta}^{sk} \end{bmatrix} = x_{r-\alpha}^{sk} + j \cdot x_{r-\beta}^{sk} = \overline{x}_{r,\alpha\beta}^{sk}$$
$$\left(x = v, i, \lambda \right) \tag{2.59}$$

where j represents the complex vector operator. By using (2.59), (2.58) is expressed as follows:

$$\begin{cases} \overline{\lambda}_{sk,\alpha\beta} = L_{l,sk} \cdot \overline{i}_{sk,\alpha\beta} + \sum_{z=1}^{n} \left(m_{sk-sz} \cdot \overline{i}_{sz,\alpha\beta} \right) + m_{sk-r} \cdot t_{sk-r} \cdot \overline{i}_{r,\alpha\beta}^{sk} \\ \lambda_{sk-0} = L_{l,sk} \cdot i_{sk-0} \end{cases} \tag{2.60}$$

The computation of (2.60) leads to the definition of the stator magnetic model in the stationary (αβ0) coordinates.

Rotor magnetic model in stationary coordinates

The computation of the rotor magnetic model in the stationary (α,β) frame is performed by following the same procedure used for the computation of the stator model. Therefore, (2.22) using the notation change of the rotor variables is below reported:

$$\left[\lambda_{r,abc}^{r} \right] = L_{l,r}^{r} \cdot \left[i_{r,abc}^{r} \right] + \sum_{z=1}^{n} \left(\left[M_{r-sz} \right] \cdot \left[i_{sz,abc} \right] \right) + \left[M_{r-r} \right] \cdot \left[i_{r,abc}^{r} \right] \tag{2.61}$$

By replacing (2.51) in (2.61), the rotor variables are referred to the *k*-set stator coordinates, obtaining the following equation system:

$$\left[\lambda_{r,abc}^{sk}\right] = L_{l,r}^{r} \cdot t_{sk-r}^{2} \cdot \left[i_{r,abc}^{sk}\right] + t_{sk-r} \cdot \sum_{z=1}^{n}\left(\left[M_{r-sz}\right] \cdot \left[i_{sz,abc}\right]\right) + t_{sk-r}^{2} \cdot \left[M_{r-r}\right] \cdot \left[i_{r,abc}^{sk}\right] \tag{2.62}$$

The application of (2.53) on (2.62) leads to the computation of the rotor magnetic model in terms of stationary (αβ0) variables, obtaining the following result:

$$\begin{aligned}\left[\lambda_{r,\alpha\beta0}^{sk}\right] = L_{l,r}^{r} \cdot t_{sk-r}^{2} \cdot \left[i_{r,\alpha\beta0}^{sk}\right] + t_{sk-r} \cdot \sum_{z=1}^{n}\left(\left[M_{r-sz,\alpha\beta0}\right] \cdot \left[i_{sz,\alpha\beta0}\right]\right) + \ldots \\ \ldots + t_{sk-r}^{2} \cdot \left[M_{r-r,\alpha\beta0}\right] \cdot \left[i_{r,\alpha\beta0}^{sk}\right]\end{aligned} \tag{2.63}$$

where:

$$\left[M_{r-sz,\alpha\beta0}\right] = \left[T_r\right] \cdot \left[M_{r-sz}\right] \cdot \left[T_{sz}\right]^{-1} = \frac{3}{2} \cdot \frac{N_{sz} \cdot N_r}{\Re_{eq}} \cdot \begin{bmatrix} 1 & 0 & 0 \\ 0 & 1 & 0 \\ 0 & 0 & 0 \end{bmatrix} \tag{2.64}$$

$$\left[M_{r-r,\alpha\beta0}\right] = \left[T_r\right] \cdot \left[M_{r-r}\right] \cdot \left[T_r\right]^{-1} = \frac{3}{2} \cdot \frac{N_r \cdot N_r}{\Re_{eq}} \cdot \begin{bmatrix} 1 & 0 & 0 \\ 0 & 1 & 0 \\ 0 & 0 & 0 \end{bmatrix} \tag{2.65}$$

With the aim at obtaining a more compact formulation, the following variables are introduced:

$$m_{r-sz} = \frac{3}{2} \cdot \frac{N_{sz} \cdot N_r}{\Re_{eq}} \quad , \quad m_{r-r} = \frac{3}{2} \cdot \frac{N_r \cdot N_r}{\Re_{eq}} \tag{2.66}$$

By separating the (α,β) components from the zero-sequence '0' one, (2.63) is expressed as follows:

$$\begin{cases} \begin{bmatrix} \lambda_{r-\alpha}^{sk} \\ \lambda_{r-\beta}^{sk} \end{bmatrix} = L_{l,r}^{r} \cdot t_{sk-r}^{2} \cdot \begin{bmatrix} i_{r-\alpha}^{sk} \\ i_{r-\beta}^{sk} \end{bmatrix} + t_{sk-r} \cdot \sum_{z=1}^{n}\left(m_{r-sz} \cdot \begin{bmatrix} i_{sz-\alpha} \\ i_{sz-\beta} \end{bmatrix}\right) + m_{r-r} \cdot t_{sk-r}^{2} \cdot \begin{bmatrix} i_{r-\alpha}^{sk} \\ i_{r-\beta}^{sk} \end{bmatrix} \\ \lambda_{r-0}^{sk} = L_{l,r}^{r} \cdot t_{sk-r}^{2} \cdot i_{r-0}^{sk} \end{cases} \tag{2.67}$$

Finally, by using (2.59), (2.67) is expressed in complex vector notation as follows:

$$\begin{cases} \overline{\lambda}_{r,\alpha\beta}^{sk} = L_{l,r}^{r} \cdot t_{sk-r}^{2} \cdot \overline{i}_{r,\alpha\beta}^{sk} + t_{sk-r} \cdot \sum_{z=1}^{n} \left(m_{r-sz} \cdot \overline{i}_{sz,\alpha\beta} \right) + m_{r-r} \cdot t_{sk-r}^{2} \cdot \overline{i}_{r,\alpha\beta}^{sk} \\ \lambda_{r-0}^{sk} = L_{l,r}^{r} \cdot t_{sk-r}^{2} \cdot i_{r-0}^{sk} \end{cases} \tag{2.68}$$

The equation system (2.68) represents the rotor magnetic model in the stationary (αβ0) coordinates, however having rotor variables referred to the *k*-set stator coordinates.

Stator electric model in stationary coordinates

The procedure for the computation of the stator electric model in stationary (α,β) frame is simpler than the one used for the computation of the magnetic equations. Starting from the *k*-set stator electric model in phase coordinates (2.23), the application of (2.53) leads to the following result:

$$\left[v_{sk,\alpha\beta0} \right] = R_{sk} \cdot \left[i_{sk,\alpha\beta0} \right] + \frac{d}{dt} \left[\lambda_{sk,\alpha\beta0} \right] \tag{2.69}$$

It is noted how the stator electric model in stationary (α,β) frame is formally identical with the one in phase coordinates (2.23). The only difference is that all vectors (voltage, flux and current) are referred to the stationary coordinates (αβ0) instead of the phase ones $(abc)_k$. As for the magnetic models, the (α,β) components can be separated from the zero-sequence '0' one, leading to the following result:

$$\begin{cases} \begin{bmatrix} v_{sk-\alpha} \\ v_{sk-\beta} \end{bmatrix} = R_{sk} \cdot \begin{bmatrix} i_{sk-\alpha} \\ i_{sk-\beta} \end{bmatrix} + \frac{d}{dt} \begin{bmatrix} \lambda_{sk-\alpha} \\ \lambda_{sk-\beta} \end{bmatrix} \\ v_{sk-0} = R_{sk} \cdot i_{sk-0} + \frac{d}{dt} \lambda_{sk-0} \end{cases} \tag{2.70}$$

Finally, by using (2.59), (2.70) is expressed as follows:

$$\begin{cases} \overline{v}_{sk,\alpha\beta} = R_{sk} \cdot \overline{i}_{sk,\alpha\beta} + \frac{d}{dt} \overline{\lambda}_{sk,\alpha\beta} \\ v_{sk-0} = R_{sk} \cdot i_{sk-0} + \frac{d}{dt} \lambda_{sk-0} \end{cases} \tag{2.71}$$

With reference to (2.71), the electric model in stationary (αβ0) coordinates of each stator *k*-set corresponds with the one of a conventional three-phase machine.

Rotor electric model in stationary coordinates

The computation of the rotor electric model in the stationary (α,β) frame is performed by following the same procedure used for the computation of the magnetic models. Therefore, (2.24) using the notation change of the rotor variables is below reported:

$$\left[v_{r,abc}^{r}\right] = R_r^r \cdot \left[i_{r,abc}^{r}\right] + \frac{d}{dt}\left[\lambda_{r,abc}^{r}\right] \tag{2.72}$$

By replacing (2.51) in (2.72), the rotor variables are referred to the *k*-set stator coordinates, obtaining the following equation system:

$$\left[v_{r,abc}^{sk}\right] = R_r^r \cdot t_{sk-r}^2 \cdot \left[i_{r,abc}^{sk}\right] + \frac{d}{dt}\left[\lambda_{r,abc}^{sk}\right] \tag{2.73}$$

The application of (2.53) on (2.73) leads to the computation of the rotor electric model in terms of stationary (αβ0) variables, obtaining the following result:

$$\left[v_{r,\alpha\beta0}^{sk}\right] = R_r^r \cdot t_{sk-r}^2 \cdot \left[i_{r,\alpha\beta0}^{sk}\right] + \frac{d}{dt}\left[\lambda_{r,\alpha\beta0}^{sk}\right] + \left[T_r\right] \cdot \left(\frac{d}{dt}\left[T_r\right]^{-1}\right) \cdot \left[\lambda_{r,\alpha\beta0}^{sk}\right] \tag{2.74}$$

where:

$$\left[T_r\right] \cdot \left(\frac{d}{dt}\left[T_r\right]^{-1}\right) = \frac{d\vartheta_r}{dt} \cdot \begin{bmatrix} 0 & 1 & 0 \\ -1 & 0 & 0 \\ 0 & 0 & 0 \end{bmatrix} = \omega_r \cdot \begin{bmatrix} 0 & 1 & 0 \\ -1 & 0 & 0 \\ 0 & 0 & 0 \end{bmatrix} \tag{2.75}$$

By separating the (α,β) components from the zero-sequence '0' one, (2.75) is expressed as follows:

$$\begin{cases} \begin{bmatrix} v_{r-\alpha}^{sk} \\ v_{r-\beta}^{sk} \end{bmatrix} = R_r^r \cdot t_{sk-r}^2 \cdot \begin{bmatrix} i_{r-\alpha}^{sk} \\ i_{r-\beta}^{sk} \end{bmatrix} + \frac{d}{dt}\begin{bmatrix} \lambda_{r-\alpha}^{sk} \\ \lambda_{r-\beta}^{sk} \end{bmatrix} + \omega_r \cdot \begin{bmatrix} 0 & 1 \\ -1 & 0 \end{bmatrix} \cdot \begin{bmatrix} \lambda_{r-\alpha}^{sk} \\ \lambda_{r-\beta}^{sk} \end{bmatrix} \\ v_{r-0}^{sk} = R_r^r \cdot t_{sk-r}^2 \cdot i_{r-0}^{sk} + \frac{d}{dt}\lambda_{r-0}^{sk} \end{cases} \tag{2.76}$$

Finally, by using (2.59), (2.76) is expressed as follows:

$$\begin{cases} \overline{v}_{r,\alpha\beta}^{sk} = R_r^r \cdot t_{sk-r}^2 \cdot \overline{i}_{r,\alpha\beta}^{sk} + \frac{d}{dt}\overline{\lambda}_{r,\alpha\beta}^{sk} - j \cdot \omega_r \cdot \overline{\lambda}_{r,\alpha\beta}^{sk} \\ v_{r-0}^{sk} = R_r^r \cdot t_{sk-r}^2 \cdot i_{r-0}^{sk} + \frac{d}{dt}\lambda_{r-0}^{sk} \end{cases} \tag{2.77}$$

With reference to (2.77), the rotor electric model in stationary (αβ0) coordinates corresponds with the one of a conventional three-phase machine.

Electromagnetic torque in stationary coordinates

Starting from (2.42), the computation of the electromagnetic torque in stationary (αβ0) coordinates is performed. Therefore, (2.42) using the notation change of the rotor variables is below reported:

$$T = p_p \cdot \sum_{k=1}^{n} \left(\left[i_{sk,abc} \right]^t \cdot \frac{d\left[M_{sk-r} \right]}{d\vartheta_r} \cdot \left[i^r_{r,abc} \right] \right) \tag{2.78}$$

By replacing (2.51) in (2.78), the rotor variables are referred to the *k*-set stator coordinates, obtaining the following equation:

$$T = p_p \cdot \sum_{k=1}^{n} \left(\left[i_{sk,abc} \right]^t \cdot \frac{d\left[M_{sk-r} \right]}{d\vartheta_r} \cdot t_{sk-r} \cdot \left[i^{sk}_{r,abc} \right] \right) \tag{2.79}$$

The application of (2.53) on (2.79) leads to the computation of the electromagnetic torque in terms of stationary (αβ0) variables, obtaining the following result:

$$T = p_p \cdot \sum_{k=1}^{n} \left(\left[i_{sk,\alpha\beta 0} \right]^t \cdot \left[\left[T_k \right]^{-1} \right]^t \cdot \frac{d\left[M_{sk-r} \right]}{d\vartheta_r} \cdot \left[T_r \right]^{-1} \cdot \left[i^{sk}_{r,\alpha\beta 0} \right] \cdot t_{sk-r} \right) \tag{2.80}$$

where:

$$\left[\left[T_k \right]^{-1} \right]^t \cdot \frac{d\left[M_{sk-r} \right]}{d\vartheta_r} \cdot \left[T_r \right]^{-1} = \frac{9}{4} \cdot \frac{N_{sk} \cdot N_r}{\Re_{eq}} \cdot \begin{bmatrix} 0 & -1 & 0 \\ 1 & 0 & 0 \\ 0 & 0 & 0 \end{bmatrix} \tag{2.81}$$

By replacing (2.81) in (2.80), the relationship of the electromagnetic torque is as follows:

$$T = p_p \cdot \sum_{k=1}^{n} \left[\frac{9}{4} \cdot t_{sk-r} \cdot \frac{N_{sk} \cdot N_r}{\Re_{eq}} \cdot \left(i^{sk}_{r-\alpha} \cdot i_{sk-\beta} - i^{sk}_{r-\beta} \cdot i_{sk-\alpha} \right) \right] \tag{2.82}$$

Finally, by using (2.57) and (2.59), (2.82) is expressed as follows:

$$T = \frac{3}{2} \cdot p_p \cdot \sum_{k=1}^{n} \left[t_{sk-r} \cdot m_{sk-r} \cdot \left(\bar{i}^{sk}_{r,\alpha\beta} \times \bar{i}_{sk,\alpha\beta} \right) \right] \tag{2.83}$$

where × indicates the cross-product operator. It is noted how each stator *k*-set torque contribution is given by the cross-product between the stator *k*-set current vector and the rotor one, thus respecting the induction machine operating principle. With the aim at obtaining a torque expression using only stator variables, (2.60) is manipulated as follows:

$$m_{sk-r} \cdot t_{sk-r} \cdot \bar{i}^{sk}_{r,\alpha\beta} = \bar{\lambda}_{sk,\alpha\beta} - L_{l,sk} \cdot \bar{i}_{sk,\alpha\beta} - \sum_{z=1}^{n} \left(m_{sk-sz} \cdot \bar{i}_{sz,\alpha\beta} \right) \tag{2.84}$$

By replacing (2.84) in (2.83), the electromagnetic torque is computed as follows:

$$T = \frac{3}{2} \cdot p_p \cdot \sum_{k=1}^{n} \left\{ \left(\overline{\lambda}_{sk,\alpha\beta} \times \overline{i}_{sk,\alpha\beta} \right) - \sum_{z=1}^{n} \left[m_{sk-sz} \cdot \left(\overline{i}_{sz,\alpha\beta} \times \overline{i}_{sk,\alpha\beta} \right) \right] \right\} \tag{2.85}$$

Using the anticommutative propriety of the cross-product, it is demonstrated as follows:

$$\left(\overline{i}_{sz,\alpha\beta} \times \overline{i}_{sk,\alpha\beta} \right) = -\left(\overline{i}_{sk,\alpha\beta} \times \overline{i}_{sz,\alpha\beta} \right) \Rightarrow \sum_{k=1}^{n} \sum_{z=1}^{n} \left[m_{sk-sz} \cdot \left(\overline{i}_{sz,\alpha\beta} \times \overline{i}_{sk,\alpha\beta} \right) \right] = 0 \tag{2.86}$$

Therefore, by replacing (2.86) in (2.85), the electromagnetic torque expression is simplified as follows:

$$T = \frac{3}{2} \cdot p_p \cdot \sum_{k=1}^{n} \left(\overline{\lambda}_{sk,\alpha\beta} \times \overline{i}_{sk,\alpha\beta} \right) \tag{2.87}$$

According to (2.87), the electromagnetic torque is given by the sum of the contributions of the *n* stator sets that interact with the three-phase rotor. Each stator *k*-set contribution is given by the cross-product between the *k*-set stator flux-linkage vector and the *k*-set stator current vector, highlighting the full modularity of the MS approach.

Electromagnetic model in stationary coordinates

In summary, the electromagnetic model in stationary (α,β) frame is composed by the combination of the following equation systems:

- Stator *k*-set Magnetic Model

$$\overline{\lambda}_{sk,\alpha\beta} = L_{l,sk} \cdot \overline{i}_{sk,\alpha\beta} + \sum_{z=1}^{n} \left(m_{sk-sz} \cdot \overline{i}_{sz,\alpha\beta} \right) + m_{sk-r} \cdot t_{sk-r} \cdot \overline{i}_{r,\alpha\beta}^{sk} \tag{2.88}$$

- Rotor Magnetic Model

$$\overline{\lambda}_{r,\alpha\beta}^{sk} = L_{l,r}^{r} \cdot t_{sk-r}^{2} \cdot \overline{i}_{r,\alpha\beta}^{sk} + t_{sk-r} \cdot \sum_{z=1}^{n} \left(m_{r-sz} \cdot \overline{i}_{sz,\alpha\beta} \right) + m_{r-r} \cdot t_{sk-r}^{2} \cdot \overline{i}_{r,\alpha\beta}^{sk} \tag{2.89}$$

- Stator *k*-set Electric Model

$$\overline{v}_{sk,\alpha\beta} = R_{sk} \cdot \overline{i}_{sk,\alpha\beta} + \frac{d}{dt} \overline{\lambda}_{sk,\alpha\beta} \tag{2.90}$$

- Rotor Electric Model

$$\overline{v}_{r,\alpha\beta}^{sk} = R_{r}^{r} \cdot t_{sk-r}^{2} \cdot \overline{i}_{r,\alpha\beta}^{sk} + \frac{d}{dt} \overline{\lambda}_{r,\alpha\beta}^{sk} - j \cdot \omega_r \cdot \overline{\lambda}_{r,\alpha\beta}^{sk} \tag{2.91}$$

Together with the (α,β) components, the MS approach defines (*n*+1) zero-sequence '0' electromagnetic models. These are computed as follows:

- Stator *k*-set Magnetic Model

$$\lambda_{sk-0} = L_{l,sk} \cdot i_{sk-0} \tag{2.92}$$

- Rotor Magnetic Model

$$\lambda_{r-0}^{sk} = L_{l,r}^{r} \cdot t_{sk-r}^{2} \cdot i_{r-0}^{sk} \tag{2.93}$$

- Stator *k*-set Electric Model

$$v_{sk-0} = R_{sk} \cdot i_{sk-0} + \frac{d}{dt}\lambda_{sk-0} \tag{2.94}$$

- Rotor Electric Model

$$v_{r-0}^{sk} = R_{r}^{r} \cdot t_{sk-r}^{2} \cdot i_{r-0}^{sk} + \frac{d}{dt}\lambda_{r-0}^{sk} \tag{2.95}$$

It is noted how the rotor magnetic and electric equations are both referred to the *k*-set stator phase coordinates. Therefore, depending be the considered stator *k*-set, the rotor electromagnetic model requires the computation of the *k*-set transformation ratio (2.50), making necessary the definition of *n* rotor models operating in parallel. With the aim at solving this issue, the following hypothesis is introduced:

7) The number of turns characterizing the three-phase stator sets are considered identical from each other.

This condition is typical for the multiple three-phase machines as a uniform design of the three-phase winding sets is performed. In terms of mathematical formulation, hypothesis 7) is expressed as follows:

$$N_{sk} = N_{sz} = N_{s} \qquad \forall k, \forall z \tag{2.96}$$

As a consequence of (2.96), a unique machine transformation ratio is defined, leading to following result:

$$t_{sk-r} = \frac{N_{sk}}{N_{r}} = \frac{N_{s}}{N_{r}} = t_{s-r} \qquad \forall k \tag{2.97}$$

In addition, the parameters in (2.57) and (2.66) are computed as follows:

$$m_{sk-sz} = m_{s-s} = \frac{3}{2} \cdot \frac{N_{s}^{2}}{\Re_{eq}} \quad , \quad m_{sk-r} = m_{r-sz} = m_{s-r} = \frac{3}{2} \cdot \frac{N_{s} \cdot N_{r}}{\Re_{eq}} \tag{2.98}$$

Therefore, by combining (2.97) and (2.98), the following results are obtained:

$$\begin{gathered} m_{sk-r} \cdot t_{sk-r} = m_{r-sz} \cdot t_{sk-r} = m_{r-r} \cdot t_{sk-r}^{2} = m_{sk-sz} = m_{s-s} = L_{m}^{s} \\ L_{l,r}^{r} \cdot t_{sk-r}^{2} = L_{l,r}^{s} \quad , \quad R_{r}^{r} \cdot t_{sk-r}^{2} = R_{r}^{s} \end{gathered} \tag{2.99}$$

Finally, by replacing (2.99) in (2.88)-(2.91), the electromagnetic model in stationary (α,β) frame is computed as follows:

$$\begin{cases} \bar{\lambda}_{sk,\alpha\beta} = L_{l,sk} \cdot \bar{i}_{sk,\alpha\beta} + L_m^s \cdot \sum_{z=1}^{n} \bar{i}_{sz,\alpha\beta} + L_m^s \cdot \bar{i}_{r,\alpha\beta}^s & k = 1,2,...,n \\ \bar{\lambda}_{r,\alpha\beta}^s = L_{l,r}^s \cdot \bar{i}_{r,\alpha\beta}^s + L_m^s \cdot \sum_{z=1}^{n} \bar{i}_{sz,\alpha\beta} + L_m^s \cdot \bar{i}_{r,\alpha\beta}^s & \\ \bar{v}_{sk,\alpha\beta} = R_{sk} \cdot \bar{i}_{sk,\alpha\beta} + \frac{d}{dt} \bar{\lambda}_{sk,\alpha\beta} & k = 1,2,...,n \\ \bar{v}_{r,\alpha\beta}^s = R_r^s \cdot \bar{i}_{r,\alpha\beta}^s + \frac{d}{dt} \bar{\lambda}_{r,\alpha\beta}^s - j \cdot \omega_r \cdot \bar{\lambda}_{r,\alpha\beta}^s & \end{cases} \tag{2.100}$$

where L_m^s represents the magnetizing inductance. Concerning the (n+1) zero-sequence '0' electromagnetic models (2.92)-(2.95), the application of (2.99) leads to following equation system:

$$\begin{cases} \lambda_{sk-0} = L_{l,sk} \cdot i_{sk-0} & k = 1,2,...,n \\ \lambda_{r-0}^s = L_{l,r}^s \cdot i_{r-0}^s & \\ v_{sk-0} = R_{sk} \cdot i_{sk-0} + \frac{d}{dt} \lambda_{sk-0} & k = 1,2,...,n \\ v_{r-0}^s = R_r^s \cdot i_{r-0}^s + \frac{d}{dt} \lambda_{r-0}^s & \end{cases} \tag{2.101}$$

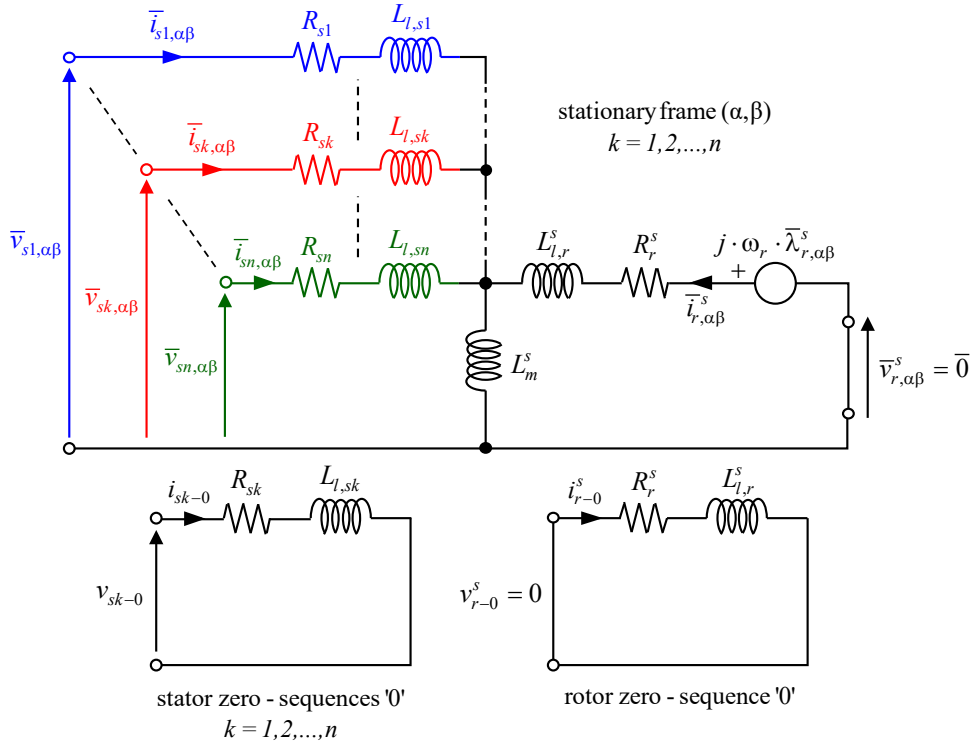

Fig. 2. 6. Equivalent MS circuit of a multiple three-phase squirrel cage IM in stationary (αβ0) components.

According to (2.100), the MS approach defines *n* stator flux-linkage vectors and *n* stator current vectors which are defined in *n* overlapped stationary (α,β) frame. Each stator *k*-set interacts with the rotor, leading to a modular electromagnetic torque production. Concerning the zero-sequence '0' components (2.101), they do not provide any contribution to the electromechanical energy conversion, leading to considerations identical to those of the three-phase machines. Therefore, the equivalent circuit of the machine, corresponding to the MS modelling approach in stationary components (αβ0), is shown in Fig. 2. 6.

Energy conversion model in stationary coordinates

Since no magnetic and electric variables are involved, the mechanical model (2.45)-(2.46) is not affected by the application of the reference transformations, making it still valid. Therefore, the electromechanical model of the machine in stationary (αβ0) components is defined as follows:

$$
\begin{cases}
\left.\begin{aligned}
&\bar{\lambda}_{sk,\alpha\beta} = L_{l,sk}\cdot\bar{i}_{sk,\alpha\beta} + L_m^s\cdot\sum_{z=1}^{n}\bar{i}_{sz,\alpha\beta} + L_m^s\cdot\bar{i}_{r,\alpha\beta}^s && k=1,2,...,n\\
&\bar{\lambda}_{r,\alpha\beta}^s = L_{l,r}^s\cdot\bar{i}_{r,\alpha\beta}^s + L_m^s\cdot\sum_{z=1}^{n}\bar{i}_{sz,\alpha\beta} + L_m^s\cdot\bar{i}_{r,\alpha\beta}^s &&\\
&\bar{v}_{sk,\alpha\beta} = R_{sk}\cdot\bar{i}_{sk,\alpha\beta} + \frac{d}{dt}\bar{\lambda}_{sk,\alpha\beta} && k=1,2,...,n\\
&\bar{v}_{r,\alpha\beta}^s = R_r^s\cdot\bar{i}_{r,\alpha\beta}^s + \frac{d}{dt}\bar{\lambda}_{r,\alpha\beta}^s - j\cdot\omega_r\cdot\bar{\lambda}_{r,\alpha\beta}^s &&
\end{aligned}\right] \quad \textit{Eq. 2.100}\\
\left.\begin{aligned}
&\lambda_{sk-0} = L_{l,sk}\cdot i_{sk-0} && k=1,2,...,n\\
&\lambda_{r-0}^s = L_{l,r}^s\cdot i_{r-0}^s &&\\
&v_{sk-0} = R_{sk}\cdot i_{sk-0} + \frac{d}{dt}\lambda_{sk-0} && k=1,2,...,n\\
&v_{r-0}^s = R_r^s\cdot i_{r-0}^s + \frac{d}{dt}\lambda_{r-0}^s &&
\end{aligned}\right] \quad \textit{Eq. 2.101}\\
T = \frac{3}{2}\cdot p_p\cdot\sum_{k=1}^{n}\left(\bar{\lambda}_{sk,\alpha\beta}\times\bar{i}_{sk,\alpha\beta}\right) \quad \textit{Eq. 2.87}\\
\frac{d\omega_r}{dt} = \frac{p_p}{I_{eq}}\cdot\left(T - T_L\right) \quad \textit{Eq. 2.45}\\
\frac{d\vartheta_r}{dt} = \omega_r \quad \textit{Eq. 2.46}
\end{cases}
\tag{2.102}
$$

It is noted how (2.102) has the same structure of the electromechanical model in phase coordinates (2.47). The only difference is related to electromagnetic model together with the torque relationship, which are expressed in a form more suitable for control purposes.

2.1.3 Electromechanical model in rotating coordinates

Like the three-phase machines, the stator and rotor models can be referred to a generic rotating frame, obtaining a suitable formulation for most of the machine control schemes like the Vector Control (VC) ones.

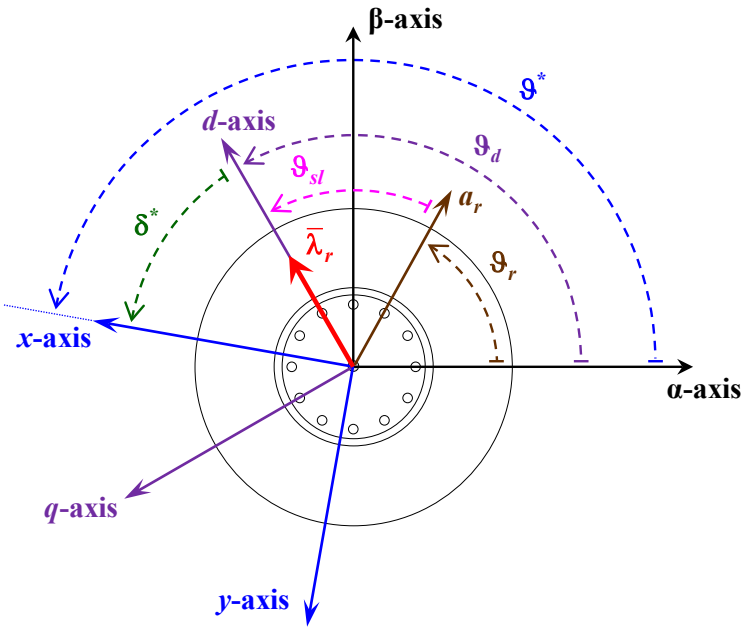

Fig. 2. 7. Representation of stationary (α,β) frame, rotating (*d*,*q*) frame and generic (*x*,*y*) frame.

With reference to the three-phase IM theory [2], the rotating *d*-axis usually corresponds with the position of the rotor flux vector $\bar{\lambda}_r$, being this angle defined with respect to the stationary α-axis. For consistency, this naming convention is here respected, thus indicating with (*x*,*y*) the generic rotating frame, as shown in Fig. 2. 7. To obtain the highest degree of versatility, the position of the rotating *x*-axis ϑ^* is defined in terms of deviation angle δ^* with respect to the position of the electromagnetic *d*-axis ϑ_d, leading to the following formulation (Fig. 2. 7):

$$\vartheta^* = \vartheta_d + \delta^* \tag{2.103}$$

In this way, by defining ϑ^* properly, it is possible to select any frame as follows:

$$\begin{aligned}
&(a) \quad \delta^* = 0 && \Rightarrow \quad \vartheta^* = \vartheta_d && \Rightarrow \quad (x,y) \equiv (d,q) \\
&(b) \quad \delta^* = -\vartheta_d && \Rightarrow \quad \vartheta^* = 0 && \Rightarrow \quad (x,y) \equiv (\alpha,\beta) \\
&(c) \quad \delta^* = -\vartheta_{sl} && \Rightarrow \quad \vartheta^* = \vartheta_r && \Rightarrow \quad (x,y) \equiv (d_r,q_r) \\
&(d) \quad \delta^* = \angle\bar{\lambda}_{sk} - \angle\bar{\lambda}_r && \Rightarrow \quad \vartheta^* = \vartheta_{sk-\lambda} && \Rightarrow \quad (x,y) \equiv (d_{sk},q_{sk})
\end{aligned} \tag{2.104}$$

The condition (2.104)(a) is useful for Field Oriented Control (FOC) with rotor flux orientation. The condition (2.104)(b) corresponds to make coincident the rotating (x,y) frame with the stationary (α,β) one, resulting suitable for the implementation of Stationary Current Control (SCC) schemes. Conversely, (2.104)(c) corresponds to make coincident the x-axis with the rotor electrical position, thus setting δ^* equal to the negation of the rotor flux vector' slip angle ϑ_{sl}. Finally, (2.104)(d) corresponds to make coincident the x-axis with the position $\vartheta_{sk-\lambda}$ of the k-set stator flux vector $\overline{\lambda}_{sk}$, thus setting δ^* equal to the load angle of the k-set unit. This condition is useful when Direct Torque Control (DTC) and Direct Flux Vector Control (DFVC) schemes must be implemented.

The MS approach requires the application of the rotational transformation to get the machine model in the generic rotating (x,y) frame; this one is defined as follows:

$$[T_{rot}] = \begin{bmatrix} \cos(\vartheta^*) & \sin(\vartheta^*) \\ -\sin(\vartheta^*) & \cos(\vartheta^*) \end{bmatrix} \tag{2.105}$$

Starting from a generic variable defined in the stationary (α,β) frame, the application of the rotational transformation (2.105) leads to the computation of the rotating (x,y) components. In terms of mathematical formulation, this operation is described as follows:

$$\left[z_{sk,xy}\right] = \begin{bmatrix} z_{sk-x} \\ z_{sk-y} \end{bmatrix} = [T_{rot}] \cdot \left[z_{sk,\alpha\beta}\right] \quad , \quad \left[z_{r,xy}\right] = \begin{bmatrix} z_{r-x} \\ z_{r-y} \end{bmatrix} = [T_{rot}] \cdot \left[z_{r,\alpha\beta}\right] \quad (z = v, i, \lambda) \tag{2.106}$$

In terms of complex notation, (2.106) is expressed as follows:

$$\overline{z}_{sk,xy} = [T_{rot}] \cdot \overline{z}_{sk,\alpha\beta} \quad , \quad \overline{z}_{r,xy} = [T_{rot}] \cdot \overline{z}_{r,\alpha\beta} \quad (z = v, i, \lambda) \tag{2.107}$$

Using the same procedure for the computation of the electromagnetic model in stationary (αβ0) coordinates, the application of the rotational transformation to both electric and magnetic models is following reported.

Stator magnetic model in rotating coordinates

According with the MS approach, the computation of the stator magnetic model in rotating (x,y) frame must be performed by considering each k-set separately. For convenience, the stator magnetic model in stationary (α,β) frame (2.100) is following reported:

$$\overline{\lambda}_{sk,\alpha\beta} = L_{l,sk} \cdot \overline{i}_{sk,\alpha\beta} + L_m \cdot \sum_{z=1}^{n} \overline{i}_{sz,\alpha\beta} + L_m \cdot \overline{i}_{r,\alpha\beta} \tag{2.108}$$

It is noted how the superscript '*s*' on the rotor variables is not used, since a unique machine transformation ratio has been defined (2.97), leading to a simpler notation of the equations.

To have more manageable equations, this simplification will also be extended on the rotor parameters, leading to use the same names already employed in the phase coordinates model. Since this one will not be used anymore, no ambiguity case will arise.

The application of (2.107) on (2.108) leads to the computation of the *k*-set stator magnetic model in terms of rotating (*x*,*y*) components, obtaining the following result:

$$\overline{\lambda}_{sk,xy} = L_{l,sk} \cdot \overline{i}_{sk,xy} + L_m \cdot \sum_{z=1}^{n} \overline{i}_{sz,xy} + L_m \cdot \overline{i}_{r,xy} \tag{2.109}$$

It is noted how the stator electric model in rotating (*x*,*y*) frame is formally identical with the one in stationary (α,β) coordinates (2.100). The only difference is that all vectors (voltage, flux and current) are referred to the rotating (*x*,*y*) coordinates instead of the stationary ones (α,β).

Concerning the zero-sequence '0' model, this is not involved by the rotational transformation, making the equation (2.101) still valid.

Rotor magnetic model in rotating coordinates

Concerning the computation of rotor magnetic model in the rotating (*x*,*y*) frame, they are valid the same considerations made for the computation of stator model. Therefore, the application of (2.107) on (2.100) leads to the following result:

$$\overline{\lambda}_{r,xy} = L_{l,r} \cdot \overline{i}_{r,xy} + L_m \cdot \sum_{z=1}^{n} \overline{i}_{sz,xy} + L_m \cdot \overline{i}_{r,xy} \tag{2.110}$$

Similarly, the zero-sequence '0' model is not involved by the rotational transformation, making the equation (2.101) still valid.

Stator electric model in rotating coordinates

The procedure for the computation of the stator electric model in rotating (*x*,*y*) frame is similar to the one used for the computation of the magnetic equations. Starting from the *k*-set stator electric model in stationary (α,β) frame, the application of (2.107) on (2.90) leads to the following result:

$$\overline{v}_{sk,xy} = R_{sk} \cdot \overline{i}_{sk,xy} + \frac{d}{dt}\overline{\lambda}_{sk,xy} + \left[T_{rot}\right] \cdot \frac{d\left[T_{rot}\right]^{-1}}{dt} \cdot \overline{\lambda}_{sk,xy} \tag{2.111}$$

where:

$$\left[T_{rot}\right] \cdot \frac{d\left[T_{rot}\right]^{-1}}{dt} = \frac{d\vartheta^*}{dt} \cdot \begin{bmatrix} 0 & -1 \\ 1 & 0 \end{bmatrix} = \omega^* \cdot \begin{bmatrix} 0 & -1 \\ 1 & 0 \end{bmatrix} = j \cdot \omega^* \tag{2.112}$$

In (2.112), the variable ω^* represents the synchronous speed of the rotating (x,y) frame which meaning depends by (2.104). By replacing (2.112) in (2.111), the k-set stator electric model in rotating (x,y) frame is as follows:

$$\overline{v}_{sk,xy} = R_{sk} \cdot \overline{i}_{sk,xy} + \frac{d}{dt}\overline{\lambda}_{sk,xy} + j \cdot \omega^* \cdot \overline{\lambda}_{sk,xy} \tag{2.113}$$

Like for the three-phase machine, the application of the rotational transformation leads to the introduction of motional voltage terms in the stator electric model. Therefore, they are valid the same considerations of the three-phase case. Finally, the zero-sequence '0' model is not involved by the rotational transformation, making the equation (2.101) still valid.

Rotor electric model in rotating coordinates

The computation of the rotor electric model in the rotating (x,y) frame is performed by following the same procedure used for the computation of the stator model. Starting from the rotor electric model in stationary (α,β) frame, the application of (2.107) on (2.100) leads to the following result:

$$\overline{v}_{r,xy} = R_r \cdot \overline{i}_{r,xy} + \frac{d}{dt}\overline{\lambda}_{r,xy} + \left[T_{rot}\right] \cdot \frac{d\left[T_{rot}\right]^{-1}}{dt} \cdot \overline{\lambda}_{r,xy} - j \cdot \omega_r \cdot \overline{\lambda}_{r,xy} \tag{2.114}$$

By replacing (2.112) in (2.114), the rotor electric model in rotating (x,y) frame is computed as follows:

$$\overline{v}_{r,xy} = R_r \cdot \overline{i}_{r,xy} + \frac{d}{dt}\overline{\lambda}_{r,xy} + j \cdot \omega_{sl}^* \cdot \overline{\lambda}_{r,xy} \tag{2.115}$$

where ω_{sl}^* is the slip speed of the rotating (x,y) frame and it is computed as follows:

$$\omega_{sl}^* = \omega^* - \omega_r \tag{2.116}$$

The rotor electric model in rotating (x,y) frame is identical with the one of the conventional three-phase IM. Therefore, they are valid the same considerations of the three-phase case. Finally, the zero-sequence '0' model is not involved by the rotational transformation, making the equation (2.101) still valid.

Electromagnetic torque in rotating coordinates

With reference to (2.87), the electromagnetic torque expression consists of the sum of n torque contributions, each of this is given by the cross-product between the k-set stator flux-linkage vector and the k-set stator current vector.

As the cross-product depends only by the position of one vector with respect to the other one, (2.87) is valid in any frame, leading to the following result:

$$T = \frac{3}{2} \cdot p_p \cdot \sum_{k=1}^{n} \left(\overline{\lambda}_{sk,\alpha\beta} \times \overline{i}_{sk,\alpha\beta} \right) = \frac{3}{2} \cdot p_p \cdot \sum_{k=1}^{n} \left(\overline{\lambda}_{sk,xy} \times \overline{i}_{sk,xy} \right) \tag{2.117}$$

Therefore, (2.117) is formally identical with the electromagnetic torque expression in stationary (α,β) frame (2.87). The only difference is that all vectors (flux and current) are referred to the rotating (*x*,*y*) coordinates instead of the stationary ones (α,β).

Electromagnetic model in rotating coordinates

As both magnetic and electric models have been computed, the electromagnetic model of the machine in rotating (*x*,*y*) frame is defined as follows:

$$\begin{cases} \bar{\lambda}_{sk,xy} = L_{l,sk} \cdot \bar{i}_{sk,xy} + L_m \cdot \sum_{z=1}^{n} \bar{i}_{sz,xy} + L_m \cdot \bar{i}_{r,xy} & k = 1,2,...,n \quad Eq.\ 2.109 \\ \bar{\lambda}_{r,xy} = L_{l,r} \cdot \bar{i}_{r,xy} + L_m \cdot \sum_{z=1}^{n} \bar{i}_{sz,xy} + L_m \cdot \bar{i}_{r,xy} & \quad Eq.\ 2.110 \\ \bar{v}_{sk,xy} = R_{sk} \cdot \bar{i}_{sk,xy} + \frac{d}{dt}\bar{\lambda}_{sk,xy} + j \cdot \omega^* \cdot \bar{\lambda}_{sk,xy} & k = 1,2,...,n \quad Eq.\ 2.113 \\ \bar{v}_{r,xy} = R_r \cdot \bar{i}_{r,xy} + \frac{d}{dt}\bar{\lambda}_{r,xy} + j \cdot \left(\omega^* - \omega_r\right) \cdot \bar{\lambda}_{r,xy} & \quad Eq.\ 2.115 \end{cases} \tag{2.118}$$

Concerning the zero-sequence electromagnetic model, (2.101) is still valid.

$$\begin{cases} \lambda_{sk-0} = L_{l,sk} \cdot i_{sk-0} & k = 1,2,...,n \\ \lambda^s_{r-0} = L^s_{l,r} \cdot i^s_{r-0} & \\ v_{sk-0} = R_{sk} \cdot i_{sk-0} + \frac{d}{dt}\lambda_{sk-0} & k = 1,2,...,n \\ v^s_{r-0} = R^s_r \cdot i^s_{r-0} + \frac{d}{dt}\lambda^s_{r-0} & \end{cases} \tag{2.101}$$

Energy conversion model in rotating coordinates

Since no magnetic and electric variables are involved, the mechanical model (2.45)-(2.46) is not affected by the application of the rotational transformation, making it still valid. Therefore, the electromechanical model of the machine in rotating (*xy*0) components is defined as follows:

$$
\begin{cases}
\left.\begin{aligned}
&\overline{\lambda}_{sk,xy} = L_{l,sk}\cdot\overline{i}_{sk,xy} + L_m\cdot\sum_{z=1}^{n}\overline{i}_{sz,xy} + L_m\cdot\overline{i}_{r,xy} \qquad k=1,2,...,n\\
&\overline{\lambda}_{r,xy} = L_{l,r}\cdot\overline{i}_{r,xy} + L_m\cdot\sum_{z=1}^{n}\overline{i}_{sz,xy} + L_m\cdot\overline{i}_{r,xy}\\
&\overline{v}_{sk,xy} = R_{sk}\cdot\overline{i}_{sk,xy} + \frac{d}{dt}\overline{\lambda}_{sk,xy} + j\cdot\omega^*\cdot\overline{\lambda}_{sk,xy} \qquad k=1,2,...,n\\
&\overline{v}_{r,xy} = R_r\cdot\overline{i}_{r,xy} + \frac{d}{dt}\overline{\lambda}_{r,xy} + j\cdot\left(\omega^*-\omega_r\right)\cdot\overline{\lambda}_{r,xy}
\end{aligned}\right\} \quad Eq.\ 2.118\\
\left.\begin{aligned}
&\lambda_{sk-0} = L_{l,sk}\cdot i_{sk-0} \qquad k=1,2,...,n\\
&\lambda_{r-0} = L_{l,r}\cdot i_{r-0}\\
&v_{sk-0} = R_{sk}\cdot i_{sk-0} + \frac{d}{dt}\lambda_{sk-0} \qquad k=1,2,...,n\\
&v_{r-0} = R_r\cdot i_{r-0} + \frac{d}{dt}\lambda_{r-0}
\end{aligned}\right\} \quad Eq.\ 2.101\\
T = \frac{3}{2}\cdot p_p\cdot\sum_{k=1}^{n}\left(\overline{\lambda}_{sk,xy}\times\overline{i}_{sk,xy}\right) \quad Eq.\ 2.117\\
\frac{d\omega_r}{dt} = \frac{p_p}{I_{eq}}\cdot\left(T-T_L\right) \quad Eq.\ 2.45\\
\frac{d\vartheta_r}{dt} = \omega_r \quad Eq.\ 2.46
\end{cases}
\tag{2.119}
$$

It is noted how (2.119) has the same structure of the electromechanical model in stationary (αβ0) coordinates (2.102). The main difference consists of the definition of both electric stator and rotor models, containing motional voltage terms introduced by the synchronous speed ω^* of the rotating (*x*,*y*) frame. It is necessary to highlight how this variable must not be computed as it represents an additional degree of freedom of the system, which is introduced for control purposes only.

The electromechanical equation system in rotating (*xy*0) coordinates represents the most generic modelling level for this kind of machine. However, with the aim at implementing MS-based control schemes, it is necessary to compute the state-space model of the machine, thus starting from the equation system (2.119).

2.1.4 State-space model in rotating coordinates

Like for the three-phase machines, the state-space model is the starting point for the implementation of any control scheme. For a multiple three-phase IM, the use of the MS modelling leads to heavy magnetic couplings among the three-phase winding sets, resulting in a complicate equation system (2.119). As a consequence, the computation of the state-space model is characterized by many mathematical manipulations. With the aim at simplifying the analysis, a fast-computational procedure will be shown, giving the possibility to compute the state-space model in straightforward way.

According with the MS modelling, the zero-sequence components do not provide any contribution to electromechanical energy conversion, resulting in an equation system totally independent from the one defined in (x,y) rotating frame. As a consequence, the state-space model related to the zero-sequence variables is computed separately.

State-space model of rotating frame components

With reference to (2.118), the magnetic model of a generic stator k-set defined in the rotating (x,y) frame is as follows:

$$\bar{\lambda}_{sk,xy} = L_{l,sk} \cdot \bar{i}_{sk,xy} + L_m \cdot \sum_{z=1}^{n} \bar{i}_{sz,xy} + L_m \cdot \bar{i}_{r,xy} \tag{2.120}$$

By considering another generic stator h-set, (2.120) is rewritten as follows:

$$\bar{\lambda}_{sh,xy} = L_{l,sh} \cdot \bar{i}_{sh,xy} + L_m \cdot \sum_{z=1}^{n} \bar{i}_{sz,xy} + L_m \cdot \bar{i}_{r,xy} \tag{2.121}$$

Therefore, by comparing (2.120) with (2.121), the following comparative magnetic equation is computed:

$$\bar{i}_{sh,xy} = \frac{1}{L_{l,sh}} \cdot \left[\left(\bar{\lambda}_{sh,xy} - \bar{\lambda}_{sk,xy} \right) + L_{l,sk} \cdot \bar{i}_{sk,xy} \right] \tag{2.122}$$

Finally, by applying the temporal derivation operator on (2.122), the following time differential equation is obtained:

$$\frac{d}{dt}\bar{i}_{sh,xy} = \frac{1}{L_{l,sh}} \cdot \left[\left(\frac{d}{dt}\bar{\lambda}_{sh,xy} - \frac{d}{dt}\bar{\lambda}_{sk,xy} \right) + L_{l,sk} \cdot \frac{d}{dt}\bar{i}_{sk,xy} \right] \tag{2.123}$$

With reference to (2.118), the electric model of a generic stator k-set defined in the rotating (x,y) frame is as follows:

$$\frac{d}{dt}\bar{\lambda}_{sk,xy} = \bar{v}_{sk,xy} - R_{sk} \cdot \bar{i}_{sk,xy} - j \cdot \omega^* \cdot \bar{\lambda}_{sk,xy} \tag{2.124}$$

By considering another generic stator *h*-set, (2.124) is rewritten as follows:

$$\frac{d}{dt}\overline{\lambda}_{sh,xy} = \overline{v}_{sh,xy} - R_{sh}\cdot\overline{i}_{sh,xy} - j\cdot\omega^{*}\cdot\overline{\lambda}_{sh,xy} \tag{2.125}$$

Therefore, by comparing (2.124) with (2.125), the following comparative electrical equation is computed:

$$\left(\frac{d}{dt}\overline{\lambda}_{sh,xy} - \frac{d}{dt}\overline{\lambda}_{sk,xy}\right) = \left(\overline{v}_{sh,xy} - \overline{v}_{sk,xy}\right) + \left(R_{sk}\cdot\overline{i}_{sk,xy} - R_{sh}\cdot\overline{i}_{sh,xy}\right) + \ldots \\ \ldots + j\cdot\omega^{*}\cdot\left(\overline{\lambda}_{sk,xy} - \overline{\lambda}_{sh,xy}\right) \tag{2.126}$$

By replacing (2.122) in (2.126), the following time differential equation is obtained:

$$\left(\frac{d}{dt}\overline{\lambda}_{sh,xy} - \frac{d}{dt}\overline{\lambda}_{sk,xy}\right) = \left(\overline{v}_{sh,xy} - \overline{v}_{sk,xy}\right) + \left(R_{sk}\cdot\overline{i}_{sk,xy} - R_{sh}\cdot\overline{i}_{sh,xy}\right) + \ldots \\ \ldots + j\cdot\omega^{*}\cdot\left(L_{l,sk}\cdot\overline{i}_{sk,xy} - L_{l,sh}\cdot\overline{i}_{sh,xy}\right) \tag{2.127}$$

Finally, by replacing (2.127) in (2.123), the following comparative electromagnetic equation is computed:

$$\frac{d}{dt}\overline{i}_{sh,xy} = \frac{1}{L_{l,sh}}\cdot\left[\begin{array}{l} L_{l,sk}\cdot\dfrac{d}{dt}\overline{i}_{sk,xy} + \left(\overline{v}_{sh,xy} - \overline{v}_{sk,xy}\right) + \left(R_{sk}\cdot\overline{i}_{sk,xy} - R_{sh}\cdot\overline{i}_{sh,xy}\right) + \ldots \\ \qquad \ldots + j\cdot\omega^{*}\cdot\left(L_{l,sk}\cdot\overline{i}_{sk,xy} - L_{l,sh}\cdot\overline{i}_{sh,xy}\right) \end{array}\right] \tag{2.128}$$

For reasons better explained later, (2.128) is used to extrapolate the following equation:

$$\sum_{\substack{h=1\\h\neq k}}^{n}\frac{d}{dt}\overline{i}_{sh,xy} = \left(\sum_{\substack{h=1\\h\neq k}}^{n}\frac{1}{L_{l,sh}}\right)\cdot\left[L_{l,sk}\cdot\frac{d}{dt}\overline{i}_{sk,xy} - \left(\overline{v}_{sk,xy} - R_{sk}\cdot\overline{i}_{sk,xy} - j\cdot\omega^{*}\cdot L_{l,sk}\cdot\overline{i}_{sk,xy}\right)\right] + \ldots \\ \ldots + \sum_{\substack{h=1\\h\neq k}}^{n}\left[\frac{1}{L_{l,sh}}\cdot\left(\overline{v}_{sh,xy} - R_{sh}\cdot\overline{i}_{sh,xy} - j\cdot\omega^{*}\cdot L_{l,sh}\cdot\overline{i}_{sh,xy}\right)\right] \tag{2.129}$$

To obtain a compact formulation of the next equations, the following variables are defined:

$$k_r = \frac{L_m}{L_m + L_{l,r}} \quad , \quad k_{sk} = \frac{L_m}{L_m + L_{l,sk}} \quad , \quad c_h = \frac{L_{l,r}\cdot k_r}{L_{l,sh}} \quad , \quad c_k = \sum_{\substack{h=1\\h\neq k}}^{n} c_h \tag{2.130}$$

Finally, by using (2.130), (2.129) is expressed as follows:

$$k_r \cdot L_{l,r} \cdot \sum_{\substack{h=1 \\ h\neq k}}^{n} \frac{d}{dt}\bar{i}_{sh,xy} = c_k \cdot L_{l,sk} \cdot \frac{d}{dt}\bar{i}_{sk,xy} + \ldots$$

$$\ldots - c_k \cdot \left(\bar{v}_{sk,xy} - R_{sk} \cdot \bar{i}_{sk,xy} - j \cdot \omega^* \cdot L_{l,sk} \cdot \bar{i}_{sk,xy}\right) + \ldots \qquad (2.131)$$

$$\ldots + \sum_{\substack{h=1 \\ h\neq k}}^{n} \left[c_h \cdot \left(\bar{v}_{sh,xy} - R_{sh} \cdot \bar{i}_{sh,xy} - j \cdot \omega^* \cdot L_{l,sh} \cdot \bar{i}_{sh,xy}\right)\right]$$

Up to now, only the magnetic and the electric stator models have been manipulated. By using (2.120), the rotor current vector is expressed as follows:

$$\bar{i}_{r,xy} = \frac{\bar{\lambda}_{sk,xy}}{L_m} - \frac{L_{l,sk}}{L_m} \cdot \bar{i}_{sk,xy} - \sum_{z=1}^{n} \bar{i}_{sz,xy} \qquad (2.132)$$

With reference to (2.118), the rotor magnetic model defined in the rotating (x,y) frame is as follows:

$$\bar{\lambda}_{r,xy} = L_{l,r} \cdot \bar{i}_{r,xy} + L_m \cdot \sum_{z=1}^{n} \bar{i}_{sz,xy} + L_m \cdot \bar{i}_{r,xy} \qquad (2.133)$$

By replacing (2.132) in (2.133), after several mathematical manipulations involving the variables defined in (2.130), the rotor magnetic model is computed as follows:

$$\bar{\lambda}_{r,xy} = \frac{1}{k_r} \cdot \left(\bar{\lambda}_{sk,xy} - \sigma_k \cdot L_{sk} \cdot \bar{i}_{sk,xy} - k_r \cdot L_{l,r} \cdot \sum_{\substack{h=1 \\ h\neq k}}^{n} \bar{i}_{sh,xy} \right) \qquad (2.134)$$

where:

$$\sigma_k = 1 - k_{sk} \cdot k_r \quad , \quad L_{sk} = L_m + L_{l,sk} \qquad (2.135)$$

By applying the temporal derivation operator on (2.134), the following time differential equation is obtained:

$$\frac{d}{dt}\bar{\lambda}_{r,xy} = \frac{1}{k_r} \cdot \left(\frac{d}{dt}\bar{\lambda}_{sk,xy} - \sigma_k \cdot L_{sk} \cdot \frac{d}{dt}\bar{i}_{sk,xy} - k_r \cdot L_{l,r} \cdot \sum_{\substack{h=1 \\ h\neq k}}^{n} \frac{d}{dt}\bar{i}_{sh,xy} \right) \qquad (2.136)$$

By replacing (2.124) and (2.131) in (2.136), after some mathematical manipulations the following equation is obtained:

$$\frac{d}{dt}\overline{\lambda}_{r,xy} = \frac{1}{k_r}\cdot\left\{\begin{array}{l}\left(1+c_k\right)\cdot\left(\overline{v}_{sk,xy} - R_{sk}\cdot\overline{i}_{sk,xy}\right) - \left(\sigma_k\cdot L_{sk} + c_k\cdot L_{l,sk}\right)\cdot\dfrac{d}{dt}\overline{i}_{sk,xy} + \ldots \\ \ldots - j\cdot\omega^*\cdot c_k\cdot L_{l,sk}\cdot\overline{i}_{sk,xy} - j\cdot\omega^*\cdot\overline{\lambda}_{sk,xy} + \ldots \\ \ldots - \sum\limits_{\substack{h=1\\h\neq k}}^{n}\left[c_h\cdot\left(\overline{v}_{sh,xy} - R_{sh}\cdot\overline{i}_{sh,xy} - j\cdot\omega^*\cdot L_{l,sh}\cdot\overline{i}_{sh,xy}\right)\right]\end{array}\right\} \tag{2.137}$$

With reference to (2.118), the rotor electric model defined in the rotating (x,y) frame is as follows:

$$\overline{v}_{r,xy} = R_r\cdot\overline{i}_{r,xy} + \frac{d}{dt}\overline{\lambda}_{r,xy} + j\cdot\left(\omega^* - \omega_r\right)\cdot\overline{\lambda}_{r,xy} \tag{2.138}$$

To reduce the complexity of the state-equations, the rotor time constant is introduced:

$$\tau_r = \frac{L_m + L_{l,r}}{R_r} \tag{2.139}$$

Finally, by replacing (2.132), (2.134) and (2.137) in (2.138), after several mathematical manipulations involving (2.139), the following equation is obtained:

$$\begin{array}{l}\left(\sigma_k\cdot L_{sk} + c_k\cdot L_{l,sk}\right)\cdot\dfrac{d}{dt}\overline{i}_{sk,xy} = \\ = -\left\{\left[R_r\cdot\dfrac{k_r}{k_{sk}} + R_{sk}\cdot\left(1+c_k\right)\right] + j\cdot\left[\omega^*\cdot\left(\sigma_k\cdot L_{sk} + c_k\cdot L_{l,sk}\right) - \omega_r\cdot\sigma_k\cdot L_{sk}\right]\right\}\cdot\overline{i}_{sk,xy} + \ldots \\ \ldots - \sum\limits_{\substack{h=1\\h\neq k}}^{n}\left\{\left[\left(R_r\cdot k_r - c_h\cdot R_{sk}\right) - j\cdot\left(\omega_r\cdot c_h\cdot L_{l,sh}\right)\right]\cdot\overline{i}_{sh,xy}\right\} + \ldots \\ \ldots + \left(\dfrac{1}{\tau_r} - j\cdot\omega_r\right)\cdot\overline{\lambda}_{sk,xy} + \left(1+c_k\right)\cdot\overline{v}_{sk,xy} - \sum\limits_{\substack{h=1\\h\neq k}}^{n}\left(c_h\cdot\overline{v}_{sh,xy}\right) - k_r\cdot\overline{v}_{r,xy}\end{array} \tag{2.140}$$

As a squirrel-cage IM is considered, the rotor voltage $\overline{v}_{r,xy}$ corresponds to zero. However, with the aim at keeping the most general form of the state-space model, the rotor voltage $\overline{v}_{r,xy}$ is not explicated.

With the only exception of $\overline{v}_{r,xy}$, it is noted how in this equation no rotor variables are used, making this formulation useful for control schemes like DTC and DFVC. However, this aspect will be better exploited in the next chapter.

The equation (2.140) does not represents the state equation of the *k*-set stator current because the *k*-set stator flux $\overline{\lambda}_{sk,xy}$ is not explicated. To solve this issue, (2.134) is replaced in (2.140), obtaining the following result:

$$\begin{aligned}
&\left(\sigma_k \cdot L_{sk} + c_k \cdot L_{l,sk}\right) \cdot \frac{d}{dt}\overline{i}_{sk,xy} = \\
&= -\left\{\left[R_r \cdot \frac{k_r}{k_{sk}} + R_{sk} \cdot \left(1 + c_k\right) - \frac{1}{\tau_r} \cdot \sigma_k \cdot L_{sk}\right] + j \cdot \left[\omega^* \cdot \left(\sigma_k \cdot L_{sk} + c_k \cdot L_{l,sk}\right)\right]\right\} \cdot \overline{i}_{sk,xy} + \ldots \\
&\ldots - \sum_{\substack{h=1 \\ h \neq k}}^{n} \left[\left(R_r \cdot k_r - c_h \cdot R_{sk} - k_r \cdot L_{l,r} \cdot \frac{1}{\tau_r}\right) \cdot \overline{i}_{sh,xy}\right] + \ldots \\
&\ldots + k_r \cdot \left(\frac{1}{\tau_r} - j \cdot \omega_r\right) \cdot \overline{\lambda}_{r,xy} + \left(1 + c_k\right) \cdot \overline{v}_{sk,xy} - \sum_{\substack{h=1 \\ h \neq k}}^{n} \left(c_h \cdot \overline{v}_{sh,xy}\right) - k_r \cdot \overline{v}_{r,xy}
\end{aligned} \tag{2.141}$$

With the computation of (2.141), the state equation of the *k*-set stator current $\overline{i}_{sk,xy}$ is obtained. It is noted how the dynamic of the stator current in each *k*-set depends only partially on the *k*-set stator voltage $\overline{v}_{sk,xy}$. Indeed, according with the MS-approach [3], [4], there are relevant coupling effects between the sets. Both are reported under the summation operator in (2.141). The first coupling effect is in terms of current while the other one in terms of voltage. In detail, the voltage coupling between the sets is dangerous because it can cause instability of a MS-based machine control scheme [5], especially when the number of three-phase sets is relevant ($n > 2$). Therefore, in the machine control scheme, decoupling algorithms with the aim at mitigating these phenomena must be implemented.

With the aim at defining the state-space model in the canonical form of the linear systems [6], (2.141) is expressed in matrix form as follows:

$$\begin{aligned}
&\frac{d}{dt}\left[i_{sk,xy}\right] = \left[A_{i,kk}\right] \cdot \left[i_{sk,xy}\right] + \sum_{\substack{h=1 \\ h \neq k}}^{n} \left(\left[A_{i,kh}\right] \cdot \left[i_{sh,xy}\right]\right) + \left[A_{i,kr}\right] \cdot \left[\lambda_{r,xy}\right] + \ldots \\
&\ldots + \left[b_{i,kk}\right] \cdot \left[v_{sk,xy}\right] + \sum_{\substack{h=1 \\ h \neq k}}^{n} \left(\left[b_{i,kh}\right] \cdot \left[v_{sh,xy}\right]\right) + \left[b_{i,kr}\right] \cdot \left[v_{r,xy}\right]
\end{aligned} \tag{2.142}$$

where the matrices in (2.142) are defined as follows:

$$\begin{aligned}
\left[A_{i,kk}\right] &= \begin{bmatrix} a_{i,kk-xx} & a_{i,kk-xy} \\ a_{i,kk-yx} & a_{i,kk-yy} \end{bmatrix} \qquad \left[b_{i,kk}\right] = \begin{bmatrix} b_{i,kk-xx} & b_{i,kk-xy} \\ b_{i,kk-yx} & b_{i,kk-yy} \end{bmatrix} \\
\left[A_{i,kh}\right]_{k\neq h} &= \begin{bmatrix} a_{i,kh-xx} & a_{i,kh-xy} \\ a_{i,kh-yx} & a_{i,kh-yy} \end{bmatrix} \quad \left[b_{i,kh}\right]_{k\neq h} = \begin{bmatrix} b_{i,kh-xx} & b_{i,kh-xy} \\ b_{i,kh-yx} & b_{i,kh-yy} \end{bmatrix} \\
\left[A_{i,kr}\right] &= \begin{bmatrix} a_{i,kr-xx} & a_{i,kr-xy} \\ a_{i,kr-yx} & a_{i,kr-yy} \end{bmatrix} \qquad \left[b_{i,kr}\right] = \begin{bmatrix} b_{i,kr-xx} & b_{i,kr-xy} \\ b_{i,kr-yx} & b_{i,kr-yy} \end{bmatrix}
\end{aligned} \tag{2.143}$$

According with (2.141), the matrices' coefficients in (2.143) are computed as follows:

$$\begin{cases} a_{i,kk-xx} = a_{i,kk-yy} = -\dfrac{R_r \cdot k_r \cdot k_{sk}^{-1} + R_{sk} \cdot (1 + c_k) - \tau_r^{-1} \cdot \sigma_k \cdot L_{sk}}{\sigma_k \cdot L_{sk} + c_k \cdot L_{l,sk}} \\ a_{i,kk-xy} = -a_{i,kk-yx} = \omega^* \end{cases} \tag{2.144}$$

$$\begin{cases} a_{i,kh-xx} = a_{i,kh-yy} = -\dfrac{R_r \cdot k_r - c_h \cdot R_{sk} - k_r \cdot L_{l,r} \cdot \tau_r^{-1}}{\sigma_k \cdot L_{sk} + c_k \cdot L_{l,sk}} \\ a_{i,kh-xy} = a_{i,kh-yx} = 0 \end{cases} \tag{2.145}$$

$$\begin{cases} a_{i,kr-xx} = a_{i,kr-yy} = \dfrac{k_r \cdot \tau_r^{-1}}{\sigma_k \cdot L_{sk} + c_k \cdot L_{l,sk}} \\ a_{i,kr-xy} = -a_{i,kr-yx} = \dfrac{k_r \cdot \omega_r}{\sigma_k \cdot L_{sk} + c_k \cdot L_{l,sk}} \end{cases} \tag{2.146}$$

$$\begin{cases} b_{i,kk-xx} = b_{i,kk-yy} = \dfrac{1 + c_k}{\sigma_k \cdot L_{sk} + c_k \cdot L_{l,sk}} \\ b_{i,kk-xy} = b_{i,kk-yx} = 0 \end{cases} \tag{2.147}$$

$$\begin{cases} b_{i,kh-xx} = b_{i,kh-yy} = -\dfrac{c_h}{\sigma_k \cdot L_{sk} + c_k \cdot L_{l,sk}} \\ b_{i,kh-xy} = b_{i,kh-yx} = 0 \end{cases} \tag{2.148}$$

$$\begin{cases} b_{i,kr-xx} = b_{i,kr-yy} = -\dfrac{k_r}{\sigma_k \cdot L_{sk} + c_k \cdot L_{l,sk}} \\ b_{i,kr-xy} = b_{i,kr-yx} = 0 \end{cases} \tag{2.149}$$

Finally, like for the three-phase IM machine, the full definition of the state-space model requires the computation of the state equation related to the rotor flux vector $\overline{\lambda}_{r,xy}$. This is computed by replacing (2.133) in (2.138), obtaining the following result:

$$\frac{d}{dt}\overline{\lambda}_{r,xy} = -\left[\frac{1}{\tau_r} + j \cdot \left(\omega^* - \omega_r\right)\right] \cdot \overline{\lambda}_{r,xy} + R_r \cdot k_r \cdot \sum_{h=1}^{n} \overline{i}_{sh,xy} + \overline{v}_{r,xy} \tag{2.150}$$

Like for the state equation of the stator current (2.141), (2.150) is expressed in matrix form as follows:

$$\begin{aligned} \frac{d}{dt}\left[\lambda_{r,xy}\right] = \sum_{h=1}^{n}\left(\left[A_{\lambda,rh}\right] \cdot \left[i_{sh,xy}\right]\right) + \left[A_{\lambda,rr}\right] \cdot \left[\lambda_{r,xy}\right] + \ldots \\ \ldots + \sum_{h=1}^{n}\left(\left[b_{\lambda,rh}\right] \cdot \left[v_{sh,xy}\right]\right) + \left[b_{\lambda,rr}\right] \cdot \left[v_{r,xy}\right] \end{aligned} \tag{2.151}$$

where the matrices in (2.142) are defined as follows:

$$\begin{aligned} \left[A_{\lambda,rh}\right] &= \begin{bmatrix} a_{\lambda,rh-xx} & a_{\lambda,rh-xy} \\ a_{\lambda,rh-yx} & a_{\lambda,rh-yy} \end{bmatrix} \quad \left[b_{\lambda,rh}\right] = \begin{bmatrix} b_{\lambda,rh-xx} & b_{\lambda,rh-xy} \\ b_{\lambda,rh-yx} & b_{\lambda,rh-yy} \end{bmatrix} \\ \left[A_{\lambda,rr}\right] &= \begin{bmatrix} a_{\lambda,rr-xx} & a_{\lambda,rr-xy} \\ a_{\lambda,rr-yx} & a_{\lambda,rr-yy} \end{bmatrix} \quad \left[b_{\lambda,rr}\right] = \begin{bmatrix} b_{\lambda,rr-xx} & b_{\lambda,rr-xy} \\ b_{\lambda,rr-yx} & b_{\lambda,rr-yy} \end{bmatrix} \end{aligned} \tag{2.152}$$

According with (2.150), the matrices' coefficients in (2.152) are computed as follows:

$$\begin{cases} a_{\lambda,rh-xx} = a_{\lambda,rh-yy} = R_r \cdot k_r \\ a_{\lambda,rh-xy} = a_{\lambda,rh-yx} = 0 \end{cases} \tag{2.153}$$

$$\begin{cases} a_{\lambda,rr-xx} = a_{\lambda,rr-yy} = -\tau_r^{-1} \\ a_{\lambda,rr-xy} = -a_{\lambda,rr-yx} = \omega^* - \omega_r \end{cases} \tag{2.154}$$

$$\left\{b_{\lambda,rh-xx} = b_{\lambda,rh-yy} = b_{\lambda,rh-xy} = b_{\lambda,rh-yx} = 0\right. \tag{2.155}$$

$$\begin{cases} b_{\lambda,rr-xx} = b_{\lambda,rr-yy} = 1 \\ b_{\lambda,rr-xy} = b_{\lambda,rr-yx} = 0 \end{cases} \tag{2.156}$$

The combination of the state equations (2.142) and (2.151) represents the state-space model of the machine in the rotating (x,y) frame. According with the MS modelling, it is composed by $2 \cdot n$ state equations related to the n stator current vectors and two state equations related the rotor flux vector.

State-space model of zero-sequence components

With reference to (2.101), the electromagnetic zero-sequence '0' model of the machine is as follows:

$$\begin{cases} \lambda_{sk-0} = L_{l,sk} \cdot i_{sk-0} & k = 1,2,...,n \\ \lambda_{r-0} = L_{l,r} \cdot i_{r-0} & \\ v_{sk-0} = R_{sk} \cdot i_{sk-0} + \dfrac{d}{dt}\lambda_{sk-0} & k = 1,2,...,n \\ v_{r-0} = R_r \cdot i_{r-0} + \dfrac{d}{dt}\lambda_{r-0} & \end{cases} \tag{2.157}$$

By using simple mathematical manipulations, (2.157) is expressed as follows:

$$\begin{cases} \dfrac{d}{dt} i_{sk-0} = -\dfrac{R_{sk}}{L_{l,sk}} \cdot i_{sk-0} + v_{sk-0} & k = 1,2,...,n \\ \dfrac{d}{dt}\lambda_{r-0} = -\dfrac{R_r}{L_{l,r}} \cdot \lambda_{r-0} + v_{r-0} & \end{cases} \tag{2.158}$$

As a squirrel cage IM is considered, the zero-sequence rotor voltage v_{r-0} is zero, leading to the following result:

$$v_{r-0} = 0 \quad \Rightarrow \quad \frac{d}{dt}\lambda_{r-0} = -\frac{R_r}{L_{l,r}} \cdot \lambda_{r-0} \tag{2.159}$$

The equation system (2.158) represents the state-space model of the machine' zero-sequence components. According with the MS modelling, it is composed by n stator equations and one rotor equation.

Like for the three-phase machines, the dynamic of the zero-sequence stator currents is related to the machine neutral points configuration. Concerning the zero-sequence rotor flux, (2.159) shows how it is always zero. Indeed, the state-space model computation has led to a homogenous differential equation, thus without any rotor voltage excitation.

State space model of the machine

The computation of the state equations for both rotating frame and zero-sequence components allows to define the state space model of the machine. With the aim at obtaining compact formulations, both rotating and zero-sequence components of each variable are merged in a single vector as follows:

$$\left[z_{sk,xy0}\right]=\begin{bmatrix} z_{sk-x} \\ z_{sk-y} \\ z_{sk-0} \end{bmatrix} \quad , \quad \left[z_{r,xy0}\right]=\begin{bmatrix} z_{r-x} \\ z_{r-y} \\ z_{r-0} \end{bmatrix} \qquad \left(z=v,i,\lambda\right) \tag{2.160}$$

Concerning the full computation of the state equation belonging to each *k*-set stator current, the following 3×3 matrices are defined:

$$\left[A_{i,kk-xy0}\right]=\begin{bmatrix} \left[A_{i,kk}\right]_{2\times 2} & 0 \\ 0 & -\dfrac{R_{sk}}{L_{l,sk}} \end{bmatrix}=\begin{bmatrix} a_{i,kk-xx} & a_{i,kk-xy} & 0 \\ a_{i,kk-yx} & a_{i,kk-yy} & 0 \\ 0 & 0 & -R_{sk}/L_{l,sk} \end{bmatrix} \tag{2.161}$$

$$\left[A_{i,kh-xy0}\right]_{k\neq h}=\begin{bmatrix} \left[A_{i,kh}\right]_{k\neq h} & 0 \\ 0 & 0 \end{bmatrix}=\begin{bmatrix} a_{i,kh-xx} & a_{i,kh-xy} & 0 \\ a_{i,kh-yx} & a_{i,kh-yy} & 0 \\ 0 & 0 & 0 \end{bmatrix} \tag{2.162}$$

$$\left[A_{i,kr-xy0}\right]=\begin{bmatrix} \left[A_{i,kr}\right] & 0 \\ 0 & 0 \end{bmatrix}=\begin{bmatrix} a_{i,kr-xx} & a_{i,kr-xy} & 0 \\ a_{i,kr-yx} & a_{i,kr-yy} & 0 \\ 0 & 0 & 0 \end{bmatrix} \tag{2.163}$$

$$\left[b_{i,kk-xy0}\right]=\begin{bmatrix} \left[b_{i,kk}\right] & 0 \\ 0 & 1 \end{bmatrix}=\begin{bmatrix} b_{i,kk-xx} & b_{i,kk-xy} & 0 \\ b_{i,kk-yx} & b_{i,kk-yy} & 0 \\ 0 & 0 & 1 \end{bmatrix} \tag{2.164}$$

$$\left[b_{i,kh-xy0}\right]_{k\neq h}=\begin{bmatrix} \left[b_{i,kh}\right]_{k\neq h} & 0 \\ 0 & 0 \end{bmatrix}=\begin{bmatrix} b_{i,kh-xx} & b_{i,kh-xy} & 0 \\ b_{i,kh-yx} & b_{i,kh-yy} & 0 \\ 0 & 0 & 0 \end{bmatrix} \tag{2.165}$$

$$\left[b_{i,kr-xy0}\right]=\begin{bmatrix} \left[b_{i,kr}\right] & 0 \\ 0 & 0 \end{bmatrix}=\begin{bmatrix} b_{i,kr-xx} & b_{i,kr-xy} & 0 \\ b_{i,kr-yx} & b_{i,kr-yy} & 0 \\ 0 & 0 & 0 \end{bmatrix} \tag{2.166}$$

Therefore, by using (2.161)-(2.166), the merging operation between (2.142) and (2.158) by means of (2.160) is performed as follows:

$$\frac{d}{dt}\left[i_{sk,xy0}\right]=\left[A_{i,kk-xy0}\right]\cdot\left[i_{sk,xy0}\right]+\sum_{\substack{h=1\\h\neq k}}^{n}\left(\left[A_{i,kh-xy0}\right]\cdot\left[i_{sh,xy0}\right]\right)+\left[A_{i,kr-xy0}\right]\cdot\left[\lambda_{r,xy0}\right]+\ldots$$

$$\ldots+\left[b_{i,kk-xy0}\right]\cdot\left[v_{sk,xy0}\right]+\sum_{\substack{h=1\\h\neq k}}^{n}\left(\left[b_{i,kh-xy0}\right]\cdot\left[v_{sh,xy0}\right]\right)+\left[b_{i,kr-xy0}\right]\cdot\left[v_{r,xy0}\right] \tag{2.167}$$

Similarly, with the aim at computing the state equation belonging to the rotor flux, the following 3×3 matrices are defined:

$$\left[A_{\lambda,rh-xy0}\right]=\begin{bmatrix}\left[A_{\lambda,rh}\right] & 0\\ 0 & 0\end{bmatrix}=\begin{bmatrix}a_{\lambda,rh-xx} & a_{\lambda,rh-xy} & 0\\ a_{\lambda,rh-yx} & a_{\lambda,rh-yy} & 0\\ 0 & 0 & 0\end{bmatrix} \tag{2.168}$$

$$\left[A_{\lambda,rr-xy0}\right]=\begin{bmatrix}\left[A_{\lambda,rr}\right] & 0\\ 0 & -\dfrac{R_r}{L_{l,r}}\end{bmatrix}=\begin{bmatrix}a_{\lambda,rr-xx} & a_{\lambda,rr-xy} & 0\\ a_{\lambda,rr-yx} & a_{\lambda,rr-yy} & 0\\ 0 & 0 & -R_r/L_{l,r}\end{bmatrix} \tag{2.169}$$

$$\left[b_{\lambda,rh-xy0}\right]=\begin{bmatrix}\left[b_{\lambda,rh}\right] & 0\\ 0 & 0\end{bmatrix}=\begin{bmatrix}b_{\lambda,rh-xx} & b_{\lambda,rh-xy} & 0\\ b_{\lambda,rh-yx} & b_{\lambda,rh-yy} & 0\\ 0 & 0 & 0\end{bmatrix} \tag{2.170}$$

$$\left[b_{\lambda,rr-xy0}\right]=\begin{bmatrix}\left[b_{\lambda,rr}\right] & 0\\ 0 & 0\end{bmatrix}=\begin{bmatrix}b_{\lambda,rr-xx} & b_{\lambda,rr-xy} & 0\\ b_{\lambda,rr-yx} & b_{\lambda,rr-yy} & 0\\ 0 & 0 & 1\end{bmatrix} \tag{2.171}$$

Therefore, by using (2.168)-(2.171), the merging operation between (2.151) and (2.158) by means of (2.160) is performed as follows:

$$\frac{d}{dt}\left[\lambda_{r,xy0}\right]=\sum_{h=1}^{n}\left(\left[A_{\lambda,rh-xy0}\right]\cdot\left[i_{sh,xy0}\right]\right)+\left[A_{\lambda,rr-xy0}\right]\cdot\left[\lambda_{r,xy0}\right]+\ldots$$
$$\ldots+\sum_{h=1}^{n}\left(\left[b_{\lambda,rh-xy0}\right]\cdot\left[v_{sh,xy0}\right]\right)+\left[b_{\lambda,rr-xy0}\right]\cdot\left[v_{r,xy0}\right] \tag{2.172}$$

By merging (2.167) for all sets k=1,2,…,n and by including (2.172), the complete state-space electromagnetic model of the machine in generic rotating (xy0) coordinates is obtained as follows:

$$\frac{d}{dt}\begin{Bmatrix}\left[i_{s1,xy0}\right]\\ \left[i_{s2,xy0}\right]\\ \dots\\ \left[i_{sn,xy0}\right]\\ \left[\lambda_{r,xy0}\right]\end{Bmatrix}=\left[\mathbf{A}\right]\cdot\begin{Bmatrix}\left[i_{s1,xy0}\right]\\ \left[i_{s2,xy0}\right]\\ \dots\\ \left[i_{sn,xy0}\right]\\ \left[\lambda_{r,xy0}\right]\end{Bmatrix}+\left[\mathbf{b}\right]\cdot\begin{Bmatrix}\left[v_{s1,xy0}\right]\\ \left[v_{s2,xy0}\right]\\ \dots\\ \left[v_{sn,xy0}\right]\\ \left[v_{r,xy0}\right]\end{Bmatrix} \tag{2.173}$$

where:

$$\left[\mathbf{A}\right]=\begin{bmatrix}\left[A_{i,11-xy0}\right] & \left[A_{i,12-xy0}\right] & \dots & \left[A_{i,1n-xy0}\right] & \left[A_{i,1r-xy0}\right]\\ \left[A_{i,21-xy0}\right] & \left[A_{i,22-xy0}\right] & \dots & \left[A_{i,2n-xy0}\right] & \left[A_{i,2r-xy0}\right]\\ \dots & \dots & \dots & \dots & \dots\\ \left[A_{i,n1-xy0}\right] & \left[A_{i,n2-xy0}\right] & \dots & \left[A_{i,nn-xy0}\right] & \left[A_{i,nr-xy0}\right]\\ \left[A_{\lambda,r1-xy0}\right] & \left[A_{\lambda,r2-xy0}\right] & \dots & \left[A_{\lambda,rn-xy0}\right] & \left[A_{\lambda,rr-xy0}\right]\end{bmatrix} \tag{2.174}$$

$$\left[\mathbf{b}\right]=\begin{bmatrix}\left[b_{i,11-xy0}\right] & \left[b_{i,12-xy0}\right] & \dots & \left[b_{i,1n-xy0}\right] & \left[b_{i,1r-xy0}\right]\\ \left[b_{i,21-xy0}\right] & \left[b_{i,22-xy0}\right] & \dots & \left[b_{i,2n-xy0}\right] & \left[b_{i,2r-xy0}\right]\\ \dots & \dots & \dots & \dots & \dots\\ \left[b_{i,n1-xy0}\right] & \left[b_{i,n2-xy0}\right] & \dots & \left[b_{i,nn-xy0}\right] & \left[b_{i,nr-xy0}\right]\\ \left[b_{\lambda,r1-xy0}\right] & \left[b_{\lambda,r2-xy0}\right] & \dots & \left[b_{\lambda,rn-xy0}\right] & \left[b_{\lambda,rr-xy0}\right]\end{bmatrix} \tag{2.175}$$

With the aim at obtaining a compact formulation of (2.175), the following variables are introduced:

$$\left\{x\right\}=\begin{Bmatrix}\left[i_{s1,xy0}\right]\\ \left[i_{s2,xy0}\right]\\ \dots\\ \left[i_{sn,xy0}\right]\\ \left[\lambda_{r,xy0}\right]\end{Bmatrix}\quad,\quad\left\{u\right\}=\begin{Bmatrix}\left[v_{s1,xy0}\right]\\ \left[v_{s2,xy0}\right]\\ \dots\\ \left[v_{sn,xy0}\right]\\ \left[v_{r,xy0}\right]\end{Bmatrix} \tag{2.176}$$

Finally, by replacing (2.176) in (2.173), the state-space model of the machine in the canonical form of the linear systems [6] is obtained:

$$\frac{d}{dt}\{x\} = [\mathbf{A}]\cdot\{x\} + [\mathbf{b}]\cdot\{u\} \tag{2.177}$$

The equation system (2.177) represents the state-space MS model of a multiple three-phase squirrel cage IM. Because of the model is defined in the generic rotating ($xy0$) coordinates, according with (2.104), it is possible to make the equation system referring to any frame. In detail, by defining ω^* properly, the following frames can be selected:

$$\begin{cases} \omega^* = \omega_d & \Rightarrow \quad (x,y,0) \equiv (d,q,0) \\ \omega^* = 0 & \Rightarrow \quad (x,y,0) \equiv (\alpha,\beta,0) \\ \omega^* = \omega_r & \Rightarrow \quad (x,y,0) \equiv (d_r,q_r,0) \\ \omega^* = \omega_{sk-\lambda} & \Rightarrow \quad (x,y,0) \equiv (d_{sk},q_{sk},0) \end{cases} \tag{2.178}$$

The meaning of the frames defined in (2.178) corresponds with the one of (2.104). In conclusion, with the definition of the state-space model, the MS modelling of the machine is fully defined. It is noted how the MS approach allows the highlight the flux and torque contribution belonging to each three-phase winding set, resulting suitable for the implementation of a modular drive scheme able to guarantee the direct control of each unit.

2.2 Vector Space Decomposition (VSD) modelling approach

The VSD approach represents the main alternative to the MS modelling. With reference to the technical literature [7], [8], it results the most employed modelling approach. Therefore, it is possible to find many paper contributions concerning the application of the VSD approach on IM, including the multiple three-phase configurations [7], [9]. As the proposed control schemes are MS-based, the VSD modelling must be considered beyond the scope of this dissertation. Consequently, a synthetic analysis is following reported, showing the main differences of the VSD modelling compared to the MS one.

2.2.1 Electromechanical model in phase coordinates

With respect to the MS approach, the following initial hypotheses must be added:

8) The stator is composed by n three-phase winding sets with angle displacements such to implement a symmetrical or asymmetrical machine configuration;
9) The three-phase winding sets are considered identical from each other, therefore characterized by the same values of the stator parameters;

10) Squirrel cage rotor modelled as an equivalent multiple three-phase winding, thus emulating the stator winding configuration.

In terms of mathematical formulation, hypotheses 9) is expressed as follows:

$$\begin{cases} N_{sk} = N_{sz} = N_s \\ R_{sk} = R_{sz} = R_s \\ L_{l,sk} = L_{l,sz} = L_{l,s} \end{cases} \quad \forall k, \forall z \tag{2.179}$$

The conditions (2.179) highlights how the VSD approach is characterized by less degrees of freedom compared to the MS one, including the angle displacements of the winding sets. Concerning hypothesis 9), it leads to the equivalent magnetic scheme shown in Fig. 2. 8.

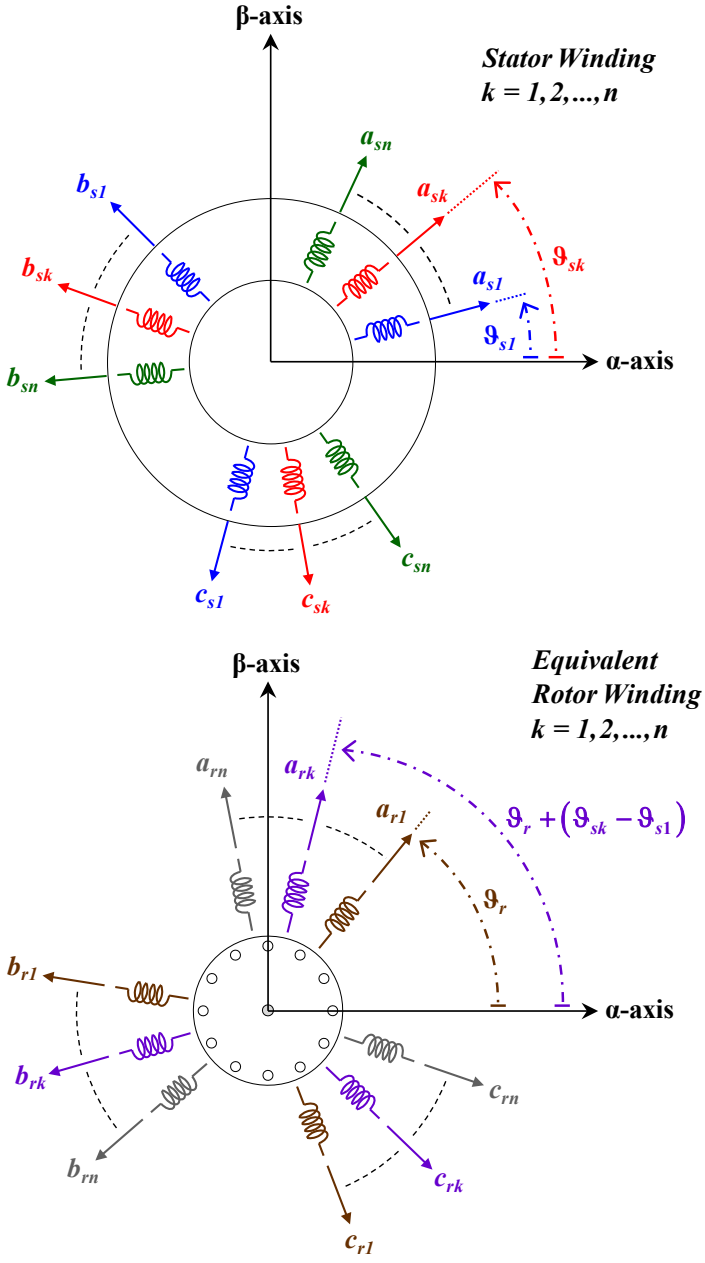

Fig. 2. 8. Equivalent VSD magnetic scheme of a multiple three-phase squirrel cage induction machine.

Therefore, according with the above assumptions, the positions of the magnetic axes belonging to the phases of a generic rotor *k*-set are expressed as follows:

$$\begin{bmatrix} \vartheta_{rk-a} \\ \vartheta_{rk-b} \\ \vartheta_{rk-c} \end{bmatrix} = \begin{bmatrix} \vartheta_{rk-a} \\ \vartheta_{rk-a} + \frac{2\pi}{3} \\ \vartheta_{rk-a} - \frac{2\pi}{3} \end{bmatrix} = \begin{bmatrix} \vartheta_{rk} \\ \vartheta_{rk} + \frac{2\pi}{3} \\ \vartheta_{rk} - \frac{2\pi}{3} \end{bmatrix} \tag{2.180}$$

The procedure for the computation of the VSD electromagnetic model in phase coordinates is similar to the one used for the MS modelling. Therefore, only the main differences will be reported.

Stator magnetic model in phase coordinates

According with hypothesis 10), it is necessary to take in account the different rotor winding structure compared to the MS modelling. By considering (2.179), the magnetic model of each three-phase stator *k*-set is expressed as follows:

$$\begin{bmatrix} \lambda_{sk-a} \\ \lambda_{sk-b} \\ \lambda_{sk-c} \end{bmatrix} = L_{l,s} \cdot \begin{bmatrix} i_{sk-a} \\ i_{sk-b} \\ i_{sk-c} \end{bmatrix} + \sum_{z=1}^{n} \left([M_{sk-sz}] \cdot \begin{bmatrix} i_{sz-a} \\ i_{sz-b} \\ i_{sz-c} \end{bmatrix} \right) + \sum_{z=1}^{n} \left([M_{sk-rz}] \cdot \begin{bmatrix} i_{rz-a} \\ i_{rz-b} \\ i_{rz-c} \end{bmatrix} \right) \tag{2.181}$$

where:

- $[i_{rz-a} \quad i_{rz-b} \quad i_{rz-c}]^t$ is the vector of the rotor currents for the three-phase rotor *z*-set defined in the own rotor phase coordinates $(abc)_{rz}$;

while:

- $[M_{sk-rz}]$ is the 3×3 mutual magnetizing inductance matrix between the stator phase windings of *k*-set and the rotor phase windings of the *z*-set.

With reference to (2.11), (2.179) and Table 2. 1, $[M_{sk-rz}]$ is computed as follows:

$$[M_{sk-rz}] = \frac{N_s \cdot N_r^{VSD}}{\Re_{eq}} \cdot \begin{bmatrix} \cos(\Delta\vartheta_{sk-rz}) & \cos\left(\Delta\vartheta_{sk-rz} - \frac{2\pi}{3}\right) & \cos\left(\Delta\vartheta_{sk-rz} - \frac{4\pi}{3}\right) \\ \cos\left(\Delta\vartheta_{sk-rz} + \frac{2\pi}{3}\right) & \cos(\Delta\vartheta_{sk-rz}) & \cos\left(\Delta\vartheta_{sk-rz} - \frac{2\pi}{3}\right) \\ \cos\left(\Delta\vartheta_{sk-rz} + \frac{4\pi}{3}\right) & \cos\left(\Delta\vartheta_{sk-rz} + \frac{2\pi}{3}\right) & \cos(\Delta\vartheta_{sk-rz}) \end{bmatrix} \tag{2.182}$$

where:

- $N_r^{VSD} = N_r / \sqrt{n}$ is the number of turns of each rotor phase winding, such at keeping the equivalence with the rotor winding structure used in the MS modelling;
- $\Delta\vartheta_{sk-rz} = \vartheta_{sk} - \vartheta_{rz}$ is the angular difference among the magnetic axes of the first phases belonging to the stator *k*-set and the rotor *z*-set.

Rotor magnetic model in phase coordinates

According with hypothesis 10), the magnetic model of each three-phase rotor *k*-set is expressed as follows:

$$\begin{bmatrix} \lambda_{rk-a} \\ \lambda_{rk-b} \\ \lambda_{rk-c} \end{bmatrix} = L_{l,r} \cdot \begin{bmatrix} i_{rk-a} \\ i_{rk-b} \\ i_{rk-c} \end{bmatrix} + \sum_{z=1}^{n} \left(\left[M_{rk-sz} \right] \cdot \begin{bmatrix} i_{sz-a} \\ i_{sz-b} \\ i_{sz-c} \end{bmatrix} \right) + \sum_{z=1}^{n} \left(\left[M_{rk-rz} \right] \cdot \begin{bmatrix} i_{rz-a} \\ i_{rz-b} \\ i_{rz-c} \end{bmatrix} \right) \quad (2.183)$$

where:

- $\left[\lambda_{rk-a} \quad \lambda_{rk-b} \quad \lambda_{rk-c} \right]^t$ is the vector of the rotor fluxes linkage for the three-phase rotor *k*-set defined in the own rotor phase coordinates $(abc)_{rk}$;

while:

- $\left[M_{rk-sz} \right]$ is the 3×3 mutual magnetizing inductance matrix between the rotor phase windings of *k*-set and the stator phase windings of the *z*-set;
- $\left[M_{rk-rz} \right]$ is the 3×3 mutual magnetizing inductance matrix between the rotor phase windings of *k*-set and the rotor phase windings of the *z*-set.

With reference to (2.11), (2.179) and Table 2. 1, $\left[M_{rk-sz} \right]$ and $\left[M_{rk-rz} \right]$ are computed as follows:

$$\left[M_{rk-sz} \right] = \frac{N_s \cdot N_r^{VSD}}{\Re_{eq}} \cdot \begin{bmatrix} \cos\left(\Delta\vartheta_{rk-sz}\right) & \cos\left(\Delta\vartheta_{rk-sz} - \frac{2\pi}{3}\right) & \cos\left(\Delta\vartheta_{rk-sz} - \frac{4\pi}{3}\right) \\ \cos\left(\Delta\vartheta_{rk-sz} + \frac{2\pi}{3}\right) & \cos\left(\Delta\vartheta_{rk-sz}\right) & \cos\left(\Delta\vartheta_{rk-sz} - \frac{2\pi}{3}\right) \\ \cos\left(\Delta\vartheta_{rk-sz} + \frac{4\pi}{3}\right) & \cos\left(\Delta\vartheta_{rk-sz} + \frac{2\pi}{3}\right) & \cos\left(\Delta\vartheta_{rk-sz}\right) \end{bmatrix} \quad (2.184)$$

$$[M_{rk-rz}] = \frac{N_r^{VSD} \cdot N_r^{VSD}}{\Re_{eq}} \cdot \begin{bmatrix} \cos(\Delta\vartheta_{rk-rz}) & \cos\left(\Delta\vartheta_{rk-rz} - \frac{2\pi}{3}\right) & \cos\left(\Delta\vartheta_{rk-rz} - \frac{4\pi}{3}\right) \\ \cos\left(\Delta\vartheta_{rk-rz} + \frac{2\pi}{3}\right) & \cos(\Delta\vartheta_{rk-rz}) & \cos\left(\Delta\vartheta_{rk-rz} - \frac{2\pi}{3}\right) \\ \cos\left(\Delta\vartheta_{rk-rz} + \frac{4\pi}{3}\right) & \cos\left(\Delta\vartheta_{rk-rz} + \frac{2\pi}{3}\right) & \cos(\Delta\vartheta_{rk-rz}) \end{bmatrix} \tag{2.185}$$

where:

- $\Delta\vartheta_{rk-sz} = \vartheta_{rk} - \vartheta_{sz}$ is the angular difference among the magnetic axes of the first phases belonging to the rotor *k*-set and the stator *z*-set;
- $\Delta\vartheta_{rk-rz} = \vartheta_{rk} - \vartheta_{rz}$ is the angular difference among the magnetic axes of the first phases belonging to the rotor *k*-set and the rotor *z*-set.

In conclusion, the VSD magnetic model of a multiple three-phase IM machine is composed by $3\cdot(n+n)$ algebraic equations, containing all the current-to-flux relationships of the phase windings.

Stator electric model in phase coordinates

The stator electric model in phase coordinates is identical to the one computed with the MS modelling, leading to the equation system (2.17). However, with the application of (2.179), the electric model of each three-phase stator *k*-set is expressed as follows:

$$\begin{bmatrix} v_{sk-a} \\ v_{sk-b} \\ v_{sk-c} \end{bmatrix} = R_s \cdot \begin{bmatrix} i_{sk-a} \\ i_{sk-b} \\ i_{sk-c} \end{bmatrix} + \frac{d}{dt} \begin{bmatrix} \lambda_{sk-a} \\ \lambda_{sk-b} \\ \lambda_{sk-c} \end{bmatrix} \tag{2.186}$$

Rotor electric model

According with hypothesis 10), the electric model of each three-phase rotor *k*-set (using the "passive sign" convention) is expressed as follows:

$$\begin{bmatrix} v_{rk-a} \\ v_{rk-b} \\ v_{rk-c} \end{bmatrix} = R_r \cdot \begin{bmatrix} i_{rk-a} \\ i_{rk-b} \\ i_{rk-c} \end{bmatrix} + \frac{d}{dt} \begin{bmatrix} \lambda_{rk-a} \\ \lambda_{rk-b} \\ \lambda_{rk-c} \end{bmatrix} \tag{2.187}$$

where:

- $[v_{rk-a} \quad v_{rk-b} \quad v_{rk-c}]^t$ is the vector of the rotor voltages for the three-phase rotor *k*-set defined in the own rotor phase coordinates $(abc)_{rk}$;

Because a squirrel cage IM typology is considered, the equivalent rotor winding is short-circuited, leading to the following equations:

$$\begin{bmatrix} v_{rk-a} & v_{rk-b} & v_{rk-c} \end{bmatrix}^t = \begin{bmatrix} 0 \end{bmatrix}_{3\times 1} = \begin{bmatrix} 0 & 0 & 0 \end{bmatrix}^t \tag{2.188}$$

In conclusion, the electric model of a multiple three-phase IM machine is composed by $3\cdot(n+n)$ differential equations, containing all the flux-to-voltage relationships of the phase windings.

Electromagnetic model in phase coordinates

With the aim at obtaining an overall electromagnetic model of the machine, it is necessary to merge the electromagnetic equations. Using (2.20), the Equations (2.181), (2.183), (2.186)-(2.187) are expressed as follows:

$$\begin{bmatrix} \lambda_{sk,abc} \end{bmatrix} = L_{l,s} \cdot \begin{bmatrix} i_{sk,abc} \end{bmatrix} + \sum_{z=1}^{n} \left(\begin{bmatrix} M_{sk-sz} \end{bmatrix} \cdot \begin{bmatrix} i_{sz,abc} \end{bmatrix} \right) + \sum_{z=1}^{n} \left(\begin{bmatrix} M_{sk-rz} \end{bmatrix} \cdot \begin{bmatrix} i_{rz,abc} \end{bmatrix} \right) \tag{2.189}$$

$$\begin{bmatrix} \lambda_{rk,abc} \end{bmatrix} = L_{l,r} \cdot \begin{bmatrix} i_{rk,abc} \end{bmatrix} + \sum_{z=1}^{n} \left(\begin{bmatrix} M_{rk-sz} \end{bmatrix} \cdot \begin{bmatrix} i_{sz,abc} \end{bmatrix} \right) + \sum_{z=1}^{n} \left(\begin{bmatrix} M_{rk-rz} \end{bmatrix} \cdot \begin{bmatrix} i_{rz,abc} \end{bmatrix} \right) \tag{2.190}$$

$$\begin{bmatrix} v_{sk,abc} \end{bmatrix} = R_s \cdot \begin{bmatrix} i_{sk,abc} \end{bmatrix} + \frac{d}{dt} \begin{bmatrix} \lambda_{sk,abc} \end{bmatrix} \tag{2.191}$$

$$\begin{bmatrix} v_{rk,abc} \end{bmatrix} = R_r \cdot \begin{bmatrix} i_{rk,abc} \end{bmatrix} + \frac{d}{dt} \begin{bmatrix} \lambda_{rk,abc} \end{bmatrix} \tag{2.192}$$

By merging (2.189) for all sets k=1,2,…,n, the stator magnetic model of the machine in phase coordinates is obtained as follows:

$$\begin{Bmatrix} \begin{bmatrix} \lambda_{s1,abc} \end{bmatrix} \\ \begin{bmatrix} \lambda_{s2,abc} \end{bmatrix} \\ \cdots \\ \begin{bmatrix} \lambda_{sn,abc} \end{bmatrix} \end{Bmatrix} = L_{l,s} \cdot \begin{Bmatrix} \begin{bmatrix} i_{s1,abc} \end{bmatrix} \\ \begin{bmatrix} i_{s2,abc} \end{bmatrix} \\ \cdots \\ \begin{bmatrix} i_{sn,abc} \end{bmatrix} \end{Bmatrix} + \begin{bmatrix} L_{SS} \end{bmatrix} \cdot \begin{Bmatrix} \begin{bmatrix} i_{s1,abc} \end{bmatrix} \\ \begin{bmatrix} i_{s2,abc} \end{bmatrix} \\ \cdots \\ \begin{bmatrix} i_{sn,abc} \end{bmatrix} \end{Bmatrix} + \begin{bmatrix} L_{SR} \end{bmatrix} \cdot \begin{Bmatrix} \begin{bmatrix} i_{r1,abc} \end{bmatrix} \\ \begin{bmatrix} i_{r2,abc} \end{bmatrix} \\ \cdots \\ \begin{bmatrix} i_{rn,abc} \end{bmatrix} \end{Bmatrix} \tag{2.193}$$

where:

$$\begin{bmatrix} L_{SS} \end{bmatrix} = \begin{bmatrix} \begin{bmatrix} M_{s1-s1} \end{bmatrix} & \begin{bmatrix} M_{s1-s2} \end{bmatrix} & \cdots & \begin{bmatrix} M_{s1-sn} \end{bmatrix} \\ \begin{bmatrix} M_{s2-s1} \end{bmatrix} & \begin{bmatrix} M_{s2-s2} \end{bmatrix} & \cdots & \begin{bmatrix} M_{s2-sn} \end{bmatrix} \\ \cdots & \cdots & \cdots & \cdots \\ \begin{bmatrix} M_{sn-s1} \end{bmatrix} & \begin{bmatrix} M_{sn-s2} \end{bmatrix} & \cdots & \begin{bmatrix} M_{sn-sn} \end{bmatrix} \end{bmatrix} \tag{2.194}$$

$$\begin{bmatrix} L_{SR} \end{bmatrix} = \begin{bmatrix} \begin{bmatrix} M_{s1-r1} \end{bmatrix} & \begin{bmatrix} M_{s1-r2} \end{bmatrix} & \cdots & \begin{bmatrix} M_{s1-rn} \end{bmatrix} \\ \begin{bmatrix} M_{s2-r1} \end{bmatrix} & \begin{bmatrix} M_{s2-r2} \end{bmatrix} & \cdots & \begin{bmatrix} M_{s2-rn} \end{bmatrix} \\ \cdots & \cdots & \cdots & \cdots \\ \begin{bmatrix} M_{sn-r1} \end{bmatrix} & \begin{bmatrix} M_{sn-r2} \end{bmatrix} & \cdots & \begin{bmatrix} M_{sn-rn} \end{bmatrix} \end{bmatrix} \tag{2.195}$$

Conversely, by merging (2.190) for all sets k=1,2,…,n, the rotor magnetic model of the machine in phase coordinates is obtained as follows:

$$\begin{Bmatrix} [\lambda_{r1,abc}] \\ [\lambda_{r2,abc}] \\ \dots \\ [\lambda_{rn,abc}] \end{Bmatrix} = L_{l,r} \cdot \begin{Bmatrix} [i_{r1,abc}] \\ [i_{r2,abc}] \\ \dots \\ [i_{rn,abc}] \end{Bmatrix} + [L_{RS}] \cdot \begin{Bmatrix} [i_{s1,abc}] \\ [i_{s2,abc}] \\ \dots \\ [i_{sn,abc}] \end{Bmatrix} + [L_{RR}] \cdot \begin{Bmatrix} [i_{r1,abc}] \\ [i_{r2,abc}] \\ \dots \\ [i_{rn,abc}] \end{Bmatrix} \tag{2.196}$$

where:

$$[L_{RS}] = \begin{bmatrix} [M_{r1-s1}] & [M_{r1-s2}] & \dots & [M_{r1-sn}] \\ [M_{r2-s1}] & [M_{r2-s2}] & \dots & [M_{r2-sn}] \\ \dots & \dots & \dots & \dots \\ [M_{rn-s1}] & [M_{rn-s2}] & \dots & [M_{rn-sn}] \end{bmatrix} \tag{2.197}$$

$$[L_{RR}] = \begin{bmatrix} [M_{r1-r1}] & [M_{r1-r2}] & \dots & [M_{r1-rn}] \\ [M_{r2-r1}] & [M_{r2-r2}] & \dots & [M_{r2-rn}] \\ \dots & \dots & \dots & \dots \\ [M_{rn-r1}] & [M_{rn-r2}] & \dots & [M_{rn-rn}] \end{bmatrix} \tag{2.198}$$

Concerning the electric models, by merging (2.191) for all sets k=1,2,…,n, the stator electric model of the machine in phase coordinates is obtained as follows:

$$\begin{Bmatrix} [v_{s1,abc}] \\ [v_{s2,abc}] \\ \dots \\ [v_{sn,abc}] \end{Bmatrix} = R_s \cdot \begin{Bmatrix} [i_{s1,abc}] \\ [i_{s2,abc}] \\ \dots \\ [i_{sn,abc}] \end{Bmatrix} + \frac{d}{dt} \cdot \begin{Bmatrix} [\lambda_{s1,abc}] \\ [\lambda_{s2,abc}] \\ \dots \\ [\lambda_{sn,abc}] \end{Bmatrix} \tag{2.199}$$

Similarly, by merging (2.191) for all sets k=1,2,…,n, the rotor electric model of the machine in phase coordinates is obtained as follows:

$$\begin{Bmatrix} [v_{r1,abc}] \\ [v_{r2,abc}] \\ \dots \\ [v_{rn,abc}] \end{Bmatrix} = R_r \cdot \begin{Bmatrix} [i_{r1,abc}] \\ [i_{r2,abc}] \\ \dots \\ [i_{rn,abc}] \end{Bmatrix} + \frac{d}{dt} \cdot \begin{Bmatrix} [\lambda_{r1,abc}] \\ [\lambda_{r2,abc}] \\ \dots \\ [\lambda_{rn,abc}] \end{Bmatrix} \tag{2.200}$$

With the aim at obtaining compact formulations, the following variables are introduced:

$$\{\mathrm{V_s}\}=\begin{Bmatrix}[v_{s1,abc}]\\[v_{s2,abc}]\\ \dots \\ [v_{sn,abc}]\end{Bmatrix} \quad , \quad \{\mathrm{I_s}\}=\begin{Bmatrix}[i_{s1,abc}]\\[i_{s2,abc}]\\ \dots \\ [i_{sn,abc}]\end{Bmatrix} \quad , \quad \{\Lambda_\mathrm{s}\}=\begin{Bmatrix}[\lambda_{s1,abc}]\\[\lambda_{s2,abc}]\\ \dots \\ [\lambda_{sn,abc}]\end{Bmatrix}$$
$$\{\mathrm{V_r}\}=\begin{Bmatrix}[v_{r1,abc}]\\[v_{r2,abc}]\\ \dots \\ [v_{rn,abc}]\end{Bmatrix} \quad , \quad \{\mathrm{I_r}\}=\begin{Bmatrix}[i_{r1,abc}]\\[i_{r2,abc}]\\ \dots \\ [i_{rn,abc}]\end{Bmatrix} \quad , \quad \{\Lambda_\mathrm{r}\}=\begin{Bmatrix}[\lambda_{r1,abc}]\\[\lambda_{r2,abc}]\\ \dots \\ [\lambda_{rn,abc}]\end{Bmatrix} \tag{2.201}$$

Therefore, by using (2.201), the Equations (2.193), (2.196), (2.199)-(2.200) are expressed as follows:

$$\{\Lambda_\mathrm{s}\}=L_{l,s}\cdot\{\mathrm{I_s}\}+[L_{SS}]\cdot\{\mathrm{I_s}\}+[L_{SR}]\cdot\{\mathrm{I_r}\} \tag{2.202}$$

$$\{\Lambda_\mathrm{r}\}=L_{l,r}\cdot\{\mathrm{I_r}\}+[L_{RS}]\cdot\{\mathrm{I_s}\}+[L_{RR}]\cdot\{\mathrm{I_r}\} \tag{2.203}$$

$$\{\mathrm{V_s}\}=R_s\cdot\{\mathrm{I_s}\}+\frac{d}{dt}\{\Lambda_\mathrm{s}\} \tag{2.204}$$

$$\{\mathrm{V_r}\}=R_r\cdot\{\mathrm{I_r}\}+\frac{d}{dt}\{\Lambda_\mathrm{r}\} \tag{2.205}$$

To compute the machine electromagnetic model, the following vectors are defined:

$$\{\mathrm{V}\}=\begin{Bmatrix}\{\mathrm{V_s}\}\\ \{\mathrm{V_r}\}\end{Bmatrix} \quad , \quad \{\mathrm{I}\}=\begin{Bmatrix}\{\mathrm{I_s}\}\\ \{\mathrm{I_r}\}\end{Bmatrix} \quad , \quad \{\Lambda\}=\begin{Bmatrix}\{\Lambda_\mathrm{s}\}\\ \{\Lambda_\mathrm{r}\}\end{Bmatrix} \tag{2.206}$$

In addition, in similar way to the MS modelling, the machine inductances matrix is defined as follows:

$$[L]=\begin{bmatrix}L_{l,s}\cdot[I_d]_{3n\times 3n}+[L_{SS}] & [L_{SR}]\\ [L_{RS}] & L_{l,r}\cdot[I_d]_{3n\times 3n}+[L_{RR}]\end{bmatrix} \tag{2.207}$$

where $[I_d]_{3n\times 3n}$ indicates the identity matrix having a ($3n\cdot 3n$) dimensions. Finally, by using (2.206)-(2.207), the models (2.202)-(2.205) are merged as follows:

$$\begin{cases}\{\mathrm{V}\}=[R]\cdot\{\mathrm{I}\}+\dfrac{d}{dt}\{\Lambda\}\\ \{\Lambda\}=[L]\cdot\{\mathrm{I}\}\end{cases} \tag{2.208}$$

Like for the MS modelling, (2.208) represents the most generic form by which the electromagnetic model of an electrical machine can be described [1].

Electromagnetic torque in phase coordinates

Because of the electromagnetic model of the machine is expressed using the generic form (2.208), the electromagnetic torque is computed by means of (2.41). With the aim at obtaining a specific formulation for the VSD modelling, (2.207) is replaced in (2.41), leading to the following result:

$$T = p_p \cdot \{\mathrm{I_s}\}^t \cdot \frac{d[L_{SR}]}{d\vartheta_r} \cdot \{\mathrm{I_r}\} \tag{2.209}$$

Energy conversion model in phase coordinates

Since no magnetic and electric variables are involved, the mechanical model (2.45)-(2.46) is not affected by the employed modelling approach. Therefore, the electromechanical VSD model of the machine in phase coordinates is defined as follows:

$$\begin{cases} \{\mathrm{V}\} = [R] \cdot \{\mathrm{I}\} + \dfrac{d}{dt}\{\Lambda\} & Eq.\ 2.208 \\ \{\Lambda\} = [L] \cdot \{\mathrm{I}\} & Eq.\ 2.208 \\ T = p_p \cdot \{\mathrm{I_s}\}^t \cdot \dfrac{d[L_{SR}]}{d\vartheta_r} \cdot \{\mathrm{I_r}\} & Eq.\ 2.209 \\ \dfrac{d\omega_r}{dt} = \dfrac{p_p}{I_{eq}} \cdot (T - T_L) & Eq.\ 2.45 \\ \dfrac{d\vartheta_r}{dt} = \omega_r & Eq.\ 2.46 \end{cases} \tag{2.210}$$

According with (2.210), the electromechanical VSD model of the machine in phase coordinates is composed as follows:

- $3 \cdot n$ stator magnetic equations (2.189);
- $3 \cdot n$ rotor magnetic equations (2.190);
- $3 \cdot n$ stator electrical equations (2.191);
- $3 \cdot n$ rotor electrical equations (2.192);
- 1 electromagnetic torque equation (2.209);
- 2 mechanical equations (2.45), (2.46).

The electromechanical model in phase coordinates can be referred to the stationary ones using the VSD reference transformation. In this way, it will be demonstrated how this approach is not able to highlight the flux and torque production of each single three-phase winding set, resulting not suitable for the implementation of modular machine control schemes.

2.2.2 Electromechanical model in stationary coordinates

The VSD approach decomposes the machine original space into several orthogonal subspaces, using a transformation matrix having a dimension equal to the total number of phases. The VSD transformation matrix is computed using an algorithm based on the harmonic decoupling [7], [10], [11]. According with this, the VSD transformation matrix of a multiple three-phase machine has a $(3\cdot n) \times (3\cdot n)$ dimension.

With the aim at computing the VSD transformation matrix for a multiple three-phase machine, it is necessary to define the vector of the positions corresponding to the magnetic axes of the phases, considering both stator and rotor windings. Starting from (2.1) and (2.180), the positions of the magnetic axes belonging to the phases of a generic three-phase *k*-set are expressed as follows:

$$\left[\vartheta_{xk,abc}\right] = \begin{bmatrix} \vartheta_{xk-a} \\ \vartheta_{xk-b} \\ \vartheta_{xk-c} \end{bmatrix} = \begin{bmatrix} \vartheta_{xk-a} \\ \vartheta_{xk-a} + \dfrac{2\pi}{3} \\ \vartheta_{xk-a} - \dfrac{2\pi}{3} \end{bmatrix} = \begin{bmatrix} \vartheta_{xk} \\ \vartheta_{xk} + \dfrac{2\pi}{3} \\ \vartheta_{xk} - \dfrac{2\pi}{3} \end{bmatrix} \qquad x = \begin{bmatrix} s \equiv stator \\ r \equiv rotor \end{bmatrix} \tag{2.211}$$

By merging (2.211) for all sets k=1,2,…,n, the vector of the angle displacements corresponding to the magnetic axes of the phases is defined as follows:

$$\left\langle \Theta_x \right\rangle_{1\times 3n} = \left\{ \left[\vartheta_{x1,abc}\right]^t \quad \left[\vartheta_{x2,abc}\right]^t \quad \ldots \quad \left[\vartheta_{xk,abc}\right]^t \right\} \qquad x = \begin{bmatrix} s \equiv stator \\ r \equiv rotor \end{bmatrix} \tag{2.212}$$

To obtain a compact formulation of the VSD transformation matrix, the following trigonometric operators are defined:

$$\begin{aligned} p\cdot C\left\langle l\cdot\Theta\right\rangle_{1\times m} &= p\cdot\left\{\cos\left(l\cdot\vartheta_1\right) \quad \cos\left(l\cdot\vartheta_2\right) \quad \ldots \quad \cos\left(l\cdot\vartheta_m\right)\right\} \\ p\cdot S\left\langle l\cdot\Theta\right\rangle_{1\times m} &= p\cdot\left\{\sin\left(l\cdot\vartheta_1\right) \quad \sin\left(l\cdot\vartheta_2\right) \quad \ldots \quad \sin\left(l\cdot\vartheta_m\right)\right\} \end{aligned} \tag{2.213}$$

With reference to [10], [11], by considering the amplitude invariant form, the VSD transformation matrix for a multiple three-phase machine is computed as follows:

symmetrical machine configuration

$$n = odd \Rightarrow \left[T_x^{VSD}\right] = \frac{2}{3 \cdot n} \cdot \begin{bmatrix} C\langle 1 \cdot \Theta_x \rangle_{1\times 3n} \\ S\langle 1 \cdot \Theta_x \rangle_{1\times 3n} \\ C\langle 2 \cdot \Theta_x \rangle_{1\times 3n} \\ S\langle 2 \cdot \Theta_x \rangle_{1\times 3n} \\ \cdots \\ \cdots \\ C\langle l \cdot \Theta_x \rangle_{1\times 3n} \\ S\langle l \cdot \Theta_x \rangle_{1\times 3n} \\ 1/2 \cdot C\langle 3 \cdot n \cdot \Theta_x \rangle_{1\times 3n} \end{bmatrix}, \quad l < \frac{3 \cdot n}{2}, \quad x = \begin{bmatrix} s \equiv stator \\ r \equiv rotor \end{bmatrix}$$

symmetrical machine configuration

$$n = even \Rightarrow \left[T_x^{VSD}\right] = \frac{2}{3 \cdot n} \cdot \begin{bmatrix} C\langle 1 \cdot \Theta_x \rangle_{1\times 3n} \\ S\langle 1 \cdot \Theta_x \rangle_{1\times 3n} \\ C\langle 2 \cdot \Theta_x \rangle_{1\times 3n} \\ S\langle 2 \cdot \Theta_x \rangle_{1\times 3n} \\ \cdots \\ \cdots \\ C\langle l \cdot \Theta_x \rangle_{1\times 3n} \\ S\langle l \cdot \Theta_x \rangle_{1\times 3n} \\ 1/2 \cdot C\langle 3 \cdot n \cdot \Theta_x \rangle_{1\times 3n} \\ 1/2 \cdot C\langle 3 \cdot n/2 \cdot \Theta_x \rangle_{1\times 3n} \end{bmatrix}, \quad l < \frac{3 \cdot n}{2}, \quad x = \begin{bmatrix} s \equiv stator \\ r \equiv rotor \end{bmatrix}$$

asymmetrical machine configuration

$$\left[T_x^{VSD}\right]=\frac{2}{3\cdot n}\cdot\begin{bmatrix} C\langle 1\cdot\Theta_x\rangle_{1\times 3n} \\ S\langle 1\cdot\Theta_x\rangle_{1\times 3n} \\ C\langle 5\cdot\Theta_x\rangle_{1\times 3n} \\ S\langle 5\cdot\Theta_x\rangle_{1\times 3n} \\ \cdots \\ \cdots \\ C\langle l\cdot\Theta_x\rangle_{1\times 3n} \\ S\langle l\cdot\Theta_x\rangle_{1\times 3n} \\ [ZS] \end{bmatrix}, \quad \begin{matrix} l=5,7,11,\ldots<\dfrac{3\cdot n}{2} \\ l\neq 3\cdot i\ ,\ i\in\mathbb{N} \end{matrix} \qquad x=\begin{bmatrix} s\equiv stator \\ r\equiv rotor \end{bmatrix}$$

$$[ZS]=\frac{1}{2}\cdot\begin{bmatrix} C\langle 3\cdot\Theta_x\rangle_{1\times 3n} \\ S\langle 3\cdot\Theta_x\rangle_{1\times 3n} \\ \cdots \\ \cdots \\ C\langle m\cdot\Theta_x\rangle_{1\times 3n} \\ S\langle m\cdot\Theta_x\rangle_{1\times 3n} \end{bmatrix}, \quad \begin{matrix} m=3\cdot(2\cdot i+1)\ ,\ i\in\mathbb{N} \\ m<\dfrac{3\cdot n}{2} \end{matrix} \tag{2.214}$$

The application of (2.214) leads to the definition of the stationary components of each variable defined in phase coordinates. In terms of mathematical formulation, this operation is described as follows:

$$\left\{\mathrm{X}_{\mathrm{s,VSD}}\right\}=\begin{bmatrix} x_{s-\alpha} \\ x_{s-\beta} \\ x_{s1-\mu+} \\ x_{s1-\mu-} \\ \cdots \\ \cdots \\ x_{sn_{hrm}-\mu+} \\ x_{sn_{hrm}-\mu+} \\ x_{s1-o+} \\ x_{s1-o-} \\ \cdots \\ \cdots \\ x_{sn_{hmp}-o+} \\ x_{sn_{hmp}-o-} \end{bmatrix}=\left[T_s^{VSD}\right]\cdot\left\{\mathrm{X_s}\right\} \quad , \quad \left\{\mathrm{X_{r,VSD}}\right\}=\begin{bmatrix} x_{r-\alpha} \\ x_{r-\beta} \\ x_{r1-\mu+} \\ x_{r1-\mu-} \\ \cdots \\ \cdots \\ x_{rn_{hrm}-\mu+} \\ x_{rn_{hrm}-\mu+} \\ x_{r1-o+} \\ x_{r1-o-} \\ \cdots \\ \cdots \\ x_{rn_{hmp}-o+} \\ x_{rn_{hmp}-o-} \end{bmatrix}=\left[T_r^{VSD}\right]\cdot\left\{\mathrm{X_r}\right\}$$

$$\left(\mathrm{X}=\mathrm{V},\mathrm{I},\Lambda\right) \tag{2.215}$$

According with [7], [10], the application of the VSD transformation on the machine original space leads to definition of $(3\cdot n)/2$ orthogonal subspaces. If the total phases number is odd, then the last subspace consists of a zero-sequence component, leading to the removal of the last row in the vectors of (2.215). The VSD subspaces are classified in three categories. The first one corresponds to the stationary (α,β) frame, having the meaning of fundamental model of the machine. The other two subspace types correspond to harmonic and homopolar patterns, without any contribution in the flux and torque production. The main advantage of the VSD approach is the possibility to obtain a harmonic decoupled model of the machine. In this way, each temporal harmonic is mapped in a specific subspace, leading to the use of a couple of resonant controllers for its regulation. Conversely, the MS modelling does not have this propriety as each temporal harmonic is mapped in the all subspaces, thus requiring a couple of resonant controllers for each of them. Other details about the harmonic propriety of the VSD transformation can be found in [10].

In conclusion, the application of the VSD transformation matrix (2.214) leads to the decomposition of the machine original space as follows:

- 1 main subspace (α,β);
- n_{hrm} harmonic subspaces (μ+, μ-);
- n_{hmp} homopolar subspaces (o+,o-).

Using the same procedure for the computation of the electromagnetic model in phase coordinates, the application of the VSD transformation to both electric and magnetic models is following reported.

Stator magnetic model in stationary coordinates

According with the VSD approach, the computation of the stator magnetic model in stationary coordinates must be performed by considering the equation system including all stator winding sets. For convenience, (2.202) is further reported:

$$\left\{\Lambda_{\mathrm{s}}\right\} = L_{l,s}\cdot\left\{\mathrm{I}_{\mathrm{s}}\right\} + \left[L_{SS}\right]\cdot\left\{\mathrm{I}_{\mathrm{s}}\right\} + \left[L_{SR}\right]\cdot\left\{\mathrm{I}_{\mathrm{r}}^{r}\right\} \tag{2.216}$$

The superscript '*r*' indicates that the considered variable is defined in the rotor coordinates, making necessary its redefinition to the stator ones. With the aim at performing this operation, according with (2.179) , the transformation ratio between the stator winding and the rotor one is introduced:

$$t_{s-r}^{VSD} = \frac{N_s}{N_r^{VSD}} = \sqrt{n}\cdot\frac{N_s}{N_r} = \sqrt{n}\cdot t_{s-r} \tag{2.217}$$

Therefore, the rotor variables can be easily referred to the stator coordinates as follows:

$$\left\{\mathrm{I}_{\mathrm{r}}^{s}\right\} = \frac{1}{t_{s-r}^{VSD}}\cdot\left\{\mathrm{I}_{\mathrm{r}}^{r}\right\} \quad , \quad \left\{\mathrm{V}_{\mathrm{r}}^{s}\right\} = t_{s-r}^{VSD}\cdot\left\{\mathrm{V}_{\mathrm{r}}^{r}\right\} \quad , \quad \left\{\Lambda_{\mathrm{r}}^{s}\right\} = t_{s-r}^{VSD}\cdot\left\{\Lambda_{\mathrm{r}}^{r}\right\} \tag{2.218}$$

By replacing (2.218) in (2.217), the stator magnetic model having rotor variables defined in stator coordinates is obtained:

$$\left\{\Lambda_{\mathrm{s}}\right\} = L_{l,s}\cdot\left\{\mathrm{I}_{\mathrm{s}}\right\} + \left[L_{SS}\right]\cdot\left\{\mathrm{I}_{\mathrm{s}}\right\} + \left[L_{SR}\right]\cdot t_{s-r}^{VSD}\cdot\left\{\mathrm{I}_{\mathrm{r}}^{s}\right\} \tag{2.219}$$

The application of (2.214) on (2.219) leads to the computation the stator magnetic model in terms of stationary variables, obtaining the following result:

$$\left\{\Lambda_{\mathrm{s,VSD}}\right\} = L_{l,s}\cdot\left\{\mathrm{I}_{\mathrm{s,VSD}}\right\} + \left[L_{SS,\mathrm{VSD}}\right]\cdot\left\{\mathrm{I}_{\mathrm{s,VSD}}\right\} + \left[L_{SR,\mathrm{VSD}}\right]\cdot t_{s-r}^{VSD}\cdot\left\{\mathrm{I}_{\mathrm{r,VSD}}^{s}\right\} \tag{2.220}$$

where:

$$\left[L_{SS,\mathrm{VSD}}\right] = \left[T_s^{VSD}\right]\cdot\left[L_{SS}\right]\cdot\left[T_s^{VSD}\right]^{-1} = \frac{3\cdot n}{2}\cdot\frac{N_s\cdot N_s}{\Re_{eq}}\cdot\begin{bmatrix} 1 & 0 & 0 & \dots & 0 \\ 0 & 1 & 0 & \dots & 0 \\ 0 & 0 & 0 & \dots & 0 \\ \dots & \dots & \dots & \dots & \dots \\ 0 & 0 & 0 & \dots & 0 \end{bmatrix} \tag{2.221}$$

$$\left[L_{SR,\mathrm{VSD}}\right]\cdot t_{s-r}^{VSD}=\left[T_s^{VSD}\right]\cdot\left[L_{SR}\right]\cdot\left[T_r^{VSD}\right]^{-1}\cdot t_{s-r}^{VSD}=\frac{3\cdot n}{2}\cdot\frac{N_s\cdot N_s}{\Re_{eq}}\cdot\begin{bmatrix}1&0&0&\dots&0\\0&1&0&\dots&0\\0&0&0&\dots&0\\\dots&\dots&\dots&\dots&\dots\\0&0&0&\dots&0\end{bmatrix} \tag{2.222}$$

With the aim at obtaining a compact formulation of the equations, (2.98)-(2.99) are replaced in (2.221)-(2.222). Therefore, by isolating each subspace' components from the other ones, (2.220) is expressed as follows:

$$\begin{cases}\begin{bmatrix}\lambda_{s-\alpha}\\\lambda_{s-\beta}\end{bmatrix}=L_{l,s}\cdot\begin{bmatrix}i_{s-\alpha}\\i_{s-\beta}\end{bmatrix}+n\cdot L_m^s\cdot\begin{bmatrix}i_{s-\alpha}\\i_{s-\beta}\end{bmatrix}+n\cdot L_m^s\cdot\begin{bmatrix}i_{r-\alpha}^s\\i_{r-\beta}^s\end{bmatrix}\\\begin{bmatrix}\lambda_{sh-\mu+}\\\lambda_{sh-\mu+}\end{bmatrix}=L_{l,s}\cdot\begin{bmatrix}i_{sh-\mu+}\\i_{sh-\mu-}\end{bmatrix}\qquad h=1,2,\dots,n_{hrm}\\\begin{bmatrix}\lambda_{sz-o+}\\\lambda_{sz-o+}\end{bmatrix}=L_{l,s}\cdot\begin{bmatrix}i_{sz-o+}\\i_{sz-o-}\end{bmatrix}\qquad z=1,2,\dots,n_{hmp}\end{cases} \tag{2.223}$$

Finally, (2.223) is further simplified by introducing the complex vector notation, leading to the following result:

$$\begin{cases}\overline{\lambda}_{s,\alpha\beta}=L_{l,s}\cdot\overline{i}_{s,\alpha\beta}+n\cdot L_m^s\cdot\overline{i}_{s,\alpha\beta}+n\cdot L_m^s\cdot\overline{i}_{r,\alpha\beta}^{\,s}\\\overline{\lambda}_{sh,\mu+\mu-}=L_{l,s}\cdot\overline{i}_{sh,\mu+\mu-}\qquad h=1,2,\dots,n_{hrm}\\\overline{\lambda}_{sz,o+o-}=L_{l,s}\cdot\overline{i}_{sz,o+o-}\qquad z=1,2,\dots,n_{hmp}\end{cases} \tag{2.224}$$

The computation of (2.224) leads to complete definition of the stator magnetic model in the stationary coordinates.

Rotor magnetic model in stationary coordinates

The procedure for the computation of the rotor magnetic model in stationary coordinates is similar to the one used for the computation of stator model. Therefore, (2.203) with the notation change of the rotor variables is reported:

$$\left\{\Lambda_{\mathrm{r}}^r\right\}=L_{l,r}^r\cdot\left\{\mathrm{I}_{\mathrm{r}}^r\right\}+\left[L_{RS}\right]\cdot\left\{\mathrm{I}_{\mathrm{s}}\right\}+\left[L_{RR}\right]\cdot\left\{\mathrm{I}_{\mathrm{r}}^r\right\} \tag{2.225}$$

By replacing (2.218) in (2.225), the rotor magnetic model having rotor variables defined in stator coordinates is obtained:

$$\left\{\Lambda_{\mathrm{r}}^s\right\}=L_{l,r}^r\cdot\left(t_{s-r}^{VSD}\right)^2\cdot\left\{\mathrm{I}_{\mathrm{r}}^s\right\}+t_{s-r}^{VSD}\cdot\left[L_{RS}\right]\cdot\left\{\mathrm{I}_{\mathrm{s}}\right\}+\left(t_{s-r}^{VSD}\right)^2\cdot\left[L_{RR}\right]\cdot\left\{\mathrm{I}_{\mathrm{r}}^s\right\} \tag{2.226}$$

Therefore, the application of (2.214) on (2.226) leads to the computation the rotor magnetic model in terms of stationary variables, obtaining the following result:

$$\begin{aligned}\left\{\Lambda^{s}_{\mathrm{r,VSD}}\right\} = L^{r}_{l,r}\cdot\left(t^{VSD}_{s-r}\right)^{2}\cdot\left\{\mathrm{I}^{s}_{\mathrm{r,VSD}}\right\} + t^{VSD}_{s-r}\cdot\left[L_{RS,\mathrm{VSD}}\right]\cdot\left\{\mathrm{I}_{\mathrm{s,VSD}}\right\} + \ldots \\ \ldots + \left(t^{VSD}_{s-r}\right)^{2}\cdot\left[L_{RR,\mathrm{VSD}}\right]\cdot\left\{\mathrm{I}^{s}_{\mathrm{r,VSD}}\right\}\end{aligned} \tag{2.227}$$

where:

$$\left[L_{RS,\mathrm{VSD}}\right] = t^{VSD}_{s-r}\cdot\left[T^{VSD}_{r}\right]\cdot\left[L_{RS}\right]\cdot\left[T^{VSD}_{s}\right]^{-1} = \frac{3\cdot n}{2}\cdot\frac{N_s\cdot N_s}{\Re_{eq}}\cdot\begin{bmatrix}1 & 0 & 0 & \ldots & 0\\ 0 & 1 & 0 & \ldots & 0\\ 0 & 0 & 0 & \ldots & 0\\ \ldots & \ldots & \ldots & \ldots & \ldots\\ 0 & 0 & 0 & \ldots & 0\end{bmatrix} \tag{2.228}$$

$$\begin{aligned}\left(t^{VSD}_{s-r}\right)^{2}\cdot\left[L_{RR,\mathrm{VSD}}\right] = \left(t^{VSD}_{s-r}\right)^{2}\cdot\left[T^{VSD}_{r}\right]\cdot\left[L_{RR}\right]\cdot\left[T^{VSD}_{r}\right]^{-1} = \ldots \\ \ldots = \frac{3\cdot n}{2}\cdot\frac{N_s\cdot N_s}{\Re_{eq}}\cdot\begin{bmatrix}1 & 0 & 0 & \ldots & 0\\ 0 & 1 & 0 & \ldots & 0\\ 0 & 0 & 0 & \ldots & 0\\ \ldots & \ldots & \ldots & \ldots & \ldots\\ 0 & 0 & 0 & \ldots & 0\end{bmatrix}\end{aligned} \tag{2.229}$$

$$L^{r}_{l,r}\cdot\left(t^{VSD}_{s-r}\right)^{2} = n\cdot L^{r}_{l,r}\cdot\left(t_{s-r}\right)^{2} = n\cdot L^{s}_{l,r} \tag{2.230}$$

With the aim at obtaining a compact formulation of the equations, (2.98)-(2.99) are replaced in (2.228)-(2.229). Therefore, by isolating each subspace' components from the other ones, (2.227) is expressed as follows:

$$\begin{cases}\begin{bmatrix}\lambda^{s}_{r-\alpha}\\ \lambda^{s}_{r-\beta}\end{bmatrix} = n\cdot L^{s}_{l,r}\cdot\begin{bmatrix}i^{s}_{r-\alpha}\\ i^{s}_{r-\beta}\end{bmatrix} + n\cdot L^{s}_{m}\cdot\begin{bmatrix}i_{s-\alpha}\\ i_{s-\beta}\end{bmatrix} + n\cdot L^{s}_{m}\cdot\begin{bmatrix}i^{s}_{r-\alpha}\\ i^{s}_{r-\beta}\end{bmatrix} \\ \begin{bmatrix}\lambda^{s}_{rh-\mu+}\\ \lambda^{s}_{rh-\mu-}\end{bmatrix} = n\cdot L^{s}_{l,r}\cdot\begin{bmatrix}i^{s}_{rh-\mu+}\\ i^{s}_{rh-\mu-}\end{bmatrix} \qquad h = 1,2,\ldots,n_{hrm} \\ \begin{bmatrix}\lambda^{s}_{rz-o+}\\ \lambda^{s}_{rz-o-}\end{bmatrix} = n\cdot L^{s}_{l,r}\cdot\begin{bmatrix}i^{s}_{rz-o+}\\ i^{s}_{rz-o-}\end{bmatrix} \qquad z = 1,2,\ldots,n_{hmp}\end{cases} \tag{2.231}$$

Finally, (2.231) is further simplified by introducing the complex vector notation, leading to the following result:

$$\begin{cases} \overline{\lambda}^{s}_{r,\alpha\beta} = n \cdot L^{s}_{l,r} \cdot \overline{i}^{s}_{r,\alpha\beta} + n \cdot L^{s}_{m} \cdot \overline{i}_{s,\alpha\beta} + n \cdot L^{s}_{m} \cdot \overline{i}^{s}_{r,\alpha\beta} & \\ \overline{\lambda}^{s}_{rh,\mu+\mu-} = n \cdot L^{s}_{l,r} \cdot \overline{i}^{s}_{rh,\mu+\mu-} & h = 1,2,...,n_{hrm} \\ \overline{\lambda}^{s}_{rz,o+o-} = n \cdot L^{s}_{l,r} \cdot \overline{i}^{s}_{rz,o+o-} & z = 1,2,...,n_{hmp} \end{cases} \tag{2.232}$$

The computation of (2.232) leads to complete definition of the rotor magnetic model in the stationary coordinates.

Stator electric model in stationary coordinates

Starting from the stator electric model in phase coordinates (2.204), the application of (2.215) leads to the following result:

$$\left\{\mathrm{V}_{\mathrm{s,VSD}}\right\} = R_s \cdot \left\{\mathrm{I}_{\mathrm{s,VSD}}\right\} + \frac{d}{dt}\left\{\Lambda_{\mathrm{s,VSD}}\right\} \tag{2.233}$$

It is noted how the stator electric model in stationary coordinates is formally identical with the one in phase coordinates (2.204). The only difference is that all vectors (voltage, flux and current) are referred to the stationary coordinates instead of the phase ones. By isolating each subspace' components from the other ones, (2.233) is expressed as follows:

$$\begin{cases} \begin{bmatrix} v_{s-\alpha} \\ v_{s-\beta} \end{bmatrix} = R_s \cdot \begin{bmatrix} i_{s-\alpha} \\ i_{s-\beta} \end{bmatrix} + \frac{d}{dt}\begin{bmatrix} \lambda_{s-\alpha} \\ \lambda_{s-\beta} \end{bmatrix} & \\ \begin{bmatrix} v_{sh-\mu+} \\ v_{sh-\mu+} \end{bmatrix} = R_s \cdot \begin{bmatrix} i_{sh-\mu+} \\ i_{sh-\mu-} \end{bmatrix} + \frac{d}{dt}\begin{bmatrix} \lambda_{sh-\mu+} \\ \lambda_{sh-\mu+} \end{bmatrix} & h = 1,2,...,n_{hrm} \\ \begin{bmatrix} v_{sz-o+} \\ v_{sz-o-} \end{bmatrix} = R_s \cdot \begin{bmatrix} i_{sz-o+} \\ i_{sz-o-} \end{bmatrix} + \frac{d}{dt}\begin{bmatrix} \lambda_{sz-o+} \\ \lambda_{sz-o-} \end{bmatrix} & z = 1,2,...,n_{hmp} \end{cases} \tag{2.234}$$

Finally, (2.234) is further simplified by introducing the complex vector notation, leading to the following result:

$$\begin{cases} \overline{v}_{s,\alpha\beta} = R_s \cdot \overline{i}_{s,\alpha\beta} + \frac{d}{dt}\overline{\lambda}_{s,\alpha\beta} & \\ \overline{v}_{sh,\mu+\mu-} = R_s \cdot \overline{i}_{sh,\mu+\mu-} + \frac{d}{dt}\overline{\lambda}_{sh,\mu+\mu-} & h = 1,2,...,n_{hrm} \\ \overline{v}_{sz,o+o-} = R_s \cdot \overline{i}_{sz,o+o-} + \frac{d}{dt}\overline{\lambda}_{sz,o+o-} & z = 1,2,...,n_{hmp} \end{cases} \tag{2.235}$$

With reference to (2.235), the electric model in stationary (α,β) frame corresponds with the one of a conventional three-phase machine.

Rotor electric model in stationary coordinates

The procedure for the computation of the rotor electric model in stationary coordinates is similar to the one used for the computation of the magnetic model. Therefore, (2.205) with the notation change of the rotor variables is reported:

$$\left\{\mathrm{V}_{\mathrm{r}}^{r}\right\}=R_{r}^{r}\cdot\left\{\mathrm{I}_{\mathrm{r}}^{r}\right\}+\frac{d}{dt}\left\{\Lambda_{\mathrm{r}}^{r}\right\} \tag{2.236}$$

By replacing (2.218) in (2.236), the rotor electric model having rotor variables defined in stator coordinates is obtained:

$$\left\{\mathrm{V}_{\mathrm{r}}^{s}\right\}=n\cdot R_{r}^{s}\cdot\left\{\mathrm{I}_{\mathrm{r}}^{s}\right\}+\frac{d}{dt}\left\{\Lambda_{\mathrm{r}}^{s}\right\} \tag{2.237}$$

where:

$$n\cdot R_{r}^{s}=R_{r}^{r}\cdot\left(t_{s-r}^{VSD}\right)^{2}=n\cdot R_{r}^{r}\cdot\left(t_{s-r}\right)^{2} \tag{2.238}$$

The application of (2.214) on (2.237) leads to the computation the rotor electric model in terms of stationary variables, obtaining the following result:

$$\left\{\mathrm{V}_{\mathrm{r,VSD}}^{s}\right\}=n\cdot R_{r}^{s}\cdot\left\{\mathrm{I}_{\mathrm{r,VSD}}^{s}\right\}+\frac{d}{dt}\left\{\Lambda_{\mathrm{r,VSD}}^{s}\right\}+\left[T_{r}^{VSD}\right]\cdot\left(\frac{d}{dt}\left[T_{r}^{VSD}\right]^{-1}\right)\cdot\left\{\Lambda_{\mathrm{r,VSD}}^{s}\right\} \tag{2.239}$$

where:

$$\left[T_{r}^{VSD}\right]\cdot\left(\frac{d}{dt}\left[T_{r}^{VSD}\right]^{-1}\right)=\omega_{r}\cdot\begin{bmatrix}0&1&0&\dots&0\\-1&0&0&\dots&0\\0&0&0&\dots&0\\\dots&\dots&\dots&\dots&\dots\\0&0&0&\dots&0\end{bmatrix} \tag{2.240}$$

Therefore, by isolating each subspace' components from the other ones, (2.239) is expressed as follows:

$$\begin{cases}\begin{bmatrix}v_{r-\alpha}^{s}\\v_{r-\beta}^{s}\end{bmatrix}=n\cdot R_{r}^{s}\cdot\begin{bmatrix}i_{r-\alpha}^{s}\\i_{r-\beta}^{s}\end{bmatrix}+\frac{d}{dt}\begin{bmatrix}\lambda_{r-\alpha}^{s}\\\lambda_{r-\beta}^{s}\end{bmatrix}+\omega_{r}\cdot\begin{bmatrix}0&1\\-1&0\end{bmatrix}\cdot\begin{bmatrix}\lambda_{r-\alpha}^{s}\\\lambda_{r-\beta}^{s}\end{bmatrix}\\\begin{bmatrix}v_{rh-\mu+}^{s}\\v_{rh-\mu-}^{s}\end{bmatrix}=n\cdot R_{r}^{s}\cdot\begin{bmatrix}i_{rh-\mu+}^{s}\\i_{rh-\mu-}^{s}\end{bmatrix}+\frac{d}{dt}\begin{bmatrix}\lambda_{rh-\mu+}^{s}\\\lambda_{rh-\mu-}^{s}\end{bmatrix} & h=1,2,\dots,n_{hrm}\\\begin{bmatrix}v_{rz-o+}^{s}\\v_{rz-o-}^{s}\end{bmatrix}=n\cdot R_{r}^{s}\cdot\begin{bmatrix}i_{rz-o+}^{s}\\i_{rz-o-}^{s}\end{bmatrix}+\frac{d}{dt}\begin{bmatrix}\lambda_{rz-o+}^{s}\\\lambda_{rz-o-}^{s}\end{bmatrix} & z=1,2,\dots,n_{hmp}\end{cases} \tag{2.241}$$

Finally, by introducing the complex vector notation, (2.241) is expressed as follows:

$$\begin{cases} \overline{v}^{s}_{r,\alpha\beta} = n \cdot R^{s}_{r} \cdot \overline{i}^{s}_{r,\alpha\beta} + \dfrac{d}{dt}\overline{\lambda}^{s}_{r,\alpha\beta} - j \cdot \omega_{r} \cdot \overline{\lambda}^{s}_{r,\alpha\beta} & \\ \overline{v}^{s}_{rh,\mu+\mu-} = n \cdot R^{s}_{r} \cdot \overline{i}^{s}_{rh,\mu+\mu-} + \dfrac{d}{dt}\overline{\lambda}^{s}_{rh,\mu+\mu-} & h = 1,2,...,n_{hrm} \\ \overline{v}^{s}_{rz,o+o-} = n \cdot R^{s}_{r} \cdot \overline{i}^{s}_{rz,o+o-} + \dfrac{d}{dt}\overline{\lambda}^{s}_{rz,o+o-} & z = 1,2,...,n_{hmp} \end{cases} \tag{2.242}$$

The computation of (2.242) leads to complete definition of the rotor electric model in the stationary coordinates.

Electromagnetic torque in stationary coordinates

Starting from (2.209), the computation of the electromagnetic torque in stationary coordinates is performed. Therefore, (2.209) using the notation change of the rotor variables is below reported:

$$T = p_{p} \cdot \left\{ \mathrm{I_s} \right\}^{t} \cdot \frac{d\left[L_{SR} \right]}{d\vartheta_{r}} \cdot \left\{ \mathrm{I_r^r} \right\} \tag{2.243}$$

By replacing (2.218) in (2.243), the rotor variables are referred to the stator coordinates, obtaining the following equation:

$$T = p_{p} \cdot \left\{ \mathrm{I_s} \right\}^{t} \cdot \frac{d\left[L_{SR} \right]}{d\vartheta_{r}} \cdot t^{VSD}_{s-r} \cdot \left\{ \mathrm{I_r^r} \right\} \tag{2.244}$$

The application of (2.215) on (2.244) leads to the computation of the electromagnetic torque in terms of stationary variables, obtaining the following result:

$$T = p_{p} \cdot \left\{ \mathrm{I_{s,VSD}} \right\}^{t} \cdot \left[\left[T^{VSD}_{s} \right]^{-1} \right]^{t} \cdot \frac{d\left[L_{SR} \right]}{d\vartheta_{r}} \cdot \left[T^{VSD}_{r} \right]^{-1} \cdot t^{VSD}_{s-r} \cdot \left\{ \mathrm{I^s_{r,VSD}} \right\} \tag{2.245}$$

where:

$$\left[\left[T^{VSD}_{s} \right]^{-1} \right]^{t} \cdot \frac{d\left[L_{SR} \right]}{d\vartheta_{r}} \cdot \left[T^{VSD}_{r} \right]^{-1} \cdot t^{VSD}_{s-r} = \frac{9 \cdot n^{2}}{4} \cdot \frac{N_{s} \cdot N_{s}}{\Re_{eq}} \cdot \begin{bmatrix} 1 & 0 & 0 & ... & 0 \\ 0 & 1 & 0 & ... & 0 \\ 0 & 0 & 0 & ... & 0 \\ ... & ... & ... & ... & ... \\ 0 & 0 & 0 & ... & 0 \end{bmatrix} \tag{2.246}$$

By replacing (2.246) in (2.245), the relationship of electromagnetic torque is as follows:

$$T = p_{p} \cdot \frac{9 \cdot n^{2}}{4} \cdot \frac{N_{s} \cdot N_{s}}{\Re_{eq}} \cdot \left(i^{s}_{r-\alpha} \cdot i_{s-\beta} - i^{s}_{r-\beta} \cdot i_{s-\alpha} \right) \tag{2.247}$$

Finally, by using (2.99), (2.247) is expressed as follows:

$$T = \frac{3 \cdot n}{2} \cdot p_p \cdot L_m^s \cdot \left(\overline{i}_{r,\alpha\beta}^{\,s} \times \overline{i}_{s,\alpha\beta} \right) \tag{2.248}$$

With the aim at obtaining a torque relationship using only stator variables, (2.224) is replaced in (2.248), leading to the following result:

$$T = \frac{3 \cdot n}{2} \cdot p_p \cdot \left(\overline{\lambda}_{s,\alpha\beta} \times \overline{i}_{s,\alpha\beta} \right) \tag{2.249}$$

According to (2.249), the electromagnetic torque is given by the cross-product between the stator flux-linkage vector and the stator current vector, both belonging to the main (α,β) subspace.

Electromagnetic model in stationary coordinates

In summary, the electromagnetic model of the machine in the main (α,β) subspace is composed by the combination of the following equation systems:

$$\begin{cases} \overline{\lambda}_{s,\alpha\beta} = L_{l,s} \cdot \overline{i}_{s,\alpha\beta} + n \cdot L_m^s \cdot \overline{i}_{s,\alpha\beta} + n \cdot L_m^s \cdot \overline{i}_{r,\alpha\beta}^{\,s} & Eq.\ 2.224 \\ \overline{\lambda}_{r,\alpha\beta}^{\,s} = n \cdot L_{l,r}^s \cdot \overline{i}_{r,\alpha\beta}^{\,s} + n \cdot L_m^s \cdot \overline{i}_{s,\alpha\beta} + n \cdot L_m^s \cdot \overline{i}_{r,\alpha\beta}^{\,s} & Eq.\ 2.232 \\ \overline{v}_{s,\alpha\beta} = R_s \cdot \overline{i}_{s,\alpha\beta} + \dfrac{d}{dt} \overline{\lambda}_{s,\alpha\beta} & Eq.\ 2.235 \\ \overline{v}_{r,\alpha\beta}^{\,s} = n \cdot R_r^s \cdot \overline{i}_{r,\alpha\beta}^{\,s} + \dfrac{d}{dt} \overline{\lambda}_{r,\alpha\beta}^{\,s} - j \cdot \omega_r \cdot \overline{\lambda}_{r,\alpha\beta}^{\,s} & Eq.\ 2.242 \end{cases} \tag{2.250}$$

Concerning the electromagnetic models of the harmonic and homopolar subspaces, they are composed by the following equation systems:

$$\begin{cases} \overline{\lambda}_{sh,\mu+\mu-} = L_{l,s} \cdot \overline{i}_{sh,\mu+\mu-} & h = 1,2,...,n_{hrm} \quad Eq.\ 2.224 \\ \overline{\lambda}_{rh,\mu+\mu-}^{\,s} = n \cdot L_{l,r}^s \cdot \overline{i}_{rh,\mu+\mu-}^{\,s} & h = 1,2,...,n_{hrm} \quad Eq.\ 2.232 \\ \overline{v}_{sh,\mu+\mu-} = R_s \cdot \overline{i}_{sh,\mu+\mu-} + \dfrac{d}{dt} \overline{\lambda}_{sh,\mu+\mu-} & h = 1,2,...,n_{hrm} \quad Eq.\ 2.235 \\ \overline{v}_{rh,\mu+\mu-}^{\,s} = n \cdot R_r^s \cdot \overline{i}_{rh,\mu+\mu-}^{\,s} + \dfrac{d}{dt} \overline{\lambda}_{rh,\mu+\mu-}^{\,s} & h = 1,2,...,n_{hrm} \quad Eq.\ 2.242 \end{cases} \tag{2.251}$$

$$\begin{cases} \overline{\lambda}_{sz,o+o-} = L_{l,s} \cdot \overline{i}_{sz,o+o-} & z = 1,2,...,n_{hmp} \quad Eq.\ 2.224 \\ \overline{\lambda}_{rz,o+o-}^{\,s} = n \cdot L_{l,r}^s \cdot \overline{i}_{rz,o+o-}^{\,s} & z = 1,2,...,n_{hmp} \quad Eq.\ 2.232 \\ \overline{v}_{sz,o+o-} = R_s \cdot \overline{i}_{sz,o+o-} + \dfrac{d}{dt} \overline{\lambda}_{sz,o+o-} & z = 1,2,...,n_{hmp} \quad Eq.\ 2.235 \\ \overline{v}_{rz,o+o-}^{\,s} = n \cdot R_r^s \cdot \overline{i}_{rz,o+o-}^{\,s} + \dfrac{d}{dt} \overline{\lambda}_{rz,o+o-}^{\,s} & z = 1,2,...,n_{hmp} \quad Eq.\ 2.242 \end{cases} \tag{2.252}$$

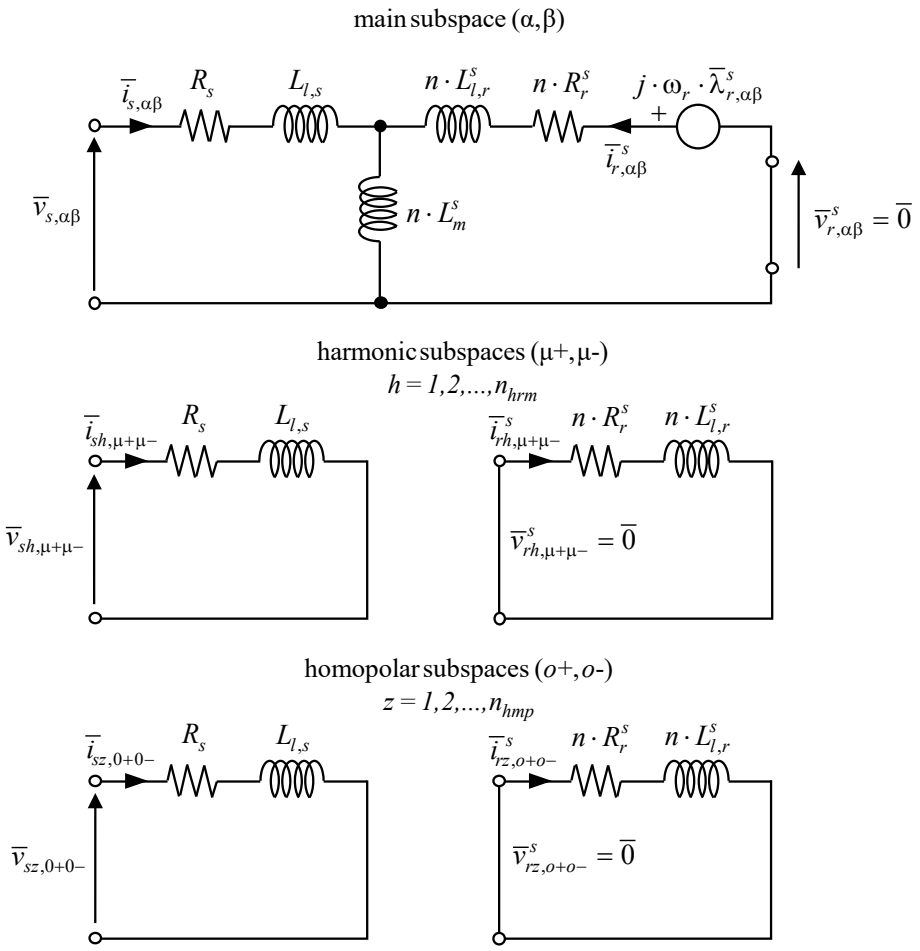

Fig. 2. 9. Equivalent VSD circuit of a multiple three-phase squirrel cage IM in stationary components.

With reference to (2.250)-(2.252), the main subspace (α,β) contains the flux- and torque-producing current components, while the other subspaces contain harmonics and homopolar components with no contribution to the electromechanical energy conversion. It is noted how the electromagnetic model of the main subspace (α,β) is identical with the one of a conventional three-phase IM. Therefore, the equivalent circuit of the machine, corresponding to the VSD modelling approach in stationary coordinates, is shown in Fig. 2. 9.

Energy conversion model in stationary coordinates

Since no magnetic and electric variables are involved, the mechanical model (2.45)-(2.46) is not affected by the application of the reference transformations, making it still valid. Therefore, the electromechanical VSD model of the machine in stationary coordinates is defined as follows:

$$
\begin{cases}
\left.\begin{aligned}
&\overline{\lambda}_{s,\alpha\beta} = L_{l,s}\cdot\overline{i}_{s,\alpha\beta} + n\cdot L_m^s\cdot\overline{i}_{s,\alpha\beta} + n\cdot L_m^s\cdot\overline{i}_{r,\alpha\beta}^s \\
&\overline{\lambda}_{r,\alpha\beta}^s = n\cdot L_{l,r}^s\cdot\overline{i}_{r,\alpha\beta}^s + n\cdot L_m^s\cdot\overline{i}_{s,\alpha\beta} + n\cdot L_m^s\cdot\overline{i}_{r,\alpha\beta}^s \\
&\overline{v}_{s,\alpha\beta} = R_s\cdot\overline{i}_{s,\alpha\beta} + \frac{d}{dt}\overline{\lambda}_{s,\alpha\beta} \\
&\overline{v}_{r,\alpha\beta}^s = n\cdot R_r^s\cdot\overline{i}_{r,\alpha\beta}^s + \frac{d}{dt}\overline{\lambda}_{r,\alpha\beta}^s - j\cdot\omega_r\cdot\overline{\lambda}_{r,\alpha\beta}^s
\end{aligned}\right\} & \textit{Eq.}\ 2.250 \\
\left.\begin{aligned}
&\overline{\lambda}_{sh,\mu+\mu-} = L_{l,s}\cdot\overline{i}_{sh,\mu+\mu-} && h=1,2,...,n_{hrm} \\
&\overline{\lambda}_{rh,\mu+\mu-}^s = n\cdot L_{l,r}^s\cdot\overline{i}_{rh,\mu+\mu-}^s && h=1,2,...,n_{hrm} \\
&\overline{v}_{sh,\mu+\mu-} = R_s\cdot\overline{i}_{sh,\mu+\mu-} + \frac{d}{dt}\overline{\lambda}_{sh,\mu+\mu-} && h=1,2,...,n_{hrm} \\
&\overline{v}_{rh,\mu+\mu-}^s = n\cdot R_r^s\cdot\overline{i}_{rh,\mu+\mu-}^s + \frac{d}{dt}\overline{\lambda}_{rh,\mu+\mu-}^s && h=1,2,...,n_{hrm}
\end{aligned}\right\} & \textit{Eq.}\ 2.251 \\
\left.\begin{aligned}
&\overline{\lambda}_{sz,o+o-} = L_{l,s}\cdot\overline{i}_{sz,o+o-} && z=1,2,...,n_{hmp} \\
&\overline{\lambda}_{rz,o+o-}^s = n\cdot L_{l,r}^s\cdot\overline{i}_{rz,o+o-}^s && z=1,2,...,n_{hmp} \\
&\overline{v}_{sz,o+o-} = R_s\cdot\overline{i}_{sz,o+o-} + \frac{d}{dt}\overline{\lambda}_{sz,o+o-} && z=1,2,...,n_{hmp} \\
&\overline{v}_{rz,o+o-}^s = n\cdot R_r^s\cdot\overline{i}_{rz,o+o-}^s + \frac{d}{dt}\overline{\lambda}_{rz,o+o-}^s && z=1,2,...,n_{hmp}
\end{aligned}\right\} & \textit{Eq.}\ 2.252 \\
T = \frac{3\cdot n}{2}\cdot p_p\cdot\left(\overline{\lambda}_{s,\alpha\beta}\times\overline{i}_{s,\alpha\beta}\right) & \textit{Eq.}\ 2.249 \\
\frac{d\omega_r}{dt} = \frac{p_p}{I_{eq}}\cdot\left(T - T_L\right) & \textit{Eq.}\ 2.45 \\
\frac{d\vartheta_r}{dt} = \omega_r & \textit{Eq.}\ 2.46
\end{cases}
$$

(2.253)

It is noted how (2.253) has the same structure of the electromechanical model in phase coordinates (2.210). The only difference is related to electromagnetic model together with the torque relationship which are both expressed using the stationary coordinates.

2.2.3 Electromechanical model in rotating coordinates

Thanks to the application of the VSD modelling, the electromagnetic model of the machine in the stationary (α,β) frame is identical to the one of a three-phase IM, as shown in (2.250). As a consequence, the computation of the electromagnetic model in generic rotating coordinates is performed in conventional way.

Therefore, to get the machine model in the generic rotating (*x*,*y*) frame, the application of the well-known rotational transformation (2.105) is required. Like for the MS modelling, its application does not change the magnetic models and the torque expression. Indeed, they are formally identical to the ones defined in the stationary (α,β) frame. The only difference is that all vectors (voltage, flux and current) are referred to the rotating (*x*,*y*) coordinates instead of the stationary (α,β) ones. As a consequence, both stator and rotor magnetic models in the rotating (*x*,*y*) frame are computed as follows:

$$\overline{\lambda}_{s,xy} = L_{l,s} \cdot \overline{i}_{s,xy} + n \cdot L_m \cdot \overline{i}_{s,xy} + n \cdot L_m \cdot \overline{i}_{r,xy} \tag{2.254}$$

$$\overline{\lambda}_{r,xy} = n \cdot L_{l,r} \cdot \overline{i}_{r,xy} + n \cdot L_m \cdot \overline{i}_{s,xy} + n \cdot L_m \cdot \overline{i}_{r,xy} \tag{2.255}$$

With reference to (2.254)-(2.255), the superscript '*s*' on the rotor variables is not used anymore, thus simplifying the formulation of the equation system. Concerning the electromagnetic torque, it is computed as follows:

$$T = \frac{3 \cdot n}{2} \cdot p_p \cdot \left(\overline{\lambda}_{s,xy} \times \overline{i}_{s,xy} \right) \tag{2.256}$$

Like for the three-phase IM modelling, the application of the rotational transformation has relevant effects just on both stator and rotor electric models, introducing the well-known motional voltage terms. Therefore, the application of (2.105) on (2.235) and (2.242) leads to the following result:

$$\overline{v}_{s,xy} = R_s \cdot \overline{i}_{s,xy} + \frac{d}{dt}\overline{\lambda}_{s,xy} + j \cdot \omega^* \cdot \overline{\lambda}_{s,xy} \tag{2.257}$$

$$\overline{v}_{r,xy} = n \cdot R_r \cdot \overline{i}_{r,xy} + \frac{d}{dt}\overline{\lambda}_{r,xy} + j \cdot \left(\omega^* - \omega_r \right) \cdot \overline{\lambda}_{r,xy} \tag{2.258}$$

Like for the MS modelling, by defining ω^* properly, the following frames can be selected:

$$\begin{cases} \omega^* = \omega_d & \Rightarrow \quad (x,y,0) \equiv (d,q,0) \\ \omega^* = 0 & \Rightarrow \quad (x,y,0) \equiv (\alpha,\beta,0) \\ \omega^* = \omega_r & \Rightarrow \quad (x,y,0) \equiv (d_r,q_r,0) \\ \omega^* = \omega_{s-\lambda} & \Rightarrow \quad (x,y,0) \equiv (d_s,q_s,0) \end{cases} \tag{2.259}$$

The meaning of the frames defined in (2.259) corresponds with the one of (2.104), excepting for the last case where the synchronous speed is defined as follows:

$$\omega_{s-\lambda} = \frac{d}{dt}\left(\vartheta_d + \vartheta_{s-\lambda} \right) = \frac{d}{dt}\left[\vartheta_d + \left(\angle\overline{\lambda}_s - \angle\overline{\lambda}_r \right) \right] = \frac{d}{dt}\left[\vartheta_d + \delta_l \right] \tag{2.260}$$

where δ_l represents the average load angle of the machine. In summary, the electromagnetic model of the machine in the rotating (*x*,*y*) frame is composed by the combination of the following equation systems:

$$\begin{cases} \overline{\lambda}_{s,xy} = L_{l,s} \cdot \overline{i}_{s,xy} + n \cdot L_m \cdot \overline{i}_{s,xy} + n \cdot L_m \cdot \overline{i}_{r,xy} & Eq.\ 2.254 \\ \overline{\lambda}_{r,xy} = n \cdot L_{l,r} \cdot \overline{i}_{r,xy} + n \cdot L_m \cdot \overline{i}_{s,xy} + n \cdot L_m \cdot \overline{i}_{r,xy} & Eq.\ 2.255 \\ \overline{v}_{s,xy} = R_s \cdot \overline{i}_{s,xy} + \dfrac{d}{dt}\overline{\lambda}_{s,xy} + j \cdot \omega^* \cdot \overline{\lambda}_{s,xy} & Eq.\ 2.257 \\ \overline{v}_{r,xy} = n \cdot R_r \cdot \overline{i}_{r,xy} + \dfrac{d}{dt}\overline{\lambda}_{r,xy} + j \cdot \left(\omega^* - \omega_r\right) \cdot \overline{\lambda}_{r,xy} & Eq.\ 2.258 \end{cases} \tag{2.261}$$

Therefore, the electromechanical VSD model of the machine in rotating coordinates is defined as follows:

$$\begin{cases} \left.\begin{aligned} &\overline{\lambda}_{s,xy} = L_{l,s} \cdot \overline{i}_{s,xy} + n \cdot L_m \cdot \overline{i}_{s,xy} + n \cdot L_m \cdot \overline{i}_{r,xy} \\ &\overline{\lambda}_{r,xy} = n \cdot L_{l,r} \cdot \overline{i}_{r,xy} + n \cdot L_m \cdot \overline{i}_{s,xy} + n \cdot L_m \cdot \overline{i}_{r,xy} \\ &\overline{v}_{s,xy} = R_s \cdot \overline{i}_{s,xy} + \frac{d}{dt}\overline{\lambda}_{s,xy} + j \cdot \omega^* \cdot \overline{\lambda}_{s,xy} \\ &\overline{v}_{r,xy} = n \cdot R_r \cdot \overline{i}_{r,xy} + \frac{d}{dt}\overline{\lambda}_{r,xy} + j \cdot \left(\omega^* - \omega_r\right) \cdot \overline{\lambda}_{r,xy} \end{aligned}\right\} & Eq.\ 2.261 \\ \left.\begin{aligned} &\overline{\lambda}_{sh,\mu+\mu-} = L_{l,s} \cdot \overline{i}_{sh,\mu+\mu-} && h = 1,2,...,n_{hrm} \\ &\overline{\lambda}^s_{rh,\mu+\mu-} = n \cdot L^s_{l,r} \cdot \overline{i}^s_{rh,\mu+\mu-} && h = 1,2,...,n_{hrm} \\ &\overline{v}_{sh,\mu+\mu-} = R_s \cdot \overline{i}_{sh,\mu+\mu-} + \frac{d}{dt}\overline{\lambda}_{sh,\mu+\mu-} && h = 1,2,...,n_{hrm} \\ &\overline{v}^s_{rh,\mu+\mu-} = n \cdot R^s_r \cdot \overline{i}^s_{rh,\mu+\mu-} + \frac{d}{dt}\overline{\lambda}^s_{rh,\mu+\mu-} && h = 1,2,...,n_{hrm} \end{aligned}\right\} & Eq.\ 2.251 \\ \left.\begin{aligned} &\overline{\lambda}_{sz,o+o-} = L_{l,s} \cdot \overline{i}_{sz,o+o-} && z = 1,2,...,n_{hmp} \\ &\overline{\lambda}^s_{rz,o+o-} = n \cdot L^s_{l,r} \cdot \overline{i}^s_{rz,o+o-} && z = 1,2,...,n_{hmp} \\ &\overline{v}_{sz,o+o-} = R_s \cdot \overline{i}_{sz,o+o-} + \frac{d}{dt}\overline{\lambda}_{sz,o+o-} && z = 1,2,...,n_{hmp} \\ &\overline{v}^s_{rz,o+o-} = n \cdot R^s_r \cdot \overline{i}^s_{rz,o+o-} + \frac{d}{dt}\overline{\lambda}^s_{rz,o+o-} && z = 1,2,...,n_{hmp} \end{aligned}\right\} & Eq.\ 2.252 \\ T = \dfrac{3 \cdot n}{2} \cdot p_p \cdot \left(\overline{\lambda}_{s,xy} \times \overline{i}_{s,xy}\right) & Eq.\ 2.256 \\ \dfrac{d\omega_r}{dt} = \dfrac{p_p}{I_{eq}} \cdot \left(T - T_L\right) & Eq.\ 2.45 \\ \dfrac{d\vartheta_r}{dt} = \omega_r & Eq.\ 2.46 \end{cases} \tag{2.262}$$

With the computation of the electromechanical model in rotating coordinates (2.262), the VSD modelling of the machine is complete. Unlike the MS modelling, the state-space model of the machine in rotating coordinates is not computed. Indeed, by considering the equation system of the main subspace, it corresponds with the one of a conventional three-phase IM [2]. In addition, the control schemes proposed in this dissertation are MS-based, thus making the computation of the VSD state-space model not necessary.

2.2.4 Comparison between VSD and MS modelling approaches

The computation of the machine model using both VSD and MS approaches allows to make some considerations. It is noted how the VSD approach allows to model the energy conversion in simpler way compared to the MS one. Indeed, the application of the VSD transformation matrix allows to obtain an electromagnetic model which is identical to the one of a three-phase IM. As a consequence, an 'average' machine model is obtained, without emphasizing the contribution of the single three-phase stator units. The proof of this is represented by the reference transformation used for each modelling approaches. Indeed, by comparing the three-phase Clarke transformation (2.48) with the VSD one (2.214), the following relationship between the VSD and MS variables is extrapolated:

$$z_{s,\alpha\beta}^{VSD} = \frac{1}{n} \cdot \sum_{k=1}^{n} z_{sk,\alpha\beta}^{MS} \quad \Rightarrow \quad z_{s,xy}^{VSD} = \frac{1}{n} \cdot \sum_{k=1}^{n} z_{sk,xy}^{MS} \qquad z = (v, i, \lambda) \tag{2.263}$$

With reference to (2.263), independently by the considered frame (stationary or rotating), each variable belonging to the VSD main subspace is computed as average value of the corresponding MS ones. Nevertheless, because of each MS variable is related to a specific winding set, it follows that each VSD variable is representative of the average behaviour of the all winding sets.

Therefore, despite the MS approach leads to a complicate electromagnetic model, characterized by strong couplings among the sets, it results the only approach able to highlight the stator flux and torque production belonging to each stator winding set. As a consequence, with the aim at implementing a machine drive scheme able to deal with a direct control of each three-phase unit, the MS approach results more convenient compared to the VSD one. For this reason, the machine control schemes proposed in this dissertation are MS-based, thus justifying the computation of the related state-space model.

2.3 Conclusion

In this chapter, the modelling of a multiple three-phase induction machine (IM) using both Multi-Stator (MS) and Vector Space Decomposition (VSD) approaches has been reported. With reference to the technical literature, the following novelties have been introduced:

- Generic MS modelling of a multiple three-phase IM, considering an arbitrary number of three-phase winding sets together with different stator parameters among the units;

- Generic VSD modelling of a multiple three-phase IM, considering an arbitrary number of three-phase winding sets and by considering both symmetrical and asymmetrical configurations.

According with the obtained results, the most relevant conclusions are the following:

- The MS approach considers the machine as multiple three-phase units operating in parallel, highlighting the flux and torque contributions produced by each individual stator winding set. This aspect represents the most important feature for the implementation of a modular control scheme able to deal with an independent control of each three-phase unit. Nevertheless, the MS approach leads to an equation system characterized by strong magnetic couplings between the units, thus requiring the definition of specific decoupling algorithms when MS-based control schemes are implemented.

- The VSD approach decomposes the machine original space into several orthogonal subspaces, using a transformation matrix based on the harmonic decoupling of the machine model. In this way, the electromechanical energy conversion is performed in a single subspace, having the meaning of fundamental model of the machine and characterized by an equation system which is identical to the one of a three-phase machine. Despite the VSD approach leads to a simpler electromagnetic model than the MS modelling, it is not suitable for the implementation of modular control schemes. Indeed, the energy conversion is modelled in average way, without highlighting the flux and torque contributions produced by each individual stator winding set.

References

[1] D. C. White and H. H. Woodson, *Electromechanical Energy Conversion*. Wiley, 1959.

[2] P. Krause, O. Wasynczuk, S. D. Sudhoff, and S. Pekarek, *Analysis of Electric Machinery and Drive Systems*. John Wiley & Sons, 2013.

[3] R. H. Nelson and P. C. Krause, 'Induction Machine Analysis for Arbitrary Displacement Between Multiple Winding Sets', *IEEE Trans. Power Appar. Syst.*, vol. PAS-93, no. 3, pp. 841–848, May 1974.

[4] R. Bojoi, S. Rubino, A. Tenconi, and S. Vaschetto, 'Multiphase electrical machines and drives: A viable solution for energy generation and transportation electrification', in *2016 International Conference and Exposition on Electrical and Power Engineering (EPE)*, 2016, pp. 632–639.

[5] Y. Hu, Z. Q. Zhu, and M. Odavic, 'Comparison of Two-Individual Current Control and Vector Space Decomposition Control for Dual Three-Phase PMSM', *IEEE Trans. Ind. Appl.*, vol. 53, no. 5, pp. 4483–4492, Sep. 2017.

[6] R. Isermann, *Digital Control Systems: Volume 1: Fundamentals, Deterministic Control*. Springer Science & Business Media, 2013.

[7] E. Levi, R. Bojoi, F. Profumo, H. A. Toliyat, and S. Williamson, 'Multiphase induction motor drives - a technology status review', *IET Electr. Power Appl.*, vol. 1, no. 4, pp. 489–516, Jul. 2007.

[8] F. Barrero and M. J. Duran, 'Recent Advances in the Design, Modeling, and Control of Multiphase Machines—Part I', *IEEE Trans. Ind. Electron.*, vol. 63, no. 1, pp. 449–458, Jan. 2016.

[9] I. Zoric, 'Multiple Three-Phase Induction Generators for Wind Energy Conversion Systems', doctoral, Liverpool John Moores University, 2018.

[10] I. Zoric, M. Jones, and E. Levi, 'Vector space decomposition algorithm for asymmetrical multiphase machines', in *2017 International Symposium on Power Electronics (Ee)*, 2017, pp. 1–6.

[11] Y. Zhao and T. A. Lipo, 'Space vector PWM control of dual three-phase induction machine using vector space decomposition', *IEEE Trans. Ind. Appl.*, vol. 31, no. 5, pp. 1100–1109, Sep. 1995.

Chapter 3

DIRECT FLUX VECTOR CONTROL OF MULTIPLE THREE-PHASE INDUCTION MOTOR DRIVES

Table of Contents

List of Figures

List of Notations

- $\hat{X}$ Observed Variable
- $\tilde{X}$ Estimated Variable/Parameter
- X^* Reference Variable

This chapter deals with the design and implementation of a Direct Flux Vector Control (DFVC) scheme for multiple three-phase Induction Motor (IM) drives. The proposed control solution performs a direct and independent regulation of both stator flux amplitude and torque contribution belonging to each three-phase winding set, thus defining an equivalent modular Direct Torque Control (DTC) scheme for this kind of machines. The proposed control scheme is designed to be fully compatible with the multiple three-phase drive topologies, using modular Voltage Supply Inverter (VSI) structures together with independent Pulse Width Modulation (PWM) voltage control of each three-phase power converter unit.

According with the machine modelling, the proposed solution is based on the Multi-Stator (MS) approach, thus extending the modularity of the multiple three-phase IM drives also in terms of machine control scheme.

3.1 Main objectives and features

The solution proposed in this dissertation is specifically designed for the control of multiple three-phase IM with a squirrel cage rotor structure. With reference to the technical literature, several attempts on the use of this machine typology for the implementation of "series/parallel" configurations have been proposed [1], [2]. Nevertheless, few control solutions able to deal with a direct control of the main variables (current, flux, torque) belonging to each three-phase winding set have been developed [2]–[6], thus exploiting all the degrees of freedom offered by the multiple three-phase IM drives. For this reason, the main goal of this work is to extend the modularity of the multiple three-phase IM structures also in terms of drive control scheme, thus without limiting itself to the machine configuration and power converter structure.

An interesting attempt to propose a Field Oriented Control (FOC) scheme able to deal with an independent control of the currents belonging to each three-phase winding set is proposed in [2]. As this control solution is based on the Vector Space Decomposition (VSD) modelling, the active regulation of the harmonic and homopolar subspaces to manage any possible unbalances among the three-phase winding sets is performed. Nevertheless, this control approach performs the computation of the reference currents belonging to the VSD' subspaces as a function of the reference (d,q) ones computed by means of the MS modelling. This aspect is a further proof how only MS-based control schemes are able to deal with a modular control of the multiple three-phase machines, as already shown in the chapter of the machine modelling (Ch. 2). Therefore, according with the main goal of the work, a MS-based control scheme is proposed.

With reference to the technical literature, no attempt to implement an independent regulation of both stator flux amplitude and torque contribution belonging to each three-phase winding set has never been reported. There are many advantages of such control solution. Like for the three-phase motor drives, the direct regulation of the stator flux amplitude allows at obtaining high dynamic

performance in the flux-weakening operation of the drive [7], including load-angle limitation that avoids the machine pull-out. Concerning the independent regulation of the torque contribution belonging to each three-phase winding set, this feature allows at implementing power sharing strategies among the three-phase winding sets, resulting useful for the proper operation of the "series/parallel" configurations [1]. With the aim at implementing such features on the drive, the Direct Flux Vector Control (DFVC) scheme is proposed [4], [7].

With reference to [7], the DFVC scheme represents a competitive alternative to the DTC ones because conventional PWM modulators are employed. Therefore, neither hysteresis regulators nor switching tables are necessary, thus overcoming the main issues related to the implementation of the Switching Table – DTC (ST-DTC) schemes on multiple three-phase motor drives characterized by a high number of units. In addition, with respect to the DTC, the DFVC linearizes the machine control as the torque is regulated indirectly by means of the direct control of the torque-producing current component, obtaining a high level of decoupling between the control axes. Therefore, the DFVC represents a competitive alternative to a DTC scheme, thus justifying its choice in this dissertation.

According with the introduction (Ch. 1), the multiple three-phase drives are usually designed to implement modular fault-tolerance strategies. After a fault event, the faulty three-phase unit is simply disconnected from the DC power supply, stopping the execution of the PWM algorithm dedicated to its voltage control [8]. Therefore, the proposed control scheme is designed to guarantee the proper operation of the motor drive after sudden turn-off of one or more three-phase units due to a fault on the power electronics side. Nevertheless, no faults detection algorithms will be provided as their implementation is beyond the scope of this dissertation. As a consequence, it is considered that each three-phase power converter unit provides a feedback signal to the control scheme, thus reporting a possible fault event. This is a standard for power modules that exhibit a dedicated fault output pin.

In conclusion, the research contributions and novelties introduced by the proposed control solution are below summarized. With the aim at proposing a modular MS-based DFVC scheme for multiple three-phase IM drives, for each three-phase unit the following features are implemented:

- **Independent stator flux amplitude regulation**
  (as for a DTC scheme)
- **Independent torque-producing current component regulation**
  (as for a FOC scheme)
- **High performance in deep flux-weakening operation**
  (as for a DFVC scheme)
- **Independent load-angle limitation**
  (aims at implementing modular strategies that avoid pull-out)

- **Independent voltage and current operational limits**
  (full modularity of the drive scheme with independent control of each three-phase unit)
- **Independent operating conditions**
  (implementation of a decoupling algorithm to compensate the MS couplings among the three-phase units)
- **Straightforward post-fault reconfiguration**
  (implementation of modular fault-tolerance strategies)

The chapter is organized as follows. Firstly, the description of the drive scheme configuration is reported. Secondly, the machine control scheme together with the full analysis of the proposed control solution is provided. Nevertheless, no experimental results are shown, thus providing the experimental validation in the next chapter.

3.2 Drive scheme configuration

The proposed control solution is designed for multiple three-phase IM drives having an arbitrary number *n* of three-phase conversion units. To deal with the most generic case, each DC source supplying any of the three-phase VSI units is considered independent from the other ones, leading to the drive topology shown in Fig. 3. 1.

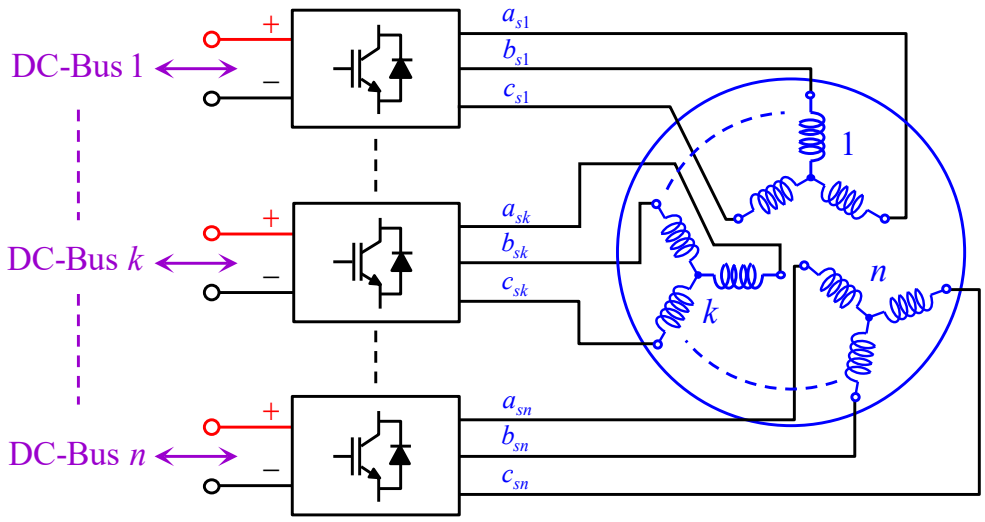

Fig. 3. 1. Multiple three-phase drive topology with independent DC sources.

According with the configuration of the multiple three-phase drives [8], each three-phase winding set has an independent and isolated neutral point. Therefore, the drive scheme configuration can be described by considering each three-phase *k*-unit separately.

In detail, for each three-phase unit *k* the following aspects are considered:

- PWM voltage control
- Measurements and feedback for the control scheme

The first point concerns the analysis of the zero-sequence variables (voltage and current) belonging to each three-phase winding set, thus demonstrating how the PWM voltage control of each unit can be performed using standard three-phase PWM modulators. The second aspect regards the description of the measurements and feedback required by the proposed control scheme in order to guarantee its specifications and features.

3.2.1 PWM voltage control of each VSI unit

As the outputs of the proposed control scheme correspond with the phase voltages references, each VSI unit may consist in any multilevel three-phase structure. However, 2-level VSI units are considered, corresponding to the most employed industrial configuration. Therefore, the analysis of the PWM voltage control of each three-phase unit *k* is performed using the scheme shown in Fig. 3. 2. With reference to it, an ideal 2-level VSI is considered, neglecting both Dead-Time (DT) effects and voltage drops related to the power switches. With reference to the figures of this chapter, the use of the Insulated Gate Bipolar Transistor (IGBT) switches is purely figurative.

It is considered that each inverter leg '*x*' is controlled by the switching function signal S_{k-x} as follows:

$$\begin{cases} S_{k-x}=0 & \text{Upper Switch OFF - Lower Switch ON} \\ S_{k-x}=1 & \text{Upper Switch ON - Lower Switch OFF} \end{cases} \quad x=a,b,c \qquad (3.1)$$

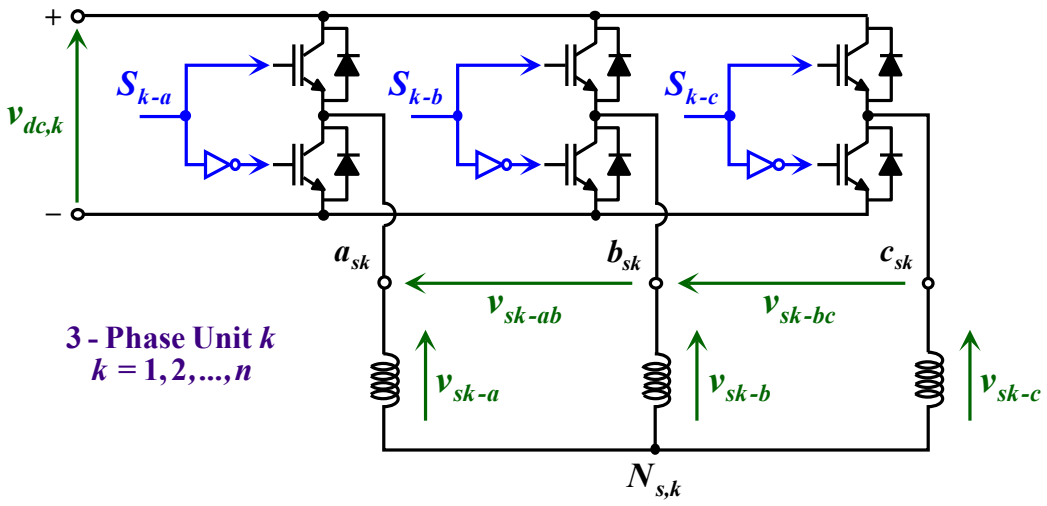

Fig. 3. 2. Generic three-phase winding set *k* fed by a 2-level VSI.

By considering each winding set of the machine as a symmetrical three-phase system, the relationships between the line voltages and the phase voltages belonging to each three-phase unit *k* are expressed as follows:

$$\begin{bmatrix} v_{sk-ab} \\ v_{sk-bc} \\ 0 \end{bmatrix} = \begin{bmatrix} 1 & -1 & 0 \\ 0 & 1 & -1 \\ 1 & 1 & 1 \end{bmatrix} \cdot \begin{bmatrix} v_{sk-a} \\ v_{sk-b} \\ v_{sk-c} \end{bmatrix} = \left[A_v\right] \cdot \begin{bmatrix} v_{sk-a} \\ v_{sk-b} \\ v_{sk-c} \end{bmatrix} \tag{3.2}$$

According with (3.1), by combining the switching functions S_{k-x} and the DC-link voltage $v_{dc,k}$, the line voltages are expressed as follows:

$$\begin{bmatrix} v_{sk-ab} \\ v_{sk-bc} \\ 0 \end{bmatrix} = \begin{bmatrix} 1 & -1 & 0 \\ 0 & 1 & -1 \\ 0 & 0 & 0 \end{bmatrix} \cdot \begin{bmatrix} S_{k-a} \\ S_{k-b} \\ S_{k-c} \end{bmatrix} \cdot v_{dc,k} = \left[B_v\right] \cdot \begin{bmatrix} S_{k-a} \\ S_{k-b} \\ S_{k-c} \end{bmatrix} \cdot v_{dc,k} \tag{3.3}$$

Therefore, by replacing (3.3) in (3.2), the phase voltages are expressed as follows:

$$\begin{bmatrix} v_{sk-a} \\ v_{sk-b} \\ v_{sk-c} \end{bmatrix} = v_{dc,k} \cdot \left[A_v\right]^{-1} \cdot \left[B_v\right] \cdot \begin{bmatrix} S_{k-a} \\ S_{k-b} \\ S_{k-c} \end{bmatrix} = v_{dc,k} \cdot \left[C_v\right] \cdot \begin{bmatrix} S_{k-a} \\ S_{k-b} \\ S_{k-c} \end{bmatrix} \tag{3.4}$$

where:

$$\left[C_v\right] = \begin{bmatrix} 2/3 & -1/3 & -1/3 \\ -1/3 & 2/3 & -1/3 \\ -1/3 & -1/3 & 2/3 \end{bmatrix} \tag{3.5}$$

According with Chapter 2, the variables expressed in phase coordinates are referred to the stationary (αβ0) ones by using the three-phase Clarke transformation defined as follows:

$$\left[T_k\right] = \frac{2}{3} \cdot \begin{bmatrix} \cos\left(\vartheta_{sk}\right) & \cos\left(\vartheta_{sk} + \frac{2\pi}{3}\right) & \cos\left(\vartheta_{sk} + \frac{4\pi}{3}\right) \\ \sin\left(\vartheta_{sk}\right) & \sin\left(\vartheta_{sk} + \frac{2\pi}{3}\right) & \sin\left(\vartheta_{sk} + \frac{4\pi}{3}\right) \\ 1/2 & 1/2 & 1/2 \end{bmatrix} \tag{3.6}$$

where ϑ_{sk} indicates the position of the magnetic axis belonging to the first phase '*a*' of the considered three-phase *k*-set. The position angle is computed with respect to the stationary α-axis by considering an anticlockwise rotation direction.

Therefore, by applying (3.6) to (3.4), the *k*-set phase voltages are computed in stationary (αβ0) coordinates as follows:

$$\begin{bmatrix} v_{sk-\alpha} \\ v_{sk-\beta} \\ v_{sk-0} \end{bmatrix} = v_{dc,k} \cdot [T_k] \cdot [C_v] \cdot \begin{bmatrix} S_{k-a} \\ S_{k-b} \\ S_{k-c} \end{bmatrix} = v_{dc,k} \cdot \left[T_{sw,k} \right] \cdot \begin{bmatrix} S_{k-a} \\ S_{k-b} \\ S_{k-c} \end{bmatrix} \tag{3.7}$$

where:

$$\left[T_{sw,k} \right] = \frac{2}{3} \cdot \begin{bmatrix} \cos(\vartheta_{sk}) & \cos\left(\vartheta_{sk} + \frac{2\pi}{3}\right) & \cos\left(\vartheta_{sk} + \frac{4\pi}{3}\right) \\ \sin(\vartheta_{sk}) & \sin\left(\vartheta_{sk} + \frac{2\pi}{3}\right) & \sin\left(\vartheta_{sk} + \frac{4\pi}{3}\right) \\ 0 & 0 & 0 \end{bmatrix} \tag{3.8}$$

Finally, the extended computation of (3.7) leads to the definition of the *k*-set voltage vectors components in the stationary (αβ0) coordinates as follows:

$$\begin{cases} v_{sk-\alpha} = \frac{2}{3} \cdot v_{dc,k} \cdot \left[S_{k-a} \cdot \cos(\vartheta_{sk}) + S_{k-b} \cdot \cos\left(\vartheta_{sk} + \frac{2\pi}{3}\right) + S_{k-c} \cdot \cos\left(\vartheta_{sk} + \frac{4\pi}{3}\right) \right] \\ v_{sk-\beta} = \frac{2}{3} \cdot v_{dc,k} \cdot \left[S_{k-a} \cdot \sin(\vartheta_{sk}) + S_{k-b} \cdot \sin\left(\vartheta_{sk} + \frac{2\pi}{3}\right) + S_{k-c} \cdot \sin\left(\vartheta_{sk} + \frac{4\pi}{3}\right) \right] \\ v_{sk-0} = 0 \end{cases} \tag{3.9}$$

Like for a 2-level three-phase VSI, there are $2^3 = 8$ possible configurations of the switching network, corresponding to the all permutations of the switching functions $\left[S_{k-a} \;\; S_{k-b} \;\; S_{k-c} \right]^t$. It is noted how, independently by the considered unit *k*, the zero-sequence voltage component v_{sk-0} is always zero. With reference to the MS modelling (Chapter 2), the electromagnetic state equation of each *k*-set zero-sequence current component is computed as follows:

$$\frac{d}{dt} i_{sk-0} = -\frac{R_{sk}}{L_{l,sk}} \cdot i_{sk-0} + v_{sk-0} \qquad \textit{Eq.}\ 2.158\ ,\ \textit{Ch.}\ 2 \tag{3.10}$$

Therefore, by replacing (3.9) in (3.10), the following equation is obtained:

$$\frac{d}{dt} i_{sk-0} = -\frac{R_{sk}}{L_{l,sk}} \cdot i_{sk-0} \tag{3.11}$$

The Equation (3.11) shows how the zero-sequence current component i_{sk-0} is always zero because a homogeneous differential equation is obtained, therefore without any voltage excitation.

This is an expected result since each three-phase winding set has two independent phase currents due to the isolated neutral point which imposes the following condition:

$$i_{sk-0} = i_{sk-a} + i_{sk-b} + i_{sk-c} = 0 \tag{3.12}$$

Concerning the (α,β) voltage vectors components, it is noted how (3.9) corresponds with the formulations of a conventional 2-level three-phase inverter [9]. The only difference is related to the position angle ϑ_{sk} whose main consequence is to introduce a rotational effect of the voltage vectors when these are mapped in the machine (α,β) subspace. However, this effect is automatically compensated by the machine control scheme whose outputs consist with the *k*-set phase voltages references, being these defined in the *k*-set phase coordinates $(abc)_k$. In this way, the algorithms implementing the consolidated PWM three-phase modulation techniques [9] can still be used without any change.

In conclusion, in a multiple three-phase drive, each three-phase unit is characterized by the following features:

- Physical rejection of the zero-sequence voltage component;
- Absence of the zero-sequence current component;
- Voltage vectors components in the stationary (α,β) subspace identical to the ones of a three-phase inverter.

As consequence of this, the PWM voltage control of each unit can be performed independently by the other ones, using a conventional three-phase PWM modulator based on a Carrier-Based approach (CB-PWM) [9]. For each unit *k* three duty-cycle signals $\left[d^*_{k-abc}\right]$ corresponding to the moving-average values of the switching functions $\left[S_{k-a} \;\; S_{k-b} \;\; S_{k-c}\right]^t$ are computed as follows:

$$\left[d^*_{k-abc}\right] = \begin{bmatrix} d^*_{k-a} \\ d^*_{k-b} \\ d^*_{k-c} \end{bmatrix} = \frac{1}{T_s} \cdot \int_{T_s} \begin{bmatrix} S_{k-a} \\ S_{k-b} \\ S_{k-c} \end{bmatrix} dt = \begin{bmatrix} 1/2 \\ 1/2 \\ 1/2 \end{bmatrix} + \frac{1}{v_{dc,k}} \cdot \begin{bmatrix} v^*_{sk-a} \\ v^*_{sk-b} \\ v^*_{sk-c} \end{bmatrix} + \begin{bmatrix} d^*_{k-0} \\ d^*_{k-0} \\ d^*_{k-0} \end{bmatrix} \tag{3.13}$$

where:

- $\left[v^*_{sk-a} \;\; v^*_{sk-b} \;\; v^*_{sk-c}\right]^t$ are the phase voltage references generated by the machine control scheme;
- T_s represents the switching period, corresponding to the time window in which the moving-average values of the switching functions are computed;
- d^*_{k-0} corresponds with a zero-sequence signal by means of which any modulation technique can be implemented [9].

In this dissertation, the PWM voltage control of each VSI unit is performed using the 'Min-Max' modulation [4], [9]. In this way, like for the three-phase case, it is possible to extend the sinusoidal voltage range of each VSI unit by a factor near to 15%, leading to relevant performance improvements especially in the flux-weakening operation of the drive.

3.2.2 Measurements and feedback for the control scheme

The control of each three-phase unit is performed using the drive scheme shown in Fig. 3. 3. It is noted how it corresponds to the one of a three-phase drive, thus without requiring additional measurements. In detail, for the control of each three-phase unit k, the following feedback are required:

- Phase currents measurements: $\left[i_{sk,abc}\right]=\left[i_{sk-a}\ \ i_{sk-b}\ \ i_{sk-c}\right]^{t}$;
- DC-link voltage measurement: $v_{dc,k}$;
- Rotor mechanical position measurement: ϑ_m ;
- VSI unit status: $x_{f,k}$ (0 = OFF/Faulty, 1 = ON/Healthy).

The mechanical position feedback is shared with the control schemes belonging to the other units. Concerning the details about the measurement methods, they are beyond the scope of this dissertation. As a consequence, they are not reported here.

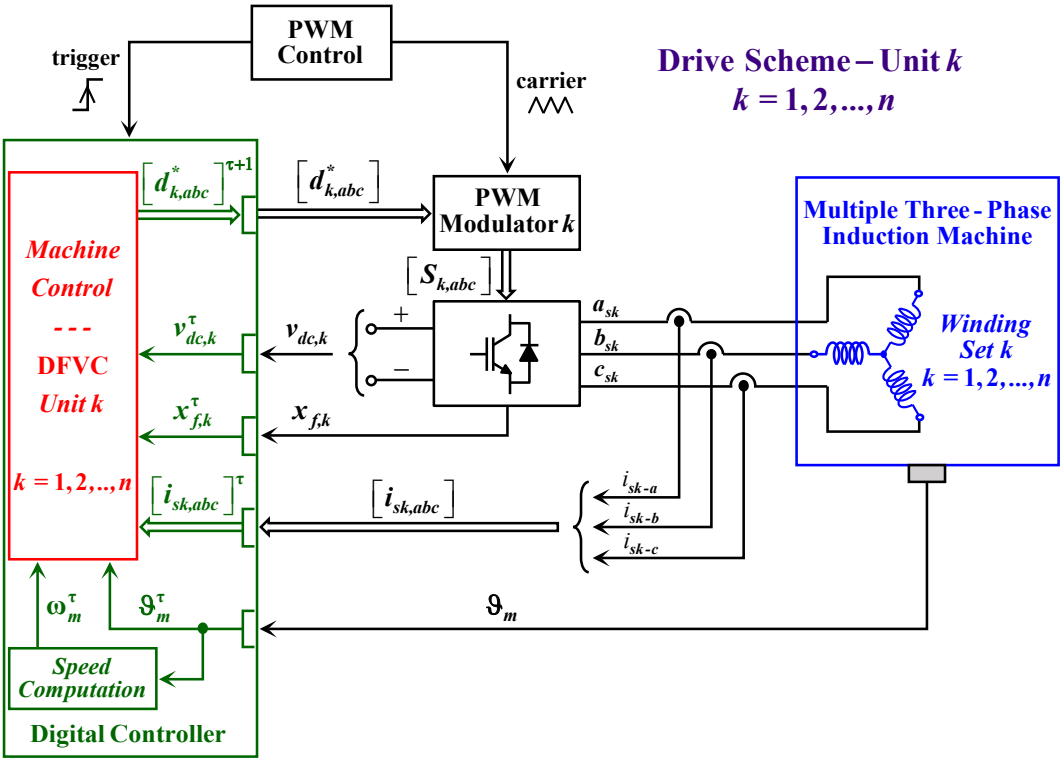

Fig. 3. 3. Drive scheme of a generic three-phase unit *k*.

According with the current technological scenario, the proposed control solution is implemented using a digital control platform (e.g. a microcontroller). Therefore, with reference to Fig. 3. 3, the above measurements are subjected to the conventional sampling and conversion operations, leading to the definition of their discrete values. These are indicated with the superscript τ, representing the considered sample time instant.

Concerning the outputs of each single unit control scheme, they correspond with the duty-cycles signals. These are indicated with the superscript (τ+1) to highlight their application for the next sample time instant, thus considering the execution delay of the digital controller.

Thanks to the use of PWM modulators, the machine control is performed at constant switching frequency. With reference to the sampling frequency, it is set identical to the switching one, thus dealing with the simplest case.

3.3 Machine control scheme configuration

The proposed control solution has a high degree of versatility such that it can be used for both motoring and generator operating modes of the machine. Nevertheless, the full modularity of a multiple three-phase drive scheme is de facto required when the machine operates as generator together with the needing to implement an independent control of each three-phase unit. A typical application example consists of the Wind Energy Conversion Systems (WECS). In this case, the DC-buses of the three-phase VSI units can be connected in different ways depending by the implemented topology [2] (parallel machine-side configurations, cascaded DC-link structures, back-to-back VSIs feeding both dc or ac microgrids).

For this reason, in this dissertation a generic configuration of a multiple three-phase drive is considered, as shown in Fig. 3. 4. Each unit *k* has its own references in terms of flux amplitude λ_{sk}^{*} and torque contribution T_k^{*}. These are provided by an outer controller which is not faced here being it beyond the scope of this dissertation. In addition, different values of the maximum phase-current $I_{max,k}$ and load-angle $\delta_{max,k}^{*}$ limits among the three-phase units are considered. Therefore, the goal of the proposed control solution is to implement an independent regulation of both stator flux amplitude and torque contribution belonging to each three-phase unit *k* according with the limitations of this one in terms of DC-link voltage $v_{dc,k}$, phase currents amplitude and load-angle.

The structure of the proposed control solution consists of multiple three-phase DFVC schemes which operate in parallel, as shown in Fig. 3. 4. Each of these is dedicated to the control of the stator flux and torque contribution of a single three-phase unit.

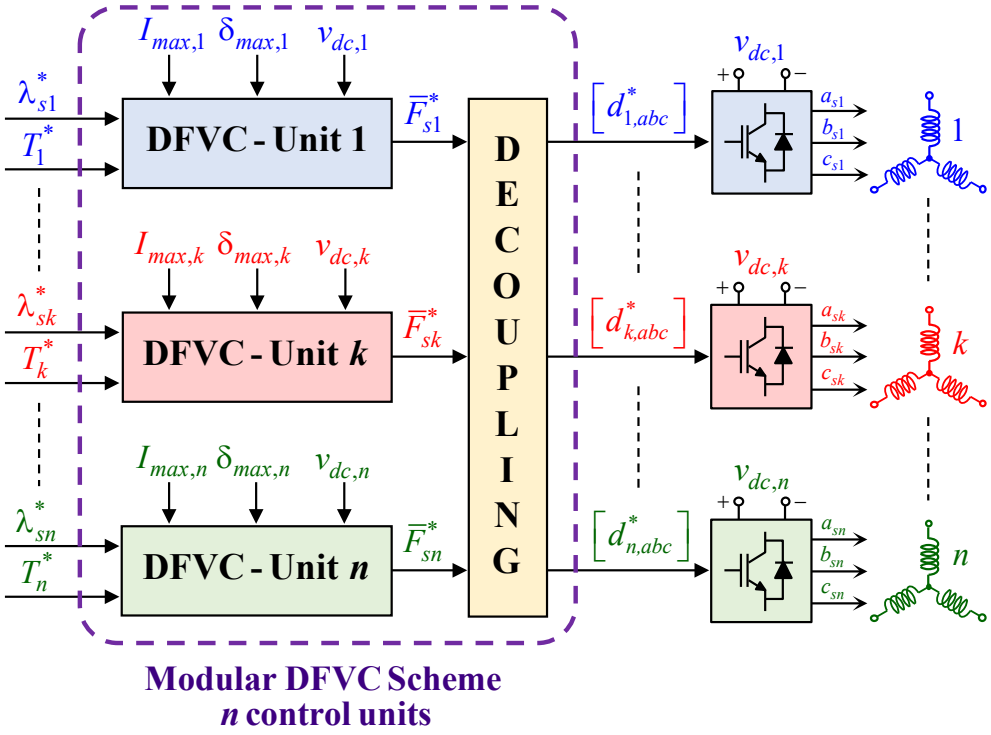

Fig. 3. 4. Modular DFVC scheme for multiple three-phase IM drives.

It is noted how for each DFVC scheme, the outputs do not correspond with the reference voltages for the considered VSI unit. Indeed, being the proposed control solution based on the MS approach, it is necessary to perform a decoupling action to compensate the electromagnetic coupling among the three-phase winding sets.

The control solution shown in Fig. 3. 4 allows at obtaining the highest degree of freedom in terms of configuration of the drive scheme. Nevertheless, in many cases the use of a single outer controller allows to satisfy the specifications of the drive. For example, the multiple three-phase drives topologies characterized by a common DC source shared by the all VSI units. In this case, the drive could operate in motoring mode, thus using the sum of the mechanical powers belonging to the units for the control of the machine mechanical speed. Conversely, the machine could operate as main alternator, thus using the sum of the electrical powers belonging to the units for the control of the DC source voltage.

For cases like these, both references of flux amplitude and torque contribution belonging to each unit can be computed using the scheme shown in Fig. 3. 5. This is designed for multiple three-phase IM drives characterized by identical three-phase units from both electrical machine and power converter point of views. In terms of mathematical formulation, these conditions are expressed as follows:

$$R_{sk} = R_s \;,\; L_{l,sk} = L_{l,s} \;,\; I_{max,k} = I_{max} \qquad \forall k = 1 \div n \tag{3.14}$$

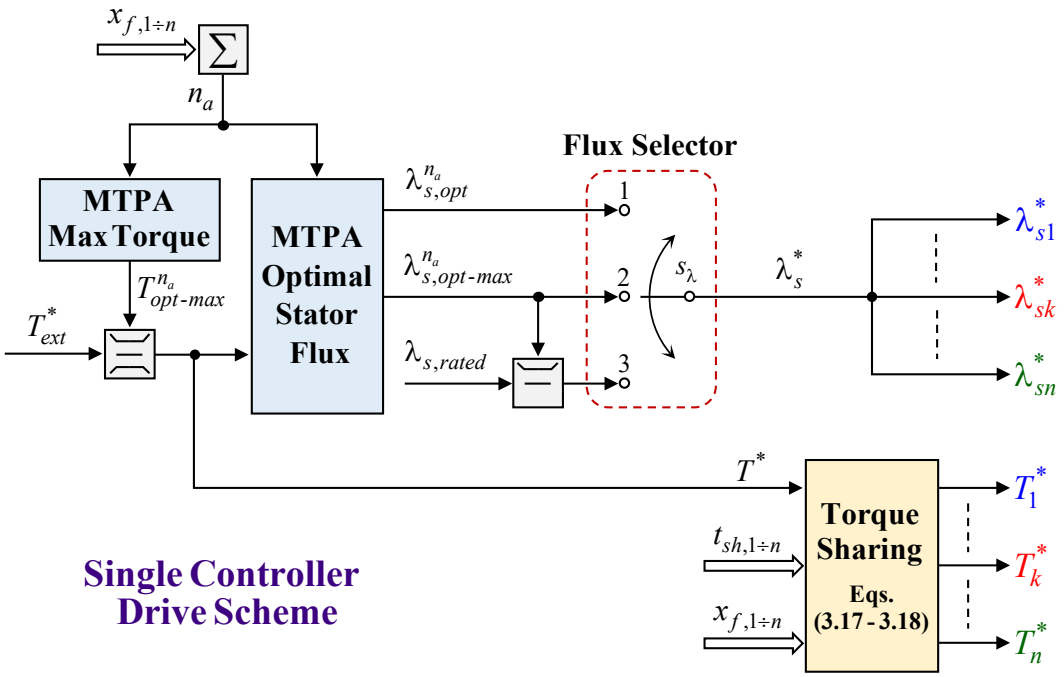

Fig. 3. 5. Drive scheme using a single outer controller.

If the conditions (3.14) are satisfied, by using the experimental procedure defined in [10], it is possible to compute the optimal stator flux amplitude profiles of the machine in both healthy and fault conditions, thus performing the Maximum Torque per Ampere (MTPA) operation of the drive. This feature allows the full exploitation of the maximum phase-current limit I_{max} together with the possibility of increasing the machine efficiency. With reference to [10], the computation of the machine optimal stator flux amplitude depends by the number of active three-phase units n_a, leading to the qualitative profiles shown in Fig. 3. 6. It is necessary to highlight how these have the meaning of optimal stator flux amplitude values belonging to the active three-phase units.

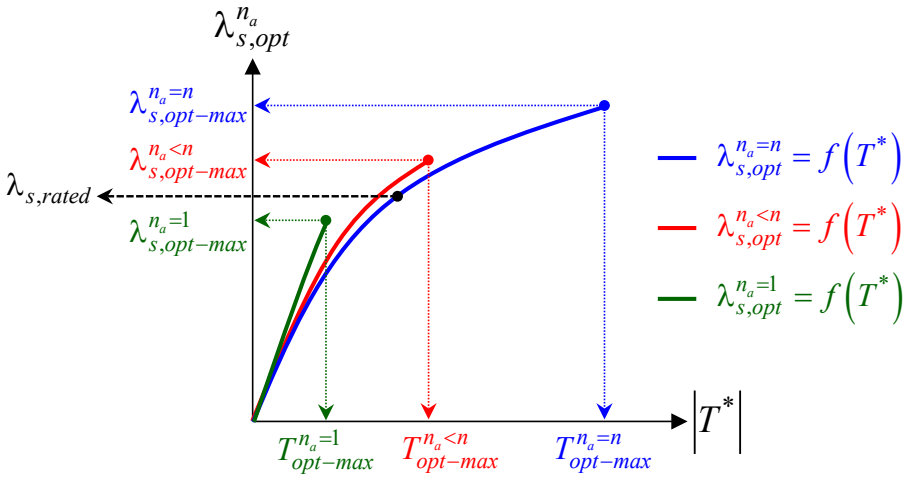

$\left(I_{\max,k} = I_{\max}\ ,\ L_{l,sk} = L_{l,s} \quad \forall k = 1 \div n\right)$ Ref. [8]

Fig. 3. 6. Optimal stator flux amplitude profiles of the machine in healthy and fault conditions.

It is noted how, for a given maximum phase-current limit I_{max}, the reduction of n_a leads to lower values of the maximum obtainable torque $T_{opt\text{-}max}^{n_a}$ (absolute value) and maximum optimal stator flux amplitude $\lambda_{s,opt\text{-}max}^{n_a}$. This result is quite obvious as the reduction of n_a leads to a natural derating of the machine performance. Concerning the optimal stator flux amplitude profiles, it is noted how the reduction of n_a leads to require a higher value of the optimal stator flux amplitude $\lambda_{s,opt}^{n_a}$ for a given value of the absolute reference torque $\left|T^*\right|$. The reason is related to the increment of the stator flux leakage contribution due to the increment of the current injected in the healthy units to guarantee the same torque production. More details can be found in [10]. To simplify the description, from now on the optimal stator flux amplitude profiles of the machine will be simply called as MTPA profiles.

Coming back to the scheme shown in Fig. 3. 5, according with the previous considerations, the total torque required to the machine T_{ext}^* is provided by a single outer controller. Therefore, by using the feedback signals providing the status of each VSI unit $x_{f,k}$, the number of active units n_a is computed as follows:

$$n_a = \sum_{z=1}^{n} x_{f,k} \tag{3.15}$$

As a consequence, by using the MTPA profiles, it is possible to define both values of maximum obtainable torque $T_{opt\text{-}max}^{n_a}$ and maximum optimal stator flux amplitude $\lambda_{s,opt\text{-}max}^{n_a}$. Therefore, the external torque reference T_{ext}^* is eventually saturated to the maximum obtainable torque value $T_{opt\text{-}max}^{n_a}$ (absolute limit), leading to the definition of the machine torque reference T^*. Finally, by using the MTPA profiles, the torque reference T^* allows to compute the optimal stator flux amplitude value $\lambda_{s,opt}^{n_a}$.

The definition of the stator flux amplitude reference λ_s^* can be performed by selecting one of the below three options:

$$\begin{cases} s_\lambda = 1 \;\rightarrow\; \lambda_s^* = \lambda_{s,opt}^{n_a} \\ s_\lambda = 2 \;\rightarrow\; \lambda_s^* = \lambda_{s,opt-max}^{n_a} \\ s_\lambda = 3 \;\rightarrow\; \lambda_s^* = \lambda_{s,rated}\ (< \lambda_{s,opt}^{n_a}) \end{cases} \tag{3.16}$$

The first choice consists of to use the optimal value of the stator flux amplitude $\lambda_{s,opt}^{n_a}$, thus performing the MTPA operation of the drive. Nevertheless, this choice is not convenient in the case of high-dynamic torque regulations must be performed.

Unlike the stator fluxes amplitudes, the dynamic of the rotor flux amplitude is strongly limited by its time constant. Therefore, like for a three-phase IM, high-dynamic variations of the stator flux amplitude reference λ_s^* may lead to relevant over-currents in the active units, corresponding to the large increments of the stator fluxes leakage contributions.

The second choice consists of using the maximum value of the optimal stator flux amplitude $\lambda_{s,opt\text{-}max}^{n_a}$. Below the base speed of the machine, both stator and rotor fluxes amplitudes are not affected by the torque reference T^* variations, allowing its regulation with high-dynamic performance. However, this condition corresponds to the injection of the maximum magnetizing current of the machine even under low-load conditions, thus leading to a reduction of the drive efficiency.

Finally, the third choice represents a compromise solution as it corresponds into use the rated stator flux amplitude of the machine $\lambda_{s,rated}$. In this way, the injection of magnetizing current in the machine is reduced. At the same time, below the base speed of the machine, both stator and rotor fluxes amplitudes are not affected by the torque variations. However, this solution does not allow the full exploitation of the maximum phase-current limit I_{max}, leading to a reduction of the maximum obtainable torque compared to the first two choices. Finally, being the rated stator flux amplitude of the machine $\lambda_{s,rated}$ defined in healthy conditions, this value should be saturated to the maximum value of the optimal stator flux amplitude $\lambda_{s,opt\text{-}max}^{n_a}$, according with Fig. 3. 6.

Once the selection of the stator flux amplitude reference λ_s^* has been performed, this corresponds with the reference value for each unit, as shown in Fig. 3. 5.

When the drive scheme employs a single outer controller, usually no torque sharing strategies are implemented, especially in the case of the maximum phase-current limits among the units are identical from each other. In this case, balanced operation of the active three-phase units is performed, corresponding to the most efficient condition of the machine [10], [11]. In terms of torque reference of the generic unit *k*, this condition corresponds to as follows:

$$T_k^* = x_{f,k} \cdot \frac{T^*}{n_a} \tag{3.17}$$

To exploit the additional degrees of freedom given by the multiple three-phase structures, it is possible to implement the so called “torque sharing”, i.e. the three-phase sets can have different torque contributions. In this case, the generic *k*-unit torque reference can be defined as follows:

$$T_k^* = x_{f,k} \cdot t_{sh,k} \cdot T^* \tag{3.18}$$

With reference to (3.18), each *k*-unit torque sharing coefficient $t_{sh,k}$ must be defined to guarantee the following condition:

$$\sum_{z=1}^{n} x_{f,z} \cdot t_{sh,z} = 1 \quad \Rightarrow \quad \sum_{z=1}^{n} T_z^* = T^* \tag{3.19}$$

In this way, the sum of the torque references belonging to the units corresponds to the machine torque reference T^*. Finally, each *k*-unit torque sharing coefficient $t_{sh,k}$ must be defined in order to guarantee the implementation of the *k*-unit torque reference T_k^*, according with the *k*-unit maximum phase-current limit $I_{max,k}$.

In conclusion, independently by the fact if single or multiple outer controllers are employed, each three-phase unit *k* is characterized by its own references in terms flux amplitude λ_{sk}^* and torque contribution T_k^*. Therefore, the DFVC scheme dedicated to the control of the considered unit *k* must be able to guarantee their regulation, according with the *k*-unit limitations in terms of DC-link voltage $v_{dc,k}^*$, phase-current amplitude $I_{max,k}$ and load-angle $\delta_{max,k}$. Therefore, it follows the full description of the DFVC scheme dedicated to the control of each three-phase unit *k*.

3.4 Modular Direct Flux Vector Control (DFVC) scheme

The DFVC scheme of each three-phase unit *k* is implemented in the rotating *k*-unit stator flux frame (d_{sk},q_{sk}). Therefore, the position of the d_{sk}-axis corresponds with the one $\vartheta_{\lambda\text{-}sk}$ of the *k*-unit flux vector $\bar{\lambda}_{sk}$, as shown in Fig. 3. 7.

The load-angle δ_{sk} of each unit *k* is defined as the angular difference between the *k*-unit flux vector $\bar{\lambda}_{sk}$ and the rotor flux vector $\bar{\lambda}_r$ (Fig. 3. 7).

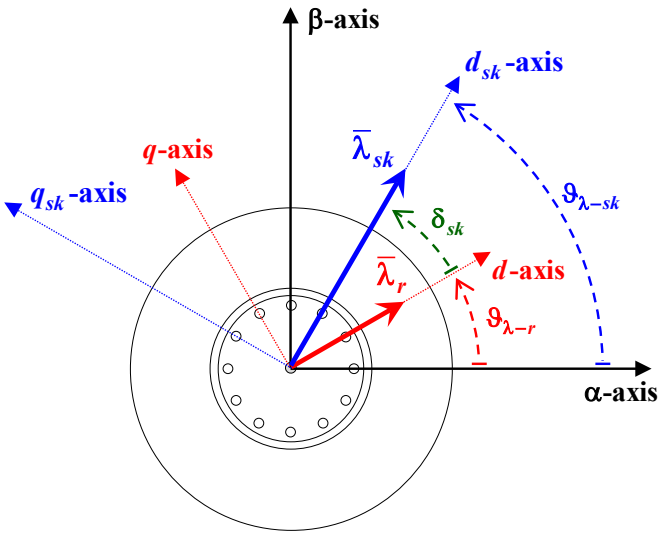

Fig. 3. 7. Rotating stator flux frame (d_{sk},q_{sk}) of a generic three-phase *k*-unit.

According with the MS machine electromechanical model (2.119), the *k*-unit electric equation defined in the rotating (d_{sk},q_{sk}) frame is computed as follows:

$$\overline{v}_{sk,dq_{sk}} = R_{sk} \cdot \overline{i}_{sk,dq_{sk}} + \frac{d}{dt}\overline{\lambda}_{sk,dq_{sk}} + j \cdot \omega_{sk} \cdot \overline{\lambda}_{sk,dq_{sk}} \tag{3.20}$$

where ω_{sk} represents the synchronous speed of the rotating (d_{sk},q_{sk}) frame with respect to the stationary (α,β) one. This is defined as follows:

$$\omega_{sk} = \frac{d\vartheta_{\lambda\text{-}sk}}{dt} \tag{3.21}$$

Therefore, with reference to (3.20), the *k*-unit stator electric equation along the d_{sk}-axis is computed as follows:

$$v_{sk,d_{sk}} = R_{sk} \cdot i_{sk,d_{sk}} + \frac{d}{dt}\lambda_{sk} \tag{3.22}$$

It is noted how the d_{sk}-axis voltage component $v_{sk,d_{sk}}$ of the unit *k* allows at performing the direct regulation of the *k*-unit flux amplitude λ_{sk}.

Concerning the regulation of the *k*-unit torque contribution, it is necessary to consider the machine electromagnetic torque expression defined in the rotating (d_{sk},q_{sk}) frame (2.119):

$$T = \frac{3}{2} \cdot p_p \cdot \sum_{k=1}^{n} \left(\overline{\lambda}_{sk,dq_{sk}} \times \overline{i}_{sk,dq_{sk}} \right) \tag{3.23}$$

By isolating the *k*-unit torque contribution T_k from (3.23), the following result is obtained:

$$T_k = \frac{3}{2} \cdot p_p \cdot \left(\overline{\lambda}_{sk,dq_{sk}} \times \overline{i}_{sk,dq_{sk}} \right) = \frac{3}{2} \cdot p_p \cdot \left(\lambda_{sk} \cdot i_{sk,q_{sk}} \right) \tag{3.24}$$

It is noted how the *k*-unit torque contribution can be regulated by means of the q_{sk}-axis current component $i_{sk,q_{sk}}$ of the unit *k*. This can be considered as an equivalent torque-producing current. Therefore, its regulation allows at obtaining a high level of decoupling among the (d_{sk},q_{sk}) control axes compared to a direct control of the *k*-unit torque contribution.

In conclusion, for each three-phase unit *k*, the Equations (3.22), (3.24) leads to the following considerations:

- The direct and independent regulation of the *k*-unit flux amplitude λ_{sk} is performed by acting on the d_{sk}-axis voltage component $v_{sk,d_{sk}}$ of the unit *k*;

- The independent regulation of the *k*-unit torque contribution T_k is performed by regulating the q_{sk}-axis current component $i_{sk,q_{sk}}$ of the *k*-unit, thus acting on the q_{sk}-axis voltage component $v_{sk,q_{sk}}$ of the unit *k*.

It follows the full description of the DFVC scheme for the control of a generic three-phase unit *k*. In detail, two regulation type are shown:

- Regulation of both stator flux amplitude and torque contribution by means of standard Proportional-Integral (PI) controllers;
- Regulation of both stator flux amplitude and torque contribution by means of Dead-Beat (DB) controllers.

It is shown how the DB-regulation leads to a control structure requiring higher computational efforts than the PI one, however able to guarantee the best dynamic performance of the drive.

In schematic way, the PI-DFVC scheme of each three-phase unit *k* is composed by the following main blocks:

- Control Inputs Elaboration
- Flux Observer
- Control Structure
- Decoupling Algorithm

Concerning the DB-DFVC scheme, it uses the same blocks of the PI-DFVC scheme with the addition of the following one:

- Model Predictive Estimator

An in-depth analysis about each of these blocks is reported below.

3.4.1 Control Inputs Elaboration

According with the drive scheme configuration, the inputs of a *k*-unit DFVC scheme correspond with the digital values of *k*-unit currents $\left[i_{sk,abc}\right]^{\tau}$, *k*-unit DC-link voltage $v_{dc,k}{}^{\tau}$ and rotor mechanical position ϑ_m^{τ}.

In addition, the *k*-unit duty-cycles $\left[d^*_{k,abc}\right]^{\tau}$ computed in the previous sample time instant (τ-1) are known. However, they are implemented in the considered one (τ) due the execution delay of the digital controller.

Therefore, the following preliminary operations are performed:

- Reconstruction of the *k*-unit ideal voltages $\left[v_{sk-rec,abc}\right]^{\tau}$;
- Estimation of the Dead-Time (DT) voltage errors $\left[\tilde{v}_{dt-k,abc}\right]^{\tau}$ introduced by the VSI unit *k*.

Both operations lead to the computation of variables defined in the *k*-unit phase coordinates $(abc)_k$. Concerning the reconstruction of the *k*-unit ideal voltages, this is performed by applying the moving-average operation on (3.4), leading to the following result:

$$\left[v_{sk-rec,abc}\right]^{\tau} = v_{dc,k} \cdot \left[C_v\right] \cdot \left[d^*_{k,abc}\right]^{\tau} = v_{dc,k} \cdot \left(\left[d^*_{k,abc}\right]^{\tau} - \begin{bmatrix} d^*_{k-0} \\ d^*_{k-0} \\ d^*_{k-0} \end{bmatrix} \right) \tag{3.25}$$

where:

$$d^*_{k-0} = \frac{d^*_{k,a} + d^*_{k,b} + d^*_{k,c}}{3} \tag{3.26}$$

Conversely, the estimation of the *k*-unit DT voltage errors $\left[\tilde{v}_{dt-k,abc}\right]^{\tau}$ is performed using the procedure described in [12], thus requiring the *k*-unit stator currents $\left[i_{sk,abc}\right]^{\tau}$.

Finally, *k*-unit currents $\left[i_{sk,abc}\right]^{\tau}$, *k*-unit ideal voltages $\left[v_{sk-rec,abc}\right]^{\tau}$ and *k*-unit DT voltage errors $\left[\tilde{v}_{dt-k,abc}\right]^{\tau}$ are expressed in stationary coordinates (αβ0), using the three-phase Clarke transformation defined in (3.6). In this way, the following stationary variables are defined:

$$\begin{cases} \left[i_{sk,\alpha\beta0}\right]^{\tau} = \left[T_k\right] \cdot \left[i_{sk,abc}\right]^{\tau} \\ \left[v_{sk-rec,\alpha\beta0}\right]^{\tau} = \left[T_k\right] \cdot \left[v_{sk-rec,abc}\right]^{\tau} \\ \left[\tilde{v}_{dt-k,\alpha\beta0}\right]^{\tau} = \left[T_k\right] \cdot \left[\tilde{v}_{dt-k,abc}\right]^{\tau} \end{cases} \tag{3.27}$$

For control purposes, the zero-sequence components of the variables are not used. For this reason, they are discarded, thus allowing the use of the complex vectors defined in the (α,β) frame.

Concerning the feedback of rotor mechanical position ϑ^{τ}_m, this is used to compute the rotor electrical position ϑ^{τ}_r as follows:

$$\vartheta^{\tau}_r = p_p \cdot \vartheta^{\tau}_m \tag{3.28}$$

The rotor mechanical position is represented as a rotating versor as:

$$\overline{\Theta}^{\tau}_m = e^{j \cdot \vartheta^{\tau}_m} = \cos\left(\vartheta^{\tau}_m\right) + j \cdot \sin\left(\vartheta^{\tau}_m\right) \tag{3.29}$$

Finally, the mechanical coordinates (3.29) are elaborated by a conventional Phase Locked Loop (PLL) in order to compute the rotor mechanical speed ω^{τ}_m. The PLL design is not reported, being this beyond the scope of this dissertation [13].

Once the rotor mechanical speed ω_m^τ has been obtained, the rotor electrical speed ω_r^τ is computed as follows:

$$\omega_r^\tau = p_p \cdot \omega_m^\tau \tag{3.30}$$

In conclusion, with reference to the execution scheme shown in Fig. 3. 8, the elaboration scheme of the *k*-unit DFVC inputs leads to the computation of the following variables:

- Current vector of the unit *k* in the stationary (α,β) frame: $\overline{i}_{sk,\alpha\beta}^\tau$
- Ideal voltage vector of the unit *k* in the stationary (α,β) frame: $\overline{v}_{sk-rec,\alpha\beta}^\tau$
- Estimated DT error voltage vector of the unit *k* in the stationary (α,β) frame: $\tilde{\overline{v}}_{dt-k,\alpha\beta}^\tau$
- Rotor electrical position: ϑ_r^τ
- Rotor mechanical speed: ω_m^τ
- Rotor electrical speed: ω_r^τ

Finally, it is necessary to highlight how the rotor electrical position together with both mechanical and electrical speeds are shared by the DFVC schemes belonging the other units.

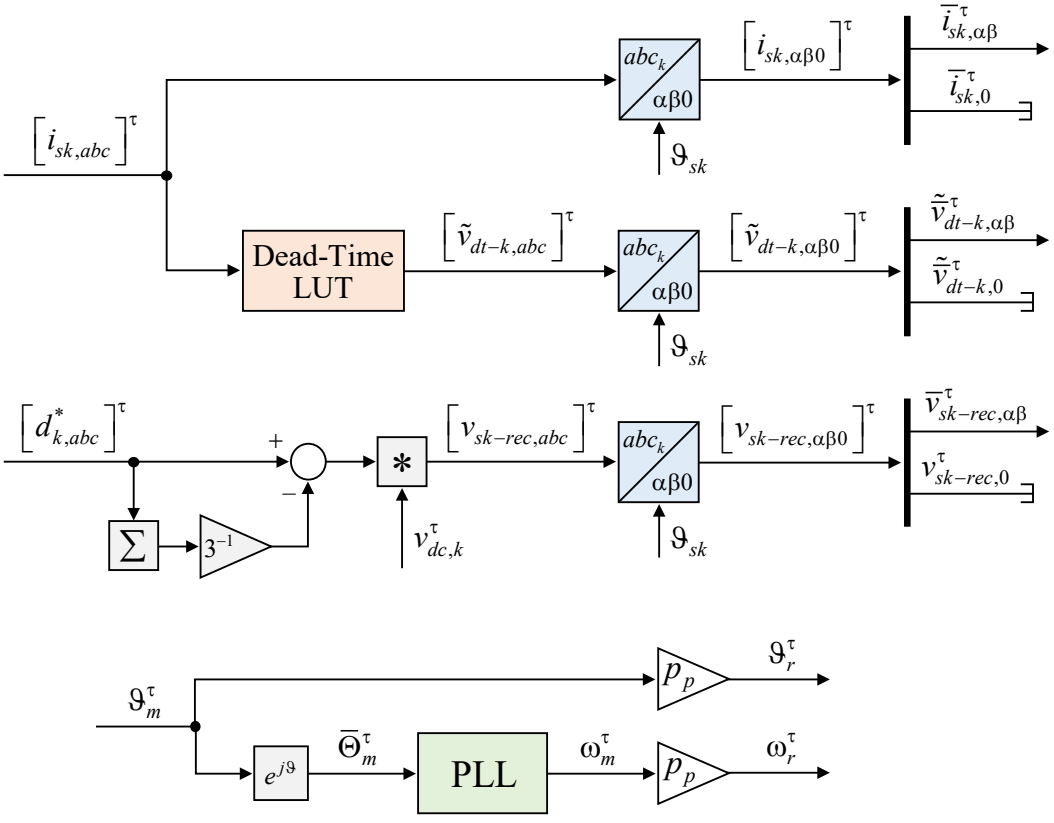

Fig. 3. 8. Execution scheme for the control inputs elaboration of the generic *k*-unit DFVC scheme.

3.4.2 Flux Observer

The DFVC scheme of each three-phase unit *k* is implemented in the rotating *k*-unit stator flux frame (d_{sk},q_{sk}). Therefore, it is necessary to implement a flux observer to get the *k*-unit flux vector in terms of amplitude and angular position.

Each unit *k* uses a flux observer consisting of the combination of two model-based estimators, as shown in Fig. 3. 9. At high speed, the flux observer is based on the "stator electric model" (blue-window). Conversely, at low speed, the flux observer is based on the "rotor electromagnetic model" (red-window). By means of a "correction mechanism" (green-window), it is established the transition operation between the two models [14].

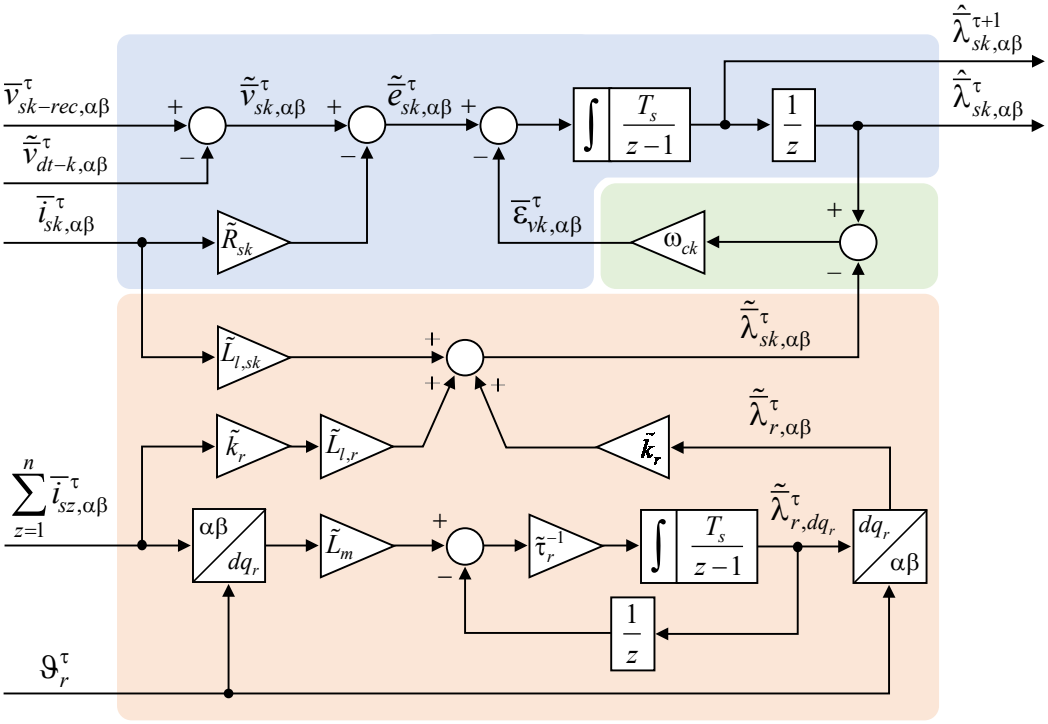

Fig. 3. 9. Flux observer structure for the generic unit *k*.

According with the MS machine electromagnetic model (2.71), the *k*-set electric equation in the stationary (α,β) frame is computed as follows:

$$\bar{v}_{sk,\alpha\beta} = R_{sk} \cdot \bar{i}_{sk,\alpha\beta} + \frac{d}{dt}\bar{\lambda}_{sk,\alpha\beta} \tag{3.31}$$

The "stator electric model" of the flux observer corresponds with the digital implementation of (3.31). In detail, with the aim at obtaining the (α,β) components of the *k*-unit flux vector $\bar{\lambda}_{sk,\alpha\beta}$, the direct integration of the *k*-unit back-emf vector $\bar{e}_{sk,\alpha\beta}$ is performed.

The integration of the *k*-unit back-emf vector is performed by using the backward-Euler method. In this way, due the execution delay of the digital controller, a straightforward prediction of the *k*-unit flux vector for the next sample time instant (τ+1) is obtained.

At high-speed, the "stator electric model" is able to guarantee an accurate estimation of the *k*-unit flux vector as both *k*-unit DT voltage errors and *k*-unit resistance detuning have negligible effects on the estimation of the *k*-unit back-emf vector.

Concerning the "rotor electromagnetic model", (2.100) is considered as follows:

$$\begin{cases} \overline{\lambda}_{sk,\alpha\beta} = L_{l,sk} \cdot \overline{i}_{sk,\alpha\beta} + L_m \cdot \sum_{z=1}^{n} \overline{i}_{sz,\alpha\beta} + L_m \cdot \overline{i}_{r,\alpha\beta} \\ \overline{\lambda}_{r,\alpha\beta} = L_{l,r} \cdot \overline{i}_{r,\alpha\beta} + L_m \cdot \sum_{z=1}^{n} \overline{i}_{sz,\alpha\beta} + L_m \cdot \overline{i}_{r,\alpha\beta} \end{cases} \tag{3.32}$$

After some mathematical manipulations, (3.32) is expressed as follows:

$$\overline{\lambda}_{sk,\alpha\beta} = L_{l,sk} \cdot \overline{i}_{sk,\alpha\beta} + k_r \cdot L_{l,r} \cdot \sum_{z=1}^{n} \overline{i}_{sz,\alpha\beta} + k_r \cdot \overline{\lambda}_{r,\alpha\beta} \tag{3.33}$$

According with the MS state-space model of the machine (2.150), the state equation of the rotor flux in the generic rotating (*x*,*y*) frame is computed as follows:

$$\frac{d}{dt}\overline{\lambda}_{r,xy} = -\left[\frac{1}{\tau_r} + j \cdot \left(\omega^* - \omega_r\right)\right] \cdot \overline{\lambda}_{r,xy} + R_r \cdot k_r \cdot \sum_{z=1}^{n} \overline{i}_{sz,xy} \tag{3.34}$$

With the aim at removing the motional terms, (3.34) is computed in the rotor (d_r,q_r) frame (2.104,c), leading to the following result:

$$\frac{d}{dt}\overline{\lambda}_{r,dq_r} = -\frac{1}{\tau_r} \cdot \overline{\lambda}_{r,dq_r} + R_r \cdot k_r \cdot \sum_{z=1}^{n} \overline{i}_{sz,dq_r} \tag{3.35}$$

The "rotor electromagnetic model" corresponds with the digital implementation of (3.33) and (3.35), as shown in Fig. 3. 9. It can be noted how the stator voltage reconstruction is not required, making this estimator quite robust against the DT voltage errors. For this reason, at low speed, the "rotor electromagnetic model" allows at performing a good estimation of the *k*-unit flux vector. However, this estimator results quite sensitive to the detuning of the rotor time constant $\tilde{\tau}_r$, thus affecting the starting operation of the machine. Concerning the inputs of this estimator, it is noted how it requires the stationary (α,β) components of the current vectors belonging to all *n* units, thus introducing a slight level of interaction between the *n* DFVC schemes. However, this aspect does not affect the modularity of the proposed control solution.

Finally, by means of the "correction mechanism", it is possible to establish the transition electrical frequency (rad/s) between the two models. With reference to Fig. 3. 9, it corresponds with the *k*-unit observer gain ω_{ck}, implementing the following transition law:

$$\hat{\bar{\lambda}}_{sk,\alpha\beta} = \tilde{\bar{\lambda}}_{sk,\alpha\beta} \cdot \frac{\omega_{ck}}{\mathcal{L} + \omega_{ck}} + \left(\frac{\tilde{\bar{e}}_{sk,\alpha\beta}}{\mathcal{L}} \right) \cdot \frac{\mathcal{L}}{\mathcal{L} + \omega_{ck}} \tag{3.36}$$

where:

- $\mathcal{L}$ represents the Laplace variable;
- $\tilde{\bar{\lambda}}_{sk,\alpha\beta}$ is the *k*-unit flux vector estimate provided by "rotor electromagnetic model";
- $\hat{\bar{\lambda}}_{sk,\alpha\beta}$ is the *k*-unit observed flux vector.

According with (3.36), in case of the electrical frequency is lower than ω_{ck}, the observed *k*-unit stator flux vector corresponds with the estimate provided by "rotor electromagnetic model". Conversely, it corresponds with the integration of the *k*-unit back-emf vector if the electrical frequency is higher than ω_{ck}.

In conclusion, with reference to Fig. 3. 9, the outputs of the *k*-unit flux observer are the following:

- Observed *k*-unit flux vector in the stationary (α,β) frame: $\hat{\bar{\lambda}}^{\tau}_{sk,\alpha\beta}$
- Predicted *k*-unit flux vector in the stationary (α,β) frame: $\hat{\bar{\lambda}}^{\tau+1}_{sk,\alpha\beta}$

Once the observed *k*-unit flux vector $\hat{\bar{\lambda}}^{\tau}_{sk,\alpha\beta}$ is obtained, by using (3.33), the observed rotor flux vector $\hat{\bar{\lambda}}^{\tau}_{r,\alpha\beta}$ is computed.

Concerning the positions of both stator and rotor fluxes vectors, they are represented by rotating versors as:

$$\hat{\bar{\Theta}}^{\tau}_{\lambda-sk} = e^{j\cdot\hat{\vartheta}^{\tau}_{\lambda-sk}} = \cos\left(\hat{\vartheta}^{\tau}_{\lambda-sk}\right) + j\cdot\sin\left(\hat{\vartheta}^{\tau}_{\lambda-sk}\right) = \frac{\hat{\bar{\lambda}}^{\tau}_{sk,\alpha\beta}}{\left|\hat{\bar{\lambda}}^{\tau}_{sk,\alpha\beta}\right|} = \frac{\hat{\bar{\lambda}}^{\tau}_{sk,\alpha\beta}}{\hat{\lambda}^{\tau}_{sk}} \tag{3.37}$$

$$\hat{\bar{\Theta}}^{\tau+1}_{\lambda-sk} = e^{j\cdot\hat{\vartheta}^{\tau+1}_{\lambda-sk}} = \cos\left(\hat{\vartheta}^{\tau+1}_{\lambda-sk}\right) + j\cdot\sin\left(\hat{\vartheta}^{\tau+1}_{\lambda-sk}\right) = \frac{\hat{\bar{\lambda}}^{\tau+1}_{sk,\alpha\beta}}{\left|\hat{\bar{\lambda}}^{\tau+1}_{sk,\alpha\beta}\right|} = \frac{\hat{\bar{\lambda}}^{\tau+1}_{sk,\alpha\beta}}{\hat{\lambda}^{\tau+1}_{sk}} \tag{3.38}$$

$$\hat{\bar{\Theta}}^{\tau}_{\lambda-r} = e^{j\cdot\hat{\vartheta}^{\tau}_{\lambda-r}} = \cos\left(\hat{\vartheta}^{\tau}_{\lambda-r}\right) + j\cdot\sin\left(\hat{\vartheta}^{\tau}_{\lambda-r}\right) = \frac{\hat{\bar{\lambda}}^{\tau}_{r,\alpha\beta}}{\left|\hat{\bar{\lambda}}^{\tau}_{r,\alpha\beta}\right|} = \frac{\hat{\bar{\lambda}}^{\tau}_{r,\alpha\beta}}{\hat{\lambda}^{\tau}_{r}} \tag{3.39}$$

Finally, the observed *k*-unit trigonometric coordinates (3.37) are elaborated by a Phase Locked Loop (PLL) to compute the synchronous speed $\hat{\omega}_{sk}^{\tau}$ of the rotating (d_{sk},q_{sk}) frame.

In conclusion, with reference to the execution scheme shown in Fig. 3. 10, the elaboration of the *k*-unit flux observer outputs leads to the computation of the following variables:

- Observed rotor flux vector in the stationary (α,β) frame: $\hat{\bar{\lambda}}_{r,\alpha\beta}^{\tau}$
- Amplitude of observed *k*-unit flux vector: $\hat{\lambda}_{sk}^{\tau}$
- Amplitude of predicted *k*-unit flux vector: $\hat{\lambda}_{sk}^{\tau+1}$
- Versor of observed *k*-unit flux vector: $\hat{\bar{\Theta}}_{\lambda-sk}^{\tau}$
- Versor of predicted *k*-unit flux vector: $\hat{\bar{\Theta}}_{\lambda-sk}^{\tau+1}$
- Versor of observed rotor flux vector: $\hat{\bar{\Theta}}_{\lambda-r}^{\tau}$
- Synchronous speed of the rotating (d_{sk},q_{sk}) frame: $\hat{\omega}_{sk}^{\tau}$

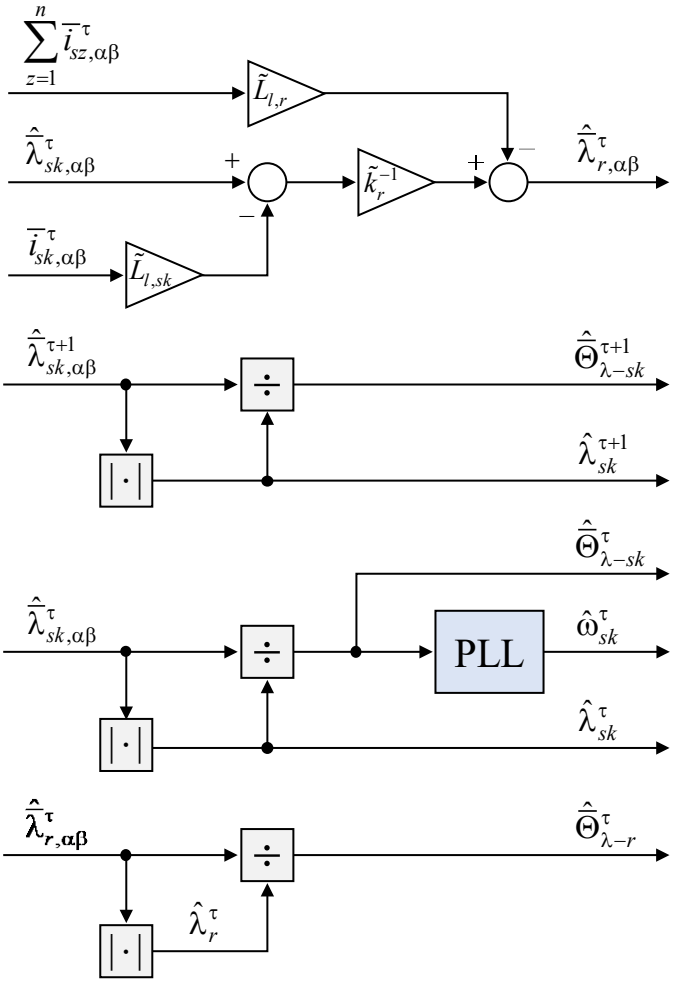

Fig. 3. 10. Execution scheme for the elaboration of the *k*-unit flux observer outputs.

3.4.3 Model Predictive Estimator

Like for the three-phase drives [15], [16], a DB regulation requires the prediction of the control variables for the next sample time instant (τ+1). Therefore, the MS state-space model of the machine (2.142) must be converted into its discrete time equivalent. However, according with [17], this operation is not easy to perform, especially for a high-order system like the considered one (2.177). For this reason, as for most of the three-phase predictive controls, the backward-Euler discretization [17] is proposed.

With reference to the *k*-unit flux observer, the predicted *k*-unit flux vector $\hat{\bar{\lambda}}_{sk,\alpha\beta}^{\tau+1}$ defined in the stationary (α,β) frame is already available. For this reason, only the prediction of the *k*-unit current vector must be performed. With the aim at performing this operation, (2.141) computed in terms of stationary (α,β) coordinates is considered, leading to as follows:

$$\begin{aligned}
&\left(\sigma_k \cdot L_{sk} + c_k \cdot L_{l,sk}\right) \cdot \frac{d}{dt} \bar{i}_{sk,\alpha\beta} = \\
&= -\left\{\left[R_r \cdot \frac{k_r}{k_{sk}} + R_{sk} \cdot \left(1 + c_k\right)\right] - j \cdot \left(\omega_r \cdot \sigma_k \cdot L_{sk}\right)\right\} \cdot \bar{i}_{sk,\alpha\beta} + \ldots \\
&\ldots - \sum_{\substack{z=1 \\ z \neq k}}^{n} \left\{\left[\left(R_r \cdot k_r - c_z \cdot R_{sk}\right) - j \cdot \left(\omega_r \cdot c_z \cdot L_{l,sz}\right)\right] \cdot \bar{i}_{sz,\alpha\beta}\right\} + \ldots \\
&\ldots + \left(\frac{1}{\tau_r} - j \cdot \omega_r\right) \cdot \bar{\lambda}_{sk,\alpha\beta} + \left(1 + c_k\right) \cdot \bar{v}_{sk,\alpha\beta} - \sum_{\substack{z=1 \\ z \neq k}}^{n} \left(c_z \cdot \bar{v}_{sz,\alpha\beta}\right)
\end{aligned} \tag{3.40}$$

To obtain a more compact formulation, the following variables are defined:

$$\begin{cases}
L_k = \sigma_k \cdot L_{sk} + c_k \cdot L_{l,sk} \\
R_k = R_r \cdot \dfrac{k_r}{k_{sk}} + R_{sk} \cdot \left(1 + c_k\right) \\
X_k = -\omega_r \cdot \sigma_k \cdot L_{sk} \\
R_z = R_r \cdot k_r - c_z \cdot R_{sk} \\
X_z = -\omega_r \cdot c_z \cdot L_{l,sz}
\end{cases} \tag{3.41}$$

By replacing (3.41) in (3.40), the following result is obtained:

$$\begin{aligned} L_k \cdot \frac{d}{dt}\overline{i}_{sk,\alpha\beta} = &-\left(R_k + j\cdot X_k\right)\cdot \overline{i}_{sk,\alpha\beta} - \sum_{\substack{z=1\\ z\neq k}}^{n}\left[\left(R_z + j\cdot X_z\right)\cdot \overline{i}_{sz,\alpha\beta}\right] + \dots \\ &\dots + \left(\tau_r^{-1} - j\cdot\omega_r\right)\cdot\overline{\lambda}_{sk,\alpha\beta} + \left(1+c_k\right)\cdot\overline{v}_{sk,\alpha\beta} - \sum_{\substack{z=1\\ z\neq k}}^{n}\left(c_z\cdot\overline{v}_{sz,\alpha\beta}\right) \end{aligned} \tag{3.42}$$

To compute the prediction of the *k*-unit current vector $\tilde{\overline{i}}_{sk,\alpha\beta}^{\tau+1}$ for the next sample time instant (τ+1), the backward-Euler discretization of (3.42) is implemented, leading to the following result:

$$\tilde{\overline{i}}_{sk,\alpha\beta}^{\tau+1} = \overline{i}_{sk,\alpha\beta}^{\tau} + \frac{T_s}{\tilde{L}_k}\cdot\left\{\begin{aligned} &-\left(\tilde{R}_k^{\tau} + j\cdot\tilde{X}_k^{\tau}\right)\cdot\overline{i}_{sk,\alpha\beta}^{\tau} - \sum_{\substack{z=1\\ z\neq k}}^{n}\left[\left(\tilde{R}_z^{\tau} + j\cdot\tilde{X}_z^{\tau}\right)\cdot\overline{i}_{sz,\alpha\beta}^{\tau}\right] + \dots \\ &\dots + \left(\tilde{\tau}_r^{-1} - j\cdot\omega_r^{\tau}\right)\cdot\hat{\overline{\lambda}}_{sk,\alpha\beta}^{\tau+\frac{1}{2}} + \left(1+\tilde{c}_k^{\tau}\right)\cdot\tilde{\overline{v}}_{sk,\alpha\beta}^{\tau} - \sum_{\substack{z=1\\ z\neq k}}^{n}\left(\tilde{c}_z^{\tau}\cdot\tilde{\overline{v}}_{sz,\alpha\beta}^{\tau}\right) \end{aligned}\right\} \tag{3.43}$$

where $\hat{\overline{\lambda}}_{sk,\alpha\beta}^{\tau+\frac{1}{2}}$ corresponds with the bilinear discretization of the *k*-unit flux vector [18]. According with the *k*-unit flux observer outputs, this is computed as follows:

$$\hat{\overline{\lambda}}_{sk,\alpha\beta}^{\tau+\frac{1}{2}} = \frac{\hat{\overline{\lambda}}_{sk,\alpha\beta}^{\tau} + \hat{\overline{\lambda}}_{sk,\alpha\beta}^{\tau+1}}{2} \tag{3.44}$$

The bilinear discretization of the *k*-unit flux vector is necessary to obtain an accurate prediction of the *k*-unit current vector. Indeed, according with the MS modelling, (3.40) does not represents a state equation because the *k*-unit flux vector cannot be considered as state variable. However, this formulation results quite useful as both observed and predicted *k*-unit flux vectors are characterized by a high-level of accuracy.

It is noted how the *k*-unit predicted current vector is denoted with the superscript ~, thus giving the meaning of estimated variable. Indeed, (3.43) represents the implementation of a Model Predictive Estimator (MPE).

Finally, it is noted how the implementation of (3.43) requires high computational efforts of the dedicated digital controller. In addition, it must be computed for the *n* DFVC schemes of the drive, corresponding to the *n* three-phase winding sets of the machine.

Similar to the flux observer, it is noted how the MPE requires the stationary (α,β) components of both current and voltage vectors belonging to all *n* units. Nevertheless, the prediction of *k*-unit current vector must not be affected by fault events regarding the other units.

Therefore, to consider the VSI units' status, compared to the definition given in (2.130), the coefficients $\tilde{c}_k$ and $\tilde{c}_z$ are re-defined as follows:

$$\tilde{c}_z = \frac{\tilde{L}_{l,r} \cdot \tilde{k}_r}{\tilde{L}_{l,sz}} \cdot x_{f,k}^{\tau} \quad , \quad \tilde{c}_k = \sum_{\substack{z=1 \\ z \neq k}}^{n} \tilde{c}_z \tag{3.45}$$

Once the *k*-unit predicted current vector is obtained, the prediction of the *k*-unit DT voltage error vector $\tilde{\bar{v}}_{dt-k,\alpha\beta}^{\tau+1}$ for the next sample time instant (τ+1) is performed, using the same procedure shown in the "Control Inputs Elaboration" block.

Finally, according with the execution scheme shown in Fig. 3. 11, the predicted *k*-unit DT voltage error vector in the rotating (d_{sk},q_{sk}) frame $\tilde{\bar{v}}_{dt-k,dq_{sk}}^{\tau+1}$ is computed. This operation is performed by means of the rotational transformation (2.105), using the trigonometric coordinates of to the *k*-unit predicted flux vector $\hat{\bar{\Theta}}_{\lambda-sk}^{\tau+1}$.

In conclusion, with reference to the execution scheme shown in Fig. 3. 11, the prediction of the *k*-unit current vector components leads to the computation of the following variables:

- Predicted *k*-unit current vector in the stationary (α,β) frame: $\tilde{\bar{i}}_{sk,\alpha\beta}^{\tau+1}$
- Predicted *k*-unit DT voltage error vector in the rotating (d_{sk},q_{sk}) frame: $\tilde{\bar{v}}_{dt-k,dq_{sk}}^{\tau+1}$

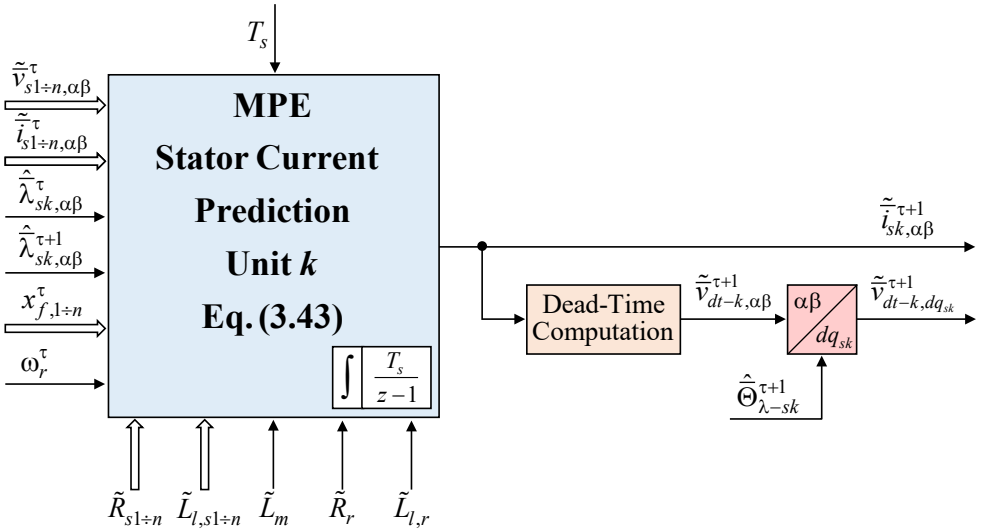

Fig. 3. 11. Execution scheme for the prediction of *k*-unit stator current vector and *k*-unit DT voltage error vector.

3.4.4 Control Structure

The *k*-unit DFVC scheme uses a control structure which is similar to the one defined for the three-phase drives [7]. In this dissertation, two configurations of the *k*-unit DFVC structure are shown, corresponding to the implementation of PI and DB regulation types. To avoid confusion, these are described separately.

Control structure using PI controllers

With reference to the execution scheme shown in Fig. 3. 12, the structure of the *k*-unit PI-DFVC scheme is composed by several blocks, thus implementing different control features. These are classified as follows:

- Stator flux amplitude limitation (green blocks)
- Torque-producing current limitation (yellow blocks)
- Unit control (blue block)

The "unit control" corresponds with the regulation of the *k*-unit flux amplitude and the *k*-unit torque-producing current. For the considered case, this is performed by means of PI regulators.

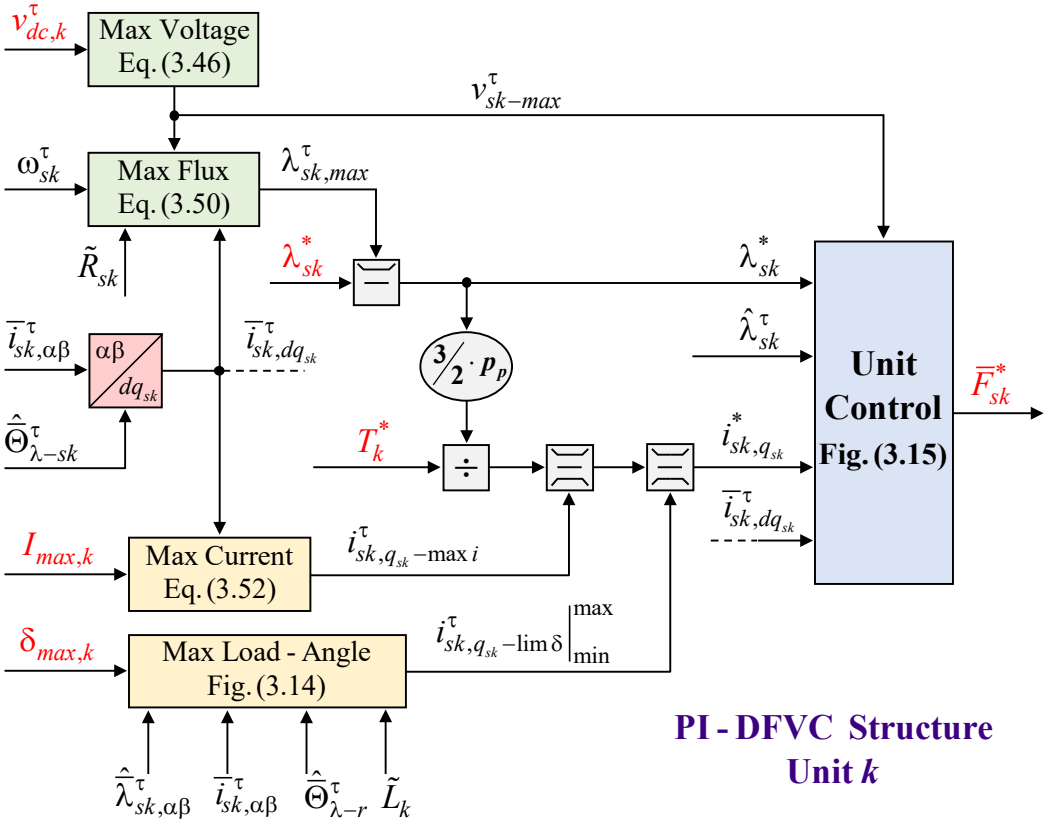

Fig. 3. 12. PI-DFVC structure for the control of the generic unit *k*.

Because a regulation type using PI controllers is considered, the computation of the *k*-unit current vector in the rotating (d_{sk},q_{sk}) frame $\bar{i}^{\tau}_{sk,dq_{sk}}$ is performed. Therefore, by using the trigonometric coordinates of the observed *k*-unit flux vector $\hat{\bar{\Theta}}^{\tau}_{\lambda-sk}$, the rotational transformation (2.105) on the *k*-unit current vector $\bar{i}^{\tau}_{sk,\alpha\beta}$ defined in the stationary (α,β) frame is implemented (Fig. 3. 12).

Concerning the observed *k*-unit flux amplitude $\hat{\lambda}^{\tau}_{sk}$, this is provided by the *k*-unit flux observer, as shown in Fig. 3. 9.

Stator flux amplitude limitation

The PWM voltage control of each VSI unit *k* is performed using the 'Min-Max' modulation [9]. As a consequence, the *k*-unit phase-voltage limit is computed as follows:

$$v^{\tau}_{sk-max} = \frac{v^{\tau}_{dc,k}}{\sqrt{3}} \tag{3.46}$$

By computing the *k*-unit electric equation (3.20) in steady-state conditions, the following result is obtained:

$$\bar{V}_{sk,dq_{sk}} = R_{sk} \cdot \bar{I}_{sk,dq_{sk}} + j \cdot \omega_{sk} \cdot \bar{\Lambda}_{sk,dq_{sk}} \tag{3.47}$$

Therefore, according with the *k*-unit phase-voltage limit, (3.47) is subjected to the following constraint:

$$\left|\bar{V}_{sk,dq_{sk}}\right| \le v^{\tau}_{sk-max} \tag{3.48}$$

Finally, by combining (3.47)-(3.48), after several mathematical manipulations, the *k*-unit flux amplitude limit is computed as follows:

$$\Lambda_{sk} \le \frac{\sqrt{v_{sk-\max} - \left(R_{sk} \cdot I_{sk,d_{sk}}\right)^2} - R_{sk} \cdot I_{sk,q_{sk}} \cdot sign\left(\omega_{sk}\right)}{\omega_{sk}} \tag{3.49}$$

Therefore, with reference to (3.49), the computation of the *k*-unit flux amplitude limit λ^{τ}_{sk-max} is implemented as follows:

$$\lambda^{\tau}_{sk-max} = k_{\lambda-\max} \cdot \frac{\sqrt{{v^{\tau}_{sk-\max}}^2 - \left(\tilde{R}_{sk} \cdot i^{\tau}_{sk,d_{sk}}\right)^2} - \tilde{R}_{sk} \cdot i^{\tau}_{sk,q_{sk}} \cdot sign\left(\hat{\omega}_{sk}\right)}{\hat{\omega}_{sk}} \tag{3.50}$$

where $k_{\lambda-\max}$ represents the exploitation degree of the *k*-unit DC-link voltage. This gain must be designed to guarantee a proper voltage margin to the *k*-unit inner controllers, especially when flux-weakening operation is performed. A reasonable value of such gain is 0.9, thus corresponding to 90% utilization of the *k*-unit phase-voltage limit.

With reference to the execution scheme shown in Fig. 3. 12, the *k*-unit flux amplitude reference λ_{sk}^{*} is eventually saturated to the limit (3.50), thus allowing the proper operation of the unit *k* under its voltage constraint (3.46). It is noted how (3.50) allows to implement a straightforward flux-weakening regulation law, without employing any outer voltage controller.

According with both references of *k*-unit flux amplitude λ_{sk}^{*} and *k*-unit torque T_k^{*}, the computation of the *k*-unit torque-producing current reference $i_{sk,q_{sk}}^{*}$ is performed. This operation corresponds with the digital implementation of (3.24) performed as follows:

$$i_{sk,q_{sk}}^{*} = \frac{T_k^{*}}{\frac{3}{2}\cdot p_p \cdot \lambda_{sk}^{*}} \tag{3.51}$$

Nevertheless, (3.51) must be limited according with the *k*-unit maximum phase-current amplitude $I_{max,k}$ and *k*-unit maximum load-angle $\delta_{max,k}$, as shown in Fig. 3. 12.

Torque-producing current limitation

With reference to the execution scheme shown in Fig. 3. 12, the *k*-unit torque-producing current reference $i_{sk,q_{sk}}^{*}$ is subjected to two consecutive limitations, corresponding to the constraints of *k*-unit maximum phase-current amplitude $I_{max,k}$ and *k*-unit maximum load-angle $\delta_{max,k}$.

Concerning the constraint of *k*-unit maximum phase-current amplitude, it leads to the definition of the saturation limit indicated as $i_{sk,q_{sk}-\max i}^{\tau}$ (Fig. 3. 12). According with the d_{sk}-axis current component of the unit *k*, this is computed as follows:

$$i_{sk,q_{sk}-\max i}^{\tau} = \sqrt{{I_{max,k}}^2 - {i_{sk,d_{sk}}^{\tau}}^2} \tag{3.52}$$

The limit (3.52) is applied independently by the sign of the torque-producing current reference. Therefore, it leads to the following saturation law:

$$\left| i_{sk,q_{sk}}^{*} \right| \le i_{sk,q_{sk}-\max i}^{\tau} \tag{3.53}$$

Concerning the constraint of *k*-unit maximum load-angle, the magnetic equation (3.33) is considered. After some mathematical manipulation involving (3.41) and (3.45), this is expressed as follows:

$$\overline{\lambda}_{sk,\alpha\beta} = \overline{\lambda}_{bk,\alpha\beta} + L_k \cdot \overline{i}_{sk,\alpha\beta} \tag{3.54}$$

where:

$$\overline{\lambda}_{bk,\alpha\beta} = k_r \cdot L_{l,r} \cdot \sum_{\substack{z=1 \\ z\neq k}}^{n} \overline{i}_{sz,\alpha\beta} + k_r \cdot \overline{\lambda}_{r,\alpha\beta} \tag{3.55}$$

For convenience, from now on the variable $\overline{\lambda}_{bk,\alpha\beta}$ is named as '*k*-unit base flux vector'. To highlight the relationship between the equation system (3.54)-(3.55) and the *k*-unit load-angle δ_{sk}, the vector diagram is shown in Fig. 3. 13. According with this, after some trigonometric considerations, the following equation is computed:

$$i_{sk,q_{sk}} = \frac{\lambda_{bk}}{L_k} \cdot \sin\left(\delta_{sk} - \vartheta_{\lambda-bk} + \vartheta_{\lambda-r}\right) \tag{3.56}$$

where λ_{bk} and $\vartheta_{\lambda-bk}$ correspond with amplitude and position of the *k*-unit base flux vector respectively. Concerning the position of the *k*-unit base flux vector, this is defined with respect to the stationary α-axis by considering an anticlockwise rotation direction, as shown in Fig. 3. 13.

According with the *k*-unit maximum load-angle $\delta_{max,k}$, (3.56) is subjected to the following constraint:

$$\left|\delta_{sk}\right| \leq \delta_{max,k} \tag{3.57}$$

Therefore, by combining (3.56)-(3.57), the operative limits of the torque producing current reference $i^*_{sk,q_{sk}}$ are computed as follows:

$$-\frac{\lambda_{bk}}{L_k} \cdot \sin\left(\delta_{max,k} + \vartheta_{\lambda-bk} - \vartheta_{\lambda-r}\right) \leq i^*_{sk,q_{sk}} \leq \frac{\lambda_{bk}}{L_k} \cdot \sin\left(\delta_{max,k} - \vartheta_{\lambda-bk} + \vartheta_{\lambda-r}\right) \tag{3.58}$$

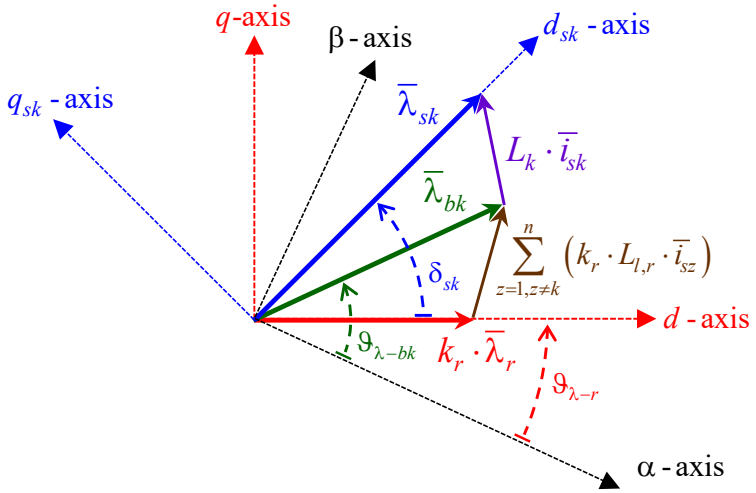

Fig. 3. 13. Vector diagram representing the magnetic model of the generic unit *k*.

As a consequence, it is proposed the digital implementation of (3.58), corresponding to the execution scheme shown in Fig. 3. 14. By means of it, the *k*-unit torque-producing current limits $i^{\tau}_{sk,q_{sk}-\lim\delta}\Big|^{\max}_{\min}$ implementing the *k*-unit load-angle limitation are computed. These limits are then used to implement the saturation of the *k*-unit torque producing current reference $i^{*}_{sk,q_{sk}}$, leading to the computation of its definitive value, as shown in Fig. 3. 12.

It is noted how the *k*-unit load-angle limitation is performed without the use of any external controller [7], leading to a model-based regulation that avoid demanding tuning procedures.

With reference to [19], in balanced operation of the units, the load angle limit that avoid pull-out corresponds with 45 electrical degrees, thus performing the Maximum Torque per Voltage (MTPV) drive operation. However, in the proposed control solution, arbitrary values of the *k*-unit load angle limit can be set, obtaining the highest degree of modularity of the proposed control solution.

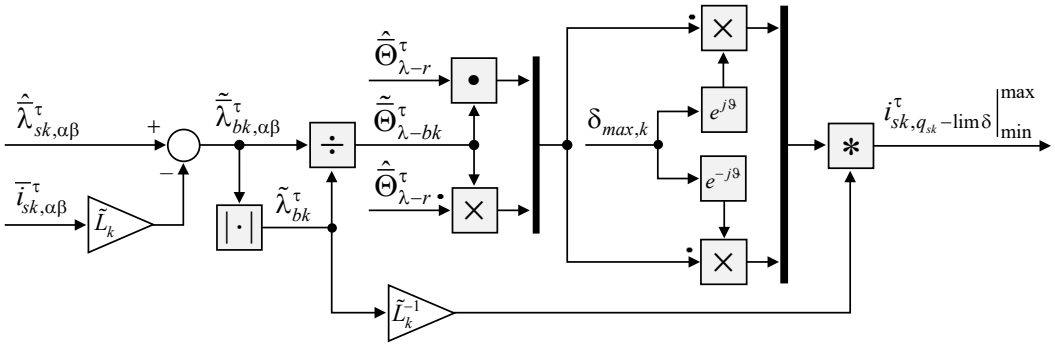

Fig. 3. 14. Execution scheme performing the load angle limitation of the unit *k*.

Once the *k*-unit references in terms of flux amplitude λ^{*}_{sk} and torque producing current $i^{*}_{sk,q_{sk}}$ are computed, the unit control is performed, as shown in Fig. 3. 12.

Unit Control

The unit control corresponds with the regulation of the *k*-unit flux amplitude and the *k*-unit torque-producing current. A regulation type using two PI controllers is considered, as shown in Fig. 3. 15. The first PI controller implements the closed loop regulation of the *k*-unit flux amplitude according with the feedback provided by the *k*-unit flux observer. The second controller implements the closed loop regulation of the *k*-unit torque-producing current according with the feedback provided by the *k*-unit measurements. It follows the analysis and design of both regulation loops. However, to avoid confusion, they are considered separately below.

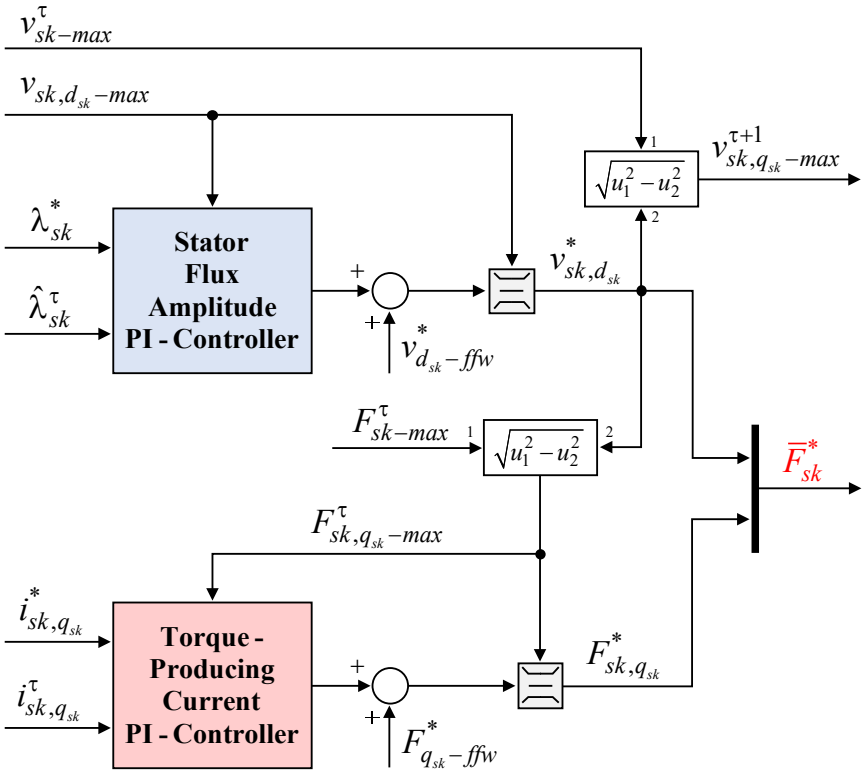

Fig. 3. 15. Execution scheme of the unit control *k* by means of PI controllers.

Design of flux amplitude control loop

The *k*-unit stator electric equation along the d_{sk}-axis (3.22) is considered. For convenience, this is further reported below:

$$v_{sk,d_{sk}} = R_{sk} \cdot i_{sk,d_{sk}} + \frac{d}{dt}\lambda_{sk} \tag{3.59}$$

According with (3.59), the d_{sk}-axis voltage component $v_{sk,d_{sk}}$ of the unit *k* allows the direct regulation of the *k*-unit flux amplitude λ_{sk}. Therefore, by means of the simplified schematic scheme in the Laplace domain shown in Fig. 3. 16, the design of the PI controller implementing the *k*-unit flux amplitude regulation is performed.

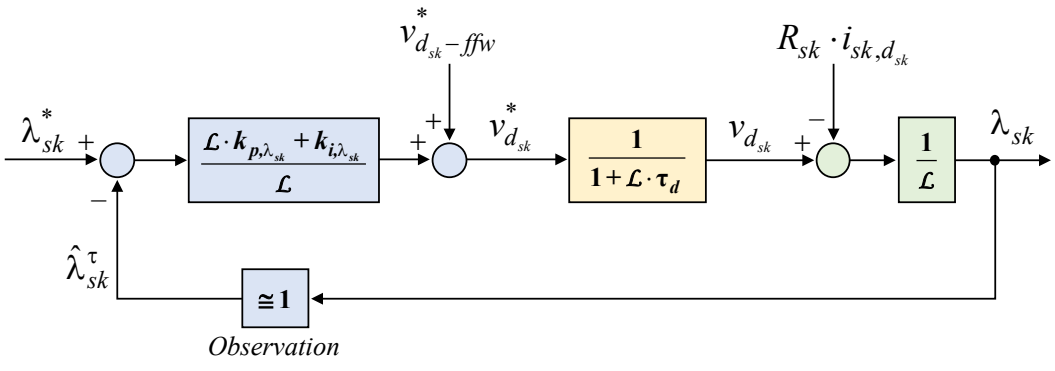

Fig. 3. 16. Schematic block of the *k*-unit flux amplitude regulation loop.

The PI flux controller gains are the proportional gain $k_{p,\lambda sk}$ and the integral gain $k_{i,\lambda sk}$. The effects of both DT voltage errors and parameter detuning are neglected in flux estimation.

Finally, to take in account the execution times of both digital controller and PWM modulator, the VSI unit *k* is modelled as a delay element (yellow block) whose time constant τ_d is defined as follows:

$$\tau_d = 1.5 \cdot T_s \tag{3.60}$$

With reference to Fig. 3. 15 and Fig. 3. 16, the *k*-unit flux amplitude regulation consists of the combination of the flux amplitude PI controller plus a feed-forward compensation $v^*_{d_{sk}-ffw}$ defined as:

$$v^*_{d_{sk}-ffw} = \tilde{R}_{sk} \cdot i^{\tau}_{sk,d_{sk}} \tag{3.61}$$

The feed-forward term (3.61) allows at improving the performance only when the resistive drop is relevant. Otherwise, this compensation results quite useless. Concerning the design of the PI gains, it is considered the open-loop transfer function $H_{\lambda k}(\mathcal{L})$ of the schematic block shown in Fig. 3. 16. This is computed as follows:

$$H_{\lambda k}(\mathcal{L}) = \left(k_{p,\lambda sk} + \frac{k_{i,\lambda sk}}{\mathcal{L}} \right) \cdot \frac{1}{\mathcal{L}} \cdot \frac{1}{1 + \mathcal{L} \cdot \tau_d} \tag{3.62}$$

With reference to (3.62), the asymptotical Bode plot of the open-loop transfer function magnitude is shown in Fig. 3. 17. The Bode frequency (rad/s) is denoted with the symbol ψ.

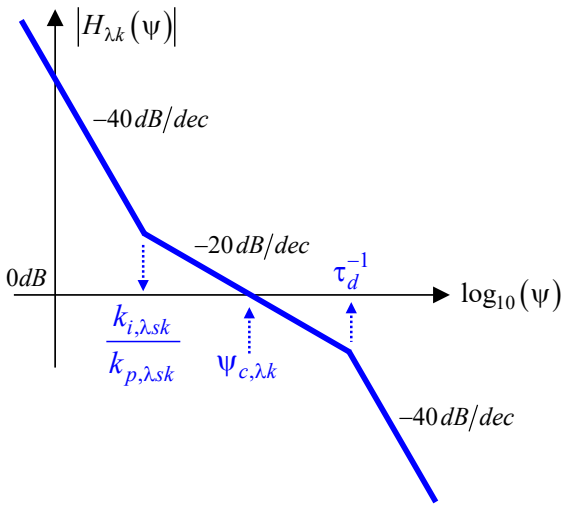

Fig. 3. 17. Asymptotic Bode plot of the open-loop transfer function magnitude for the *k*-unit flux amplitude regulation loop.

By performing the computation of both magnitude and phase belonging to the open-loop transfer function (3.62), the following results are obtained:

$$\begin{cases} \left|H_{\lambda k}\left(\psi\right)\right| = \dfrac{k_{i,\lambda sk}}{\psi^2} \cdot \sqrt{\dfrac{1+\left(\dfrac{\psi \cdot k_{p,\lambda sk}}{k_{i,\lambda sk}}\right)^2}{1+\left(\psi \cdot \tau_d\right)^2}} \\ \angle H_{\lambda k}\left(\psi\right) = -\pi + \arctan\left(\dfrac{\psi \cdot k_{p,\lambda sk}}{k_{i,\lambda sk}}\right) - \arctan\left(\psi \cdot \tau_d\right) \end{cases} \tag{3.63}$$

By computing (3.63) at the cross-over frequency $\psi_{c,\lambda k}$, when the open-loop transfer function exhibits unitary magnitude (0 dB), the following equation system is obtained:

$$\begin{cases} \dfrac{k_{i,\lambda sk}}{\psi_{c,\lambda k}^2} \cdot \sqrt{\dfrac{1+\left(\dfrac{\psi_{c,\lambda k} \cdot k_{p,\lambda sk}}{k_{i,\lambda sk}}\right)^2}{1+\left(\psi_{c,\lambda k} \cdot \tau_d\right)^2}} = 1 \\ \phi_{pm,\lambda k} = \arctan\left(\dfrac{\psi_{c,\lambda k} \cdot k_{p,\lambda sk}}{k_{i,\lambda sk}}\right) - \arctan\left(\psi_{c,\lambda k} \cdot \tau_d\right) \end{cases} \tag{3.64}$$

where $\phi_{pm,\lambda k}$ represents the phase-margin of the *k*-unit flux amplitude regulation loop. Finally, by performing several reasonable approximations, (3.64) is simplified as follows:

$$\begin{cases} k_{p,\lambda sk} \simeq \psi_{c,\lambda k} \\ k_{i,\lambda sk} \simeq \dfrac{\psi_{c,\lambda k}^2}{\tan\left[\phi_{pm,\lambda k} + \arctan\left(\psi_{c,\lambda k} \cdot \tau_d\right)\right]} \\ \phi_{pm,\lambda k} < \dfrac{\pi}{2} - \arctan\left(\psi_{c,\lambda k} \cdot \tau_d\right) \end{cases} \tag{3.65}$$

According with the computation of the closed-loop transfer function, the cross-over frequency results very close to the bandwidth (rad/s) of the *k*-unit flux amplitude loop. Therefore, when the crossover frequency becomes equal to the reciprocal of the VSI time constant τ_d^{-1}, the theoretical limit of the bandwidth is reached, leading to the following result:

$$\psi_{c,\lambda k} \le \tau_d^{-1} \Rightarrow \psi_{c,\lambda k} \le \frac{1}{1.5 \cdot T_s} \Rightarrow \psi_{c,\lambda k} \le \frac{f_s}{1.5} \tag{3.66}$$

where f_s represents the switching/sampling frequency (Hz).

Finally, by combining (3.66) with (3.65), the following equation system is obtained:

$$\begin{cases} k_{p,\lambda sk} \simeq \psi_{c,\lambda k} \\ k_{i,\lambda sk} \simeq \dfrac{\psi_{c,\lambda k}^2}{\tan\left[\phi_{pm,\lambda k} + \arctan\left(\psi_{c,\lambda k} \cdot \tau_d\right)\right]} \\ \phi_{pm,\lambda k} < \dfrac{\pi}{2} - \arctan\left(\psi_{c,\lambda k} \cdot \tau_d\right) \\ \psi_{c,\lambda k} < \tau_d^{-1} \end{cases} \tag{3.67}$$

According with the selected values of bandwidth and phase margin, the design of the PI controller implementing the *k*-unit flux amplitude regulation is performed using (3.67). It is noted how this does not depend on the *k*-unit parameters, nor the *k*-unit operating point.

Concerning the voltage margin of the *k*-unit flux amplitude regulation, this is limited to a predefined value denoted with $v_{d_{sk}-max}$, as shown in Fig. 3. 15. In this way, a useless reduction of the voltage margin for the *k*-unit torque-producing current regulation is avoided. However, the limit $v_{d_{sk}-max}$ must ensure the *k*-unit flux amplitude regulation in all operating conditions.

Finally, the output of the *k*-unit flux amplitude regulation corresponds with the d_{sk}-axis voltage reference $v^*_{sk,d_{sk}}$ of the unit *k*. However, due the execution delay of the digital controller, this is applied in the next sample time instant (τ+1). Therefore, according with (3.46), the maximum value of the q_{sk}-axis voltage reference $v^{\tau+1}_{sk,q_{sk}-max}$ of the unit *k* for the next sample time instant (τ+1) is computed as follows:

$$v^{\tau+1}_{sk,q_{sk}-max} = \sqrt{{v^{\tau}_{sk-max}}^2 - {v^*_{sk,d_{sk}}}^2} \tag{3.68}$$

In conclusion, because (3.59) does not contain any coupling term with the other units, the *k*-unit flux amplitude regulation is performed using the d_{sk}-axis voltage component of the unit *k* directly. Therefore, no decoupling action is required.

Torque-producing current loop design

The *k*-unit torque-producing current corresponds with the q_{sk}-axis current component of the unit *k*. Therefore, if (2.141) is computed in the rotating (d_{sk},q_{sk}) frame then:

$$\left(\sigma_k \cdot L_{sk} + c_k \cdot L_{l,sk}\right) \cdot \frac{d}{dt} \overline{i}_{sk,dq_{sk}} =$$

$$= -\left\{\left[R_r \cdot \frac{k_r}{k_{sk}} + R_{sk} \cdot \left(1 + c_k\right) \right] + j \cdot \left[\omega_{sk} \cdot \left(\sigma_k \cdot L_{sk} + c_k \cdot L_{l,sk}\right) - \omega_r \cdot \sigma_k \cdot L_{sk} \right] \right\} \cdot \overline{i}_{sk,dq_{sk}} + \ldots$$

$$\ldots - \sum_{\substack{z=1 \\ z \neq k}}^{n} \left\{ \left[\left(R_r \cdot k_r - c_z \cdot R_{sk} \right) - j \cdot \left(\omega_r \cdot c_z \cdot L_{l,sz} \right) \right] \cdot \overline{i}_{sz,dq_{sk}} \right\} + \ldots$$

$$\ldots + \left(\frac{1}{\tau_r} - j \cdot \omega_r \right) \cdot \overline{\lambda}_{sk,dq_{sk}} + \left(1 + c_k\right) \cdot \overline{v}_{sk,dq_{sk}} - \sum_{\substack{z=1 \\ z \neq k}}^{n} \left(c_z \cdot \overline{v}_{sz,dq_{sk}} \right)$$

(3.69)

By isolating the q_{sk}-axis component from (3.69), then:

$$\left(\sigma_k \cdot L_{sk} + c_k \cdot L_{l,sk}\right) \cdot \frac{d}{dt} i_{sk,q_{sk}} =$$

$$= -\left\{\left[R_r \cdot \frac{k_r}{k_{sk}} + R_{sk} \cdot \left(1 + c_k\right) \right] \cdot i_{sk,q_{sk}} + \left[\omega_{sk} \cdot \left(\sigma_k \cdot L_{sk} + c_k \cdot L_{l,sk}\right) - \omega_r \cdot \sigma_k \cdot L_{sk} \right] \cdot i_{sk,d_{sk}} \right\} + \ldots$$

$$\ldots - \sum_{\substack{z=1 \\ z \neq k}}^{n} \left[\left(R_r \cdot k_r - c_z \cdot R_{sk} \right) \cdot i_{sz,q_{sk}} - \left(\omega_r \cdot c_z \cdot L_{l,sz} \right) \cdot i_{sz,d_{sk}} \right] + \ldots$$

$$\ldots - \omega_r \cdot \lambda_{sk} + \left(1 + c_k\right) \cdot v_{sk,q_{sk}} - \sum_{\substack{z=1 \\ z \neq k}}^{n} \left(c_z \cdot v_{sz,q_{sk}} \right)$$

(3.70)

To obtain a compact formulation, (3.41) is replaced in (3.70), leading to as follows:

$$\begin{aligned} L_k \cdot \frac{d}{dt} i_{sk,q_{sk}} = -R_k \cdot i_{sk,q_{sk}} - X_{kk} \cdot i_{sk,d_{sk}} - \sum_{\substack{z=1 \\ z \neq k}}^{n} \left[R_z \cdot i_{sz,q_{sk}} + X_z \cdot i_{sz,d_{sk}} \right] + \ldots \\ \ldots - \omega_r \cdot \lambda_{sk} + \left(1 + c_k\right) \cdot v_{sk,q_{sk}} - \sum_{\substack{z=1 \\ z \neq k}}^{n} \left(c_z \cdot v_{sz,q_{sk}} \right) \end{aligned}$$

(3.71)

where:

$$X_{kk} = \omega_{sk} \cdot L_k - \omega_r \cdot \sigma_k \cdot L_{sk}$$

(3.72)

With reference to (3.71), the q_{sk}-axis voltage component $v_{sk,q_{sk}}$ of the unit k allows to perform the regulation of the k-unit torque-producing current $i_{sk,q_{sk}}$. However, according with the MS modelling, there are relevant coupling effects between the units. Both are reported under the summation operator in (3.71). The first coupling effect is in terms of current while the other one in terms of voltage.

Because of the voltage coupling, the k-unit torque-producing current is partially controlled also by the regulators belonging the other units. For this reason, the output of the k-unit torque-producing current regulator must not be considered as q_{sk}-axis voltage reference of the unit k. Otherwise, this would lead to relevant conflicts with the torque-producing current regulations performed in the other units, causing the instability of the machine control scheme [20].

With the aim at solving this issue, it is proposed to consider the output of each torque-producing current regulator as combination of the voltage references belonging to all n units. Therefore, according with (3.71), the k-unit torque-producing current regulator output is defined as follows:

$$F_{sk,q_{sk}} = \left(1+c_k\right)\cdot v_{sk,q_{sk}} - \sum_{\substack{z=1 \\ z\neq k}}^{n}\left(c_z \cdot v_{sz,q_{sk}}\right) \tag{3.73}$$

As a consequence, (3.73) is replaced in (3.71), leading to the following result:

$$\begin{aligned} L_k \cdot \frac{d}{dt} i_{sk,q_{sk}} = &-R_k \cdot i_{sk,q_{sk}} - X_{kk} \cdot i_{sk,d_{sk}} - \sum_{\substack{z=1 \\ z\neq k}}^{n}\left[R_z \cdot i_{sz,q_{sk}} + X_z \cdot i_{sz,d_{sk}} \right] + \ldots \\ &\ldots - \omega_r \cdot \lambda_{sk} + F_{sk,q_{sk}} \end{aligned} \tag{3.74}$$

To obtain a compact formulation, the following variable is defined:

$$f_{q_{sk}} = X_{kk} \cdot i_{sk,d_{sk}} + \sum_{\substack{z=1 \\ z\neq k}}^{n}\left[R_z \cdot i_{sz,q_{sk}} + X_z \cdot i_{sz,d_{sk}} \right] + \omega_r \cdot \lambda_{sk} \tag{3.75}$$

Finally, by replacing (3.75) in (3.74), it is obtained as follows:

$$L_k \cdot \frac{d}{dt} i_{sk,q_{sk}} = -R_k \cdot i_{sk,q_{sk}} - f_{q_{sk}} + F_{sk,q_{sk}} \tag{3.76}$$

Therefore, by means of the simplified schematic scheme shown in Fig. 3. 18, the design of the PI controller implementing the k-unit torque-producing current regulation is performed. With reference to it, the Equation (3.76) is modelled using the green blocks. Conversely, the red blocks implement the k-unit torque-producing current regulation. It is noted how the PI torque-producing current controller is modelled by means of the conventional proportional $k_{p,iq_{sk}}$ and integral $k_{i,iq_{sk}}$ gains. Concerning the k-unit torque-producing current measurement process, this is considered ideal.

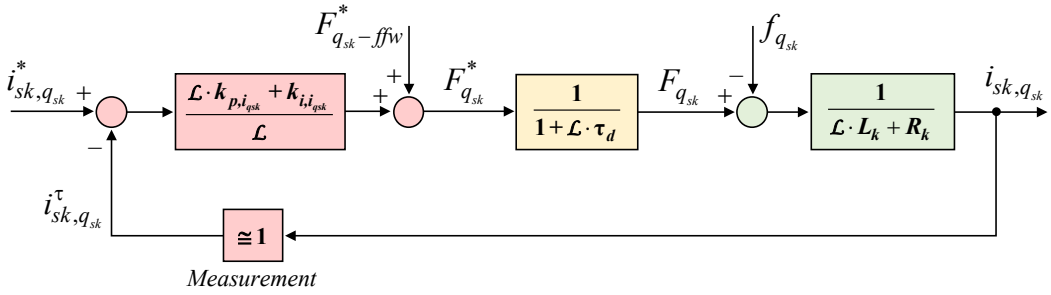

Fig. 3. 18. Schematic block of the *k*-unit torque-producing current regulation loop.

According with (3.76), the yellow block is representative of the all VSI units. However, the transfer function defined for a single one (3.60) can still be considered valid.

With reference to Fig. 3. 15 and Fig. 3. 18, the *k*-unit torque-producing current regulation consists of the combination of the torque-producing current PI regulator plus a feed-forward compensation $F^*_{q_{sk}-ffw}$. According with (3.75), the last should be computed as follows:

$$F^*_{q_{sk}-ffw} = \tilde{X}^{\tau}_{kk}\cdot i^{\tau}_{sk,d_{sk}} + \sum_{\substack{z=1\\ z\neq k}}^{n}\left[\tilde{R}^{\tau}_{z}\cdot i^{\tau}_{sz,q_{sk}} + \tilde{X}^{\tau}_{z}\cdot i^{\tau}_{sz,d_{sk}}\right] + \omega^{\tau}_{r}\cdot\hat{\lambda}^{\tau}_{sk} \tag{3.77}$$

It is noted how (3.77) needs the (d_{sk},q_{sk}) components of the current vectors belonging to the other (n-1)-units, thus requiring high computational efforts of the dedicated digital controller. Indeed, this operation must be performed for the torque-producing current regulations belonging to all n-units, thus leading to the implementation of (n-1)^2 additional rotational transformations. However, in the case of balanced operation of the machine, (3.77) is drastically simplified as follows:

$$F^*_{q_{sk}-ffw} = \tilde{X}^{\tau}_{kk}\cdot i^{\tau}_{sk,d_{sk}} + \sum_{\substack{z=1\\ z\neq k}}^{n}\left[\tilde{R}^{\tau}_{z}\cdot i^{\tau}_{sz,q_{sz}} + \tilde{X}^{\tau}_{z}\cdot i^{\tau}_{sz,d_{sz}}\right] + \omega^{\tau}_{r}\cdot\hat{\lambda}^{\tau}_{sk} \tag{3.78}$$

Compared to (3.77), (3.78) needs the (d_{sz},q_{sz}) components of the current vectors belonging to the other (n-1)-units. Nevertheless, according with the control structure shown in Fig. 3. 12, these are already computed in the DFVC schemes of the other units. Therefore, no additional rotational transformations are required. Nevertheless, by accepting a slight performance drop of the *k*-unit torque producing current regulation, (3.77) can be further simplified as follows:

$$F^*_{q_{sk}-ffw} = \tilde{X}^{\tau}_{kk}\cdot i^{\tau}_{sk,d_{sk}} + \omega^{\tau}_{r}\cdot\hat{\lambda}^{\tau}_{sk} \tag{3.79}$$

Compared to (3.77), (3.79) corresponds with the simple compensation of the *k*-unit back-emf contribution plus the cross term related to the d_{sk}-axis current component of the unit *k*, thus neglecting the coupling effects in terms of current.

However, this operation does not imply any instability in the *k*-unit torque-producing current regulation. Indeed, because each three-phase winding set is fed by a VSI, the coupling effects among the units in terms of current must be considered as simple additive disturbance in the *k*-unit torque-producing current regulation. Therefore, its compensation is not mandatory.

Concerning the design of the PI gains, it is considered the open-loop transfer function $H_{ik}(\mathcal{L})$ of the schematic block shown in Fig. 3. 18. This is computed as follows:

$$H_{ik}(\mathcal{L}) = \left(k_{p,i_{qsk}} + \frac{k_{i,i_{qsk}}}{\mathcal{L}} \right) \cdot \frac{1}{1+\mathcal{L}\cdot\tau_d} \cdot \frac{1}{R_k + \mathcal{L}\cdot L_k} \tag{3.80}$$

The design of the torque-producing current PI regulator can be performed in many ways. In this case, the pole-zero cancellation method is proposed, corresponding into making coincident the PI's zero with the *k*-unit pole. In terms of mathematical formulation, this operation is expressed as follows:

$$\frac{k_{i,i_{qsk}}}{k_{p,i_{qsk}}} = \frac{R_k}{L_k} \tag{3.81}$$

By replacing (3.80) in (3.81), the open-loop transfer function is simplified as follows:

$$H_{ik}(\mathcal{L}) = \frac{k_{p,i_{qsk}}}{L_k} \cdot \frac{1}{1+\mathcal{L}\cdot\tau_d} \cdot \frac{1}{\mathcal{L}} \tag{3.82}$$

With reference to (3.82), the asymptotical Bode plot of the open-loop transfer function magnitude is shown in Fig. 3. 19.

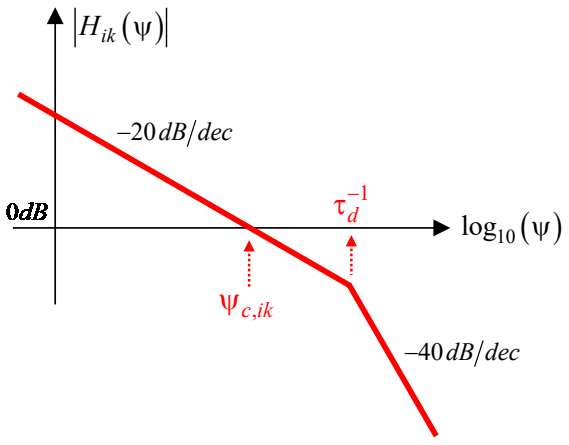

Fig. 3. 19. Asymptotic Bode plot of the open-loop transfer function magnitude for the *k*-unit torque-producing current regulation loop.

By performing the computation of both magnitude and phase belonging to the open-loop transfer function (3.82), the following results are obtained:

$$\begin{cases} \left|H_{ik}\left(\psi\right)\right| = \dfrac{k_{p,i_{qsk}}}{L_k} \cdot \dfrac{1}{\psi} \cdot \sqrt{\dfrac{1}{1+\left(\psi \cdot \tau_d\right)^2}} \\ \angle H_{ik}\left(\psi\right) = -\dfrac{\pi}{2} - \arctan\left(\psi \cdot \tau_d\right) \end{cases} \tag{3.83}$$

By computing (3.83) at the cross-over frequency $\psi_{c,ik}$, corresponding to the condition in which the open-loop transfer function exhibits unitary magnitude (0 dB), the following equation system is obtained:

$$\begin{cases} \dfrac{k_{p,i_{qsk}}}{L_k} \cdot \dfrac{1}{\psi_{c,ik}} \cdot \sqrt{\dfrac{1}{1+\left(\psi_{c,ik} \cdot \tau_d\right)^2}} = 1 \\ \phi_{pm,ik} = \dfrac{\pi}{2} - \arctan\left(\psi_{c,ik} \cdot \tau_d\right) \end{cases} \tag{3.84}$$

where $\phi_{pm,ik}$ represents the phase-margin of the *k*-unit torque-producing current regulation loop. Finally, by performing several reasonable approximations, (3.84) is simplified as follows:

$$\begin{cases} k_{p,i_{qsk}} \simeq \psi_{c,ik} \cdot L_k \\ \phi_{pm,ik} = \dfrac{\pi}{2} - \arctan\left(\psi_{c,ik} \cdot \tau_d\right) \end{cases} \tag{3.85}$$

Because of the initial condition (3.81), it is noted how (3.85) does not allow the setting of both phase-margin and cross-over frequency, thus making necessary to perform a trade-off choice among the desired values of these. Therefore, in case the phase-margin is chosen as main variable, by combining (3.81) and (3.85), it is obtained as follows:

$$\begin{cases} k_{p,i_{qsk}} \simeq \dfrac{L_k}{\tau_d \cdot \tan\left(\phi_{pm,ik}\right)} \\ k_{i,i_{qsk}} \simeq \dfrac{R_k}{\tau_d \cdot \tan\left(\phi_{pm,ik}\right)} \end{cases} \tag{3.86}$$

Conversely, by choosing the cross-over frequency as main variable, the combination of (3.81) and (3.85) leads to as follows:

$$\begin{cases} k_{p,i_{qsk}} \simeq \psi_{c,ik} \cdot L_k \\ k_{i,i_{qsk}} \simeq \psi_{c,ik} \cdot R_k \end{cases} \tag{3.87}$$

According with the computation of the closed-loop transfer function, the cross-over frequency results very close to the bandwidth (rad/s) of the *k*-unit torque-producing current regulation loop. Therefore, when the crossover frequency becomes equal to the reciprocal of the VSI time constant τ_d^{-1}, the theoretical limit of the bandwidth is reached, leading to the following result:

$$\psi_{c,ik} \leq \tau_d^{-1} \Rightarrow \psi_{c,ik} \leq \frac{1}{1.5 \cdot T_s} \Rightarrow \psi_{c,ik} \leq \frac{f_s}{1.5} \tag{3.88}$$

By replacing (3.88) in (3.85), the phase-margin limit condition is computed as follows:

$$\frac{\pi}{4} \leq \phi_{pm,ik} < \frac{\pi}{2} \tag{3.89}$$

Therefore, by replacing (3.89) in (3.86), the following equation system is obtained:

$$\begin{cases} k_{p,i_{qsk}} \simeq \dfrac{L_k}{\tau_d \cdot \tan\left(\phi_{pm,ik}\right)} \\ k_{i,i_{qsk}} \simeq \dfrac{R_k}{\tau_d \cdot \tan\left(\phi_{pm,ik}\right)} \\ \dfrac{\pi}{4} \leq \phi_{pm,ik} < \dfrac{\pi}{2} \end{cases} \tag{3.90}$$

By replacing (3.88) in (3.87), the following equation system is obtained:

$$\begin{cases} k_{p,i_{qsk}} \simeq \psi_{c,ik} \cdot L_k \\ k_{i,i_{qsk}} \simeq \psi_{c,ik} \cdot R_k \\ \psi_{c,ik} \leq \tau_d^{-1} \end{cases} \tag{3.91}$$

With reference to (3.90) and (3.91), according with the trade-off choice among the desired values of bandwidth and phase margin, the design of the PI controller implementing the *k*-unit torque-producing current is performed. Compared to the *k*-unit flux amplitude regulation, it is noted how the one for the *k*-unit torque-producing current strictly depends by the *k*-unit parameters.

Finally, with reference to Fig. 3. 15, the voltage margin of the *k*-unit torque-producing current regulation $F_{sk,q_{sk}-max}^{\tau}$ is computed as follows:

$$F_{sk,q_{sk}-max}^{\tau} = \sqrt{{F_{sk-max}^{\tau}}^2 - {v_{sk,d_{sk}}^*}^2} \tag{3.92}$$

where F_{sk-max}^{τ} corresponds with the voltage limit of the unit control *k*. This value must be defined to ensure the *k*-unit torque-producing current regulation in all operating conditions. However, as the output of the *k*-unit torque-producing current

regulation $F^{*}_{sk,q_{sk}}$ corresponds with the definition given in (3.73), F^{τ}_{sk-max} must be defined according with the implemented torque-sharing strategies. However, in the case of balanced operation of the machine, F^{τ}_{sk-max} can be set equal to the *k*-unit phase-voltage limit v^{τ}_{sk-max}, leading to as follows:

$$F^{\tau}_{sk,q_{sk}-max} = \sqrt{{v^{\tau}_{sk-max}}^{2} - {v^{*}_{sk,d_{sk}}}^{2}} \tag{3.93}$$

In conclusion, due to the voltage coupling among the units, the *k*-unit torque-producing current regulation cannot be performed using the q_{sk}-axis voltage component of the unit *k* directly. Therefore, according with (3.73), the *k*-unit torque-producing current regulator output must consist in a linear combination of the q_{sk}-axis voltage references belonging to all units. As consequence, with the aim at extrapolating the q_{sk}-axis voltage reference of the unit *k*, a decoupling action must be implemented.

DFVC structure using DB controllers

With reference to Fig. 3. 20, the structure of the *k*-unit DB-DFVC scheme is similar to that using the PI controllers (Fig. 3. 12). Indeed, because in this case a DB-regulation is performed, the main difference among the two structures consists of the definition of the unit control block.

Because the *k*-unit DB-DFVC scheme performs a predictive regulation of *k*-unit flux amplitude and *k*-unit torque producing current, the computation of the predicted *k*-unit current vector in the rotating (d_{sk},q_{sk}) frame $\tilde{\tilde{i}}^{\tau+1}_{sk,dq_{sk}}$ is performed. Therefore, by using the trigonometric coordinates of the predicted *k*-unit flux vector $\hat{\bar{\Theta}}^{\tau+1}_{\lambda-sk}$, the rotational transformation (2.105) on the predicted *k*-unit current vector defined in the stationary (α,β) frame $\tilde{\tilde{i}}^{\tau+1}_{sk,\alpha\beta}$ is implemented (Fig. 3. 20).

Concerning the predicted *k*-unit flux amplitude $\hat{\lambda}^{\tau+1}_{sk}$, this is provided by the *k*-unit flux observer, as shown in Fig. 3. 9.

Unit Control

According with the DB approach [15], [16], the *k*-unit control corresponds with the predictive regulation of *k*-unit flux amplitude and *k*-unit torque-producing current. However, compared to a Model Predictive Control (MPC) scheme, no cost function is implemented. Indeed, with the aim computing the *k*-unit control outputs, the *k*-unit DB regulation uses the discrete *k*-unit electromagnetic equations, leading the execution scheme shown in Fig. 3. 21.

For the sake of clarity, it follows a brief description of the DB regulation.

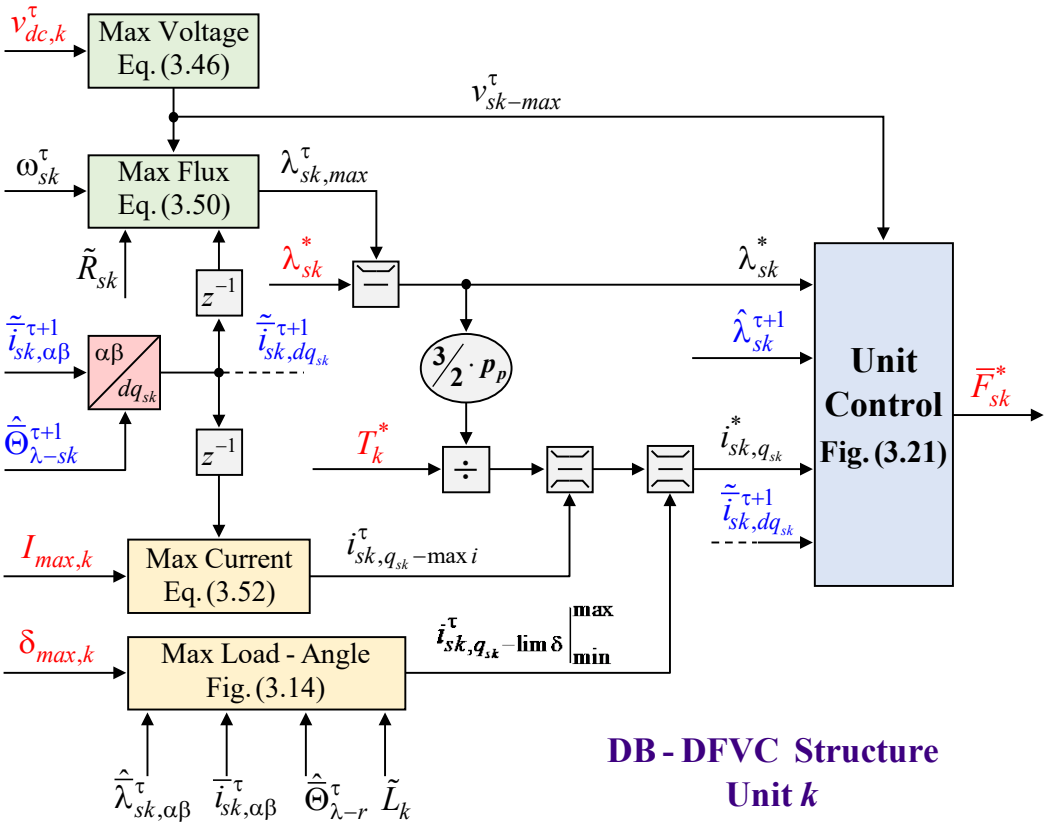

Fig. 3. 20. DB-DFVC structure for the control of the generic unit *k*.

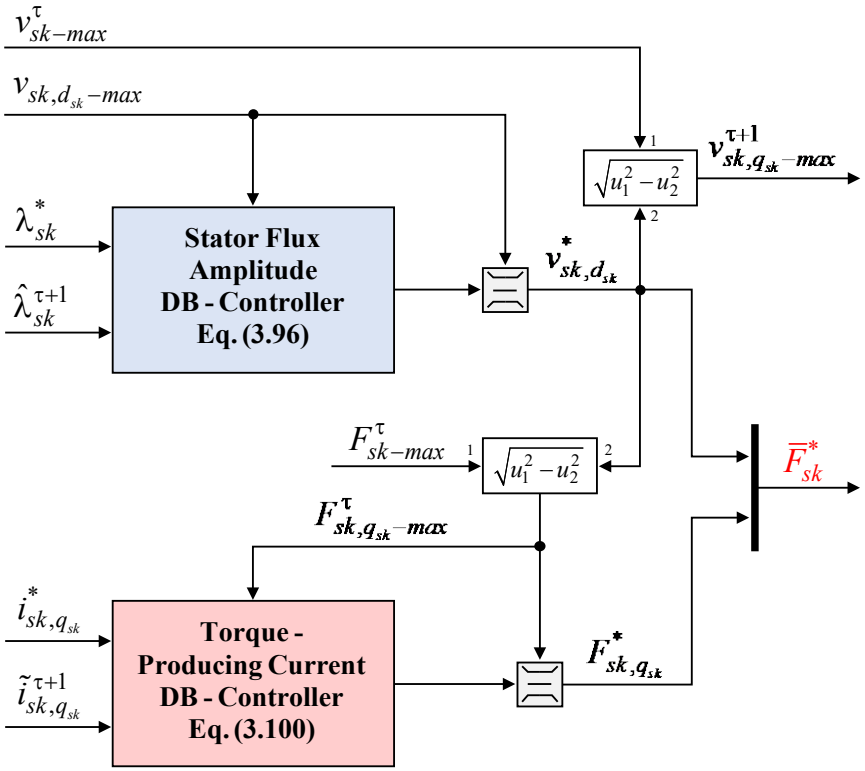

Fig. 3. 21. Execution scheme of the unit control *k* by means of DB controllers.

Because of the digital controller execution delay, the *k*-unit control outputs are applied in the sample time instant (τ+1), thus defining the values of the *k*-unit state variables for the next step (τ+2). As a consequence, by considering the backward-Euler discretization of each *k*-unit state equation [17], it is possible to assert as follows:

$$x_k^{\tau+2} = x_k^{\tau+1} + T_s \cdot f_k^{\tau+1} \tag{3.94}$$

where x_k represents the generic *k*-unit state variable whose dynamic evolution is established by the generic *k*-unit forcing term f_k.

Therefore, with the aim at setting the value of the generic *k*-unit state variable to a reference target x_k^*, (3.94) must be inverted as follows:

$$f_k^{\tau+1} = \frac{x_k^* - x_k^{\tau+1}}{T_s} \tag{3.95}$$

The application of (3.95) corresponds into implementing a DB regulation of the generic *k*-unit state variable. As a consequence, with reference to the *k*-unit control scheme shown in Fig. 3. 21, both regulations of *k*-unit flux amplitude and *k*-unit torque-producing current correspond to the implementation of (3.95) on their respective control equations. However, to avoid confusion, they are considered separately below.

Deadbeat regulation of stator flux amplitude

The *k*-unit stator electric equation along the d_{sk}-axis is considered. Therefore, the application of (3.94) on (3.59) leads to as follows:

$$v_{sk,d_{sk}}^* = \tilde{R}_{sk} \cdot \tilde{i}_{sk,d_{sk}}^{\tau+1} + \frac{\lambda_{sk}^* - \hat{\lambda}_{sk}}{T_s} \tag{3.96}$$

With reference to (3.96), the DB regulation of the *k*-unit flux amplitude results quite simple and robust, especially in the high-speed range of the machine. In these operating conditions, the *k*-unit flux observer allows at obtaining an accurate prediction of the *k*-unit flux amplitude, thus leading to high regulation performance of (3.96).

As regards the estimation error on the predicted value of d_{sk}-axis resistive voltage drop, this has negligible effects on the *k*-unit flux amplitude regulation, especially in case of the *k*-unit stator resistance exhibits a low value.

Like for the PI-DFVC scheme, the voltage margin of the *k*-unit flux amplitude regulation is limited to the predefined value $v_{sk,d_{sk}-max}$, thus leading to the same considerations (Fig. 3. 21).

Finally, with reference to the execution scheme shown in Fig. 3. 21, the maximum value of the q_{sk}-axis voltage reference $v_{sk,q_{sk}-max}^{\tau+1}$ of the unit k for the next sample time instant (τ+1) is computed as in (3.68).

In conclusion, the regulation of the k-unit flux amplitude using a DB controller is quite similar to one defined for the PI-DFVC scheme. The only difference is related to d_{sk}-axis voltage reference computation, which is performed by means of a predictive algorithm, thus without using any PI regulator.

Deadbeat regulation of torque-producing current

Like for the PI-DFVC scheme, the output of the k-unit torque-producing current regulation must be defined as (3.73), thus leading to the same considerations. Therefore, the application of (3.94) on (3.76) is considered, leading to as follows:

$$F_{sk,q_{sk}}^{*} = \tilde{R}_k \cdot \tilde{i}_{sk,q_{sk}}^{\tau+1} + \tilde{L}_k \cdot \frac{i_{sk,q_{sk}}^{*} - \tilde{i}_{sk,q_{sk}}^{\tau+1}}{T_s} + \tilde{f}_{q_{sk}}^{\tau+1} \tag{3.97}$$

where:

$$\tilde{f}_{q_{sk}}^{\tau+1} = \tilde{X}_{kk}^{\tau} \cdot \tilde{i}_{sk,d_{sk}}^{\tau+1} + \sum_{\substack{z=1 \\ z\neq k}}^{n} \left[\tilde{R}_z^{\tau} \cdot \tilde{i}_{sz,q_{sk}}^{\tau+1} + \tilde{X}_z^{\tau} \cdot \tilde{i}_{sz,d_{sk}}^{\tau+1} \right] + \omega_r^{\tau} \cdot \hat{\lambda}_{sk}^{\tau+1} \tag{3.98}$$

Similar to (3.77), the Equation (3.98) needs the predicted (d_{sk},q_{sk}) components of the current vectors belonging to the other (n-1)-units, thus requiring high computational efforts of the dedicated digital controller. Indeed, this operation must be performed for the torque-producing current regulations belonging to all n-units, thus leading to the implementation of (n-1)^2 additional rotational transformations. However, in the case of balanced operation of the machine, (3.98) is drastically simplified as follows:

$$\tilde{f}_{q_{sk}}^{\tau+1} = \tilde{X}_{kk}^{\tau} \cdot \tilde{i}_{sk,d_{sk}}^{\tau+1} + \sum_{\substack{z=1 \\ z\neq k}}^{n} \left[\tilde{R}_z^{\tau} \cdot \tilde{i}_{sz,q_{sz}}^{\tau+1} + \tilde{X}_z^{\tau} \cdot \tilde{i}_{sz,d_{sz}}^{\tau+1} \right] + \omega_r^{\tau} \cdot \hat{\lambda}_{sk}^{\tau+1} \tag{3.99}$$

Compared to (3.98), (3.99) needs the predicted (d_{sz},q_{sz}) components of the current vectors belonging to the other (n-1)-units. Nevertheless, according with the control structure shown in Fig. 3. 20, these are already computed in the DB-DFVC schemes of the other units, thus without requiring additional rotational transformations.

In any case, with reference to (3.97), it is noted how the k-unit torque-producing current regulation could be characterized by steady state permanent error. The main causes are the employed discretization method and the machine parameters detuning. Concerning the backward-Euler discretization, it loses its accuracy when the ratio between the sampling frequency and the fundamental electrical frequency of the machine becomes too low (< 20).

With the aim at solving this issue, the proposed implementation of the *k*-unit torque-producing current regulation is:

$$F^*_{sk,q_{sk}} = \tilde{R}_k \cdot \tilde{i}^{\tau+1}_{sk,q_{sk}} + \tilde{L}_k \cdot \frac{i^*_{sk,q_{sk}} - \tilde{i}^{\tau+1}_{sk,q_{sk}}}{T_s} + \tilde{f}^{\tau+1}_{q_{sk}} + f^{\tau}_{comp} \tag{3.100}$$

where:

$$f^{\tau}_{comp} = f^{\tau-1}_{comp} + T_s \cdot k_{comp} \cdot \left(i^*_{sk,q_{sk}} - i^{\tau}_{sk,q_{sk}} \right) \tag{3.101}$$

It is noted how (3.101) represents an integral regulation of the *k*-unit torque-producing current. Nevertheless, this must be designed just to compensate the inaccuracy of (3.97). As a consequence, the steady state permanent error converges to zero with a dynamic related to both integral gain value k_{comp} and allocated voltage margin for the integral regulation (a good compromise is 5÷10% of the *k*-unit phase voltage limit v^{τ}_{sk-max}). It is necessary to highlight how the integral compensation (3.101) does not affect the dynamic behaviour of the *k*-unit torque-producing current regulation but only the steady state operation.

Finally, like for the PI-DFVC scheme, the voltage margin of the *k*-unit torque-producing current regulation is limited by the value $F^{\tau}_{sk,q_{sk}-max}$ (Fig. 3. 20), thus leading to the same considerations.

In conclusion, the regulation of the *k*-unit torque-producing current using a DB controller is quite similar to one defined for the PI-DFVC scheme. The only difference consists of the output computation which is performed by means of a predictive algorithm. However, with the aim at compensating the inaccuracy of this last one, a slight integral compensation action must be implemented.

3.4.5 Decoupling Algorithm

Regardless of the regulation type performed in the *k*-unit DVFC scheme, the outputs of this correspond to as follows:

- d_{sk}-axis reference voltage of the unit *k*: $v^*_{sk,d_{sk}}$
- q_{sk}-axis reference voltages combination belonging to the all units: $F^*_{sk,q_{sk}}$

With reference to the figures of this chapter, for the generic unit *k* this couple of values is merged in a single vector indicated as $\overline{F}^*_{sk}$.

Therefore, with the aim at extrapolating the q_{sk}-axis reference voltage of the unit *k*, a decoupling algorithm must be implemented. In this way, both (d_{sk},q_{sk}) reference components of the *k*-unit voltage vector are obtained, thus allowing their elaboration in order to compute the duty-cycle commands of the VSI unit *k*, as shown in Fig. 3. 22.

It follows the mathematical description of the decoupling algorithm.

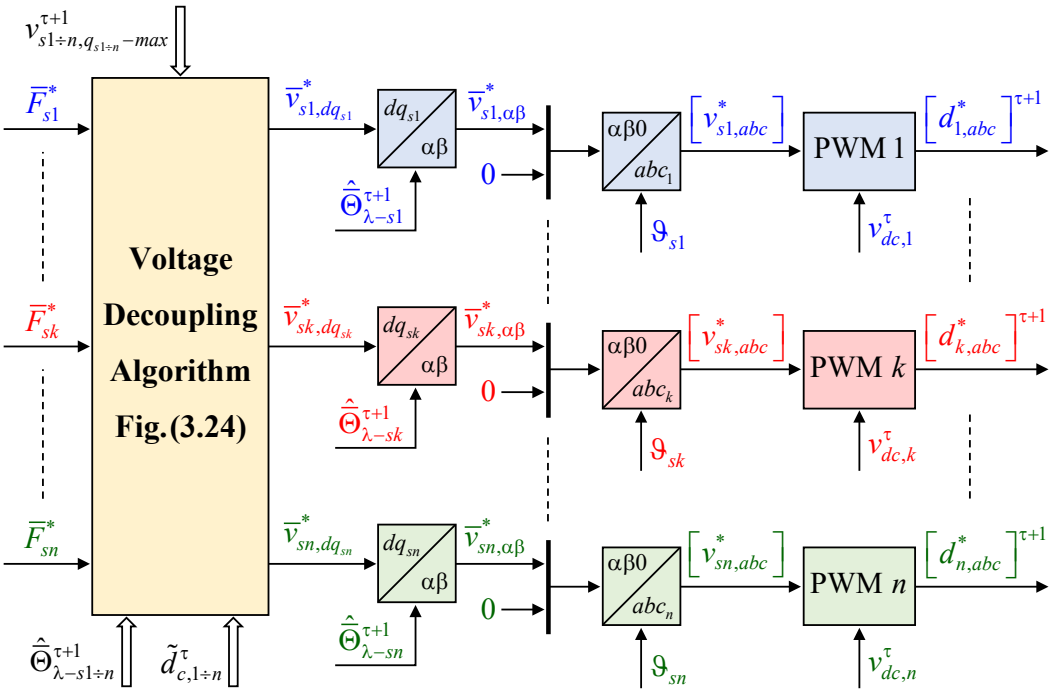

Fig. 3. 22. Execution scheme for the computation of the duty-cycles belonging the all VSI units.

With reference to (3.73), the output of each *k*-unit torque-producing current regulation is defined as follows:

$$F^*_{sk,q_{sk}} = \left(1+\tilde{c}_k\right)\cdot v^*_{sk,q_{sk}} - \sum_{\substack{z=1 \\ z\neq k}}^{n}\left(\tilde{c}_z \cdot v^*_{sz,q_{sk}}\right) \tag{3.102}$$

where:

- $v^*_{sk,q_{sk}}$ represents the reference *k*-unit voltage vector defined in the *k*-unit rotating (d_{sk},q_{sk}) frame;
- $v^*_{sz,q_{sk}}$ represents the reference *z*-unit voltage vector defined in the *k*-unit rotating (d_{sk},q_{sk}) frame.

To highlight the relationship between the *k*-unit rotating (d_{sk},q_{sk}) frame and the *z*-unit rotating (d_{sz},q_{sz}) frame, the vector diagram is shown in Fig. 3. 23. According with this, after some trigonometric considerations, the following equation system is computed:

$$\begin{cases} v_{sz,d_{sk}} = \cos\left(\delta_{sz}-\delta_{sk}\right)\cdot v_{sz,d_{sz}} - \sin\left(\delta_{sz}-\delta_{sk}\right)\cdot v_{sz,q_{sz}} \\ v_{sz,q_{sk}} = \sin\left(\delta_{sz}-\delta_{sk}\right)\cdot v_{sz,d_{sz}} + \cos\left(\delta_{sz}-\delta_{sk}\right)\cdot v_{sz,q_{sz}} \end{cases} \tag{3.103}$$

According with (3.103), each single unit DFVC scheme is implemented in the own rotating stator flux frame. Therefore, the angular difference among two generic rotating frames corresponds with the load-angles difference belonging to the considered units.

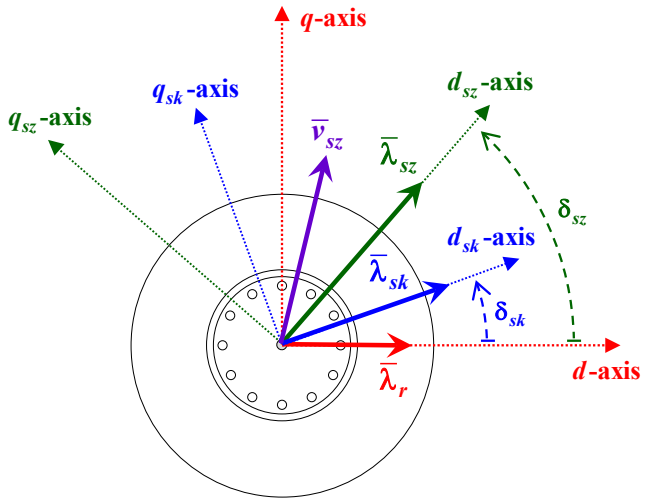

Fig. 3. 23. Vector diagram representing the relationship between the *k*-unit rotating (d_{sk},q_{sk}) frame and *z*-unit rotating (d_{sz},q_{sz}) frame.

By considering the second equation of (3.103), the following result is extrapolated:

$$v^*_{sz,q_{sk}} = \sin\left(\delta^{\tau+1}_{sz} - \delta^{\tau+1}_{sk}\right)\cdot v^*_{sz,d_{sz}} + \cos\left(\delta^{\tau+1}_{sz} - \delta^{\tau+1}_{sk}\right)\cdot v^*_{sz,q_{sz}} \tag{3.104}$$

With reference to (3.104), the angular difference between the predicted load-angles values is considered. Because of the digital controller execution delay, the reference voltages computed in the current sample instant (τ) are applied in the next step (τ+1), thus justifying this choice.

By replacing (3.104) in (3.102), the following *k*-unit equation is obtained:

$$\begin{aligned} F^*_{sk,q_{sk}} &= \left(1+\tilde{c}_k\right)\cdot v^*_{sk,q_{sk}} - \sum_{\substack{z=1\\ z\neq k}}^{n}\left[\tilde{c}_z\cdot v^*_{sz,d_{sz}}\cdot\sin\left(\hat{\delta}^{\tau+1}_{sz} - \hat{\delta}^{\tau+1}_{sk}\right)\right] + \ldots \\ &\ldots - \sum_{\substack{z=1\\ z\neq k}}^{n}\left[\tilde{c}_z\cdot v^*_{sz,q_{sz}}\cdot\cos\left(\hat{\delta}^{\tau+1}_{sz} - \hat{\delta}^{\tau+1}_{sk}\right)\right] \end{aligned} \tag{3.105}$$

Compared to (3.102), it is noted how (3.105) allows at highlighting the q_{sz}-axis reference voltage of the generic unit *z*, thus representing one of the decoupling algorithm results. Concerning the d_{sz}-axis voltage component of the generic unit *z*, this value is provided by the *z*-unit flux amplitude regulation directly, as shown in Fig. 3. 15 and Fig. 3. 21. Therefore, to obtain a compact formulation of the next equations, the already known voltage terms are combined follows:

$$C^*_{sk,q_{sk}} = F^*_{sk,q_{sk}} + \sum_{\substack{z=1\\ z\neq k}}^{n}\left[\tilde{c}_z\cdot v^*_{sz,d_{sz}}\cdot\sin\left(\hat{\delta}^{\tau+1}_{sz} - \hat{\delta}^{\tau+1}_{sk}\right)\right] \tag{3.106}$$

Finally, by replacing (3.106) in (3.105), the output of each *k*-unit torque-producing current regulation is expressed as follows:

$$C^*_{sk,q_{sk}} = \left(1+\tilde{c}_k\right)\cdot v^*_{sk,q_{sk}} - \sum_{\substack{z=1\\ z\neq k}}^{n}\left[\tilde{c}_z \cdot v^*_{sz,q_{sz}} \cdot \cos\left(\hat{\delta}^{\tau+1}_{sz} - \hat{\delta}^{\tau+1}_{sk}\right)\right] \tag{3.107}$$

To avoid any confusion, the following notation change of (3.45) is introduced:

$$\tilde{d}^{\tau}_{c,z} = \tilde{c}_z = \frac{\tilde{L}_{l,r}\cdot\tilde{k}_r}{\tilde{L}_{l,sz}}\cdot x^{\tau}_{f,k} \quad , \quad \tilde{c}_k = \sum_{\substack{z=1\\ z\neq k}}^{n}\tilde{c}_z = \sum_{\substack{z=1\\ z\neq k}}^{n}\tilde{d}^{\tau}_{c,z} \tag{3.108}$$

Therefore, by using (3.108), (3.107) is formally changed as follows:

$$C^*_{sk,q_{sk}} = \left(1+\sum_{\substack{z=1\\ z\neq k}}^{n}\tilde{d}^{\tau}_{c,z}\right)\cdot v^*_{sk,q_{sk}} - \sum_{\substack{z=1\\ z\neq k}}^{n}\left[\tilde{d}^{\tau}_{c,z} \cdot v^*_{sz,q_{sz}} \cdot \cos\left(\hat{\delta}^{\tau+1}_{sz} - \hat{\delta}^{\tau+1}_{sk}\right)\right] \tag{3.109}$$

By merging (3.109) for all units k=1,2,…,n, the following equation system is obtained:

$$\begin{bmatrix} C^*_{s1,q_{s1}} \\ \dots \\ C^*_{sk,q_{sk}} \\ \dots \\ C^*_{sn,q_{sn}} \end{bmatrix} = \begin{bmatrix} m^{\tau+1}_{(1,1)} & \dots & m^{\tau+1}_{(1,k)} & \dots & m^{\tau+1}_{(1,n)} \\ \dots & \dots & \dots & \dots & \dots \\ m^{\tau+1}_{(k,1)} & \dots & m^{\tau+1}_{(k,k)} & \dots & m^{\tau+1}_{(k,n)} \\ \dots & \dots & \dots & \dots & \dots \\ m^{\tau+1}_{(n,1)} & \dots & m^{\tau+1}_{(n,k)} & \dots & m^{\tau+1}_{(n,n)} \end{bmatrix} \cdot \begin{bmatrix} v^*_{s1,q_{s1}} \\ \dots \\ v^*_{sk,q_{sk}} \\ \dots \\ v^*_{sn,q_{sn}} \end{bmatrix} = \left[M\right]^{\tau+1} \cdot \begin{bmatrix} v^*_{s1,q_{s1}} \\ \dots \\ v^*_{sk,q_{sk}} \\ \dots \\ v^*_{sn,q_{sn}} \end{bmatrix} \tag{3.110}$$

where the coefficients belonging to the matrix $\left[M\right]^{\tau+1}$ are defined as follows:

$$m^{\tau+1}_{(i,j)} = \begin{cases} 1+\sum_{\substack{z=1\\ z\neq i,j}}^{n}\tilde{d}^{\tau}_{c,z} & i = j \\ -\tilde{d}^{\tau}_{c,j}\cdot\cos\left(\hat{\delta}^{\tau+1}_{sj} - \hat{\delta}^{\tau+1}_{si}\right) & i \neq j \end{cases} \tag{3.111}$$

With the aim at computing the q_{sk}-axis reference voltage $v^*_{sk,q_{sk}}$ of the generic unit k, (3.110) must be inverted as follows:

$$\begin{bmatrix} v^*_{s1,q_{s1}} \\ \dots \\ v^*_{sk,q_{sk}} \\ \dots \\ v^*_{sn,q_{sn}} \end{bmatrix} = \left(\left[M\right]^{\tau+1}\right)^{-1} \cdot \begin{bmatrix} C^*_{s1,q_{s1}} \\ \dots \\ C^*_{sk,q_{sk}} \\ \dots \\ C^*_{sn,q_{sn}} \end{bmatrix} = \left[S\right]^{\tau+1} \cdot \begin{bmatrix} C^*_{s1,q_{s1}} \\ \dots \\ C^*_{sk,q_{sk}} \\ \dots \\ C^*_{sn,q_{sn}} \end{bmatrix} \tag{3.112}$$

where:

$$\left[S\right]^{\tau+1}=\begin{bmatrix} s_{(1,1)}^{\tau+1} & \cdots & s_{(1,k)}^{\tau+1} & \cdots & s_{(1,n)}^{\tau+1} \\ \cdots & \cdots & \cdots & \cdots & \cdots \\ s_{(k,1)}^{\tau+1} & \cdots & s_{(k,k)}^{\tau+1} & \cdots & s_{(k,n)}^{\tau+1} \\ \cdots & \cdots & \cdots & \cdots & \cdots \\ s_{(n,1)}^{\tau+1} & \cdots & s_{(n,k)}^{\tau+1} & \cdots & s_{(n,n)}^{\tau+1} \end{bmatrix} \tag{3.113}$$

With reference to (3.112)-(3.113), the real-time computation of the coefficients belonging to the matrix $\left[S\right]^{\tau+1}$ must be implemented, corresponding to the more complex operation performed in the proposed decoupling algorithm. After several mathematical manipulations, it is demonstrated how the computation of (3.113) leads to as follows:

$$s_{(i,j)}^{\tau+1}=\begin{cases} \dfrac{1}{S_c^{\tau+1}}\cdot\left[(1+\tilde{d}_{c,i}^{\tau})+\dfrac{1}{2}\cdot\left(1+\sum_{z=1}^{n}\tilde{d}_{c,z}^{\tau}\right)^{-1}\cdot S_{i-i}^{\tau+1}\right] & i=j \\ \dfrac{1}{S_c^{\tau+1}}\cdot\left[\tilde{d}_{c,j}^{\tau}\cdot\left(1+\sum_{z=1}^{n}\tilde{d}_{c,z}^{\tau}\right)^{-1}\cdot S_{i-j}^{\tau+1}\right] & i\neq j \end{cases} \tag{3.114}$$

where:

$$S_c^{\tau+1}=\left(1+\sum_{z=1}^{n}\tilde{d}_{c,z}^{\tau}\right)+\frac{1}{2}\cdot\sum_{z=1}^{n}\sum_{l=1}^{n}\left[\tilde{d}_{c,z}^{\tau}\cdot\tilde{d}_{c,l}^{\tau}\cdot\sin^2\left(\hat{\delta}_{sz}^{\tau+1}-\hat{\delta}_{sl}^{\tau+1}\right)\right] \tag{3.115}$$

$$S_{i-i}^{\tau+1}=\sum_{\substack{z=1\\z\neq i}}^{n}\sum_{\substack{l=1\\l\neq i}}^{n}\left[\tilde{d}_{c,z}^{\tau}\cdot\tilde{d}_{c,l}^{\tau}\cdot\sin^2\left(\hat{\delta}_{sz}^{\tau+1}-\hat{\delta}_{sl}^{\tau+1}\right)\right] \tag{3.116}$$

$$S_{i-j}^{\tau+1}=\left(1+\tilde{d}_{c,i}^{\tau}+\tilde{d}_{c,j}^{\tau}\right)\cdot\cos\left(\hat{\delta}_{si}^{\tau+1}-\hat{\delta}_{sj}^{\tau+1}\right)+\sum_{\substack{z=1\\z\neq i,j}}^{n}\left[\tilde{d}_{c,z}^{\tau}\cdot\cos\left(\hat{\delta}_{si}^{\tau+1}-\hat{\delta}_{sz}^{\tau+1}\right)\cdot\cos\left(\hat{\delta}_{sj}^{\tau+1}-\hat{\delta}_{sz}^{\tau+1}\right)\right] \tag{3.117}$$

Finally, the computation of the q_{sk}-axis reference voltage belonging to the unit k is performed as follows:

$$v_{sk,q_{sk}}^{*}=s_{(k,k)}^{\tau+1}\cdot C_{sk,q_{sk}}^{*}+\sum_{\substack{z=1\\z\neq k}}^{n}\left[s_{(k,z)}^{\tau+1}\cdot C_{sz,q_{sz}}^{*}\right] \tag{3.118}$$

To implement (3.118), high computational efforts of the dedicated digital controller are required, especially in case multiple three-phase IM drives having a high number of conversion units *n* are considered. However, in the case of balanced operation of the machine, corresponding into having same load-angles values among the units, (3.118) is drastically simplified as follows:

$$v^{*}_{sk,q_{sk}} = \left[F^{*}_{sk,q_{sk}} + \sum_{z=1}^{n} \left(\tilde{d}^{\tau}_{c,z} \cdot F^{*}_{sz,q_{sz}} \right) \right] \cdot \left(1 + \sum_{z=1}^{n} \tilde{d}^{\tau}_{c,z} \right)^{-1} \tag{3.119}$$

As the coefficients (3.108) are defined by considering the VSI units' status, the decoupling action of (3.118) is not affected by fault events, thus obtaining fault-tolerance capability of the proposed solution.

With reference to (3.114), the computation of the angular differences among the predicted load-angles values of the units is required. However, these are always expressed in terms of sine and cosine values, thus allowing their computation by means of the stationary (α,β) versors belonging to the predicted flux vectors of the units (3.38). Therefore, by considering two generic units (*i*,*j*), the following is implemented:

$$\begin{cases} \cos\left(\hat{\delta}^{\tau+1}_{si} - \hat{\delta}^{\tau+1}_{sj}\right) = \cos\left(\hat{\delta}^{\tau+1}_{si}\right) \cdot \cos\left(\hat{\delta}^{\tau+1}_{sj}\right) + \sin\left(\hat{\delta}^{\tau+1}_{si}\right) \cdot \sin\left(\hat{\delta}^{\tau+1}_{sj}\right) = \hat{\bar{\Theta}}^{\tau+1}_{\lambda-si} \bullet \hat{\bar{\Theta}}^{\tau+1}_{\lambda-sj} \\ \sin\left(\hat{\delta}^{\tau+1}_{si} - \hat{\delta}^{\tau+1}_{sj}\right) = \cos\left(\hat{\delta}^{\tau+1}_{sj}\right) \cdot \sin\left(\hat{\delta}^{\tau+1}_{si}\right) - \sin\left(\hat{\delta}^{\tau+1}_{sj}\right) \cdot \cos\left(\hat{\delta}^{\tau+1}_{si}\right) = \hat{\bar{\Theta}}^{\tau+1}_{\lambda-sj} \times \hat{\bar{\Theta}}^{\tau+1}_{\lambda-si} \end{cases} \tag{3.120}$$

The implementation of (3.120) results quite fast and robust, thus without requiring the computation of the load angle value belonging to each unit.

In conclusion, by means of (3.118), the q_{sk}-axis reference voltage $v^{*}_{sk,q_{sk}}$ of the unit *k* is computed. Finally, this value is eventually saturated to the q_{sk}-axis voltage limit $v^{\tau+1}_{sk,q_{sk}-max}$ of the unit *k* (3.68), as shown in Fig. 3. 24.

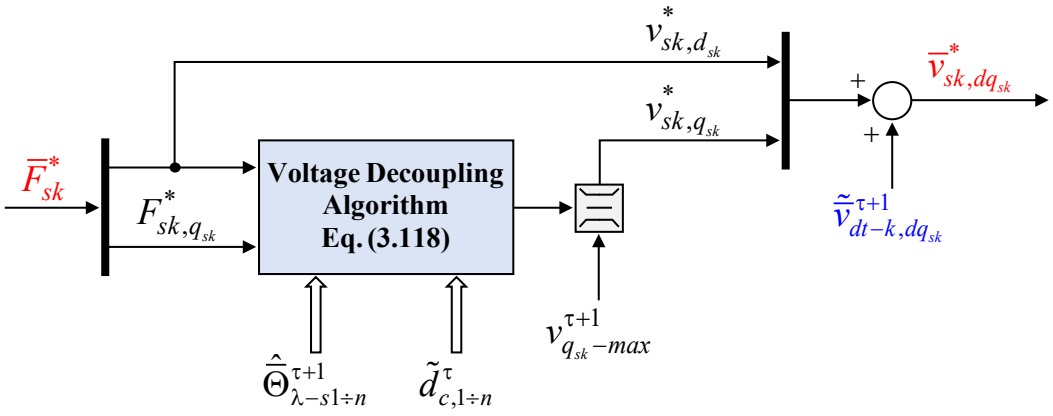

Fig. 3. 24. Execution scheme of the voltage decoupling algorithm.

If a DB-DFVC scheme is implemented, the prediction of the *k*-unit DT voltage error vector in the rotating (d_{sk},q_{sk}) frame $\tilde{\bar{v}}_{dt-k,dq_{sk}}^{\tau+1}$ is performed, as shown in Fig. 3. 11. Therefore, with reference to the execution scheme shown in Fig. 3. 24, a predictive compensation of the DT voltage errors introduced by the VSI unit *k* is implemented. In this way, relevant improvements in the *k*-unit currents waveforms are obtained, especially at low speed and for no-load condition.

With reference to Fig. 3. 22, once the *k*-unit reference voltage vector in the rotating (d_{sk},q_{sk}) frame $\bar{v}_{sk,dq_{sk}}^{*}$ is obtained, this is computed in terms of *k*-unit phase coordinates $(abc)_k$.

Therefore, by using the trigonometric coordinates of the predicted *k*-unit flux vector $\hat{\bar{\Theta}}_{\lambda-sk}^{\tau+1}$, the inverse rotational transformation (2.105) on the *k*-unit reference voltage vector in the rotating (d_{sk},q_{sk}) frame $\bar{v}_{sk,dq_{sk}}^{*}$ is implemented. In this way, the *k*-unit reference voltage vector in the stationary (α,β) frame $\bar{v}_{sk,\alpha\beta}^{*}$ is computed.

Finally, by discarding the zero-sequence voltage reference, the inverse Clarke transformation (3.6) on the *k*-unit reference voltage vector in stationary (αβ0) coordinates is implemented, thus leading to the computation of the *k*-unit reference voltage vector $\left[v_{sk,abc}\right]^{*}$ in the *k*-unit phase coordinates $(abc)_k$.

With reference to Fig. 3. 22, once the *k*-unit reference voltage vector in the *k*-unit phase coordinates $(abc)_k$ is obtained, the computation of the *k*-unit duty-cycles $\left[d_{k,abc}^{*}\right]^{\tau+1}$ is performed. According with the previous considerations, the 'Min-Max' modulation is implemented [9], leading to execution scheme shown in Fig. 3. 25. Therefore, with reference to (3.13), the zero-sequence signal d_{k-0}^{*} is computed as follows:

$$d_{k-0}^{*}=-\frac{1}{4}\cdot\left[\max\left(\frac{\left[v_{sk,abc}\right]^{*}}{v_{dc}^{\tau}}\right)+\min\left(\frac{\left[v_{sk,abc}\right]^{*}}{v_{dc}^{\tau}}\right)\right] \tag{3.121}$$

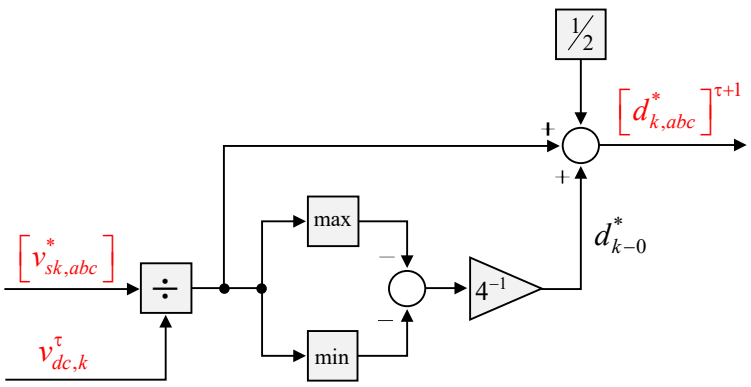

Fig. 3. 25. Execution scheme implementing the "Min-Max" modulation of the unit *k*.

3.4.6 Schematic block diagram of the *k*-unit DFVC scheme

In summary, each unit *k* is characterized by its own references in terms of *k*-unit flux amplitude and *k*-unit torque contribution. The *k*-unit DFVC scheme must be able to guarantee their regulation, according with the *k*-unit limitations in terms of DC-link voltage, phase-current amplitude and load-angle.

Two regulation types have been shown:

- Regulation by means of Proportional-Integral (PI) controllers, leading to a PI-DFVC scheme;
- Regulation by means of Dead-Beat (DB) controllers, leading to a DB-DFVC scheme.

The schematic block diagram of the *k*-unit PI-DFVC scheme is shown in Fig. 3. 26. With reference to it, the following main blocks are individuated:

- Control Inputs Elaboration (Section 3.4.1)
  This block implements the elaboration of both mechanical and electrical feedback belonging to the *k*-unit PI-DFVC scheme. By elaborating the electrical feedback, the computation of *k*-unit current and *k*-unit voltage in stationary coordinates is performed. Concerning the rotor mechanical position feedback, this is used to perform the computation of the rotor electrical position together with both mechanical and electrical speeds.
- Flux Observer (Section 3.4.2)
  By implementing a flux observer, the computation of the *k*-unit flux vector in terms of amplitude and angular position is performed. Two estimates are carried out, corresponding to the observed and predicted components of the *k*-unit flux vector in stationary coordinates. These are then used to obtain the observed and predicted position of the *k*-unit flux vector together with the estimation of the *k*-unit synchronous speed. In addition, the computation of the rotor flux vector in terms of amplitude and angular position is performed.
- Control Structure (Section 3.4.4)
  This block implements the *k*-unit DFVC structure. According with the *k*-unit limitations in terms of DC-link voltage, phase-current amplitude and load-angle, the *k*-unit references in terms of flux amplitude and torque-producing current are properly computed. Finally, by using PI controllers, the *k*-unit control is performed.
- Decoupling Algorithm (Section 3.4.5)
  To extrapolate the *k*-unit reference voltage vector components, a voltage decoupling algorithm is implemented. It follows the computation of the *k*-unit phase voltage references. Finally, by implementing the selected PWM modulation technique, the *k*-unit duty-cycles are computed, corresponding to the outputs of the *k*-unit DFVC scheme.

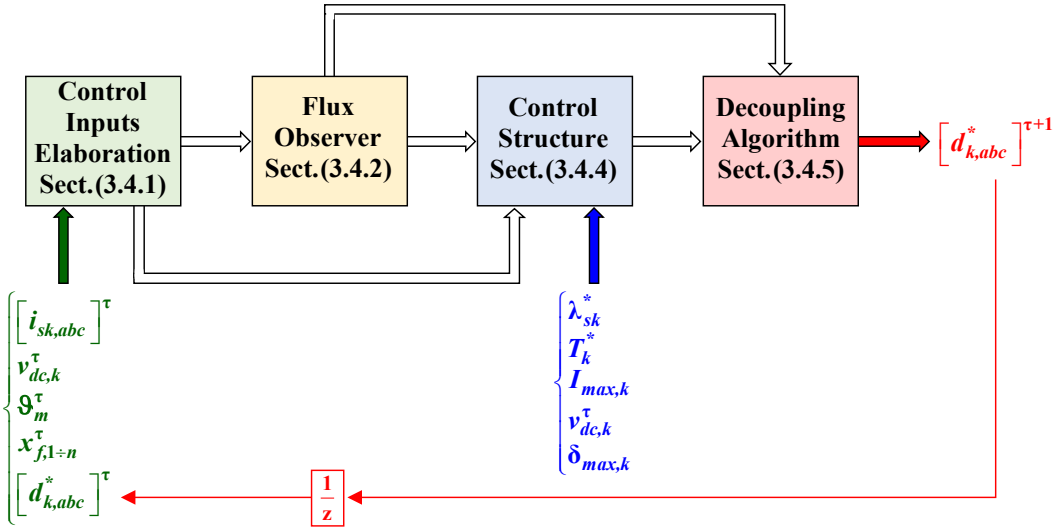

Fig. 3. 26. Schematic block diagram of the *k*-unit PI-DFVC scheme.

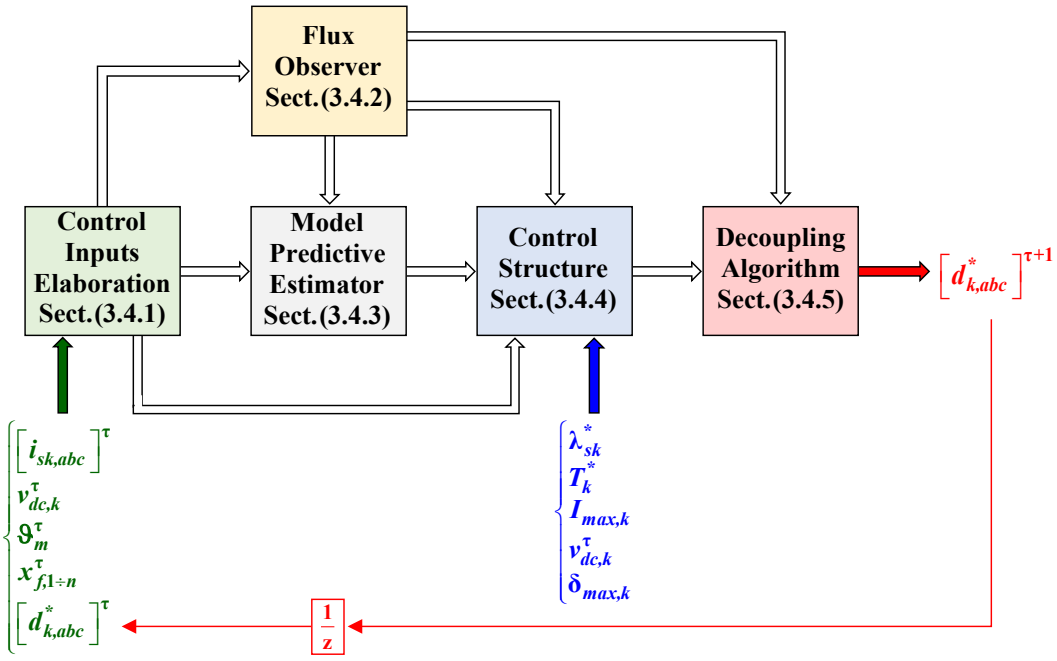

Fig. 3. 27. Schematic block diagram of the *k*-unit DB-DFVC scheme.

The schematic block diagram of the *k*-unit DB-DFVC scheme is shown in Fig. 3. 27. Concerning the Control Structure block (Section 3.4.4), the only difference consists of performing the *k*-unit control by means of DB controllers. Compared to *k*-unit PI-DFVC scheme, the following additional block is individuated:

- Model Predictive Estimator (Section 3.4.3)
  Implementation of a model-based estimator for the prediction of the *k*-unit current vector, thus allowing the DB regulation of the *k*-unit torque-producing current. In addition, with the aim at improving the *k*-unit phase currents waveforms, it follows the prediction of the *k*-unit DT voltage errors, thus allowing their feed-forward compensation.

3.5 Conclusion

In this chapter, the design and digital implementation of a Direct Flux Vector Control (DFVC) scheme for multiple three-phase Induction Motor (IM) drives has been reported. The proposed control solution is based on the Multi-Stator (MS) approach, thus allowing a straightforward control of the main variables (current, flux, torque) belonging to each three-phase unit. In this way, the modularity of the multiple three-phase IM drives is extended also in terms of control scheme, without limiting itself to the machine configuration and power converter structure.

With reference to the technical literature, the research contributions and novelties introduced by the proposed control solution are below summarized. With the aim at proposing a modular MS-based DFVC scheme for multiple three-phase IM drives, for each three-phase unit the following features have been implemented:

- Independent stator flux amplitude regulation
- Independent torque regulation
- Independent voltage and current operational limits
- Independent load-angle limitation
- Independent post-fault reconfiguration

The proposed control solution has been developed by considering two different regulation types, corresponding to as follows:

- Regulation by means of Proportional-Integral (PI) controllers, leading to a control scheme characterized by good dynamic performance and acceptable computational efforts in order to be implemented;
- Regulation by means of Dead-Beat (DB) controllers, leading to a control scheme characterized by high dynamic performance but high computational efforts in order to be implemented;

According with proposed control solution, for each DFVC scheme dedicated to the control of a generic unit, the most relevant conclusions are the following:

- The torque contribution is regulated by means of the torque-producing current component, thus obtaining a high level of decoupling between the control axes;
- The control scheme is implemented in the rotating stator flux frame, thus requiring the implementation of a flux observer to get the stator vector in terms of amplitude and position;
- The control structure allows a straightforward regulation of the stator flux amplitude and torque contribution, however considering the limitations in terms of DC-link voltage, phase-current amplitude and load-angle;
- The regulation using DB controllers requires the prediction of the stator current vector, leading to the implementation of a model-based predictive estimator;

- Due the voltage coupling introduced by the MS approach, the output of the torque-producing current regulation must be considered as combination of the voltage references belonging to all units, thus requiring the implementation of a voltage decoupling algorithm;
- The computation of the duty-cycles can be performed using any of the conventional three-phase PWM modulation techniques.

References

[1] M. J. Duran and F. Barrero, 'Recent Advances in the Design, Modeling, and Control of Multiphase Machines—Part II', *IEEE Trans. Ind. Electron.*, vol. 63, no. 1, pp. 459–468, Jan. 2016.

[2] I. Zoric, M. Jones, and E. Levi, 'Arbitrary Power Sharing Among Three-Phase Winding Sets of Multiphase Machines', *IEEE Trans. Ind. Electron.*, vol. 65, no. 2, pp. 1128–1139, Feb. 2018.

[3] R. Bojoi, M. Lazzari, F. Profumo, and A. Tenconi, 'Digital field-oriented control for dual three-phase induction motor drives', *IEEE Trans. Ind. Appl.*, vol. 39, no. 3, pp. 752–760, May 2003.

[4] R. Bojoi, A. Cavagnino, A. Tenconi, and S. Vaschetto, 'Control of Shaft-Line-Embedded Multiphase Starter/Generator for Aero-Engine', *IEEE Trans. Ind. Electron.*, vol. 63, no. 1, pp. 641–652, Jan. 2016.

[5] I. Subotic, O. Dordevic, B. Gomm, and E. Levi, 'Active and Reactive Power Sharing Between Three-Phase Winding Sets of a Multiphase Induction Machine', *IEEE Trans. Energy Convers.*, pp. 1–1, 2019.

[6] A. Galassini, A. Costabeber, M. Degano, C. Gerada, A. Tessarolo, and R. Menis, 'Enhanced Power Sharing Transient With Droop Controllers for Multithree-Phase Synchronous Electrical Machines', *IEEE Trans. Ind. Electron.*, vol. 66, no. 7, pp. 5600–5610, Jul. 2019.

[7] G. Pellegrino, R. I. Bojoi, and P. Guglielmi, 'Unified Direct-Flux Vector Control for AC Motor Drives', *IEEE Trans. Ind. Appl.*, vol. 47, no. 5, pp. 2093–2102, Sep. 2011.

[8] R. Bojoi, S. Rubino, A. Tenconi, and S. Vaschetto, 'Multiphase electrical machines and drives: A viable solution for energy generation and transportation electrification', in *2016 International Conference and Exposition on Electrical and Power Engineering (EPE)*, 2016, pp. 632–639.

[9] D. G. Holmes and T. A. Lipo, *Pulse Width Modulation for Power Converters: Principles and Practice*. John Wiley & Sons, 2003.

[10] S. Rubino, R. Bojoi, M. Mengoni, and L. Zarri, 'Optimal flux selection for multi three-phase machines in normal and fault conditions', in *2017 IEEE International Electric Machines and Drives Conference (IEMDC)*, 2017, pp. 1–8.

[11] I. Zoric, 'Multiple Three-Phase Induction Generators for Wind Energy Conversion Systems', doctoral, Liverpool John Moores University, 2018.

[12] I. R. Bojoi, E. Armando, G. Pellegrino, and S. G. Rosu, 'Self-commissioning of inverter nonlinear effects in AC drives', in *2012 IEEE International Energy Conference and Exhibition (ENERGYCON)*, 2012, pp. 213–218.

[13] V. Kaura and V. Blasko, 'Operation of a phase locked loop system under distorted utility conditions', *IEEE Trans. Ind. Appl.*, vol. 33, no. 1, pp. 58–63, Jan. 1997.

[14] P. L. Jansen and R. D. Lorenz, 'A physically insightful approach to the design and accuracy assessment of flux observers for field oriented induction machine drives', *IEEE Trans. Ind. Appl.*, vol. 30, no. 1, pp. 101–110, Jan. 1994.

[15] C. Choi, J. Seok, and R. D. Lorenz, 'Wide-Speed Direct Torque and Flux Control for Interior PM Synchronous Motors Operating at Voltage and Current Limits', *IEEE Trans. Ind. Appl.*, vol. 49, no. 1, pp. 109–117, Jan. 2013.

[16] J. S. Lee, C. Choi, J. Seok, and R. D. Lorenz, 'Deadbeat-Direct Torque and Flux Control of Interior Permanent Magnet Synchronous Machines With Discrete Time Stator Current and Stator Flux Linkage Observer', *IEEE Trans. Ind. Appl.*, vol. 47, no. 4, pp. 1749–1758, Jul. 2011.

[17] R. Isermann, *Digital Control Systems: Volume 1: Fundamentals, Deterministic Control*. Springer Science & Business Media, 2013.

[18] 'Bilinear transform', *Wikipedia*. 08-Oct-2018.

[19] R. Bojoi, A. Tenconi, and S. Vaschetto, 'Direct Stator Flux and Torque Control for asymmetrical six-phase induction motor drives', in *2010 IEEE International Conference on Industrial Technology*, 2010, pp. 1507–1512.

[20] Y. Hu, Z. Q. Zhu, and M. Odavic, 'Comparison of Two-Individual Current Control and Vector Space Decomposition Control for Dual Three-Phase PMSM', *IEEE Trans. Ind. Appl.*, vol. 53, no. 5, pp. 4483–4492, Sep. 2017.

Chapter 4

EXPERIMENTAL VALIDATION

Table of Contents

List of Figures

Fig. 4. 22. From top to bottom: single units observed torque (Nm); single units observed flux amplitude (mVs); single units measured d_{sk}-axis current (A); single units measured q_{sk}-axis current (A); single units observed load-angle (deg).
Fig. 4. 23. For each *k*-unit DFVC scheme, from top to bottom: reference and observed torque (Nm); reference and observed flux amplitude (mVs); measured d_{sk}-axis current (A); reference and measured q_{sk}-axis current (A); observed load-angle (deg).
Fig. 4. 24. Ch1: $i_{s1\text{-}a}$ (10 A/div), Ch2: $i_{s2\text{-}a}$ (10 A/div), Ch3: $i_{s3\text{-}a}$ (10 A/div), Ch4: $i_{s4\text{-}a}$ (10 A/div).
Fig. 4. 25. From top to bottom: measured speed (10^3 · r/min); reference and observed machine torque (Nm); estimated mechanical power (kW).
Fig. 4. 26. From top to bottom: single units observed torque (Nm); single units observed flux amplitude (mVs); single units measured d_{sk}-axis current (A); single units measured q_{sk}-axis current (A); single units observed load-angle (deg).
Fig. 4. 27. For each *k*-unit DFVC scheme, from top to bottom: reference and observed torque (Nm); reference and observed flux amplitude (mVs); measured d_{sk}-axis current (A); reference and measured q_{sk}-axis current (A); observed load-angle (deg).
Fig. 4. 28. Ch1: $i_{s1\text{-}a}$ (10 A/div), Ch2: $i_{s2\text{-}a}$ (10 A/div), Ch3: $i_{s3\text{-}a}$ (10 A/div), Ch4: $i_{s4\text{-}a}$ (10 A/div).
Fig. 4. 29. From top to bottom: measured speed (10^3 · r/min); reference and observed machine torque (Nm); estimated mechanical power (kW).
Fig. 4. 30. From top to bottom: single units observed torque (Nm); single units observed flux amplitude (mVs); single units measured d_{sk}-axis current (A); single units measured q_{sk}-axis current (A); single units observed load-angle (deg).
Fig. 4. 31. For each *k*-unit DFVC scheme, from top to bottom: reference and observed torque (Nm); reference and observed flux amplitude (mVs); measured d_{sk}-axis current (A); reference and measured q_{sk}-axis current (A); observed load-angle (deg).
Fig. 4. 32. Ch1: $i_{s1\text{-}a}$ (10 A/div), Ch2: $i_{s2\text{-}a}$ (10 A/div), Ch3: $i_{s3\text{-}a}$ (10 A/div), Ch4: $i_{s4\text{-}a}$ (10 A/div).
Fig. 4. 33. From top to bottom: measured speed (10^3 · r/min); reference and observed machine torque (Nm); estimated mechanical power (kW).
Fig. 4. 34. From top to bottom: single units observed torque (Nm); single units observed flux amplitude (mVs); single units measured d_{sk}-axis current (A); single units measured q_{sk}-axis current (A); single units observed load-angle (deg).
Fig. 4. 35. For each *k*-unit DFVC scheme, from top to bottom: reference and observed torque (Nm); reference and observed flux amplitude (mVs); measured d_{sk}-axis current (A); reference and measured q_{sk}-axis current (A); observed load-angle (deg).
Fig. 4. 36. Ch1: $i_{s1\text{-}a}$ (10 A/div), Ch2: $i_{s2\text{-}a}$ (10 A/div), Ch3: $i_{s3\text{-}a}$ (10 A/div), Ch4: $i_{s4\text{-}a}$ (10 A/div).
Fig. 4. 37. Machine phase-currents for 200% of the rated torque (32 Nm) in generation at -3500 r/min using the optimal stator flux amplitude reference. Ch1:

$i_{s1\text{-}a}$ (7.5 A/div), Ch2: $i_{s2\text{-}a}$ (7.5 A/div), Ch3: $i_{s3\text{-}a}$ (7.5 A/div), Ch4: $i_{s4\text{-}a}$ (7.5 A/div). Time resolution: 10ms/div.

Fig. 4. 38. From top to bottom: measured speed (10^3 · r/min); reference and observed machine torque (Nm); estimated mechanical power (kW).

Fig. 4. 39. From top to bottom: single units observed torque (Nm); single units observed flux amplitude (mVs); single units measured d_{sk}-axis current (A); single units measured q_{sk}-axis current (A); single units observed load-angle (deg).

Fig. 4. 40. For each k-unit DFVC scheme, from top to bottom: reference and observed torque (Nm); reference and observed flux amplitude (mVs); measured d_{sk}-axis current (A); reference, measured and maximum limit q_{sk}-axis current (A); observed load-angle (deg).

Fig. 4. 41. From top to bottom: measured speed (10^3 · r/min); reference and observed machine torque (Nm); estimated mechanical power (kW).

Fig. 4. 42. From top to bottom: single units observed torque (Nm); single units observed flux amplitude (mVs); single units measured d_{sk}-axis current (A); single units measured q_{sk}-axis current (A); single units observed load-angle (deg).

Fig. 4. 43. For each k-unit DFVC scheme, from top to bottom: reference and observed torque (Nm); reference and observed flux amplitude (mVs); measured d_{sk}-axis current (A); reference and measured q_{sk}-axis current (A); observed load-angle (deg).

Fig. 4. 44. Ch1: $i_{s1\text{-}a}$ (7.5 A/div), Ch2: $i_{s2\text{-}a}$ (7.5 A/div), Ch3: $i_{s3\text{-}a}$ (7.5 A/div), Ch4: $i_{s4\text{-}a}$ (7.5 A/div).

Fig. 4. 45. Ch1: $i_{s1\text{-}a}$ (7.5 A/div), Ch2: $i_{s2\text{-}a}$ (7.5 A/div), Ch3: $i_{s3\text{-}a}$ (7.5 A/div), Ch4: $i_{s4\text{-}a}$ (7.5 A/div).

Fig. 4. 46. From top to bottom: measured speed (10^3 · r/min); reference and observed machine torque (Nm); estimated mechanical power (kW).

Fig. 4. 47. From top to bottom: single units observed torque (Nm); single units observed flux amplitude (mVs); single units measured d_{sk}-axis current (A); single units measured q_{sk}-axis current (A); single units observed load-angle (deg).

Fig. 4. 48. For each k-unit DFVC scheme, from top to bottom: reference and observed torque (Nm); reference and observed flux amplitude (mVs); measured d_{sk}-axis current (A); reference and measured q_{sk}-axis current (A); observed load-angle (deg).

Fig. 4. 49. Ch1: $i_{s1\text{-}a}$ (7.5 A/div), Ch2: $i_{s2\text{-}a}$ (7.5 A/div), Ch3: $i_{s3\text{-}a}$ (7.5 A/div), Ch4: $i_{s4\text{-}a}$ (7.5 A/div).

Fig. 4. 50. From top to bottom: measured speed (10^3 · r/min); reference and observed machine torque (Nm); estimated mechanical power (kW).

Fig. 4. 51. From top to bottom: single units observed torque (Nm); single units observed flux amplitude (mVs); single units measured d_{sk}-axis current (A); single units measured q_{sk}-axis current (A); single units observed load-angle (deg).

Fig. 4. 52. For each k-unit DFVC scheme, from top to bottom: reference and observed torque (Nm); reference and observed flux amplitude (mVs); measured d_{sk}-axis current (A); reference, measured and maximum limit q_{sk}-axis current (A); observed load-angle (deg).

Fig. 4. 53. From top to bottom: measured speed (10^3 · r/min); reference and observed machine torque (Nm); estimated mechanical power (kW).
Fig. 4. 54. From top to bottom: single units observed torque (Nm); single units observed flux amplitude (mVs); single units measured d_{sk}-axis current (A); single units measured q_{sk}-axis current (A); single units observed load-angle (deg).
Fig. 4. 55. For each k-unit DFVC scheme, from top to bottom: reference and observed torque (Nm); reference and observed flux amplitude (mVs); measured d_{sk}-axis current (A); reference, measured and maximum limit q_{sk}-axis current (A); observed and maximum limit load-angle (deg).
Fig. 4. 56. Ch1: $i_{s1\text{-}a}$ (7.5 A/div), Ch2: $i_{s2\text{-}a}$ (7.5 A/div), Ch3: $i_{s3\text{-}a}$ (7.5 A/div), Ch4: $i_{s4\text{-}a}$ (7.5 A/div).
Fig. 4. 57. Ch1: $i_{s1\text{-}a}$ (7.5 A/div), Ch2: $i_{s2\text{-}a}$ (7.5 A/div), Ch3: $i_{s3\text{-}a}$ (7.5 A/div), Ch4: $i_{s4\text{-}a}$ (7.5 A/div).
Fig. 4. 58. From top to bottom: measured speed (10^3 · r/min); reference and observed machine torque (Nm); estimated mechanical power (kW).
Fig. 4. 59. From top to bottom: single units observed torque (Nm); single units observed flux amplitude (mVs); single units measured d_{sk}-axis current (A); single units measured q_{sk}-axis current (A); single units observed load-angle (deg).
Fig. 4. 60. For each k-unit DFVC scheme, from top to bottom: reference and observed torque (Nm); reference and observed flux amplitude (mVs); measured d_{sk}-axis current (A); reference, measured and maximum limit q_{sk}-axis current (A); observed and maximum limit load-angle (deg).
Fig. 4. 61. From top to bottom: measured speed (10^3 · r/min); reference and observed machine torque (Nm); estimated mechanical power (kW).
Fig. 4. 62. From top to bottom: single units observed torque (Nm); single units observed flux amplitude (mVs); single units measured d_{sk}-axis current (A); single units measured q_{sk}-axis current (A); single units observed load-angle (deg).
Fig. 4. 63. For each k-unit DFVC scheme, from top to bottom: reference and observed torque (Nm); reference and observed flux amplitude (mVs); measured d_{sk}-axis current (A); reference, measured and maximum limit q_{sk}-axis current (A); observed and maximum limit load-angle (deg).
Fig. 4. 64. Single units flux amplitude and rotor flux amplitude (mVs).
Fig. 4. 65. From top to bottom: measured speed (10^3 · r/min); reference, observed and predicted machine torque (Nm); estimated mechanical power (kW).
Fig. 4. 66. From top to bottom: single units observed and predicted torque (Nm); single units observed and predicted flux amplitude (mVs); single units measured and predicted d_{sk}-axis current (A); single units measured and predicted q_{sk}-axis current (A); single units observed and predicted load-angle (deg).
Fig. 4. 67. For each k-unit DFVC scheme, from top to bottom: reference, observed and predicted torque (Nm); reference, observed and predicted flux amplitude (mVs); measured and predicted d_{sk}-axis current (A); reference, measured and predicted q_{sk}-axis current (A); observed and predicted load-angle (deg).

Fig. 4. 68. For each *k*-unit model predictive estimator (MPE), from top to bottom: reference, observed and predicted torque (Nm); (α,β) observed and predicted fluxes (mVs); (α,β) measured and predicted currents (A).
Fig. 4. 69. From top to bottom: measured speed (10^3 · r/min); reference, observed and predicted machine torque (Nm); estimated mechanical power (kW).
Fig. 4. 70. From top to bottom: single units observed and predicted torque (Nm); single units observed and predicted flux amplitude (mVs); single units measured and predicted d_{sk}-axis current (A); single units measured and predicted q_{sk}-axis current (A); single units observed and predicted load-angle (deg).
Fig. 4. 71. For each *k*-unit DFVC scheme, from top to bottom: reference, observed and predicted torque (Nm); reference, observed and predicted flux amplitude (mVs); measured and predicted d_{sk}-axis current (A); reference, measured and predicted q_{sk}-axis current (A); observed and predicted load-angle (deg).
Fig. 4. 72. For each *k*-unit model predictive estimator (MPE), from top to bottom: reference, observed and predicted torque (Nm); (α,β) observed and predicted fluxes (mVs); (α,β) measured and predicted currents (A).
Fig. 4. 73. Ch1: $i_{s1\text{-}a}$ (10 A/div), Ch2: $i_{s2\text{-}a}$ (10 A/div). Time resolution: 5 ms/div.
Fig. 4. 74. From top to bottom: measured speed (10^3 · r/min); reference, observed and predicted machine torque (Nm); estimated mechanical power (kW).
Fig. 4. 75. From top to bottom: single units observed and predicted torque (Nm); single units observed and predicted flux amplitude (mVs); single units measured and predicted d_{sk}-axis current (A); single units measured and predicted q_{sk}-axis current (A); single units observed and predicted load-angle (deg).
Fig. 4. 76. For each *k*-unit DFVC scheme, from top to bottom: reference, observed and predicted torque (Nm); reference, observed and predicted flux amplitude (mVs); measured and predicted d_{sk}-axis current (A); reference, measured and predicted q_{sk}-axis current (A); observed and predicted load-angle (deg).
Fig. 4. 77. For each *k*-unit model predictive estimator (MPE), from top to bottom: reference, observed and predicted torque (Nm); (α,β) observed and predicted fluxes (mVs); (α,β) measured and predicted currents (A).
Fig. 4. 78. Ch1: $i_{s1\text{-}a}$ (10 A/div), Ch2: $i_{s2\text{-}a}$ (10 A/div). Time resolution: 5 ms/div.
Fig. 4. 79. From top to bottom: measured speed (10^3 · r/min); reference, observed and predicted machine torque (Nm); estimated mechanical power (kW).
Fig. 4. 80. From top to bottom: single units observed and predicted torque (Nm); single units observed and predicted flux amplitude (mVs); single units measured and predicted d_{sk}-axis current (A); single units measured and predicted q_{sk}-axis current (A); single units observed and predicted load-angle (deg).
Fig. 4. 81. For each *k*-unit DFVC scheme, from top to bottom: reference, observed and predicted torque (Nm); reference, observed and predicted flux amplitude (mVs); measured and predicted d_{sk}-axis current (A); reference, measured and predicted q_{sk}-axis current (A); observed and predicted load-angle (deg).
Fig. 4. 82. For each *k*-unit model predictive estimator (MPE), from top to bottom: reference, observed and predicted torque (Nm); (α,β) observed and predicted fluxes (mVs); (α,β) measured and predicted currents (A).

List of Tables

This chapter deals with the experimental validation of the Direct Flux Vector Control (DFVC) scheme for multiple three-phase Induction Motor (IM) drives. The proposed control solution has been validated with a multi-modular power converter feeding a quadruple three-phase induction machine prototype.

According with the previous chapter, two regulation types have been implemented. The first one has led to a DFVC scheme employing standard Proportional-Integral (PI) controllers. The second regulation type has consisted of the implementation of a Dead-Beat (DB) control solution, thus obtaining the best dynamic performance of the drive. Due to the high computational efforts required to the digital controller, the experimental validation of the DB scheme has been performed on the prototype configured as an asymmetrical 6-phase machine.

The chapter is organized as follows. The first section concerns the test rig, thus including the data of power converter and machine prototype. It follows the presentation of the obtained experimental results, thus providing the experimental validation of the proposed control solutions.

4.1 Test rig

The experimental validation has been carried using a test rig consisted of the following main elements:

- Quadruple three-phase induction machine prototype
- Multiphase modular power converter
- Digital controller

With the aim at testing the machine in open-loop torque control mode, the rotor shaft has been coupled to a driving machine acting as active mechanical load, as shown in Fig. 4. 1.

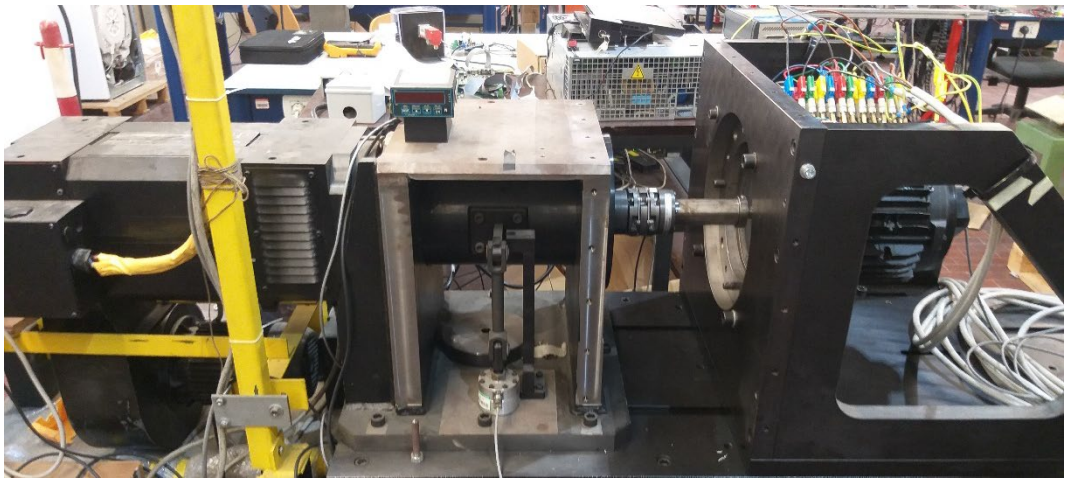

Fig. 4. 1. View of the machine under test (right) and the driving machine (left).

Finally, according with the power converter structure (Section 4.1.2), a single DC voltage source is employed. This consisted of a battery emulator whose details are beyond the scope of this dissertation.

The description of the main elements composing the test rig is provided below.

4.1.1 Quadruple three-phase induction machine prototype

The machine used for the experimental validation is an asymmetrical 12-phase squirrel cage induction prototype (Fig. 4. 2). The main features of the machine are reported in Table 4. 1 [1]. The stator has twelve phases with one slot/pole/phase, forming a quadruple three-phase winding with a phase shift of 15 electrical degrees among two three-phase winding sets, as shown in Fig. 4. 3. The machine has been designed with distributed windings and full-pitch layout, thus avoiding leakage mutual couplings between the stator phases. The three-phase winding sets are characterized by identical parameters, thus leading to univocal values of both stator resistance and mutual leakage inductance.

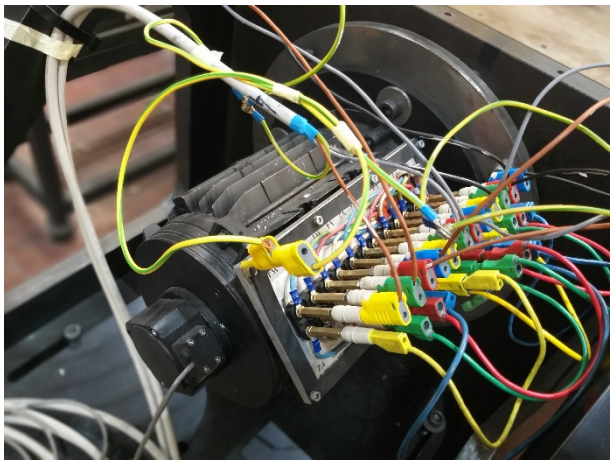

Fig. 4. 2. View of the 12-phase induction machine prototype.

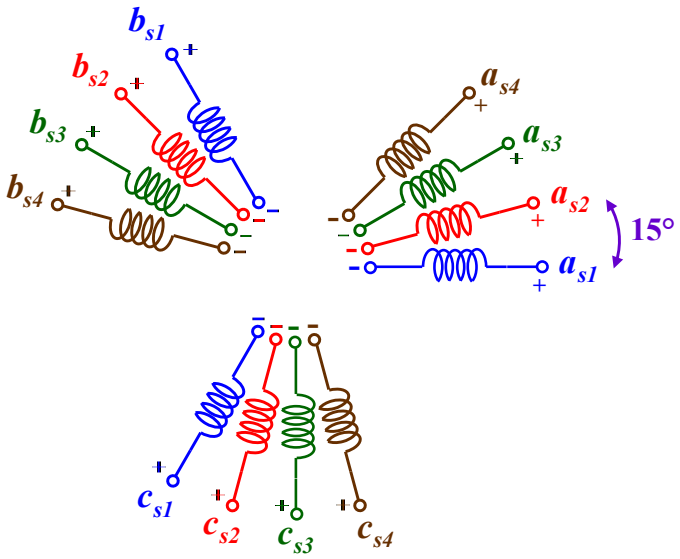

Fig. 4. 3 Asymmetrical 12-phase induction machine configuration.

Design Data	
Phase number	12 (4x3-phase)
Rotor type	Squirrel-cage
Winding configuration	Asymmetrical
Pole number	4
Slot/pole/phase number	1
Winding type	Distributed
Winding layout	Full-pitched
Cooling system	Forced air ventilation
Mechanical Data	
Rated power	10 kW
Rated speed	6000 r/min
Maximum speed	15000 r/min
Electrical Data	
Rated phase-voltage	115 V (rms)
Rated current	10 A (rms)
Rated frequency	200 Hz
Overload capability	150% - 5 min / 200% - 5 sec
Machine Parameters	
Stator resistance R_s	145 mΩ
Stator leakage inductance L_{ls}	0.94 mH
Magnetizing inductance L_m	4.3 mH
Rotor resistance R_r	45 mΩ
Rotor leakage inductance L_{lr}	0.235 mH
Rated stator flux $\lambda_{s,rated}$	0.115 Vs

Table 4. 1. Main data of the quadruple three-phase induction machine prototype.

By using the experimental procedure defined in [2], the computation of the machine optimal stator flux amplitude profiles in both healthy and fault conditions has been performed. In this way, according to experimental results shown in the next paragraph, the Maximum Torque per Ampere (MTPA) operation of the drive has been tested.

With reference to Chapter 3 (Section 3.3), the maximum phase-current limit of the units has been defined to meet the overload requirement (Table 4. 1), thus leading to the results shown in Fig. 4. 4, synthetically reported in Table 4. 2. According to these, it is noted how the fault-tolerance capability is extremely compromised if a single unit is active, leading to a maximum stator flux amplitude value lower than the rated one, as shown in Table 4. 1.

Finally, with the aim at implementing a multiple three-phase topology, each three-phase winding sets have isolated neutral points.

Maximum optimal limits of stator flux amplitude and torque @ I_{max} = 24 A		
Active Units n_a	Stator Flux Amplitude (Vs) $\lambda_{s,opt\text{-}max}^{n_a}$	Torque (Nm) $T_{opt\text{-}max}^{n_a}$
1	0.0934	3.8
2	0.1324	12.8
3	0.1459	23.0
4	0.1535	33.4

Table 4. 2. Optimal maximum reference values.

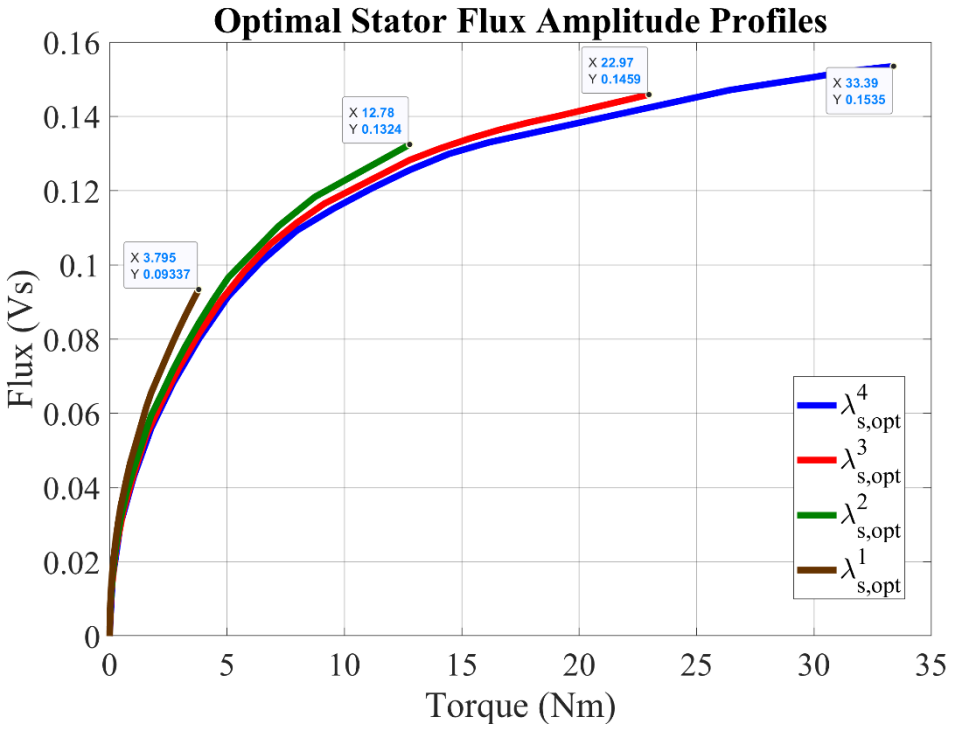

Fig. 4. 4. Optimal stator flux amplitude profiles of the machine in healthy and faulty conditions.

Asymmetrical 6-phase configuration

With reference Fig. 4. 3, the quadruple three-phase prototype employs an open-end winding configuration, thus allowing the series connection of the following three-phase winding sets:

$$(Set\ 1 \rightarrow Set\ 2) \Rightarrow \begin{cases} a_{s1}^{-} \rightarrow a_{s2}^{+} \\ b_{s1}^{-} \rightarrow b_{s2}^{+} \\ c_{s1}^{-} \rightarrow c_{s2}^{+} \end{cases} \quad ; \quad (Set\ 3 \rightarrow Set\ 4) \Rightarrow \begin{cases} a_{s3}^{-} \rightarrow a_{s4}^{+} \\ b_{s3}^{-} \rightarrow b_{s4}^{+} \\ c_{s3}^{-} \rightarrow c_{s4}^{+} \end{cases} \quad (4.1)$$

By performing the series connections (4.1), an asymmetrical 6-phase induction prototype has been obtained, leading to the features reported in Table 4. 3 [3]. With reference to these, the stator has six phases with two slot/pole/phase, forming a double three-phase winding with a relative shift of 30 electrical degrees among the three-phase winding sets, as shown in Fig. 4. 5.

Design Data	
Phase number	6 (2x3-phase)
Rotor type	Squirrel-cage
Winding configuration	Asymmetrical
Pole number	4
Slot/pole/phase number	2
Winding type	Distributed
Winding layout	Full-pitched
Cooling system	Forced air ventilation
Mechanical Data	
Rated power	10 kW
Rated speed	6000 r/min
Maximum speed	15000 r/min
Electrical Data	
Rated phase-voltage	230 V (rms)
Rated current	10 A (rms)
Rated frequency	200 Hz
Overload capability	150% - 5 min / 200% - 5 sec
Machine Parameters	
Stator resistance R_s	289 mΩ
Stator leakage inductance L_{ls}	1.88 mH
Magnetizing inductance L_m	15.7 mH
Rotor resistance R_r	181 mΩ
Rotor leakage inductance L_{lr}	0.94 mH
Rated stator flux $\lambda_{s,rated}$	0.230 Vs

Table 4. 3. Main data of the asymmetrical 6-phase prototype.

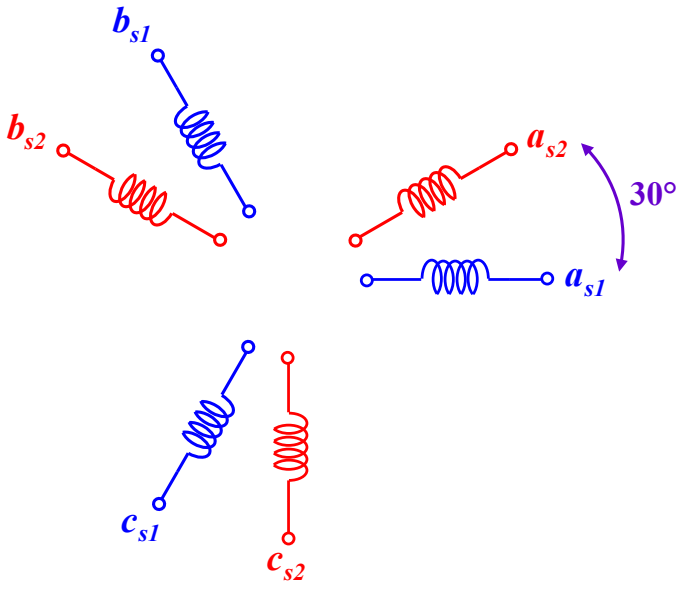

Fig. 4. 5. Asymmetrical 6-phase induction machine configuration.

Compared to the quadruple three-phase configuration, the machine optimal stator flux amplitude profiles have not been computed, thus representing a future work of this research activity. As for the quadruple three-phase configuration, both three-phase windings have isolated neutral points.

By using the machine asymmetrical 6-phase configuration, the experimental validation of the DB-DFVC scheme has been carried out, thus overcoming the limits of the digital controller in terms of computational power.

Machine sensors

The machine prototype has two integrated sensors. The first one consists of a thermocouple used to monitor the stator winding temperature. This can be used to implement a protection procedure to reduce the demanded power or even the drive shut-down. The other sensor consists of an incremental encoder having a resolution of 1024 pulses/rev (Fig. 4. 2), thus obtaining the rotor mechanical position measurement. This has represented the mechanical feedback of the proposed control scheme.

4.1.2 Multiphase modular power converter

The power converter is consists of six Power Electronic Building Block (PEBB) units [4]. Each of these consists of a three-phase Voltage Supply Inverter (VSI) with local controller implemented on a Field Programmable Gate Array (FPGA) board, as shown in Fig. 4. 6.

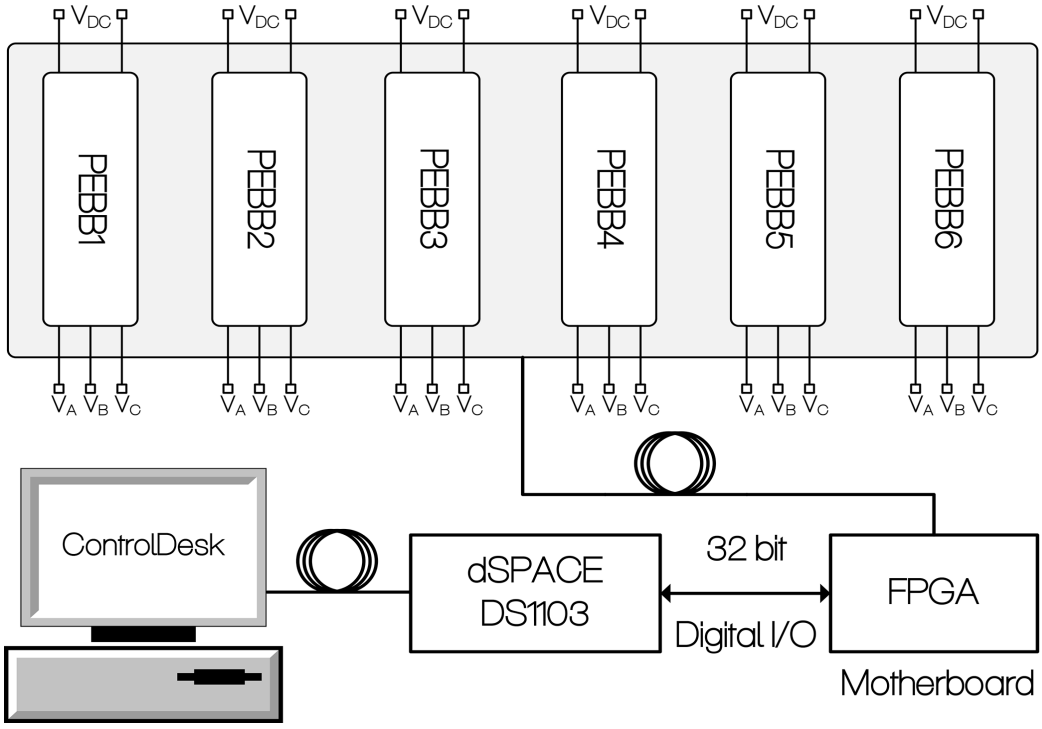

Fig. 4. 6. Schematic block of the modular power converter [4].
Picture reported by courtesy of the authors.

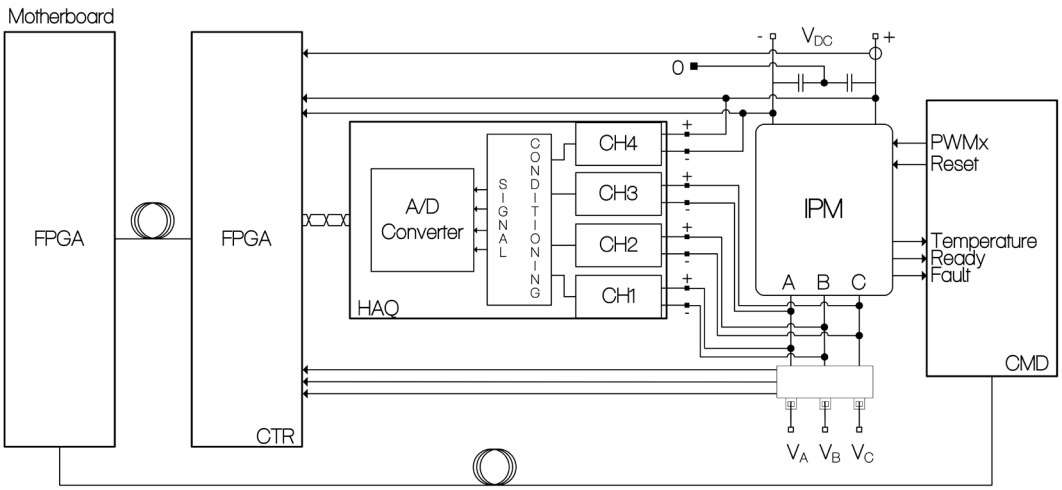

Fig. 4. 7. Schematic block of a single PEBB [4].
Picture reported by courtesy of the authors.

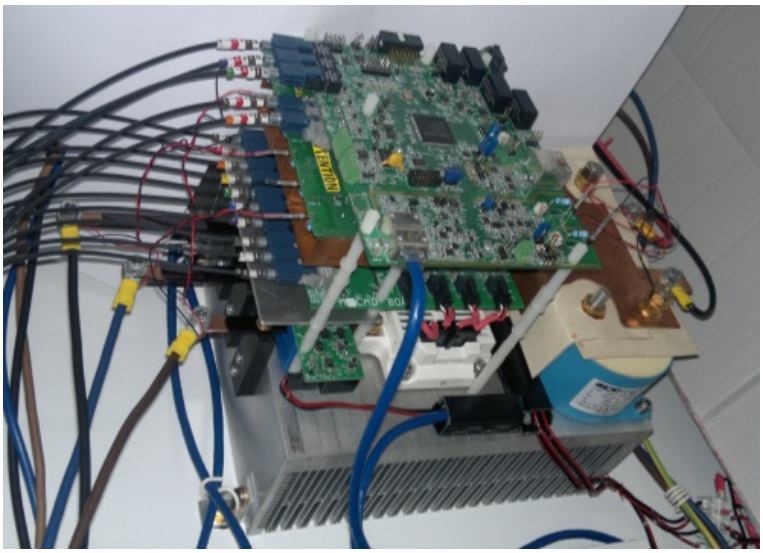

Fig. 4. 8. View of a single PEBB [4].
Picture reported by courtesy of the authors.

The power converter digital controller is the dSPACE® "DS1103 PPC Controller Board" [5]. The communication between the dSPACE board and the VSI units is performed by means of an FPGA-based motherboard, using a 32-bit I/O bus with dedicated communication protocol (Fig. 4. 6). Conversely, the communications between the FPGA motherboard and the VSI units are performed by means of optical fibers.

Each single PEBB unit consists of one three-phase Intelligent Power Module (IPM) with local DC-link obtained by means of two series-connected polypropylene capacitors, as shown in Fig. 4. 7 and Fig. 4. 8. Concerning the IPM modules, rated 100A-1200V, are the Infineon® "MIPAQ" series [6], using the Insulated Gate Bipolar Transistor (IGBT) technology.

With reference to Fig. 4. 7, each single PEBB unit is equipped with several boards. According to the dissertation scope, the most relevant ones are the following:

- Command board (CMD) – receives the switching commands for the IGBTs and transmits the feedback fault signals generated by the IPM;
- Hall-effect board – contains 3 Hall-effect sensors performing the measurement of the PEBB output currents;
- Control board – acquires the PEBB output currents and DC-link voltage.

Each single PEBB unit can be fed by an independent DC source. Nevertheless, due to several reasons beyond the scope of this dissertation, the power converter structure has been designed to be fed by a single DC source, shared by all six PEBB units.

A general view of the power converter structure is shown in Fig. 4. 9. With reference to it, the cooling system consists of six fans whose speed is regulated by the FPGA motherboard according with the highest temperature among the ones belonging to the PEBB units.

Finally, the communications performed by the FPGA motherboard include the one with the machine mechanical sensor, thus allowing the reception of the rotor mechanical position feedback by the dSPACE board.

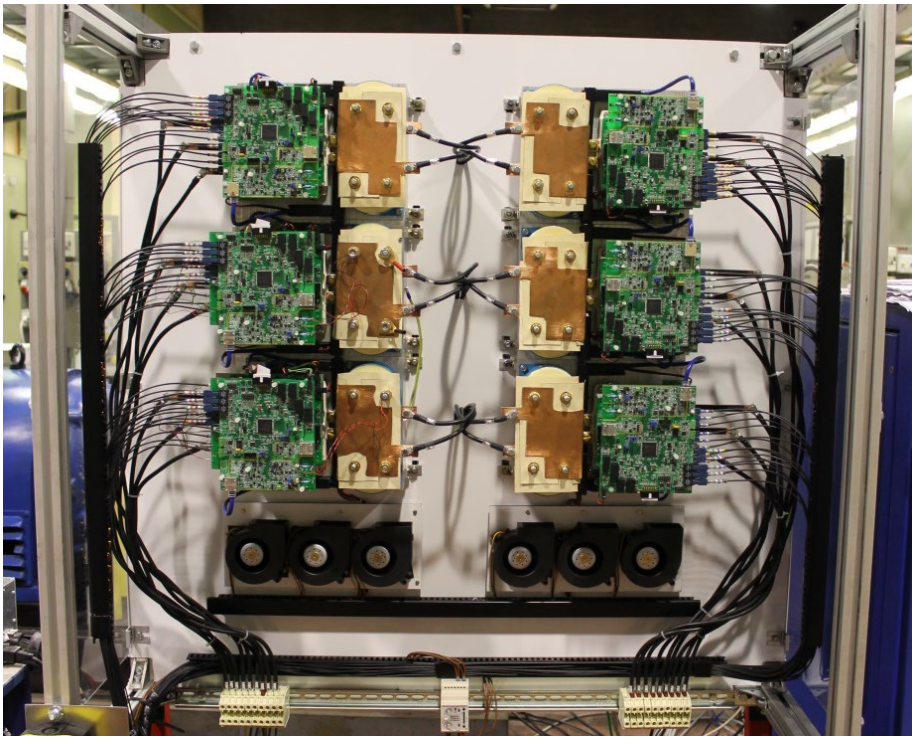

Fig. 4. 9. View of the modular power converter [4].
Picture reported by courtesy of the authors.

4.1.3 Digital controller

According with Section 4.1.2, the control algorithm has been implemented on the development system dSPACE® "DS1103 PPC Controller Board" [5] (Fig. 4. 10). The description of the digital controller is not reported, being it beyond the scope of this dissertation.

By using the experimenting software dSPACE® "ControlDesk", the on-line operations of setup and monitoring of the experimental tests have been performed, including the real-time data acquisition. Finally, concerning the control algorithm, this has been totally developed in C-code environment.

Fig. 4. 10. View of the digital controller DS1103 PPC Controller Board (left) and the power converter FPGA motherboard (right).

4.1.4 Schematic block diagram of the test rig

The schematic block diagram of the test rig is shown in Fig. 4. 11 and Fig. 4. 12. With reference to it, the following elements are individuated:

- DC Source
  It consists of a battery emulator system, thus allowing the regulation of the DC source voltage feeding the VSI units.
- Modular power converter (Section 4.1.2)
  It consists of six independent three-phase VSI units. Depending on if a double or quadruple three-phase machine configuration is considered, two or four VSI units are employed.
- Quadruple three-phase induction machine prototype (Section 4.1.1)
  Depending on the tested control scheme (PI-DFVC or DB-DFVC), a double or quadruple three-phase machine configuration is implemented.
- Active mechanical load
  It consists of a driving machine. In this way, the open-loop torque control operations are tested.
- Digital controller (Section 4.1.3)
  It consists of the dSPACE® control board.

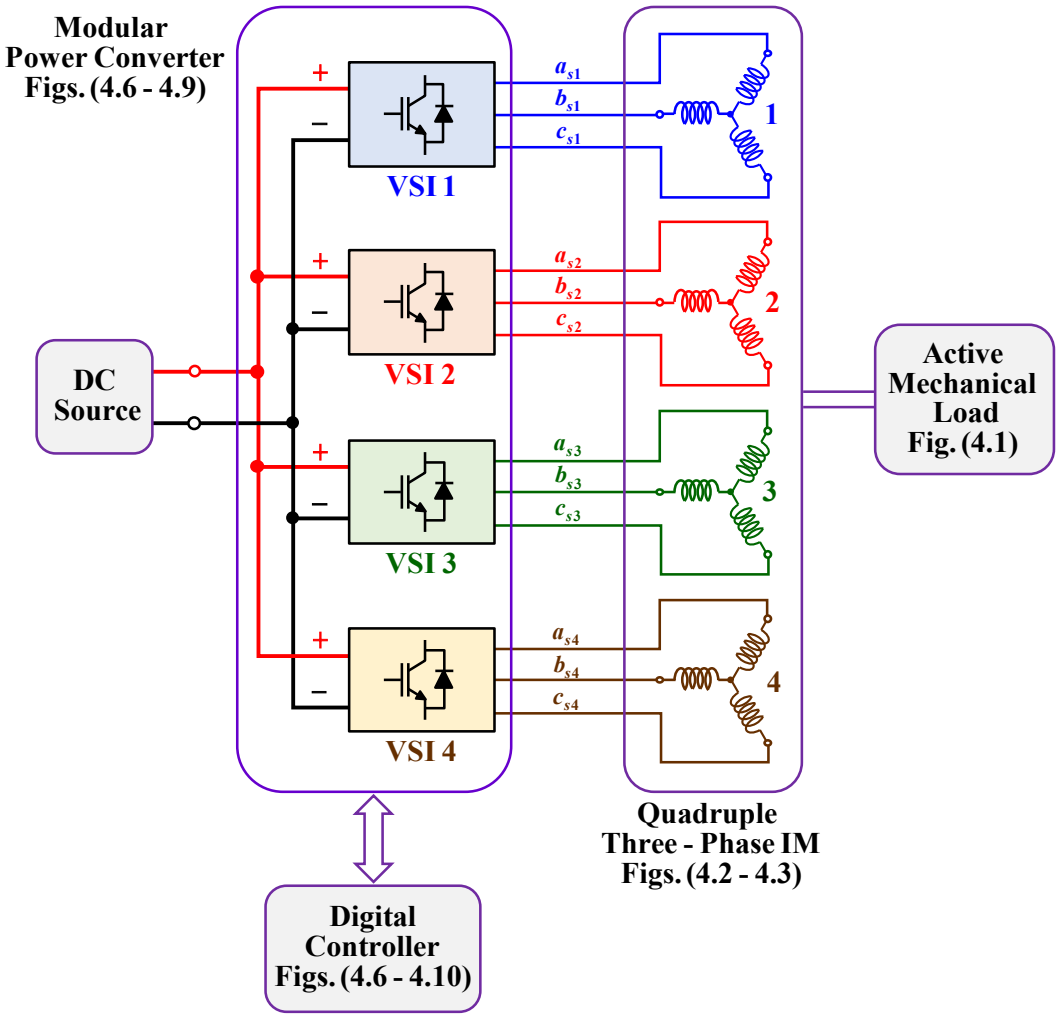

Fig. 4. 11. Schematic block diagram of the test rig for the experimental validation of the DFVC scheme using PI controllers.

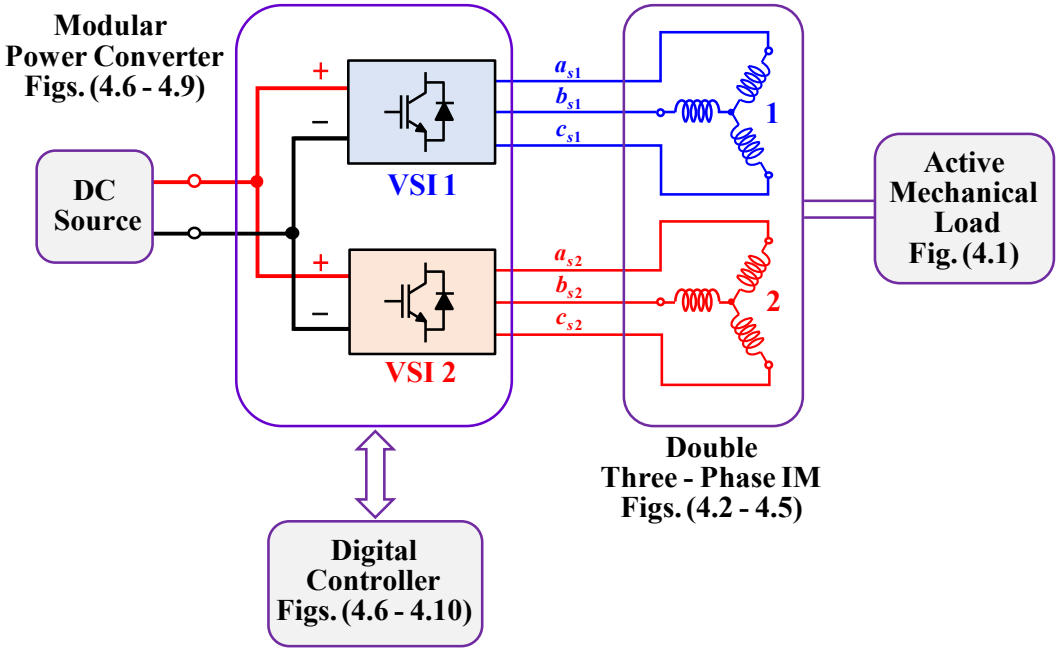

Fig. 4. 12. Schematic block diagram of the test rig for the experimental validation of the DFVC scheme using DB controllers.

4.2 Experimental results

The experimental results concerns the validation of the DFVC scheme for both solutions employing PI and DB regulators respectively. However, to avoid confusion, these are considered separately.

As the power converter employs a single DC voltage source, a drive scheme using a single outer controller has been tested, thus referring to the units' references generation system shown in Fig. 3. 5. For convenience, this is further reported in Fig. 4. 13. Therefore, according with the Chapter 3 - Section 3.3, the definition of the flux reference belonging to all the units has been performed by selecting one of the below three options:

$$\begin{cases} s_\lambda = 1 \rightarrow \lambda_s^* = \lambda_{s,opt}^{n_a} \\ s_\lambda = 2 \rightarrow \lambda_s^* = \lambda_{s,opt-max}^{n_a} \\ s_\lambda = 3 \rightarrow \lambda_s^* = \lambda_{s,rated} \left(< \lambda_{s,opt}^{n_a}\right) \end{cases} \qquad Eq.\ (3.16) \qquad (4.2)$$

Concerning the torque reference of the generic unit *k*, this has been generated as follows:

$$T_k^* = x_{f,k} \cdot t_{sh,k} \cdot T^* \qquad Eq.\ (3.18) \qquad (4.3)$$

By setting the input conditions (4.2)-(4.3) properly, each proposed experimental test has uniquely been defined.

The experimental results are related to the drive operation in open loop torque control and closed loop speed control. In the first case, the machine torque reference T^* has been set by the user directly. Conversely, in the case of closed loop speed control, the machine torque reference has been provided by the outer controller shown in Fig. 4. 13, corresponding to a simple PI regulator.

Due to the mechanical limitations of the driving machine, the speed has been limited at ±6000 r/min. Therefore, to perform deep-flux weakening drive operation, the DC source voltage has been imposed to lower values than the rated one. With reference to Table 4. 1 and Table 4. 3, the rated DC source voltage values correspond at 270 V for the quadruple three-phase configuration and 550 V for the double three-phase one.

For each VSI unit, the Dead-Time (DT) value has been set to 1.5 μs.

Finally, the sampling frequency and the VSI units switching frequency have been set to proper values such to guarantee the real-time execution of the control algorithm, thus overcoming the limits of the digital controller in terms of computational power. However, this aspect represents a further validation element because it provides a realistic scenario that is representative of the industrial implementations.

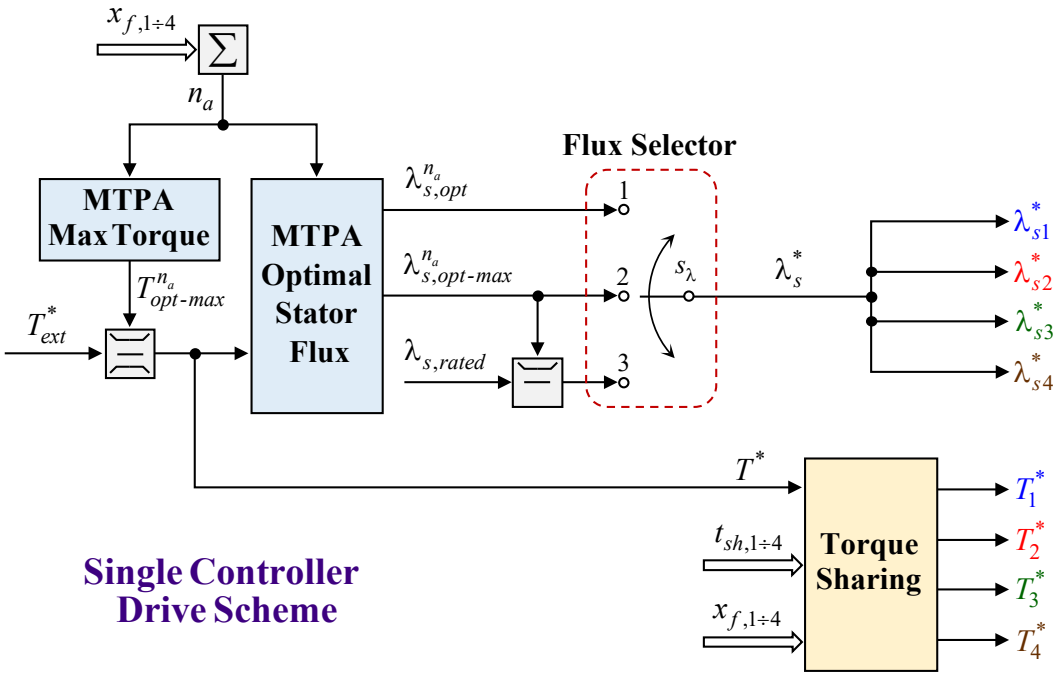

Fig. 4. 13. Drive scheme using a single outer controller.

4.2.1 Experimental validation of the PI-DFVC scheme

The validation of the PI-DFVC scheme has been carried out on the quadruple three-phase configuration.

According with the descriptions of both electrical machine and power converter, the DFVC schemes of the units have been designed using common values of the respective control parameters, as reported in Table 4. 4.

Flux Observer	
Observer gain ω_{ck}	125 rad/s
Control Structure	
DC-link voltage exploitation degree $k_{\lambda\text{-max}}$	0.9
Maximum phase-current limit $I_{max,k}$	24 A
Unit Control – Flux Amplitude PI Controller	
Proportional gain $k_{p,\lambda sk}$	1250 rad/s
Integral gain $k_{i,\lambda sk}$	132000 rad/s^2
Unit Control – Torque-producing current PI Controller	
Proportional gain k_{p,i_qsk}	2.3 V/A
Integral gain k_{i,i_qsk}	380 V/(A·s)

Table 4. 4. Values of the control parameters belonging to the k-unit PI-DFVC scheme (k=1,2,3,4).

In the next subsections, the obtained experimental results for the following tests are provided:

- Open loop torque control
  - Fast torque transients in healthy conditions
  - Fault ride-through capability for open three-phase set
  - Optimal torque control operation
  - Torque sharing operations
- Closed loop speed control
  - Deep flux-weakening operation

Open loop torque control tests

The mechanical speed has been imposed by the driving machine (speed controlled), while the machine under test was torque controlled. The experimental results concerns the drive operation under healthy and open-winding fault conditions.

The faulty condition means open phases after sudden shut-off of one or more VSI units due to a failure in power electronics.

Fast torque transients in healthy conditions

The drive has been tested in both motoring and generating operation. With reference to (4.2)-(4.3), the following conditions have been set:

$$\begin{cases} f_s = 5\,\text{kHz} & \\ v_{dc,k} = 270\,\text{V} & (k = 1 \div 4) \\ \omega_m = -6000\,\text{r/min} & \\ \delta_{max,k} = 45° & (k = 1 \div 4) \\ s_\lambda = 3 \rightarrow \lambda_s^* = \lambda_{s,rated} & \\ T_k^* = \dfrac{T^*}{4} & (k = 1 \div 4) \end{cases} \tag{4.4}$$

Settings (4.4) correspond to the balanced operation of the machine. Since the drive is characterized by identical three-phase units, this testing condition represents a realistic operating scenario for the considered machine.

It is noted how the tests have been performed by imposing the machine's rated flux value to all units (0.115 Vs), allowing high-dynamic torque variations together with a proper magnetizing current injection.

The execution of the fast torque transients has led to the performance validation of each *k*-unit PI-based regulation (*k*=1,2,3,4). In addition, the effectiveness of the proposed decoupling algorithm has been verified.

The experimental results for the fast torque transient (10 Nm/ms) from -24 Nm to +24 Nm (150% of rated value) are shown in Fig. 4. 14 - Fig. 4. 16. Each three-phase winding set provides a quarter of the total torque, corresponding to ±6 Nm. In motoring mode, the drive has been operated under both unit limitations in terms of voltage (flux-weakening) and current, thus not allowing the satisfaction of the torque target.

Despite the high slew-rate of the mechanical power from -15 kW to +15 kW in just 5 ms, the good dynamic torque response is noted, as shown in Fig. 4. 14 and Fig. 4. 16. Due to internal asymmetries, the three-phase set 2 is imbalanced with respect to the other ones, leading to more oscillations in terms of torque contribution and (d_{s2},q_{s2}) currents.

In addition, the phase currents of the unit 2 are more distorted with respect to the ones belonging to the other units. This is confirmed in Fig. 4. 20 that shows the machine currents ($i_{s1\text{-}a}$,$i_{s2\text{-}a}$,$i_{s3\text{-}a}$,$i_{s3\text{-}a}$) for the fast torque transient (10 Nm/ms) from zero up to 24 Nm (Fig. 4. 17 - Fig. 4. 19). Despite these asymmetries related to the machine manufacturing, each *k*-unit DFVC scheme is able to deal with the direct and independent control of both *k*-unit flux amplitude and *k*-unit torque contribution.

Experimental results for fast torque transient (10 Nm/ms) from 150% rated torque in motoring to 150% rated torque in generation at -6000 r/min

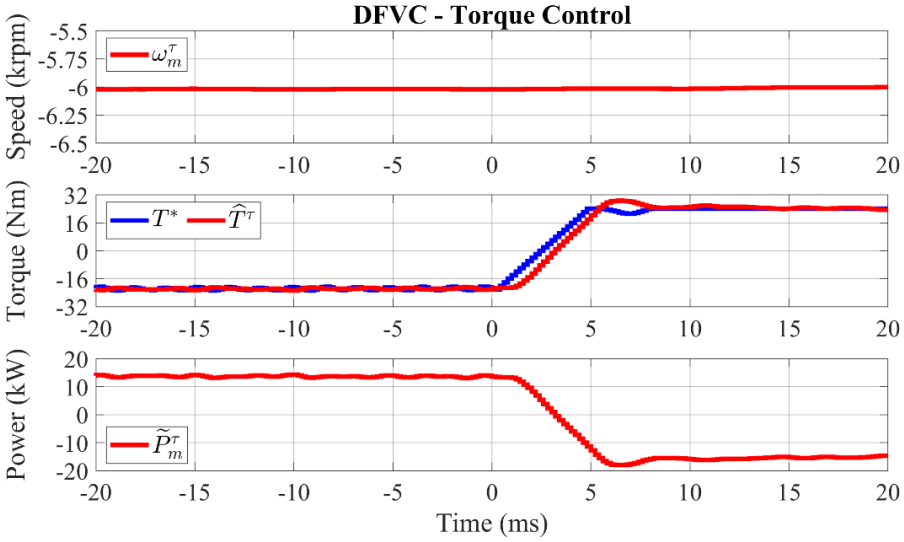

Fig. 4. 14. From top to bottom: measured speed (10^3 · r/min); reference and observed machine torque (Nm); estimated mechanical power (kW).

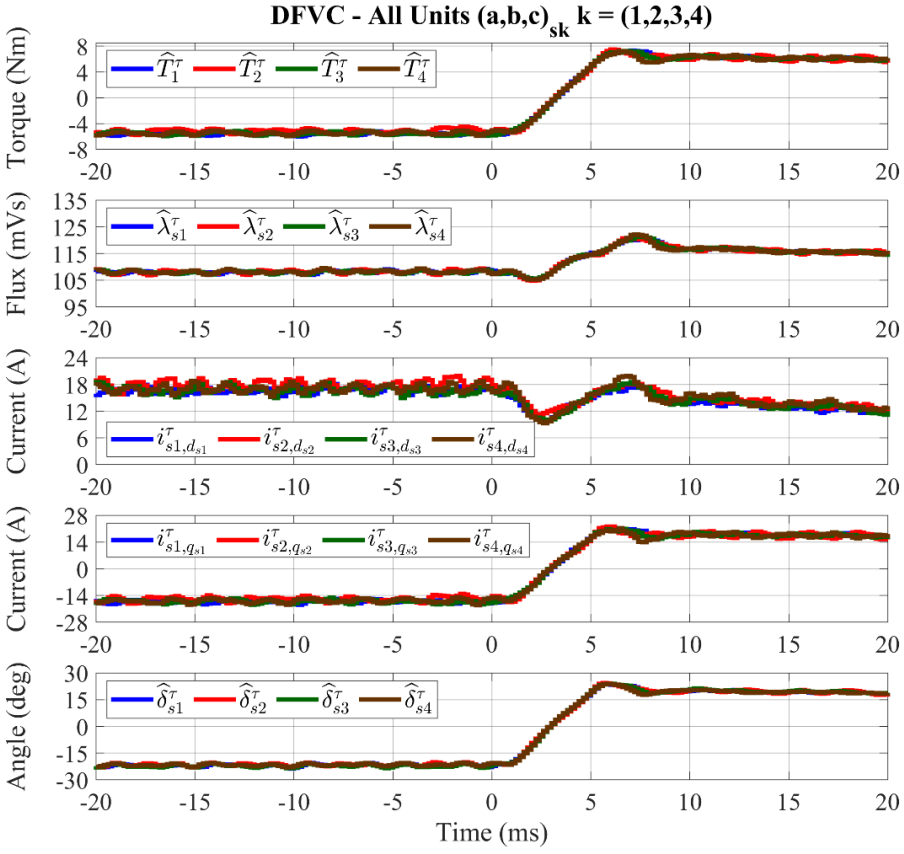

Fig. 4. 15. From top to bottom: single units observed torque (Nm); single units observed flux amplitude (mVs); single units measured d_{sk}-axis current (A); single units measured q_{sk}-axis current (A); single units observed load-angle (deg).

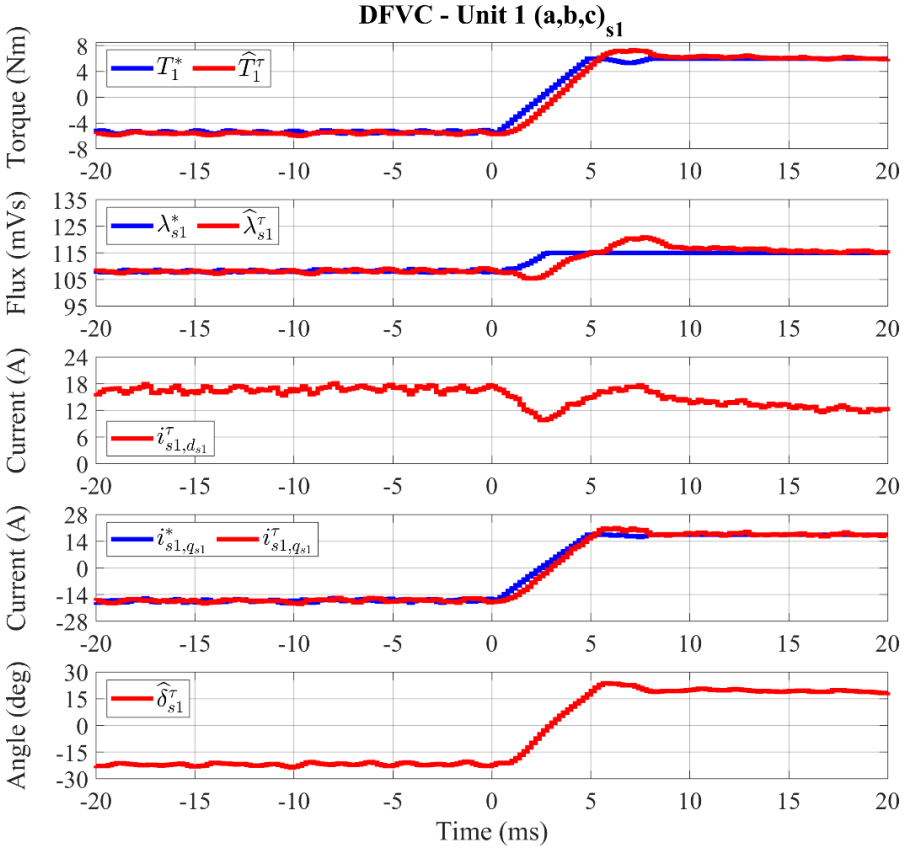

See figure caption: Fig. 4. 16

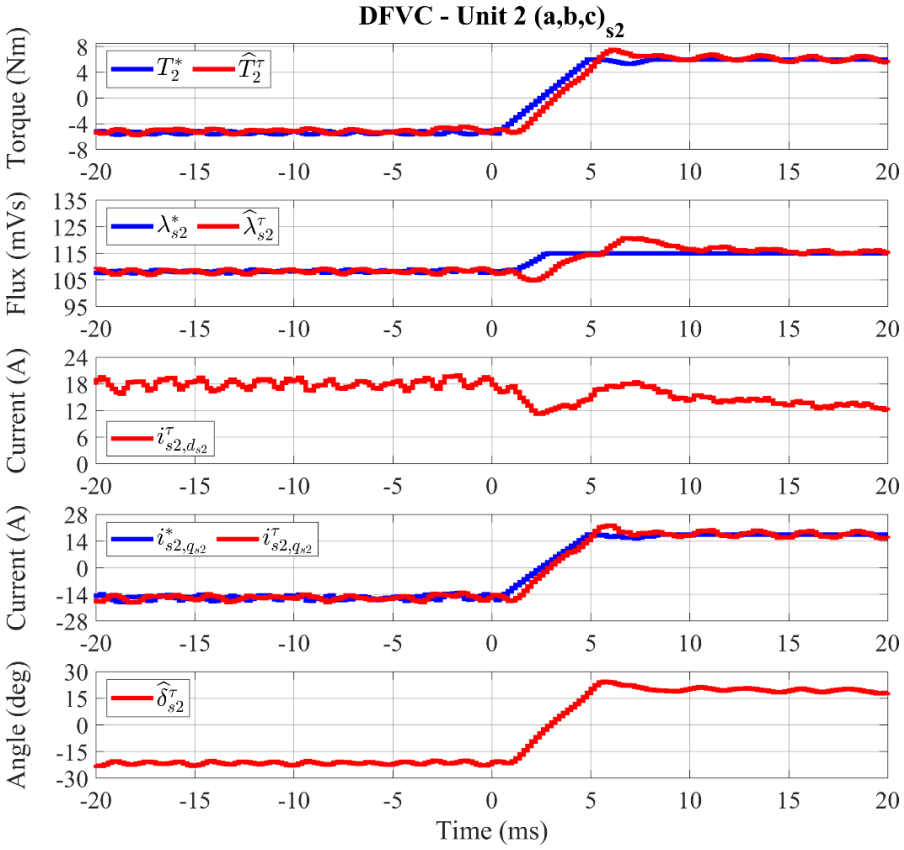

See figure caption: Fig. 4. 16

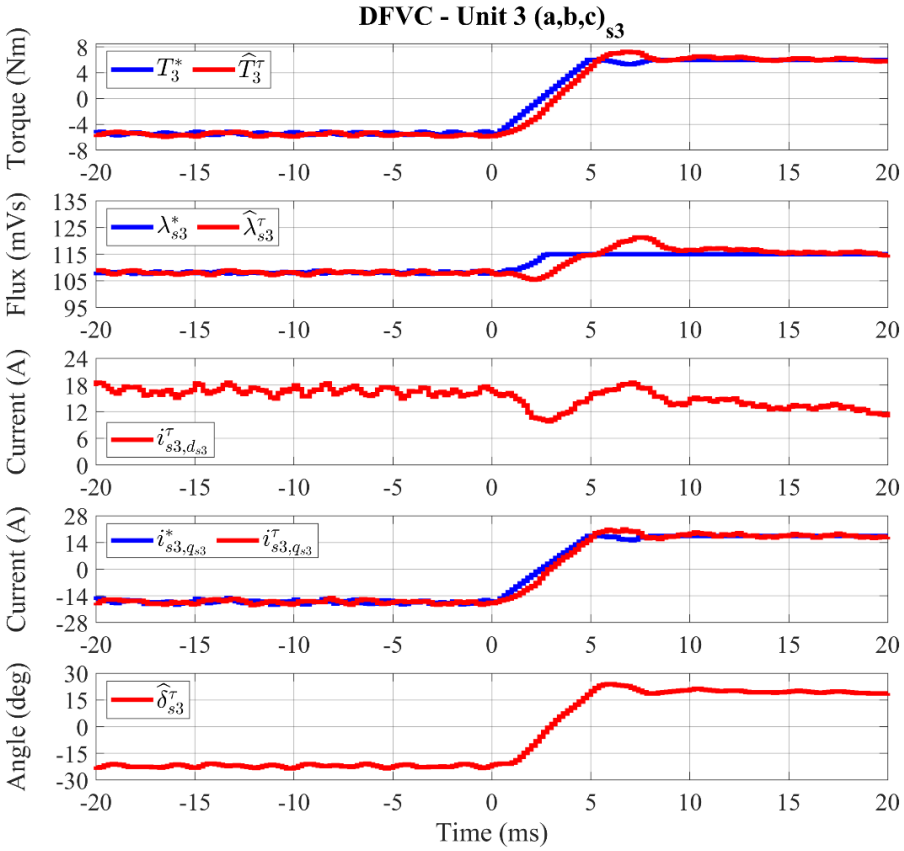

See figure caption: Fig. 4. 16

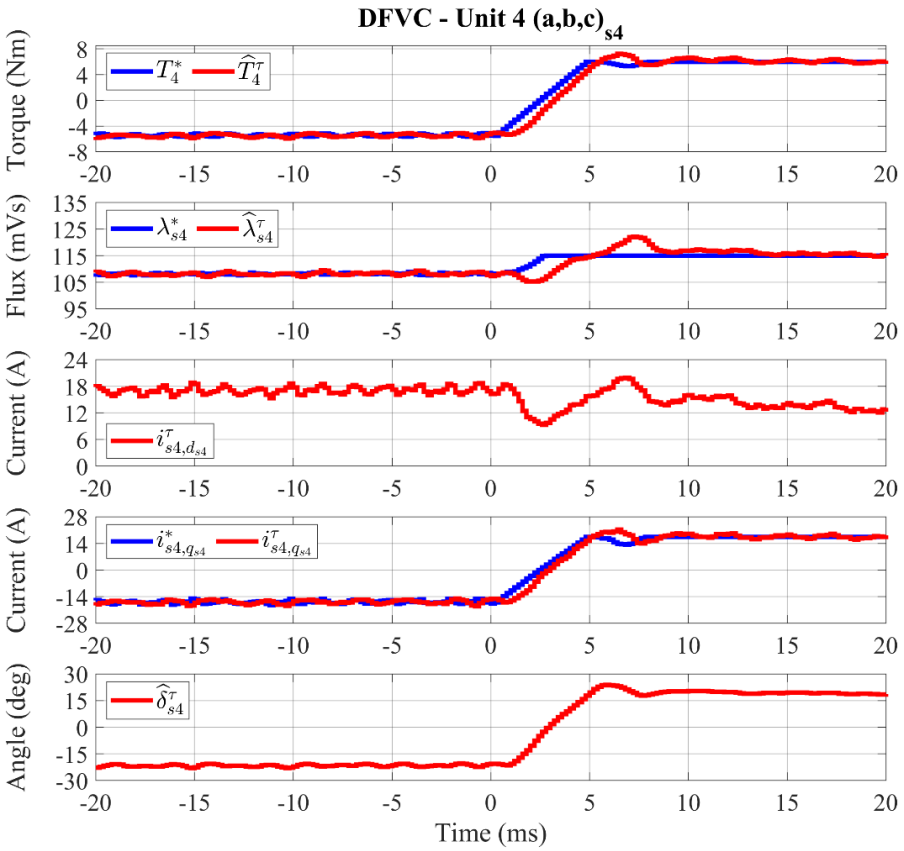

Fig. 4. 16. For each *k*-unit DFVC scheme, from top to bottom: reference and observed torque (Nm); reference and observed flux amplitude (mVs); measured d_{sk}-axis current (A); reference and measured q_{sk}-axis current (A); observed load-angle (deg).

Experimental results for fast torque transient (10 Nm/ms) from no-load (0 Nm) up to 150% rated torque (24 Nm) in generation at -6000 r/min

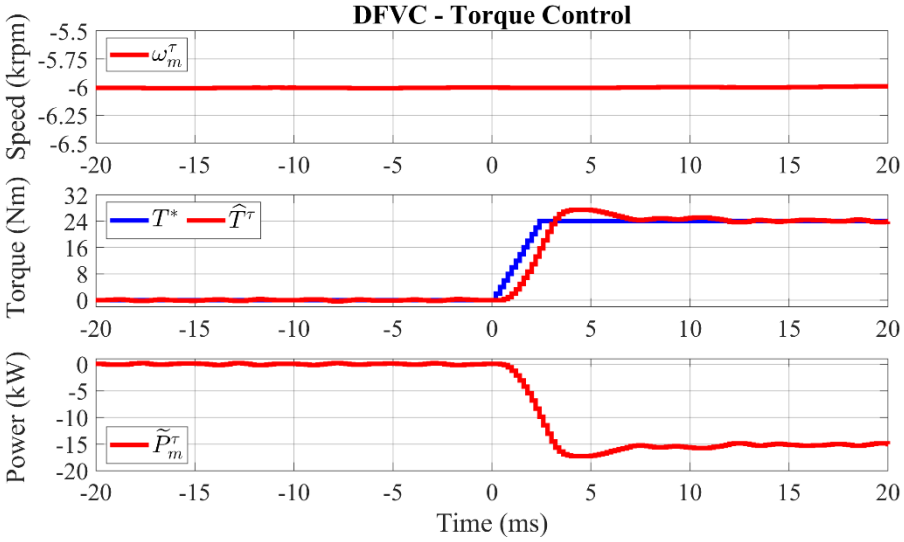

Fig. 4. 17. From top to bottom: measured speed (10^3 · r/min); reference and observed machine torque (Nm); estimated mechanical power (kW).

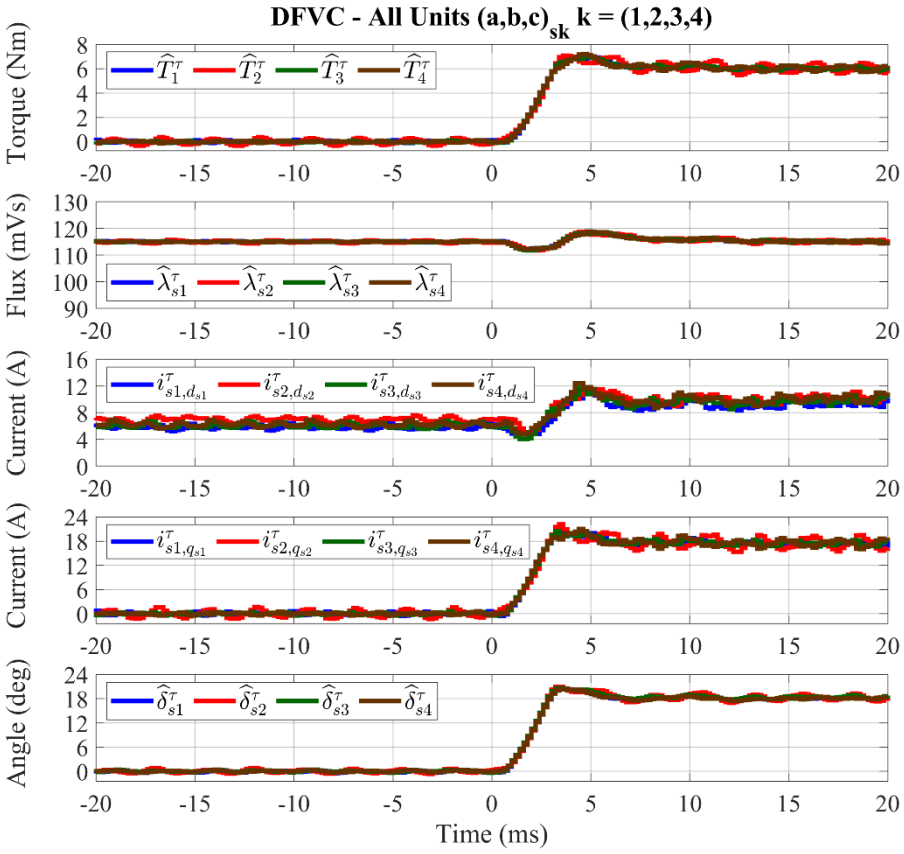

Fig. 4. 18. From top to bottom: single units observed torque (Nm); single units observed flux amplitude (mVs); single units measured d_{sk}-axis current (A); single units measured q_{sk}-axis current (A); single units observed load-angle (deg).

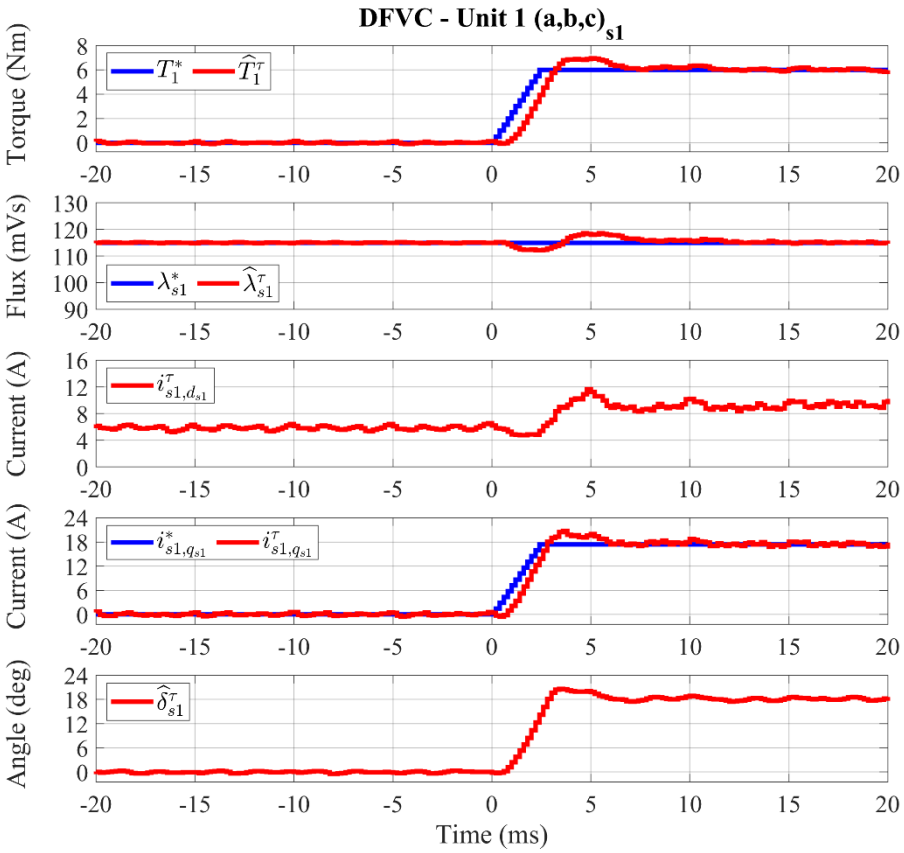

See figure caption: Fig. 4. 19

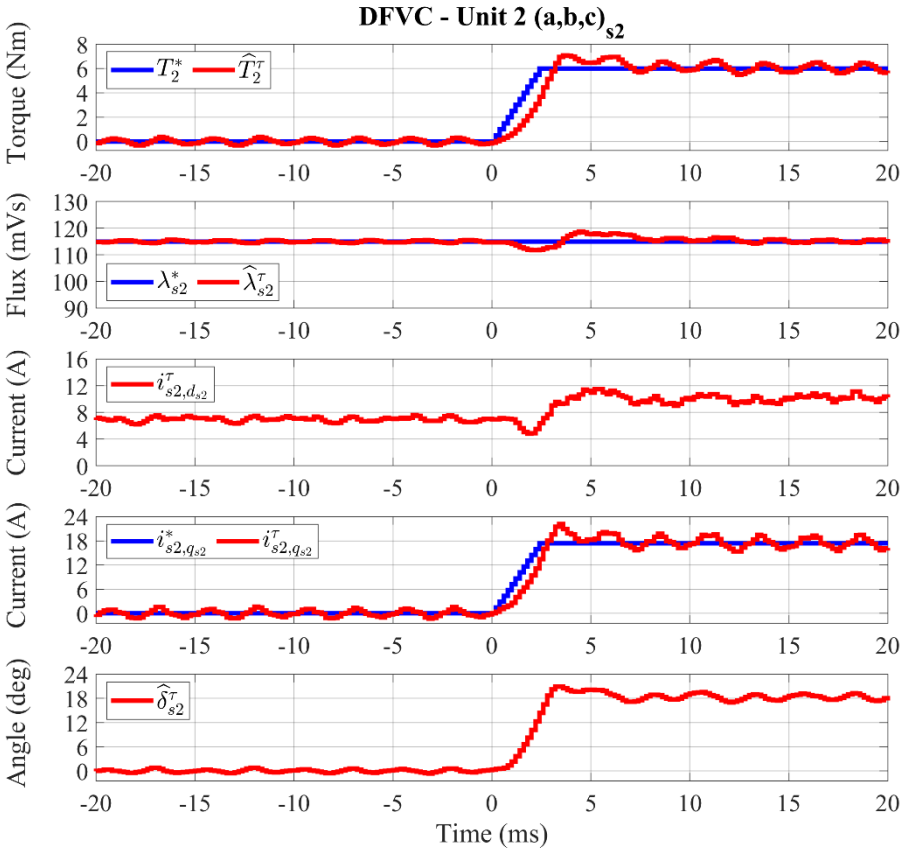

See figure caption: Fig. 4. 19

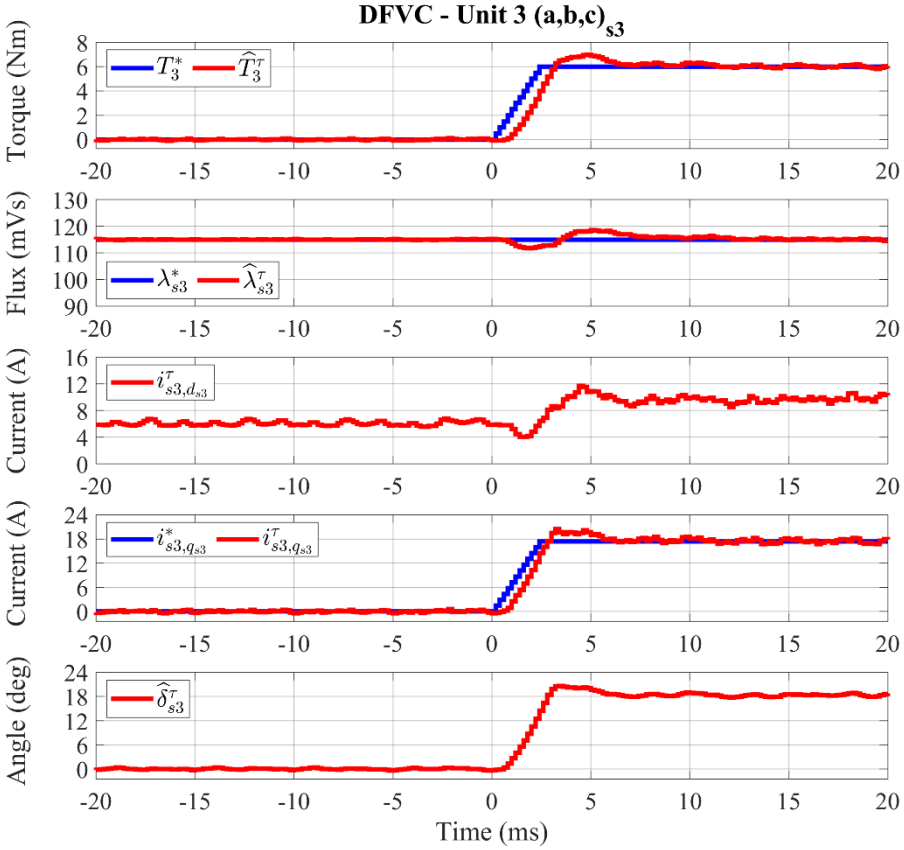

See figure caption: Fig. 4. 19

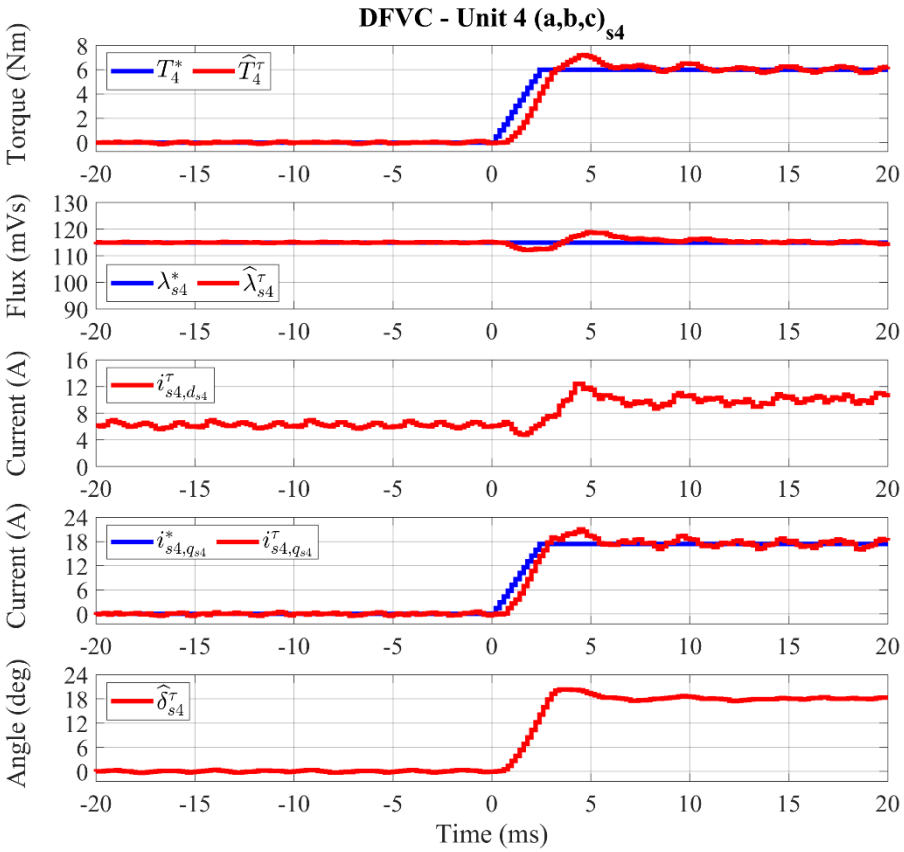

Fig. 4. 19. For each *k*-unit DFVC scheme, from top to bottom: reference and observed torque (Nm); reference and observed flux amplitude (mVs); measured d_{sk}-axis current (A); reference and measured q_{sk}-axis current (A); observed load-angle (deg).

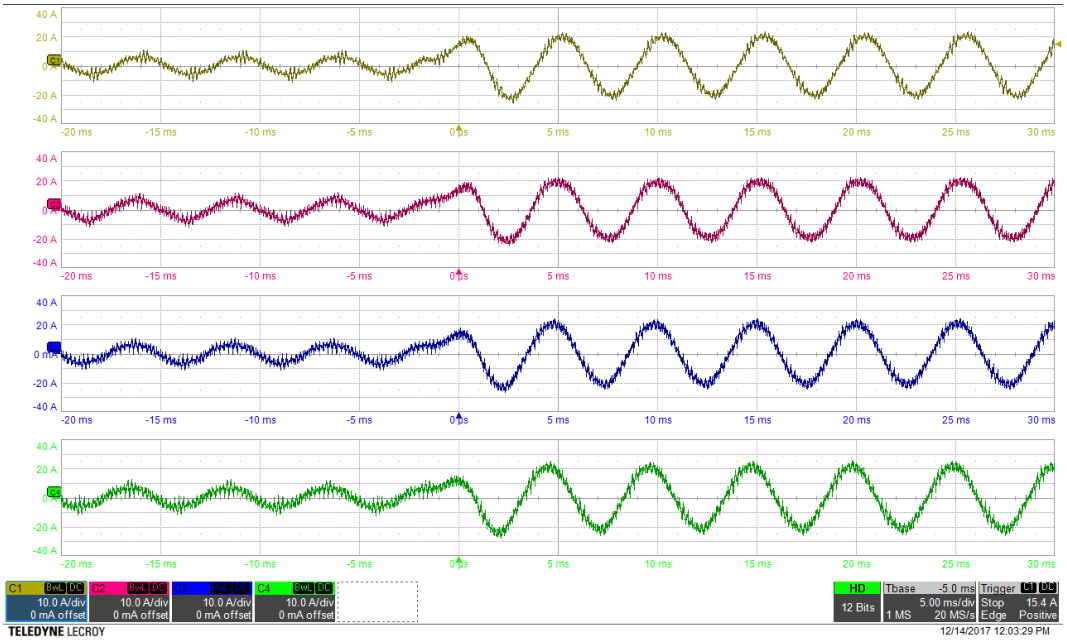

Fig. 4. 20. Fast torque transient from no-load up to 150% rated torque (24 Nm) at -6000 r/min. Ch1: $i_{s1\text{-}a}$ (10 A/div), Ch2: $i_{s2\text{-}a}$ (10 A/div), Ch3: $i_{s3\text{-}a}$ (10 A/div), Ch4: $i_{s4\text{-}a}$ (10 A/div). Time resolution: 5 ms/div.

Fault ride-through capability for open three-phase set

The drive has been tested in generating operation. With reference to (4.2)-(4.3), the following conditions have been set:

$$\begin{cases} f_s = 5\,\text{kHz} & \\ v_{dc,k} = 270\,\text{V} & (k = 1 \div 4) \\ \omega_m = -6000\,\text{r/min} & \\ \delta_{max,k} = 45° & (k = 1 \div 4) \\ s_\lambda = 3 \rightarrow \lambda_s^* = \lambda_{s,rated} & \\ T_k^* = x_{f,k}^{\tau} \cdot \dfrac{T^*}{n_a} & (k = 1 \div 4) \end{cases} \tag{4.5}$$

To demonstrate the drive "fault ride-through" capability when one or more VSI units are suddenly disabled, they are shown the experimental results for the following tests:

- Open-phase operation for sudden VSI 2 turn-off at the rated torque 16 Nm (Fig. 4. 21 - Fig. 4. 24);
- Open-phase operation for sudden VSI 3 turn-off with VSI 2 already OFF at 10 Nm (Fig. 4. 25 - Fig. 4. 28);
- Open-phase operation for sudden VSI 4 turn-off with VSIs 2-3 already OFF at 2 Nm (Fig. 4. 29 - Fig. 4. 32).

It is noted how the healthy units exhibit sinusoidal currents that increase within the allowed limits to keep the same torque and machine flux, as shown in Fig. 4. 24, Fig. 4. 28 and Fig. 4. 32. However, the phase-currents amplitudes for the healthy units are slightly different, demonstrating some machine asymmetries that is mitigated without problem by the control scheme. This is the proof of the modularity of the MS-based control schemes, with the maximum degree of freedom in the control of each single unit.

Finally, to demonstrate the torque capability with one or more disabled VSI units, the fast torque transient (10 Nm/ms) from no-load up to 10 Nm using only the VSI units 1 and 4 is shown in Fig. 4. 33 - Fig. 4. 36.

Experimental results for sudden VSI 2 turn-off during generation mode with torque control at -6000 r/min with 16 Nm (rated torque)

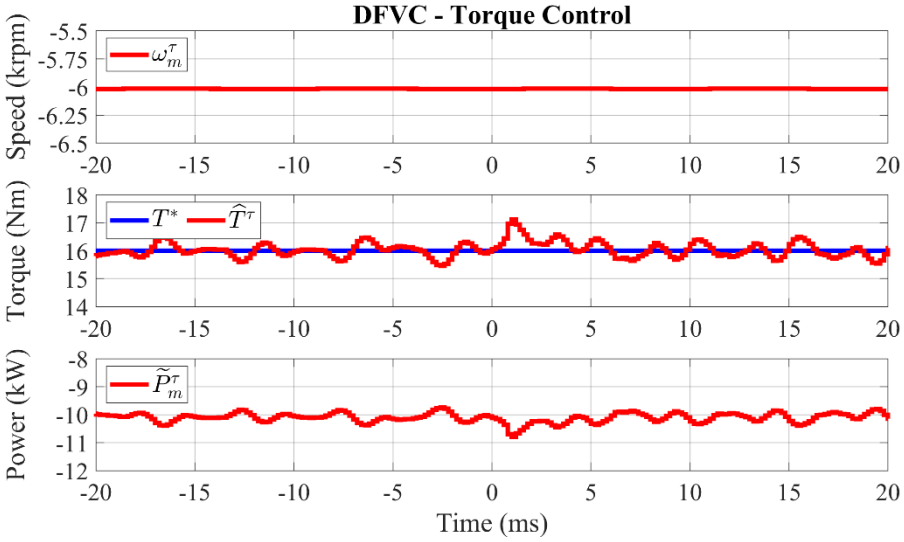

Fig. 4. 21. From top to bottom: measured speed (10^3 · r/min); reference and observed machine torque (Nm); estimated mechanical power (kW).

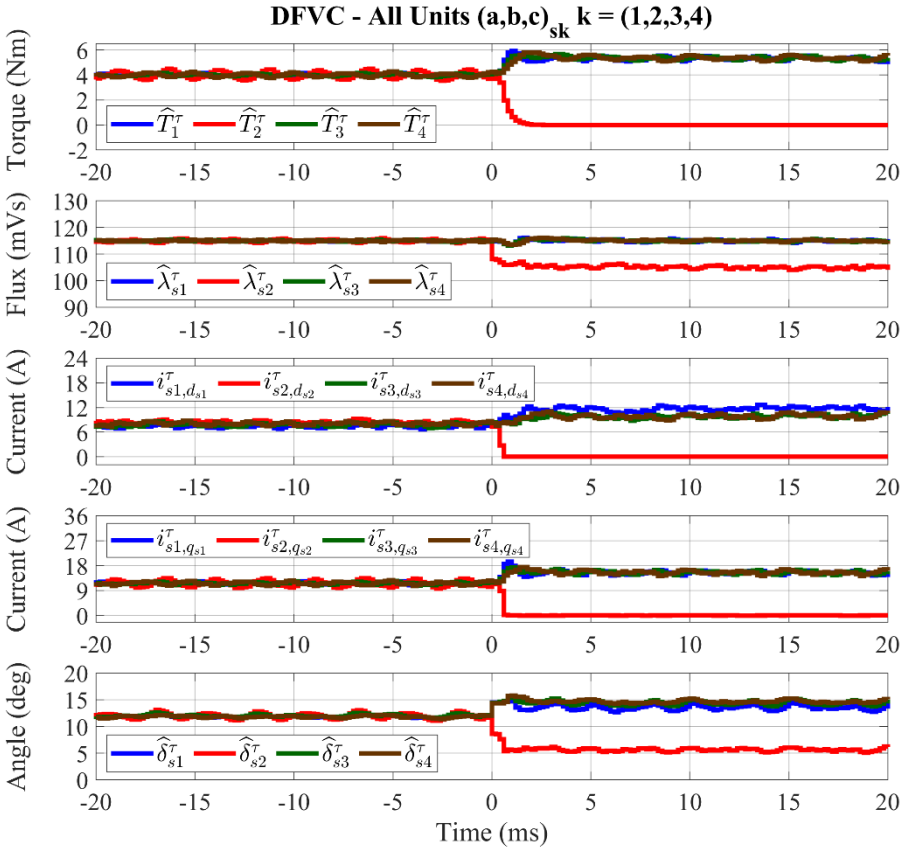

Fig. 4. 22. From top to bottom: single units observed torque (Nm); single units observed flux amplitude (mVs); single units measured d_{sk}-axis current (A); single units measured q_{sk}-axis current (A); single units observed load-angle (deg).

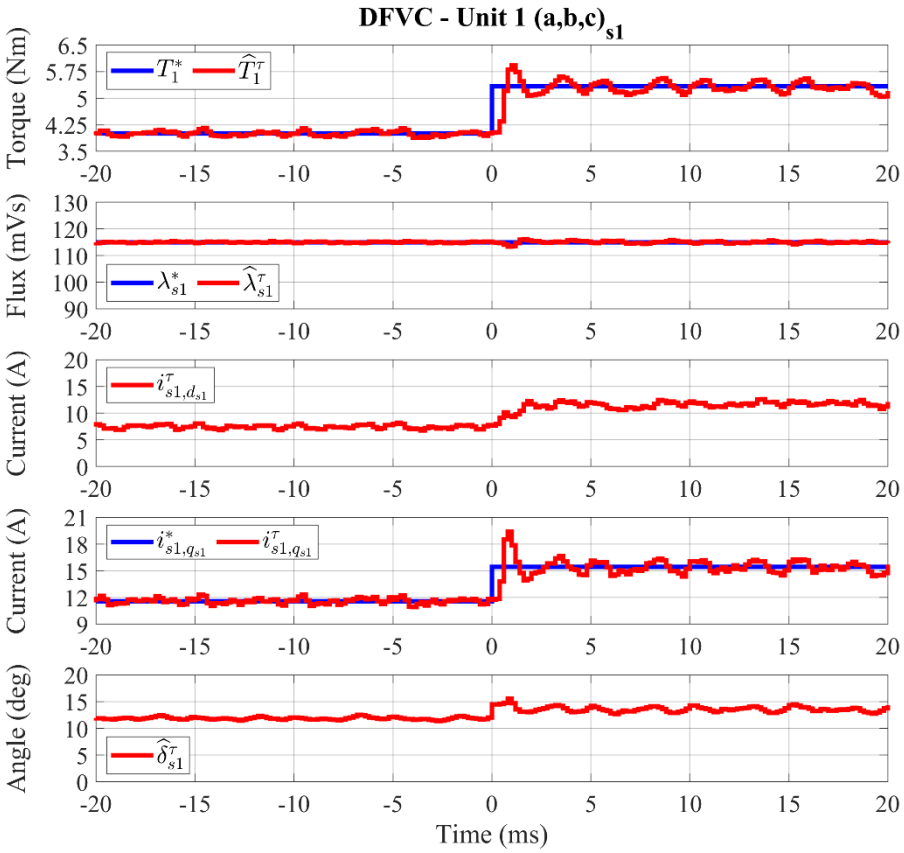

See figure caption: Fig. 4. 23

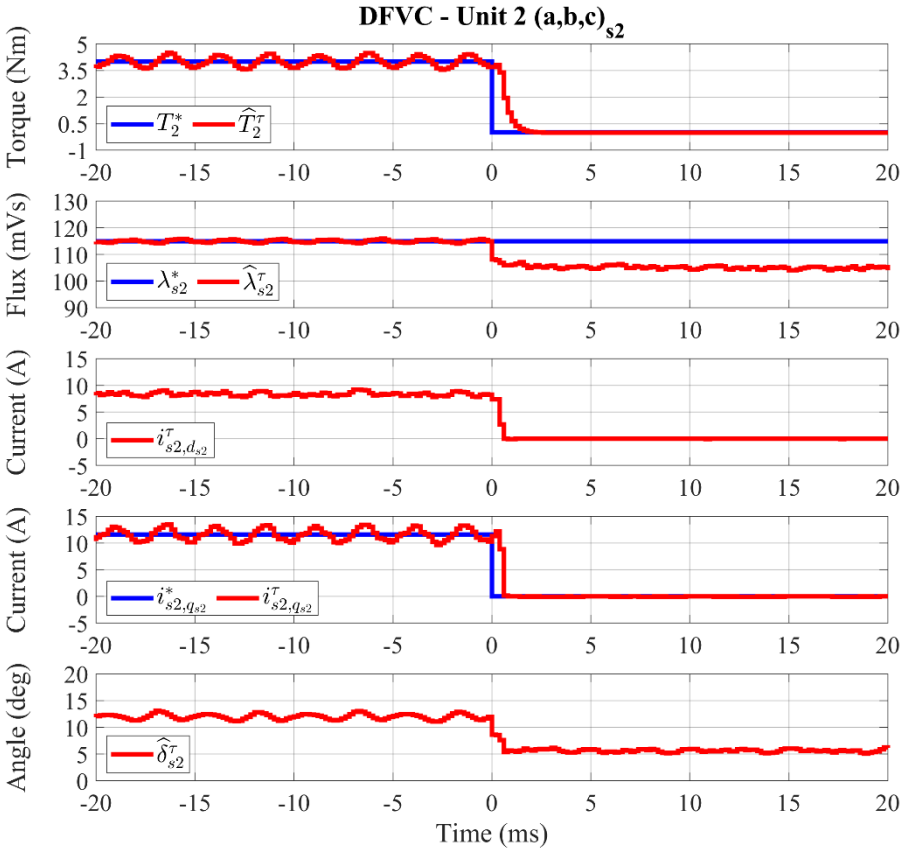

See figure caption: Fig. 4. 23

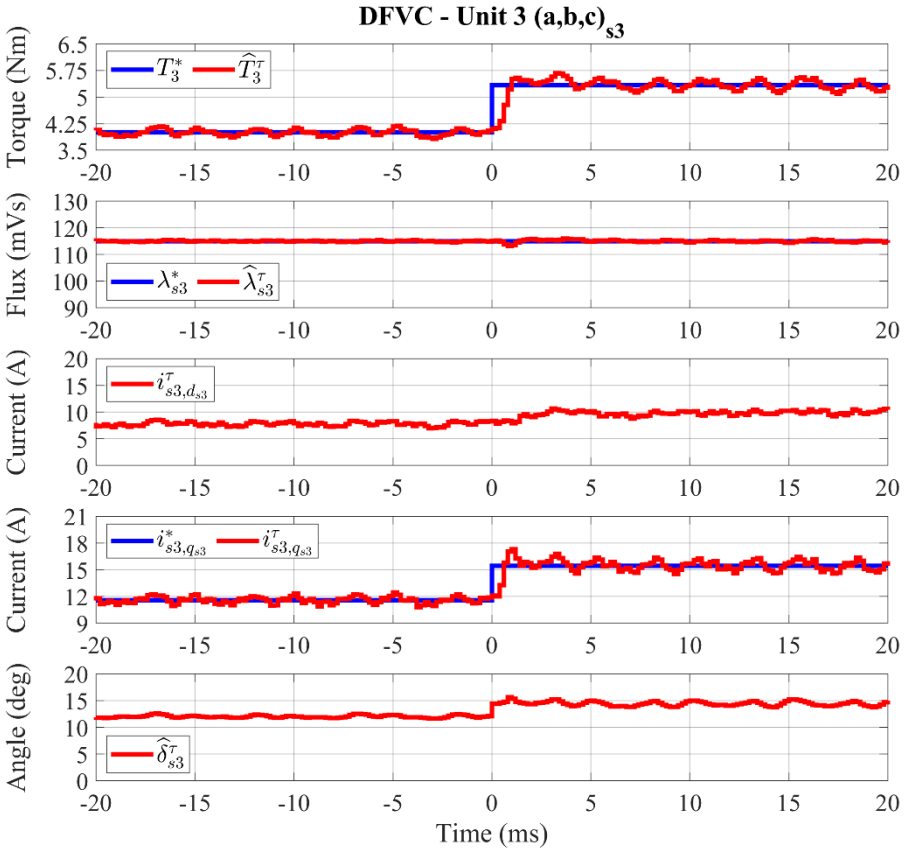

See figure caption: Fig. 4. 23

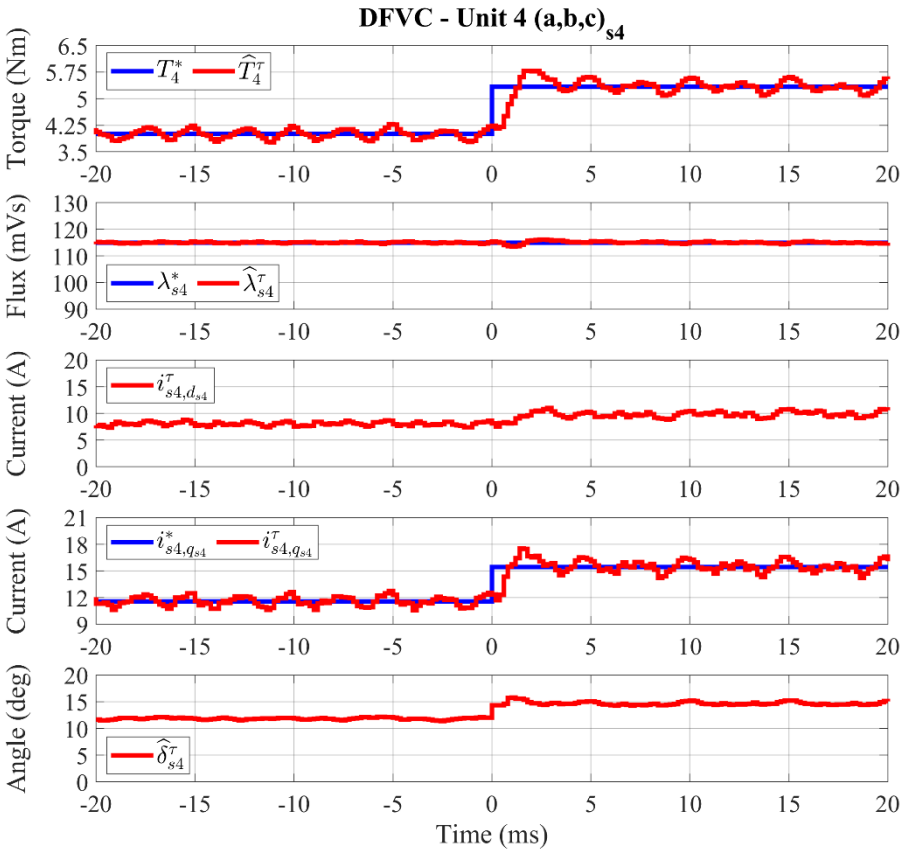

Fig. 4. 23. For each *k*-unit DFVC scheme, from top to bottom: reference and observed torque (Nm); reference and observed flux amplitude (mVs); measured d_{sk}-axis current (A); reference and measured q_{sk}-axis current (A); observed load-angle (deg).

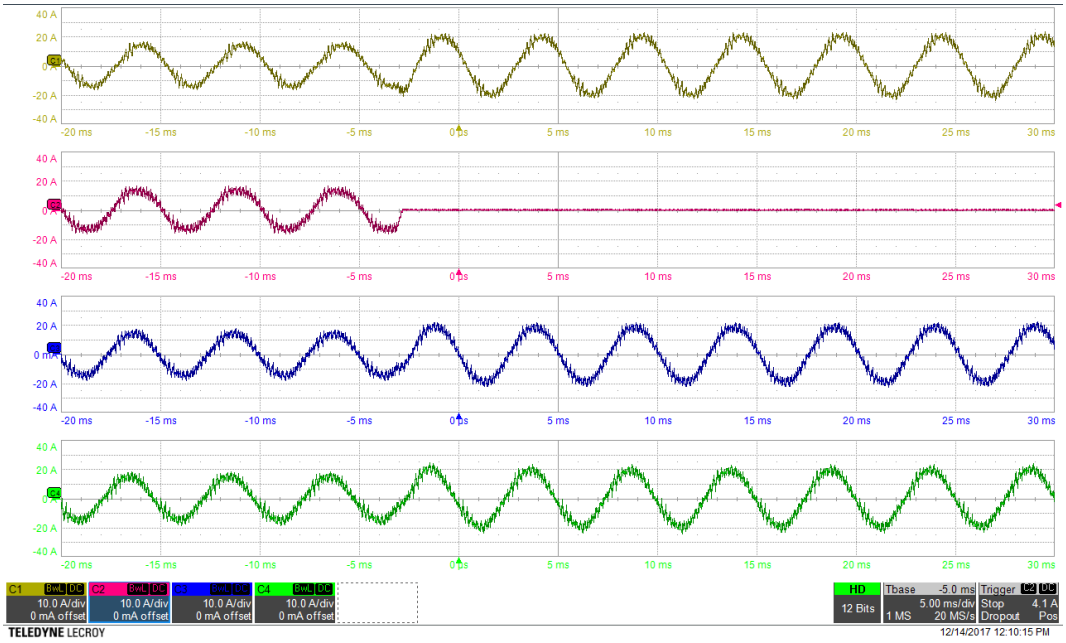

Fig. 4. 24. Ch1: $i_{s1\text{-}a}$ (10 A/div), Ch2: $i_{s2\text{-}a}$ (10 A/div), Ch3: $i_{s3\text{-}a}$ (10 A/div), Ch4: $i_{s4\text{-}a}$ (10 A/div). Time resolution: 5 ms/div.

Experimental results for sudden VSI 3 turn-off with VSI 2 already OFF during generation mode with torque control at -6000 r/min with 10 Nm

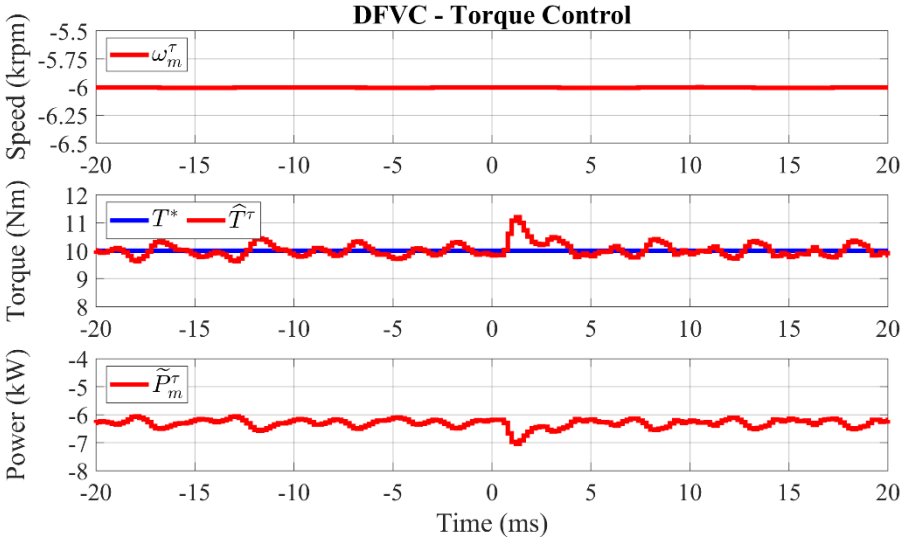

Fig. 4. 25. From top to bottom: measured speed (10^3 · r/min); reference and observed machine torque (Nm); estimated mechanical power (kW).

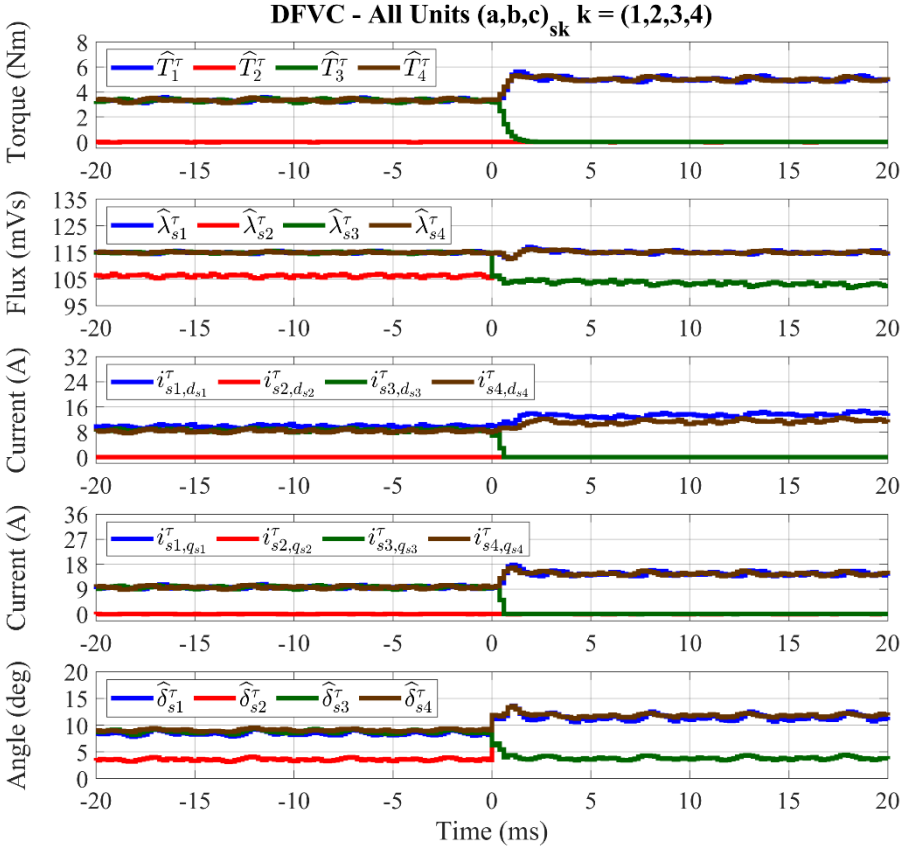

Fig. 4. 26. From top to bottom: single units observed torque (Nm); single units observed flux amplitude (mVs); single units measured d_{sk}-axis current (A); single units measured q_{sk}-axis current (A); single units observed load-angle (deg).

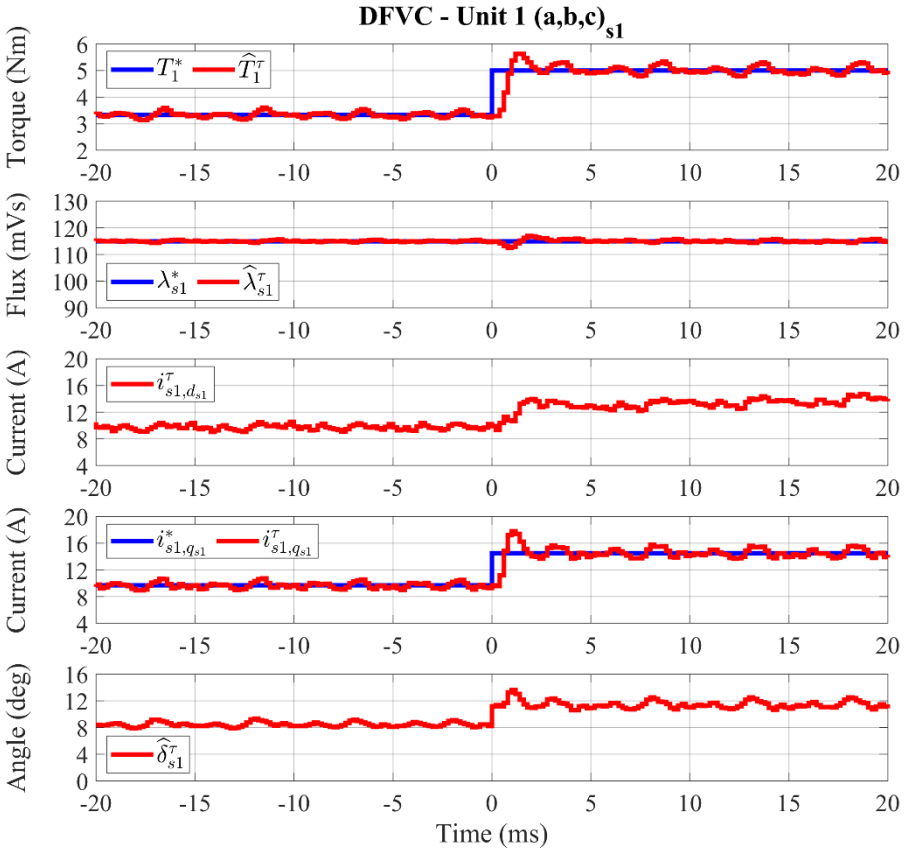

See figure caption: Fig. 4. 27

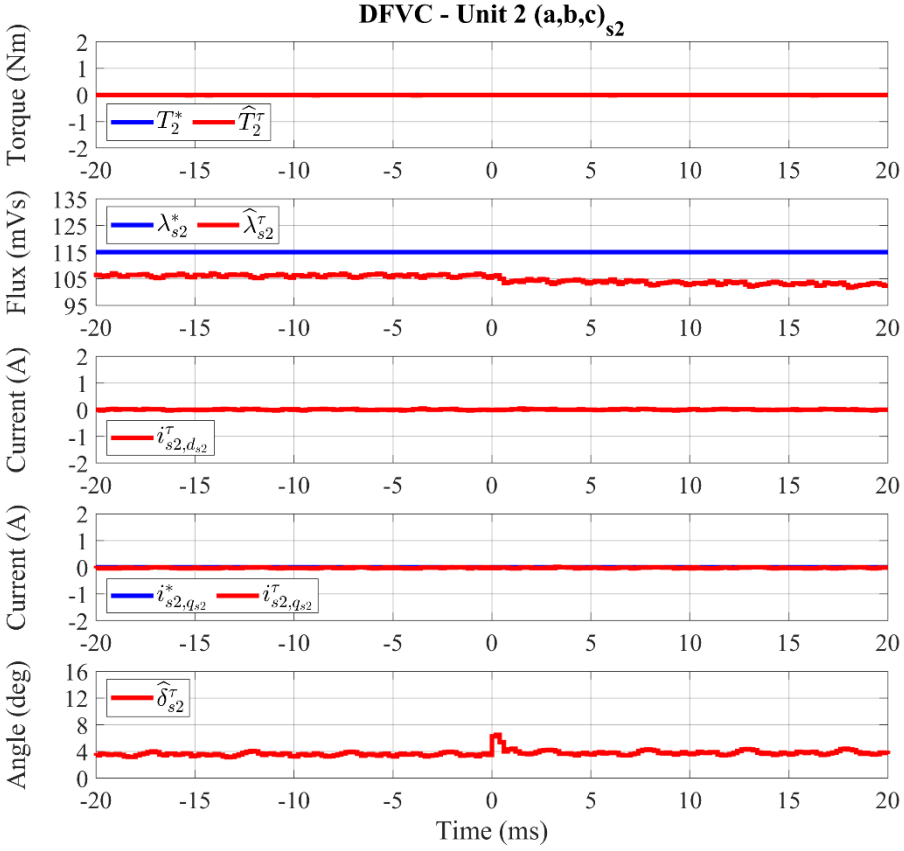

See figure caption: Fig. 4. 27

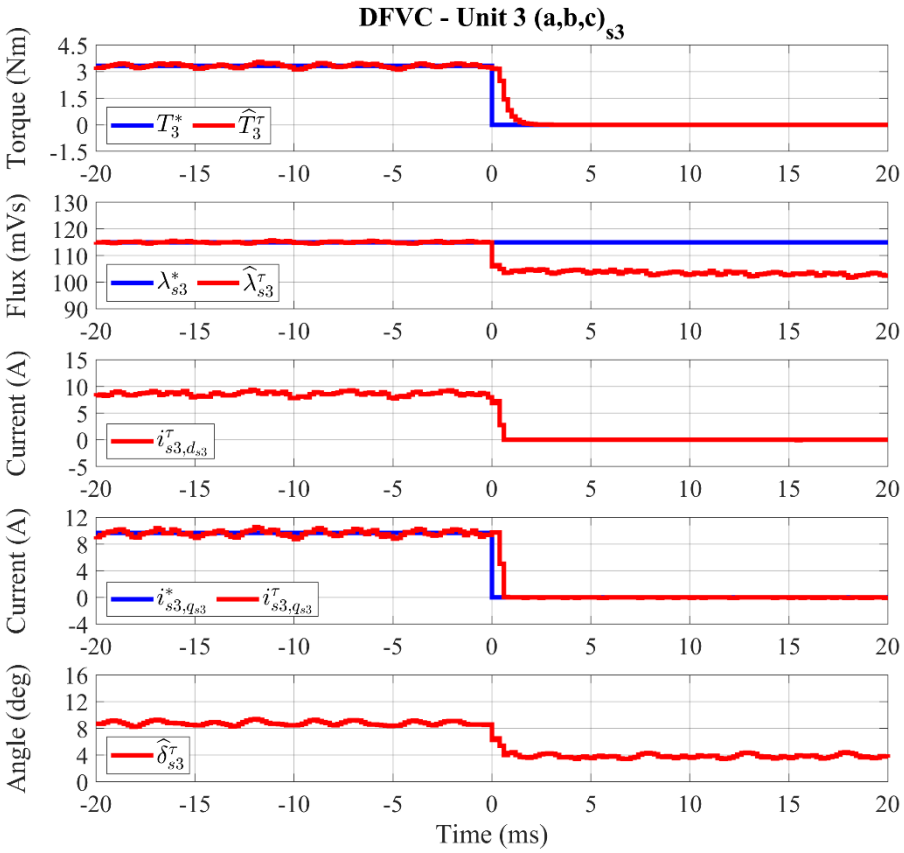

See figure caption: Fig. 4. 27

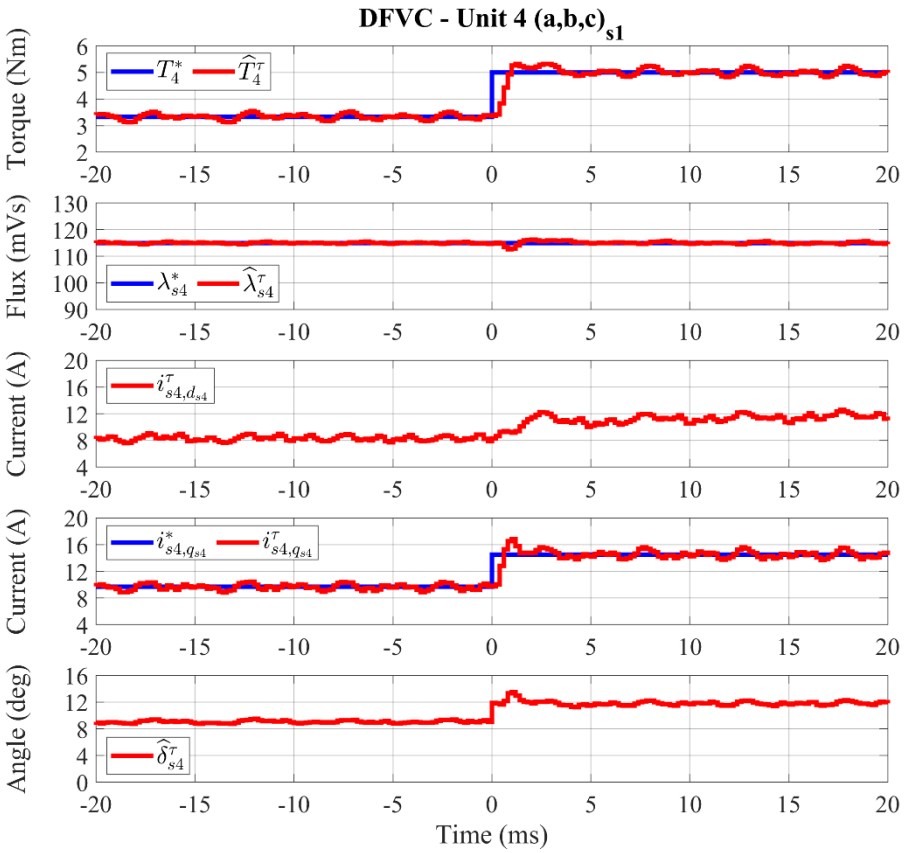

Fig. 4. 27. For each *k*-unit DFVC scheme, from top to bottom: reference and observed torque (Nm); reference and observed flux amplitude (mVs); measured d_{sk}-axis current (A); reference and measured q_{sk}-axis current (A); observed load-angle (deg).

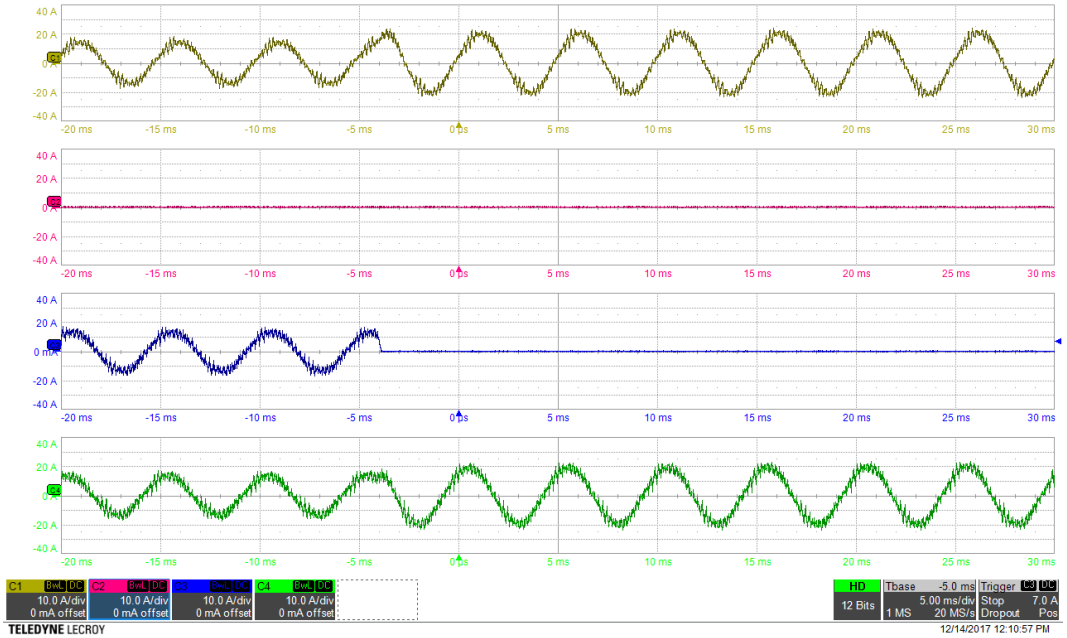

Fig. 4. 28. Ch1: $i_{s1\text{-}a}$ (10 A/div), Ch2: $i_{s2\text{-}a}$ (10 A/div), Ch3: $i_{s3\text{-}a}$ (10 A/div), Ch4: $i_{s4\text{-}a}$ (10 A/div). Time resolution: 5 ms/div.

Experimental results for sudden VSI 3 turn-off with VSIs 2-3 already OFF during generation mode with torque control at -6000 r/min with 2 Nm

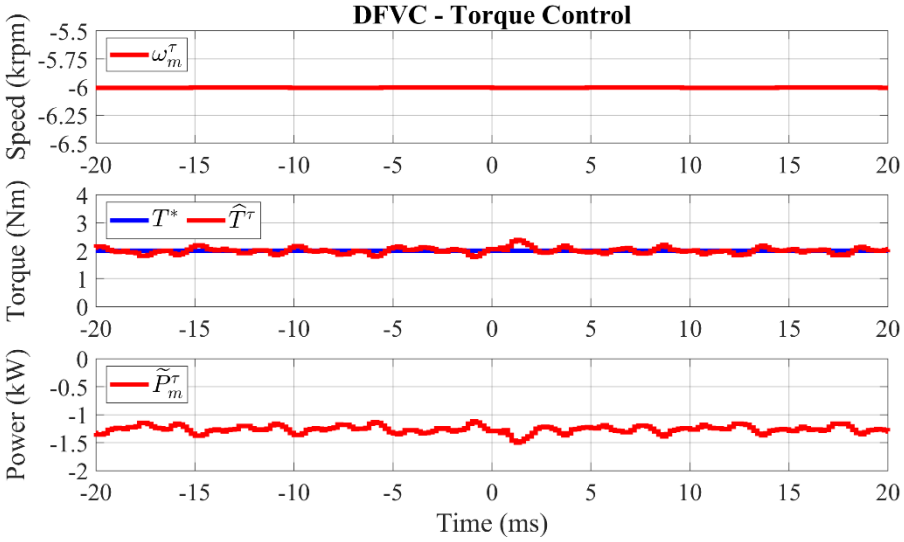

Fig. 4. 29. From top to bottom: measured speed (10^3 · r/min); reference and observed machine torque (Nm); estimated mechanical power (kW).

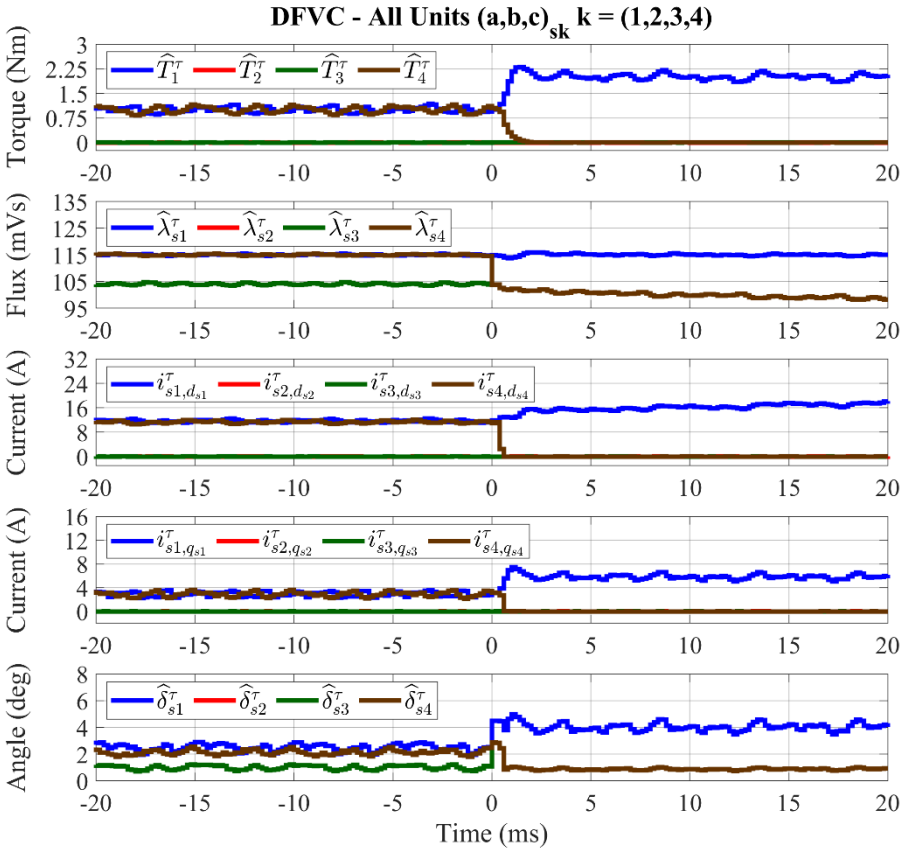

Fig. 4. 30. From top to bottom: single units observed torque (Nm); single units observed flux amplitude (mVs); single units measured d_{sk}-axis current (A); single units measured q_{sk}-axis current (A); single units observed load-angle (deg).

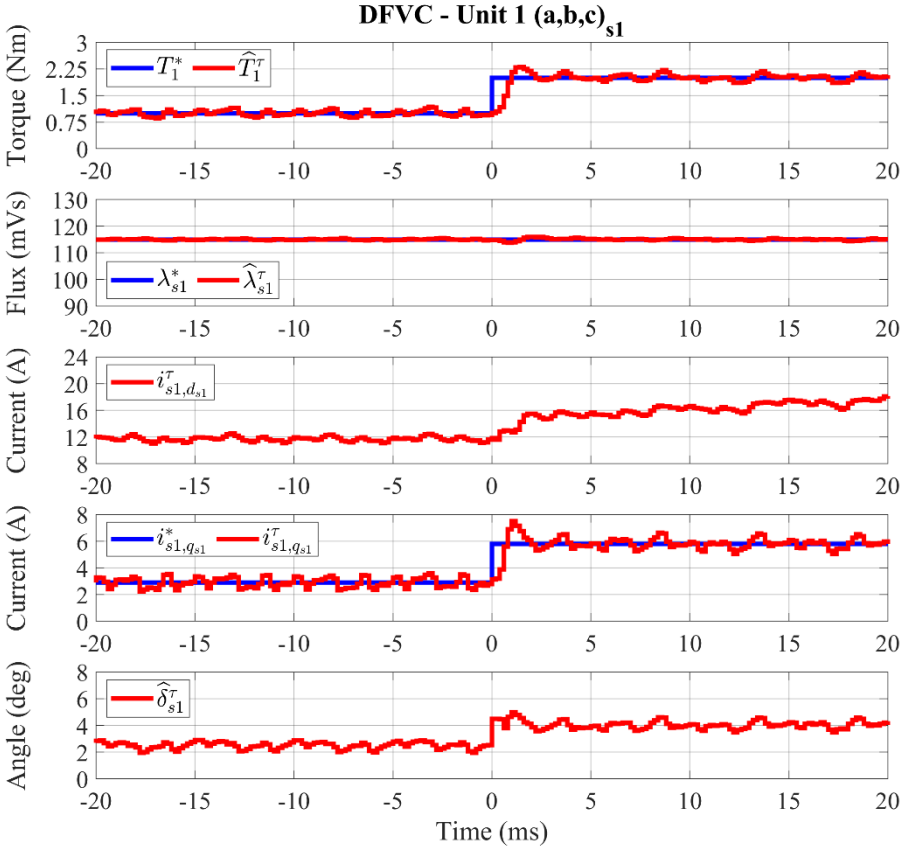

See figure caption: Fig. 4. 31

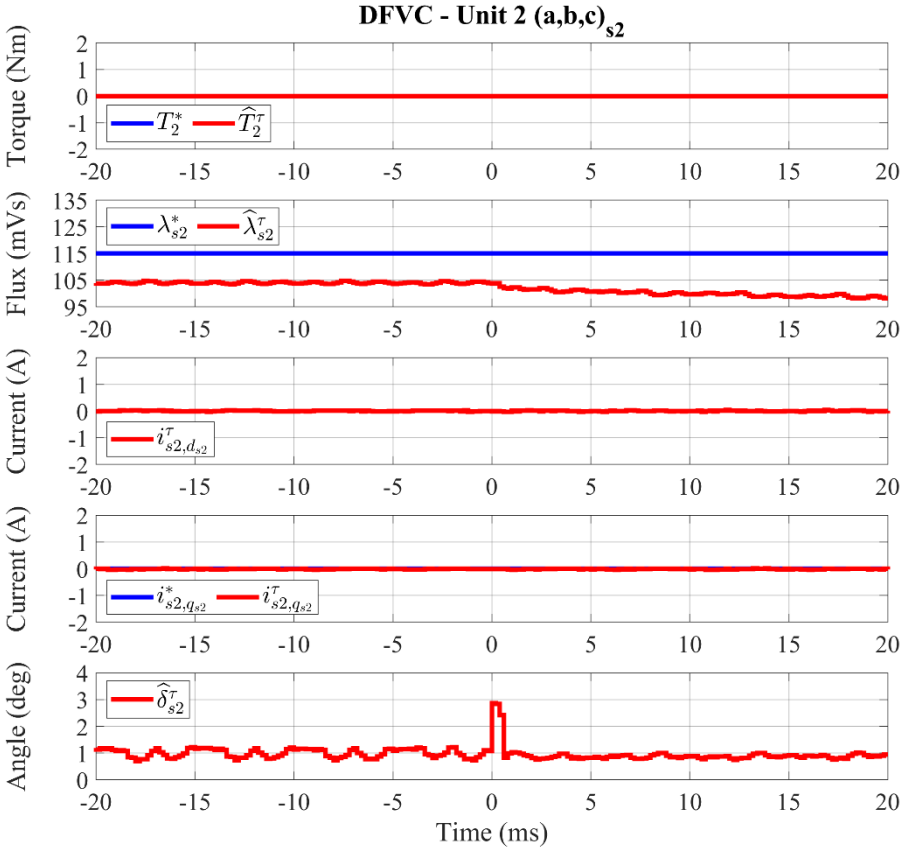

See figure caption: Fig. 4. 31

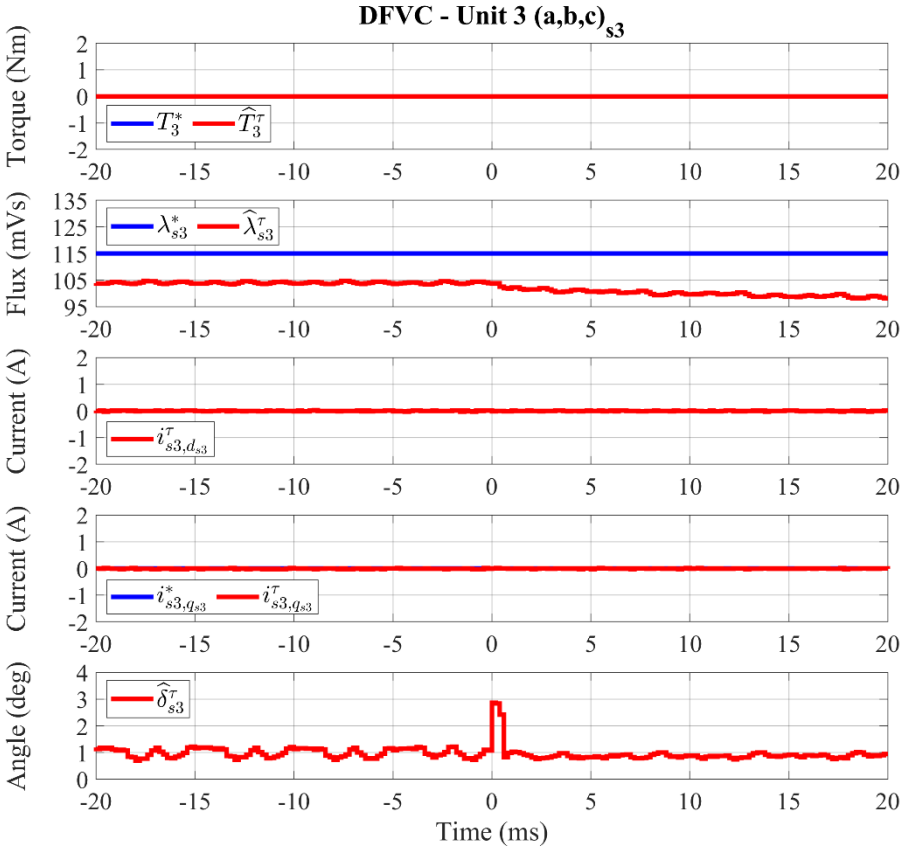

See figure caption: Fig. 4. 31

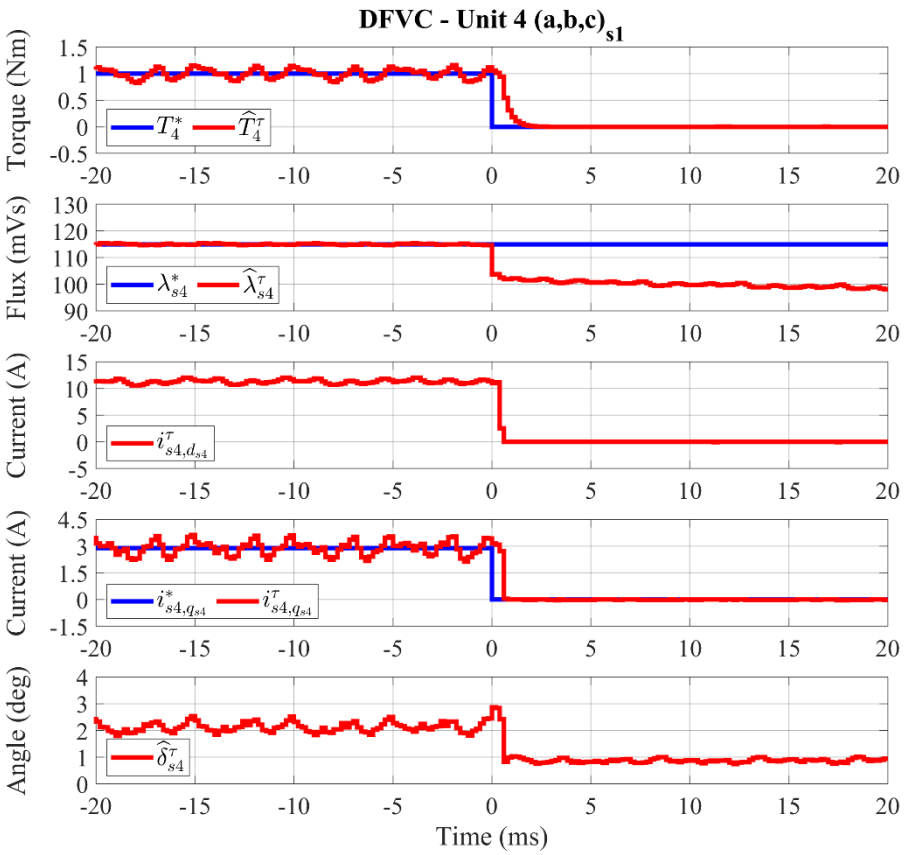

Fig. 4. 31. For each *k*-unit DFVC scheme, from top to bottom: reference and observed torque (Nm); reference and observed flux amplitude (mVs); measured d_{sk}-axis current (A); reference and measured q_{sk}-axis current (A); observed load-angle (deg).

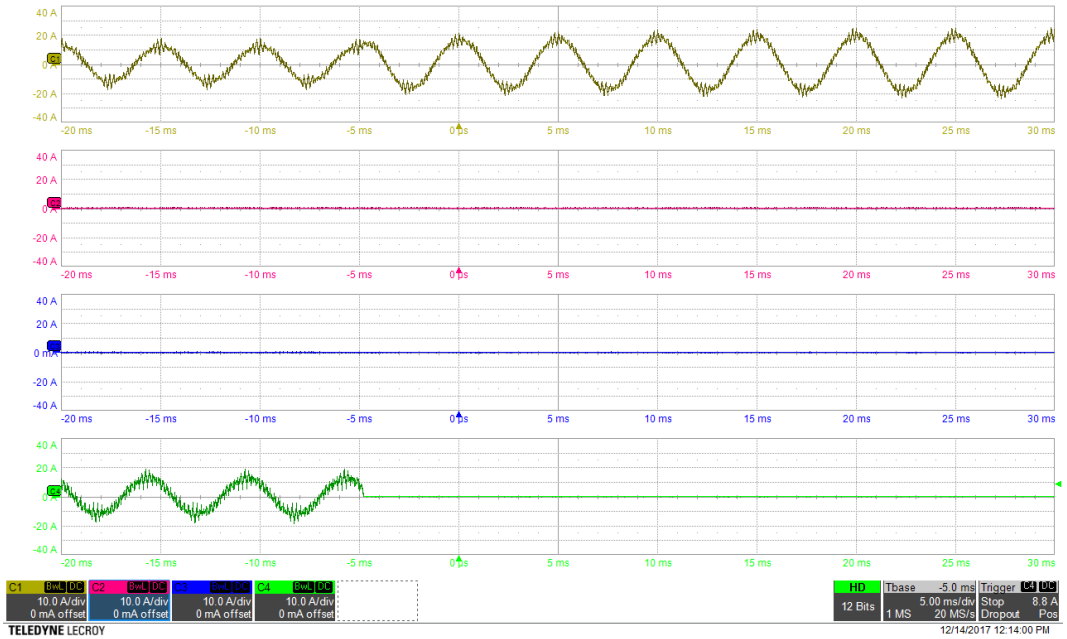

Fig. 4. 32. Ch1: $i_{s1\text{-}a}$ (10 A/div), Ch2: $i_{s2\text{-}a}$ (10 A/div), Ch3: $i_{s3\text{-}a}$ (10 A/div), Ch4: $i_{s4\text{-}a}$ (10 A/div). Time resolution: 5 ms/div.

Experimental results for fast torque transient (10 Nm/ms) from no-load (0 Nm) up to 10 Nm using the VSI units 1 and 4 during generation mode with torque control at -6000 r/min

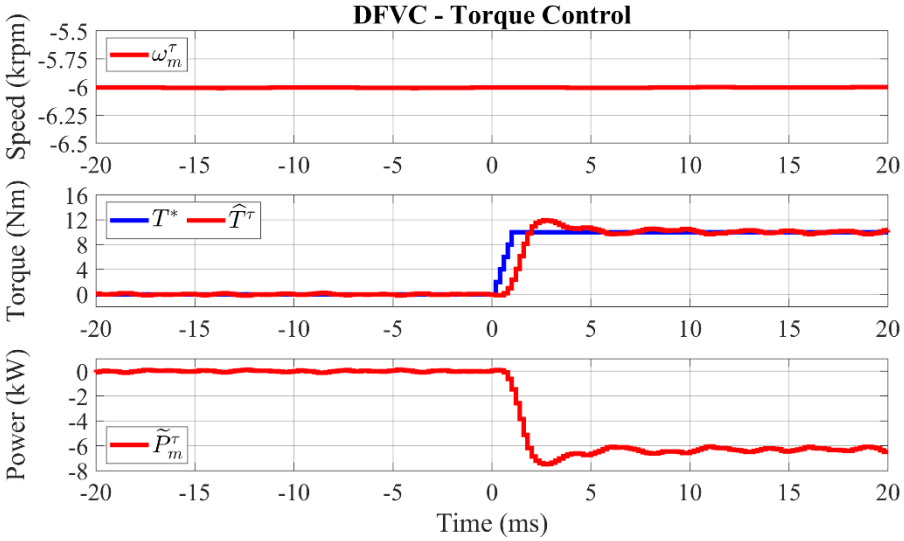

Fig. 4. 33. From top to bottom: measured speed (10^3 · r/min); reference and observed machine torque (Nm); estimated mechanical power (kW).

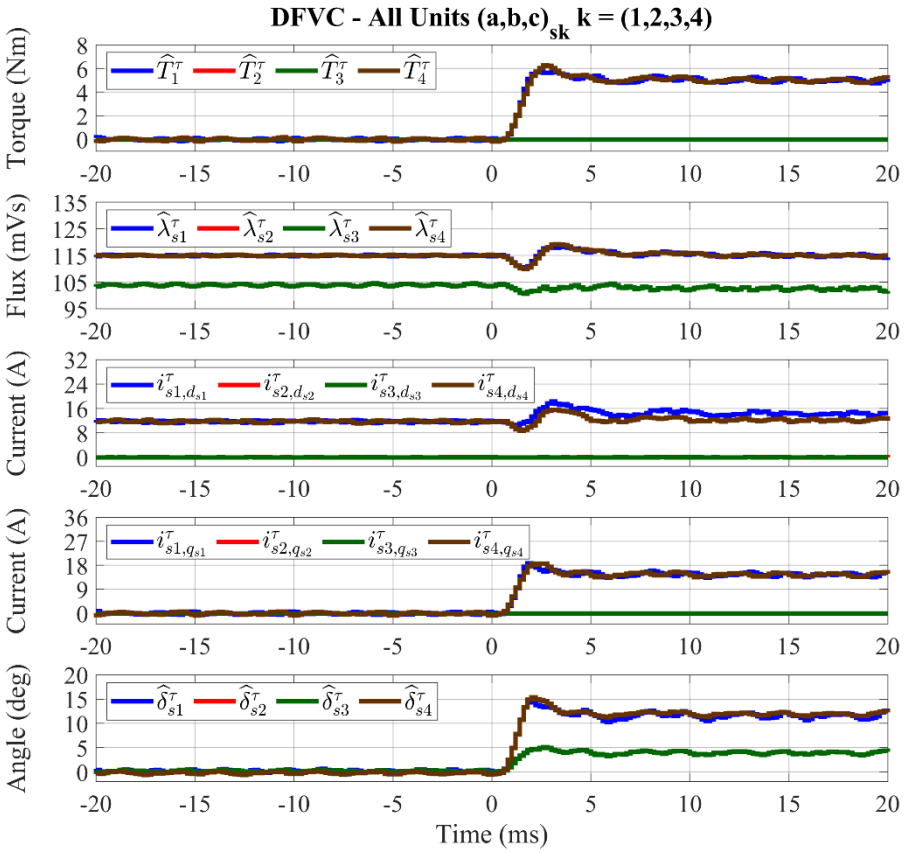

Fig. 4. 34. From top to bottom: single units observed torque (Nm); single units observed flux amplitude (mVs); single units measured d_{sk}-axis current (A); single units measured q_{sk}-axis current (A); single units observed load-angle (deg).

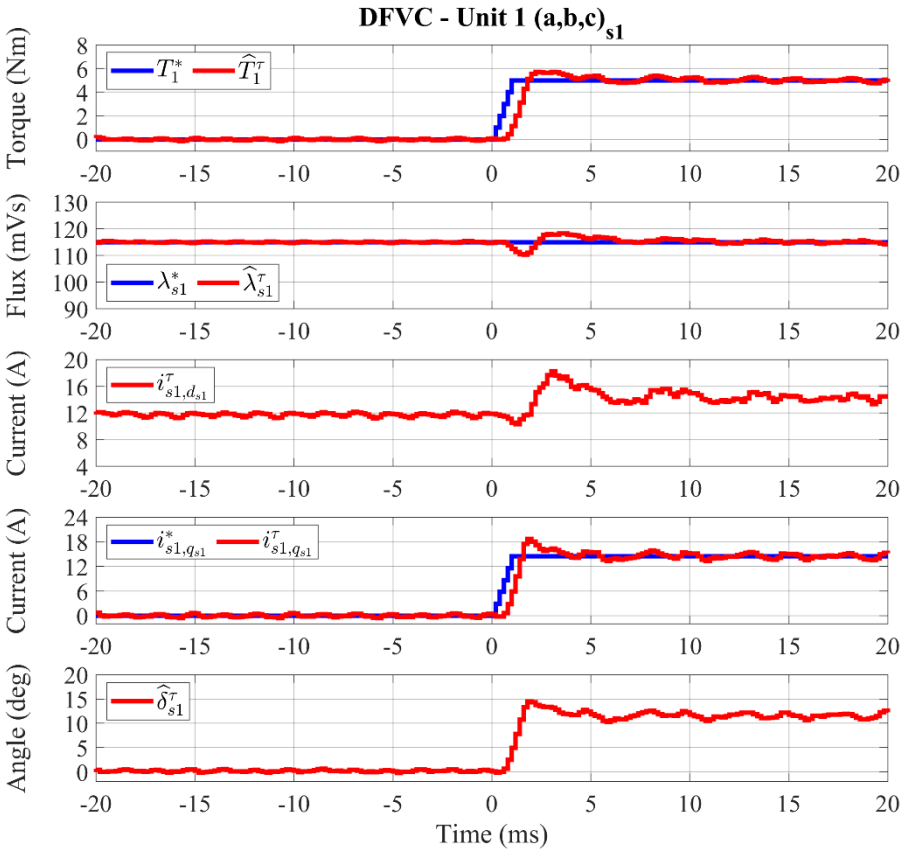

See figure caption: Fig. 4. 35

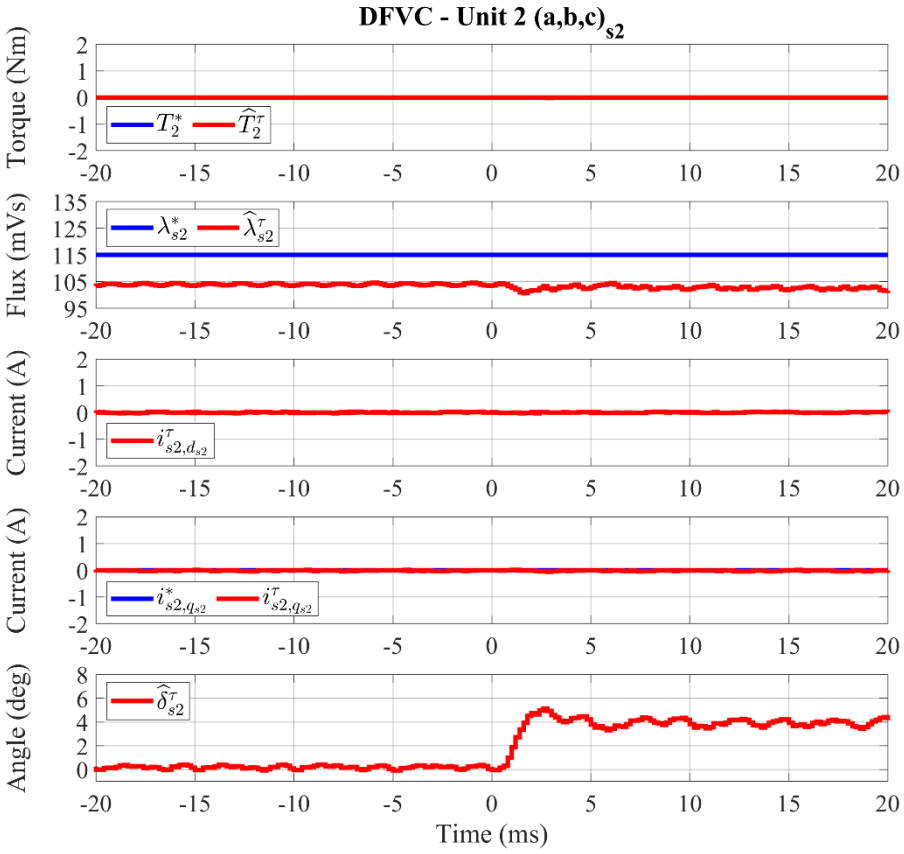

See figure caption: Fig. 4. 35

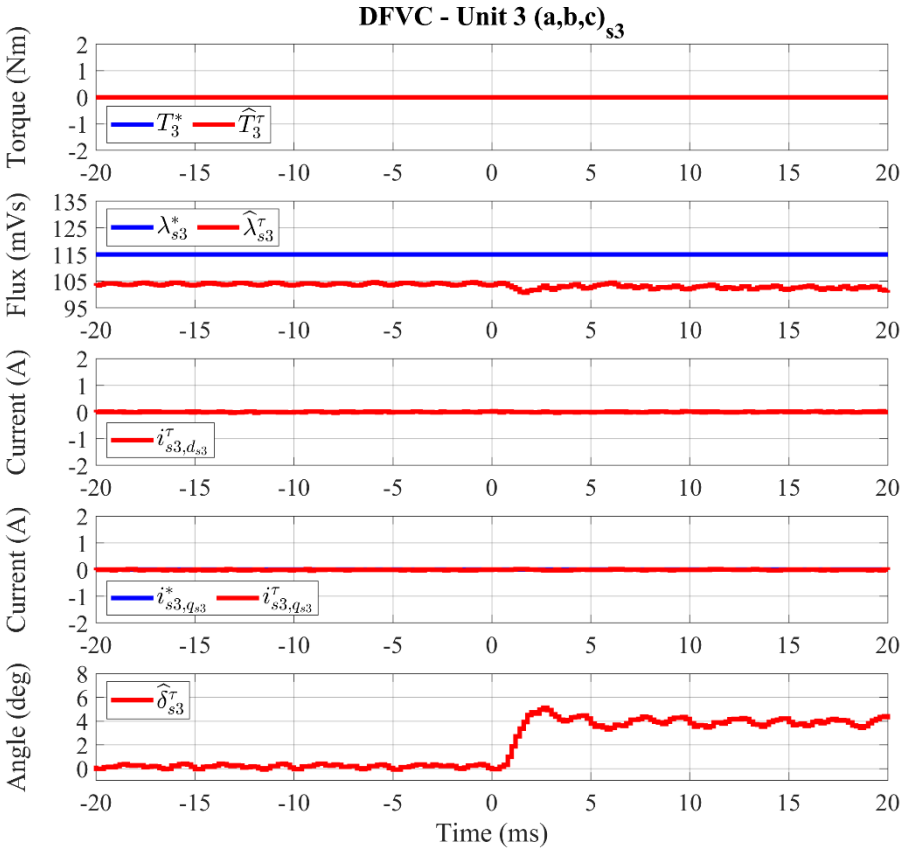

See figure caption: Fig. 4. 35

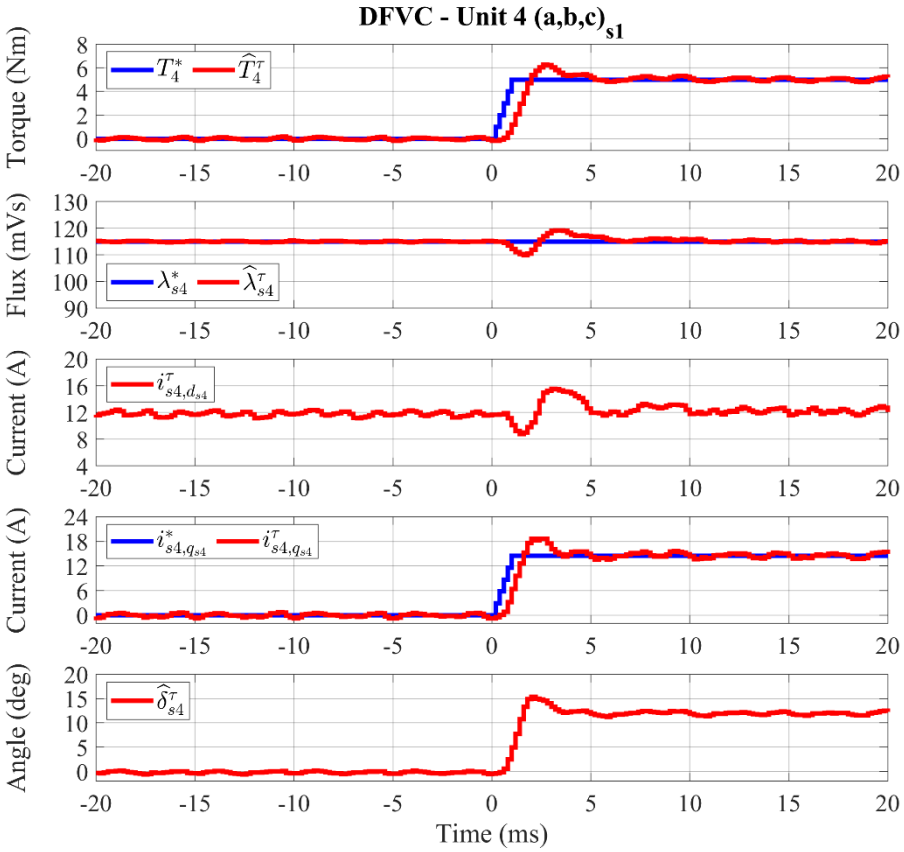

Fig. 4. 35. For each *k*-unit DFVC scheme, from top to bottom: reference and observed torque (Nm); reference and observed flux amplitude (mVs); measured d_{sk}-axis current (A); reference and measured q_{sk}-axis current (A); observed load-angle (deg).

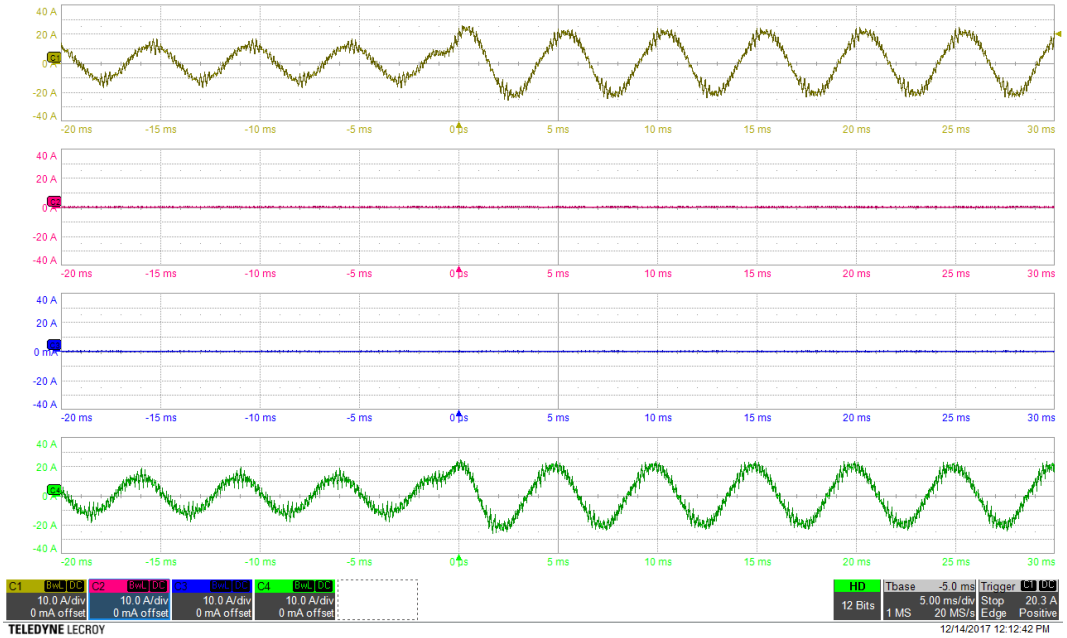

Fig. 4. 36. Ch1: $i_{s1\text{-}a}$ (10 A/div), Ch2: $i_{s2\text{-}a}$ (10 A/div), Ch3: $i_{s3\text{-}a}$ (10 A/div), Ch4: $i_{s4\text{-}a}$ (10 A/div). Time resolution: 5 ms/div.

Optimal torque control operation

The drive has been tested in generating operation. With reference to (4.2)-(4.3), the following conditions have been set:

$$\begin{cases} f_s = 5\,\text{kHz} & \\ v_{dc,k} = 270\,\text{V} & (k = 1 \div 4) \\ \omega_m = -3500\,\text{r/min} & \\ \delta_{max,k} = 45° & (k = 1 \div 4) \\ s_\lambda = 1 \rightarrow \lambda_s^* = \lambda_{s,opt}^{n_a} & \\ T_k^* = \dfrac{T^*}{4} & (k = 1 \div 4) \end{cases} \tag{4.6}$$

To obtain the full exploitation of the VSI units current limit, the Maximum Torque per Ampere (MTPA) operation of the drive has been tested. Therefore, according with the machine torque reference, the flux amplitude reference of the units has been computed using the experimental optimal profiles shown in Fig. 4. 4. Nevertheless, because the validation of these is beyond the scope of this dissertation, only the optimal stator flux amplitude profile in healthy condition has been tested.

According with Chapter 3 – Section 3.3, the MTPA drive operation does not allow high-dynamic torque regulations. As a consequence, to avoid over-currents in the units, a very slow torque transient (32 Nm/s) from zero up to 32 Nm (200 % of the rated torque) has been performed, leading to the experimental results shown in Fig. 4. 37 - Fig. 4. 40. With reference to these, it is noted how the maximum torque condition (32 Nm) corresponds with the maximum current injection in the machine (24 A), thus providing the validation of the optimal stator flux amplitude profile in healthy condition.

Finally, it is noted how initially the rotor flux amplitude has not followed the torque variations, leading to a relevant increment of the units' load-angles (Fig. 4. 40).

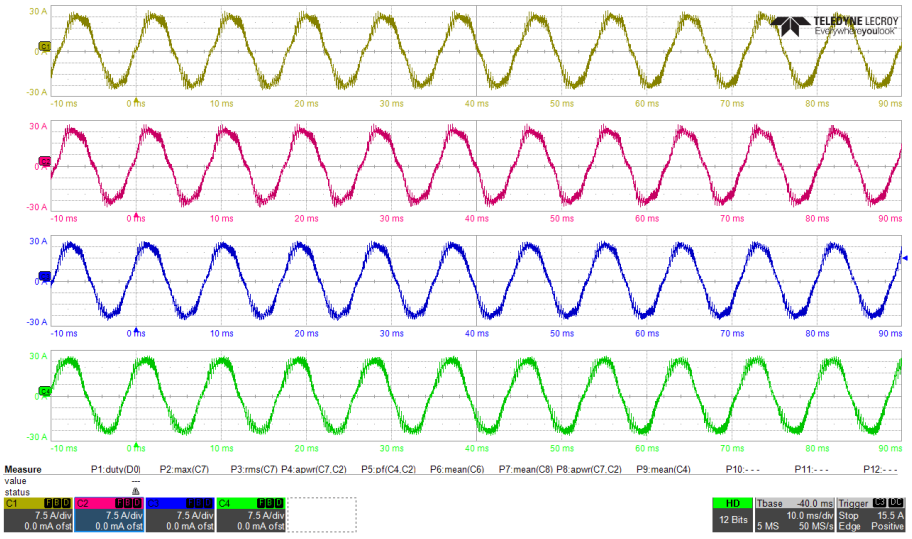

Fig. 4. 37. Machine phase-currents for 200% of the rated torque (32 Nm) in generation at -3500 r/min using the optimal stator flux amplitude reference. Ch1: $i_{s1\text{-}a}$ (7.5 A/div), Ch2: $i_{s2\text{-}a}$ (7.5 A/div), Ch3: $i_{s3\text{-}a}$ (7.5 A/div), Ch4: $i_{s4\text{-}a}$ (7.5 A/div). Time resolution: 10ms/div.

Experimental results for torque transient (32 Nm/s) from no-load up to 200% rated torque (32 Nm) in generation at -3500 r/min using the optimal stator flux reference profile

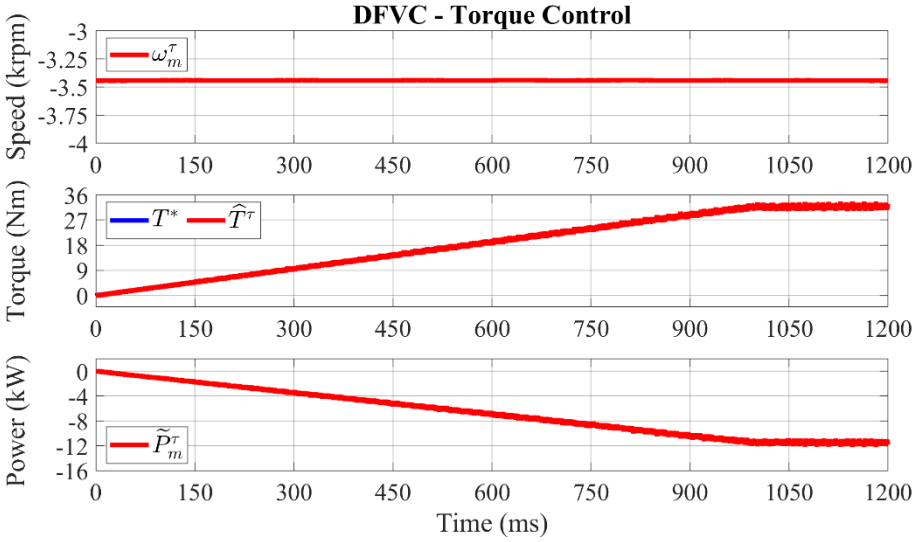

Fig. 4. 38. From top to bottom: measured speed (10^3 · r/min); reference and observed machine torque (Nm); estimated mechanical power (kW).

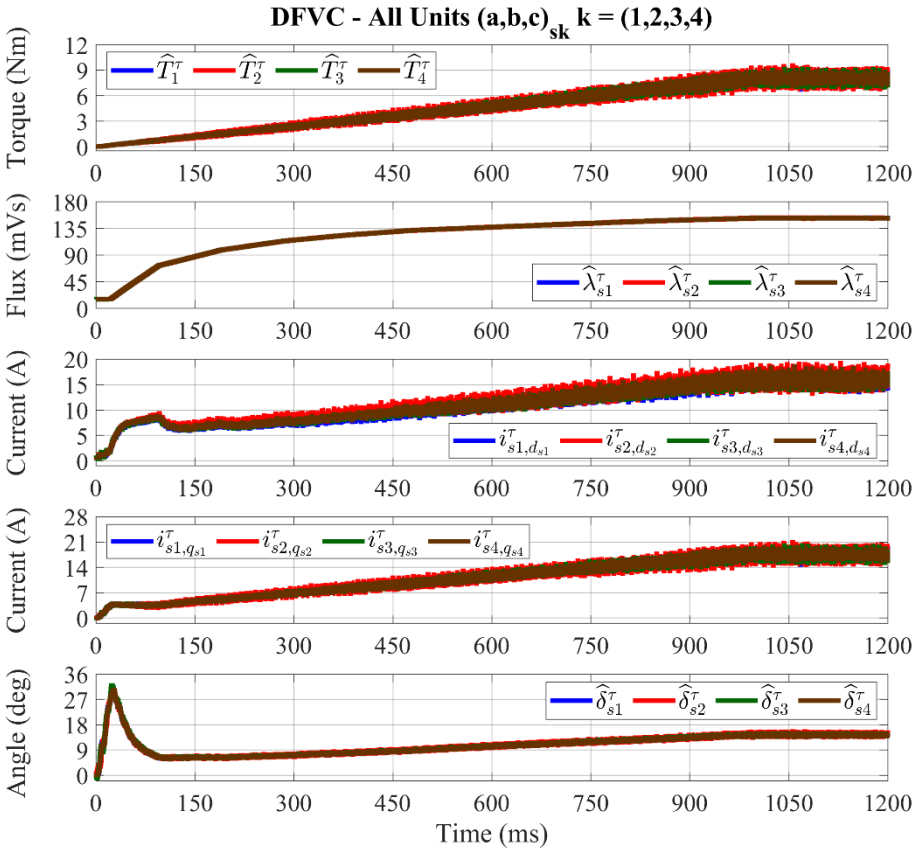

Fig. 4. 39. From top to bottom: single units observed torque (Nm); single units observed flux amplitude (mVs); single units measured d_{sk}-axis current (A); single units measured q_{sk}-axis current (A); single units observed load-angle (deg).

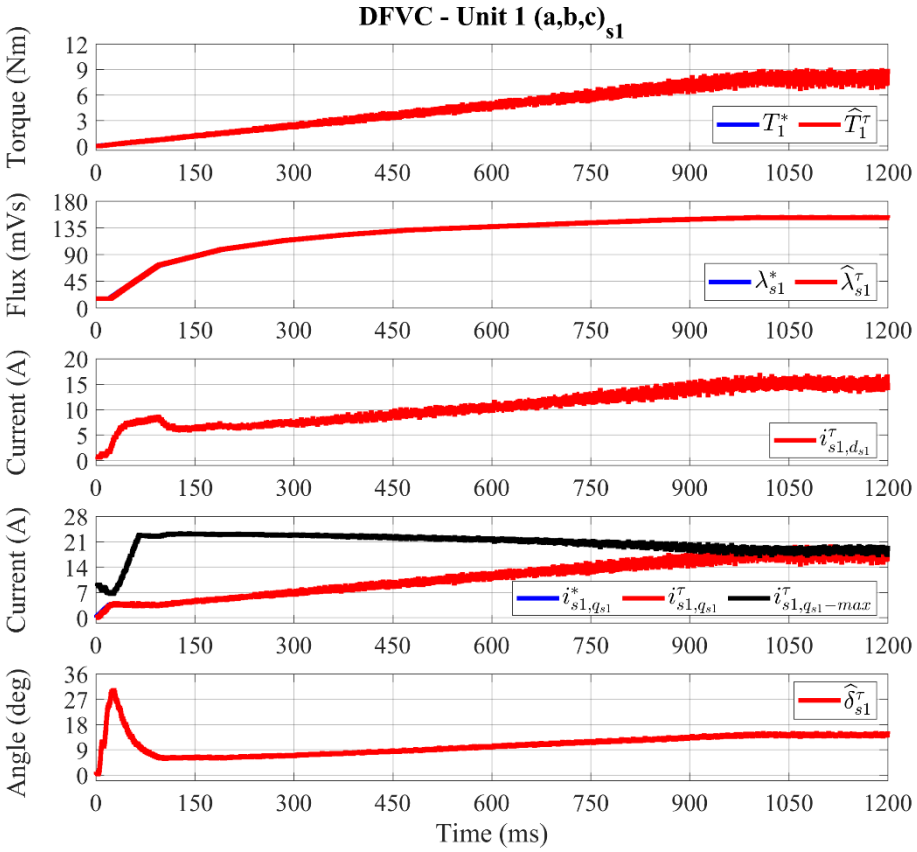

See figure caption: Fig. 4. 40

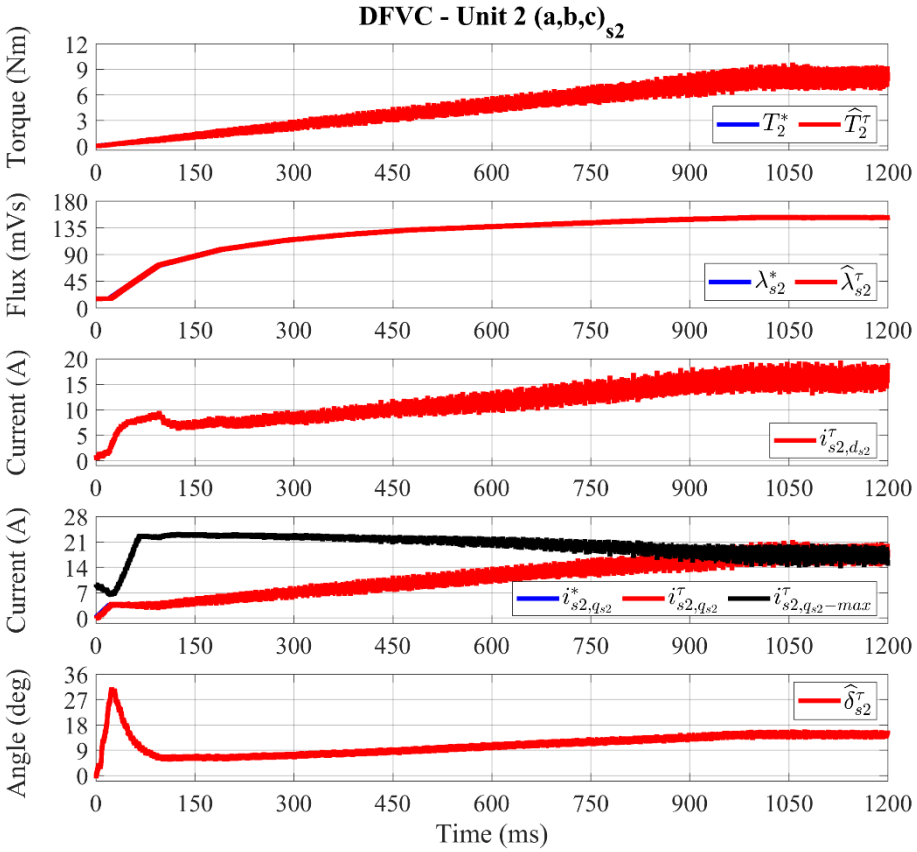

See figure caption: Fig. 4. 40

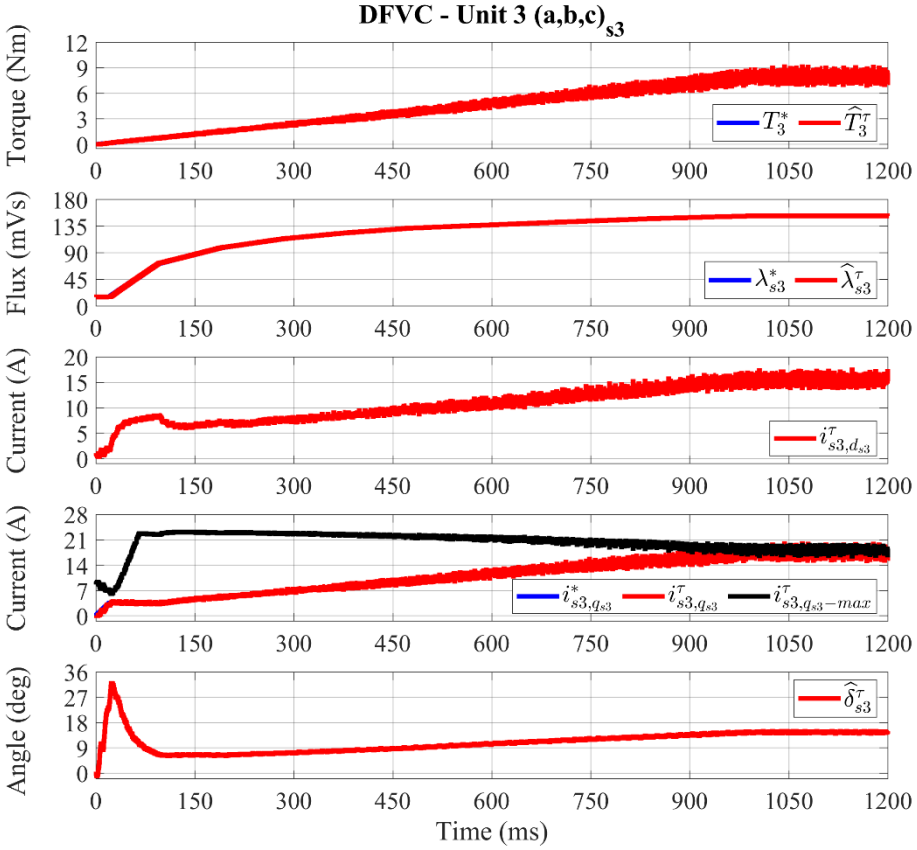

See figure caption: Fig. 4. 40

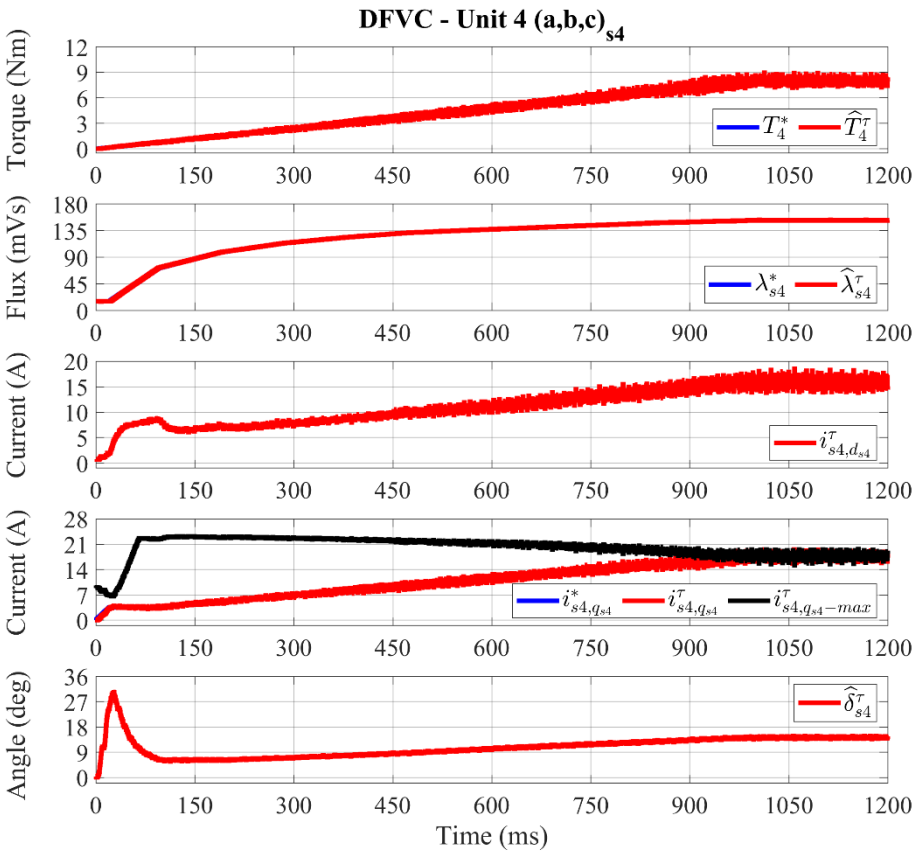

Fig. 4. 40. For each *k*-unit DFVC scheme, from top to bottom: reference and observed torque (Nm); reference and observed flux amplitude (mVs); measured d_{sk}-axis current (A); reference, measured and maximum limit q_{sk}-axis current (A); observed load-angle (deg).

Torque sharing operations

The proposed control solution allows to implement an independent regulation of the torque contribution belonging to each unit. As a consequence, to validate the performance of the proposed control scheme also in case of different operating conditions among the units, specific torque sharing strategies have been tested. The main goal of these has consisted into obtaining large differences among the load-angle values of the units, allowing the full validation of the proposed decoupling algorithm. In detail, they are provided the experimental results related to the following tests:

- Power recirculation between the units
- Sinusoidal torque sharing under voltage constraint
- Sinusoidal torque sharing under both voltage and current constraints
- Sinusoidal torque sharing under both voltage and load-angle constraints
- Sinusoidal torque sharing in deep flux-weakening conditions

Experimental results for power recirculation between the units

The following conditions have been set:

$$\begin{cases} f_s = 4\,\text{kHz} & \\ v_{dc,k} = 270\,\text{V} & (k = 1 \div 4) \\ \omega_m = -6000\ \text{r/min} & \\ \delta_{max,k} = 45° & (k = 1 \div 4) \\ s_\lambda = 3 \rightarrow \lambda_s^* = \lambda_{s,rated} & \\ T^* = 0 & \end{cases} \tag{4.7}$$

With reference to (4.7), the machine torque reference has been set to zero. Nevertheless, the torque references of the units have been set as follows:

$$\begin{cases} T_1^* = T_4^* = +6\ \text{Nm} \\ T_2^* = T_3^* = -6\ \text{Nm} \end{cases} \tag{4.8}$$

According with Table 4. 1, (4.8) corresponds into overloading each unit by a factor equal to 175% . Nevertheless, two units are controlled in motoring mode (unit s 2 and 3) while the other two in generation mode (units 1 and 4), thus implementing a mechanical power recirculation. As a consequence, despite the mechanical power related to each unit is near to 3.8 kW (absolute value), the overall one of machine is zero.

This test is useless from the practical point of view. In addition, it leads to relevant distortion effects on the magnetomotive force at the machine air-gap. Indeed, the stator currents waveforms results quite distorted, as shown in Fig. 4. 44. However, it has been possible to obtain opposite load-angle values among the units controlled in motoring mode and the ones controlled in generation mode, as shown in Fig. 4. 41 - Fig. 4. 44. It can be noted how in each unit the reference torque has been fulfilled without any problem.

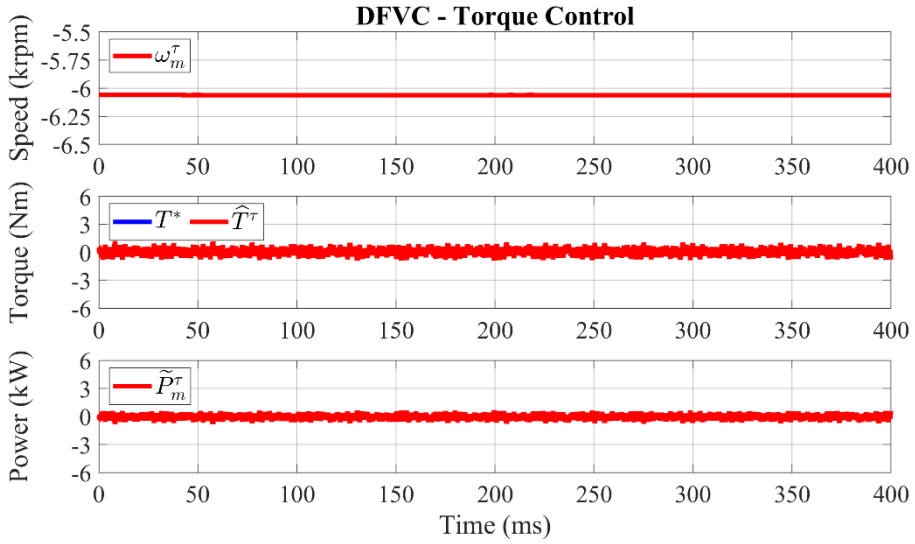

Fig. 4. 41. From top to bottom: measured speed (10^3 · r/min); reference and observed machine torque (Nm); estimated mechanical power (kW).

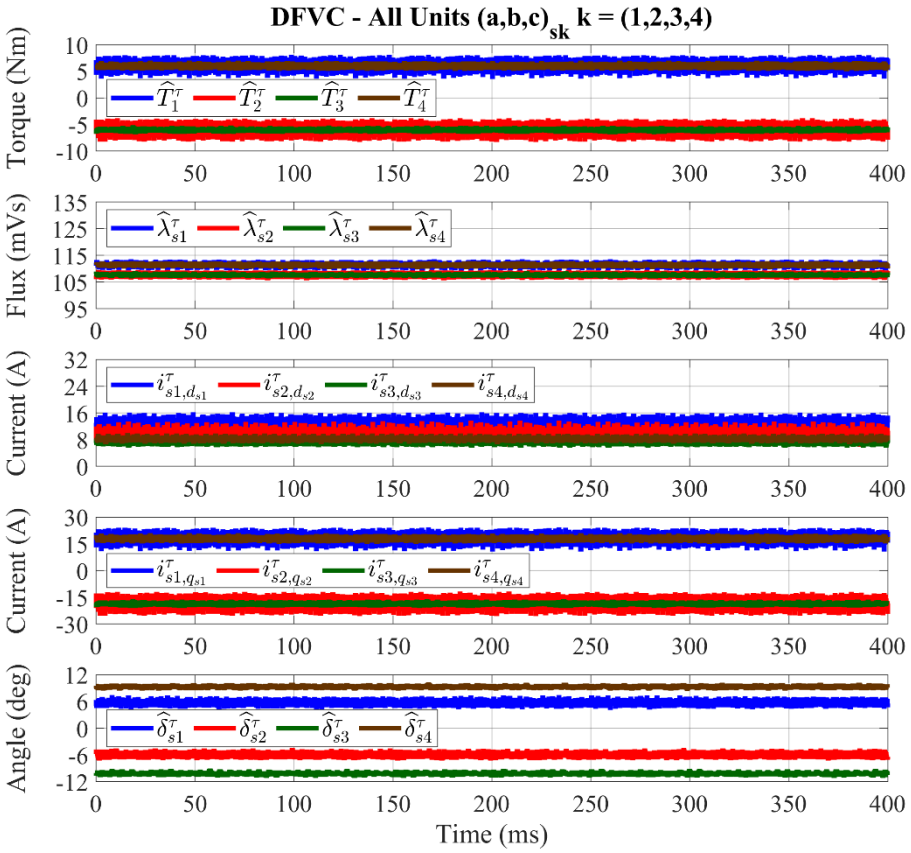

Fig. 4. 42. From top to bottom: single units observed torque (Nm); single units observed flux amplitude (mVs); single units measured d_{sk}-axis current (A); single units measured q_{sk}-axis current (A); single units observed load-angle (deg).

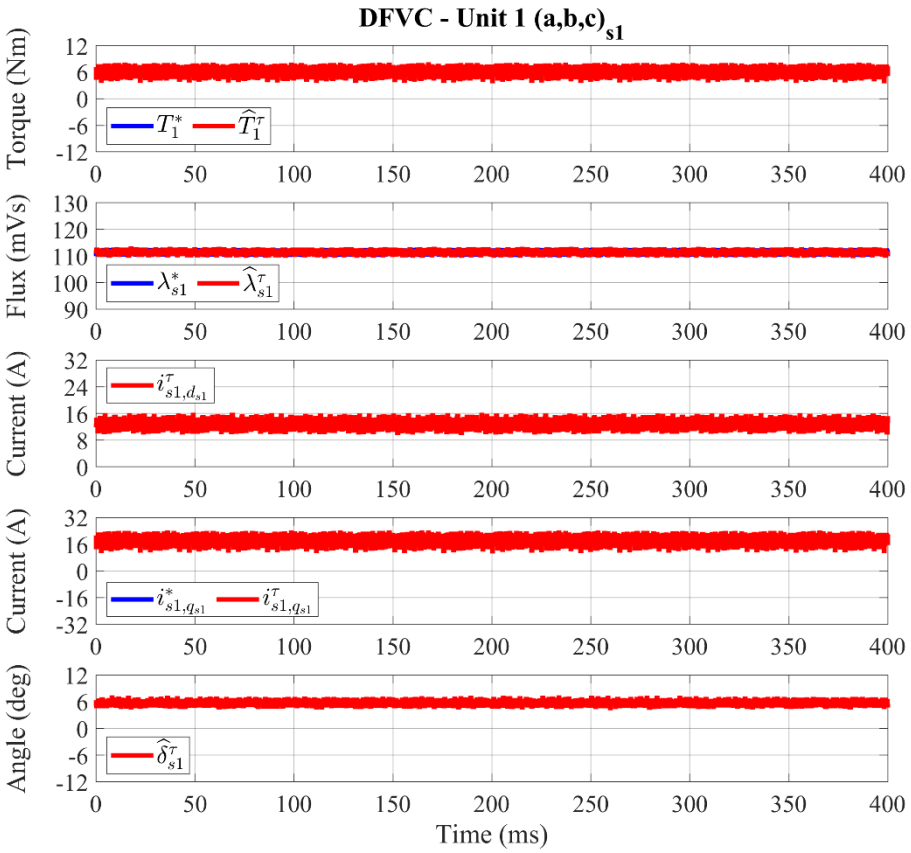

See figure caption: Fig. 4. 43

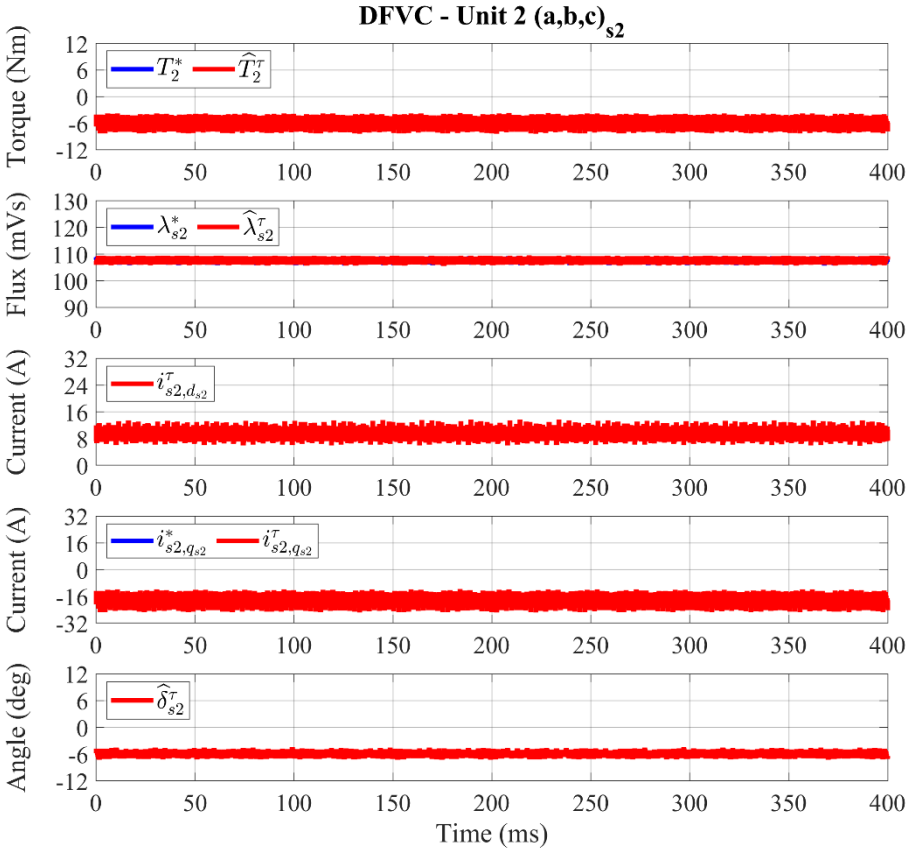

See figure caption: Fig. 4. 43

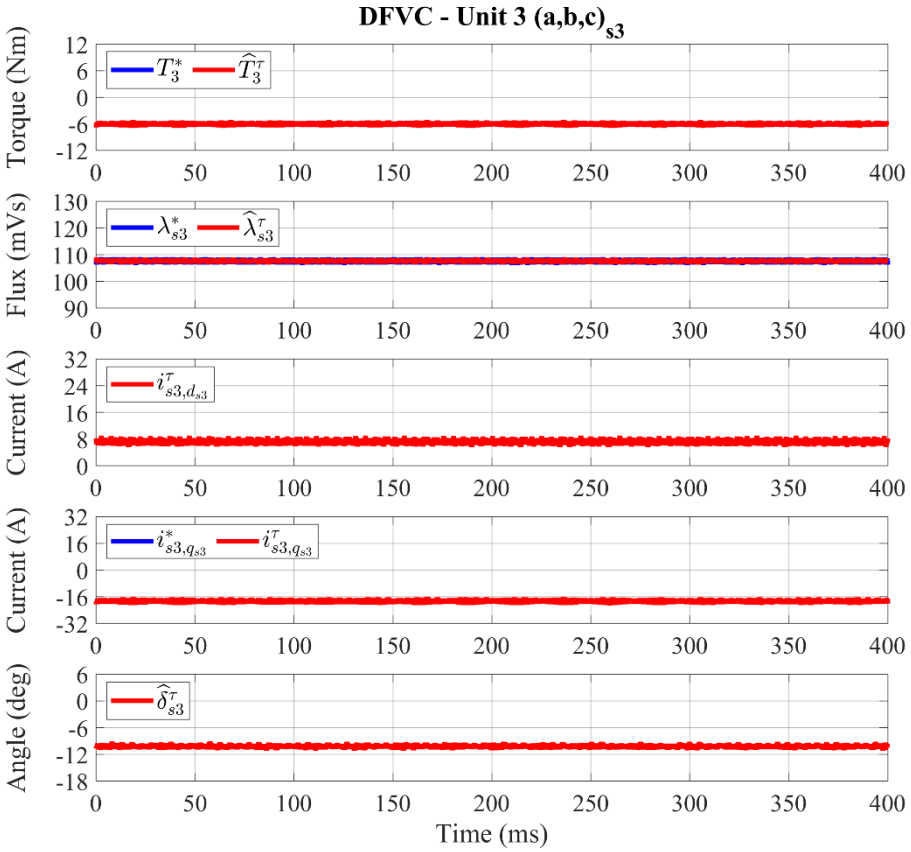

See figure caption: Fig. 4. 43

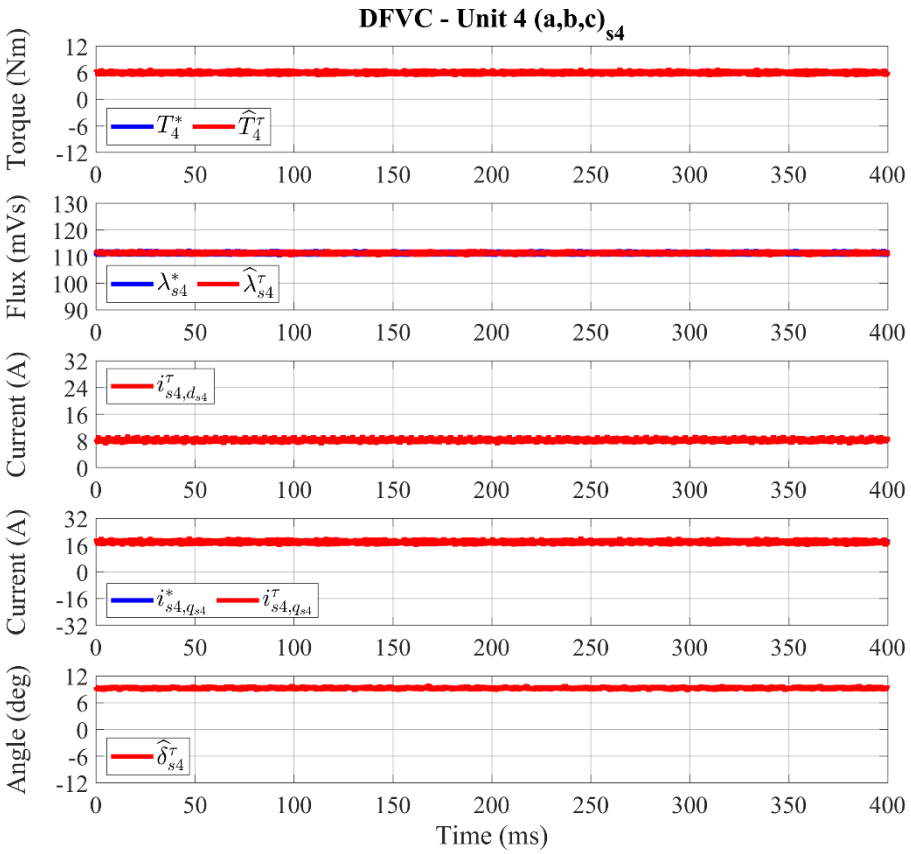

Fig. 4. 43. For each *k*-unit DFVC scheme, from top to bottom: reference and observed torque (Nm); reference and observed flux amplitude (mVs); measured d_{sk}-axis current (A); reference and measured q_{sk}-axis current (A); observed load-angle (deg).

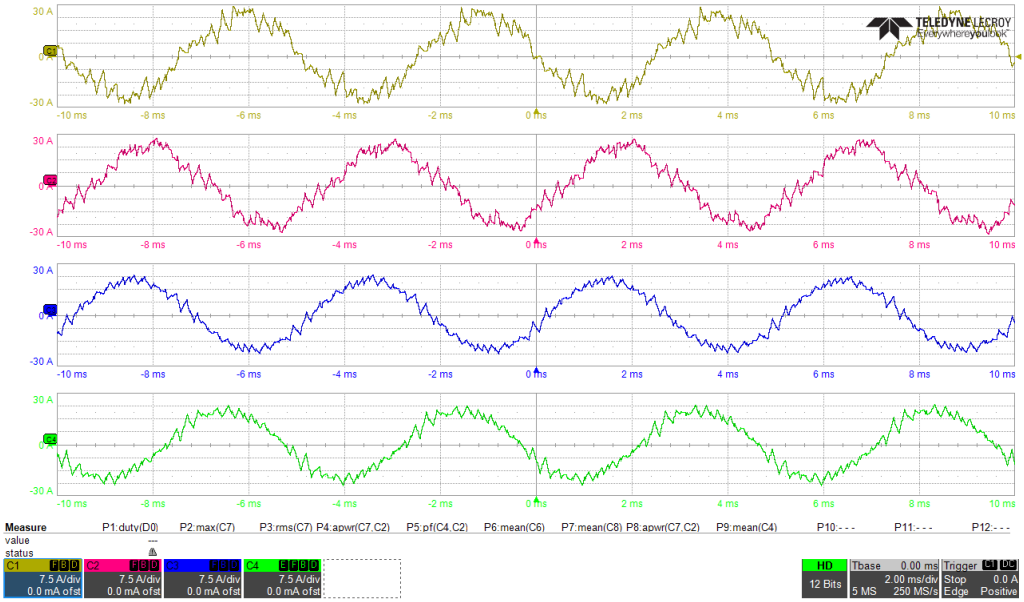

Fig. 4. 44. Ch1: $i_{s1\text{-}a}$ (7.5 A/div), Ch2: $i_{s2\text{-}a}$ (7.5 A/div), Ch3: $i_{s3\text{-}a}$ (7.5 A/div), Ch4: $i_{s4\text{-}a}$ (7.5 A/div). Time resolution: 2 ms/div.

Experimental results for sinusoidal torque sharing operation under voltage constraint

The drive has been tested in generating operation. The following conditions have been set:

$$\begin{cases} f_s = 4\,\text{kHz} & \\ v_{dc,k} = 135\,\text{V} & (k = 1 \div 4) \\ \omega_m = -4000\ \text{r/min} & \\ \delta_{max,k} = 45° & (k = 1 \div 4) \\ s_\lambda = 3 \rightarrow \lambda_s^* = \lambda_{s,rated} & \\ T_k^* = t_{sh,k} \cdot T^* & (k = 1 \div 4) \end{cases} \tag{4.9}$$

With reference to (4.9), the DC source voltage has been reduced to an half of the rated value, thus allowing to test the flux-weakening drive operation. The machine torque reference has been set to 6 Nm, corresponding at an overall mechanical power of 2.5 kW. Concerning the torque sharing coefficients, they have been defined as follows:

$$\begin{cases} t_{sh,1} = \dfrac{1}{4} + \dfrac{1}{2} \cdot \sin\left(2\pi \cdot 10 \cdot t\right) \\ t_{sh,2} = \dfrac{1}{4} + \dfrac{1}{2} \cdot \sin\left(2\pi \cdot 10 \cdot t - \dfrac{\pi}{2}\right) \\ t_{sh,3} = \dfrac{1}{4} + \dfrac{1}{2} \cdot \sin\left(2\pi \cdot 10 \cdot t - \pi\right) \\ t_{sh,4} = \dfrac{1}{4} + \dfrac{1}{2} \cdot \sin\left(2\pi \cdot 10 \cdot t - \dfrac{3\pi}{2}\right) \end{cases} \tag{4.10}$$

According with (4.10), for each unit a base torque reference value of 1.5 Nm in generation has been set. In addition, a torque reference oscillation having an amplitude of 3 Nm and frequency of 10 Hz has been added. Nevertheless, with the aim at forcing strong differences among the load-angle values of the units, the torque oscillations references have been temporally shifted each other in order to emulate a symmetrical four-phase system. In this way, the overall torque of the machine has been kept constant (6 Nm), but instant by instant the torque contributions of the units have been always kept different each other. Therefore, at any moment some units have operated in generation mode, while the others have operated in motoring mode to keep the total torque constant at 6 Nm, as shown in Fig. 4. 45 - Fig. 4. 48. Although this test does not have a direct application, it has preliminary demonstrated the torque sharing capability of proposed scheme.

The phase currents of the units are characterized by oscillations which are quite similar to the ones of the radio waves using an amplitude modulation, as shown in Fig. 4. 45. However, for each unit this amplitude modulation corresponds to a mechanical power oscillation of 1.2 kW having a frequency of 10 Hz and superimposed to an average value of 600 W.

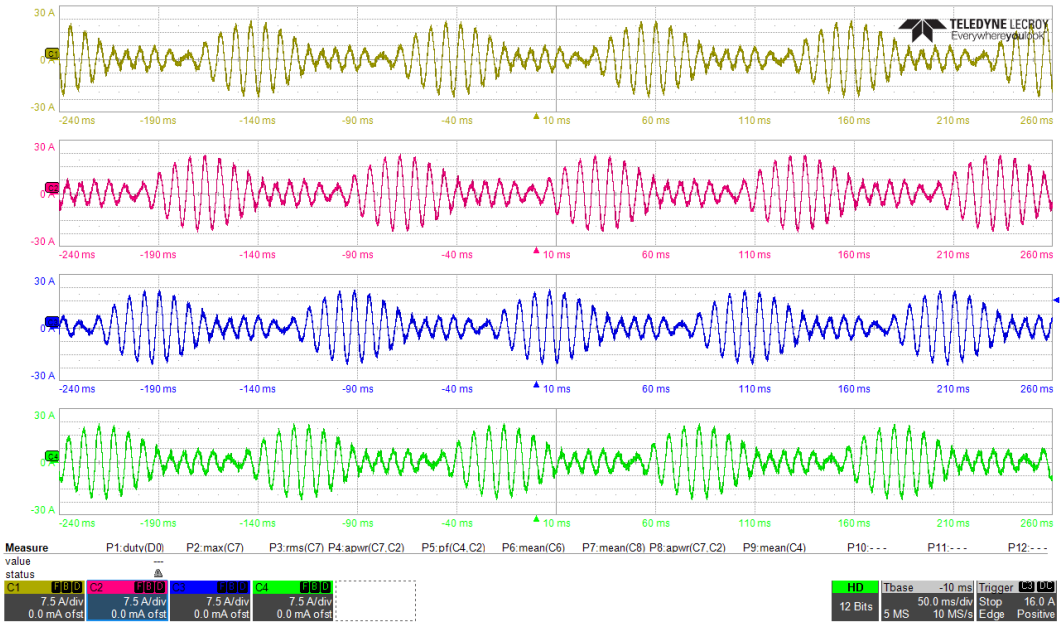

Fig. 4. 45. Ch1: $i_{s1\text{-}a}$ (7.5 A/div), Ch2: $i_{s2\text{-}a}$ (7.5 A/div), Ch3: $i_{s3\text{-}a}$ (7.5 A/div), Ch4: $i_{s4\text{-}a}$ (7.5 A/div). Time resolution: 50 ms/div.

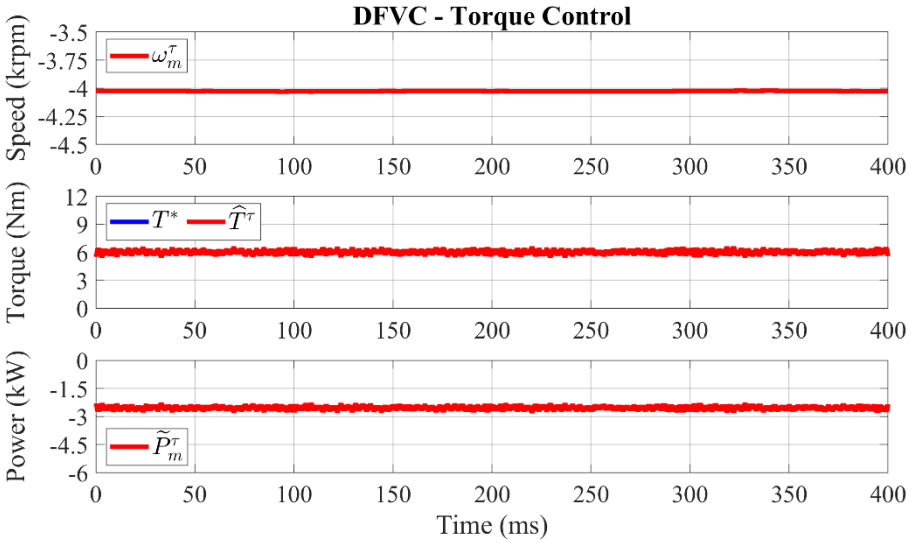

Fig. 4. 46. From top to bottom: measured speed (10^3 · r/min); reference and observed machine torque (Nm); estimated mechanical power (kW).

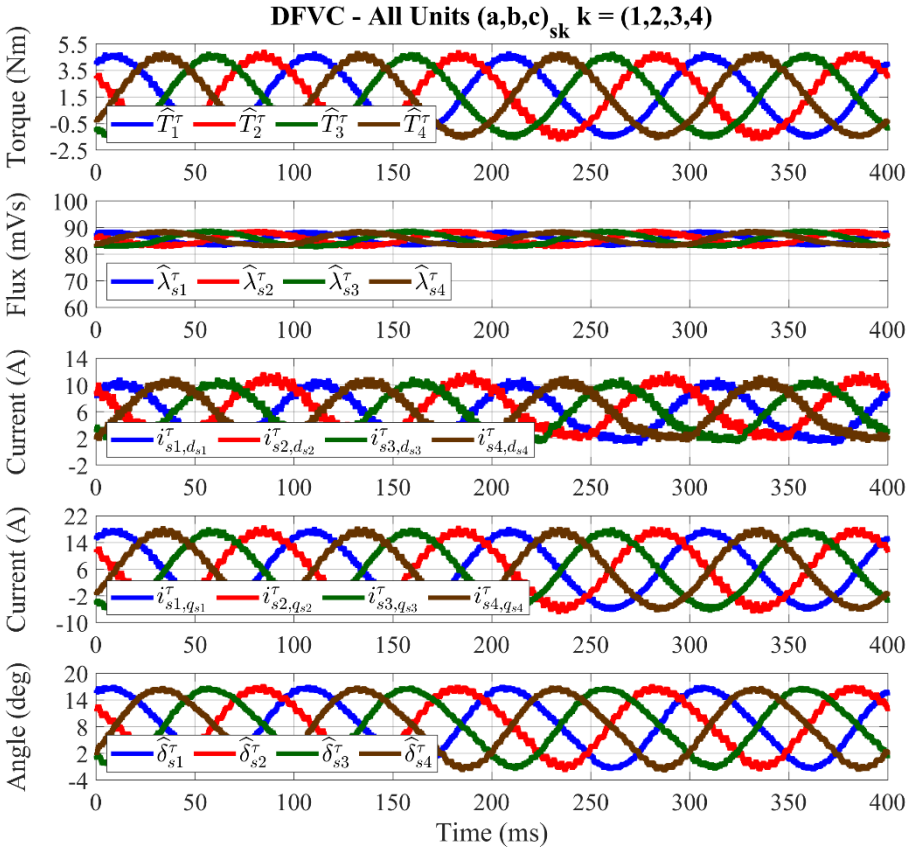

Fig. 4. 47. From top to bottom: single units observed torque (Nm); single units observed flux amplitude (mVs); single units measured d_{sk}-axis current (A); single units measured q_{sk}-axis current (A); single units observed load-angle (deg).

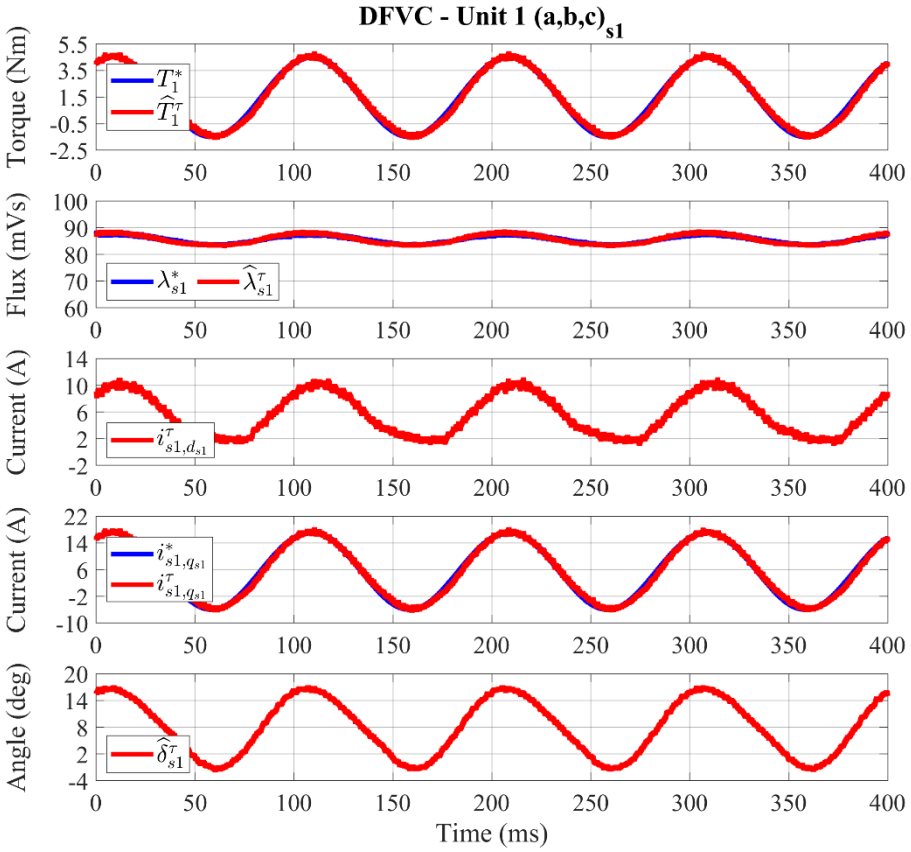

See figure caption: Fig. 4. 48

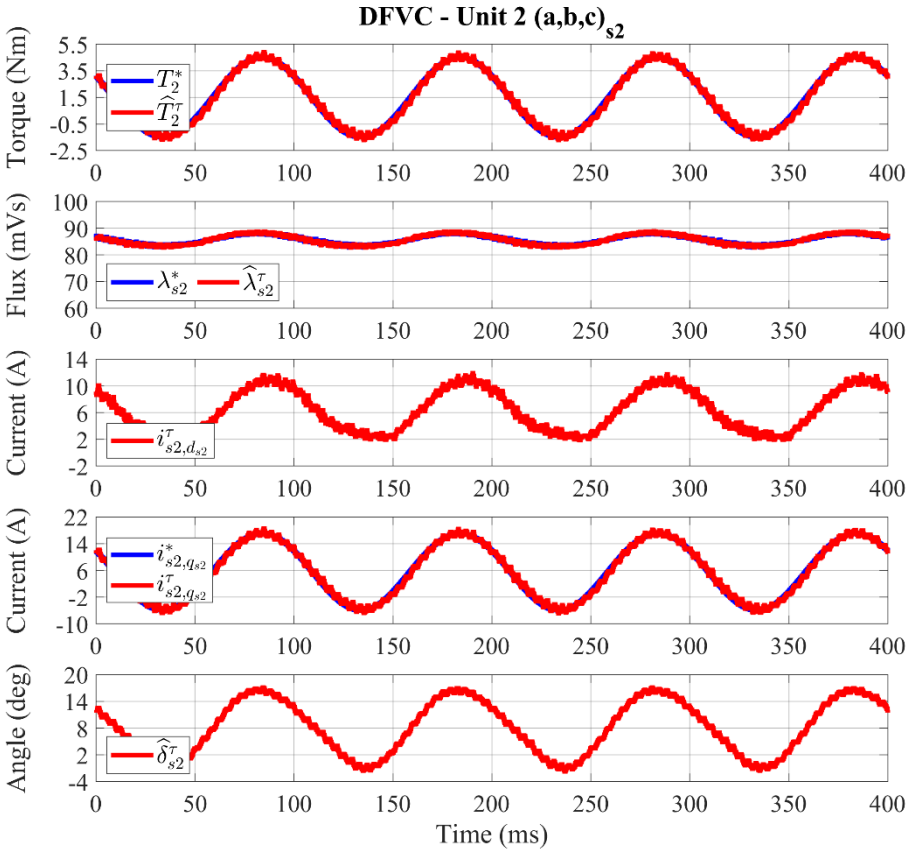

See figure caption: Fig. 4. 48

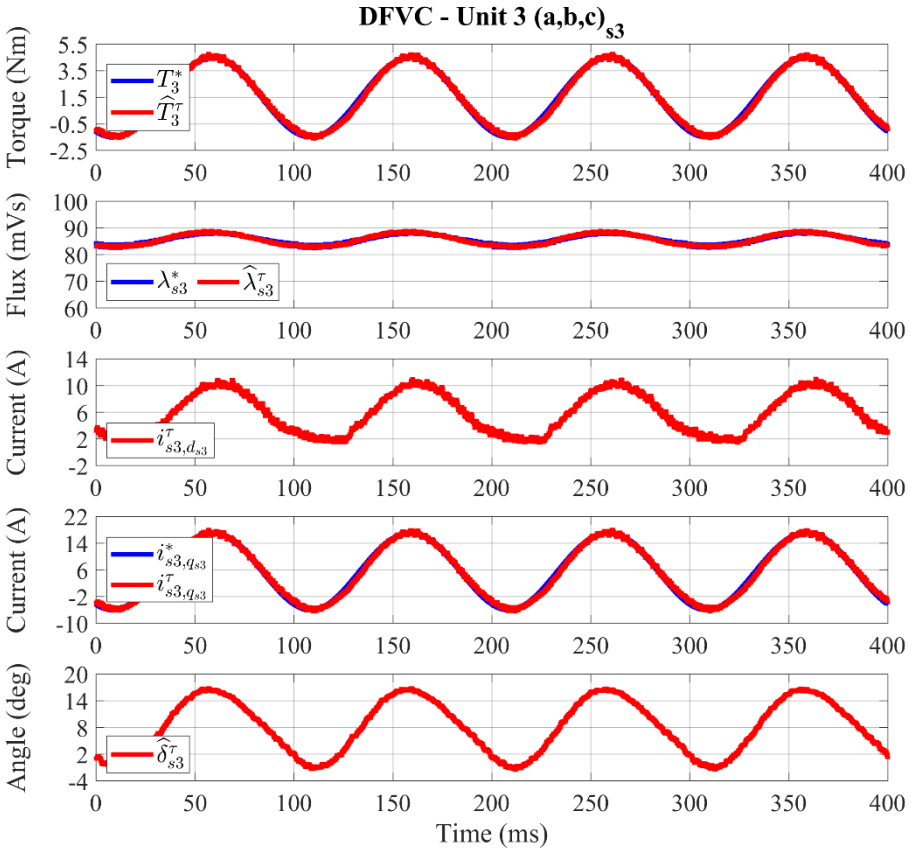

See figure caption: Fig. 4. 48

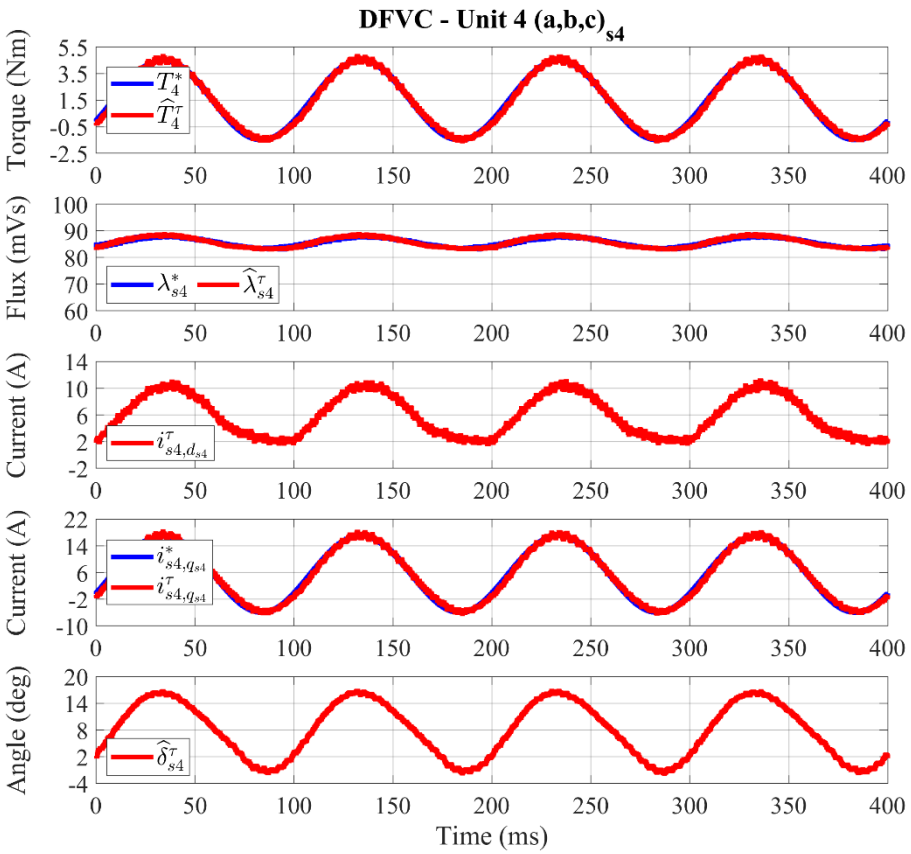

Fig. 4. 48. For each *k*-unit DFVC scheme, from top to bottom: reference and observed torque (Nm); reference and observed flux amplitude (mVs); measured d_{sk}-axis current (A); reference and measured q_{sk}-axis current (A); observed load-angle (deg).

Experimental results for sinusoidal torque sharing under both voltage and current constraints

The drive has been tested in generating operation, using the settings (4.9). The machine torque reference has been set to 9 Nm, corresponding at an overall mechanical power of 3.75 kW. Initially, the drive has operated in balanced conditions of the units. Therefore, for each of these a base torque reference value of 2.25 Nm in generation has been set. However, from a certain moment of time onwards, the torque sharing operations (4.10) have been suddenly enabled. As a consequence, for each unit a torque reference oscillation having an amplitude of 4.5 Nm and frequency of 10 Hz has been added, leading to the experimental results shown in Fig. 4. 49 - Fig. 4. 52.

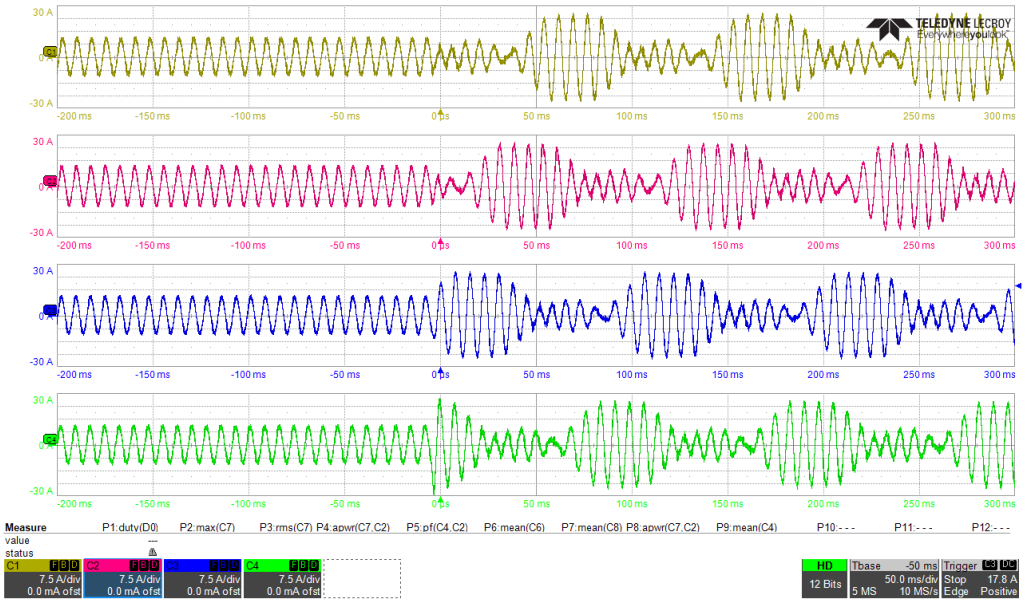

See figure caption: Fig. 4. 49

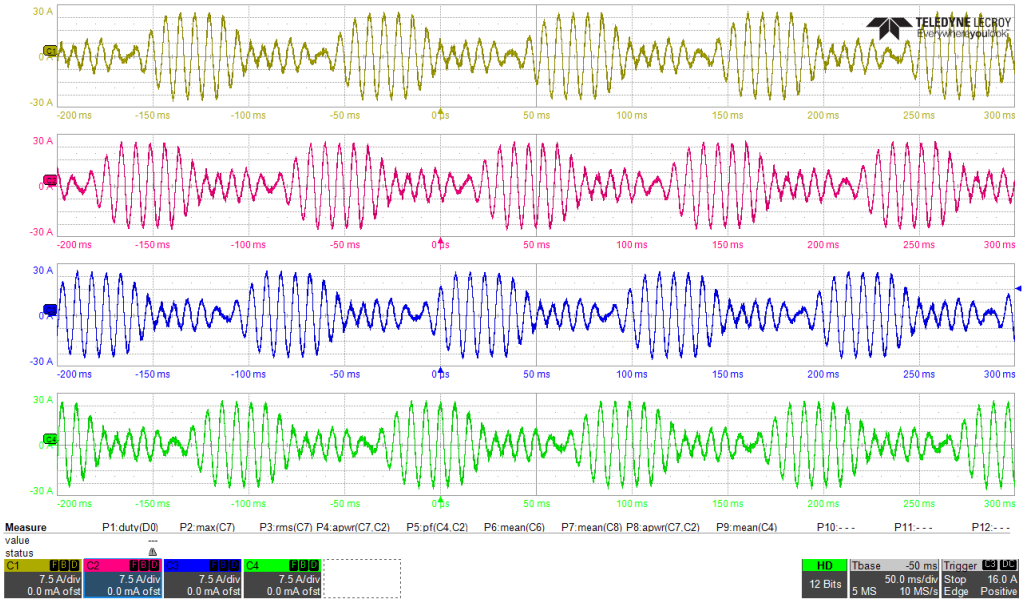

Fig. 4. 49. Ch1: $i_{s1\text{-}a}$ (7.5 A/div), Ch2: $i_{s2\text{-}a}$ (7.5 A/div), Ch3: $i_{s3\text{-}a}$ (7.5 A/div), Ch4: $i_{s4\text{-}a}$ (7.5 A/div). Time resolution: 50 ms/div.

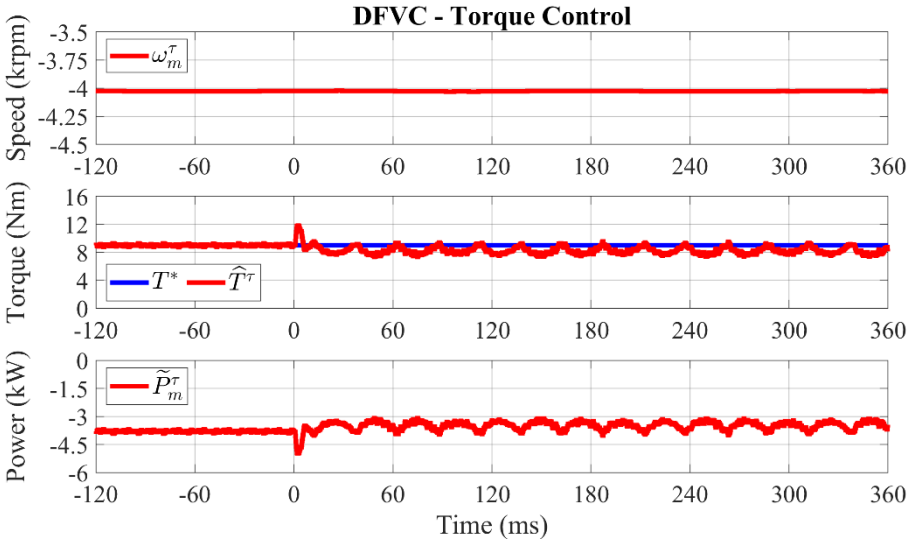

Fig. 4. 50. From top to bottom: measured speed (10^3 · r/min); reference and observed machine torque (Nm); estimated mechanical power (kW).

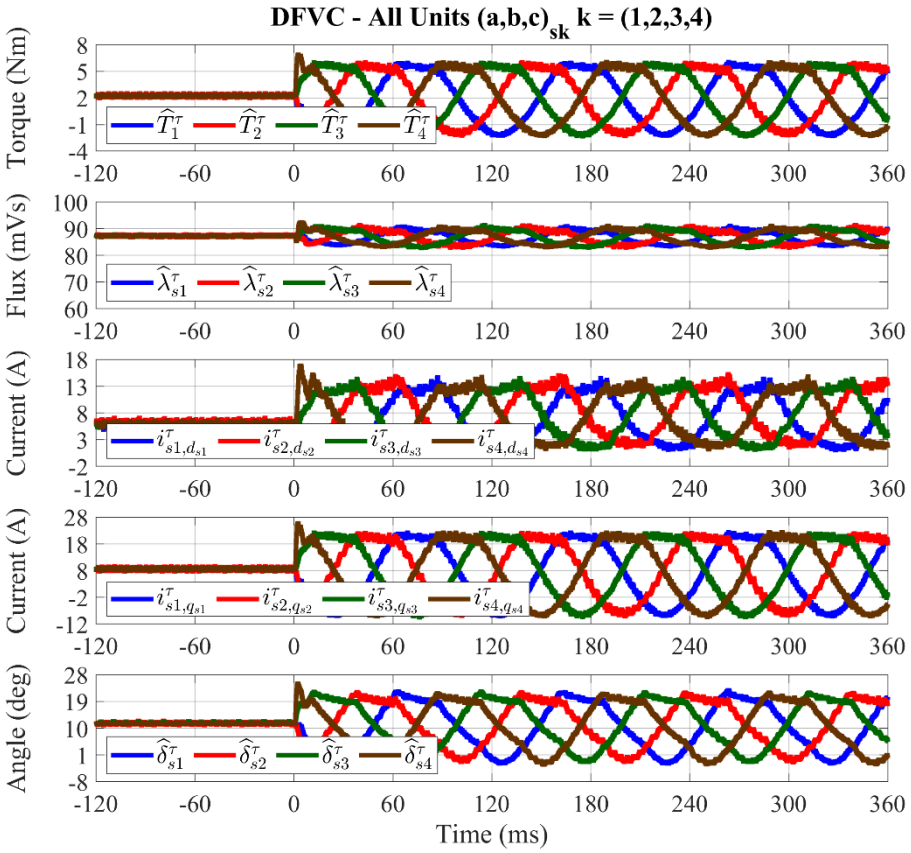

Fig. 4. 51. From top to bottom: single units observed torque (Nm); single units observed flux amplitude (mVs); single units measured d_{sk}-axis current (A); single units measured q_{sk}-axis current (A); single units observed load-angle (deg).

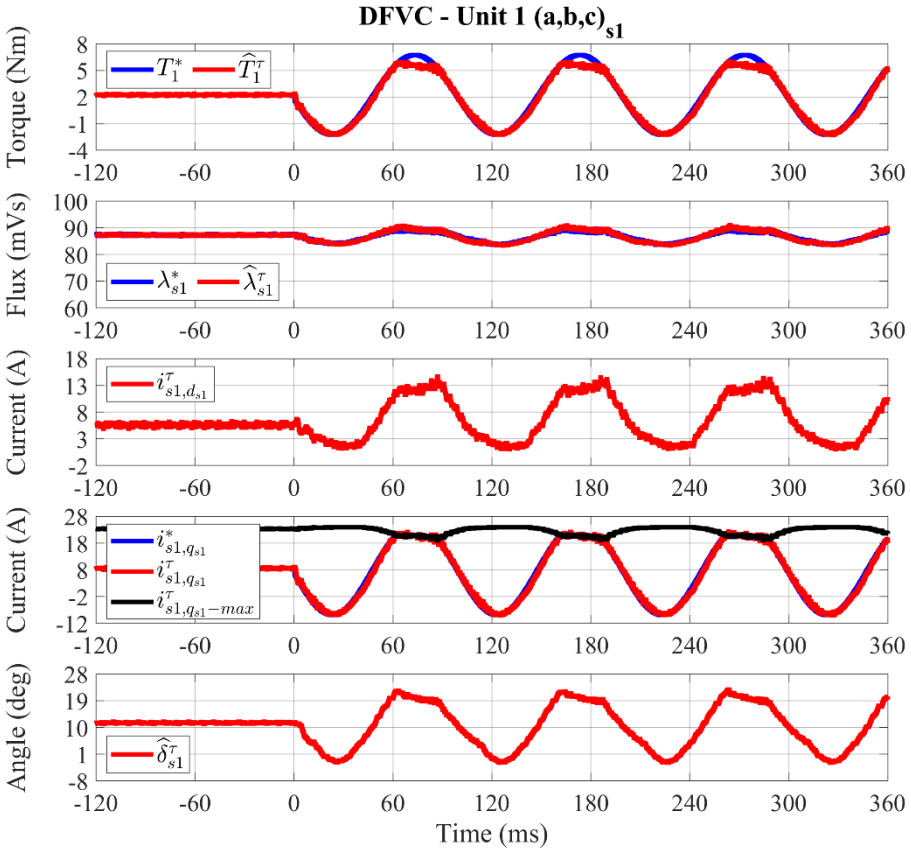

See figure caption: Fig. 4. 52

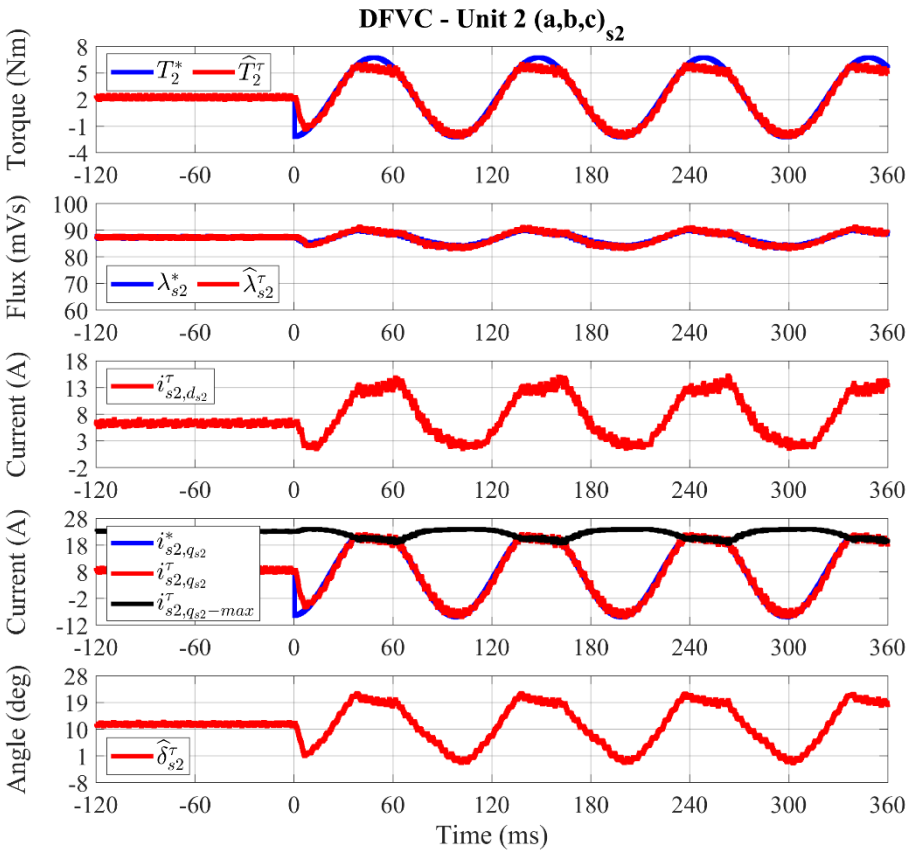

See figure caption: Fig. 4. 52

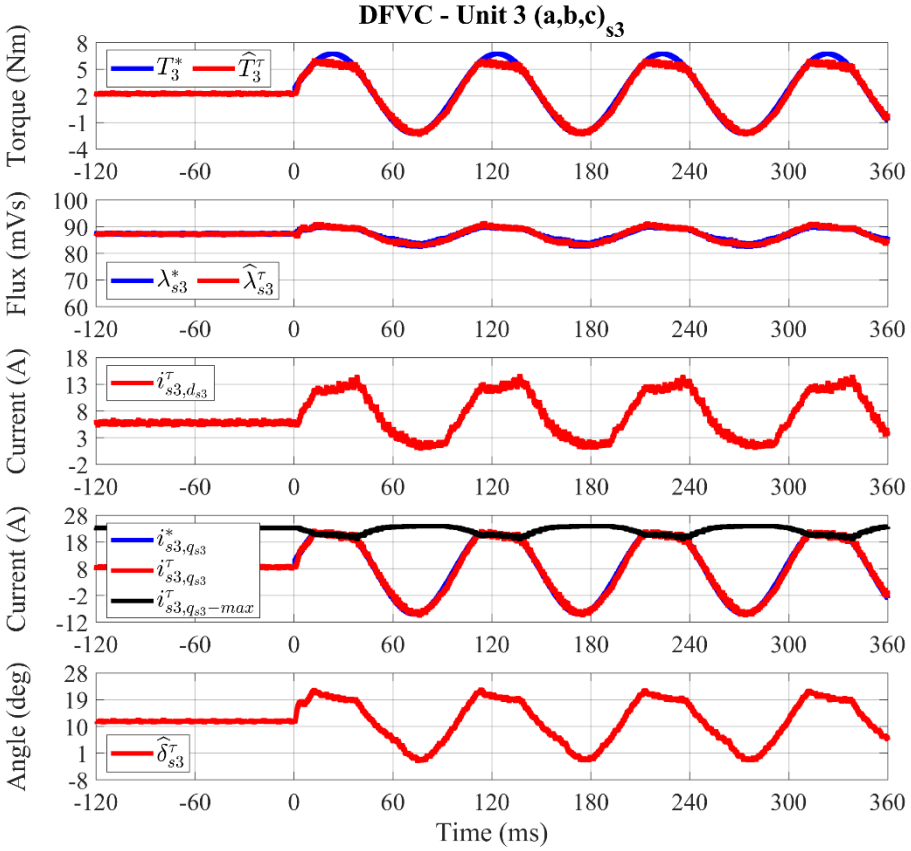

See figure caption: Fig. 4. 52

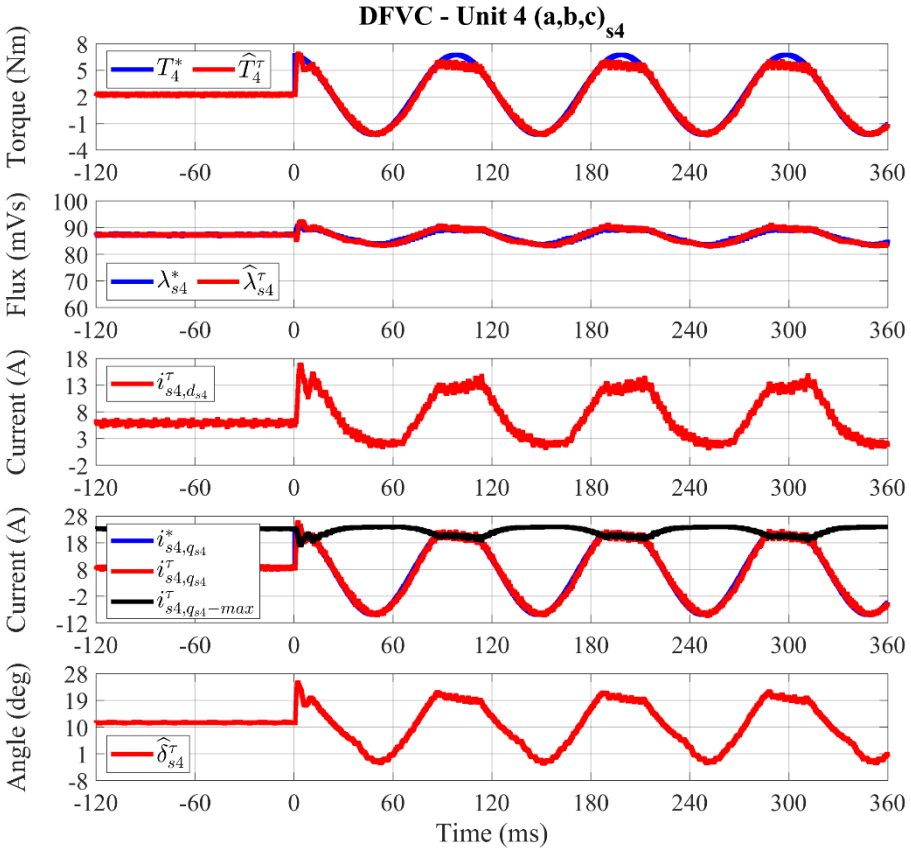

Fig. 4. 52. For each *k*-unit DFVC scheme, from top to bottom: reference and observed torque (Nm); reference and observed flux amplitude (mVs); measured d_{sk}-axis current (A); reference, measured and maximum limit q_{sk}-axis current (A); observed load-angle (deg).

Compared to the previous test, it is noted how the torque reference of each unit *k* has not continuously been fulfilled. Indeed, with the aim at keeping the *k*-unit phase-currents within the maximum allowable amplitude limit, the *k*-unit DFVC scheme has performed a proper saturation of the *k*-unit torque-producing current reference. Therefore, through this test it has been demonstrated the torque sharing capability of the proposed scheme however considering the maximum phase-current limit of each unit.

Experimental results for sinusoidal torque sharing under both voltage and load-angle constraints

The drive has been tested in generating operation. The following conditions have been set:

$$\begin{cases} f_s = 4\,\text{kHz} & \\ v_{dc,k} = 135\,\text{V} & (k = 1 \div 4) \\ \omega_m = -6000\ \text{r/min} & \\ \delta_{max,k} = 25° & (k = 1 \div 4) \\ s_\lambda = 3 \rightarrow \lambda_s^* = \lambda_{s,rated} & \\ T_k^* = t_{sh,k} \cdot T^* & (k = 1 \div 4) \end{cases} \tag{4.11}$$

The machine torque reference has been set to 9 Nm, corresponding at an overall mechanical power of 5.7 kW. Concerning the torque sharing coefficients, they have been defined as follows:

$$\begin{cases} t_{sh,1} = \dfrac{1}{4} + \dfrac{2}{5} \cdot \sin\left(2\pi \cdot 10 \cdot t\right) \\ t_{sh,2} = \dfrac{1}{4} + \dfrac{2}{5} \cdot \sin\left(2\pi \cdot 10 \cdot t - \dfrac{\pi}{2}\right) \\ t_{sh,3} = \dfrac{1}{4} + \dfrac{2}{5} \cdot \sin\left(2\pi \cdot 10 \cdot t - \pi\right) \\ t_{sh,4} = \dfrac{1}{4} + \dfrac{2}{5} \cdot \sin\left(2\pi \cdot 10 \cdot t - \dfrac{3\pi}{2}\right) \end{cases} \tag{4.12}$$

According with (4.12), for each unit a base torque reference value of 2.25 Nm in generation has been set. In addition, a torque reference oscillation having an amplitude of 3.6 Nm and frequency of 10 Hz has been added, leading to the experimental results shown in Fig. 4. 53 - Fig. 4. 56.

Similar to the previous case, it is noted how the torque reference of each unit *k* has not continuously been fulfilled. Indeed, with the aim at keeping the *k*-unit load-angle within the maximum allowable limit (4.11), the *k*-unit DFVC scheme has performed a proper saturation of the *k*-unit torque-producing current reference. Therefore, through this test it has been demonstrated the torque sharing capability of the proposed scheme however taking in account the maximum load-angle limit of each unit.

Finally, it is noted how the load-angle limit has arbitrary been set to the value of 25° for all units, thus highlighting one of the many degrees of freedom characterizing the proposed control solution.

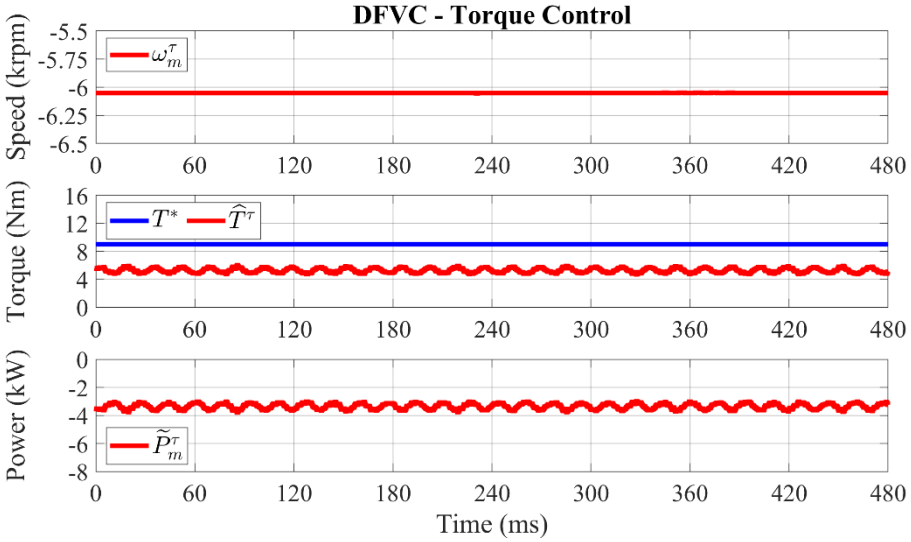

Fig. 4. 53. From top to bottom: measured speed (10^3 · r/min); reference and observed machine torque (Nm); estimated mechanical power (kW).

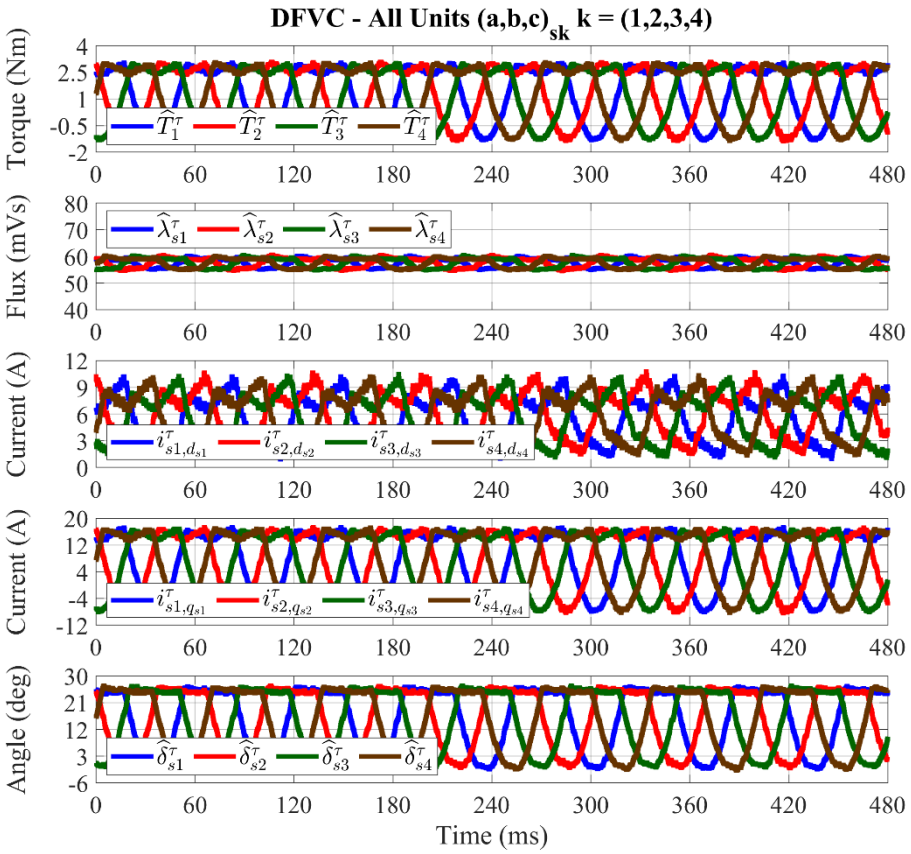

Fig. 4. 54. From top to bottom: single units observed torque (Nm); single units observed flux amplitude (mVs); single units measured d_{sk}-axis current (A); single units measured q_{sk}-axis current (A); single units observed load-angle (deg).

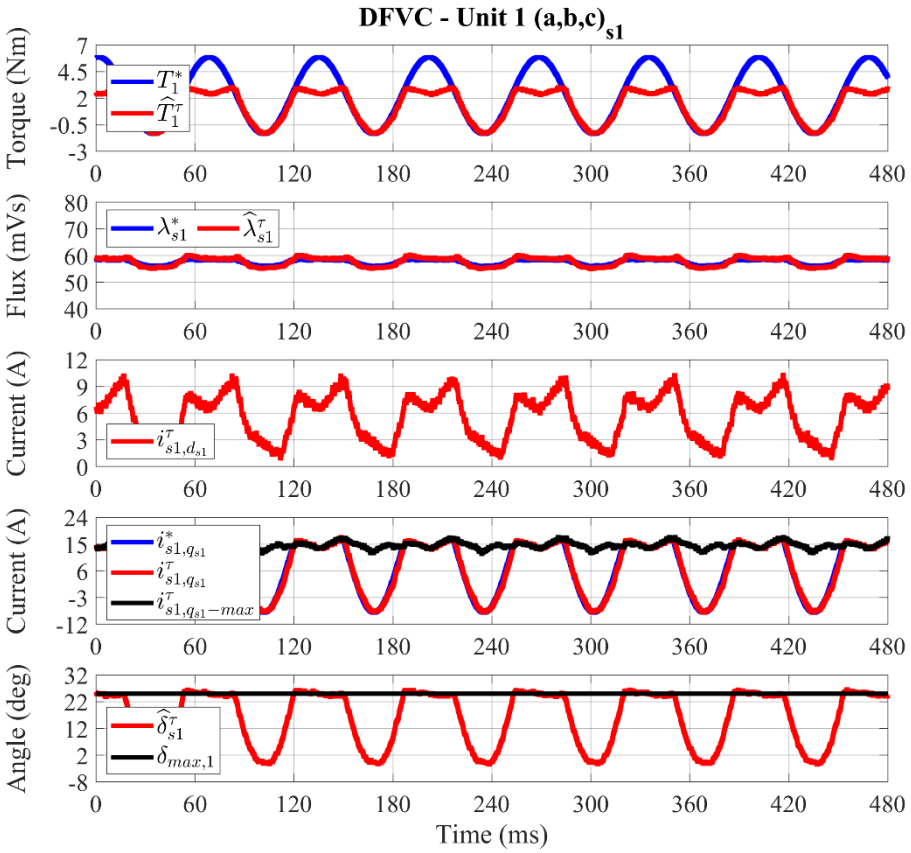

See figure caption: Fig. 4. 55

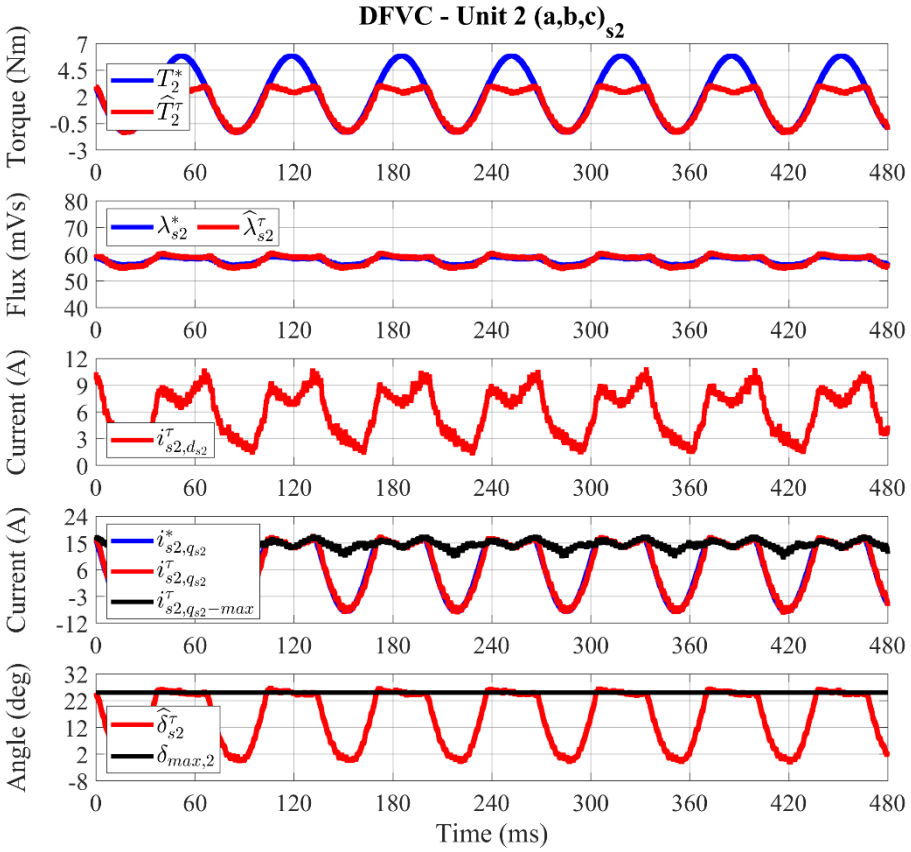

See figure caption: Fig. 4. 55

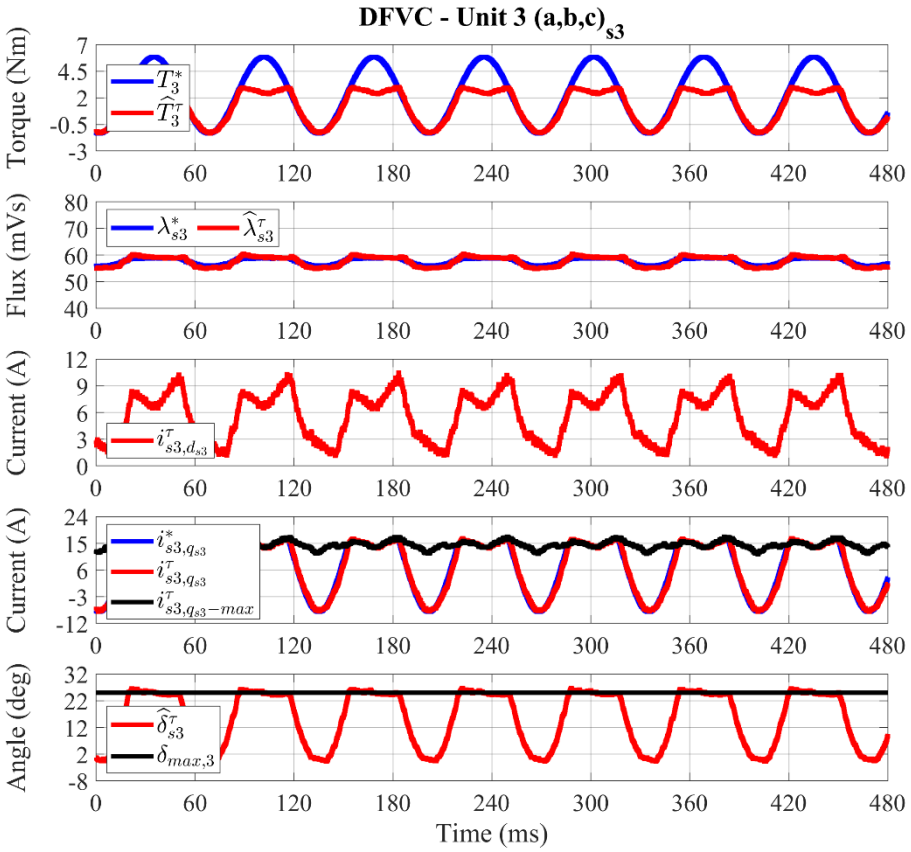

See figure caption: Fig. 4. 55

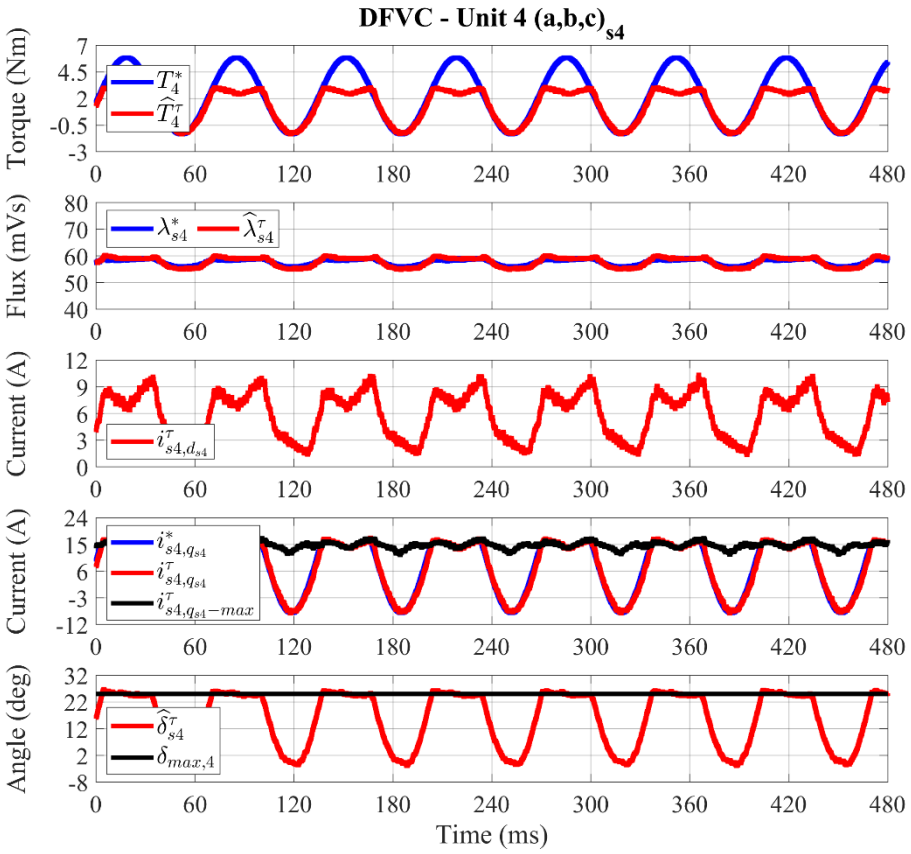

Fig. 4. 55. For each *k*-unit DFVC scheme, from top to bottom: reference and observed torque (Nm); reference and observed flux amplitude (mVs); measured d_{sk}-axis current (A); reference, measured and maximum limit q_{sk}-axis current (A); observed and maximum limit load-angle (deg).

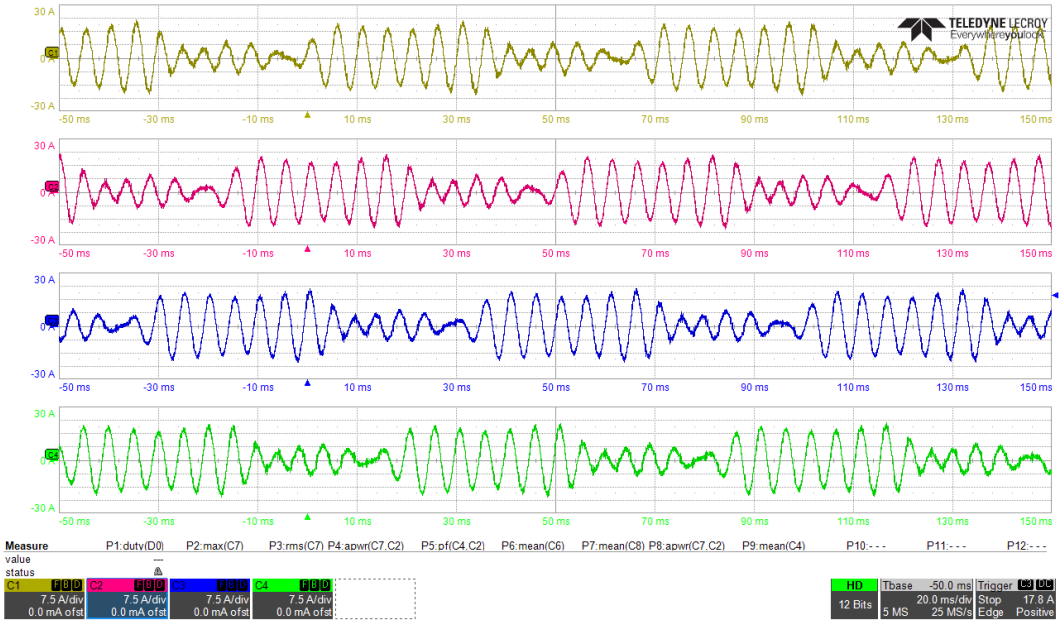

Fig. 4. 56. Ch1: $i_{s1\text{-}a}$ (7.5 A/div), Ch2: $i_{s2\text{-}a}$ (7.5 A/div), Ch3: $i_{s3\text{-}a}$ (7.5 A/div), Ch4: $i_{s4\text{-}a}$ (7.5 A/div). Time resolution: 20 ms/div.

Experimental results for sinusoidal torque sharing in deep flux-weakening conditions

The drive has been tested in generating operation. The following conditions have been set:

$$\begin{cases} f_s = 4\,\text{kHz} & \\ v_{dc,k} = 100\,\text{V} & (k = 1 \div 4) \\ \omega_m = -6000\ \text{r/min} & \\ \delta_{max,k} = 45° & (k = 1 \div 4) \\ s_\lambda = 3 \rightarrow \lambda_s^* = \lambda_{s,rated} & \\ T_k^* = t_{sh,k} \cdot T^* & (k = 1 \div 4) \end{cases} \tag{4.13}$$

With reference to (4.13), it is noted how the DC source voltage has been reduced to about one third of the rated value, thus allowing to test the deep flux-weakening drive operation. Concerning the torque sharing coefficients, they have been defined as follows:

$$\begin{cases} t_{sh,1} = \dfrac{1}{4} + \dfrac{1}{2} \cdot \sin\left(2\pi \cdot 10 \cdot t\right) \\ t_{sh,2} = \dfrac{1}{4} + \dfrac{1}{2} \cdot \sin\left(2\pi \cdot 10 \cdot t - \dfrac{\pi}{2}\right) \\ t_{sh,3} = \dfrac{1}{4} + \dfrac{1}{2} \cdot \sin\left(2\pi \cdot 10 \cdot t - \pi\right) \\ t_{sh,4} = \dfrac{1}{4} + \dfrac{1}{2} \cdot \sin\left(2\pi \cdot 10 \cdot t - \dfrac{3\pi}{2}\right) \end{cases} \tag{4.14}$$

Initially, the machine has operated in no-load condition, leading to a balanced operation of the units. From a certain moment of time onwards, the machine torque reference has suddenly been set to 5 Nm. In addition, the also the torque sharing operations (4.14) have been enabled. Therefore, for each unit a base torque reference value of 1.25 Nm in generation has been set. In addition, a torque reference oscillation having an amplitude of 2.5 Nm and frequency of 10 Hz has been added, leading to the experimental results shown in Fig. 4. 57 - Fig. 4. 60.

It is noted how the torque reference of each unit k has not continuously been fulfilled. Indeed, like for the previous test, the k-unit DFVC scheme has performed a proper saturation of the k-unit torque-producing current reference, thus allowing to keep the k-unit load angle within the maximum allowable limit (4.13).

Nevertheless, with reference to Fig. 4. 54, in this case the load-angles of the units have been limited to the critical value that avoids the machine pull-out. Therefore, through this test it has been demonstrated the torque sharing capability of the proposed scheme in the most critical drive operating condition, corresponding to the Maximum Torque per Volt (MTPV) operation under deep flux-weakening.

Finally, with reference to Fig. 4. 59, it can be noted how the load-angle value of each unit has oscillated within the range of (-7.5 degrees, 45 degrees), thus leading to strong angular differences among the stator flux frames of the units (up to 52.5 degrees). Therefore, through this test, the full validation of the proposed decoupling algorithm has been also performed.

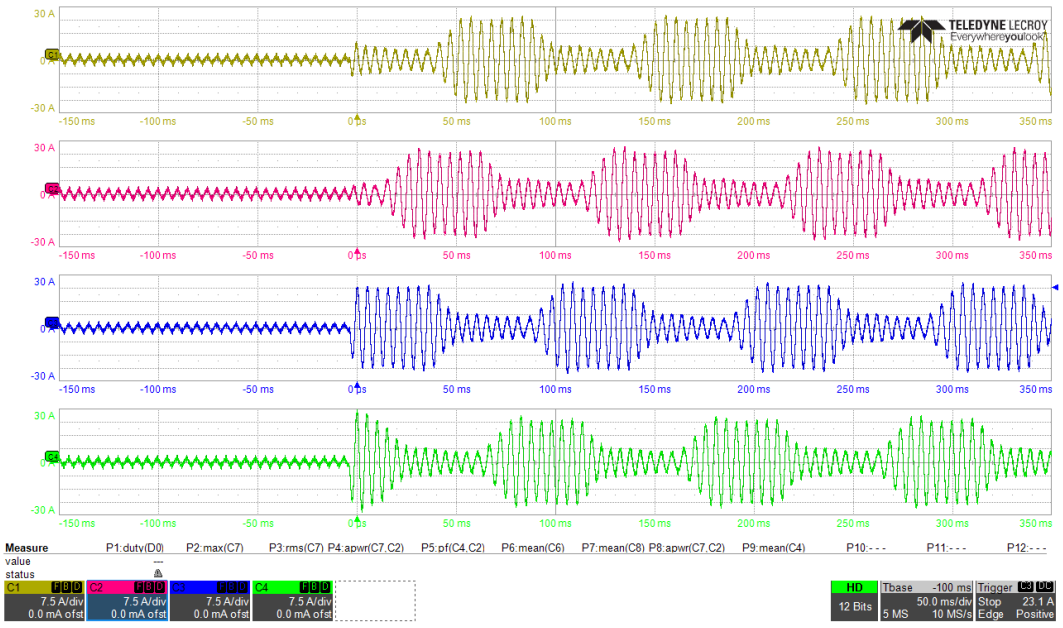

Fig. 4. 57. Ch1: $i_{s1\text{-}a}$ (7.5 A/div), Ch2: $i_{s2\text{-}a}$ (7.5 A/div), Ch3: $i_{s3\text{-}a}$ (7.5 A/div), Ch4: $i_{s4\text{-}a}$ (7.5 A/div). Time resolution: 20 ms/div.

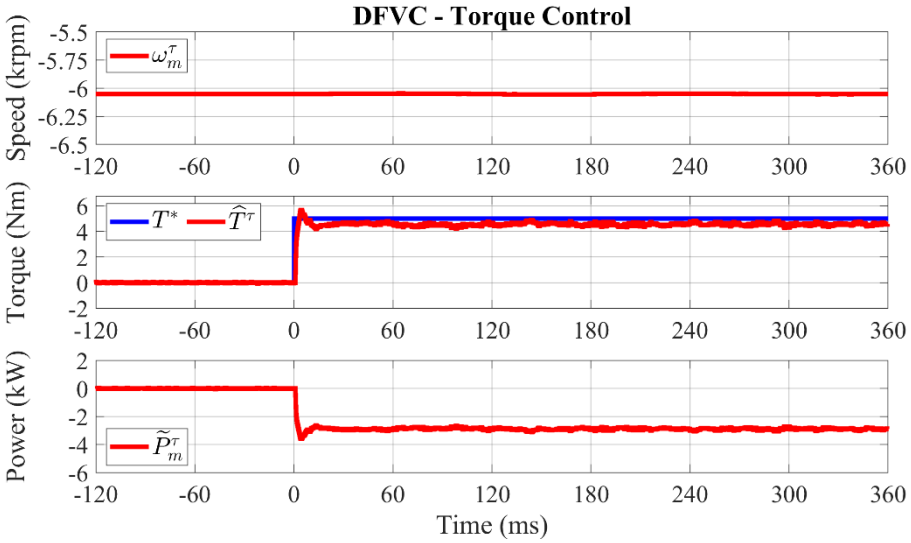

Fig. 4. 58. From top to bottom: measured speed (10^3 · r/min); reference and observed machine torque (Nm); estimated mechanical power (kW).

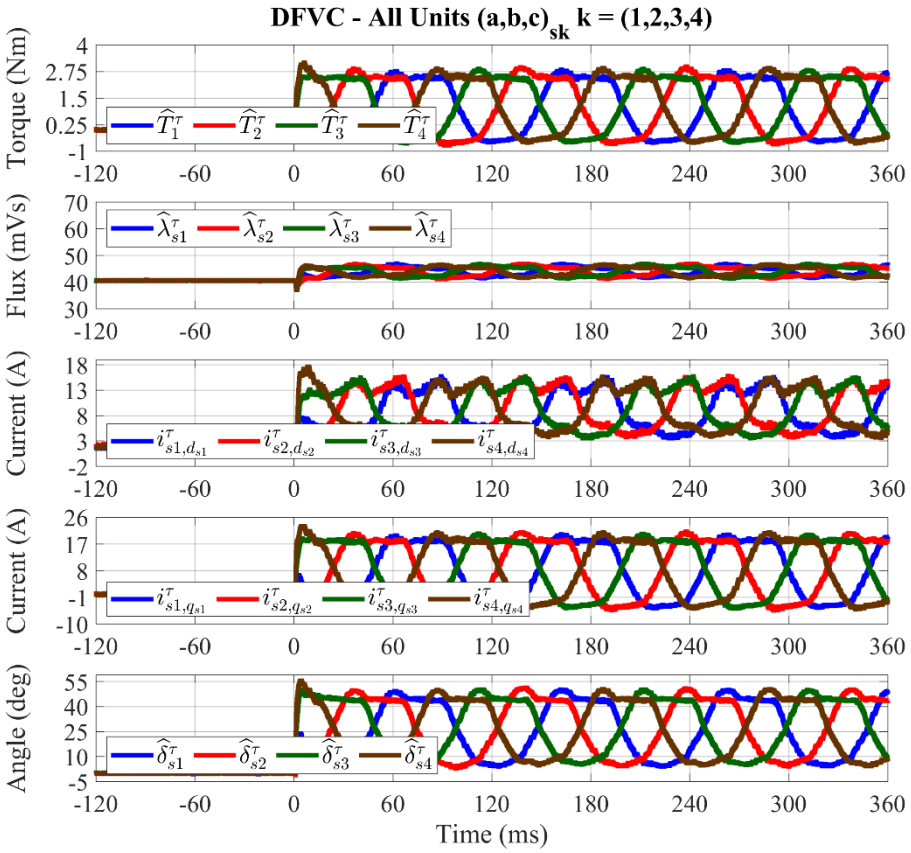

Fig. 4. 59. From top to bottom: single units observed torque (Nm); single units observed flux amplitude (mVs); single units measured d_{sk}-axis current (A); single units measured q_{sk}-axis current (A); single units observed load-angle (deg).

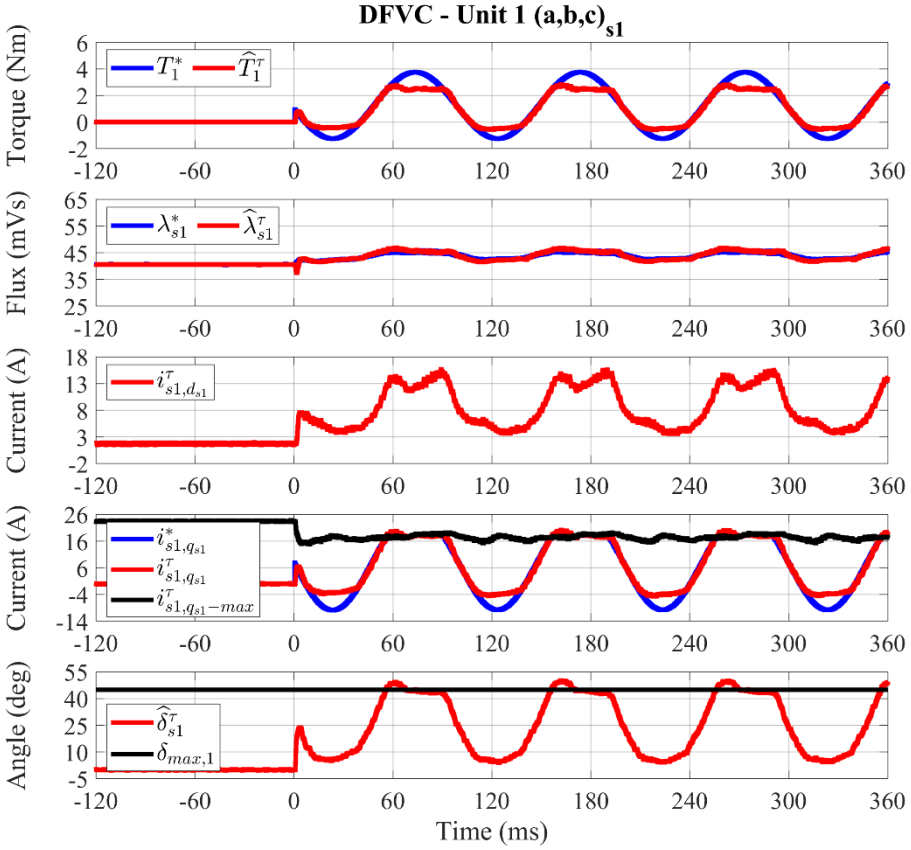

See figure caption: Fig. 4. 60

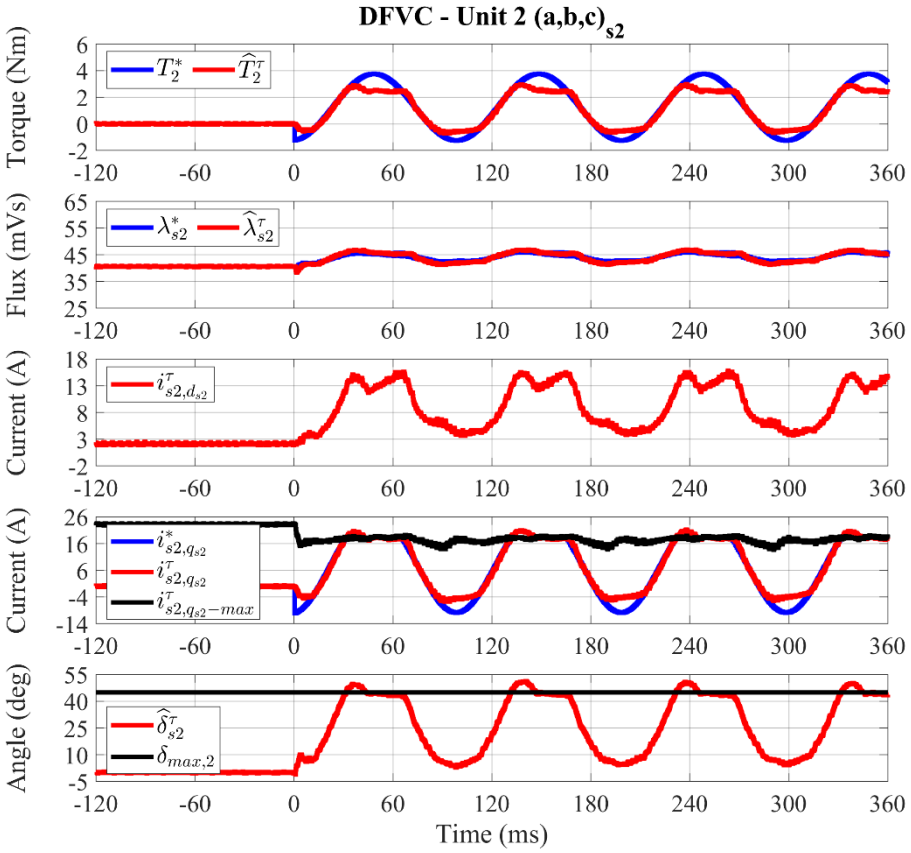

See figure caption: Fig. 4. 60

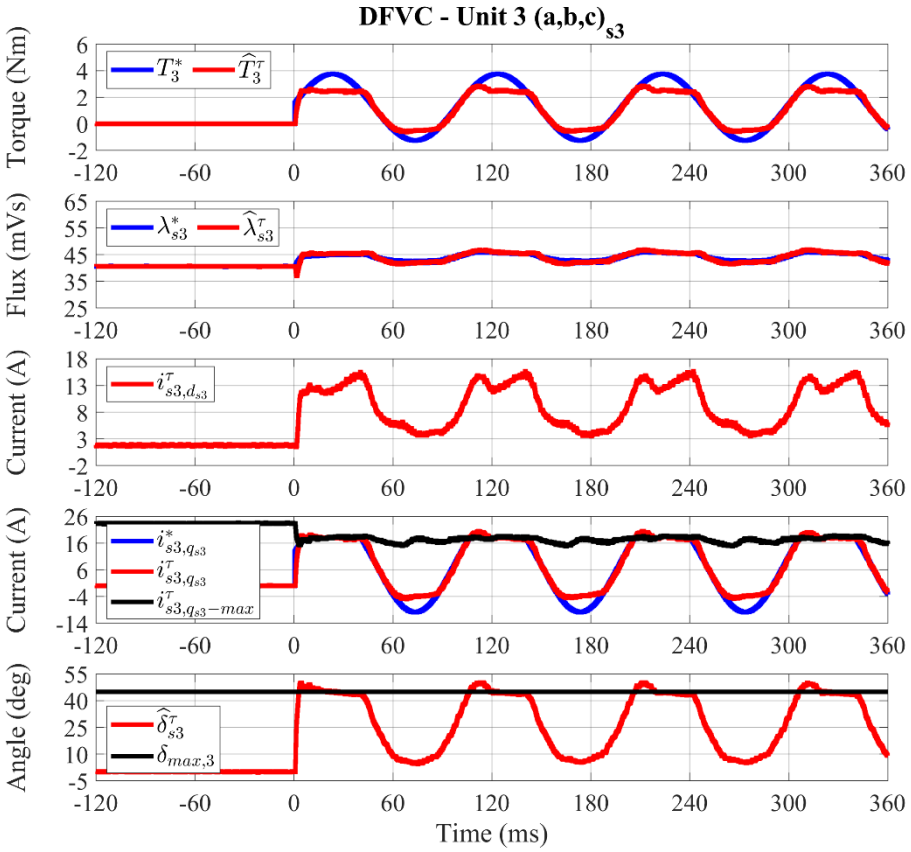

See figure caption: Fig. 4. 60

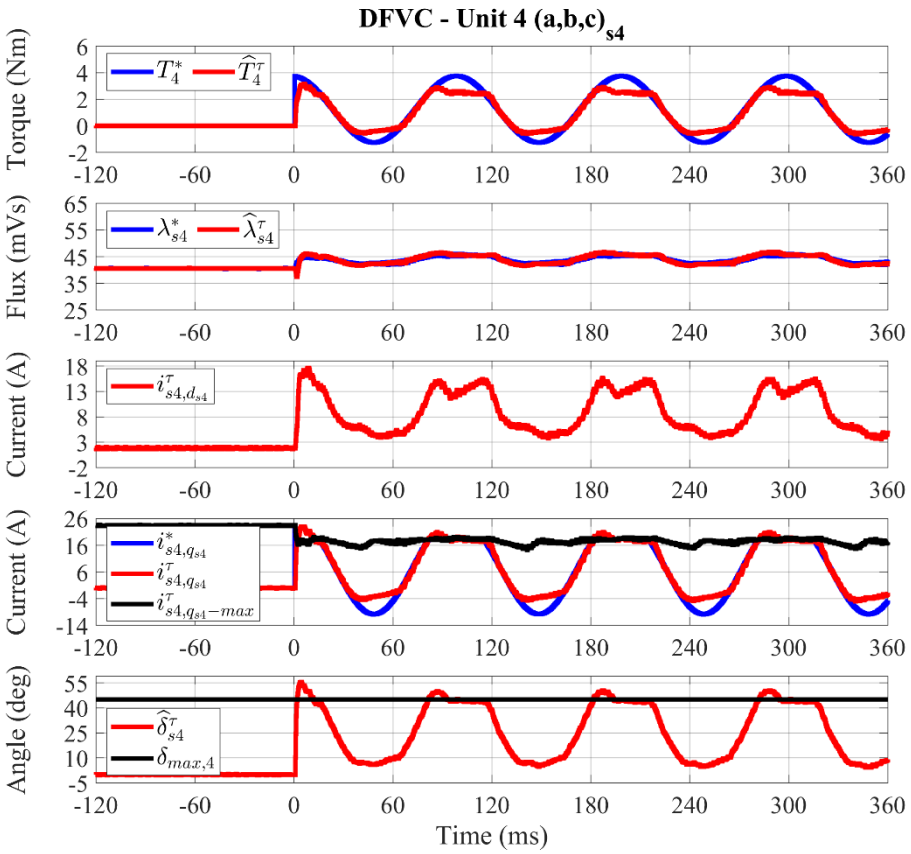

Fig. 4. 60. For each *k*-unit DFVC scheme, from top to bottom: reference and observed torque (Nm); reference and observed flux amplitude (mVs); measured d_{sk}-axis current (A); reference, measured and maximum limit q_{sk}-axis current (A); observed and maximum limit load-angle (deg).

Closed loop speed control test

In this test, the driving machine has been switched-off, thus acting as passive inertial load. Due to the mechanical limitations of the test rig, the speed has been limited within the range of ±6000 r/min. Therefore, the DC source voltage has been reduced to test the flux-weakening and MTPV operation below the speed limit of the test rig. Concerning the other testing conditions, they have been set as follows:

$$\begin{cases} f_s = 5\,\text{kHz} & \\ v_{dc,k} = 100\,\text{V} & (k = 1 \div 4) \\ \delta_{max,k} = 40° & (k = 1 \div 4) \\ s_\lambda = 2 \rightarrow \lambda_s^* = \lambda_{s,opt-max}^{n_a} & \\ T_k^* = \dfrac{T^*}{4} & (k = 1 \div 4) \end{cases} \tag{4.15}$$

It is noted how the test has been performed by imposing the machine's maximum optimal flux value to all units (0.1535 Vs), allowing high-dynamic torque variations together with the full exploitation of the VSI units current limit.

The machine torque reference has been provided by an outer speed controller. This has consisted of a PI regulator whose design is beyond the scope of this dissertation. The obtained results for a step speed reference from zero up to 6000 r/min are shown in Fig. 4. 61 - Fig. 4. 63.

At low speed and without any voltage limitation, the torque has been limited only by the VSI units current limit. The single units torques are slightly different due to the difference values of the d_{sk}-axis currents which define the torque-producing current limits of each unit. The flux-weakening becomes active for a speed that is near to 1500 r/min. The stator fluxes and stator currents are perfectly controlled, as shown in Fig. 4. 63. The MTPV limitation becomes active when the maximum load-angle is reached, at a speed of about 2500 r/min. For safety, the maximum load angle has been set to 40 degrees to avoid the pull-out of the machine. It is noted how the load-angles of the units are perfectly limited, as shown in Fig. 4. 62. The results presented at flux-weakening with closed loop speed control clearly have demonstrated that the proposed scheme is able to work properly under MTPV conditions with load-angle limitation.

Finally, it is noted the deep flux-weakening operation, corresponding to a ratio 1:5 in terms of stator flux amplitude and 1:8 for the rotor one, as shown in Fig. 4. 64.

Experimental results for speed control with inertial load from zero up to 6000 r/min

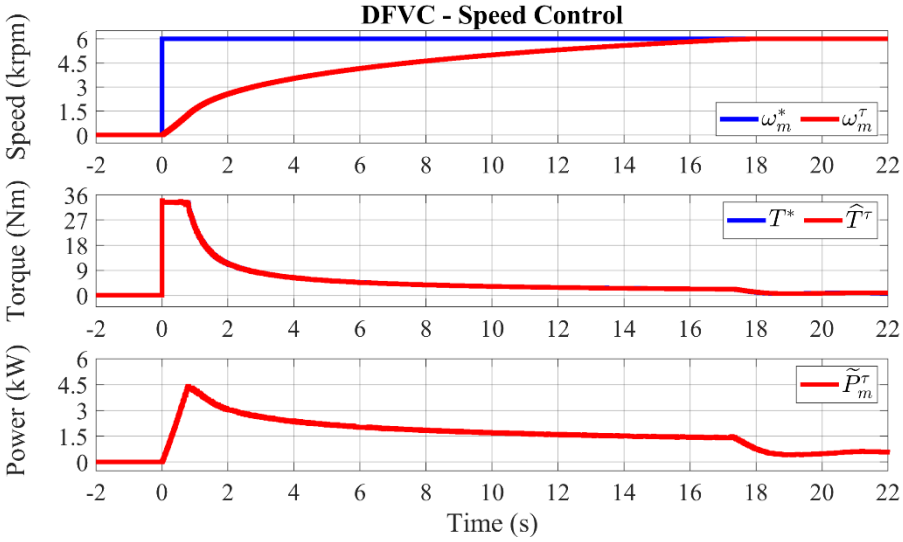

Fig. 4. 61. From top to bottom: measured speed (10^3 · r/min); reference and observed machine torque (Nm); estimated mechanical power (kW).

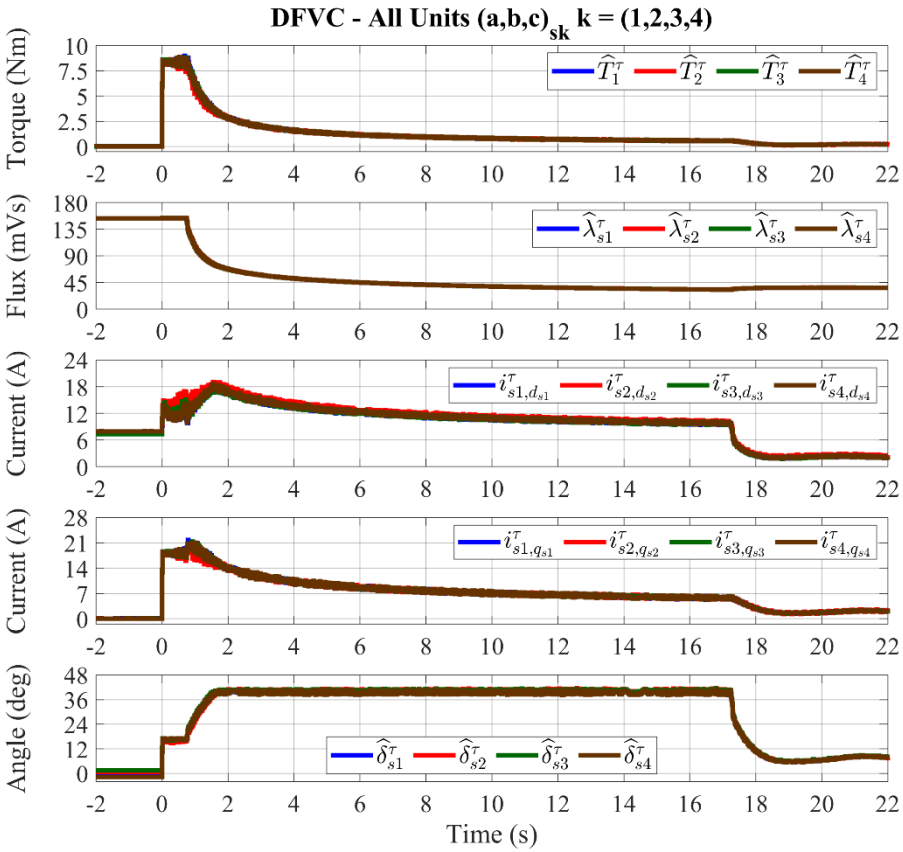

Fig. 4. 62. From top to bottom: single units observed torque (Nm); single units observed flux amplitude (mVs); single units measured d_{sk}-axis current (A); single units measured q_{sk}-axis current (A); single units observed load-angle (deg).

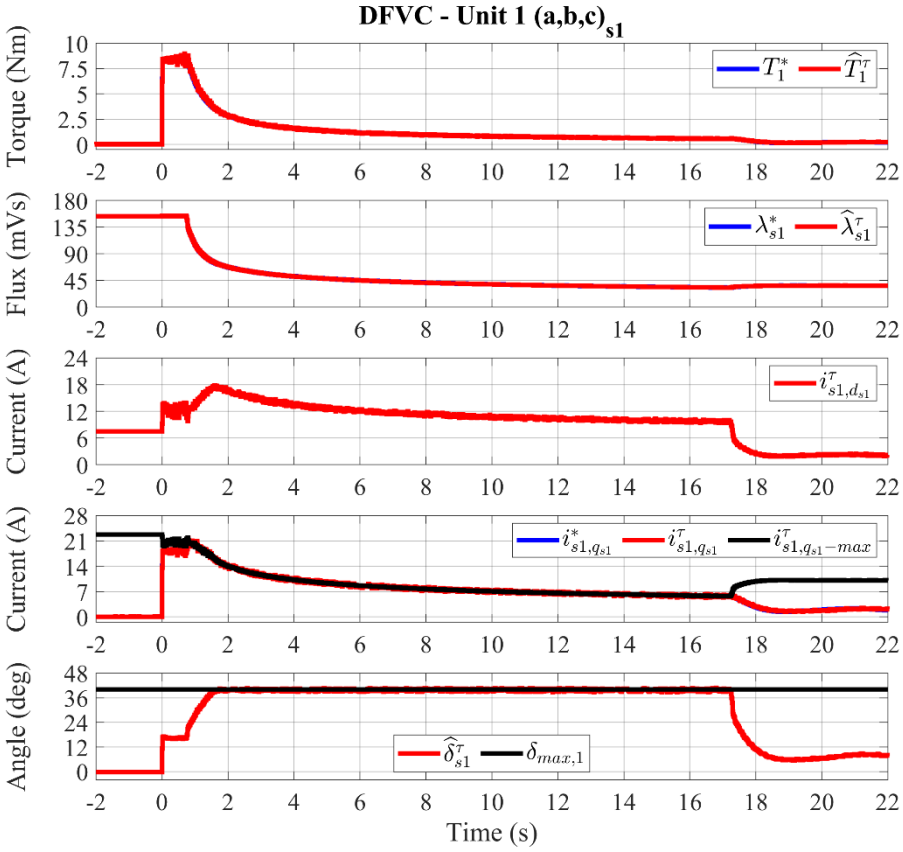

See figure caption: Fig. 4. 63

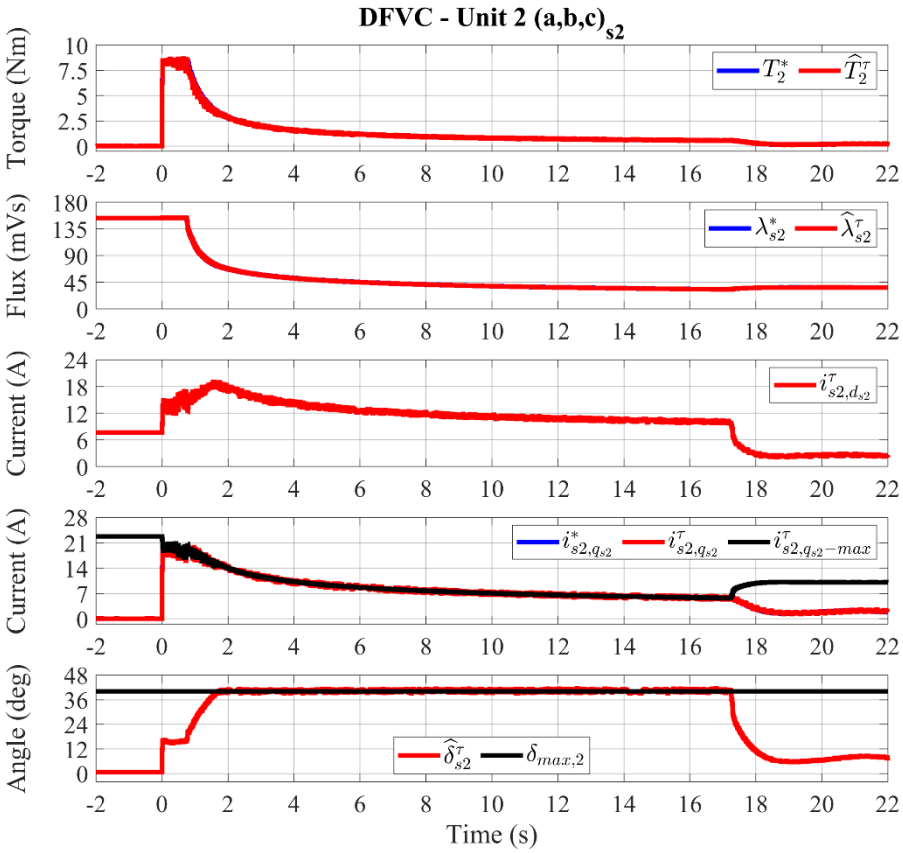

See figure caption: Fig. 4. 63

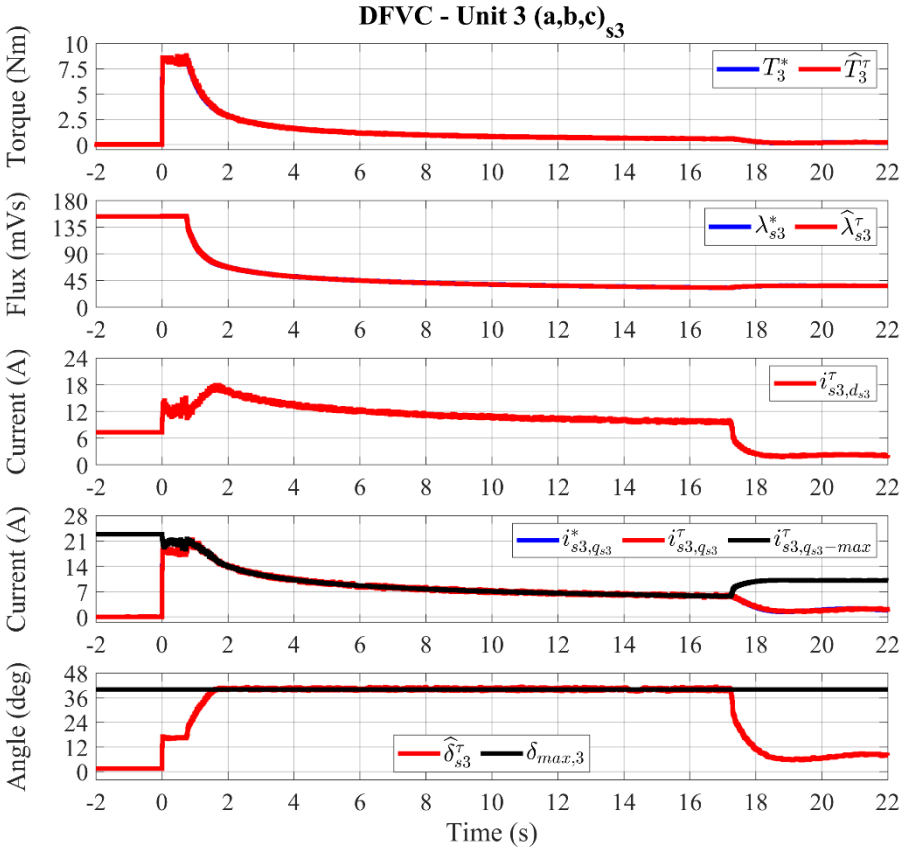

See figure caption: Fig. 4. 63

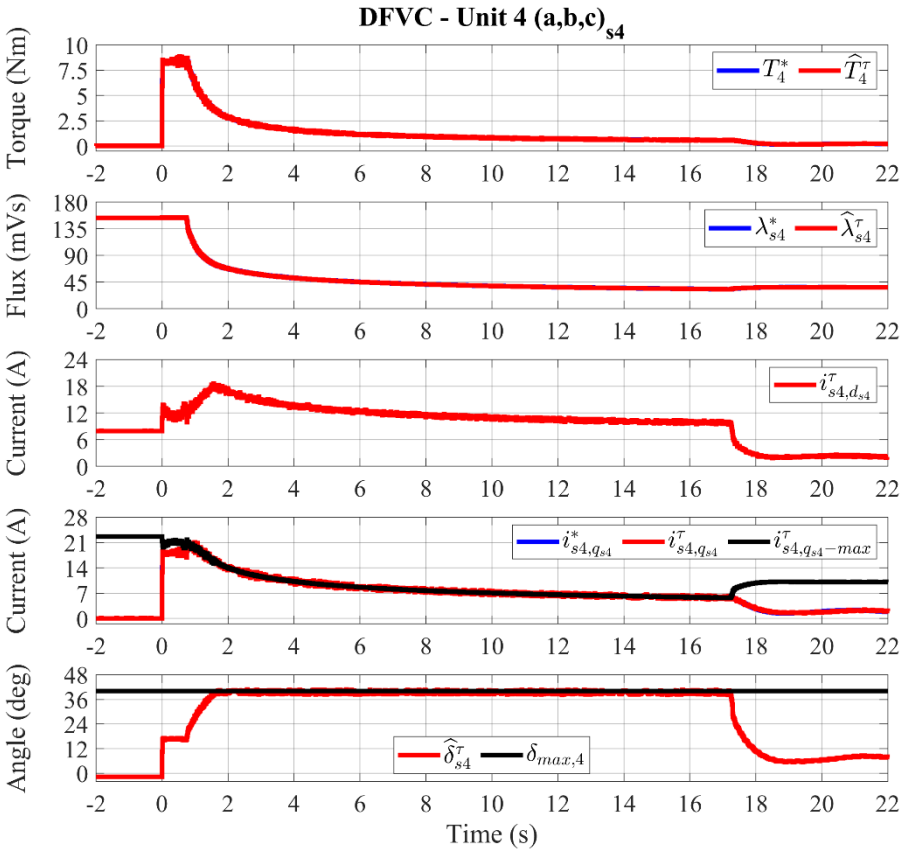

Fig. 4. 63. For each *k*-unit DFVC scheme, from top to bottom: reference and observed torque (Nm); reference and observed flux amplitude (mVs); measured d_{sk}-axis current (A); reference, measured and maximum limit q_{sk}-axis current (A); observed and maximum limit load-angle (deg).

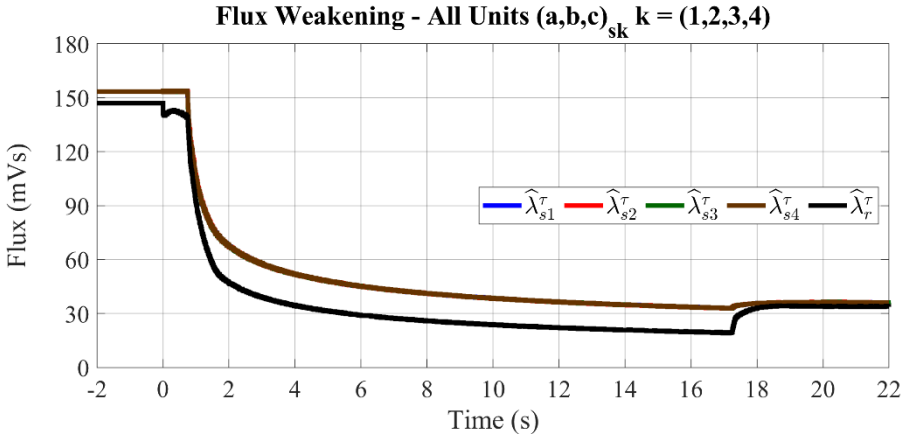

Fig. 4. 64. Single units flux amplitude and rotor flux amplitude (mVs).

4.2.2 Experimental validation of the DB-DFVC scheme

The validation of the DB-DFVC scheme has been carried out on the asymmetrical 6-phase configuration. Due to the high computational efforts required to the digital controller, only the balanced operation of the machine has been tested.

According with the descriptions of both electrical machine and power converter, the DFVC schemes of the units have been designed using common values of the respective control parameters, as reported in Table 4. 5.

For the all performed experimental tests, the sampling frequency and the VSI units switching frequency have been set at 6 kHz.

In the next subsections, the obtained experimental results for the following tests are provided:

- Open loop torque control
  - Fast torque transients in healthy conditions
  - Fault ride-through capability for open three-phase set
- Closed loop speed control
  - Deep flux-weakening operation

Flux Observer	
Observer gain ω_{ck}	125 rad/s
Control Structure	
DC-link voltage exploitation degree $k_{\lambda\text{-max}}$	0.9
Maximum phase-current limit $I_{max,k}$	24 A
Maximum load angle $\delta_{max,k}$	40°
Unit Control – Torque-producing current Integral Compensator	
Integral gain k_{comp}	100 V/(A·s)
Voltage margin	0.1 (p.u.)

Table 4. 5. Values of the control parameters belonging to the k-unit DB-DFVC scheme (k=1,2).

Open loop torque control tests

The mechanical speed has been imposed by the driving machine (speed controlled), while the machine under test was torque controlled. The experimental results concerns the drive operation under healthy and open-winding fault conditions.

Fast torque transients in healthy conditions

The drive has been tested in both motoring and generating operation. With reference to (4.2)-(4.3), the following conditions have been set:

$$\begin{cases} v_{dc,k} = 550\,\text{V} & (k=1,2) \\ \omega_m = -6000\,\text{r/min} & \\ s_\lambda = 3 \rightarrow \lambda_s^* = \lambda_{s,rated} & \\ T_k^* = \dfrac{T^*}{2} & (k=1,2) \end{cases} \tag{4.16}$$

The execution of the fast torque transients has led to the performance validation of each *k*-unit DB-based regulation (*k*=1,2). In addition, the effectiveness of the proposed decoupling algorithm has been verified.

The experimental results for the fast torque transient (40 Nm/ms) from -24 Nm to +24 Nm (150% of rated value) are shown in Fig. 4. 65 - Fig. 4. 68. Each three-phase winding set has produced a half of the total torque, corresponding to ±12 Nm. In motoring mode, the target torque is not reached due to the voltage and current limitations. Conversely, in generation mode the target torque can be reached, as shown in Fig. 4. 67 - Fig. 4. 68.

With reference to Fig. 4. 68, it is clearly noted the one-step ahead prediction of the currents and fluxes belonging to each unit, as well as the DB torque response, despite the high slew-rate of the torque reference that corresponds to an inversion of the mechanical power from -15 kW to +15 kW in just 1.5 ms (Fig. 4. 65).

The currents of the units are perfectly balanced under both no-load and load conditions. This is demonstrated by the experimental results related to the fast torque transients (40 Nm/ms) from zero up to -24 Nm in motoring (Fig. 4. 69 - Fig. 4. 73) and from zero up to 24 Nm in generation (Fig. 4. 74 - Fig. 4. 78).

Experimental results for fast torque transient (40 Nm/ms) from 150% rated torque in motoring to 150% rated torque in generation at -6000 r/min

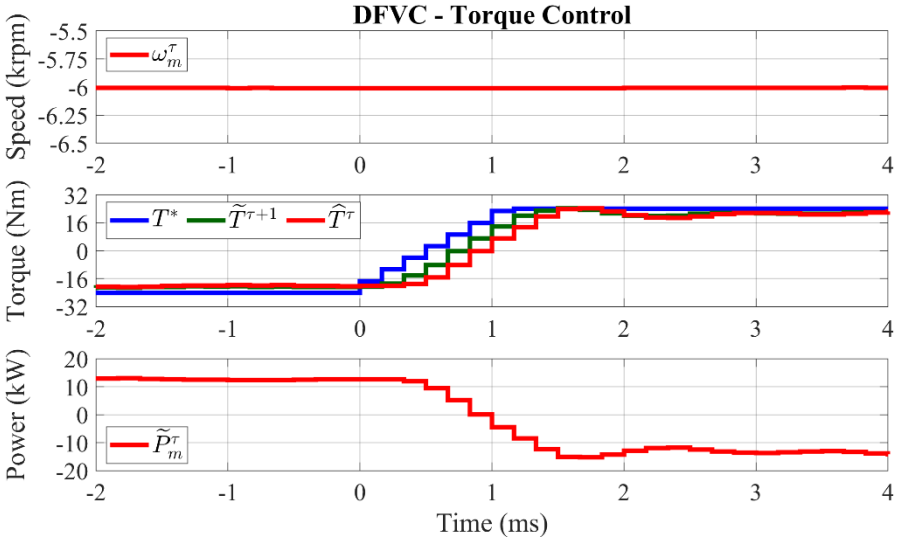

Fig. 4. 65. From top to bottom: measured speed (10^3 · r/min); reference, observed and predicted machine torque (Nm); estimated mechanical power (kW).

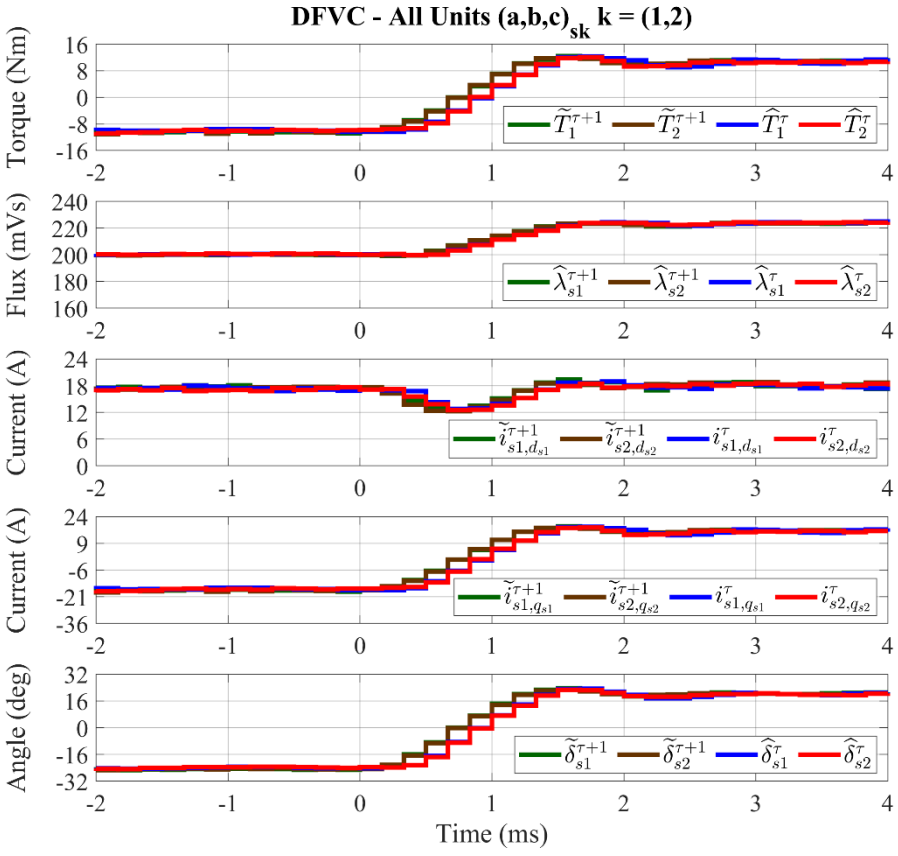

Fig. 4. 66. From top to bottom: single units observed and predicted torque (Nm); single units observed and predicted flux amplitude (mVs); single units measured and predicted d_{sk}-axis current (A); single units measured and predicted q_{sk}-axis current (A); single units observed and predicted load-angle (deg).

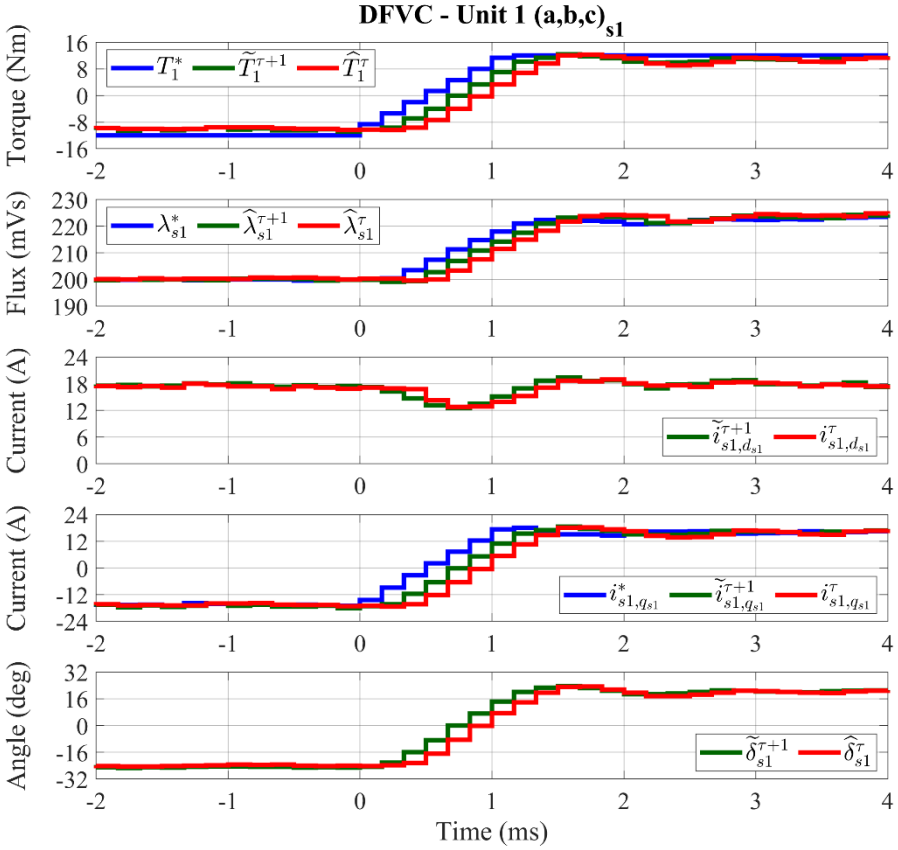

See figure caption: Fig. 4. 67

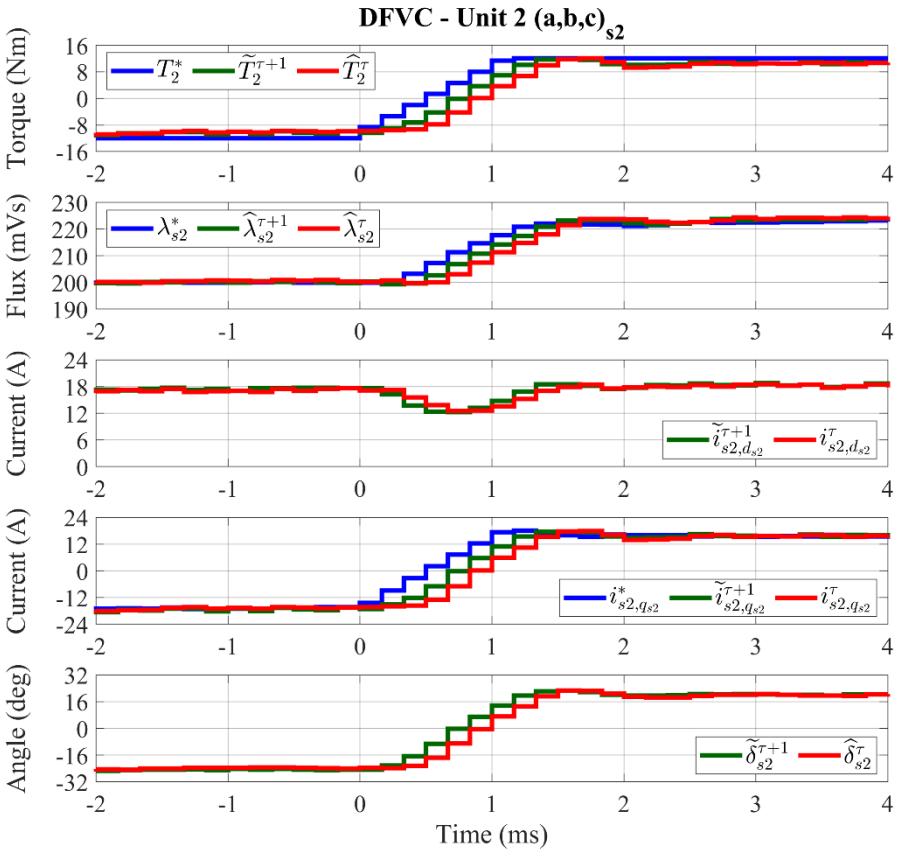

Fig. 4. 67. For each *k*-unit DFVC scheme, from top to bottom: reference, observed and predicted torque (Nm); reference, observed and predicted flux amplitude (mVs); measured and predicted d_{sk}-axis current (A); reference, measured and predicted q_{sk}-axis current (A); observed and predicted load-angle (deg).

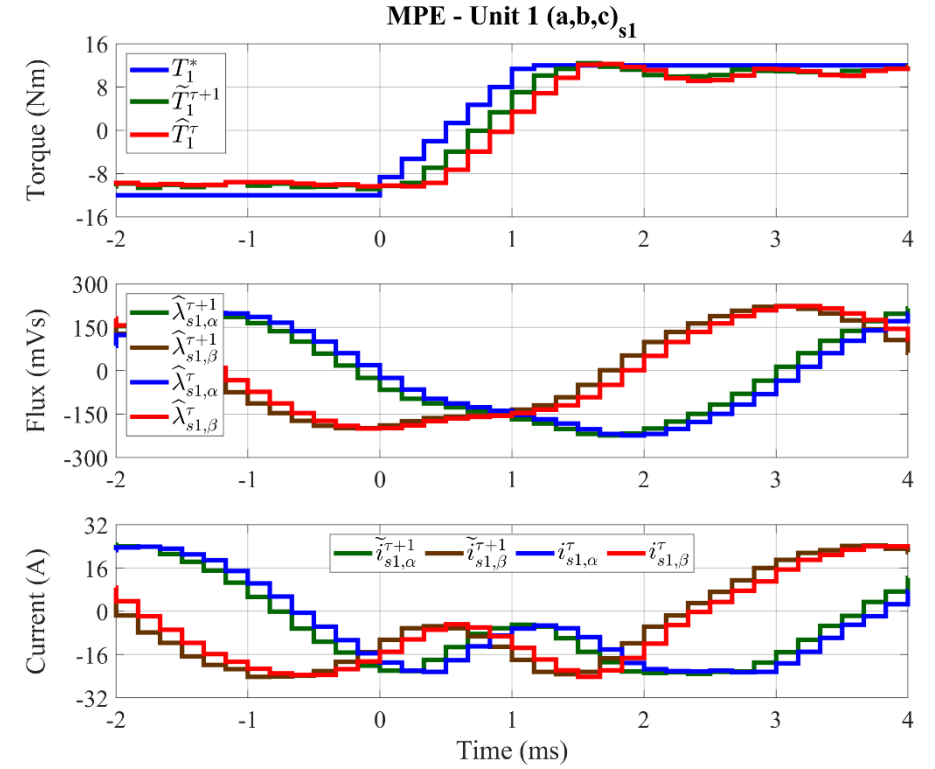

See figure caption: Fig. 4. 68

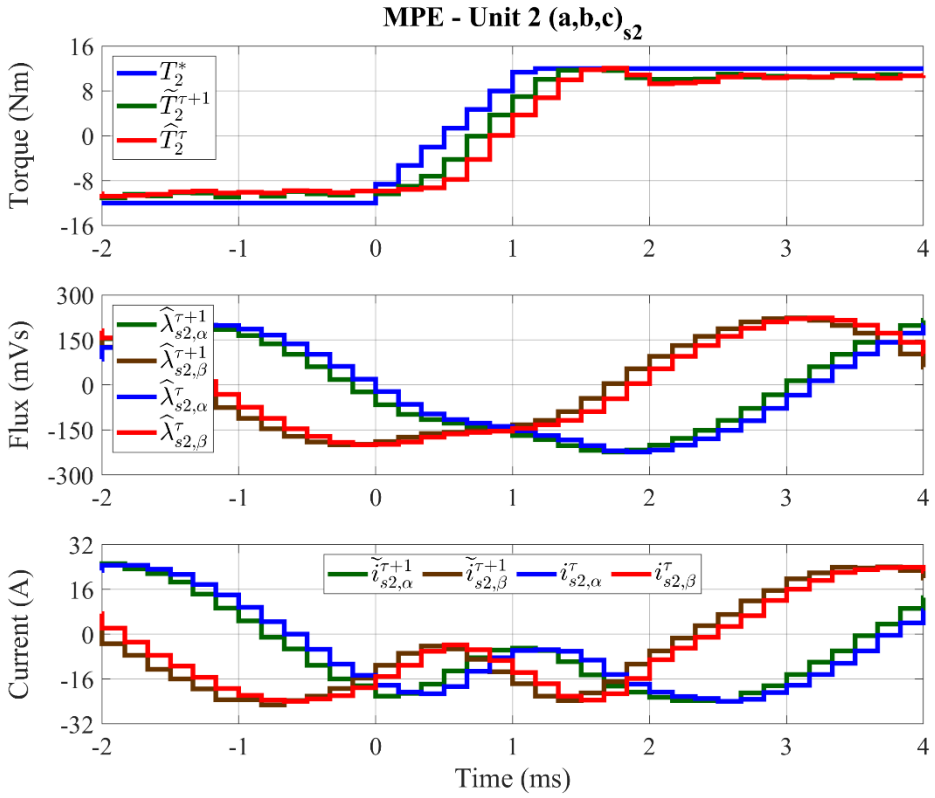

Fig. 4. 68. For each *k*-unit model predictive estimator (MPE), from top to bottom: reference, observed and predicted torque (Nm); (α,β) observed and predicted fluxes (mVs); (α,β) measured and predicted currents (A).

Experimental results for fast torque transient (40 Nm/ms) from no-load (0 Nm) up to 150% rated torque (24 Nm) in motoring at -6000 r/min

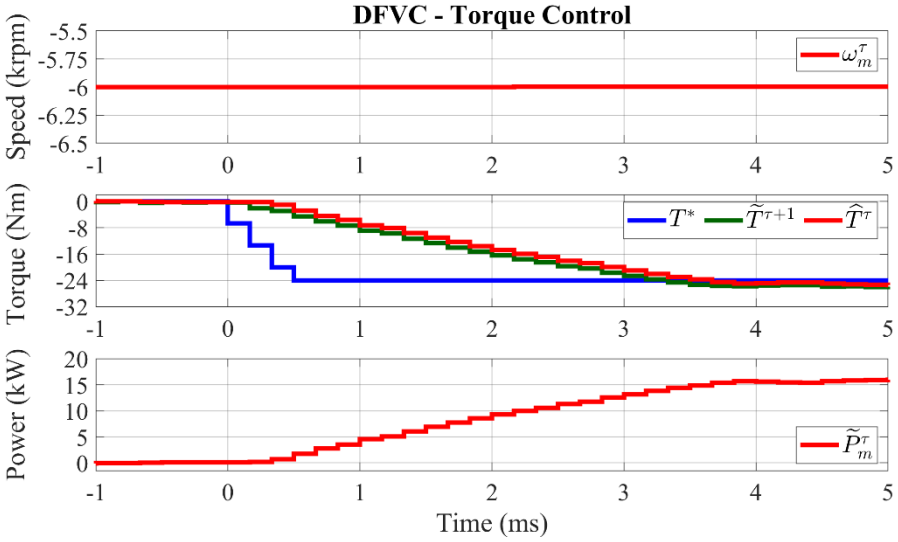

Fig. 4. 69. From top to bottom: measured speed (10^3 · r/min); reference, observed and predicted machine torque (Nm); estimated mechanical power (kW).

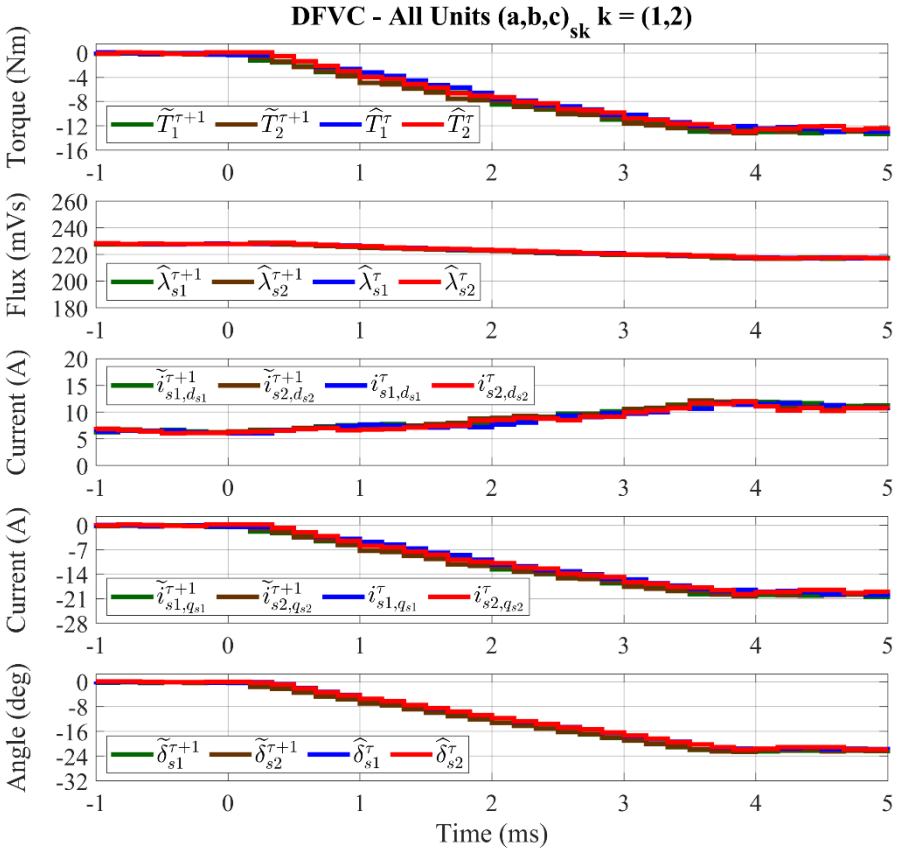

Fig. 4. 70. From top to bottom: single units observed and predicted torque (Nm); single units observed and predicted flux amplitude (mVs); single units measured and predicted d_{sk}-axis current (A); single units measured and predicted q_{sk}-axis current (A); single units observed and predicted load-angle (deg).

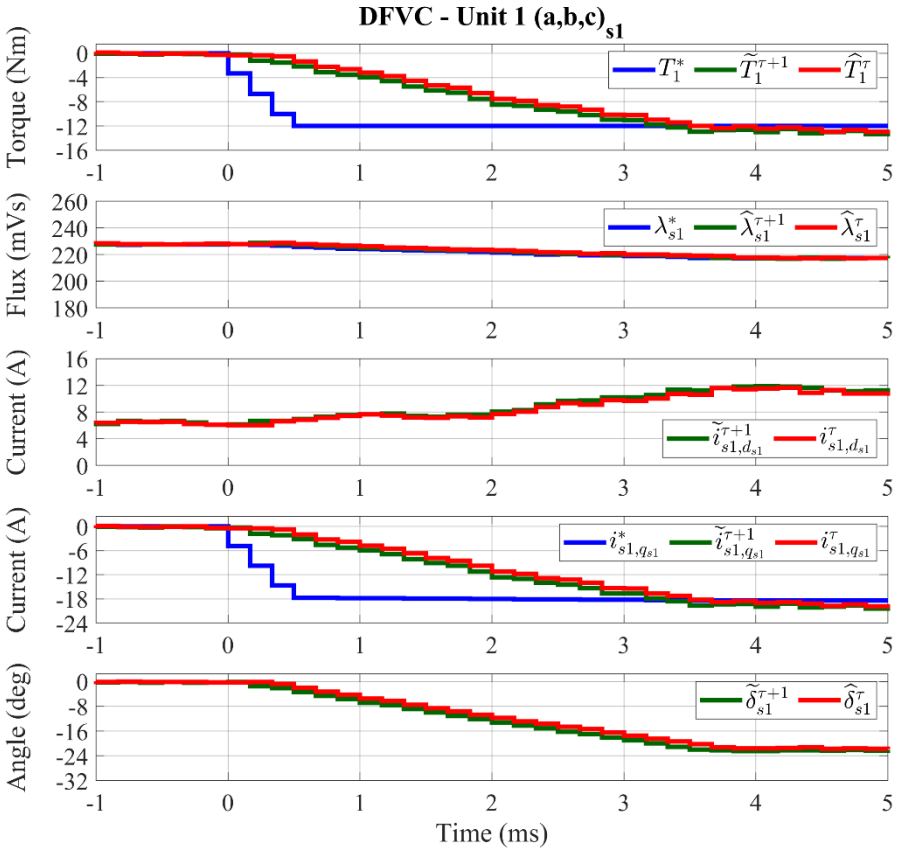

See figure caption: Fig. 4. 71

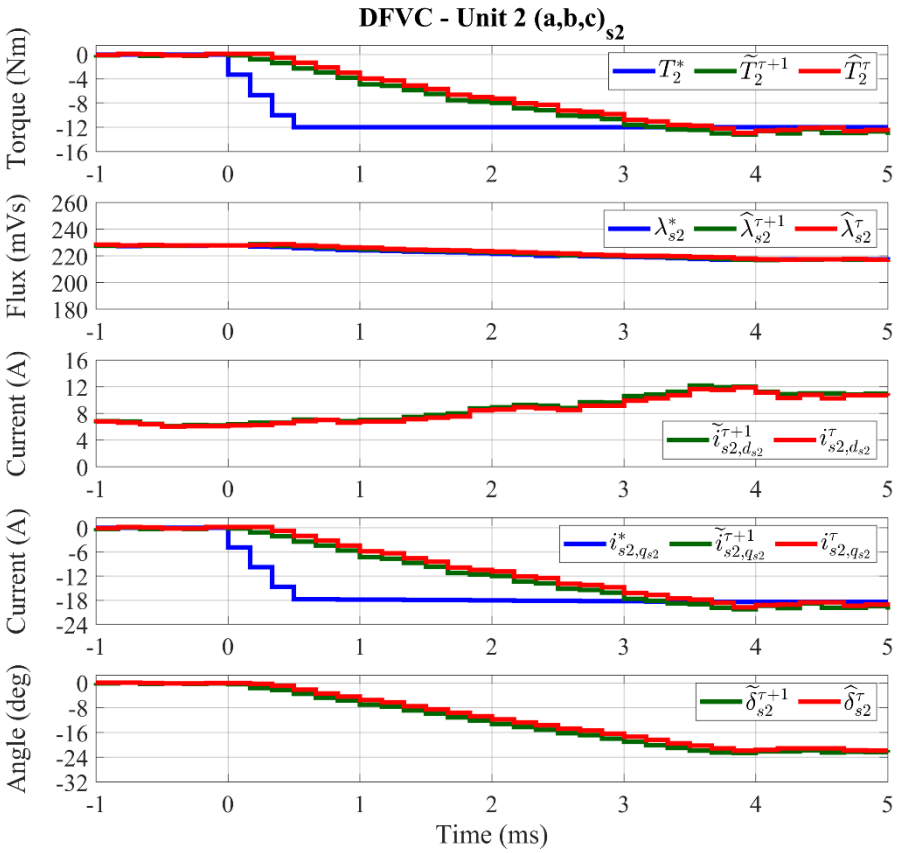

Fig. 4. 71. For each *k*-unit DFVC scheme, from top to bottom: reference, observed and predicted torque (Nm); reference, observed and predicted flux amplitude (mVs); measured and predicted d_{sk}-axis current (A); reference, measured and predicted q_{sk}-axis current (A); observed and predicted load-angle (deg).

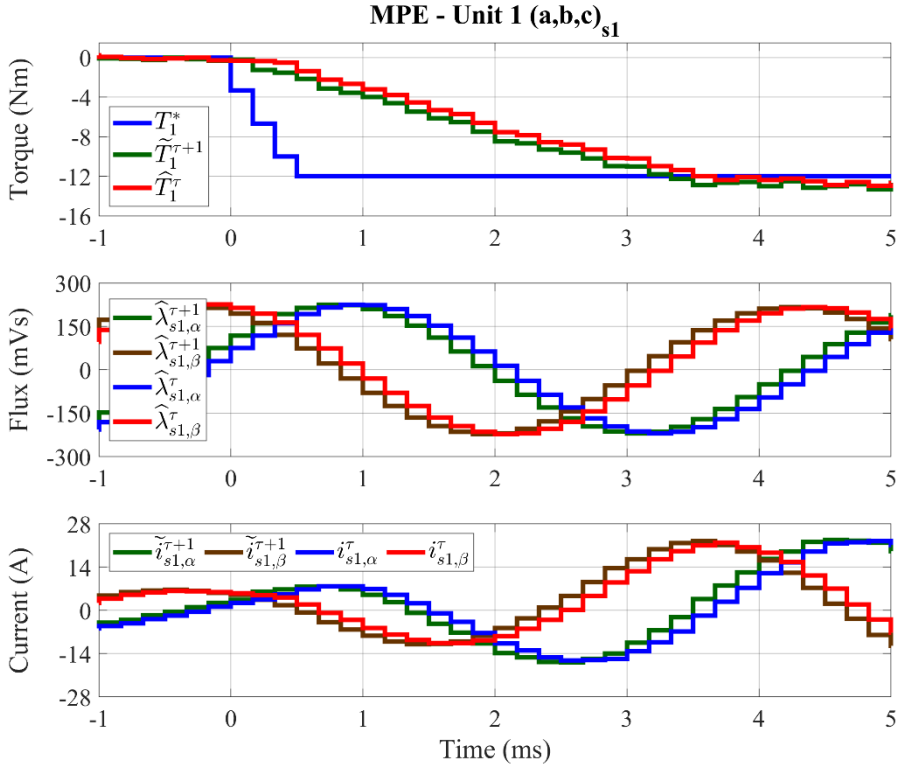

See figure caption: Fig. 4. 72

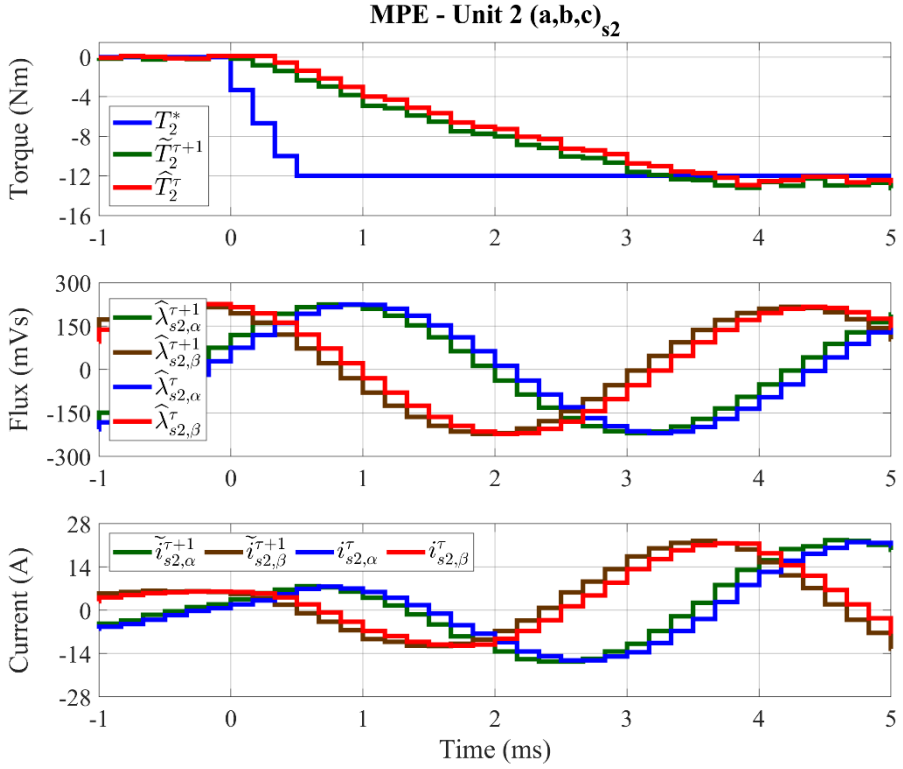

Fig. 4. 72. For each *k*-unit model predictive estimator (MPE), from top to bottom: reference, observed and predicted torque (Nm); (α,β) observed and predicted fluxes (mVs); (α,β) measured and predicted currents (A).

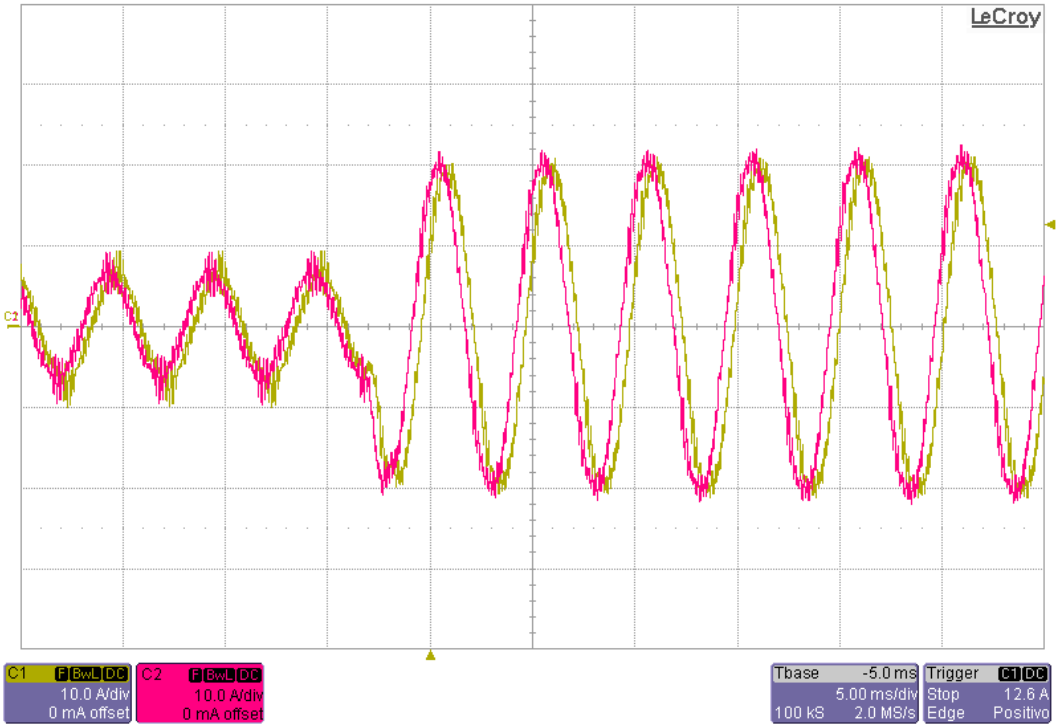

Fig. 4. 73. Ch1: $i_{s1\text{-}a}$ (10 A/div), Ch2: $i_{s2\text{-}a}$ (10 A/div). Time resolution: 5 ms/div.

Experimental results for fast torque transient (40 Nm/ms) from no-load (0 Nm) up to 150% rated torque (24 Nm) in generation at -6000 r/min

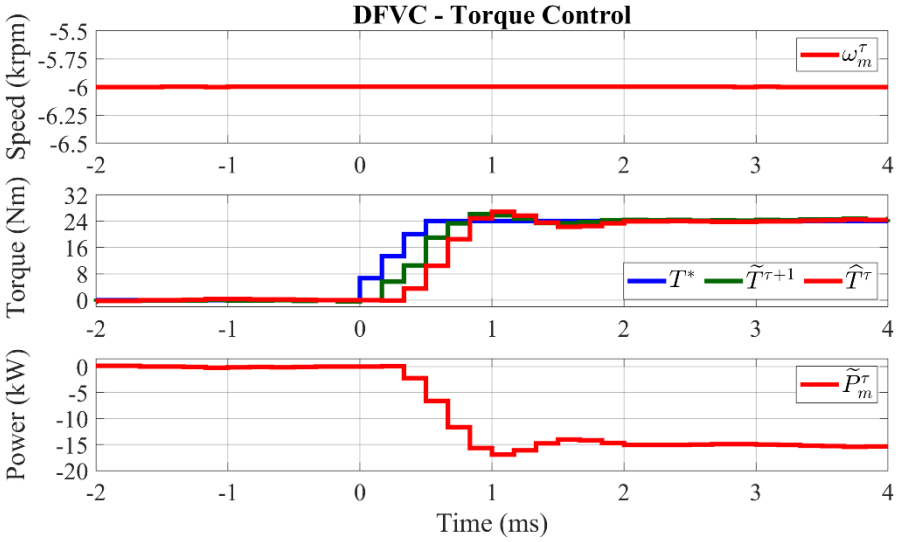

Fig. 4. 74. From top to bottom: measured speed (10^3 · r/min); reference, observed and predicted machine torque (Nm); estimated mechanical power (kW).

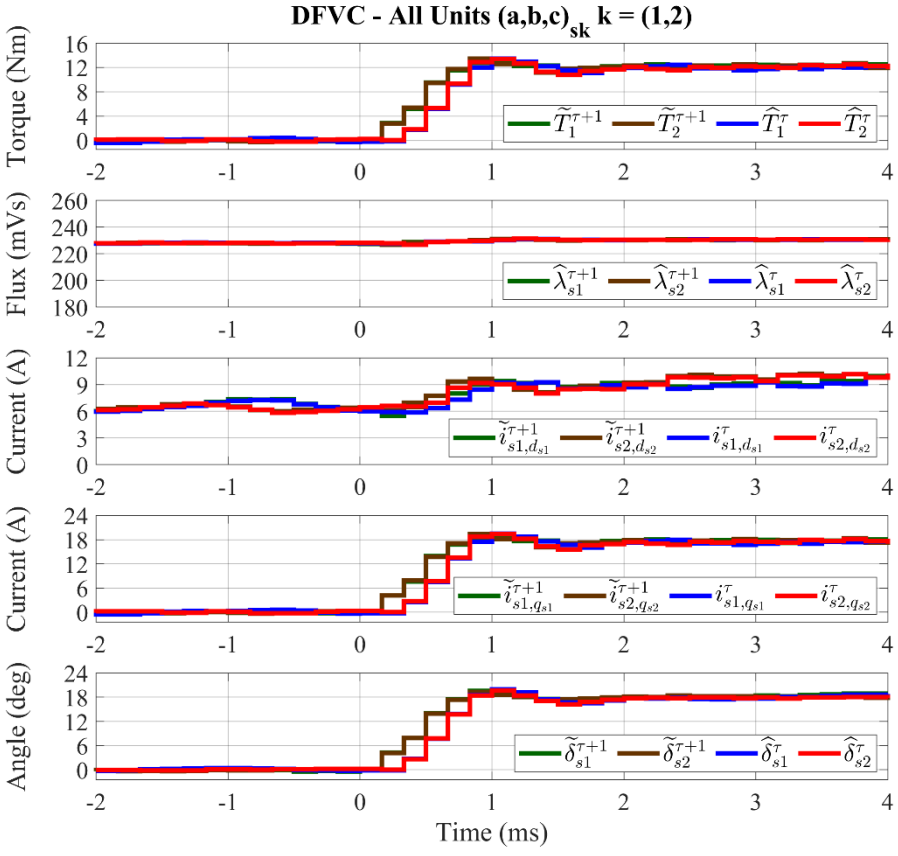

Fig. 4. 75. From top to bottom: single units observed and predicted torque (Nm); single units observed and predicted flux amplitude (mVs); single units measured and predicted d_{sk}-axis current (A); single units measured and predicted q_{sk}-axis current (A); single units observed and predicted load-angle (deg).

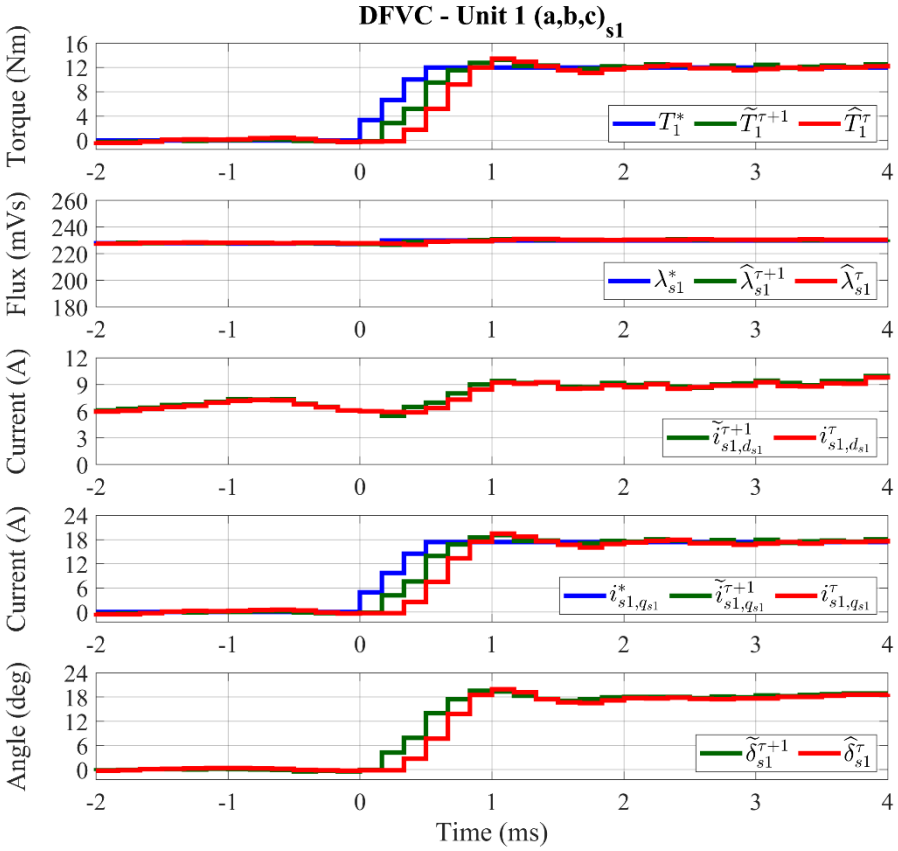

See figure caption: Fig. 4. 76

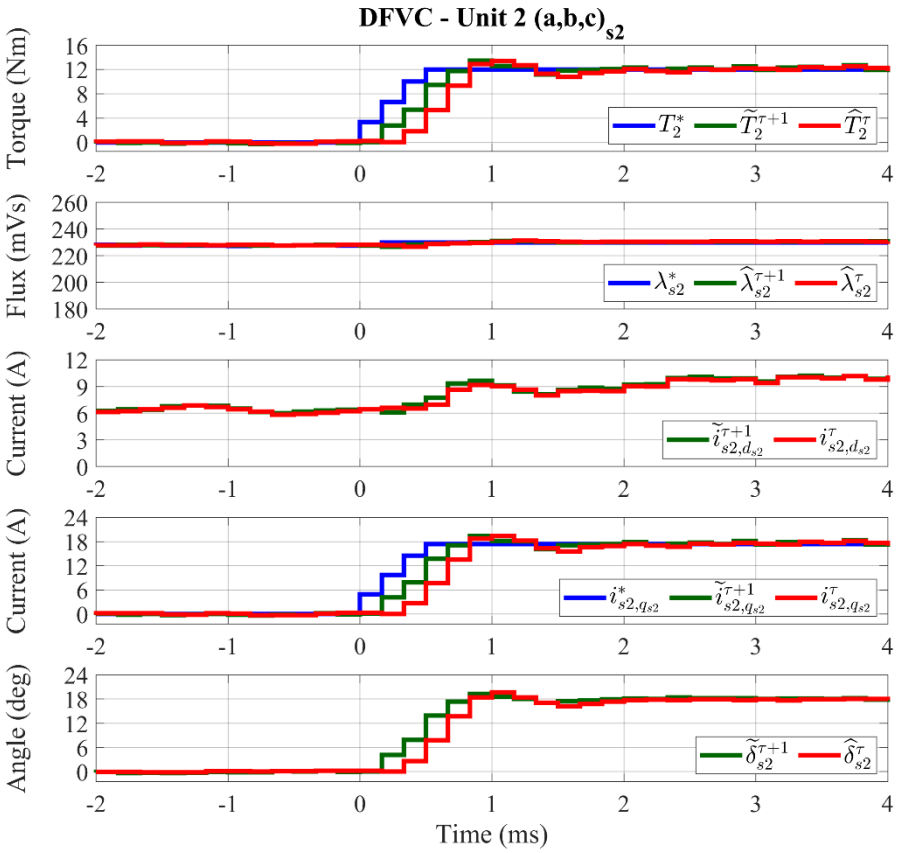

Fig. 4. 76. For each *k*-unit DFVC scheme, from top to bottom: reference, observed and predicted torque (Nm); reference, observed and predicted flux amplitude (mVs); measured and predicted d_{sk}-axis current (A); reference, measured and predicted q_{sk}-axis current (A); observed and predicted load-angle (deg).

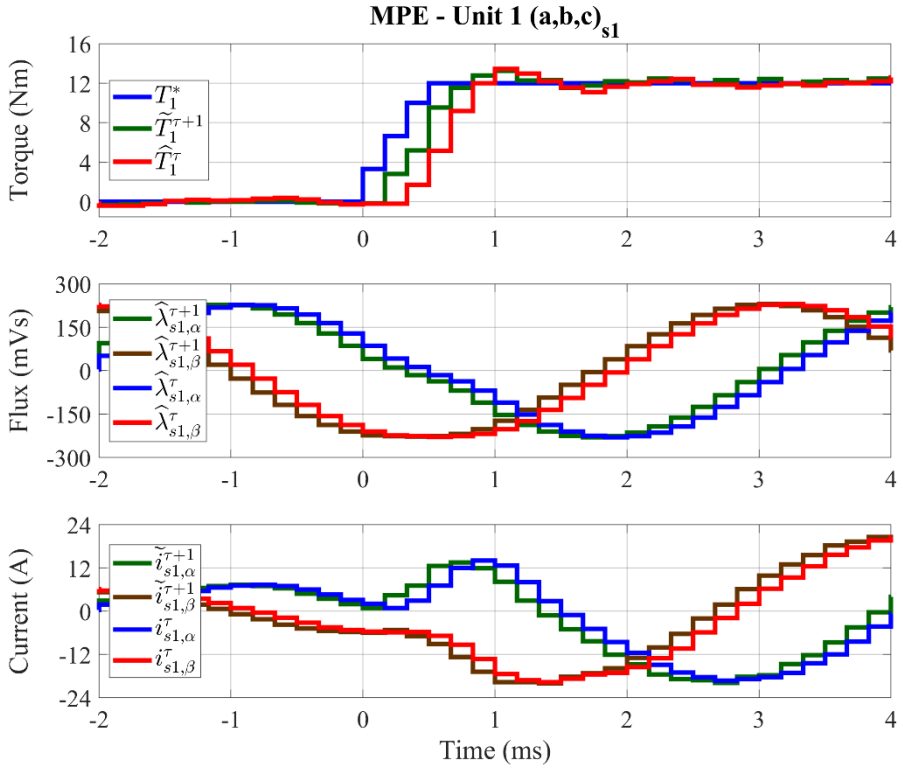

See figure caption: Fig. 4. 77

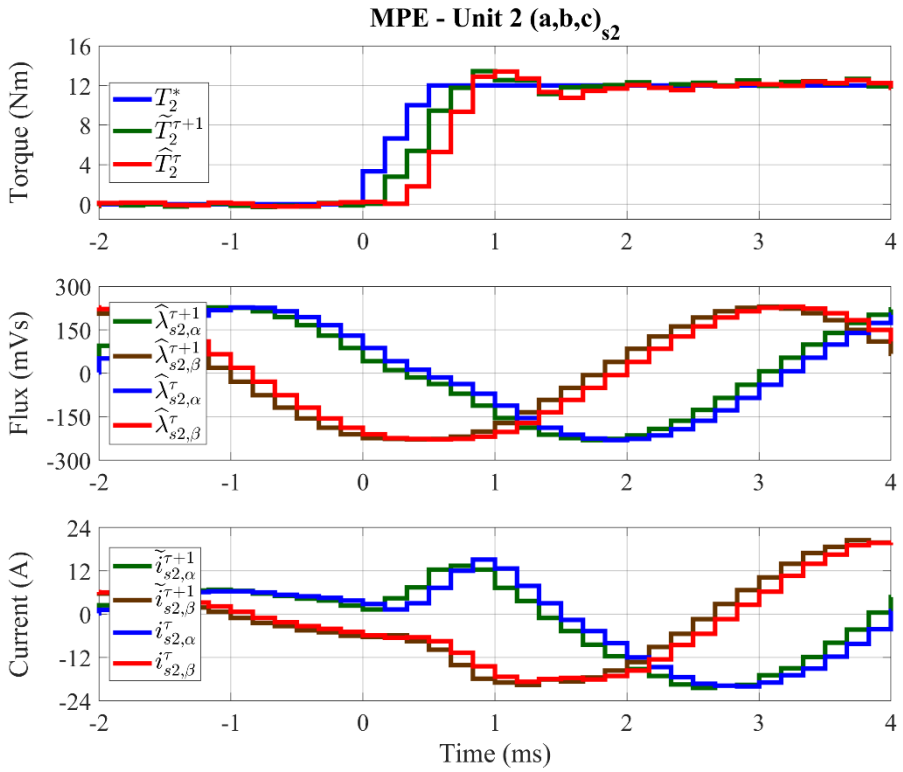

Fig. 4. 77. For each *k*-unit model predictive estimator (MPE), from top to bottom: reference, observed and predicted torque (Nm); (α,β) observed and predicted fluxes (mVs); (α,β) measured and predicted currents (A).

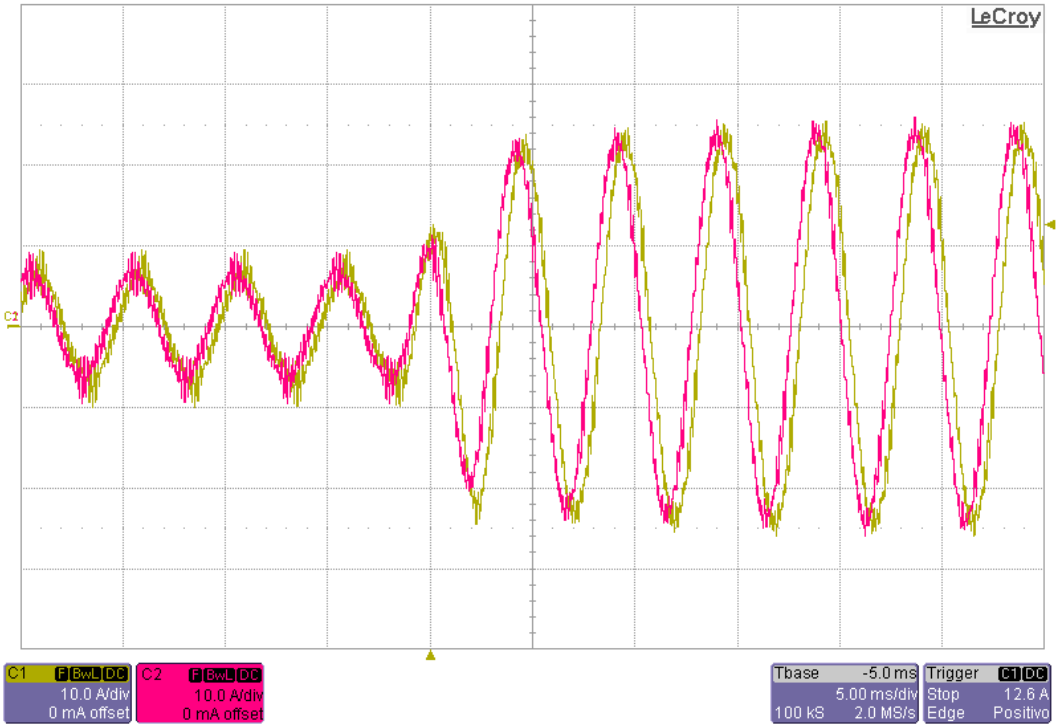

Fig. 4. 78. Ch1: $i_{s1\text{-}a}$ (10 A/div), Ch2: $i_{s2\text{-}a}$ (10 A/div). Time resolution: 5 ms/div.

Fault ride-through capability for open three-phase set

The drive has been tested in generating operation. With reference to (4.2)-(4.3), the following conditions have been set:

$$\begin{cases} v_{dc,k} = 550\,\text{V} & (k=1,2) \\ \omega_m = -6000\,\text{r/min} & \\ s_\lambda = 3 \rightarrow \lambda_s^* = \lambda_{s,rated} & \\ T_k^* = x_{f,k}^{\tau} \cdot \dfrac{T^*}{n_a} & (k=1,2) \end{cases} \tag{4.17}$$

To demonstrate the drive "fault ride-through" capability when one VSI unit is suddenly disabled, they are shown the experimental results for the open-phase operation for sudden VSI 2 turn-off at 10 Nm (Fig. 4. 79 - Fig. 4. 83).

It is noted how the healthy unit exhibits sinusoidal currents that increase within the allowed limits to keep the same torque and machine flux, as shown in Fig. 4. 83. The torque response and the torque-producing current response of the healthy unit exhibit slight overshoots due to the shut-off dynamic of the faulty unit. Indeed, the current transient of the faulty unit is slow and acts as disturbance on the DB regulation of the healthy unit (Fig. 4. 81). Nevertheless, this test has provided the proof of the modularity of the MS-based control schemes, with the maximum degree of freedom in the control of each single unit.

Experimental results for sudden VSI 2 turn-off during generation mode with torque control at -6000 r/min with 10 Nm (rated torque)

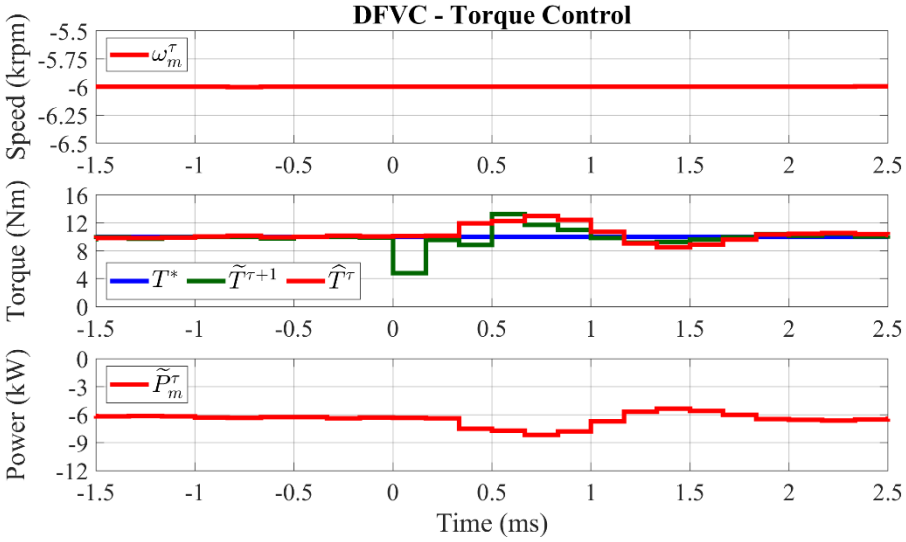

Fig. 4. 79. From top to bottom: measured speed (10^3 · r/min); reference, observed and predicted machine torque (Nm); estimated mechanical power (kW).

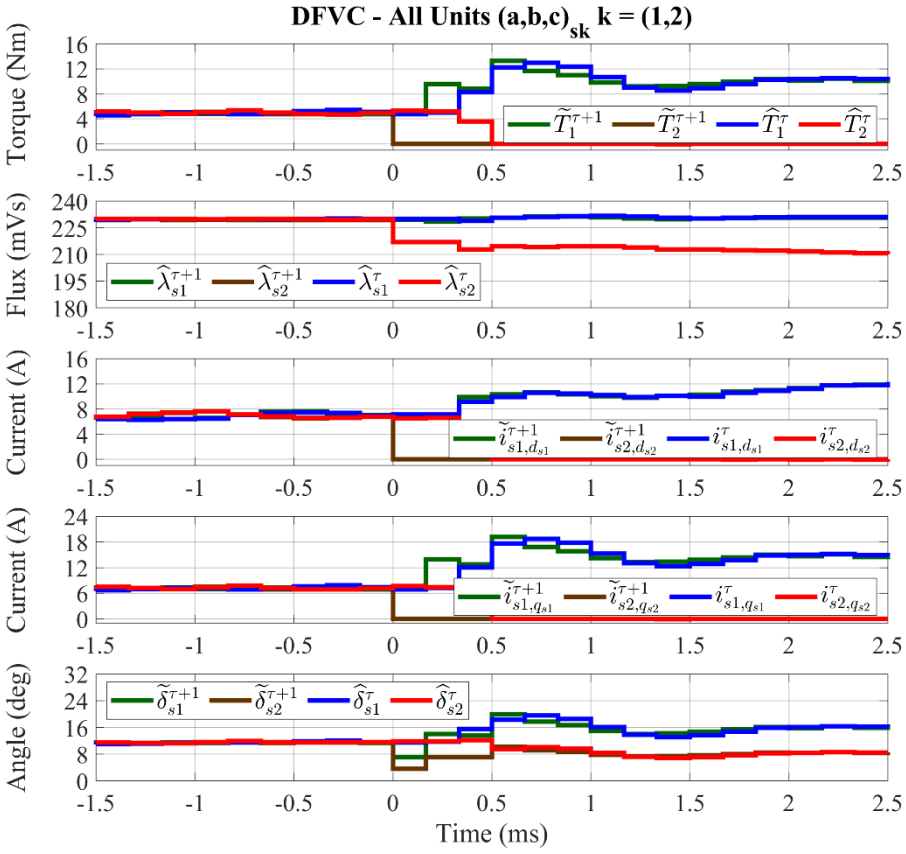

Fig. 4. 80. From top to bottom: single units observed and predicted torque (Nm); single units observed and predicted flux amplitude (mVs); single units measured and predicted d_{sk}-axis current (A); single units measured and predicted q_{sk}-axis current (A); single units observed and predicted load-angle (deg).

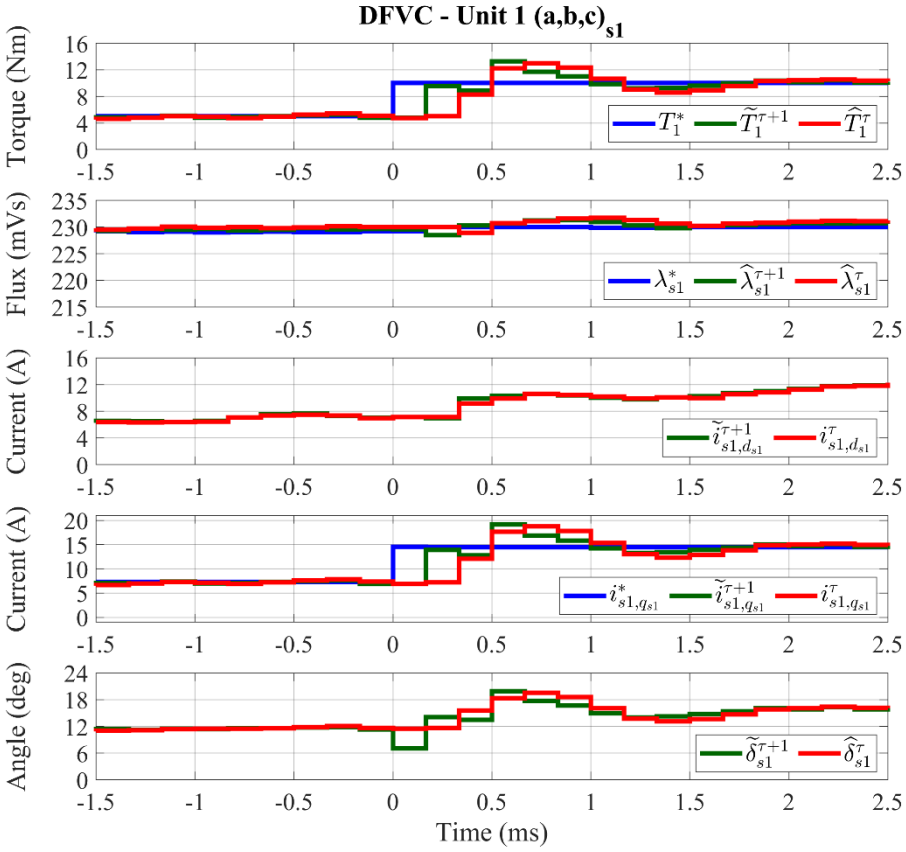

See figure caption: Fig. 4. 81

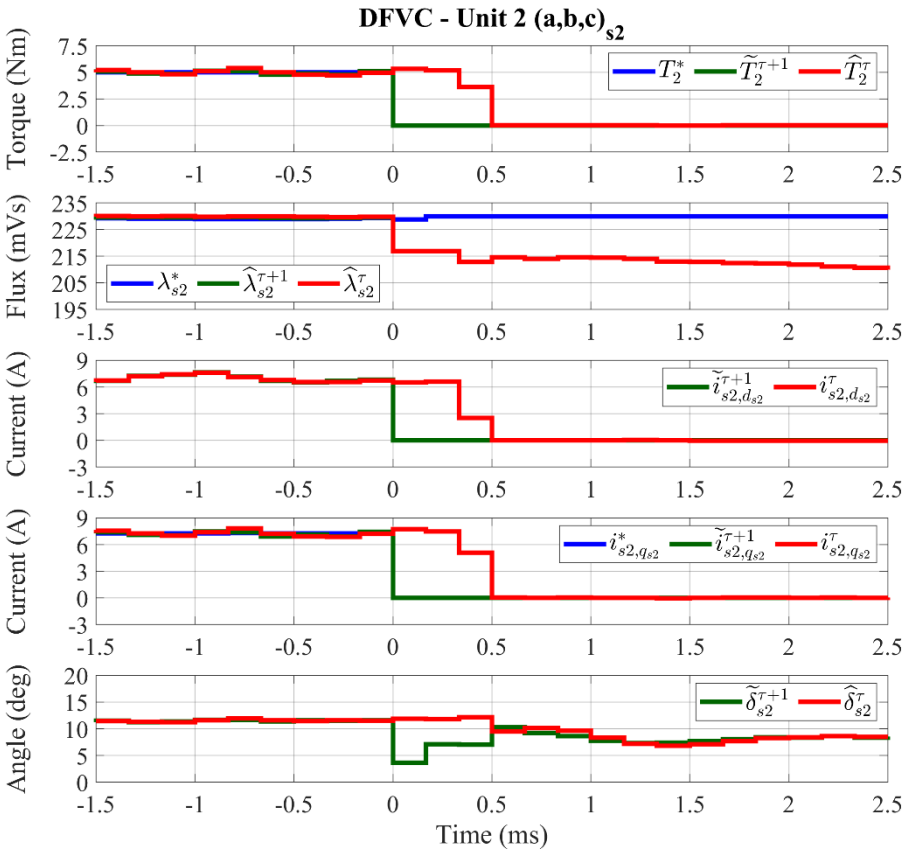

Fig. 4. 81. For each *k*-unit DFVC scheme, from top to bottom: reference, observed and predicted torque (Nm); reference, observed and predicted flux amplitude (mVs); measured and predicted d_{sk}-axis current (A); reference, measured and predicted q_{sk}-axis current (A); observed and predicted load-angle (deg).

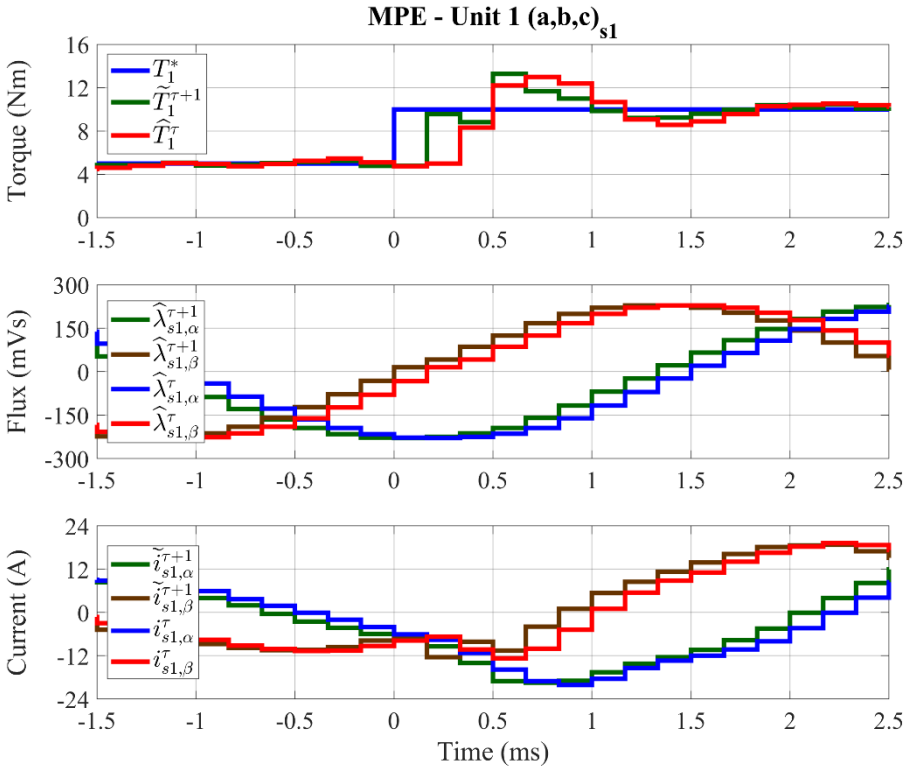

See figure caption: Fig. 4. 82

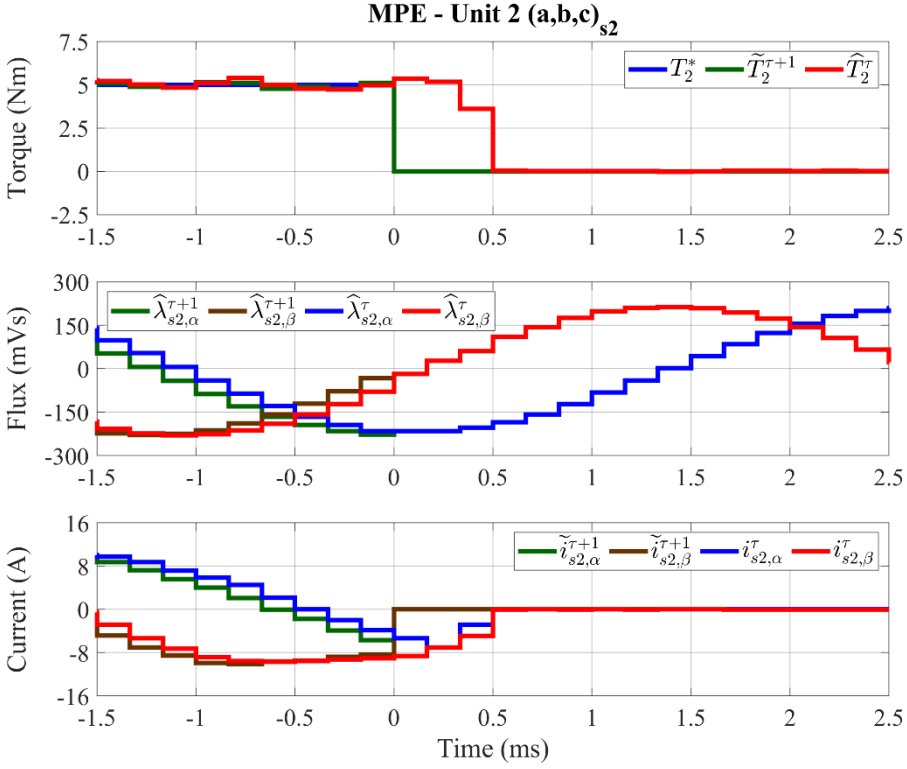

Fig. 4. 82. For each *k*-unit model predictive estimator (MPE), from top to bottom: reference, observed and predicted torque (Nm); (α,β) observed and predicted fluxes (mVs); (α,β) measured and predicted currents (A).

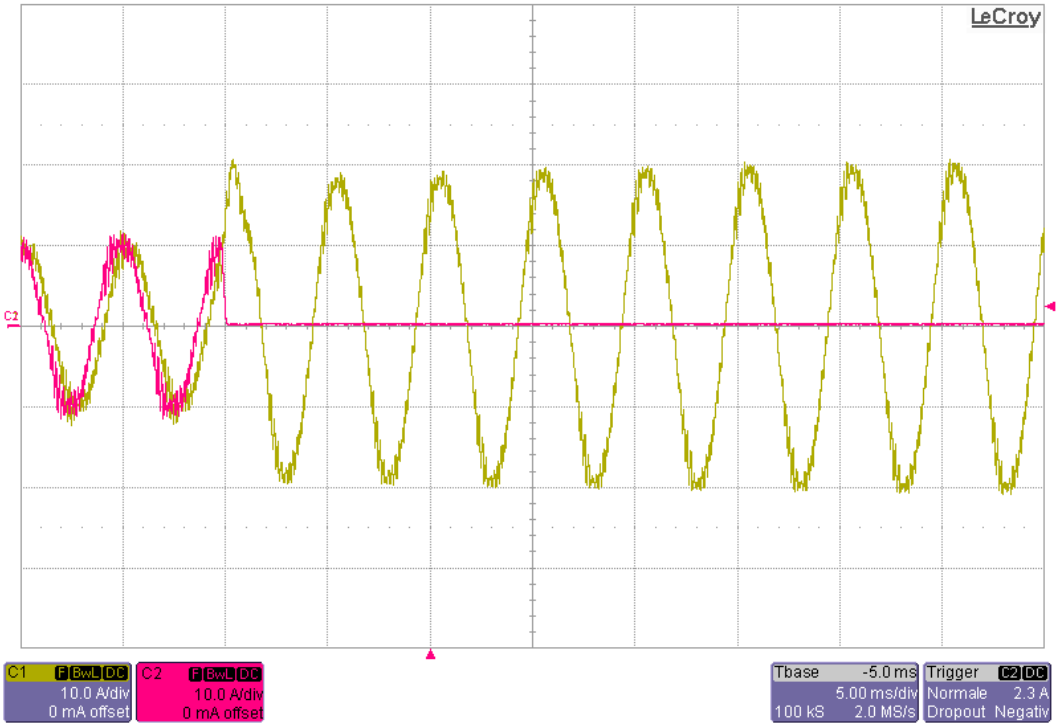

Fig. 4. 83. Ch1: $i_{s1\text{-}a}$ (10 A/div), Ch2: $i_{s2\text{-}a}$ (10 A/div). Time resolution: 5 ms/div.

Closed loop speed control test

In this test, the driving machine has been switched-off, thus acting as passive inertial load. Due to the mechanical limitations of the test rig, the speed has been limited within the range of ±6000 r/min. Therefore, the DC source voltage has been reduced to a half of the rated value, thus testing the flux-weakening and MTPV operation below the speed limit of the test rig. Concerning the other testing conditions, they have been set as follows:

$$\begin{cases} v_{dc,k} = 275\,\mathrm{V} & (k=1,2) \\ s_\lambda = 3 \rightarrow \lambda_s^* = \lambda_{s,rated} & \\ T_k^* = \dfrac{T^*}{2} & (k=1,2) \end{cases} \tag{4.18}$$

It is noted how the tests have been performed by imposing the machine's rated flux value to all units (0.23 Vs), allowing high-dynamic torque variations together with a proper magnetizing current injection.

The machine torque reference has been provided by an outer speed controller. This has consisted of a PI regulator whose design is beyond the scope of this dissertation. The obtained results for a step speed reference from zero up to 6000 r/min are shown in Fig. 4. 84 - Fig. 4. 87.

At low speed and without any limitation, the torque has been limited only by the current limit of the VSI units. The flux-weakening becomes active for a speed that is near to 3000 r/min. The stator fluxes and stator currents are perfectly controlled, as shown in Fig. 4. 86. The MTPV limitation becomes active when the maximum load-angle is reached, at a speed of about 4500 r/min. For safety, the maximum load angle has been set to 40 degrees to avoid the pull-out of the machine. It is noted how the load-angles of the units are perfectly limited, as shown in Fig. 4. 85. The results presented at flux-weakening with closed loop speed control clearly have demonstrated that the proposed scheme is able to work properly under MTPV conditions with load-angle limitation.

Finally, it is noted the deep flux-weakening operation, corresponding to a ratio 1:2 in terms of stator flux amplitude and 1:4 for the rotor one, as shown in Fig. 4. 87.

Experimental results for speed control with inertial load from zero up to 6000 r/min

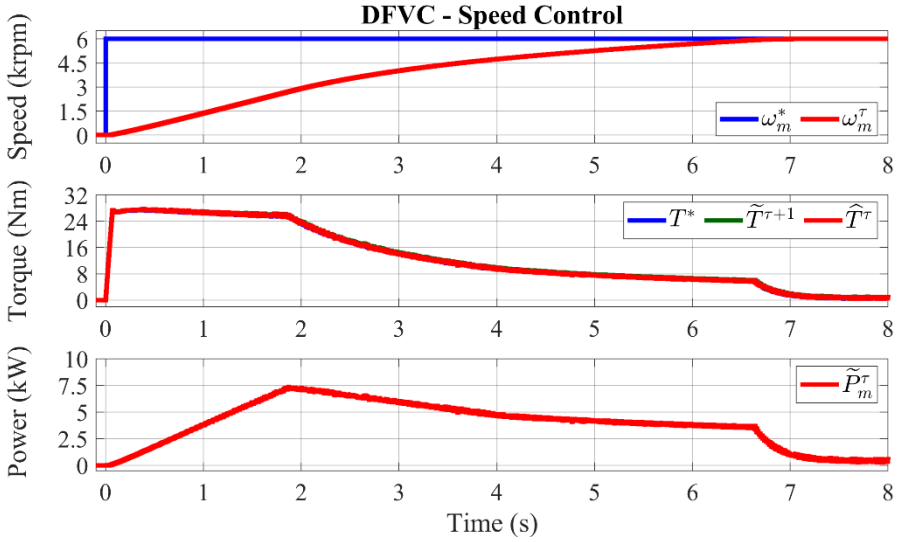

Fig. 4. 84. From top to bottom: measured speed (10^3 · r/min); reference, observed and predicted machine torque (Nm); estimated mechanical power (kW).

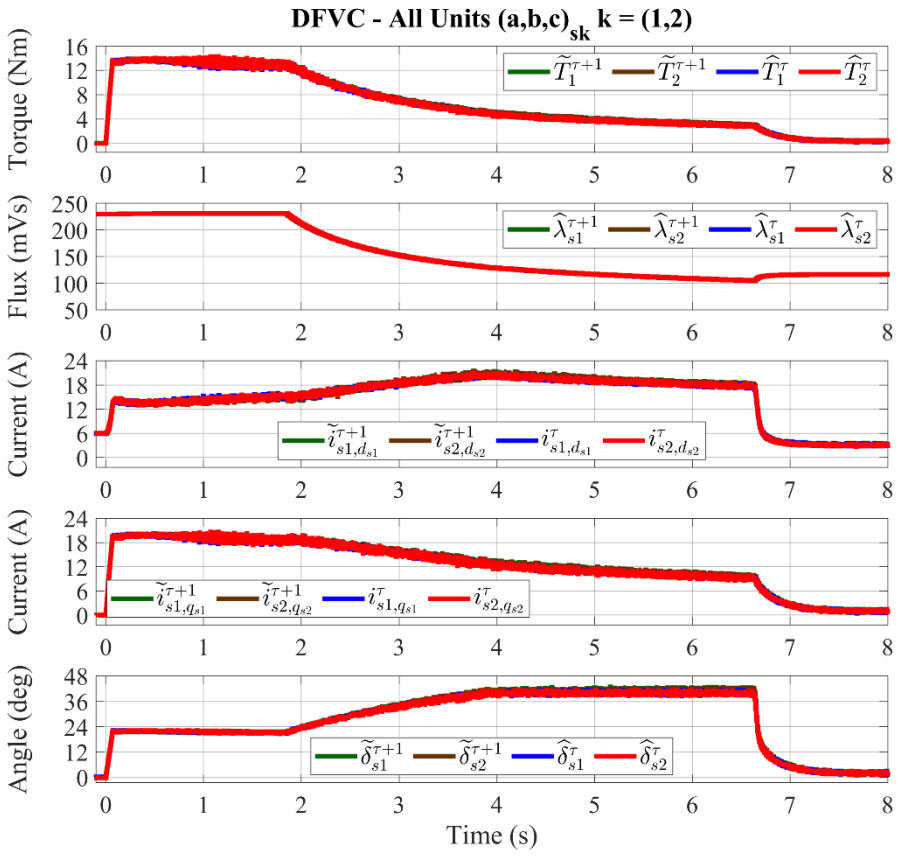

Fig. 4. 85. From top to bottom: single units observed and predicted torque (Nm); single units observed and predicted flux amplitude (mVs); single units measured and predicted d_{sk}-axis current (A); single units measured and predicted q_{sk}-axis current (A); single units observed and predicted load-angle (deg).

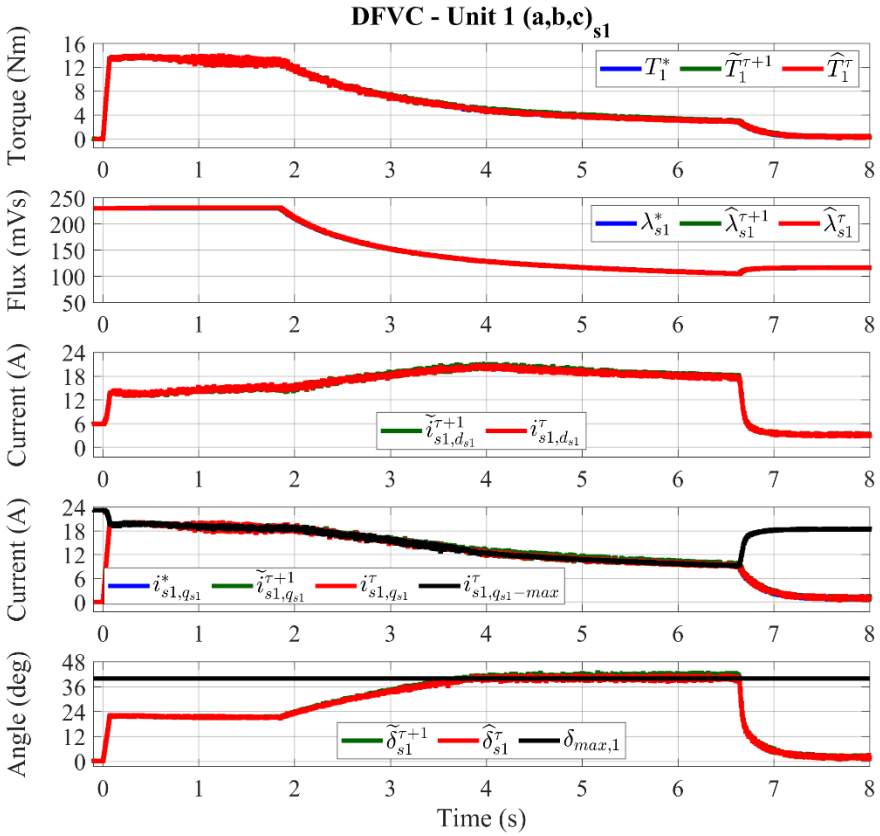

See figure caption: Fig. 4. 86

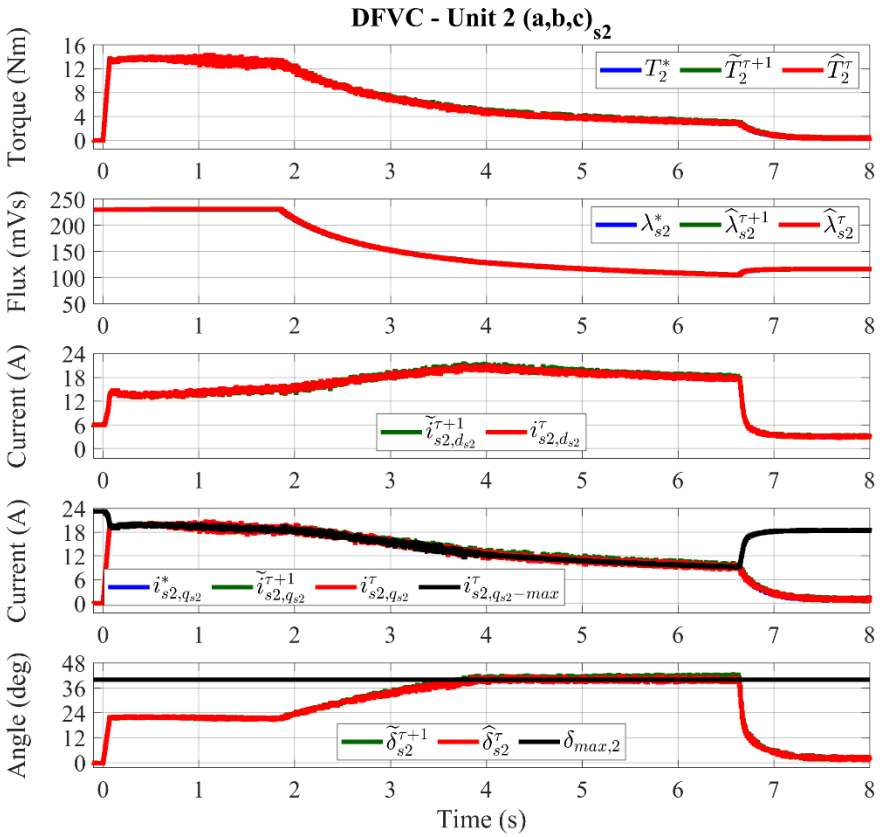

Fig. 4. 86. For each *k*-unit DFVC scheme, from top to bottom: reference, observed and predicted torque (Nm); reference, observed and predicted flux amplitude (mVs); measured and predicted d_{sk}-axis current (A); reference, measured, predicted and maximum limit q_{sk}-axis current (A); observed, predicted and maximum limit load-angle (deg).

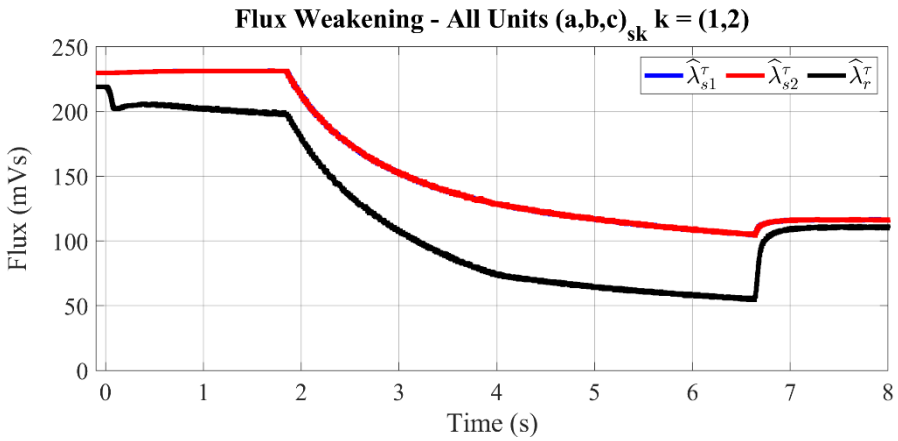

Fig. 4. 87. Single units flux amplitude and rotor flux amplitude (mVs).

4.3 Conclusion

In this chapter, the experimental validation of the Direct Flux Vector Control (DFVC) scheme for multiple three-phase Induction Motor (IM) drives has been reported.

The proposed control solution has been validated with a multi-modular power converter feeding a quadruple three-phase induction machine prototype. The digital controller has consisted of a rapid-prototyping development board. Concerning the control algorithm, it has been totally developed in C-code environment.

Two regulation types have been tested, corresponding to the implementation of the DFVC scheme using Proportional-Integral (PI) and Dead-Beat (DB) controllers respectively. The experimental validation of the DB regulation has been performed on a double three-phase configuration, this obtained by reconfiguring the stator winding of the quadruple three-phase prototype properly.

The experimental results have been related to the drive operation in healthy and open-winding fault conditions, as well as open loop torque control and closed loop speed operation. The faulty condition has consisted of open phases after sudden shut-off of one or more three-phase inverter power modules.

According with the obtained experimental results, the most relevant conclusions are the following:

- The DFVC scheme obtains a direct and independent control of both stator flux amplitude and torque contribution belonging to each three-phase unit, however taking in account the limitation of this in terms of DC-link voltage, phase-current amplitude and load-angle;
- The implementation of the DFVC scheme using PI controllers (PI-DFVC) has required acceptable computational efforts to the digital controller. As a consequence, many kinds of experimental tests have been performed like the ones concerning the torque sharing strategies;
- The PI-DFVC scheme has allowed at obtaining good dynamic performance of the drive in all operating conditions, including Max Torque per Volt (MTPV) operation in deep flux-weakening;
- Due to the high computational efforts required to the digital controller, the validation of the DFVC scheme using DB controllers (DB-DFVC) has been performed by only testing the balanced operation of the units;
- The DB-DFVC scheme has led to the best dynamic performance of the drive in all operating conditions, especially in the fast torque transients thanks to the one-step ahead prediction of the fluxes and currents belonging to each unit.

References

[1] G. Rizzoli, G. Serra, P. Maggiore, and A. Tenconi, 'Optimized design of a multiphase induction machine for an open rotor aero-engine shaft-line-embedded starter/generator', in *IECON 2013 - 39th Annual Conference of the IEEE Industrial Electronics Society*, 2013, pp. 5203–5208.

[2] S. Rubino, R. Bojoi, M. Mengoni, and L. Zarri, 'Optimal flux selection for multi three-phase machines in normal and fault conditions', in *2017 IEEE International Electric Machines and Drives Conference (IEMDC)*, 2017, pp. 1–8.

[3] R. Bojoi, A. Cavagnino, A. Tenconi, and S. Vaschetto, 'Control of Shaft-Line-Embedded Multiphase Starter/Generator for Aero-Engine', *IEEE Trans. Ind. Electron.*, vol. 63, no. 1, pp. 641–652, Jan. 2016.

[4] F. Mariut, S. Rosu, and R. B. A. Tenconi, 'Multiphase modular power converter using the PEBB concept and FPGA-based direct high speed voltage measurement', in *2015 17th European Conference on Power Electronics and Applications (EPE'15 ECCE-Europe)*, 2015, pp. 1–10.

[5] 'Home - dSPACE'. [Online]. Available: https://www.dspace.com/en/inc/home.cfm. [Accessed: 19-Feb-2019].

[6] I. T. AG, 'Semiconductor & System Solutions - Infineon Technologies'. [Online]. Available: https://www.infineon.com/cms/en/. [Accessed: 19-Feb-2019].

CONCLUSIONS

The dissertation has dealt with the analysis, design and implementation of high-performance control techniques for multiphase induction motor drives using multiple three-phase configurations.

In detail, the main goal of the research activity has consisted in the development of a modular control scheme able to fully exploit all the degrees of freedom offered by the multiple three-phase structures.

The dissertation has been structured in the following main chapters:

- Chapter 1 - Introduction
- Chapter 2 - Machine modelling
- Chapter 3 - Control scheme
- Chapter 4 - Experimental validation

Chapter 1 - Introduction

A literature survey providing the state of the art on the multiphase systems has been reported, with a particular focus on:

- Applications
- Machine configurations and modelling
- Machine design
- Power converter and modulation techniques
- Drive topologies
- Drive control techniques
- Fault analysis and post-fault control strategies

The literature survey empathizes the reasons why the multiple three-phase drives are gaining a growing attention in the current technological scenario, thus justifying their choice as main research context of this dissertation.

Chapter 2 - Machine modelling

The general modelling of a multiple three-phase induction machine (IM) using both Multi-Stator (MS) and Vector Space Decomposition (VSD) approaches has been reported. With reference to the technical literature, the following contribution has been introduced:

- Generic MS state-space model of a multiple three-phase IM, considering an arbitrary number of three-phase winding sets together with different stator parameters among the units.

To show how the MS modelling allows to better highlight the flux and torque contributions produced by each individual stator winding set, a generic VSD modelling of a multiple three-phase IM has been reported. This model considers an arbitrary number of three-phase winding sets and both symmetrical and asymmetrical configurations. In this way, it has been demonstrated how the MS results the most suitable modelling approach for the implementation of modular control schemes able to deal with a direct and independent control of each three-phase unit.

Chapter 3 – Control scheme

The design and digital implementation of a Direct Flux Vector Control (DFVC) scheme for multiple three-phase IM drives has been reported. The proposed control solution is based on the MS approach, thus allowing a straightforward control of the main variables (current, flux, torque) belonging to each three-phase unit. In this way, the modularity of the multiple three-phase IM drives has been extended also in terms of control scheme, without limiting itself to the machine configuration and power converter structure.

The proposed control scheme has been designed to be fully compatible with the multiple three-phase drive topologies, using modular Voltage Supply Inverter (VSI) structures together with independent Pulse Width Modulation (PWM) voltage control of each three-phase power converter unit.

With reference to the technical literature, the research contributions and novelties introduced by the proposed control solution are summarized below. With the aim at proposing a modular MS-based DFVC scheme for multiple three-phase IM drives, for each three-phase unit the following features have been implemented:

- Independent stator flux amplitude regulation
- Independent torque regulation
- Independent voltage and current operational limits
- Independent load-angle limitation
- Independent post-fault reconfiguration

Finally, the proposed control solution has been developed by considering two different regulation types, corresponding to as follows:

- Regulation by means of Proportional-Integral (PI) controllers, leading to a control scheme (PI-DFVC) characterized by good dynamic performance and acceptable computational efforts in order to be implemented;
- Regulation by means of Dead-Beat (DB) controllers, leading to a control scheme (DB-DFVC) characterized by high dynamic performance but high computational efforts in order to be implemented.

According with the technical literature, the DB-DFVC scheme represents the first ever made attempt to implement a multiphase predictive solution having the features above summarized.

Chapter 4 – Experimental validation

The experimental validation of the proposed control scheme has been reported. The test rig has consisted of a multi-modular power converter feeding a quadruple three-phase induction machine prototype. Concerning the digital controller, it has consisted of a rapid-prototyping development board.

Two regulation types have been tested, corresponding to the implementation of the DFVC scheme using Proportional-Integral (PI) and Dead-Beat (DB) controllers respectively. The experimental validation of the DB regulation has been carried out with an asymmetrical 6-phase machine, this obtained by reconfiguring the stator winding of the quadruple three-phase prototype properly.

The experimental results have been related to the drive operation in healthy and open-winding fault conditions, as well as open loop torque control and closed loop speed operation. The faulty condition consisted of open phases after sudden shut-off of one or more three-phase inverter power modules.

According with the obtained experimental results, the most relevant conclusions have been the following:

- The PI-DFVC scheme has led to good dynamic performance of the drive in all operating conditions, including Max Torque per Volt (MTPV) operation in deep flux-weakening;
- The DB-DFVC scheme has led to the best dynamic performance of the drive in all operating conditions, especially in the fast torque transients thanks to the one-step ahead prediction of the fluxes and currents belonging to each unit.

In conclusion, the experimental results have demonstrated the full drive controllability in all operating conditions, thus providing the validation of the proposed control solution.

Future research work

The future research work includes:

- Extension of the MS-based DFVC scheme to the multiple three-phase synchronous motor drives.